

Miroslav Zbořil

**Feste Elektronenquellen
für die Energieskalaüberwachung
im KATRIN Experiment**

**Solid electron sources
for the energy scale monitoring
in the KATRIN experiment**

 2011 

Experimentelle Physik

Dissertationsthema

Feste Elektronenquellen
für die Energieskalaüberwachung
im KATRIN Experiment

Inaugural-Dissertation
zur Erlangung des Doktorgrades der
Naturwissenschaften
im Fachbereich Physik
der Mathematisch-Naturwissenschaftlichen Fakultät
der Westfälischen Wilhelms-Universität Münster

vorgelegt von
Miroslav Zbořil
aus Karlsbad, Tschechische Republik

 2011 

Dekan:	Prof. Dr. T. Kuhn
Erster Gutachter:	Prof. Dr. C. Weinheimer
Zweiter Gutachter:	Mgr. D. Vénos, CSc.
Tag der mündlichen Prüfung:	13.12.2011
Tag der Promotion:	13.12.2011

Zusammenfassung

Das KATRIN-Experiment (KARlsruhe TRITium Neutrino) stellt ein Tritium Beta-Zerfall Experiment der nächsten Generation dar, mit dem Ziel, die direkte hochpräzise Messung der Elektron-Antineutrinomasse $m(\nu_e)$ mit einer Empfindlichkeit von $0,2 \text{ eV } c^{-2}$ (90 % C.L.) durchzuführen. KATRIN stellt das Nachfolge-Experiment der Neutrinomassenexperimente in Mainz (Deutschland) und Troitsk (Russland) dar, die die Obergrenze für $m(\nu_e)$ auf $2 \text{ eV } c^{-2}$ festlegten. Das Ziel des KATRIN-Experiments ist die Verbesserung der Neutrinomassenempfindlichkeit um eine Größenordnung. Die Untersuchung der Neutrinomassenskala mit der sub-eV Empfindlichkeit ist besonders wichtig für Teilchenphysik, Astrophysik und Kosmologie. Im Gegensatz zu anderen Methoden wie der Suche nach neutrinolosem Doppel-Betazerfall oder kosmologischen Neutrinomassenstudien unter Verwendung der großskaliger Strukturen und der kosmischen Mikrowellenhintergrundstrahlung, stellt KATRIN eine vollständig modellunabhängige Methode der Neutrinomassenbestimmung dar: Es basiert nur auf kinematischen Relationen der Energie- und Impulserhaltung.

Für die Beobachtung der Signatur einer nichtverschwindenden Neutrinomasse in der Endpunktsregion des Beta-Spektrums (Endpunktsenergie $Q = 18,6 \text{ keV}$) sind die Methoden der hochauflösenden Elektronenspektroskopie, zusammen mit einem sehr niedrigen Untergrundniveau, notwendig. Zu diesem Zweck benutzt das bevorstehende KATRIN-Experiment eine Kombination aus zwei elektrostatischen Retardierungsspektrometern mit magnetischer adiabatischer Kollimation ("MAC-E-Filter"). Allerdings sind hohe Auflösung und geringer Untergrund nur zwei der vielen Anforderungen, die mit der anspruchsvollen Realisierung des KATRIN-Experiments verbunden sind. Die Stabilität der Energieskala der KATRIN-Spektrometer ist eine der wichtigsten systematischen Effekte: Das Prinzip der MAC-E-Filter-Technik beruht auf der genauen Kenntnis des Retardierungspotentials, welches die Beta-Elektronen auf ihrem Weg durch das Spektrometer erfahren. Die Herausforderung besteht darin, dass das Retardierungspotential in jedem Moment der Messung hinreichend genau bekannt ist. Neben dem Einsatz eines hochpräzisen Hochspannungsteilers für eine direkte Messung der Hochspannung, werden mehrere Kalibrationselektronenquellen bei KATRIN eingesetzt, basierend auf atomaren/nuklearen Standards. Eine der Elektronenquellen wird kontinuierlich durch ein zusätzliches MAC-E-Filter-Spektrometer ("Monitor-Spektrometer") vermessen, welches gleichzeitig auf dem selben Hochspannungspotential liegt wie das KATRIN-Hauptspektrometer, um die Stabilität des Retardierungspotentials zu beobachten. Auf diese Weise wird das zweifache Energieskalaüberwachungssystem gebildet.

In der vorliegenden Arbeit wurde der Einsatz einer festen Elektronenquelle—basierend auf den metastabilen Isotop Krypton-83m ($^{83\text{m}}\text{Kr}$, $t_{1/2} = 1,83 \text{ h}$)—erfolgreich getestet. Bei dieser Art der Quelle bedient man sich des Prozesses der Inneren Konversion von $^{83\text{m}}\text{Kr}$, wobei dieses kontinuierlich von Rubidium-83 (^{83}Rb , $t_{1/2} \simeq 86 \text{ d}$) erzeugt wird. Die Kontrolle der KATRIN-Stabilität erfordert eine Energiestabilität $\Delta E/E$ der $K-32$ Konversionselektronen (kinetische Energie der Elektronen $E = 17,8 \text{ keV}$, Linienbreite $\Gamma = 2,7 \text{ eV}$) von $\pm 1,6 \text{ ppm}$ pro Monat. Im Rahmen dieses Dissertationsprojektes wurden insgesamt acht Proben der festen $^{83}\text{Rb}/^{83\text{m}}\text{Kr}$ Quellen, hergestellt durch zwei verschiedene Techniken der Vakuumverdampfung und der Ionenimplantation, mithilfe des Mainzer MAC-E-Filter-Spektrometers untersucht. Im Verlauf der Messkampagne wurden die strengen Anforderun-

gen an die energetische Stabilität erfüllt. Zusätzlich wurden die Form und die absolute kinetische Energie der $^{83\text{m}}\text{Kr}$ Konversionselektronen-Linien im Detail studiert und ihre Abhängigkeit von der Umgebung untersucht. Die ionenimplantierten $^{83}\text{Rb}/^{83\text{m}}\text{Kr}$ -Quellen können als das Standardwerkzeug für die kontinuierliche Überwachung der KATRIN-Energieskalastabilität mit sub-ppm Präzision empfohlen werden.

Abstract

The Karlsruhe TRITium Neutrino (KATRIN) experiment represents a next-generation tritium beta-decay experiment designed to perform a high precision direct measurement of the electron antineutrino mass $m(\nu_e)$ with the sensitivity of $0.2 \text{ eV } c^{-2}$ (90% C.L.). KATRIN is a successor experiment of the neutrino mass experiments carried out in Mainz (Germany), and Troitsk (Russia), which set the upper limit on $m(\nu_e)$ of $2 \text{ eV } c^{-2}$. Therefore, the aim of the KATRIN experiment represents the improvement of the neutrino mass sensitivity by one order of magnitude. The investigation of the neutrino mass scale with the sub-eV sensitivity is of particular interest for particle physics, astrophysics and cosmology. In contrast to other methods, such as the search for neutrinoless double beta-decay or cosmological neutrino mass studies using large scale structures and cosmic microwave background radiation data, KATRIN will provide a completely model-independent measurement of the neutrino mass, based only on kinematic relations and energy-momentum conservation.

For the observation of a non-zero neutrino mass signature in the endpoint region of the beta-spectrum (endpoint energy $Q = 18.6 \text{ keV}$) the methods of high-resolution electron spectroscopy are necessary together with a very low background level. For this purpose the upcoming KATRIN experiment uses two successive electrostatic retardation filters with the magnetic adiabatic collimation (called “MAC-E filters”). However, high resolution and low background are only two of many stringent requirements which are connected to the challenging realization of the KATRIN experiment. The stability of the energy scale of the KATRIN spectrometers is one of the main systematic effects: the principle of the MAC-E filter technique relies on the precise knowledge of the retarding potential which is experienced by the beta-electrons on their path through the spectrometer. Therefore, the challenge of knowing the retarding potential precisely enough in every moment during the measurement is inevitable in the KATRIN experiment. Besides the use of the state-of-the-art equipment for a direct measurement of the high voltage, including specially developed precision high voltage dividers, several very stable calibration electron sources will be utilized in KATRIN, based on atomic/nuclear standards. One of the electron sources will be continuously measured by an additional MAC-E filter spectrometer (“monitor spectrometer”) to which the high voltage will be applied, corresponding at the same time to the filtering potential of KATRIN. This way a two-fold monitoring system will be formed.

In this work the feasibility of solid electron source based on the metastable isotope krypton-83m ($^{83\text{m}}\text{Kr}$, $t_{1/2} = 1.83 \text{ h}$) was successfully tested. In this type of source the process of internal conversion of $^{83\text{m}}\text{Kr}$ is utilized, where $^{83\text{m}}\text{Kr}$ is continuously generated by rubidium-83 (^{83}Rb , $t_{1/2} \simeq 86 \text{ d}$). The monitoring task of KATRIN demands the energy stability $\Delta E/E$ of the K_{32} conversion electron line (kinetic energy $E = 17.8 \text{ keV}$, line width $\Gamma = 2.7 \text{ eV}$) of $\pm 1.6 \text{ ppm}$ per month. In the course of this dissertation project altogether eight samples of the solid $^{83}\text{Rb}/^{83\text{m}}\text{Kr}$ sources, produced by two different techniques of vacuum evaporation and ion implantation, were investigated with the help of the former Mainz MAC-E filter spectrometer. In the course of the measurement campaign the stringent demand on the energy stability was fulfilled. In addition, the shapes and the absolute kinetic energies of the $^{83\text{m}}\text{Kr}$ conversion electron lines were studied in detail and their dependence on the $^{83\text{m}}\text{Kr}$ atom environment was investigated. The ion-implanted $^{83}\text{Rb}/^{83\text{m}}\text{Kr}$ sources can be recommended as a standard tool for continuous monitoring of the KATRIN energy scale

stability with the sub-ppm precision.

Acknowledgments

I am truly indebted to my supervisors Prof. Dr. Christian Weinheimer and Mgr. Drahoslav Vénos, CSc. for their sincere and constant support throughout my doctoral studies. I would like to thank my Doktorvater C. Weinheimer for the opportunity to study physics in such a beautiful city of Münster and for his unremitting interest and encouragement during my experimental work as well as during writing down this thesis. I also appreciate his support and advice in practical things beyond the laboratory walls. I am very grateful to my second supervisor D. Vénos for his practical help during the measurements carried out in Mainz and for his unceasing effort for perfection and deep understanding of new features which occurred during the measurements and the interpretation of results. I acknowledge many stimulating discussions and valuable encouragement from his side.

The measurements carried out in the Institute of Physics, University of Mainz, would not be possible without the kind hospitality of the group QUANTUM of Prof. Dr. Immanuel Bloch and the great support of Prof. Dr. Dr. h.c. Ernst-Wilhelm Otten and Dr. Jochen Bonn. I would like to thank E.-W. Otten for his constant interest, fruitful discussions and all the organizational support of our measurements. I am very much obliged to J. Bonn: his exceptional experimental skills and experience were praised in each and every diploma thesis and dissertation elaborated in the former group EXAKT and this dissertation is no exception. I would like to express my sincere gratitude for all his kind support ranging from practical help during the measurement campaign running practically non-stop on numerous weekends and holidays, over the organizational support of the measurements, to his expertise in the interpretation of results. His “Never give up!” attitude was very inspiring when problems arose. It was a great pleasure to work with him in the laboratory of the former Mainz Neutrino Mass Experiment and to take part in actually the last test experiment carried out at Mainz MAC-E filter spectrometer.

I am grateful to Dr. Alojz Kovalík, Dr. Klaus Schlösser and Martin Slezák for their great and enthusiastic help during the experiment, their frequent stays in Mainz are highly appreciated. I would like to thank A. Kovalík for his kind support and moral as well as practical help since the time we met in Dubna. Thanks to K. Schlösser it was possible to accomplish the ion implantation of the isotope ^{83}Rb at the ISOLDE facility, CERN, which turned out to be an uneasy task. I thank him for his encouragement at desperate moments when it seemed that no useful samples would be obtained. I would like to thank Dr. Beatrix Ostrick for the introduction to the experimental setup of the MAC-E filter spectrometer and for her kind support throughout the measurements. I gratefully acknowledge the support of Dr. Marcus Beck during my doctoral studies and his kind help during the measurements. My big thanks go to Dr. Thomas Thümmler, Stephan Bauer and Stephan Rosendahl for providing us with the two high precision high voltage dividers which were crucial for the measurements reported in this dissertation. Thanks to their prompt help the measurement could continue even when serious problems concerning the high voltage occurred. No measurement would be possible without the perfect logistics of H. Geibel und Erwin Gries who provided us with liquid nitrogen and helium. The same holds for the mechanical workshop of the Institute of Physics which helped us promptly with various details of the experimental setup. It is my pleasure to thank Christine Best, Marta Ubieto-Díaz, Prof. Dr. Dr. h.c. Gerhard Fricke with his wife, Dr. Sergei Karpuk and Elvira Stuck-Kerth for their support during my stays

in Mainz.

I acknowledge the help of Dr. Alexander Herlert, Dr. Karl Johnston and Dr. Erwin Siesling during the collections at the ISOLDE facility. Thanks to their organizational and practical support it was possible to obtain the ion-implanted samples and thus to achieve very promising results in Mainz.

I am grateful to Cornelia Noll and PD Dr. Reiner Vianden for the non-radioactive samples of the isotope ^{85}Rb produced at the radioisotope separator and implanter of the Helmholtz-Institut für Strahlen- und Kernphysik, University of Bonn. I acknowledge the support of Prof. Dr. Helmut Zacharias to the measurements carried out with the help of X-ray photoelectron spectroscopy at the Physikalisches Institut, University of Münster. It would not be possible to carry out these measurements without the efforts of Steffen Linden, thank you.

I would like to thank my colleagues in the Nuclear Physics Institute of the ASCR in Řež near Prague: Ing. Otokar Dragoun, DrSc., Jaromír Kašpar, Ph.D., Ondřej Lebeda, Ph.D., RNDr. Miloš Ryšavý, CSc. and Ing. Antonín Špalek, CSc. I sincerely acknowledge the constant support and interest expressed by O. Dragoun since the time I first came to the Electron spectroscopy group, thank you. Many thanks to O. Lebeda for his expertise in the production of the isotope ^{83}Rb for the purposes of our experiments. I appreciate the discussions with M. Ryšavý which helped to improve the analysis tools used in this work. I am very much indebted to A. Špalek for providing me with the results of his Monte Carlo simulations of the electron transport in solids. I am sincerely grateful to Prof. Ing. Zdeněk Janout, CSc. and Doc. Ing. Ivan Štekl, CSc. for their valuable encouragement throughout my undergraduate studies in Prague.

It is my pleasure to thank all the members of the group of C. Weinheimer in the Institute of Nuclear Physics, University of Münster, for pleasant working atmosphere. Especially I would like to thank Karen Bokeloh, Dr. Volker Hannen, Anna Sejersen Riis, Daniel Spitzer, Dr. Kathrin Valerius and Michael Zacher for their moral as well as practical help during my doctoral studies. I very much appreciate the technical support of K. Valerius with the \LaTeX code of this thesis. I am grateful to Prof. Dr. Johannes P. Wessels for his organizational help during my doctoral studies. The support of the mechanical and electronic workshops of the Institute of Nuclear Physics is appreciated, namely the help of Hans-Werner Ortjohann, Helmut Baumeister and Wladimir Buglak. Many thanks to Michaela Erdmann and Uta Mayer for their kind organizational support.

Last but not the least, I am happy to express my sincere gratitude to my family in Czech Republic and my wife's family in Russia for all the warm support.

Above all I am truly indebted to my beloved wife Alexandra for all her patience, faith and unremitting support. To her I dedicate this thesis.

Thank you. Besten Dank. Спасибо. Děkuji. 

A subtle thought that is in error may yet give rise to fruitful inquiry that can establish truths of great value.

— Isaac Asimov

Contents

Zusammenfassung	v
Abstract	vii
Acknowledgments	ix
1 Introduction	1
1.1 Neutrino physics	1
1.1.1 Brief history of neutrino	1
1.1.2 Motivation for neutrino mass determination	3
1.1.3 Towards the absolute scale of neutrino masses	8
1.2 Process of internal conversion	13
Thesis outline	19
2 The KATRIN experiment	21
2.1 Tritium beta-decay	21
2.2 The MAC-E filter technique	25
2.3 Brief overview of the KATRIN experimental setup	28
2.4 Systematic and statistical uncertainties	32
3 Stability monitoring and calibration of the energy scale in KATRIN	37
3.1 Motivation for continuous monitoring and absolute calibration of the energy scale	37
3.2 Concept of monitoring of the KATRIN energy scale stability	43
3.2.1 High precision high voltage divider	44
3.3 Candidates for quasi-monoenergetic electron sources for KATRIN	47
3.3.1 Photoelectrons from $^{241}\text{Am}/\text{Co}$	48
3.3.2 Conversion electrons from $^{83\text{m}}\text{Kr}$	50
4 Solid $^{83}\text{Rb}/^{83\text{m}}\text{Kr}$ electron sources for KATRIN	59
4.1 Vacuum-evaporated sources	60
4.1.1 Vacuum evaporation of ^{83}Rb	60
4.1.2 Samples investigated in this work	62
4.2 Ion-implanted sources	65
4.2.1 Basic processes of ion implantation	66
4.2.2 Ion implantation of ^{83}Rb at the ISOLDE facility	74
4.2.3 Samples investigated in this work	76
4.3 Conversion electrons from solid $^{83}\text{Rb}/^{83\text{m}}\text{Kr}$ sources	83

4.3.1	Shifts of electron binding energies	83
4.3.2	Shake-up and shake-off effects	89
4.3.3	Inelastically scattered electrons	90
5	Mainz MAC-E filter used for conversion electron spectroscopy	101
5.1	Experimental setup	101
5.1.1	MAC-E filter	102
5.1.2	Source section	104
5.1.3	Detector section	106
5.1.4	Vacuum system	107
5.1.5	High voltage system	109
5.1.6	Control and data acquisition system	110
5.2	Data analysis	112
5.2.1	Typical measurement and data treatment	113
5.2.2	Energy scale corrections	117
5.2.3	Dead time correction	120
5.2.4	Expected count rate of zero-energy-loss electrons	123
5.2.5	Transmission function	125
5.2.6	Description of the conversion electron line shape	128
5.2.7	Cross-correlation method	131
5.2.8	Comparison of cross-correlation and many-parameters fit methods . .	133
6	Long-term measurements of the conversion electrons energy stability at Mainz	
	MAC-E filter	137
6.1	Pilot studies of the energy stability of the $^{83}\text{Rb}/^{83\text{m}}\text{Kr}$ sources	138
6.1.1	Proof of principle	138
6.1.2	Measurements with vacuum-evaporated sources mounted onto CKrS setup	138
6.2	First measurement phase: single vacuum-evaporated source	145
6.2.1	Systematic measurements of the long-term drifts	146
6.2.2	Sudden unexpected shift of the high voltage scale	152
6.2.3	Measurements with the shifted high voltage scale	157
6.2.4	Influence of the source position on the K -32 line	161
6.3	Second measurement phase: one ion-implanted and two vacuum-evaporated sources investigated simultaneously	165
6.3.1	Comparison of drifts of individual sources	167
6.3.2	Changes of vacuum conditions due to breakdowns and bake-out . . .	172
6.3.3	Tests with deliberate venting of the vacuum setup	176
6.3.4	Sudden unexpected change of the high voltage divider scale factor . .	178
6.3.5	Influence of the source position on the K -32 line at two different spec- trometer resolutions	184
6.3.6	Background and transmission properties of Mainz MAC-E filter	185
6.4	Third measurement phase: four ion-implanted sources investigated simulta- neously	191
6.4.1	Comparison of drifts of individual sources	192
6.4.2	Change of residual gas composition in spectrometer vessel resulting from vacuum breakdown	200

6.5	Summary of results	205
6.5.1	Energy stability of conversion electrons emitted by the solid sources	205
6.5.2	Overview of systematic effects	208
7	Conversion electron spectrum of ^{83m}Kr in solid sources	213
7.1	Choice of data and estimate of analysis precision	214
7.2	Shapes of the conversion electron lines	216
7.2.1	Description of the conversion lines of the vacuum-evaporated sources with a singlet	216
7.2.2	Doublet structure of the conversion lines of the ion-implanted sources	220
7.2.3	Verification of the many-parameters fit procedure	230
7.2.4	Discussion of amplitude and background of the conversion electron lines	234
7.3	Absolute kinetic energies of the conversion electrons from solid sources	238
7.3.1	Conversion electrons of the 9.4 keV gamma transition	239
7.3.2	Conversion electrons of the 32 keV gamma transition	243
7.3.3	Influence of ^{83m}Kr atom environment on the electron binding energy	246
7.3.4	Energy difference of the 9.4 keV and 32 keV gamma transitions	247
7.4	Hypotheses for the explanation of the asymmetry and splitting in the ^{83m}Kr conversion electron spectra of the ion-implanted $^{83}\text{Rb}/^{83m}\text{Kr}$ sources	253
7.4.1	Different environments of the ^{83}Rb atoms	253
7.4.2	Surface plasmons	256
7.4.3	Electron-hole interaction in metals	256
7.4.4	Strong electric fields in polycrystalline foils	257
7.4.5	Internal conversion at neighboring atoms	258
7.5	Electron energy loss spectra of the solid sources	260
8	Conclusions and outlook	265
A	Electron binding energies of gaseous krypton	275
B	Evaluation of the energy shifts of the ^{83m}Kr conversion lines resulting from abrupt changes of vacuum conditions	277
B.1	Second measurement phase	277
B.2	Third measurement phase	280
C	Investigation of different environments of the ^{83}Rb atoms in the ion-implanted $^{83}\text{Rb}/^{83m}\text{Kr}$ sources with the XPS method	283
	Bibliography	289

1. Introduction

In this chapter a brief introduction will be given to the fields of physics most relevant to this work. Firstly, in Sect. 1.1 the neutrino physics will be shortly reviewed while the focus will be made on the neutrino masses and methods to determine the absolute neutrino mass scale. Secondly, Sect. 1.2 will describe the effect of internal conversion of gamma radiation. The electron sources based on this effect will be investigated later in this work.

1.1. Neutrino physics

Neutrino is definitely one of the most interesting elementary particles known up to date. At this place only the basic properties of neutrinos will be reviewed. For a thorough description of the neutrino physics the reader is kindly referred to [Cal01, Alt03, Zub04].

1.1.1. Brief history of neutrino

The “birth” of the neutrino can be dated back to December 4, 1930 when W. Pauli postulated in his famous letter [Pau30] the existence of electrically neutral spin $1/2$ particles with a mass “of the same order of magnitude as the electron mass and in any event not larger than 0.01 proton masses” in the nucleus. This way he attempted to save the energy conservation law which was suddenly questioned by J. Chadwick’s observation of continuous energy spectrum of the β -decay electrons [Cha14]. By introducing the neutrino (originally denoted as “neutron” by W. Pauli), the β -decay becomes a three-body decay where the surplus energy is shared by the emitted electron and neutrino and, thus, the energy spectrum of the electrons is naturally continuous. As the neutrino was assumed to be a lepton (*i. e.* not participating in strong interactions) with zero charge (no electromagnetic interactions), it was clear that the experimental observation of the neutrino would be extremely difficult. The neutrino mass was anticipated to be very small or even vanishing¹.

In 1932 J. Chadwick discovered the heavy fermion, called nowadays neutron, and clearly this particle was too heavy to be the “neutron” that W. Pauli had predicted. However, Pauli’s particle played a crucial role in the first theory of the nuclear β -decay formulated by E. Fermi in 1934 [Fer34]. According to Fermi’s theory, electron and neutrino are to be created at the moment when the neutron transforms itself into the proton, and not to be inhabiting

¹In the case of a non-vanishing mass the electromagnetic and gravitational interactions would be possible.

1. Introduction

the nucleus as constituents as has been believed so far. Thus, the conception of the atomic nucleus had to be changed as well.

The first experimental evidence of the neutrino induced interaction was brought by F. Reines and C. Cowan who performed experiments in the years 1951–1956 utilizing a nuclear reactor as an intense source of neutrinos [Rei96]. Reines and Cowan elected to search for the evidence of the interaction $\nu + p \rightarrow n + e^+$, which could be well observed in the organic scintillator owing to the annihilation of positron, followed several microseconds later by the neutron capture. In fact, (electron) antineutrinos, not neutrinos participate in this “inverse β -decay” interaction, but the distinction between the two was not clear until after Reines and Cowan had completed their experiments. Moreover, no distinction was made between the neutrino flavors ν_e , ν_μ and ν_τ at the time of the experiment. Finally, after full 26 years from Pauli’s prediction the existence of the neutrino was proved without doubt.

After the existence of the neutrino was definitely proved, its properties were experimentally studied. M. Goldhaber *et al.* [Gol58] found in 1958 by the means of the inverse β -decay of ^{152}Eu that neutrinos are left-handed. In the framework of the Standard Model (see below), this result implied that neutrinos have to be exactly massless and distinctly different from their antiparticles. One year earlier, C.S. Wu *et al.* [Wu57] demonstrated that the parity is violated in the weak interaction.

In 1962 G. Danby *et al.* [Dan62] detected the muon neutrino and it was confirmed that it is different from the electron neutrino. Consequently, the idea of B. Pontecorvo of neutrino-antineutrino oscillations [Pon67] (analogous to the K^0 - \bar{K}^0 oscillations) was further changed by Z. Maki, M. Nakagawa and S. Sakata [Mak62] who introduced the theory of neutrino flavor mixing and the consequent phenomenon: flavor oscillations. According to the theory of neutrino mixing, each neutrino flavor², ν_e or ν_μ , is comprised by the mixture of the mass eigenstates. Unlike the ν - $\bar{\nu}$ oscillations suggested by B. Pontecorvo, Z. Maki *et al.* had in mind the ν_e - ν_μ oscillations which can take place only if the two neutrino flavors have different masses.

Another primacy was achieved in 1965 when the first natural (atmospheric) neutrinos were observed by two teams of F. Reines *et al.* and G. Menon *et al.* After preceding calculations done by R. Davis and J. Bahcall in 1964, one epochal experiment was started: R. Davis *et al.* began to measure the flux of neutrinos coming from the sun. A tank filled with 380 000 liters of C_2Cl_4 placed 1.5 km under ground was utilized for detection of the solar neutrinos by means of the reaction $^{37}\text{Cl} + \nu \rightarrow e^- + ^{37}\text{Ar}$. Stringent requirements on the very low background, tank properties *etc.* were met and the results were surprising: a deficit in the solar neutrino flux was observed. Shortly after, V. Gribov and B. Pontecorvo interpreted this deficit as the evidence for oscillations. The theory of neutrino oscillations seemed to be the solution of the “solar neutrino problem”.

In the time period from 1970 till the end of 1980’s many experiments were made to investigate the neutrino mass and the phenomenon of the flavor oscillations with more precision. In addition, the family of neutrinos was enlarged in this era: the discovery of the tau lepton by M. Perl *et al.* [Per75] in 1975 at the SLAC, Stanford, and the consequent analysis of tau decay modes led to the conclusion that tau lepton is accompanied by its own neutrino ν_τ

²At the time when the neutrino mixing was introduced, only two neutrino types ν_e and ν_μ were known, in fact. The third neutrino flavor ν_τ was introduced after 1976 when the tau lepton was discovered. The tau neutrino was experimentally observed in 2000 by the DONuT experiment [DON08].

which is neither ν_e nor ν_μ . The direct measurement of the electron antineutrino mass by means of tritium β -decay was performed by many experimental teams, setting the upper limit on the electron antineutrino mass of the order of tens of $\text{eV } c^{-2}$.

The neutrino oscillations were studied by a number of experiments, among which the Kamiokande experiment was the largest: a spectrometer with $\approx 2\,000$ tones of extra clean water placed 825 m under ground was utilized as the Cherenkov detector. The deficit of solar neutrinos was confirmed by Kamiokande team in 1986. On February 23, 1987, the Kamiokande spectrometer detected 11 events from the burst of neutrinos released by the eruption of the supernova SN 1987A about 168 000 years earlier (the upper limit on the neutrino mass derived from this observation is discussed below). Not only the spectrometer in Kamioka, but also other Cherenkov detectors in the world—built especially to monitor the proton decay as predicted by quark-lepton symmetries in early 1970's—observed some neutrinos from this supernova. This event can be denoted as the birth of the neutrino astronomy.

In the end of 1980's, two measurements of the decay width of the Z^0 boson were performed at the electron-positron colliders LEP, CERN and SLAC, Stanford. The number of the neutrino flavors was determined as 2.984(8) [PDG10] in a good agreement with the three observed generations of the fundamental fermions in the Standard Model. The neutrino physics has showed nearly a boom since 1990. The solar neutrino deficit was once more confirmed by the experiments SAGE and GALLEX. In 1996 the Super-Kamiokande detector was completed and the search for neutrino interactions began. Two years later the Super-Kamiokande experiment reported the observation of oscillations of the atmospheric neutrinos [Sup05]. The Sudbury neutrino observatory (SNO) provided in 2002 a convincing evidence for the oscillations of the solar neutrinos [SNO07]—the long-standing solar neutrino problem was definitely solved with no doubt. In the same year the KamLAND collaboration observed oscillations of the reactor neutrinos [Kam05].

In the first decade of the 21st century, two tritium β -decay experiments in Mainz [Kra05], Germany, and Troitsk [Lob03], Russia, pushed the upper limit on the electron antineutrino mass down to the $2 \text{ eV } c^{-2}$ range, see Sect. 1.1.3. Their direct successor is the KATRIN experiment (described in Chap. 2) which aims to perform a high precision direct measurement of the electron antineutrino mass with the sensitivity of $0.2 \text{ eV } c^{-2}$. On the other hand, a number of experiments (COBRA, CUORE, EXO, GERDA, NEMO-3, SNO+ and others) is nowadays searching for the evidence of the neutrinoless double β -decay which would directly imply that neutrino is a Majorana particle, *i.e.* it is identical to its own antiparticle (see below). The knowledge of the absolute mass scale of neutrinos, bearing fundamental implications to particle physics, astrophysics and cosmology, represents one of the most intriguing and challenging tasks of modern physics.

1.1.2. Motivation for neutrino mass determination

The evidence for non-vanishing neutrino masses was collected over the past decade in a large number of experiments observing the neutrino flavor oscillations. In order to explain the effect of flavor oscillations it is necessary to introduce the mixing of neutrinos, *i.e.* the flavor states $|\nu_\alpha\rangle$, where $\alpha = e, \mu, \tau$, are not identical to the eigenstates $|\nu_i\rangle$ ($i = 1, 2, 3$) of the mass operator M . The two sets of states are connected by a unitary mixing matrix U

1. Introduction

according to

$$|\nu_\alpha\rangle = \sum_i U_{\alpha i} |\nu_i\rangle, \quad (1.1)$$

$$|\nu_i\rangle = \sum_\alpha U_{i\alpha}^\dagger |\nu_\alpha\rangle = \sum_\alpha U_{\alpha i}^* |\nu_\alpha\rangle. \quad (1.2)$$

In the weak interaction process a neutrino of the flavor state $|\nu_\alpha\rangle$ ($\alpha = e, \mu, \tau$) is created together with its corresponding charged lepton partner ℓ_α . The flavor state is not an eigenstate of the mass operator M , but can be expressed as a linear superposition of the mass eigenstates $|\nu_i\rangle$ with the eigenvalues m_i ($i = 1, 2, 3$) via the mixing matrix U . The matrix U is often denoted as the PMNS (Pontecorvo-Maki-Nakagawa-Sakata) matrix and it is analogous to the CKM (Cabibbo-Kobayashi-Maskawa) matrix used in the quark sector of the Standard Model. In a unitary $n \times n$ matrix there are altogether $(n-1)^2$ independent parameters which can be expressed by $\frac{1}{2}n(n-1)$ mixing angles of an n -dimensional rotation matrix and by $\frac{1}{2}(n-1)(n-2)$ phases. Thus, in the case of $n = 3$ one obtains three mixing angles θ_{ij} and one phase δ ,

$$U = \begin{pmatrix} 1 & 0 & 0 \\ 0 & \cos \theta_{23} & \sin \theta_{23} \\ 0 & -\sin \theta_{23} & \cos \theta_{23} \end{pmatrix} \begin{pmatrix} \cos \theta_{13} & 0 & \sin \theta_{13} e^{i\delta} \\ 0 & 1 & 0 \\ -\sin \theta_{13} e^{-i\delta} & 0 & \cos \theta_{13} \end{pmatrix} \\ \times \begin{pmatrix} \cos \theta_{12} & \sin \theta_{12} & 0 \\ -\sin \theta_{12} & \cos \theta_{12} & 0 \\ 0 & 0 & 1 \end{pmatrix}. \quad (1.3)$$

The phase factor δ can be linked to the violation of the CP symmetry, however, up to now δ has not been measured in neutrino oscillation experiments. Observation on non-zero δ would indicate the violation of the CP symmetry similar to that observed in the quark sector. In the case of Majorana type neutrinos³ two additional phases $\alpha_{1,2}$ have to be included, which changes the mixing matrix as follows:

$$U_{\text{Majorana}} = U \begin{pmatrix} 1 & 0 & 0 \\ 0 & e^{\frac{i\alpha_1}{2}} & 0 \\ 0 & 0 & e^{\frac{i\alpha_2}{2}} \end{pmatrix} \quad (1.4)$$

It should be noted that the phases α_1 and α_2 cannot be detected in the neutrino oscillations. Assuming that the mass eigenstates $|\nu_i\rangle$ are different, *i.e.* $m_i \neq m_j$ for $i \neq j$, it follows from the Schrödinger equation that in the oscillation experiment the eigenstates $|\nu_i\rangle$ will exhibit a different time evolution. In a simplified case of two flavor eigenstates ν_α and ν_β , which are composed of two mass eigenstates ν_1 and ν_2 via one mixing angle θ as

$$\begin{pmatrix} \nu_\alpha \\ \nu_\beta \end{pmatrix} = \begin{pmatrix} \cos \theta & \sin \theta \\ -\sin \theta & \cos \theta \end{pmatrix} \begin{pmatrix} \nu_1 \\ \nu_2 \end{pmatrix}, \quad (1.5)$$

³A neutrino which is identical to its own antiparticle ($\nu = \bar{\nu}$) is called a Majorana particle, while for the Dirac type neutrinos the lepton number distinguishes neutrinos from antineutrinos.

it can be shown [Zub04] that the oscillation probability reads (using $\hbar = 1$ and $c = 1$)

$$P(\nu_\alpha \rightarrow \nu_\beta) = \sin^2(2\theta) \sin^2\left(\frac{\Delta m^2 L}{4 E}\right) \quad (1.6)$$

with $\Delta m^2 := m_2^2 - m_1^2$. The mixing angle θ defines the amplitude of the oscillation, whereas Δm^2 determines the oscillation frequency. It should be noted that Eq. 1.6 is valid in the case of neutrino flavor oscillations in vacuum.

In Fig. 1.1 an overview of the results obtained in a number of neutrino oscillation experiments is depicted. From a combined analysis of the data the following limits of on the oscillation parameters can be deduced [PDG10]⁴:

$$\begin{aligned} \sin^2(2\theta_{12}) &= 0.861^{+0.026}_{-0.022}, & \frac{m_2^2 - m_1^2}{10^{-5} \text{ eV}^2 c^{-4}} &= 7.59 \pm 0.21, \\ 0.92 < \sin^2(2\theta_{23}) &\leq 1, & \frac{|m_3^2 - m_2^2|}{10^{-3} \text{ eV}^2 c^{-4}} &= 2.43 \pm 0.13, \\ \sin^2(2\theta_{13}) &< 0.15. \end{aligned} \quad (1.7)$$

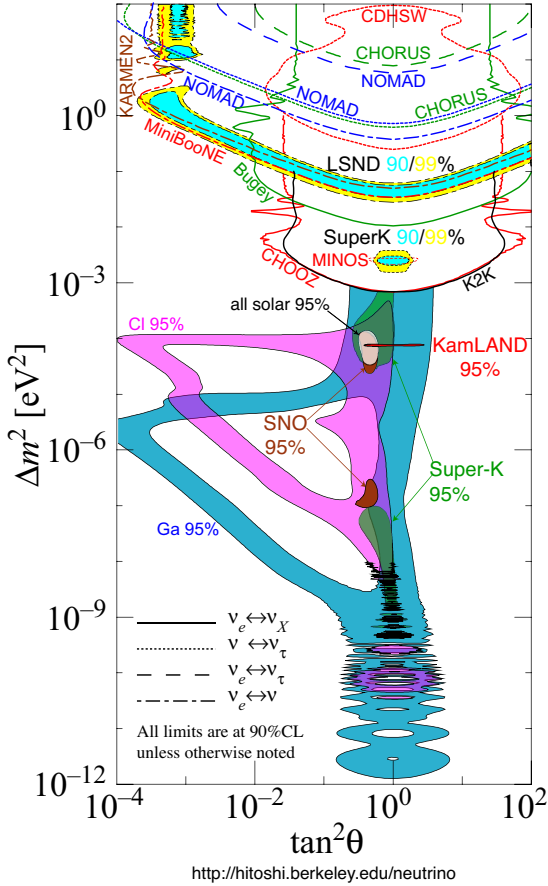


Fig. 1.1: The overview of the regions of squared-mass splitting and mixing angle favored or excluded by various oscillation experiments using solar and atmospheric neutrinos as well as neutrinos from accelerators and reactors. The various oscillation channels are depicted: $\nu_e \leftrightarrow \nu_x$, $\nu_\mu \leftrightarrow \nu_\tau$, $\nu_e \leftrightarrow \nu_\tau$, $\nu_e \leftrightarrow \nu_\mu$. The figure is taken from [PDG10] and based on data compilation done by H. Murayama.

From Eq. 1.7 the following conclusions can be drawn: a) the neutrinos have a small non-zero rest mass and b) the splittings between the squared masses are small and unequal in

⁴The latest results of the T2K experiment indicate a non-zero mixing angle θ_{13} : $0.03 < \sin^2(2\theta_{13}) < 0.28$ [T2K11].

1. Introduction

the sense that there is a closely spaced pair m_1^2, m_2^2 while the squared mass m_3^2 is set off. The statement (a) indicates that the present description of neutrinos in the Standard Model is incomplete. The conclusion (b) raises questions concerning the actual ordering of the mass states m_i ($i = 1, 2, 3$). The ordering within the doublet m_1^2, m_2^2 can be fixed by an analysis of the solar neutrino oscillation data where the matter-induced effect is taken into account. The ordering of m_3^2 with respect to the doublet m_1^2, m_2^2 is ambiguous: two scenarios denoted as normal and inverted hierarchy are possible, see Fig. 1.2. On the other hand, if the smallest neutrino mass would be larger than about $0.1\text{--}0.2\text{ eV } c^{-2}$ the splittings would become negligible. This scenario $m_1 \approx m_2 \approx m_3$ is denoted as degenerate hierarchy.

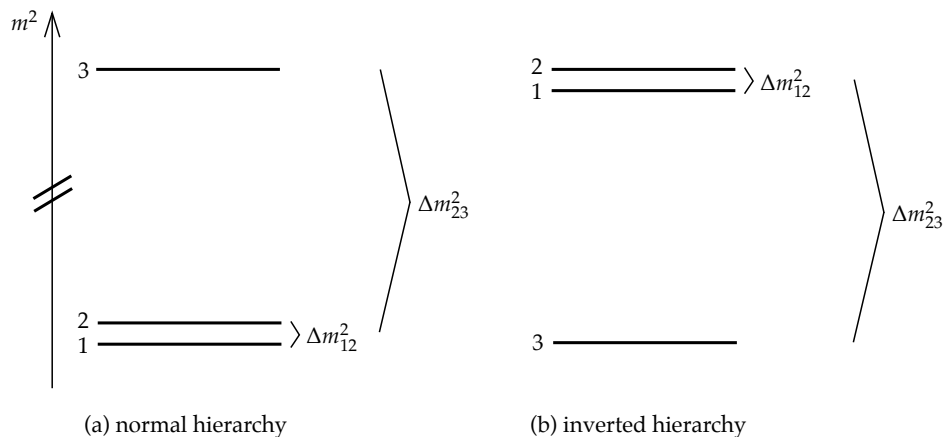


Fig. 1.2: The sketch of hierarchical neutrino mass scenarios showing the arrangement of neutrino mass eigenvalues $m(\nu_i)$ in (a) normal and (b) inverted hierarchy. See Eq. 1.7 for the limits on the splittings Δm_{12}^2 and Δm_{23}^2 . The figure is taken from [Val09a].

The Standard Model of particle physics, describing very precisely the present experimental data up to the electroweak scale, offers no explanation for the observed pattern of the fermion masses or the mixing among the fermion generations. In particular, it offers no explanation for neutrino masses and neutrino mixing: in this model the neutrinos are considered as being massless and are assumed to have no electric or magnetic dipole moment, thus, they cannot interact electromagnetically. Generally, fermions in the Standard Model acquire their mass via Yukawa couplings between the left- and right-handed components of the fermion fields. The values of the masses, however, are not predicted by the model and have to be inserted as free parameters. The recent evidence for the neutrino masses and mixing is a clear indication for physics beyond the Standard Model: in order to incorporate the tiny neutrino masses, the Yukawa couplings for neutrinos need to be at least 6 orders of magnitude smaller than the ones for all other charged fermions, which seems rather unsatisfactory.

Many theories explore the origins of neutrino masses and mixing [Zub04]. In these theories, which often work within the framework of Supersymmetry, neutrinos naturally acquire mass. A large group of models makes use of the so-called seesaw mechanism to generate neutrino masses. Other classes of theories are based on completely different possible origins of neutrino masses, such as radiative corrections arising from an extended Higgs sector. As neutrino masses are much smaller than the masses of the other fermions, the knowledge of the absolute value of neutrino masses is crucial for our understanding of the fermion masses in general: it will probably be the absolute mass scale of neutrinos which will determine the

dimensions of new physics. Moreover, theoretical models come to different conclusions of whether neutrino masses are of the Dirac or Majorana type.

A second motivation for the precise knowledge of the neutrino masses originates from the role of neutrinos in astrophysics and cosmology. In 1965 the cosmic microwave background (CMB) radiation was discovered by A.A. Penzias and R.W. Wilson [Pen65]. The CMB radiation can be well explained as radiation left over from early development stage of the Universe. This discovery turned out to be one of the proofs of the so-called ‘‘Big Bang’’ model of cosmology. According to this model the Universe had a very hot and dense origin from which it cooled and expanded into its present state. The Big Bang theory predicts (among other effects) that a large number of neutrinos could have been created by frequent weak interactions at high temperatures in the early Universe. These primordial neutrinos ceased to be in thermal equilibrium with the other particle species when their interaction rate became smaller than the expansion rate of the Universe (given by the Hubble parameter $H(T)$). This effect occurred at the time of about 1 s after the Big Bang when the temperature decreased to $T \approx 10^{10}$ K ($E \approx 1$ MeV). The present-day density $n_{\nu 0}$ of these relic neutrinos can be estimated on the basis of the of photon density $n_{\gamma 0}$ derived from the CMB,

$$\begin{aligned} n_{\nu 0} &= \frac{3}{4} \frac{g_\nu}{g_\gamma} \frac{4}{11} n_{\gamma 0} \\ &\approx \frac{9}{11} \cdot 411 \text{ cm}^{-3} \simeq 336 \text{ cm}^{-3}. \end{aligned} \quad (1.8)$$

Thus, neutrinos are the second second-most abundant particle species in the Universe right after the photons. Here, $g_\nu = 6$ and $g_\gamma = 2$ denote the relativistic degrees of freedom for three flavors of neutrinos and for photons, respectively. Similarly, the present-day temperature of such cosmic neutrino background (CNB) can be estimated as

$$T_{\nu 0} = T_{\gamma 0} \left(\frac{4}{11} \right)^{1/3} \simeq 1.95 \text{ K}, \quad (1.9)$$

where $T_{\gamma 0} = 2.725(1)$ K is the measured temperature of the CMB [Fix02]. Such a low temperature corresponds to thermal energies in the sub-meV range. Due to the high density of the relic neutrinos, their contribution to the total energy density Ω_{tot} of the Universe cannot be neglected, despite their small mass. In the current Concordance Model of cosmology, Ω_{tot} is composed of the following components (in relative units):

$$\begin{aligned} \Omega_{\text{tot}} &= \Omega_\Lambda + \Omega_m + \Omega_r + \Omega_k \\ &\quad \text{dark energy} \quad \text{matter} \quad \text{radiation} \quad \text{curvature} \\ &\approx 0.76 + 0.24 + \mathcal{O}(10^{-5}) + 0 \end{aligned} \quad (1.10)$$

where the matter contribution Ω_m contains cold dark matter ($\Omega_{\text{cdm}} \approx 0.20$), baryonic matter ($\Omega_b \approx 0.04$) and neutrinos (Ω_ν). The origin of the dark energy is still fully unknown nowadays.

Without going into details of the Concordance Model, it can be summarized that from the assumption on the sum of the neutrino mass states of $\sum m(\nu_i) = 6 \text{ eV } c^{-2}$ (according to the present upper limits on $m(\nu_e)$ from laboratory experiments, cf. Eq. 1.19 below) it can be deduced $\Omega_\nu < 0.13$. In addition, from the Super-Kamiokande results on the atmospheric neutrino oscillations (cf. Eq. 1.7) it follows $\Omega_\nu \gtrsim 0.001$. Thus, the experimentally allowed

1. Introduction

range for the neutrino contribution to the total energy density spans two order of magnitude as can be seen in Fig. 1.3. The neutrino mass sensitivity aimed for by the KATRIN experiment can be interpreted as $\Omega_\nu \approx 0.013$ (assuming the degenerate hierarchy of neutrinos with $m_1 \approx m_2 \approx m_3 = 0.2 \text{ eV } c^{-2}$). On the other hand, present astrophysical observations can deduce limits on the neutrino mass. However, the main disadvantage of this procedure is its dependence on model assumptions and the fact that the cosmological parameters are correlated. Therefore, improving the precision in the laboratory neutrino mass measurements can provide an important feedback to astrophysics. In addition, cosmological models of the large-scale structure formation and evolution strongly depend on the relative amounts of the so-called hot (relativistic particles, *e. g.* neutrino) and cold (non-relativistic particles, *e. g.* supersymmetric particles) dark matter in the Universe, thus, these models can profit from the precise knowledge of the neutrino mass as well.

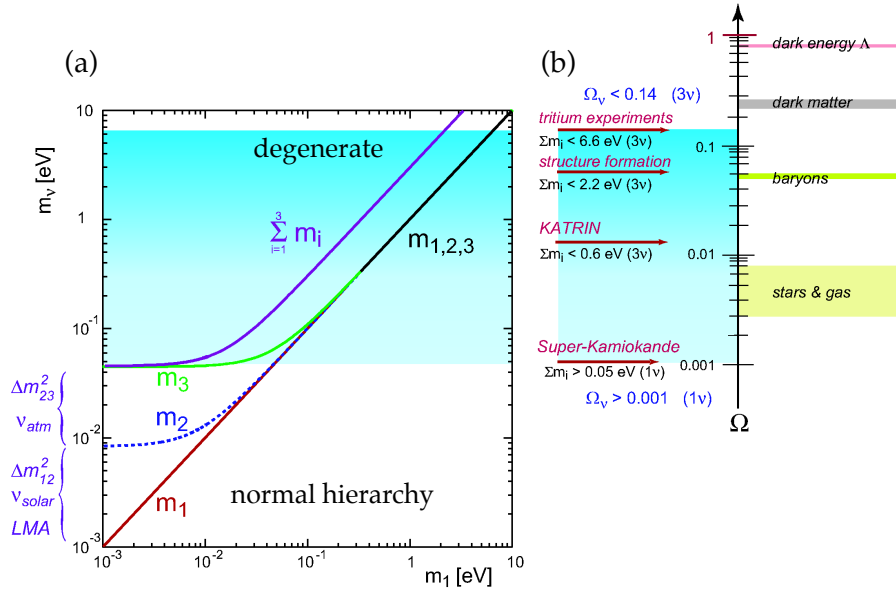


Fig. 1.3: The neutrino masses and their contribution Ω_ν to the energy density of the Universe: **(a)** Neutrino mass eigenvalues m_1 , m_2 and m_3 as a function of m_1 in the hierarchical and the degenerate scenario. The splittings of the neutrino masses (cf. Eq. 1.7) are taken into account. The KATRIN sensitivity roughly marks the border between the hierarchical and the degenerate case. **(b)** Composition of the total energy density Ω_{tot} of the Universe according to the Concordance Model of cosmology. Present bounds on the neutrino contribution Ω_ν from laboratory experiments (upper limit) and from neutrino oscillations (lower limit) cover two orders of magnitude (cyan band). The figure is taken from [KAT04, Val09a].

1.1.3. Towards the absolute scale of neutrino masses

It was shown in the previous section that it is desirable to determine the absolute scale of neutrino masses. However, the oscillation experiments can “only” deliver the splittings Δm_{12}^2 and Δm_{23}^2 between the neutrino mass eigenstates m_i , $i = 1, 2, 3$ (and the mixing angles θ_{ij} , of course). Therefore, other techniques are necessary for determining the absolute neutrino mass scale. At this point these various techniques will be briefly compared.

Cosmological bounds on neutrino mass

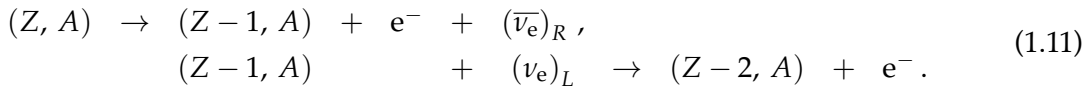
In Sect. 1.1.2 it was already stated that in the cosmological observations the sum $M_\nu = \sum m(\nu_i)$ of the neutrino mass plays a role. One of the two principal ways of deducing M_ν from the cosmological data is based on the fact that massive neutrinos modify the anisotropy spectrum of the CMB temperature. The latest 7-years data of the WMAP experiment, combined with the data of the power spectrum of the matter distribution in the Universe, allowed to set the upper limit of $M_\nu < 0.58 \text{ eV } c^{-2}$ (95% C.L.) [WMA11]. Anyhow, the analysis relies on the validity of the Λ CDM model and does not represent a model-independent method.

Neutrinoless double beta decay

Double β -decay (denoted as $\beta\beta$ -decay) is a rare spontaneous nuclear transition in which the nuclear charge changes by two units while the mass number remains the same. It was first proposed by M. Goeppert-Mayer in 1935 [Goe35] and since that time it has been recognized as a powerful tool to study the lepton number conservation in general, and neutrino properties in particular. Being a second-order process of the weak interaction, half-lives are expected to be very long ($\approx 10^{20}$ a or even more).

For the $\beta\beta$ -decay to proceed, the initial nucleus must be less bound than the final one, but more bound than the intermediate nucleus⁵. In nature these conditions can be realized for even-even nuclei (and never for nuclei with an odd number of protons or neutrons). All ground states of even-even nuclei have spin and parity 0^+ and thus, in all the cases the transitions $0^+ \rightarrow 0^+$ are expected. Occasionally, population of the low-lying excited states of the daughter nucleus is energetically possible, giving rise to $0^+ \rightarrow 2^+$ transitions or to transitions to the excited 0^+ state. Since the half-life of the $\beta\beta$ -decay is always much longer than the age of the Universe, both the initial and the final nuclei can exist in nature⁶. The transition of two neutrons into two protons is energetically possible in many candidates.

The nuclear $\beta\beta$ -transition can proceed in two ways. One of them is the so-called two-neutrino $\beta\beta$ -decay ($2\nu\beta\beta$), during which the nucleus undergoes two β -disintegrations at a time and emits two electrons and two neutrinos. This form of $\beta\beta$ -decay does not carry any information on the neutrino mass and conserves the lepton number. The process was first observed for the isotope ^{82}Se [Ell87]. However, in the second form of $\beta\beta$ -decay, the so-called neutrinoless $\beta\beta$ -decay ($0\nu\beta\beta$), a virtual neutrino is exchanged and no neutrino is emitted. This process violates the lepton number by two units and is therefore forbidden in the standard electroweak theory. The decay scheme of $0\nu\beta\beta$ can be decomposed into two steps:



The right-handed antineutrino $(\bar{\nu}_e)_R$ emitted in the first interaction step has to be absorbed

⁵Thus, $M(Z+1, A) > M(Z, A) > M(Z+2, A)$ for the $\beta^-\beta^-$ decay.

⁶Due to a very long half-life the initial nucleus definitely still exists in nature. However, the final nucleus might be still missing in nature.

1. Introduction

in the second step as a left-handed neutrino $(\nu_e)_L$. Thus, the $0\nu\beta\beta$ process will only take place on the condition that neutrino is of Majorana type. Furthermore, only massive neutrinos can change helicity with the probability of the neutrino to be found in the “wrong” helicity state being proportional to $(m_\nu/E_\nu)^2$.

The observable in the $0\nu\beta\beta$ -decay is the so-called effective Majorana neutrino mass $m_{ee}(\nu)$ which is equal to the coherent sum over all neutrino mass eigenvalues m_j contributing to the electron neutrino and it can be expressed [Ott08] in terms of the mixing parameters θ_{12} , θ_{23} , θ_{13} , δ and $\alpha_{1,2}$ from Eq. 1.3 and Eq. 1.4,

$$\begin{aligned} m_{ee}(\nu) &:= \left| \sum_j U_{ej}^2 m_j \right| \\ &= \left| |U_{e1}|^2 m_1 + |U_{e2}|^2 e^{i\alpha_1} m_2 + |U_{e3}|^2 e^{i\alpha_2} m_3 \right| \\ &= \left| (m_1 \cos^2 \theta_{12} + m_2 e^{i\alpha_1} \sin^2 \theta_{12}) \cos^2 \theta_{13} + m_3 e^{i(\alpha_2+2\delta)} \sin^2 \theta_{13} \right|. \end{aligned} \quad (1.12)$$

It can be seen that the Majorana phases $\alpha_{1,2}$ entering the summation can lead to a (partial) cancellation of terms in $m_{ee}(\nu)$. This feature is the key difference to the observable $m(\nu_e)$ in the neutrino mass searches based on kinematic method (see below). In particular, the term containing m_3 can be neglected for degenerate masses or inverse hierarchy (*i. e.* $m_3 \ll m_1, m_2$) since θ_{13} is small. In either of the two scenarios, m_1 and m_2 are about equal, and a destructive phase $\alpha_1 \approx \pi$ might yield a strong cancellation effect.

The half-life $t_{1/2}^{0\nu}$ of the $0\nu\beta\beta$ -decay is related to $m_{ee}(\nu)$ via

$$(t_{1/2}^{0\nu})^{-1} = G^{0\nu} |\mathcal{M}^{0\nu}|^2 \left(\frac{m_{ee}(\nu)}{m_e} \right)^2, \quad (1.13)$$

where $G^{0\nu}$ is the phase space integral for the two electrons and $\mathcal{M}^{0\nu}$ is the nuclear matrix element. Thus, the mass $m_{ee}(\nu)$ can be derived from a measured decay rate for the $0\nu\beta\beta$ -process. In the absence of a detected signal, a lower limit on the half-life $t_{1/2}^{0\nu}$ transforms into an upper limit on the neutrino mass. The main uncertainty in extracting a bound on $m_{ee}(\nu)$ from experimental half-life limits stems from the nuclear matrix element. It can be calculated on the basis of several theoretical models, *e. g.* the nuclear shell model or the quasiparticle random phase approximation (QRPA). Nowadays, the uncertainties and an overall agreement of the various models represent an open problem, making the precise determination of $m_{ee}(\nu)$ with the $0\nu\beta\beta$ -decay searches more difficult [Sim10].

Up to now, the highest sensitivity was achieved by the Heidelberg-Moscow experiment searching for the $0\nu\beta\beta$ -decay in ^{76}Ge . The $0\nu\beta\beta$ -signal $^{76}\text{Ge} \rightarrow ^{76}\text{Se} + 2e^-$ would be based on the observation of a statistically significant peak in the Ge sum energy spectrum at the Q value of the $\beta\beta$ -decay at $Q_{\beta\beta} = 2039$ keV. In 2001, the collaboration published the upper limit on the effective Majorana neutrino mass $m_{ee}(\nu) < 0.35$ eV (90% C.L.) [Kla01]. A subgroup of the collaboration claimed in 2004 the finding of an evidence [Kla04] for the signal at the right decay energy with the 4.2σ significance. From this the range for the effective Majorana neutrino mass $0.1 \text{ eV } c^{-2} \leq m_{ee}(\nu) \leq 0.9 \text{ eV } c^{-2}$ could be deduced, with the best-fit value of $m_{ee}(\nu) = 0.44 \text{ eV } c^{-2}$. Although the significance could be in the meantime increased to 6σ [Kla06], the claim was criticized by parts of the community due to problematic assumptions and uncertainties. The upcoming next-generation experiments searching for

the $0\nu\beta\beta$ -decay are expected to probe Majorana neutrino masses with increased sensitivity and to clarify the aforementioned claim.

Direct kinematic methods

In contrast to the $\beta\beta$ -decay experiments, direct investigations of the neutrino mass do not rely on further assumptions on the neutrino mass type (Majorana or Dirac). Direct kinematic experiments can be classified into two categories of a) the so-called Time-of-flight (TOF) method and b) the method utilizing the kinematics of weak decays. Both methods are essentially model-independent as they are mainly based on the relativistic energy-momentum relation

$$E^2 = p^2c^2 + m^2c^4. \quad (1.14)$$

The TOF method is represented by the famous case of detecting the burst of neutrinos released by the eruption of the nearby type II supernova SN 1987A. The events were observed independently by three experiments and they represented the first neutrinos to be investigated from an astrophysical source other than the Sun. From the correlation between the energy and the arrival time of the supernova neutrinos the upper limit on the electron antineutrino mass of $m_{\bar{\nu}_e} < 5.7 \text{ eV } c^{-2}$ (95 % C.L.) could be deduced [Lor02]. Although it is anticipated that a future nearby core-collapse supernova explosion will be observed by large underground neutrino experiments (Super-Kamiokande, SNO+ and others) with better sensitivity, it is not expected that the upper limit on $m_{\bar{\nu}_e}$ will reach a value below $1 \text{ eV } c^{-2}$. Moreover, the estimated rate of the supernova type II collisions is only in the range of one event per several tens of years in our galaxy.

The investigation of the kinematics of weak decays is based on the measurement of the charged decay products of the weak decays. The observable in such experiments is the weighted sum over the squared neutrino mass eigenvalues, according to the mixing matrix U (cf. Eq. 1.3):

$$m^2(\nu_\alpha) := \sum_j |U_{\alpha j}|^2 m_j^2, \quad \alpha = e, \mu, \tau. \quad (1.15)$$

Similarly to Eq. 1.12, the observable can be explicitly written (for the case of the electron neutrino) as

$$\begin{aligned} m^2(\nu_e) &:= \sum_j |U_{ej}|^2 m_j^2 \\ &= |U_{e1}|^2 m_1^2 + |U_{e2}|^2 m_2^2 + |U_{e3}|^2 m_3^2 \\ &= (m_1^2 \cos^2 \theta_{12} + m_2^2 \sin^2 \theta_{12}) \cos^2 \theta_{13} + m_3^2 \sin^2 \theta_{13}. \end{aligned} \quad (1.16)$$

So far only the upper bounds were found. For $m(\nu_\mu)$ and $m(\nu_\tau)$, these were derived from pion and tau decay, respectively:

$$m(\nu_\mu) < 0.19 \text{ MeV } c^{-2} \quad (90 \% \text{ C.L.}) \quad [\text{Ass96, PDG10}] \quad (1.17)$$

$$m(\nu_\tau) < 18.2 \text{ MeV } c^{-2} \quad (95 \% \text{ C.L.}) \quad [\text{ALE98}] \quad (1.18)$$

In comparison, the present upper limit on $m(\nu_e)$ derived from the precise measurement of the tritium β -spectrum near its endpoint (see Sect. 2.1) is more stringent by about five and

1. Introduction

seven orders of magnitude, respectively [PDG10]:

$$m(\nu_e) < 2 \text{ eV } c^{-2}. \quad (1.19)$$

This upper limit is based on the results of the neutrino mass experiments at Troitsk and Mainz, which both used the MAC-E filter technique (see Sect. 2.2). This technique will also be employed in the KATRIN experiment. The final results of the two experiments are:

$$\begin{aligned} m^2(\nu_e) &= -0.6 \pm 2.2 \pm 2.1 \text{ eV}^2 c^{-4}, \\ m(\nu_e) &< 2.3 \text{ eV } c^{-2} \end{aligned} \quad (\text{Mainz, [Kra05]}), \quad (1.20)$$

$$\begin{aligned} m^2(\nu_e) &= -2.3 \pm 2.5 \pm 2.0 \text{ eV}^2 c^{-4}, \\ m(\nu_e) &< 2.1 \text{ eV } c^{-2} \end{aligned} \quad (\text{Troitsk, [Lob03]}). \quad (1.21)$$

Besides tritium, the isotope ^{187}Re is a suitable β -emitter for direct neutrino mass measurements. It possesses an extremely low endpoint energy of 2.47 keV which helps to maximize the relative fraction of useful events close to the endpoint of the spectrum (where the sensitivity on $m(\nu_e)$ is highest). Its half-life of 4.3×10^{10} a implies the use of the bolometer technique (detector = source). As the present upper limit on the neutrino mass derived from such method amounts to $m(\nu_e) < 15 \text{ eV } c^{-2}$ (90% C.L.) [Sis04], the bolometer technique is not yet competitive with the tritium β -decay measurements. However, the upcoming two-staged project MARE [MAR10] aims at the sensitivity corresponding to the present limit achieved by the tritium experiments, (see Eq. 1.19). The second stage of MARE is aimed at attacking the sub-eV range of the neutrino mass by scaling up the number of bolometer crystals and further improving the experimental technique. Concerning the tritium β -decay method, the sub-eV sensitivity is now within reach with the KATRIN experiment, see Chap. 2.

Since the search for the $0\nu\beta\beta$ -decay and the direct kinematic neutrino mass experiments provide different neutrino mass parameters, both types of experiments are complementary to each other. The comparison of the neutrino mass observables $m_{ee}(\nu)$ and $m(\nu_e)$ is depicted in Fig. 1.4.

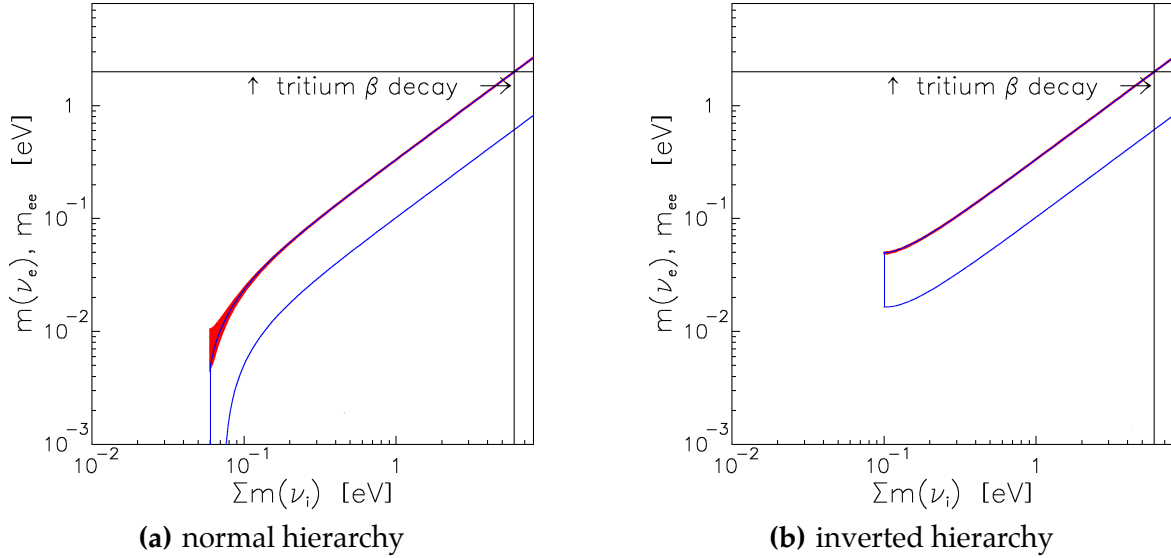


Fig. 1.4: The comparison of the neutrino mass observables in the neutrinoless $\beta\beta$ -decay ($m_{ee}(\nu)$ in Eq. 1.12, blue open band) and the single β -decay ($m(\nu_e)$ in Eq. 1.16, red solid band). Two scenarios are considered: **(a)** normal and **(b)** inverted hierarchy. The correlation of both observables with the cosmologically relevant sum of neutrino mass eigenvalues $\Sigma m(\nu_i)$ is shown together with the present upper limit from the tritium β -decay experiments in Mainz and Troitsk. The width of the bands reflects the experimental uncertainties of the mixing angles as well as the unknown phases α_1 , $(\alpha_2 + 2\delta)$ in the expression for $m_{ee}(\nu)$. Further uncertainties of $m_{ee}(\nu)$ which arise from the calculations of the nuclear matrix elements are not taken into account. The figure is taken from [Ott08].

1.2. Process of internal conversion

Internal conversion is an electromagnetic process that competes with the emission of gamma radiation: instead of emitting a photon, the excited state of the nucleus leads to the emission of one of the atomic electrons⁷. The process was first observed by O. von Baeyer and O. Hahn in 1910 [Bae10] when a discrete distribution of β -particles was observed. In 1924 O. Hahn and L. Meitner [Hah24, Mei24] proved that this radiation does not originate in the nucleus, but on the contrary, it consists of electrons ejected from the atomic shells by the nuclear gamma radiation. Since that time it was denoted as “conversion of the gamma radiation”. The first correct theoretical description of this process was provided by H.R. Hulme in 1932 [Hul32]. The internal conversion is fully analogous to the Auger effect. The only difference is that instead of two orbital electrons making the transition, here one electron and the nucleus are involved. The process of internal conversion is the underlying principle of the electron source concept which will be utilized in this work for the purpose of monitoring the stability of the energy scale in the KATRIN experiment. In this section the process of internal conversion will be shortly described on the basis of works [Sie68, Ros78, Dra83, Kra88].

⁷The excited nuclear state can also de-excite (if the excitation energy is high enough) via emission of an electron-positron pair or via higher order processes such as simultaneous emission of two photons or two electrons. These processes are not considered here.

Brief theoretical consideration

A nucleus in an excited state, possessing excitation energy E_γ lower than the binding energy of a nuclear particle, will almost always make a transition to a lower state by either one of two competing processes. These are a) the emission of a gamma ray or b) the ejection of one of the orbital electrons. The ratio of the transition probability λ_e for process (b) to the probability λ_γ for process (a) is denoted as the internal conversion coefficient (ICC) α ,

$$\alpha = \frac{\lambda_e}{\lambda_\gamma}. \quad (1.22)$$

Clearly, α can be any positive number. The total decay probability λ_{tot} (equal to $\ln 2/t_{1/2}$, $t_{1/2}$ being the half-life) can be expressed as

$$\lambda_{\text{tot}} = \lambda_\gamma + \lambda_e = \lambda_\gamma (1 + \alpha). \quad (1.23)$$

The ICC α used in Eq. 1.22 and Eq. 1.23 is often denoted as the total ICC α_{tot} (in the sense that all the atomic shells and subshells are taken into account). The total ICC depends strongly on the following parameters:

1. the transition energy E_γ ,
2. the atomic number Z of the emitter,
3. the multipolarity L , or angular momentum of the radiated field, *i. e.* of the competing gamma radiation,
4. the character of the nuclear transition, electric (E) or magnetic (M), which, in turn, uniquely determines the nuclear parity change once L is fixed.

The multipolarity (EL or ML) determines the multipole order 2^L of the radiation: $L = 1$ represents the dipole, $L = 2$ denotes the quadrupole *etc.* The angular momentum and the parity obey the so-called selection rules. Considering the gamma transition from the initial excited state of angular momentum I_i and parity π_i (usually designated in the form $I_i^{\pi_i}$) to the final state of I_f and π_f , from the conservation of angular momentum it follows

$$|I_i - I_f| \leq L \leq I_i + I_f \quad (\text{no } L = 0). \quad (1.24)$$

In addition, the relative parity of the initial and final states determines whether the emitted radiation is of the electric or magnetic type:

$$\begin{aligned} \pi_i &= (-1)^L \pi_f && \text{for EL radiation,} \\ \pi_i &= (-1)^{L+1} \pi_f && \text{for ML radiation.} \end{aligned} \quad (1.25)$$

In the case of $I_i = I_f = 0$ the selection rules give only $L = 0$ which is not permitted for radiative transitions. Thus, for the $0^+ \rightarrow 0^+$ transitions (E0 type) the only possible de-excitation process is the internal conversion (besides the electron-positron pair production).

From a comparison of observation and accurate theoretical values of the ICCs the information about the parity change and angular momentum change of the nucleus can be obtained. Except for low $Z \lesssim 20$ and high $E_\gamma \gtrsim 2.5$ MeV the ICCs are usually large enough to be measured. In some cases— E_γ near the threshold and especially for the larger L values (2^4 or 2^5 -poles)— α may become so large that it is difficult to observe any gamma radiation. In

such cases the useful information may be derived from ratios of the so-called partial ICCs for different shells or subshells. The partial ICCs α_i , representing the individual atomic shells i , are defined as

$$\begin{aligned}\lambda_{\text{tot}} &= \lambda_\gamma + \lambda_{e,K} + \lambda_{e,L} + \lambda_{e,M} + \dots \\ &= \lambda_\gamma (1 + \alpha_K + \alpha_L + \alpha_M + \dots),\end{aligned}\quad (1.26)$$

and thus

$$\alpha_{\text{tot}} = \alpha_K + \alpha_L + \alpha_M + \dots \quad (1.27)$$

Similarly, for the subshells one can write *e. g.* $\alpha_L = \alpha_{L_1} + \alpha_{L_2} + \alpha_{L_3}$. For a nuclear transition of mixed multipolarity it can be written

$$\alpha_i = \sum_L p_L \alpha_i(\tau L), \quad (1.28)$$

where τ sets the transition type (E or M) and p_L is the admixture⁸ of the multipolarity τL . For a particular transition, only one or two (and, very rarely, three) lowest multiplicities can be deduced from comparison of the experimental data with theoretical predictions. In accordance with the aforementioned dependencies of the ICC, α can be expressed as

$$\alpha = \alpha(Z, \tau L, E_\gamma, n, \kappa), \quad (1.31)$$

where n and κ are the principal and relativistic angular momentum quantum numbers of the orbital electron, respectively. To specify the atomic subshell, nlj with $j = |\kappa| - \frac{1}{2}$, spectroscopic notation is often used, *e. g.* $1s_{1/2}$, $2p_{3/2}$, $5d_{5/2}$, ..., or K , L_3 , O_5 , ...

The internal conversion process can be described theoretically as the interaction between one of the nucleons⁹ and the orbital electron. In the initial state the nucleus is excited with energy E_γ above the ground state (or state of lower excitation) and the electron is in its ground state. In the final state the electron is in an excited (continuum) state with the energy E_{kin} and the nucleus has lost the energy E_γ . The number of quanta present is zero in both initial and final states. The transition probability $\lambda_{\text{if}}(i \rightarrow f)$ of the internal conversion can be expressed with the help of the Fermi's golden rule as

$$\lambda_{\text{if}} = \frac{2\pi}{\hbar} |\mathcal{M}_{\text{if}}|^2 \rho_f, \quad (1.32)$$

where ρ_f denotes the density of final states and \mathcal{M}_{if} is the nuclear matrix element of the multipole operator $M(\tau L)$ (corresponding to the multipole moment),

$$\mathcal{M}_{\text{if}} = \int \psi_f^* M(\tau L) \psi_i \, dv. \quad (1.33)$$

⁸Besides the admixture p_L , the mixing ratio $\delta_\gamma^2(L)$ is often used. It is defined as

$$\delta_\gamma^2(L) = \frac{\lambda_\gamma(L)}{\lambda_\gamma(L_{\text{min}})}, \quad (1.29)$$

and connected with the admixture p_L via

$$p_L = \frac{\delta_\gamma^2(L)}{\sum_{L'=L_{\text{min}}}^{L_{\text{max}}} \delta_\gamma^2(L')}. \quad (1.30)$$

⁹The fact that all the nucleons in the emitting nucleus are involved is taken care of by a summation over all nucleons. This plays a role when the corrections due to finite size of the nucleus are introduced.

1. Introduction

Here the initial state $\psi_i = \psi_{i,n} \psi_{i,e}$ (n denoting the nuclear wave function and e indicating the electron wave function) includes a bound electron. Similarly, the final state $\psi_f = \psi_{f,n} \psi_{f,e}$, where $\psi_{f,e} = e^{-ik \cdot r_e}$ is the free-particle wave function. The integration in Eq. 1.33 is carried out over the volume of the nucleus. For the details of the calculations of the ICCs the reader is kindly referred to [Sie68] and references therein.

In a very crude approximation (non-relativistic treatment of the electron and point model of the nucleus) the ICC can be expressed [Kra88] for the electric multipoles as

$$\alpha(\text{EL}) \approx \frac{Z^3}{n^3} \frac{L}{L+1} \left(\frac{e^2}{4\pi\epsilon_0\hbar c} \right)^4 \left(\frac{2m_e c^2}{E_\gamma} \right)^{L+\frac{5}{2}}, \quad (1.34)$$

and for the magnetic multipoles as

$$\alpha(\text{ML}) \approx \frac{Z^3}{n^3} \left(\frac{e^2}{4\pi\epsilon_0\hbar c} \right)^4 \left(\frac{2m_e c^2}{E_\gamma} \right)^{L+\frac{3}{2}}. \quad (1.35)$$

Here the factor $(Z/n)^3$ comes from the term $|\psi_{i,e}(0)|^2$ appearing in the conversion rate and the dimensionless term $e^2/(4\pi\epsilon_0\hbar c)$ is the fine structure constant $\alpha \simeq 1/137$ (not to be confused with α designating the ICC). The dependence of the ICC on the subshell is neglected in this approximation, therefore κ is not present in Eq. 1.34 and Eq. 1.35.

Internal conversion coefficients

It was stated in Eq. 1.31 that the ICC is dependent on a number of parameters. The approximate expressions Eq. 1.34 and Eq. 1.35 illustrate the following features of the ICCs:

- They increase as Z^3 , thus, the conversion process is more important for heavy nuclei than for light nuclei.
- The ICC decreases rapidly with increasing transition energy E_γ . In contrast to this, the probability for the emission of the gamma radiation increases rapidly with E_γ .
- The ICC increase rapidly as the multipole order 2^L increases, also because the gamma ray emission is hindered for higher L .
- For higher atomic shells the ICC decreases as n^{-3} . Thus, for a given transition one might roughly expect $\alpha_K/\alpha_L \simeq 8$.

In sum, relatively large values of α_K can be expected for low energy, high multipolarity transitions in heavy nuclei, while in other cases (higher atomic shells, higher transition energy, lighter nuclei, lower multipoles) the ICC decreases. In Fig. 1.5 the dependence of the ICC α_K on the transition energy, the multipolarity and the atomic number is illustrated.

For quantitative comparison with experimental results, the tabulated ICCs are often used, based on detailed computations where the finite size of the nucleus, proper atomic wave functions and other corrections are taken into account. In [Ros78] the ICCs for all natural atomic shells and the total ICCs of all atoms with $30 \leq Z \leq 104$ for energies ranging from 2 keV above threshold to about 5 MeV for the K shell and to about 1.5 MeV for all other shells. The multiplicities of the four lowest orders of the electric and of the magnetic type are included. Nowadays, sophisticated databases of the ICCs are accessible also on the Internet, *e. g.* the BrIcc database [Kib08].

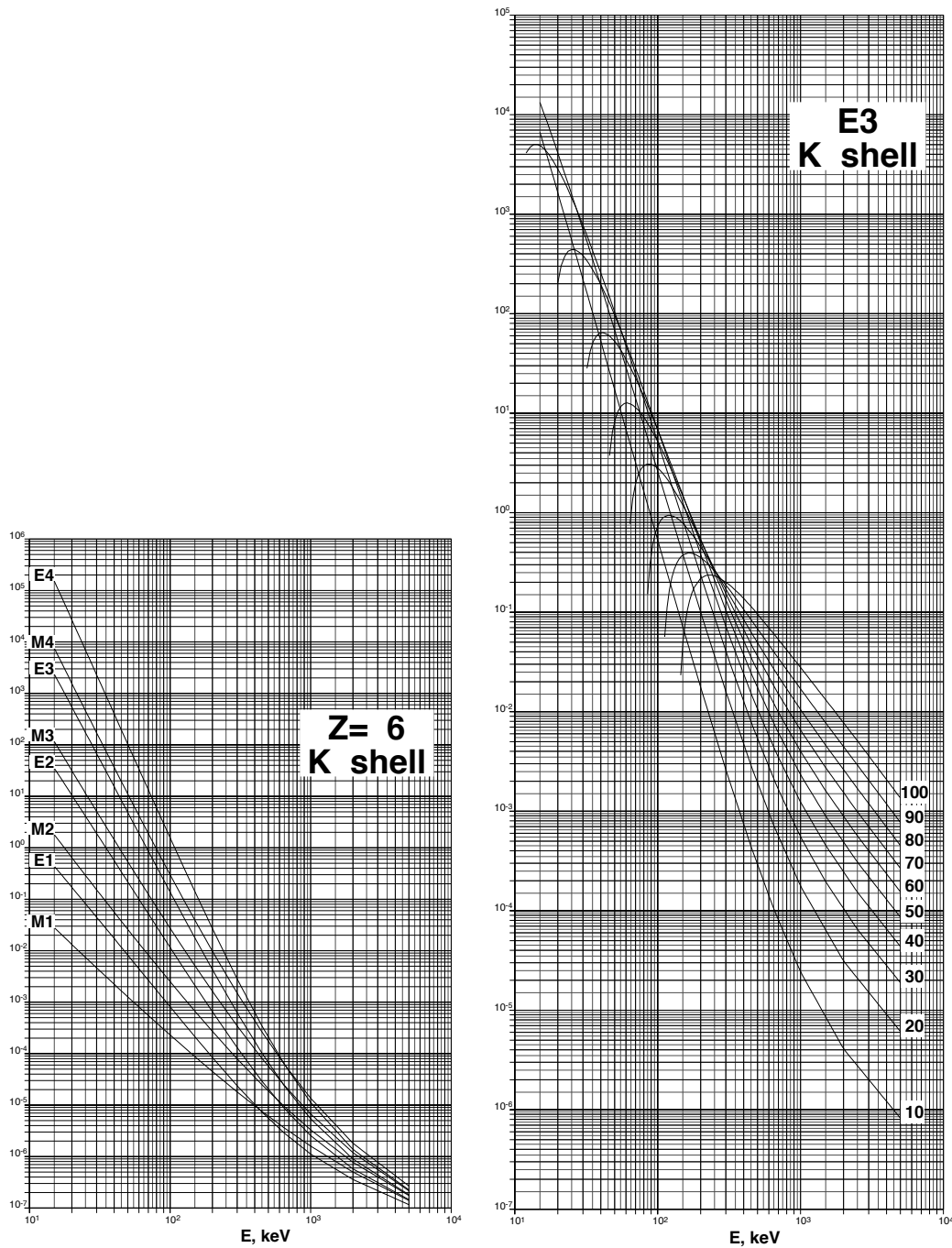


Fig. 1.5: The graphs of theoretical ICCs α_K illustrate the dependence on a) the multipolarity for the case of carbon, $Z = 6$ (graph on the left side) and b) the atomic number Z for the case of multipolarity E3 (graph on the right side). The x axis denotes the transition energy [keV]. Both x and y are plotted in the log scale. The y scale covers 13 (left graph) and 12 (right graph) orders of magnitude. The accuracy of the coefficients amounts to 3–5%. Smooth curves were drawn through the calculated data points by using a cubic spline fit to the logarithms of both energy and conversion coefficient. The graphs are taken from [Fir96].

Width of the conversion line

The kinetic energy E_{kin} of the conversion electrons is discussed in detail below in Sect. 3.3.2. At this point only the width of the conversion line will be shortly mentioned. The shape of the conversion line follows directly from the solution of the Schrödinger equation. It can be shown [Wei27] that the intensity distribution of the conversion electrons around the central energy E_0 is of the form of the Lorentz function,

$$L(E, E_0, \Gamma) = \frac{1}{\pi} \frac{\Gamma/2}{(E - E_0)^2 + (\Gamma/2)^2}, \quad (1.36)$$

where Γ denotes the width (full width at half maximum, FWHM) of the distribution. The width Γ is influenced by the lifetimes τ_γ , τ_e of the nuclear transition and the electron hole, respectively, as on the basis of the uncertainty principle $\Gamma \cdot \tau = \hbar$ one can write

$$\Gamma \propto \frac{1}{\tau_\gamma} + \frac{1}{\tau_e}. \quad (1.37)$$

The width corresponding to the electron hole lifetime τ_e is often the decisive one. The natural width Γ of an atomic level is given by the sum of the radiative width Γ_R (X-ray emission), the Auger width Γ_A (emission of an Auger electron), and the Coster-Kronig width Γ_{CK} (special case of the Auger process in which the vacancy is filled by an electron from a higher subshell of the same major shell) [Cam01]. These three components of the level width are related to the corresponding transition rates S_i , $i = R, A, \text{CK}$, for the filling of a hole in that level, while $\Gamma_i = \hbar \cdot S_i$ holds. The Γ values range from 0.07 to 70 eV depending on Z and the atomic subshell [Dra83]. Thus, the width of the line is not negligible in the analysis of the conversion electron spectra measured with the instrumental resolution at the eV level as will be seen later in this work.

Thesis outline

This work is organized as follows:

Chap. 2 introduces the KATRIN experiment which aims at the direct determination of the neutrino mass on the basis of precise measurement of the tritium β -spectrum. The setup of the KATRIN experiment and, in particular, the principle of the MAC-E filter are presented. The systematic and statistical uncertainties of the experiment are discussed. The possible instability of the energy scale of the β -spectrometers is identified as one of the six main systematic uncertainties of the KATRIN experiment.

The importance of continuous monitoring of the energy scale stability and of absolute calibration of the energy scale is discussed in detail in Chap. 3. The two-fold concept of monitoring of the KATRIN energy scale is presented. In addition, possible candidates for quasi-monoenergetic electron sources, based on atomic/nuclear standards, are described and their feasibility for the KATRIN experiment is discussed.

Probably the most promising and most suitable tool for the continuous monitoring of the KATRIN energy scale stability is the concept based on conversion electrons of the metastable ^{83m}Kr . In the KATRIN experiment the ^{83m}Kr source will be utilized in three different forms: as a gas, as a condensed source and as a solid source. The latter option is thoroughly discussed in Chap. 4. Two production techniques of the $^{83}\text{Rb}/^{83m}\text{Kr}$ solid sources are introduced and the actual samples, investigated in this work at the MAC-E filter spectrometer in the Institute of Physics, University of Mainz, are presented. The chapter concludes with a discussion of surface and solid state effects affecting the conversion electrons emitted from the solid sources.

The first part of Chap. 5 covers the experimental setup of Mainz MAC-E filter spectrometer used in this work for long-term measurements of energy stability of the ^{83m}Kr conversion lines of the solid $^{83}\text{Rb}/^{83m}\text{Kr}$ sources. In the second part of this chapter the analysis of the collected data is described. Basic notions are also introduced which will be later used throughout the following chapters.

The long-term measurements of the conversion electrons energy stability carried out at Mainz MAC-E filter are reported in Chap. 6. Altogether four measurement phases are described in a chronological manner so that the progress of the measurements can be easily seen. Besides the long-term measurements of the various conversion lines, additional systematic measurements are described in the course of the measurement phases as well, allowing to assess the overall sensitivity and systematic uncertainties of the method. These are summarized in the last section of this chapter.

Whereas in Chap. 6 the focus was made on the relative energy stability of the ^{83m}Kr conversion lines, in Chap. 7 the absolute kinetic energies of the various conversion lines of the solid $^{83}\text{Rb}/^{83m}\text{Kr}$ sources are of main interest. Detailed analysis of rather complicated shapes of the conversion lines is presented, together with several hypotheses for the explanation of the doublet structure observed in the electron spectra. In addition, the influence of environment on the electron binding energy is discussed. The absolute calibration of the experimental setup is verified as well. Finally, the electron energy loss spectra of the solid $^{83}\text{Rb}/^{83m}\text{Kr}$ sources are investigated.

Conclusions of this work and an outlook are presented in Chap. 8.

2. The KATRIN experiment

It was shown in Sect. 1.1 that the direct investigations of the neutrino mass, based on the kinematics of weak decays, are model-independent. Moreover, the direct kinematic searches represent the only model-independent method of the neutrino mass determination which is realizable in laboratory. The Karlsruhe TRITium Neutrino experiment (KATRIN) represents a next-generation tritium β -decay experiment designed to perform a high precision direct measurement of the electron antineutrino mass with the sensitivity of $0.2 \text{ eV } c^{-2}$. KATRIN is a successor experiment of the neutrino mass experiments carried out in Mainz and Troitsk which set the upper limit on the electron neutrino mass of $2 \text{ eV } c^{-2}$ (see Eq. 1.19 to Eq. 1.21 in previous Chap. 1). Therefore, the aim of the KATRIN experiment represents the improvement of the neutrino mass sensitivity by one order of magnitude.

This chapter provides a brief review of the main features and components of this project. Firstly, the β -decay of tritium (Sect. 2.1) and the MAC-E filter technique (Sect. 2.2) will be described. Secondly, the major components of the KATRIN experimental setup will be reviewed in Sect. 2.3. Lastly, Sect. 2.4 discusses the systematic and statistical uncertainties. It is not the scope of this work to provide a complete overview of the very complex experimental setup of KATRIN with all its details and challenges. The reader is kindly referred to the KATRIN documents of Letter of Intent [KAT01] and Design Report [KAT04] for a comprehensive review. The topics of the β -decay and the MAC-E filter technique were thoroughly described in [Ott08] which was used here as a reference.

2.1. Tritium beta-decay

The β^- -decay (denoted here as β -decay henceforth) is a three-body decay during which an electron and electron-antineutrino are emitted:

$$(A, Z) \rightarrow (A, Z + 1)^+ + e^- + \bar{\nu}_e + Q, \quad (2.1)$$

where A and Z denote the atomic mass number and nuclear charge of the parent isotope. The total surplus energy Q of the decay is released in three different forms: a) as a kinetic energy obtained by the electron and the neutrino, b) as a small recoil energy E_{rec} transferred to the daughter $(A, Z + 1)^+$, and c) as an excited state of energy V_k of the daughter, created with the probability P_k .

The energy spectrum of the electrons can be deduced theoretically from the Fermi's golden rule. The rate \dot{N} of electrons emitted into the kinetic energy interval between E and $E + dE$

2. The KATRIN experiment

is

$$\frac{d\dot{N}}{dE} = \frac{d^2N}{dE dt} = \frac{2\pi}{\hbar} |\mathcal{M}|^2 \rho(E_{\text{tot}}, E_{\text{tot } \nu}), \quad (2.2)$$

where \mathcal{M} is the transition matrix element and $\rho(E_{\text{tot}}, E_{\text{tot } \nu})$ is the density of final states, where E_{tot} and $E_{\text{tot } \nu}$ represent the total energy of the electron and neutrino, respectively. The matrix element can be decomposed into leptonic and hadronic parts via

$$\mathcal{M} = G_F \cos \theta_C \mathcal{M}_{\text{nuc}} \mathcal{M}_{\text{lep}}, \quad (2.3)$$

where G_F stands for the Fermi coupling constant and θ_C for the Cabibbo angle. The leptonic part of the matrix element can be written as

$$|\mathcal{M}_{\text{lep}}|^2 = \frac{1}{V^2} F(Z+1, E). \quad (2.4)$$

The Fermi function $F(Z+1, E)$ accounts for the Coulomb interaction of the outgoing electron with the daughter nucleus, while V denotes the normalization volume.

The phase space factors for neutrino and electron may be treated separately (thanks to the fact that the momenta of electron and neutrino are not directly correlated¹) and expressed as a function of the kinetic energy E of the electron,

$$\begin{aligned} \rho(E_{\text{tot}}, E_{\text{tot } \nu}) &= \frac{dn_e}{dE_e} \frac{dn_\nu}{dE_\nu} = \frac{V^2 p E_{\text{tot}} p_\nu E_{\text{tot } \nu}}{4\pi^4 \hbar^6} \\ &= \frac{V^2}{4\pi^4 \hbar^6} p (E + m_e c^2) (E_0 - E) \cdot \sqrt{(E_0 - E)^2 - m^2(\nu_e) c^4}. \end{aligned} \quad (2.5)$$

E_0 denotes the endpoint energy corresponding to zero neutrino mass, p and p_ν stand for the electron and neutrino momenta. Thus, one can rewrite Eq. 2.2 with the help of Eq. 2.3 to Eq. 2.5 as

$$\frac{d^2N}{dE dt} = R(E) \cdot \sqrt{(E_0 - E)^2 - m^2(\nu_e) c^4} \Theta(E_0 - E - m(\nu_e) c^2), \quad (2.6)$$

with

$$R(E) = \frac{G_F^2 \cos^2 \theta_C}{2\pi^3 \hbar^7} |\mathcal{M}_{\text{nuc}}|^2 F(Z+1, E) p (E + m_e c^2) (E_0 - E). \quad (2.7)$$

Here the step function Θ ensures the energy conservation. Finally, the excited states V_k and the incoherent sum

$$m^2(\nu_e) = \sum_j |U_{ej}|^2 m^2(\nu_j), \quad (2.8)$$

representing the neutrino mass observable in this direct kinematic method, shall be incorporated, and one obtains

$$\begin{aligned} \frac{d^2N}{dE dt} &= \text{const.} \cdot |\mathcal{M}_{\text{nuc}}|^2 F(Z+1, E) p (E + m_e c^2) \\ &\quad \cdot \sum_j \sum_k |U_{ej}|^2 P_k \epsilon_k \sqrt{\epsilon_k^2 - m^2(\nu_j) c^4} \Theta(\epsilon_k - m(\nu_j) c^2), \end{aligned} \quad (2.9)$$

$$\text{with} \quad \epsilon_k = E_0 - E - V_k. \quad (2.10)$$

¹The nucleus is so heavy that it takes nearly no energy but balances all the momenta [Zub04].

It can be seen that the signature of a non-zero neutrino mass is pronounced most strongly in the region close to the endpoint E_0 as illustrated in Fig. 2.1 for the case of tritium β -decay. In principle, the non-zero neutrino mass causes the β -spectrum to vanish at the energy $E_0 - m(\nu_e)c^2$, lower than the endpoint E_0 . However, the considerable background make this method difficult to realize. From the considerations based on Eq. 2.9 and Fig. 2.1 it follows that any β -decay experiment aiming at the neutrino mass sensitivity in the sub-eV range has to deal with several major challenges:

- A strong source with high β -decay rate is needed for a sufficient count rate in the region just below the endpoint energy E_0 . In Fig. 2.1 it is shown that for a hypothetical neutrino mass of $m(\nu_e) = 1 \text{ eV}c^{-2}$ only a fraction of about 2×10^{-13} of all tritium β -events lies within the interval of 1 eV below E_0 .
- As the absolute energy resolution ΔE required scales with the value of the neutrino mass aimed for, a spectrometer with very high resolution is needed.
- Very low background in the endpoint region is required.

It will be shown in the next section that the β -spectrometer based on the MAC-E filter technique fulfills the aforementioned requirements.

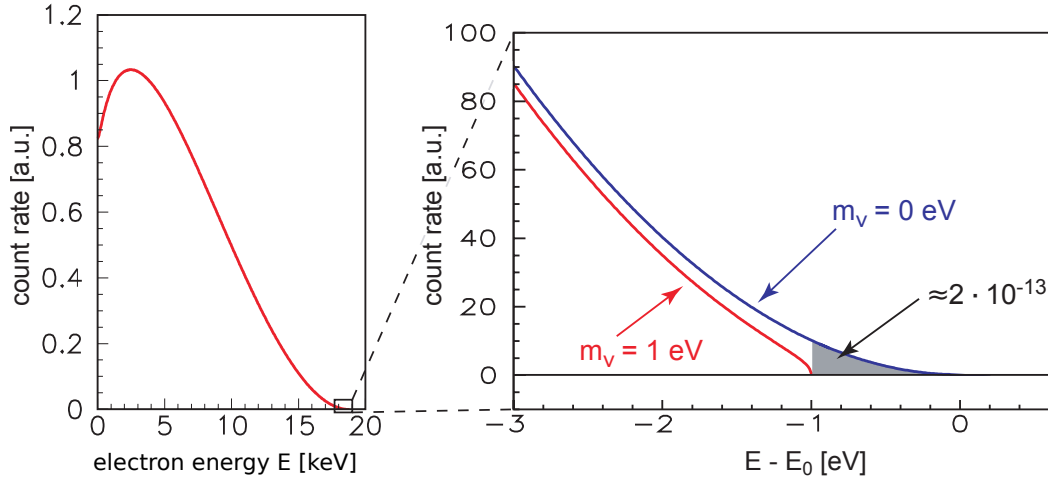
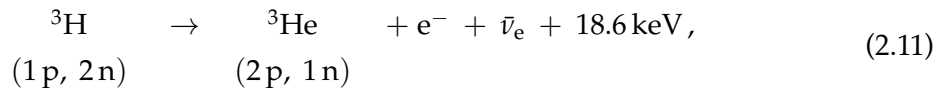


Fig. 2.1: The electron energy spectrum of tritium β -decay: complete spectrum (left side) and narrow region around the endpoint E_0 (right side). Two calculated β -spectra for zero neutrino mass (red) and for a small non-vanishing neutrino mass (blue) are shown. The signature of $m(\nu_e) \neq 0$ is seen as an offset throughout the entire spectrum and as a shift of the point where the spectrum vanishes. The gray-shaded area, representing the fraction of only $\approx 2 \times 10^{-13}$ of all decays, denotes the effect of a hypothetical neutrino mass of $m(\nu_e) = 1 \text{ eV}c^{-2}$. The figure is based on [Ott08].

Tritium, undergoing the β -decay in the form



has the following advantages as the β -emitter in the neutrino mass investigations:

1. Tritium has the second lowest total decay energy of all β -emitters. Only ${}^{187}\text{Re}$ with $Q \simeq 2.5 \text{ keV}$ has a lower endpoint energy. Since the portion of decay electrons with energies just slightly below the endpoint E_0 is proportional to E_0^{-3} , the rate of those electrons is high for tritium compared to other β -emitters.

2. The KATRIN experiment

2. Thanks to its short half-life of $t_{1/2} = 12.3$ a, tritium exhibits a high specific decay activity. Thus, high count rates can be obtained with a small amount of the source material, which in turn implies a reduced probability for the inelastic scattering of electrons.
3. Tritium β -decay represents a super-allowed nuclear transition. Therefore, the nuclear matrix element $|\mathcal{M}_{\text{nuc}}|^2$ is energy-independent and no energy corrections have to be applied.
4. In addition, the Fermi function $F(Z + 1, E)$ for the daughter nucleus is nearly constant over a wide range of electron energies and can be approximated with a constant close to unity in the interesting region just below E_0 .
5. Molecular tritium as well as its daughter possess a simple electronic structure which permits to quite accurately calculate the final state distribution and to model its influence on the theoretical β -spectrum.
6. Due to the low charge number $Z = 1$ of tritium the cross section for inelastic scattering of electrons is relatively low compared to other elements.

It should be noted, though, that some of the advantages summarized here are important only for the experimental setups where the source is not identical to the detector. The discussion of the calorimetric β -spectroscopy of ^{187}Re using bolometers is presented in [Ott08]. The combination of the advantageous features of tritium and the MAC-E filter technique made it possible to explore the absolute neutrino masses in the eV-range during 1990s. This breakthrough is clearly presented in Fig. 2.2 where the results of recent tritium β -decay experiments are plotted. Equally important was the better understanding of systematic effects and improvements in the experimental setups.

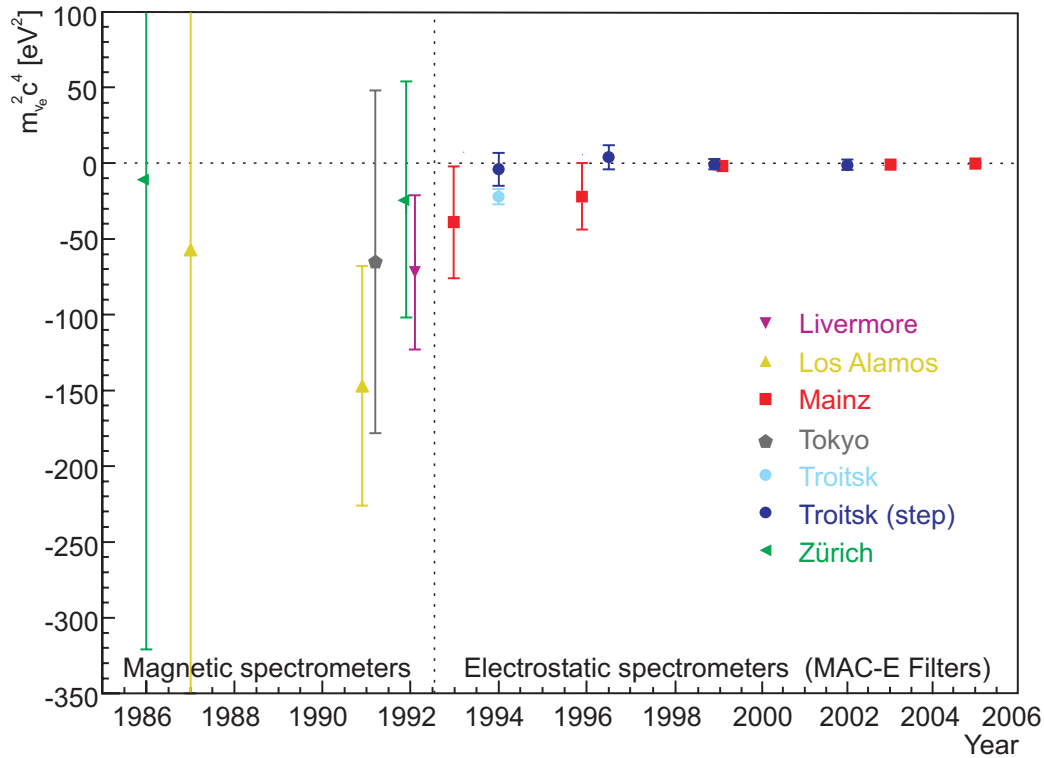


Fig. 2.2: The historical overview of the results of neutrino mass experiments based on direct kinematic method. Early experiments, using magnetic spectrometers, suffered from moderate energy resolution and systematic effects, resulting in the problem of negative values of $m^2(\nu_e)$. The advent of the MAC-E filter spectrometers during 1990s made it possible to reduce the uncertainties by two orders of magnitude. The figure is taken from [Eic09].

2.2. The MAC-E filter technique

A sensitive search for the neutrino mass in the tritium β -spectrum requires measuring close to a low endpoint with high luminosity as well as with high resolution. Both these basic requirements are fulfilled in the concept of “magnetic adiabatic collimation with an electrostatic filter”, abbreviated as MAC-E filter. This principle, firstly introduced in 1970s, was later adopted for the use in the neutrino mass experiments at Troitsk [Lob85] and Mainz [Pic92a].

The main components of the MAC-E filter are described in Fig. 2.3. Two superconducting solenoids are placed on both sides of a cascading system of cylindrical electrodes. The solenoids generate a highly inhomogeneous magnetic field guiding the electrons along the magnetic field lines from their origin in the source to the detector. The magnetic field is symmetrical with respect to the central plane (so-called analyzing plane) of the spectrometer. The minimum field strength B_A at the central plane is suppressed by several orders of magnitude with respect to the maximum B_{\max} occurring at the center of the solenoids. The second important ingredient of the MAC-E filter is the retardation of the electrons by an electrostatic field, which at the center of the spectrometer is nearly parallel to the magnetic field lines.

The magnetic gradient force transforms most of the transverse energy E_{\perp} of the electron

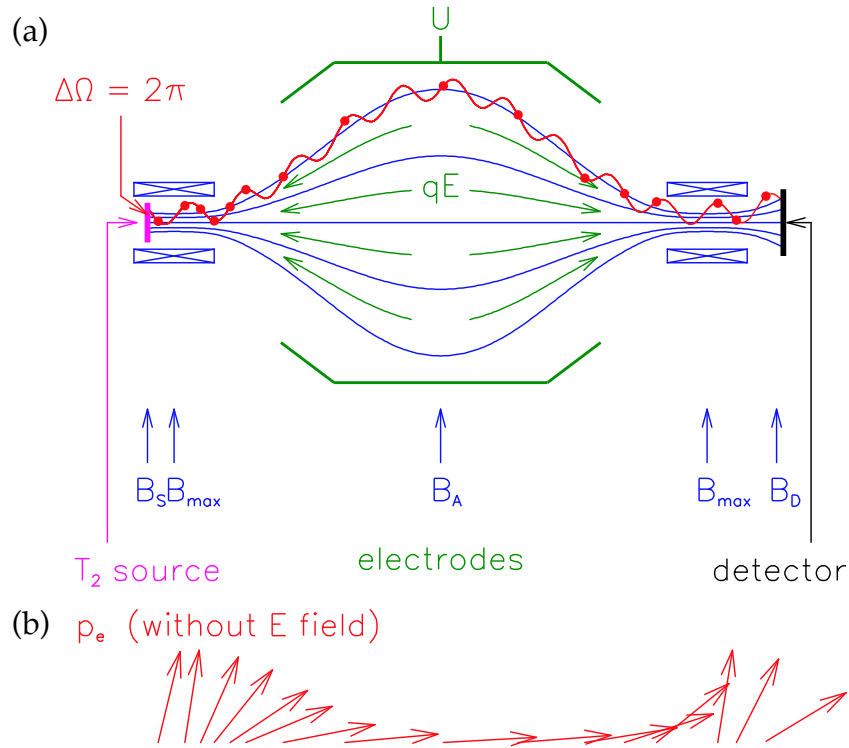


Fig. 2.3: The principle of the MAC-E filter. **(a)** Schematic view of the experimental setup: the electrons created in the source are guided along magnetic field lines towards the detector. Only those electrons with sufficient longitudinal energy can overcome the electrostatic retardation barrier and get reaccelerated onto the detector. **(b)** Momentum transformation due to the adiabatic invariance of the magnetic orbit momentum μ in the inhomogeneous magnetic field. Here, the electrostatic retardation is left out and only the magnetic gradient force is considered. The figure is taken from [Wei09].

into the longitudinal motion. This is illustrated in Fig. 2.3(b) by a smooth variation of the momentum vector. Due to the slowly varying magnetic field the momentum transforms adiabatically, therefore the magnetic moment μ keeps constant [KAT04]²:

$$\mu = \frac{E_{\perp}}{B} = \text{const.} \quad (2.12)$$

The criterion of adiabatic motion can be represented as a condition that the magnetic field B varies only slightly during one cyclotron circulation of the electron. Thus, the β -electrons, isotropically emitted at the source, are transformed into a broad beam of electrons flying almost parallel to the magnetic field lines. This parallel beam of electrons is running against an electrostatic potential formed by a set of cylindrical electrodes. All electrons with enough energy to pass the electrostatic barrier are reaccelerated and collimated onto a detector, all others are reflected. Therefore the spectrometer acts as an integrating high-pass filter. Varying the electrostatic retarding potential allows the measurement of the β -spectrum (or any other electron spectrum) in an integrating mode.

The energy resolution of a MAC-E filter follows from Eq. 2.12. In the extreme case where the total kinetic energy of the electron at the starting point, E_{start} , is given in the form of

²Since the electrons generated in tritium β -decay reach a maximum value of $\gamma = 1.04 \approx 1$, the non-relativistic approximation may be used.

transverse energy, the adiabatic transformation according to Eq. 2.12 will result in a small remainder of transverse energy left over at the analyzing plane. This maximum amount of non-analyzable energy defines the theoretical resolution ΔE ,

$$\Delta E \equiv (E_{\perp})_{\max} = E_{\text{start}} \cdot \frac{B_A}{B_{\max}}. \quad (2.13)$$

The resolution is therefore in principle only limited by the minimum ratio B_A/B_{\max} of the magnetic fields that can be realized experimentally.

In order to suppress electrons which have a very long path within the tritium source and therefore exhibit a high scattering probability, the electron source is placed in a magnetic field B_S which is lower than the maximal magnetic field B_{\max} . This restricts the maximum accepted starting angle of the electrons $\theta_{\text{start}}^{\max}$ due to Eq. 2.12 to

$$\theta_{\text{start}}^{\max} = \arcsin \left(\sqrt{\frac{B_S}{B_{\max}}} \right). \quad (2.14)$$

The normalized transmission function of the MAC-E filter with the retarding potential $U < 0$ can be analytically expressed for an isotropically emitting electron source as [Pic92a, KAT04]

$$T(E_{\text{start}}, qU) = \begin{cases} 0 & \text{for } E_{\text{start}} < qU \\ \frac{1 - \sqrt{1 - \frac{(E_{\text{start}} - qU) B_S}{E_{\text{start}} B_A}}}{1 - \sqrt{1 - \frac{B_S}{B_{\max}}}} & \text{for } qU \leq E_{\text{start}} \leq qU \frac{B_{\max}}{B_{\max} - B_A} \\ 1 & \text{for } E_{\text{start}} > qU \frac{B_{\max}}{B_{\max} - B_A}. \end{cases} \quad (2.15)$$

Here

- E_{start} is the starting kinetic energy of the electron in the source,
- B_S is the magnetic field strength in the source,
- B_A is the magnetic field strength in the analyzing plane,
- B_{\max} is the magnetic field strength in the centre of the solenoids,
- U is the maximum retardation potential reached in the analyzing plane, and
- q is the electron charge, $q = -|e|$.

The normalized transmission function is depicted in Fig. 2.4 for the case of the KATRIN main spectrometer where the following features will be realized: $\Delta E = 0.93$ eV at $E_{\text{start}} = 18.6$ keV, therefore $\Delta E/E_{\text{start}} \approx 1 : 20\,000$, and $\theta_{\text{start}}^{\max} = 50.77^\circ$. Finally, it should be noted that the magnetic flux

$$\Phi = \int B \, dA \quad (2.16)$$

is conserved during the transport of the electrons from the β -emitter to the detector. Therefore, at the analyzing plane the electrons form a broad beam of area

$$A_A = A_S \cdot \frac{B_S}{B_A}, \quad (2.17)$$

where A_S is the effective source area. This relationship illustrates the need for a large diameter of the MAC-E filter spectrometer vessel.

2. The KATRIN experiment

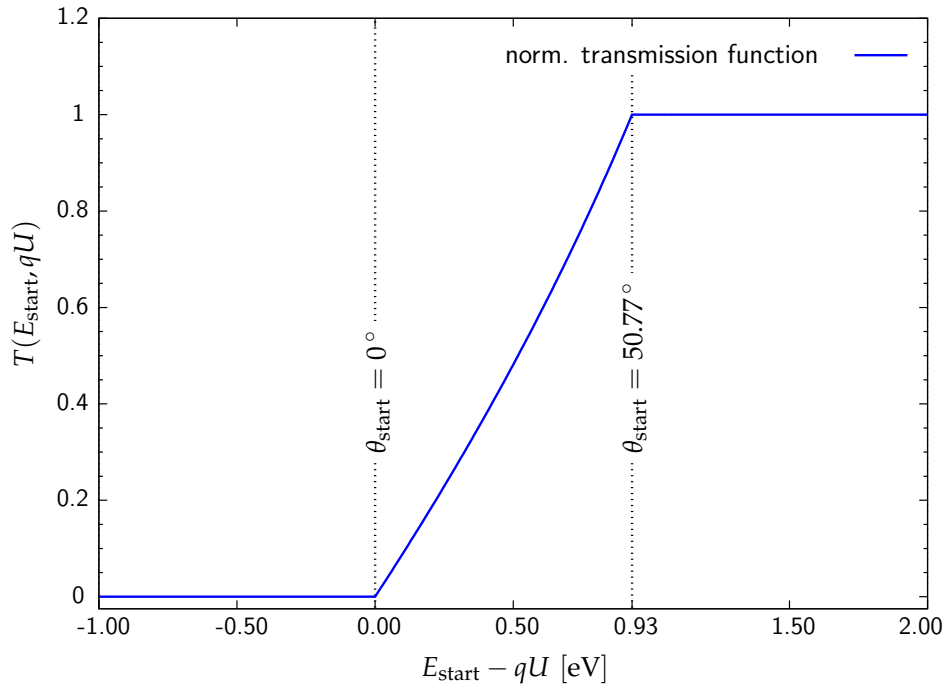


Fig. 2.4: The normalized transmission function of an electron spectrometer of the MAC-E filter type. The transmission function shown was calculated according to Eq. 2.15 for the case of the KATRIN main spectrometer with the following parameters of the magnetic field: $B_S = 3.6$ T, $B_A = 0.3$ mT and $B_{\max} = 6$ T. The figure is taken from [Val09a].

2.3. Brief overview of the KATRIN experimental setup

The key components of the KATRIN experimental setup, depicted in Fig. 2.5, shall be briefly discussed in the following paragraphs. Basically, the very complex setup, currently being built and commissioned at the Karlsruhe Institute of Technology and spanning over 70 m in length, can be described as follows: the high luminosity tritium source ensures a constant count rate of β -electrons which are magnetically guided to a tandem of spectrometers (both of the MAC-E filter type). The so-called pre-spectrometer rejects the large low-energy part of the tritium β -spectrum which does not carry significant information for the determination of $m(\nu_e)$. Thus, only the electrons originating from the last ≈ 300 eV below the tritium endpoint enter the so-called main spectrometer. Here the high precision energy analysis takes place. The electrons which pass the analyzing voltage are counted in the detector. Not shown in the overview scheme in Fig. 2.5 is the so-called monitor spectrometer. Its purpose is the continuous monitoring of the stability of the high voltage (HV) applied to the main spectrometer. The monitor spectrometer, which is directly related to the topic of this work, will be described in Chap. 3. For the discussion of the various sources of background in the KATRIN experiment the reader is referred to [KAT04].

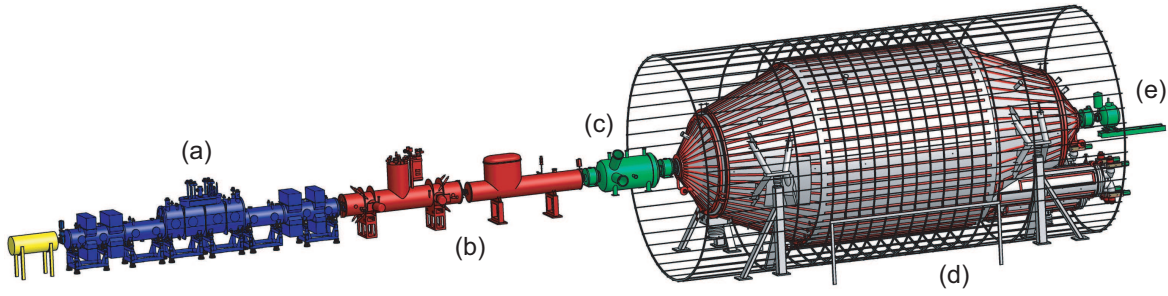


Fig. 2.5: The schematic overview of the ≈ 70 m long experimental setup of the KATRIN experiment. The major components shown left to right are: **(a)** calibration and monitoring system (CMS) and windowless gaseous tritium source (WGTS), **(b)** transport and pumping section (differential pumping section, DPS, and cryogenic pumping section, CPS), **(c)** pre-spectrometer, **(d)** main spectrometer, and **(e)** detector system. The monitor spectrometer is not shown. The figure is based on [KAT04].

Tritium source

The windowless gaseous tritium source (WGTS) delivers 10^{10} β -decay electrons per second. Such a high luminosity is crucial for obtaining sufficient count rate of electrons in the end-point region of the tritium β -spectrum. Ultra-cold molecular tritium (T_2) gas of high isotopic purity ($> 95\%$) and stable temperature ($T = 30$ K) will be injected through a set of capillaries in the middle of the 10 m long beam tube³. The diameter of the beam tube amounts to 90 mm and the magnetic guiding field in the source area was chosen as $B_S = 3.6$ T. The gas injection pressure allows adjustment of the column density ρd of tritium molecules. The optimal working point of $\rho d = 5 \times 10^{17}$ cm^{-2} was determined for KATRIN. The demand for high sensitivity of KATRIN requires a stabilization of the column density to the level of 0.1%. This in turn implies the stabilization of the source temperature and the injection pressure at the level of 30 mK and 10^{-6} mbar, respectively. It was shown in [Gro09] how the stringent KATRIN requirements can be fulfilled.

Transport and pumping section

The background generated by the tritium decay within the spectrometers must be less than 10^{-3} counts s^{-1} which was thought⁴ to correspond to the partial pressure of tritium of 10^{-20} mbar in the main spectrometer [KAT04]. In order to achieve such a low background in the β -spectrum endpoint region the flow of tritium into the spectrometer section has to be lower than 10^{-14} mbar l s^{-1} . Therefore, the system connecting the WGTS with the tandem of spectrometers is not only responsible for the adiabatic transport of the β -electrons, but also for preventing the tritium to reach the spectrometers. This very important task will be realized by the combination of differential and cryogenic pumping. The latter relies on the

³About 40 g of gaseous T_2 will have to be cycled through KATRIN's tritium source per day, which corresponds to an injection rate of 1.7×10^{11} Bq s^{-1} .

⁴It was pointed out recently [Fra11] that radon atoms, which emanate from materials inside the vacuum region of the KATRIN spectrometers, are able to penetrate deep into the magnetic flux tube. Thus, the α -decay of Rn, during which a significant number of low energy electrons can be created, contributes to the background in the region of β -spectrum endpoint. In this regard not only tritium has to be avoided in the KATRIN spectrometers, but also radon.

2. The KATRIN experiment

concept of cryotrapping at cold surfaces. The inner walls of the CPS beam tube will be covered with argon frost at a temperature of 4.5 K to enhance the pumping rate by increasing the effective surface area (see [Kaz08, Eic09] for details). A scheme of the WGTS connected to the transport and pumping section is depicted in Fig. 2.6.

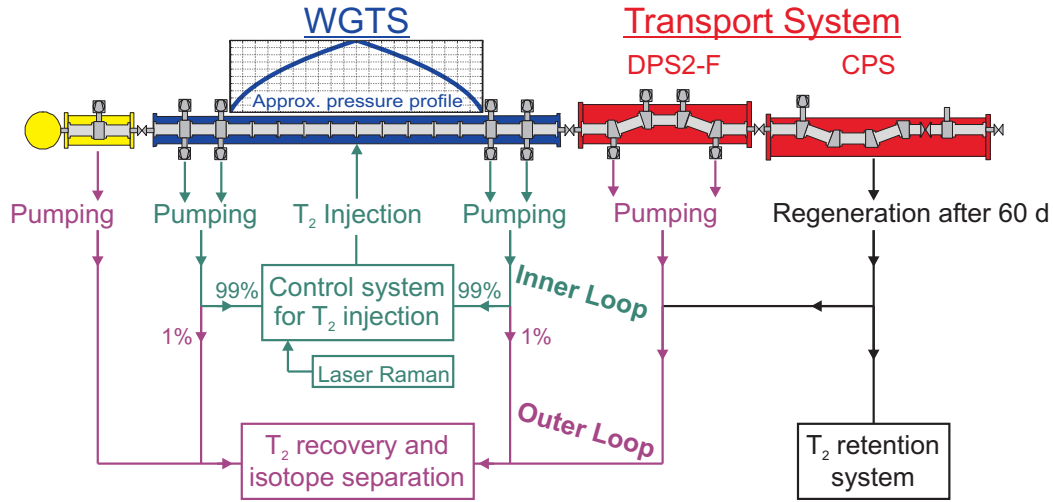


Fig. 2.6: The schematic view of the tritium-related parts of the KATRIN experimental setup. The WGTS is operated in closed loops in order to achieve stable injection rate and purity of tritium. Tritium is injected in the middle of the WGTS tube and pumped out at its ends. About 99% of the tritium is retransferred to the control system for T₂ injection (Inner Loop), 1% is redirected into the laboratory tritium recovery and isotope separation system for purification (Outer Loop). Tritium from the transport system is transferred to the Outer Loop and the retention system. The figure is taken from [Eic09].

Spectrometers

The tandem setup of the pre- and main spectrometers is schematically shown in Fig. 2.7. The pre-spectrometer (length of $\simeq 3.4$ m, diameter of $\simeq 1.7$ m) is intended to act as a “pre-filter”, *i. e.* only the electrons with kinetic energies very close to the β -spectrum endpoint will pass its fixed analyzing voltage. This feature will cut down the flux of β -electrons from 10^{10} to 10^3 electrons per second. For this purpose the rather moderate energy resolution of $\Delta E/E \simeq 1 : 200$ will be fully sufficient. The adiabatic motion of the electrons within the pre-spectrometer is ensured. Further, the electrons carrying the information on the neutrino mass enter the large main spectrometer (length of $\simeq 23$ m, diameter of $\simeq 10$ m) where their kinetic energy is analyzed with the energy resolution of 0.93 eV at 18.6 keV. In order to minimize the background events from ionization of the residual gas both spectrometer vessels are operated at ultrahigh vacuum conditions (base pressure below 10^{-11} mbar, see [Wol09]).

The large dimensions of the main spectrometer vessel together with the requirements for mechanical precision and ultrahigh vacuum present challenges of its own. However, the task is further complicated by the necessity of ultra-low background in the main spectrometer. A sophisticated concept of the background reduction by a double-layer screening wire electrode was developed [Fla04, Val06, Val09a, Val10] and realized [Pra11].

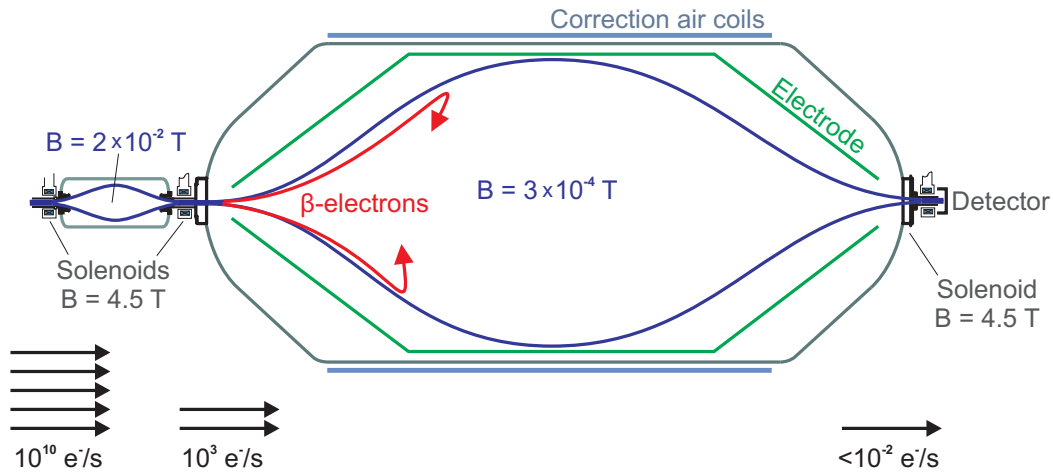


Fig. 2.7: The schematic view of the tandem of KATRIN electron spectrometers. The pre-spectrometer acts as a pre-filter for the main spectrometer where the precise energy analysis of the electrons takes place. The spectrometers are connected by one superconducting transport solenoid. The blue lines indicate the magnetic field lines. The electrode inside the main spectrometer marked green is only a schematic representation: in reality, the whole vessel of the main spectrometer lies on HV and inside the vessel there are two layers of “massless” wire electrode set to more negative analyzing potential. The correction air coils (light blue) compensate the Earth's magnetic field in the region of the analyzing plane where the guiding magnetic field reaches its minimum of 0.3 mT. In red the paths of the β -electrons rejected by the analyzing voltage in the main spectrometer are illustrated. Typical electron count rates are denoted in the figure: the pre-spectrometer suppresses the electron rate from 10^{10} electrons s^{-1} down to 10^3 electrons s^{-1} . The count rate of 10^{-2} electrons s^{-1} impinging on the detector denotes only the background rate. The electron rate achieved during the actual tritium measurement may differ from this value. The figure is taken from [Eic09].

The spectrometers share one superconducting solenoid which lies at ground potential. The electrons which do not pass the retarding voltage of the main spectrometer are reflected back to the high magnetic field region between the spectrometer vessels. In such conditions the Penning trap is easily formed and the electrons stored there can significantly increase the background rate. This potential source of background was recognized and measures will be taken for periodical emptying the Penning trap [Val09a, Bec10, Hil11].

Parallel to the main KATRIN beam line, the MAC-E filter of the former Mainz Neutrino Mass Experiment will be operated using the same HV source as the main spectrometer in order to continuously check the stability of its retardation potential with calibration sources based on atomic and nuclear energy standards [KAT04]. In Chap. 3 the purpose of the monitor spectrometer will be discussed in detail.

Detector

The electrons passing the analyzing voltage in the middle of the main spectrometer will be counted by a sophisticated detector system. The main component of this system is the large-area silicon PIN diode with high energy resolution ($\simeq 1$ keV for 18.6 keV electrons) and very thin entrance window. The Si PIN diode is segmented in a dartboard manner into 148 segments including a central “bull's eye” part with four segments. The pixel layout will

enable to monitor the radial density of the WGTS and the electron transport properties of the spectrometers. In addition, it will be possible to reject the background events originating outside of the analyzed magnetic flux [Dun08].

2.4. Systematic and statistical uncertainties

When aiming for the unprecedented sensitivity on the neutrino mass in the sub-eV range, it is crucial to assess possible systematic uncertainties of the experiment critically. In addition, corresponding measures in terms of systematic studies and control of many experimental parameters have to be undertaken. The main sources of systematic uncertainties can be briefly listed as follows [KAT04]:

1. final states of the $(^3\text{He T})^+$ daughter molecule

The distribution of the final states of the $(^3\text{He T})^+$ daughter molecule must be considered when the molecular tritium is used. The excitation energy of the lowest electronic excited state of the $(^3\text{He T})^+$ molecule is 27 eV. Therefore, it can be cut out by an appropriate choice of the analyzing interval of the β -spectrum. However, the uncertainty comes from the rotational and vibrational excitations of the electronic ground state. The mean excitation energy of the rotational-vibrational excitations is 1.7 eV while the width is $\Gamma \simeq 0.36$ eV. The width Γ limits the energy resolution which can be achieved with a β -decay experiment using molecular tritium source. Reliable quantum-chemical calculations, necessary for modeling the final states distribution, are available [Sae00].

2. elastic and inelastic scattering within the WGTS

The inelastic scattering of the electron on its way through the tritium source will lead to energy losses δE . Such an effect obviously changes the shape of the β -spectrum. In addition, an elastic collision of the electron within the source may change the angle θ of the electron momentum with respect to the applied magnetic field. This in turn may cause the electron to lose a fraction of its longitudinal kinetic energy (in the case of increase of θ) or bring the electron into the transmitted angular range (if θ decreases below the maximal accepted angle). Therefore, the electron energy loss function $f(\delta E)$ has to be known precisely. For this purpose dedicated calibration runs with an electron gun are planned [Val09b, Hug10, Val11]. The inelastic scattering within the WGTS represents the dominant systematic uncertainty of the experiment.

3. fluctuations of the column density of the WGTS

Fluctuations of the column density ρd of the WGTS will directly influence the signal rate and the aforementioned energy loss δE of electrons by scattering. Thus, the column density has to be stabilized and regularly monitored. Repeated measurements with an electron gun in breaks between successive neutrino mass measurement runs are foreseen for such purposes. Moreover, the column density can be monitored via laser Raman spectrometer [Stu10] as well as with the help of a detector placed in the rear wall (the very left side of the experimental setup shown in Fig. 2.5). Generally, this uncertainty can be reduced by high isotopic purity of tritium and temperature stabilization of the WGTS.

4. charging of the WGTS due to remaining ions

The β -decay activity of the tritium gas inside the WGTS is about 10^{11} Bq. One β -electron creates on average 15 secondary electron-ion pairs. Thus, various positive ions (T^+ , T_2^+ and T_3^+) can be formed in the source. Moreover, electrons colliding with T_2 molecules can produce T_2^- ions. As a result of the various states of tritium in the WGTS the observed β -spectrum will correspond to the sum of β -spectra with different endpoint energies. The effects of the plasma phenomena on the neutrino mass measurement were discussed in [Nas05]. The measurements of the ion concentration via Fourier transform ion cyclotron resonance [Ubi09] will address this issue.

5. transmission function of the main spectrometer

In reality, the sharp transmission function (cf. Eq. 2.15 and Fig. 2.4) of the MAC-E filter is complicated by inhomogeneities of the electric potential and magnetic field in the region of the analyzing plane. Such effects are intrinsic to the concept of the MAC-E filter spectrometer and will be especially noticeable in the case of the main spectrometer where the diameter of the analyzing plane amounts to $\simeq 9$ m. These effects lead to broadening and smearing of the transmission function and must be accounted for in the analysis. Using a segmented detector helps to reduce the influence of these effects, but nevertheless extensive calibration measurements (performed for each pixel of the detector) need to be carried out to achieve a detailed understanding of the transmission properties of the main spectrometer. For this purpose the calibration source based on condensed ^{83m}Kr [Ost08] will be utilized (see below).

6. fluctuations of the absolute energy scale

The kinetic energy of the β -electrons will be analyzed on the energy scale which is defined by the difference between the source potential and the analyzing potential of the main spectrometer. Any time instability of the energy scale directly influences the measured β -spectrum. Details of the concept aiming for ultra-precise monitoring of the energy scale stability are discussed in Chap. 3.

To summarize the various systematic uncertainties, the final state distribution (1) of the daughter molecule is inevitable due to the use of molecular tritium. The effects described in items (2) to (4) stem from the gaseous tritium source. Finally, the effects (5) and (6) result from the utilization of the MAC-E filter technique. None of the individual systematic effects is expected to give the uncertainty contribution of more than about $\Delta m_{\text{syst},i}^2 = 0.007 \text{ eV}^2 c^{-4}$ [KAT04]. The total systematic uncertainty (where further minor contributions are included as well [KAT04]) with respect to the observable $m^2(\nu_e)$ is therefore estimated as

$$\Delta m_{\text{syst}}^2 = \sqrt{\sum_i \left(\Delta m_{\text{syst},i}^2 \right)^2} = 0.017 \text{ eV}^2 c^{-4}. \quad (2.18)$$

In the integral β -spectrum measured with a spectrometer of the MAC-E filter type there exist a certain point (narrow energy region) few eV below the endpoint where the highest sensitivity on $m^2(\nu_e)$ can be reached. Such a point is found to be in the region where the signal-to-background ratio is equal to 2 [Ott94]. Considering the parameters of the KATRIN experiment, this region lies about 3 eV below the endpoint E_0 . Therefore, it seems rather inconvenient to use a uniform distribution of the measurement time. Instead, given an effective measurement time of KATRIN of three years, an optimal distribution of mea-

2. The KATRIN experiment

measuring time spent at various settings of the retardation energy should be followed. Such a distribution, illustrated in Fig. 2.8, optimizes the statistical uncertainty [Kas08]. It should be noted that the optimal measurement time distribution depends also strongly on the background rate and the width of the transmission function.

The dependence of the statistical uncertainty on the lower limit of the measuring interval is shown in Fig. 2.9 for several configurations of the KATRIN setup. It can be seen that increasing the measuring interval more than $\simeq 35$ eV below the endpoint does not further reduce the statistical error. For an interval of $[E_0 - 30 \text{ eV}, E_0 + 5 \text{ eV}]$ and three years of effective measurement time at a total background rate of $0.01 \text{ counts s}^{-1}$, a statistical uncertainty of similar size as the total systematic uncertainty will be reached [KAT04]:

$$\Delta m_{\text{stat}}^2 = 0.018 \text{ eV}^2 c^{-4}. \quad (2.19)$$

The total uncertainty, obtained from quadratically adding the systematic (Eq. 2.18) and statistic (Eq. 2.19) uncertainties, amounts to

$$\Delta m_{\text{tot}}^2 = 0.025 \text{ eV}^2 c^{-4}, \quad (2.20)$$

which leads to a discovery potential [KAT04] of

$$\begin{aligned} m(\nu_e) &= 0.30 \text{ eV } c^{-2} & (3\sigma) \\ \text{or } m(\nu_e) &= 0.35 \text{ eV } c^{-2} & (5\sigma). \end{aligned} \quad (2.21)$$

Should no neutrino mass signal be found, the sensitivity of the KATRIN experiment will allow to set an upper limit of

$$m(\nu_e) < 0.2 \text{ eV } c^{-2} \quad (90\% \text{ C.L.}). \quad (2.22)$$

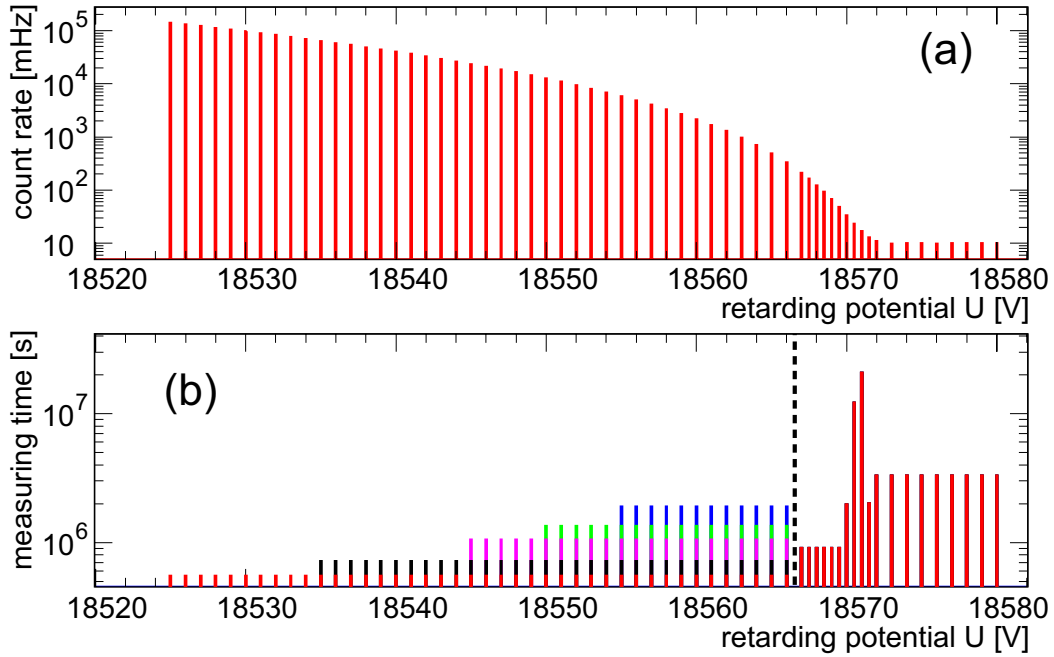


Fig. 2.8: The optimized distribution of measurement time of the β -spectrum. **(a)** Simulated count rate at various settings of the retardation potential for a given background rate of $0.01 \text{ counts s}^{-1}$. **(b)** Optimized measurement time per retarding potential of the above spectrum for widths from 50 eV (red) to 20 eV (blue) below E_0 of analyzed intervals, total measurement time 3 years. The height of the entries represents the integrated time over many scans. At $U > 18566$ V, qU being the spectrometer retarding energy, the measurement time is not influenced by the lower limit of the energy interval. Such optimization allows to improve the statistical accuracy by about 40–50% as compared to a uniform distribution of the measurement time. The figure is taken from [KAT04].

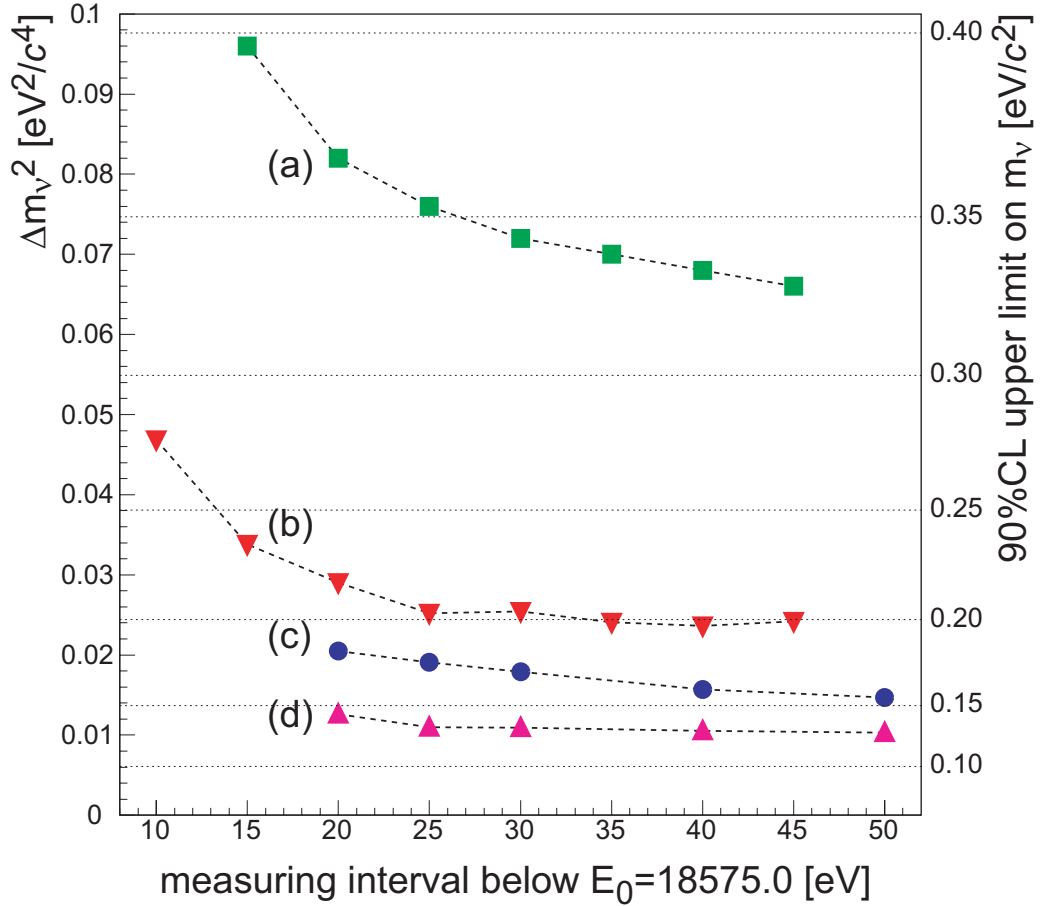


Fig. 2.9: The statistical uncertainty Δm_{stat}^2 (for the measurement time of three years) and the corresponding 90% C.L. upper limit on $m(\nu_e)$ (right y axis) as a function of the lower limit of the measuring interval below E_0 . Different configurations and background rates are compared: **(a)** values stated in the KATRIN Letter of Intent [KAT01], **(b)** increased source strength and isotopic purity of the T_2 gas, spectrometer diameter enlarged to 10 m, uniform measurement time, **(c)** same parameters as in **(b)**, but taking into account the optimized measurement point distribution shown in Fig. 2.8, **(d)** reduction of the background rate from $0.01 \text{ counts s}^{-1}$ as in **(a)** to **(c)** down to $0.001 \text{ counts s}^{-1}$. The figure is taken from [KAT04].

3. Stability monitoring and calibration of the energy scale in KATRIN

In Sect. 2.4 the possible instability of the energy scale of the KATRIN spectrometers was recognized as one of the six major sources of the systematic uncertainties in the KATRIN experiment. The principle of the MAC-E filter technique (see Sect. 2.2) relies on the precise knowledge of the retarding potential which is experienced by the β -electrons in the analyzing plane of the spectrometer. Therefore, the challenge of knowing the retarding potential precisely enough in every moment during the measurement is inevitable in the KATRIN experiment.

In this chapter firstly the motivation for the continuous monitoring of the energy scale stability as well as for the absolute calibration of the scale is discussed (Sect. 3.1). In Sect. 3.2 the concept of monitoring of the KATRIN energy scale stability is described. Finally, the possible sources of electrons of well-defined energies are considered in detail in Sect. 3.3.

3.1. Motivation for continuous monitoring and absolute calibration of the energy scale

It was shown in Eq. 2.18 that the total systematic uncertainty of KATRIN with respect to the observable $m^2(\nu_e)$ is expected to be $\Delta m_{\text{sys}}^2 = 0.017 \text{ eV}^2 c^{-4}$, where each of the six major systematic uncertainties is limited by $\Delta m_{\text{sys},i}^2 = 0.007 \text{ eV}^2 c^{-4}$. The same constraint holds for the instability of the retarding high voltage (HV), thus

$$\Delta m_{\text{HV}}^2(\nu_e) = 0.007 \text{ eV}^2 c^{-4}. \quad (3.1)$$

The relationship between such a requirement and a quantity relevant to the HV stability can be derived in the following way [Rob88]. The β -spectrum, precisely described by Eq. 2.9, can be approximated in the vicinity of the endpoint E_0 as

$$\frac{d\dot{N}}{dE} = a \cdot (E_0 - E) \sqrt{(E_0 - E)^2 - m^2(\nu_e) c^4}, \quad (3.2)$$

where a includes all constant factors in Eq. 2.9 which can be omitted in this approximation. The observable $m^2(\nu_e)$ is used here in accordance with Eq. 2.8. Assuming the neutrino mass to be small, one can rewrite Eq. 3.2 with the help of Taylor series in the vicinity of the point

3. Stability monitoring and calibration...

$m^2(\nu_e) = 0$ as

$$\frac{d\dot{N}}{dE} (m^2(\nu_e) \simeq 0) \approx a \cdot (E_0 - E)^2 - \frac{a}{2} m^2(\nu_e) c^4, \quad (3.3)$$

where the terms of $\mathcal{O}(m^4(\nu_e) c^8)$ and higher orders were omitted. Evidently, for $m^2(\nu_e) = 0$ one can introduce

$$g(E) \equiv \frac{d\dot{N}}{dE} (m^2(\nu_e) = 0) = a \cdot (E_0 - E)^2, \quad (3.4)$$

where $g(E)$ denotes the simplified shape of the β -spectrum for zero neutrino mass.

In order to assess the influence of the instability of HV scale on the spectrum, a periodic fluctuation of the HV shall be introduced. The fluctuation can be described by a Gaussian distribution with a given width σ and mean value μ equal to zero:

$$f(x) = \frac{1}{\sigma\sqrt{2\pi}} e^{-\frac{(x-\mu)^2}{2\sigma^2}} = \frac{1}{\sigma\sqrt{2\pi}} e^{-\frac{x^2}{2\sigma^2}}. \quad (3.5)$$

The instability of the HV can be interpreted in terms of fluctuations of the energy barrier in the analyzing plane which is experienced by the β -electrons. This way the width σ can be expressed in energy units. The shape of the β -spectrum $g(E)$ affected by the HV fluctuation follows from the convolution

$$\begin{aligned} (f \otimes g)(E) &= \int_{-\infty}^{\infty} f(x) \cdot g(E-x) dx \\ &= \int_{-\infty}^{\infty} \frac{1}{\sigma\sqrt{2\pi}} e^{-\frac{x^2}{2\sigma^2}} a (E_0 - E + x)^2 dx \\ &= a (E_0 - E)^2 \underbrace{\frac{1}{\sigma\sqrt{2\pi}} \int_{-\infty}^{\infty} e^{-\frac{x^2}{2\sigma^2}} dx}_{=1} + 2a (E_0 - E) \underbrace{\frac{1}{\sigma\sqrt{2\pi}} \int_{-\infty}^{\infty} x e^{-\frac{x^2}{2\sigma^2}} dx}_{=\mu=0} \\ &\quad + a \underbrace{\frac{1}{\sigma\sqrt{2\pi}} \int_{-\infty}^{\infty} x^2 e^{-\frac{x^2}{2\sigma^2}} dx}_{=\sigma^2} \\ &= a (E_0 - E)^2 + a \sigma^2. \end{aligned} \quad (3.6)$$

From the comparison of the simplified β -spectrum in Eq. 3.3 with the result of the convolution in Eq. 3.6 it follows that the introduced HV fluctuation affects the β -spectrum as a shift towards negative $m^2(\nu_e)$ values,

$$m^2(\nu_e) c^4 = -2\sigma^2. \quad (3.7)$$

This relationship shows that an *unrecognized* fluctuation of the retarding potential in the form of a Gaussian broadening of the width σ imprints on the β -spectrum in the manner of reducing the neutrino mass squared:

$$\Delta m^2(\nu_e) c^4 = -2\sigma^2. \quad (3.8)$$

Finally, comparing Eq. 3.8 with the KATRIN requirement stated in Eq. 3.1, the upper limit on the unrecognized fluctuation of the HV scale is obtained:

$$\Delta m_{\text{HV}}^2(\nu_e) = 0.007 \text{ eV}^2 c^{-4} \Rightarrow \sigma \leq 0.059 \text{ eV}. \quad (3.9)$$

The upper limit on σ stated in Eq. 3.9 can be interpreted as the requirement on the HV scale stability of $\Delta_{\text{abs}}(\text{HV}) = \pm 60 \text{ meV}$ which represents the portion of $\Delta_{\text{rel}}(\text{HV}) = \pm 3.2 \text{ ppm}$ of the retarding potential of 18.6 keV corresponding to the tritium endpoint. This requirement defines the aim of the task ‘‘Calibration and Monitoring’’ within the KATRIN project. At first sight it may seem that the stringent limit on the HV scale stability has to be fulfilled over the whole three years period of KATRIN data taking. However, the requirement is relieved by the fact that the procedure of data taking in KATRIN will consist of a series of individual tritium runs of two months length. The absolute energy scale is not relevant here as from each run a separate value of $m^2(\nu_e)$ will be determined. On the other hand, the successful stabilization of the HV scale over more than one tritium run would allow to combine the data series obtained in the runs. Stabilizing and, moreover, monitoring the HV of $\approx 20 \text{ kV}$ on the ppm level over time periods spanning several months is an uneasy task as will be seen later in this work. In addition, it should be noted that foreseen length of the single tritium run may change slightly in the future which would alter the aforementioned requirements on the HV scale stability correspondingly.

The influence of the imperfections of the energy scale on the observable $m^2(\nu_e)$ was studied in detail in [Kas04, KAT04] with the help of the β -spectra simulated for parameters very close to those of the KATRIN experimental setup. In Fig. 3.1 the systematic shift $\Delta m^2(\nu_e)$ is plotted for four cases of the imperfections. In the first plot (a) the absolute HV scale varies over time in two exemplified schemes: having an unaccounted shift of amplitude d of the HV divider and the digital voltmeter in 50% of the total measuring time or having a Gaussian variation of the energy scale with an appropriate value of σ . Taking the maximal allowed systematic shift of $\Delta m_{\text{HV}}^2(\nu_e) = 0.007 \text{ eV}^2 c^{-4}$ (illustrated by the horizontal dotted line), the Gaussian variations of the HV have to be limited to $\sigma \leq 60 \text{ mV}$ in a good agreement with the analytical description given in Eq. 3.9. Another potential source of the HV imperfections could be inaccuracies δ of the HV slope of the calibration line of the voltmeter along the energy interval under analysis (plot (b)). For the two cases of an unaccounted constant or a Gaussian-varying HV slope error δ , inaccuracies have to be limited to the 10^{-3} level, *e. g.* less than 50 mV along the analyzing interval of 50 eV below the endpoint energy.

So far only the stability of the HV scale was discussed. Here the absolute calibration shall be mentioned as well. The effect of a wrong calibration can be visualized as an unrecognized constant shift (bias) of the HV scale over the whole energy range used for evaluation. In [Kas04] it was demonstrated that the unrecognized energy bias is much less critical with respect to $m^2(\nu_e)$ than the unrecognized instability of the energy scale. It was found that the results are insensitive to constant energy scale bias, *e. g.* an unrecognized constant energy bias of 10 eV implies the shift $\Delta m^2(\nu_e)$ of the order of $10^{-12} \text{ eV}^2 c^{-4}$ which is negligible for KATRIN. Actually, the notable insensitivity of the observable $m^2(\nu_e)$ with respect to the constant energy bias comes by no surprise as the endpoint energy E_0 of the tritium β -spectrum was a fitted parameter in [Kas04]. This is a usual procedure in fitting the β -spectrum. It is a well known fact that in the least-squares fit of the β -spectrum the endpoint energy E_0 is strongly correlated with the observable $m^2(\nu_e)$. An example of such correlation is shown in Fig. 3.2.

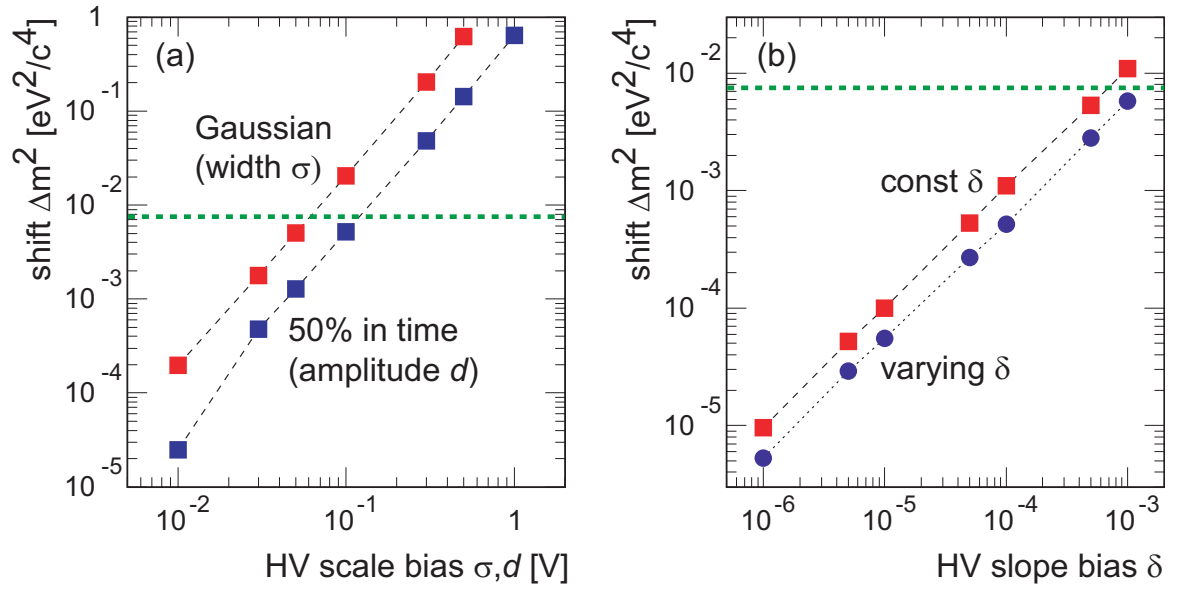


Fig. 3.1: The systematic shift $\Delta m^2(\nu_e)$ of the observable $m^2(\nu_e)$ due to uncertainties (a) in the HV scale and (b) in the HV slope [Kas04]. The horizontal dotted line corresponds to the maximal individual systematic shift of $\Delta m^2(\nu_e) = 0.007 \text{ eV}^2 c^{-4}$. See text for details. The figure is taken from [KAT04].

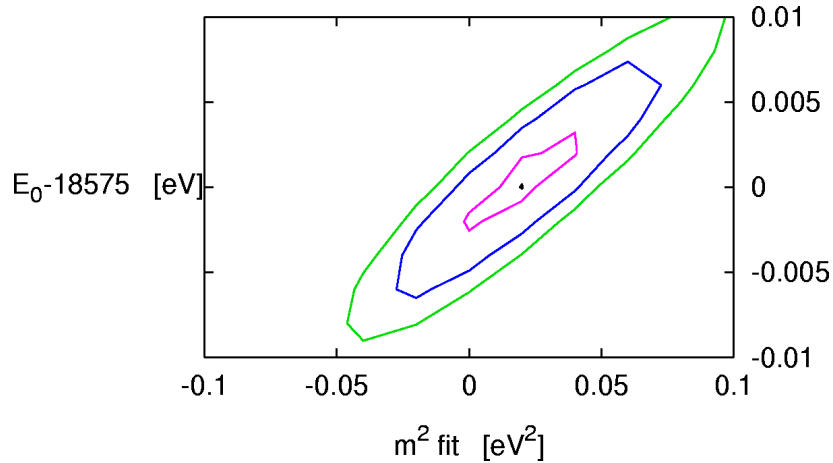


Fig. 3.2: The χ^2 contour plot illustrating the correlation between the fitted endpoint E_0 and the fitted neutrino mass squared $m^2(\nu_e)$ from Monte Carlo simulations with conditions similar to the KATRIN experiment [KAT04] for a measurement interval of 25 eV below the endpoint. The ellipses correspond to 1σ , 2σ and 3σ contours. The 2σ uncertainty of $m^2(\nu_e)$ amounts to about 0.1 eV^2 and corresponds to an endpoint uncertainty of $\Delta E_0 = \pm 5 \text{ meV}$. The figure is taken from [Ott06].

Therefore, one may consider not to fit E_0 together with the other parameters from the data, but instead to use a fixed E_0 value determined from external measurements. In other words, knowing the E_0 precisely enough would help to check the systematic uncertainties of KATRIN: any significant difference would point to unaccounted systematic errors. There is a direct relation between endpoint energy E_0 (and thus the Q value of the tritium decay¹) and the mass difference $\Delta M = M(\text{T}) - M(^3\text{He})$ of neutral parent and daughter atoms. This fact is illustrated in Fig. 3.3. The most recent determination [Nag06] of the mass difference $\Delta M(\text{T}, ^3\text{He})$ is based on high precision mass spectrometry utilizing the Penning trap. From this measurement the value of the endpoint energy of molecular tritium follows as

$$E_0(\text{T}_2) = 18\,571.8(12) \text{ eV}. \quad (3.10)$$

Unfortunately, the uncertainty of 1.2 eV is not sufficient for the purpose of KATRIN. Future measurements are anticipated to improve this uncertainty by one order of magnitude [Bla10]. Such a precision would still be insufficient for including the external value of E_0 as a fixed parameter in the analysis, on the other hand, a comparison of the fitted E_0 with the external value will be a significant check of systematic effects.

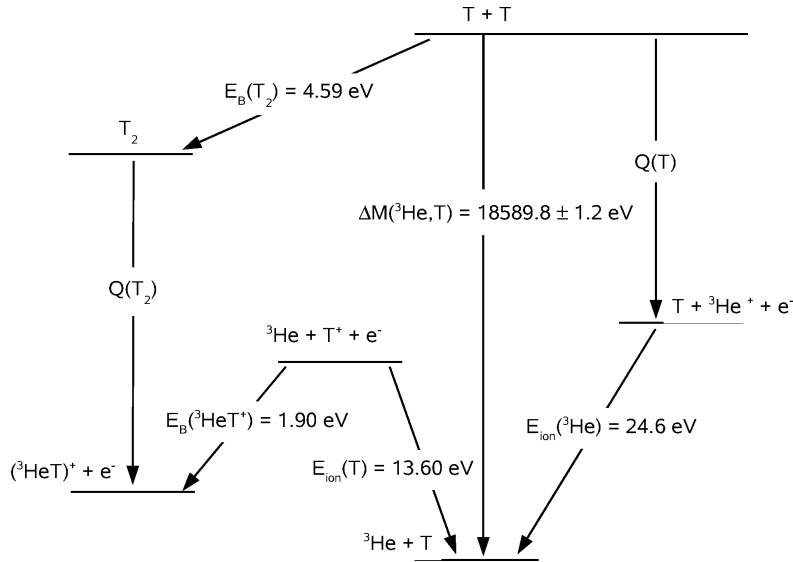


Fig. 3.3: The level diagram illustrating the relation between the mass difference $\Delta M(^3\text{He}, \text{T})$ measured by cyclotron resonance in a Penning trap [Nag06] and the Q values of molecular and atomic tritium decay. The figure is taken from [Ott08].

At this point it shall be discussed what physical quantity is actually of our concern with respect to the HV scale stability. In Fig. 3.4 a simplified overview of the various HV levels applied in the KATRIN experimental setup is presented. The measurement procedure of the tritium β -spectrum can be summarized in the following way [KAT04, Thu07, Thu11]:

- The scanning of the β -spectrum is performed by varying the potential difference between the windowless gaseous tritium source (WGTS) and the main spectrometer. The HV applied to the main spectrometer (marked as (d) in Fig. 3.4) will be fixed and actively stabilized (level of $\pm 20 \text{ mV}$) to the value U_{ana} which will be close to -18.6 kV .

¹Using the notation defined in Sect. 2.1, one can write $Q = E + E_{\text{tot } \nu} + E_{\text{rec}} + V_j = E_0 + E_{\text{rec}}$.

3. Stability monitoring and calibration...

However, it will be possible to apply up to -35 kV on the main spectrometer vessel. This approach is convenient with respect to technical difficulties connected with huge dimensions of the main spectrometer vessel. The stability of the U_{ana} voltage is crucial regarding the observable $m^2(\nu_e)$.

- Strictly speaking, the β -electrons flying through the main spectrometer will encounter the HV by about 200 V more negative with respect to U_{ana} . The reason for this is the presence of the “massless” double-layer wire electrode installed inside the main spectrometer vessel for the purpose of the background reduction. Flexible connections of the HV to the individual electrode modules will allow to produce various HV schemes (e.g. dipole). However, the stability of this additional voltage shall not represent a major technical difficulty and therefore it will be further omitted here.
- The β -electrons created in the WGTS with the starting kinetic energy of about 18.6 keV will be accelerated (or decelerated) by the voltage U_{source} of the order of 1 kV. The variation of this relatively low voltage will result in the actual scanning of the tritium β -spectrum. Direct measurement and active stabilization of U_{source} at the level of ± 20 mV is intended. The region where U_{source} will be applied is marked as (a) in Fig. 3.4 and it spans the WGTS together with the differential pumping section.
- The cryogenic pumping section (marked as (b) in Fig. 3.4) will be kept at ground potential.
- The pre-spectrometer ((c) in Fig. 3.4) will pre-filter the electrons of kinetic energies below a certain value. The stability of the retarding potential in the pre-spectrometer is not crucial regarding the neutrino mass. On the other hand, the adiabatic motion of electrons within the pre-spectrometer and low background are of concern here.
- The electrons passing the retarding potential of the main spectrometer will be focused onto the detector ((e) in Fig. 3.4). Here the post-acceleration of the electrons by up to $+25$ kV takes place prior to their impact on the detector. This measure reduces the backscatter effects of the electrons and lowers the intrinsic detector background. However, the stability of this HV is not critical.
- Lastly, the fixed HV U_{ana} will also be connected to the monitor spectrometer, noted as (f) in Fig. 3.4. This spectrometer is intended as a “direct high precision meter” of U_{ana} and it represents the main part of the HV scale monitoring concept described below in Sect. 3.2.

To summarize the considerations, the β -electrons will be analyzed according to the “effective” potential difference ΔU_{eff} between U_{ana} and U_{source} . However, the situation is complicated by several effects occurring in the WGTS and in the main spectrometer:

$$\Delta U_{\text{eff}}(t) = \left(U_{\text{ana}}(t) + \delta U_{\text{inhom.}} + \phi_{\text{spec}}(t) \right) - \left(U_{\text{source}}(t) + \delta U_{\text{space charge}}(t) + \phi_{\text{source}}(t) \right). \quad (3.11)$$

Here the time dependence of the individual terms was expressed. Firstly, the inhomogeneities $\delta U_{\text{inhom.}}$ of the retarding potential in the main spectrometer have to be investigated with the help of a suitable calibration source. For this purpose the angular-resolved electron gun is intended [Hug10]. However, such inhomogeneities can be corrected by the flexible schemes of the voltages attached to the wire electrode modules and their stability in time does not represent an issue as this voltage is of the order of 200 V. Further, the work function $\phi_{\text{spec}}(t)$ of the main spectrometer plays an important role. Its stability has to be

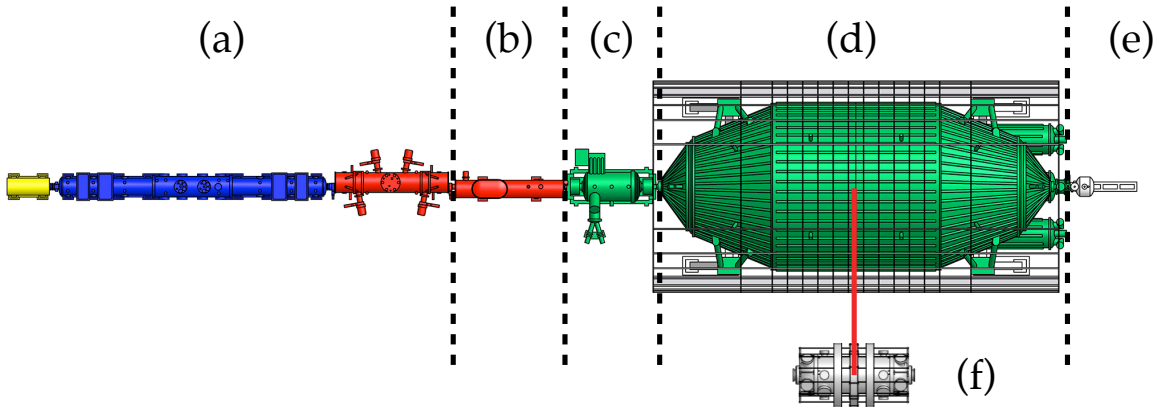


Fig. 3.4: The schematic overview of the KATRIN experimental setup from the point of view of the HV stability requirements. To the WGTS and DPS sections marked (a) the voltage of U_{source} of the order of 1 kV will be applied. The CPS section (b) will be kept at ground potential. The pre-spectrometer denoted (c) will be set to HV about 300 V “below” the tritium endpoint E_0 in order to pre-filter the β -spectrum. The HV applied to the main spectrometer (d) will be simultaneously applied to the monitor spectrometer (f) as well, this fact is represented by the red line. In the detector region (e) the post-acceleration of electrons will take place.

ensured and this should be achievable with the help of the sophisticated vacuum system of the main spectrometer [Wol09] that keeps the base pressure in the main spectrometer vessel below 10^{-11} mbar. Similarly, the work function $\phi_{\text{source}}(t)$ of the rear wall of the tritium source [Nas05] is of main concern. Any unrecognized change of $\phi_{\text{spec}}(t)$ and $\phi_{\text{source}}(t)$ has to be prevented. Finally, the charging of the WGTS due to remaining ions, mentioned in Sect. 2.4, may affect the electron kinetic energy and the stability of $\delta U_{\text{space charge}}(t)$ has to be monitored.

3.2. Concept of monitoring of the KATRIN energy scale stability

Previous Sect. 3.1 emphasized the necessity of continuous monitoring of the HV scale stability at the level of ± 60 meV per one tritium run at 18.6 keV. The schematic overview of the concept of monitoring the HV scale stability in KATRIN is depicted in Fig. 3.5 and can be summarized as follows [KAT04, Thu11]:

- A commercial HV power supply, marked in Fig. 3.5 as “HV PS #1”, will deliver the HV of value U_1 to the main spectrometer vessel including the vacuum pumps and various sensors. The ripple of the AC noise will amount to about 50 mV peak-to-peak. Post-regulation circuit will accomplish an active stabilization of the HV.
- Another commercial HV power supply “HV PS #2” featuring very high stability and very low ripple of the AC noise (20 mV peak-to-peak) will produce HV of value U_2 which will be fed to a) the HV distribution unit where surplus voltages to individual modules of the “massless” wire electrode will be created, b) the high precision HV di-

3. Stability monitoring and calibration...

vider, and c) the electrodes of the monitor spectrometer placed in a separate building.

- In the HV distribution unit in total 46 individual voltages $U_{\text{wire el.}, i}$ will be created with the AC noise of 10 mV peak-to-peak and applied to the wire electrode modules inside the main spectrometer. The central part of the wire electrode system defines the retarding potential of the MAC-E filter. Moreover, the double-layer wire electrode causes a screening offset of the applied HV.
- The high precision HV divider will divide the HV of U_2 down to a low voltage in the 20 V range which can be easily measured with the help of the commercial digital voltmeter. This way the direct measurement of the retarding HV is accomplished. Both the HV divider and the digital voltmeter are regularly calibrated and the calibration procedure can be traced back to the PTB standards.
- The main beam line will be regularly calibrated via adding suitable gaseous source (“calibration source #1” in Fig. 3.5) of well defined electrons as an admixture to the WGTS.
- Another well defined electron source (“calibration source #2” in Fig. 3.5) will be attached to the cryogenic pumping section in the main beam line and will be regularly used for the energy calibration. Prior to the whole series of tritium measurement runs, such a source may be used for detailed studies of the transmission function of the main spectrometer.
- The third electron spectrometer of the MAC-E filter type, denoted as monitor spectrometer, will form the monitor beam line parallel to the main beam line. Its purpose is to monitor the instabilities of $U_2 \approx -18.6$ kV with the precision at the ppm level. The monitor spectrometer will continuously measure the energy of a well defined sharp electron line (denoted as “calibration source #3” in Fig. 3.5). The MAC-E filter of the former Mainz Neutrino Mass Experiment [Kra05] will be utilized as the monitor spectrometer.

The working principle of the HV divider will be briefly described in the coming section. The candidates for suitable monoenergetic electron sources will be discussed separately in Sect. 3.3. The calibration source marked as #3, which is intended to be used in the combination with the monitor spectrometer, is the main subject of this work.

3.2.1. High precision high voltage divider

In the KATRIN experiment the HV divider will be utilized for scaling the HV of about -19 kV down to about -10 V. Such a low voltage can be then measured by a commercial digital voltmeter with high precision. In the framework of the KATRIN project two high precision HV dividers were developed at the Institute of Nuclear Physics, University of Münster, in cooperation with Physikalisch-Technische Bundesanstalt (PTB) Braunschweig. The HV divider concept was similar to the one used before for producing the PTB standard divider “MT100” [Mar01], although very different types of resistors were used in these two concepts. The HV divider MT100 allows to perform a HV measurement up to 100 kV with the ppm-scale precision. The dividers developed within the KATRIN project will be denoted as K35 and K65 henceforth.

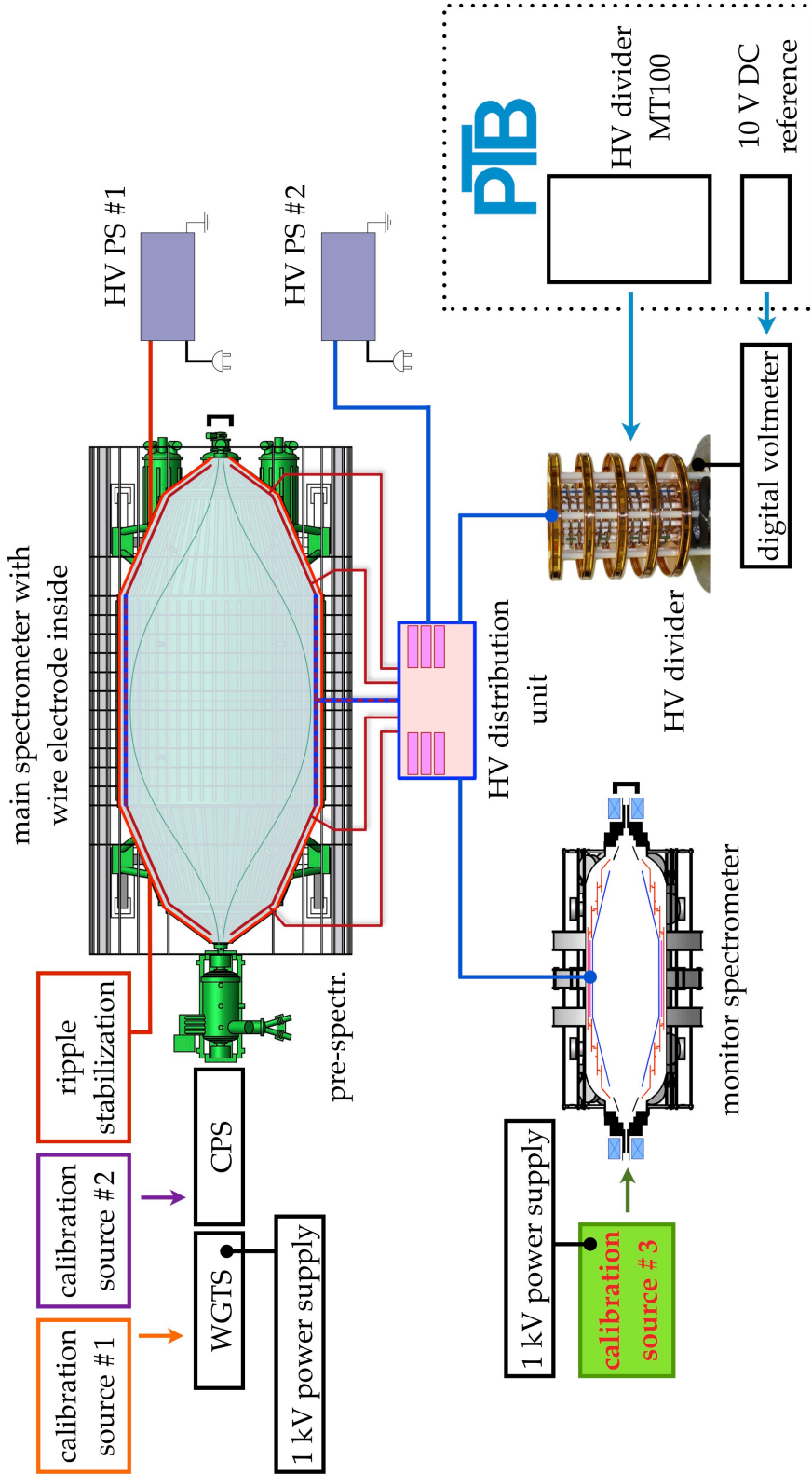


Fig. 3.5: The schematic overview of the HV scale monitoring concept of the KATRIN experiment. The first HV power supply “HV PS #1” applies HV to the main spectrometer vessel, the HV line is marked red. From the second HV power supply “HV PS #2” the HV line marked blue connects to the HV divider, the monitor spectrometer and the HV distribution unit. From this unit the voltage shown in dark red is applied to the modules of the wire electrode system inside the main spectrometer. The calibration source denoted as #1 will be applied in the gaseous form in the WGTS setup. The calibration source #2 will be connected to the CPS setup. The calibration source #3, highlighted with green box, is intended to be used together with the monitor spectrometer. This source represents the field of study described in this work. The dotted box marked as “PTB” illustrates the fact that the HV dividers, digital voltmeters and other auxiliary devices (e.g. the 1 000 V calibrator) used in the KATRIN experiment are calibrated with the standards of the PTB Braunschweig. See text for details. The figure is based on [KAT04, Thu07, Thu11].

3. Stability monitoring and calibration...

The HV divider K35 was built in 2005 and consists of 106 precision resistors of type Bulk Metal Foil, company Vishay [Thu07, Thu09]. The inner setup comprises four sections subdivided by five control electrodes made of polished copper and supported by a set of polyoxymethylene rods, see Fig. 3.6. The HV is fed to the top electrode by an appropriate sealed HV bushing. The whole structure is supported by polyoxymethylene rods on the bottom flange of the stainless steel vessel. In the four upper sections of the divider, 100 resistors of the resistance of $1.84\text{ M}\Omega$ are arranged in a helix structure, each section comprises 25 resistors. Every such section is shielded by electrodes creating a smooth potential distribution at the mounting position of the resistors, in order to reduce leak currents across the insulators and to prevent sparking. The remaining six resistors of the resistance of $140\text{ k}\Omega$ each, provide two low voltage outputs. Therefore, two groups of three resistors in parallel are arranged subsequent to the 100 precision resistors. One such group provides the dividing ratio (also called scale factor) of $3\,945 : 1$, both together provide the dividing ratio of $1\,972 : 1$, thus allowing precise measurements in the 20 V range, as needed by KATRIN. During the KATRIN test runs, the input voltages in the range of $7\text{--}35\text{ kV}$ are expected.

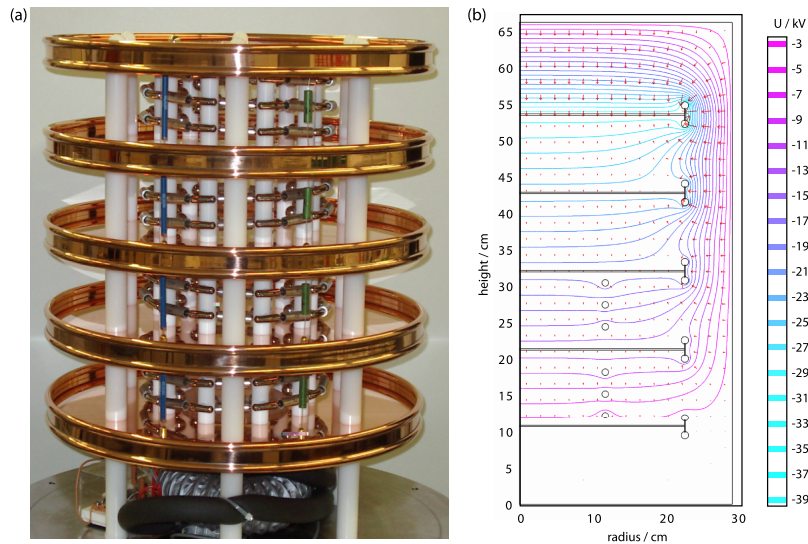


Fig. 3.6: The inner view and the electric field map of the HV divider K35. **(a)** The photograph of the inner layout of the divider. Five copper electrodes are visible which divide the setup into four sections, each containing 25 resistors. In the bottom part the voltage output can be recognized. **(b)** The electric field map simulated for the actual configuration of the HV divider. The figure is taken from [Thu07].

The resistors are specified for voltages up to 600 V and according to the published specifications they show the long-term stability of the resistance of $\pm 5 \times 10^{-6}$ in one year shelf life and $\pm 2 \times 10^{-5}$ in load life². This drift is mainly caused by an ageing effect of the resistor material and is supposed to decrease with time [Thu09]. The specified voltage coefficient of resistance is of the order of 10^{-7} V^{-1} and the temperature coefficient of the resistors is of the order of 10^{-6} K^{-1} . However, under load each resistor shows a characteristic warm-up deviation of the resistance value, which is strongly correlated to the internal temperature increase and the temperature coefficient of resistance [Thu09]. Therefore, the warm-up deviation of each resistor was checked and the resistors were chosen from a lot of 200 pieces so

²After 2000 h operation at a power of 0.1 W and a temperature of 60°C .

that the warm-up deviation of pairs or triplets of neighboring resistors cancels out. Moreover, the temperature inside the divider device is stabilized at 25.0(1)°C.

While the HV divider K35 is designed for HV up to 35 kV, the second HV divider K65 built in 2008 [Bau09] is used for HV measurement up to 65 kV. It consists of 170 resistors of the same type as in the case of K35. However, the resistors of resistance 880 kΩ were pre-aged during their production process. This is one of the main improvements of the divider design with respect to K35. The use of the pre-aged resistors should in principle minimize the ageing effect of the HV divider, thus delivering even better long-term stability of the dividing ratio M . In general, the long-term dependency of the dividing ratio can be described as exponential [Thu07] which—after sufficient time has passed from the divider production date—can be simplified to a linear function

$$M(t) = M_0 \cdot \left(1 + \underbrace{\frac{1}{M_0} \frac{\partial M}{\partial t}}_{=m} \cdot t\right), \quad (3.12)$$

where the long-term drift m is typically of the order of 0.1 ppm month⁻¹ for a high precision device.

Both HV dividers were extensively tested and calibrated against the PTB standard HV divider MT100 and also against each other. The fact that two such devices are available for KATRIN is of great importance with respect to their mutual cross-checks and overall redundancy. The dividers K35 and K65 were also recently utilized as the HV reference for calibration of the HV installation at the ISOLDE facility at CERN [Kri11].

3.3. Candidates for quasi-monoenergetic electron sources for

KATRIN

High order of redundancy in the concept of monitoring of the HV scale stability in KATRIN can be achieved by relying not only on the state-of-the-art electronics, but also on the natural standards of the atomic and nuclear physics. It should be noted that on the contrary to *e. g.* gamma spectroscopy, where various gamma ray standards [Fir96] are commercially available, the situation in the electron spectroscopy is much less favorable. There exists no commercial standard of electron source with the stability required by KATRIN (cf. Eq. 3.9).

This section introduces two main candidates for the source which could be utilized as the standard source at the monitor spectrometer. Firstly, the ²⁴¹Am/Co source of photoelectrons will be discussed. Then the ^{83m}Kr source of conversion electrons will be introduced. The third possible candidate for monoenergetic electron source, the ¹⁰⁹Cd source of Auger electrons will not be discussed here. The reader is kindly referred to [KAT04] for the description of this source.

3.3.1. Photoelectrons from $^{241}\text{Am}/\text{Co}$

Precise energy calibration of electron spectrometers at energies up to several keV is often performed by means of photoelectrons induced by X-rays. However, increasing the natural width of exciting X-radiation from heavier elements decreases the accuracy of this method at higher electron energies [KAT04]. A sharp electron source with an energy very close to the endpoint energy of the tritium β -spectrum can be based on the photoelectrons ejected by gamma ray photons of ^{241}Am from a thin foil of metallic cobalt. The kinetic energy $E_{\text{kin}}(i)$ of the photoelectrons ejected from a given atomic shell i , measured by the spectrometer, can be determined as

$$E_{\text{kin}}(i) = E_{\gamma} - E_{\text{bin}}^{\text{Fermi}}(i) - E_{\text{rec},e}(i) - \phi_{\text{spec}}, \quad (3.13)$$

where

- E_{γ} is the gamma ray energy,
- $E_{\text{bin}}^{\text{Fermi}}(i)$ is the electron binding energy of the shell i related to the Fermi level,
- $E_{\text{rec},e}(i)$ is the energy of the recoil atom after photoelectron emission, and
- ϕ_{spec} is the work function of the retarding electrode of the electron spectrometer measuring the electrons.

The balance of the individual terms is illustrated in Fig. 3.7 (where the recoil energy was neglected). The electron binding energy is related to the Fermi level since the photoelectrons are created in metallic environment which is electrically connected to the ground of the electron spectrometer. Of particular interest for KATRIN is the combination of the ^{241}Am gamma transition of energy $E_{\gamma} = 26\,344.6(2)$ eV [Hel00] with the photoelectric effect on the cobalt K shell where the electron binding energy amounts to $E_{\text{bin}}^{\text{Fermi}}(K) = 7\,708.78(2)$ eV [Des03]. Thus, in accordance with Eq. 3.13 the kinetic energy of the “ K -26” electron line is

$$E_{\text{kin}}(K) + \phi_{\text{spec}} \simeq 18\,635.7(2) \text{ eV}, \quad (3.14)$$

where $E_{\text{rec},e}(K) = 0.14$ eV was taken into account. The value of the work function ϕ_{spec} of a stainless steel electrode is typically 4–5 eV.

The features of the $^{241}\text{Am}/\text{Co}$ photoelectron source can be summarized as follows [KAT04, Kas08, Dra11a]:

- The energy of the photoelectrons intended for HV scale monitoring, $E_{\text{kin}}(K) \simeq 18\,631$ eV, differs from the tritium endpoint E_0 only by about 60 eV. Moreover, the calibration line lies “above” the tritium endpoint, therefore, it would not be affected by the β -spectrum if one would consider applying such source in the main spectrometer directly.
- The recoil energy and the natural width of the exciting gamma rays together with its Doppler broadening at 300 K are less than 0.02 eV, *i. e.* completely negligible for this purpose.
- The natural width of the atomic K shell of Co, caused by the lifetime of the K hole, is rather narrow: 1.28 eV.
- The ^{241}Am half-life of 432 a is practical for long-term monitoring.
- The $^{241}\text{Am}/\text{Co}$ source may suffer from physical-chemical changes of the binding energy. Differences of the binding energies of the Co metal component and possible Co oxides are in the range of 1.9–2.1 eV. Photoelectrons corresponding to the metal Co

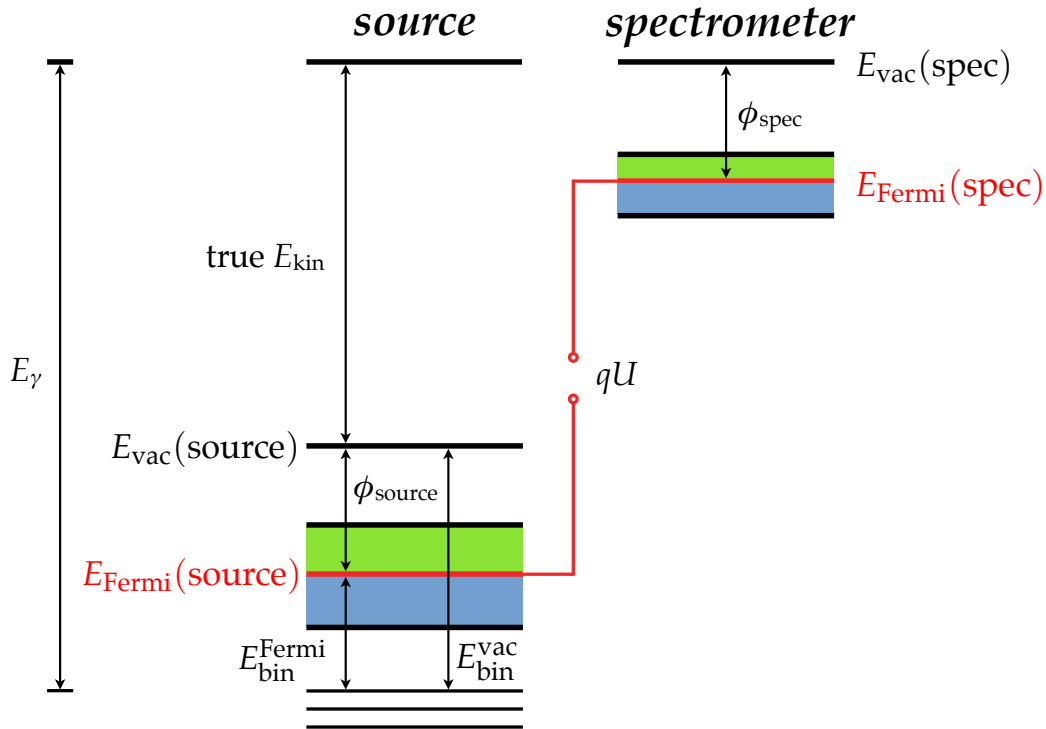


Fig. 3.7: The energy diagram for an electrically conducting sample (source of electrons) that is connected with the ground of the electron spectrometer. A scan of the spectrum of emitted electrons is obtained by varying the voltage $U < 0$ between the Fermi levels (marked red) of the source and the spectrometer electrode. In the depicted situation exactly the electrons from the conversion electron line are transmitted. When $U = 0$ the Fermi levels of the source and the spectrometer electrode are aligned, $E_{\text{Fermi}}(\text{source}) = E_{\text{Fermi}}(\text{spec})$. The bands of conducting electrons are shown in green whereas the bands of valence electrons are denoted blue. The notion of spectrometer work function ϕ_{spec} denotes, more precisely, the work function of the retardation electrode. The work functions difference $\phi_{\text{spec}} - \phi_{\text{source}}$, which is introduced via $E_{\text{bin}}^{\text{Fermi}} = E_{\text{bin}}^{\text{vac}} - \phi_{\text{source}}$, can be positive or negative. In the diagram the terms of recoil energy were omitted. For the sake of simplicity, the dip of the retarding potential across the analyzing plane of the spectrometer (see Sect. 5.2.2 below) is also not drawn. The same holds for the shift of the electron binding energy $E_{\text{bin}}^{\text{vac}}$ resulting from the surface or solid state effects (see Sect. 4.3.1 below). The figure is based on [Rat09].

3. Stability monitoring and calibration...

component originate with higher kinetic energy than the ones corresponding to Co oxide states. The differences are both well described and observable in the monitor spectrometer. Moreover, the effect may be suppressed by cleaning the Co foil with the help of ion etching.

The electron source based on such principle of the $^{241}\text{Am}/\text{Co}$ convertor is very promising regarding the long-term monitoring of the HV scale (time scale of two or more months) as the metallic convertor is expected to be physically and chemically stable. The source was tested in 2005 at Mainz MAC-E filter spectrometer [Kas08, Dra11a]. The main drawback of the source was found to be a rather low count rate (of the order of 10 counts s^{-1}) of the zero-energy-loss electrons coming from the source. Moreover, the high energy X-rays and gamma rays produced considerable background upon which the useful electron line was superimposed. The stability of the source was not studied in detail.

3.3.2. Conversion electrons from $^{83\text{m}}\text{Kr}$

An electron source based on the internal conversion in $^{83\text{m}}\text{Kr}$ was already used in the past for the calibration purposes in Mainz Neutrino Mass Experiment [Pic92b] and other experiments [Rob91, Bel08]. Similarly to the $^{241}\text{Am}/\text{Co}$ source, the initial energy is available upon the gamma transition. However, in the source based on $^{83\text{m}}\text{Kr}$ the process of internal conversion is utilized. The process of internal conversion was described above in Sect. 1.2.

The $^{83\text{m}}\text{Kr}$ source will be applied in KATRIN in three different physical states: as a gas, as a condensed film of the sub-monolayer thickness and as a solid source. Regardless of the physical state of the given source, the parent isotope ^{83}Rb with the half-life of 86.2(1) d [Fir96] will be exploited, since ^{83}Rb decays via electron capture to $^{83\text{m}}\text{Kr}$. Thus, ^{83}Rb conveniently serves as a generator of the short-lived isomeric state $^{83\text{m}}\text{Kr}$ with the half-life of 1.83 h [Fir96]. The decay schemes of ^{83}Rb and $^{83\text{m}}\text{Kr}$ are depicted in Fig. 3.8. About 77.9% of ^{83}Rb decays to the metastable state of $^{83\text{m}}\text{Kr}$ of energy 41.5 keV and nuclear spin of $I^\pi = \frac{1}{2}^-$. This state decays further to the short-lived state (147 ns) of energy 9.4 keV and spin of $I^\pi = \frac{7}{2}^+$. Lastly, the stable state has the spin of $I^\pi = \frac{9}{2}^+$. The conversion electrons produced in electromagnetic transitions from the krypton nuclear levels above the isomeric state are not usable for our purpose due to high energies [Ven09]. However, the isomeric state decays via a cascade of suitable low energy transitions of 32.2 and 9.4 keV possessing high intensity of conversion electrons. The first transition (32.2 keV) with the multipolarity E3 is especially highly converted: the total internal conversion coefficient (ICC, cf. Eq. 1.23) amounts to $\alpha_{\text{tot}} = 2010$ [Ros78]. The second transition of 9.4 keV energy is practically a pure M1 transition (the amount of the E2 multipolarity admixture is given by the mixing parameter $\delta = 0.0130(8)$) and the total ICC amounts to $\alpha_{\text{tot}} = 17$ [Ros78].

In the case of gaseous $^{83\text{m}}\text{Kr}$, the kinetic energy of an electron emitted from atomic shell i , measured by the spectrometer, reads (cf. Fig. 3.7)

$$E_{\text{kin}}^{\text{gas}}(i) = E_\gamma + E_{\text{rec}, \gamma} - E_{\text{rec}, e}(i) - E_{\text{bin}}^{\text{vac}}(\text{gas}, i) - (\phi_{\text{spec}} - \phi_{\text{source}}) - C, \quad (3.15)$$

where

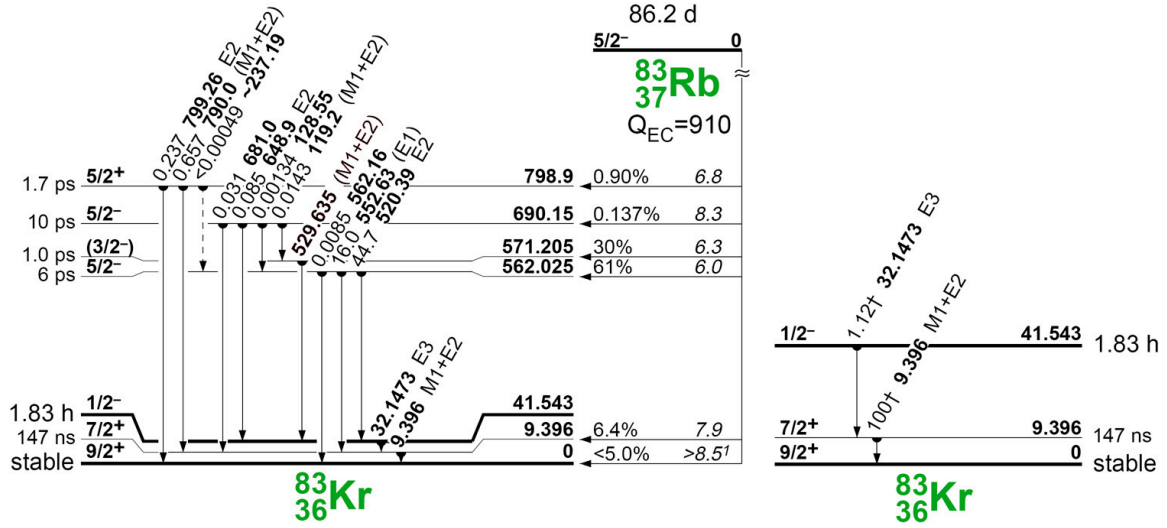


Fig. 3.8: The decay schemes of ^{83}Rb (left scheme) and $^{83\text{m}}\text{Kr}$ (right scheme). The decay of $^{83\text{m}}\text{Kr}$ is visible also in the bottom part of the decay scheme of ^{83}Rb but for the sake of clarity it is plotted separately. The ^{83}Rb (half-life 86.2 d) decays by the pure electron capture with the branching ratio of 77.9% into the short-lived isomeric state $^{83\text{m}}\text{Kr}$ (1.83 h). Detail on the right side shows its 32.2 keV (intensity 0.0358(45)%, multipolarity E3) and 9.4 keV (5.86(134)%, M1+E2) gamma transitions. The schemes are taken from [Fir96].

- E_γ is the gamma ray energy,
- $E_{\text{rec}, \gamma}$ is the energy of the recoil atom after gamma ray emission and is equal to 0.007 and 0.002 eV for the E3 and M1 transitions, respectively,
- $E_{\text{rec}, e(i)}$ is the energy of the recoil atom after emission of the conversion electron from shell i ,
- $E_{\text{bin}}^{\text{vac}}(\text{gas}, i)$ is the electron binding energy of the shell i (related to the vacuum level) of the free atom,
- ϕ_{spec} is the work function of the spectrometer electrode,
- ϕ_{source} is the work function of the source, and
- C is an additional term accounting for possible space and surface charges within the gaseous source.

The electron binding energies of krypton in gaseous form are tabulated in App. A. The gamma ray energy E_γ of the aforementioned 9.4 and 32.2 keV transitions was determined by high precision gamma ray spectroscopy with semiconductor detectors. In [Ven06] the calibration method of closely spaced lines in the gamma spectrum was used. The soft gamma ray lines with the energies of 26 and 33 keV of ^{241}Am were utilized (their energy is known with the precision of 0.2 and 0.1 eV, respectively) and the energy $E_\gamma \equiv E_\gamma(32)$ of the E3 transition in $^{83\text{m}}\text{Kr}$ was determined as

$$E_\gamma(32) = 32\,151.7(5) \text{ eV}. \quad (3.16)$$

Similarly, in [Sle11] the energy $E_\gamma \equiv E_\gamma(9.4)$ of the M1 transition was measured as

$$E_\gamma(9.4) = 9\,405.8(4) \text{ eV}. \quad (3.17)$$

3. Stability monitoring and calibration...

The values stated in Eq. 3.16 and Eq. 3.17, representing the most recent values, were found to be in a very good agreement with the values 32 151.5(11) eV and 9 405.9(8) eV published in [Pic92b]. There the values were obtained from the analysis of the $^{83\text{m}}\text{Kr}$ conversion electron spectrum measured at Mainz MAC-E filter with the $^{83\text{m}}\text{Kr}$ atoms condensed onto cooled copper substrate. A similar analysis was carried out in [Ost08] where the $^{83\text{m}}\text{Kr}$ was condensed onto cooled highly ordered pyrolytic graphite and the values of 32 151.74(35) eV and 9 404.71(35) eV were determined. While the E3 transition energy values are in an overall agreement, there is a certain discrepancy concerning the M1 transition values. This issue will be addressed later in this work. In addition, the values in Eq. 3.16 and Eq. 3.17 agree well with the previous measurements carried out with semiconductor detectors. Similarly to the $^{241}\text{Am}/\text{Co}$ source, the most interesting conversion electron line of $^{83\text{m}}\text{Kr}$ regarding the application in KATRIN is the conversion on the K shell. The precision of the electron binding energy of this core shell was increased in the recent reevaluation [Dra04] and the value of $E_{\text{bin}}^{\text{vac}}(K)$ reads

$$E_{\text{bin}}^{\text{vac}}(K) = 14\,327.26(4) \text{ eV}, \quad (3.18)$$

which, combined with Eq. 3.15 and Eq. 3.16, gives the kinetic energy of the “K-32” electron as

$$E_{\text{kin}}^{\text{gas}}(K) + (\phi_{\text{spec}} - \phi_{\text{source}}) = 17\,824.3(5) \text{ eV}. \quad (3.19)$$

Here the values $E_{\text{rec}, \gamma} = 0.007 \text{ eV}$ and $E_{\text{rec}, e}(K) = 0.12 \text{ eV}$ were taken into account while other effects were omitted via taking $C = 0$. In the same way the kinetic energies of the other electron lines of the $^{83\text{m}}\text{Kr}$ conversion spectrum were calculated, using the $E_{\text{bin}}^{\text{vac}}(i)$ values stated in App. A. The following quantities are summarized in Tab. 3.1:

- recoil atom energy $E_{\text{rec}, e}(i)$,
- kinetic energy $E_{\text{kin}}^{\text{gas}}(i)$ of the electron line, calculated according to Eq. 3.15, while the difference of the work functions was omitted, *i. e.* $\phi_{\text{spec}} = \phi_{\text{source}}$,
- intensity $I(i)$ of the electron line in % per ^{83}Rb decay, based on the interpolation of the ICC values tabulated in [Ros78],
- the Lorentzian width $\Gamma(i)$ of the electron line as recommended in [Cam01],
- the width $\Gamma(i)$ of the electron line as measured at Mainz MAC-E filter with the $^{83\text{m}}\text{Kr}$ condensed onto cooled copper [Pic92b] and highly ordered pyrolytic graphite [Ost08] substrate, and
- the instrumental energy resolution ΔE of Mainz spectrometer used in this work (as well as in [Ost08]) for measuring the given conversion line³.

³From Eq. 2.13 in Sect. 2.2 it follows that the energy resolution of the MAC-E filter increases linearly with the starting energy of the electron. The ratio of maximal and minimal magnetic field strengths is kept constant.

Tab. 3.1: The overview of the conversion electron lines of $^{83\text{m}}\text{Kr}$.

Electron level and notation	Atom rec. energy $E_{\text{rec}, e}(i)$	Kinetic energy $E_{\text{kin}}^{\text{gas}}(i)$	Intensity $I(i)$ [%] per ^{83}Rb decay	Lorentzian line width $\Gamma(i)$			Instr. resol. ΔE
				recomm. [Cam01]	exp. (cond. Kr) [Pic92b]	[Ost08]	
γ transition M1		9 405.8(4)	5.86(134)				
$2s_{1/2}$ L_1	0.05	7 481.2(9)	70.32	3.75	5.30(4)	3.72(19)	0.4
$2p_{1/2}$ L_2	0.05	7 673.8(4)	7.91	1.25	1.84(5)	1.29(14)	0.4
$2p_{3/2}$ L_3	0.05	7 726.5(4)	5.07	1.19	1.40(2)	1.58(16)	0.4
$3s_{1/2}$ M_1	0.06	9 113.0(5)	11.60	3.5	4.27(5)	3.123(4)	0.5
$3p_{1/2}$ M_2	0.06	9 183.5(4)	1.30	1.6	1.99(32)	0.63(39)	0.5
$3p_{3/2}$ M_3	0.06	9 191.3(4)	0.98	1.1	1.66(8)	1.1(4)	0.5
$4s_{1/2}$ N_1	0.06	9 378.2(4)	1.43	0.4	0.19(4)	0.288(93)	0.5
$4p_{1/2}$ N_2	0.06	9 391.1(4)	0.12	0.03 ^a	–	0 ^b	0.5
$4p_{3/2}$ N_3	0.06	9 391.7(4)	0.09	0.03 ^a	–	0 ^b	0.5
γ transition E3		32 151.7(5)	0.035 8(45)				
$1s_{1/2}$ K	0.12	17 824.3(5)	17.07	2.71	2.83(12)	2.70(6)	0.9
$2s_{1/2}$ L_1	0.20	30 226.9(9)	1.13	3.75	–	–	1.6
$2p_{1/2}$ L_2	0.20	30 419.6(5)	17.61	1.25	1.84(5)	1.165(69)	1.6
$2p_{3/2}$ L_3	0.21	30 472.3(5)	27.42	1.19	1.40(2)	1.108(13)	1.6
$3s_{1/2}$ M_1	0.21	31 858.8(6)	0.19	3.5	–	–	1.6
$3p_{1/2}$ M_2	0.21	31 929.3(5)	2.99	1.6	1.99(32)	1.230(61)	1.6
$3p_{3/2}$ M_3	0.21	31 937.0(5)	4.65	1.1	1.66(8)	1.322(18)	1.6
$3d_{1/2}$ M_4	0.21	32 056.5(5)	4.69	0.07	–	–	1.7
$3d_{3/2}$ M_5	0.21	32 057.7(5)	6.59	0.072	–	–	1.7
$4s_{1/2}$ N_1	0.21	32 124.0(5)	0.02	0.4	0.19(4)	0.4	1.7
$4p_{1/2}$ N_2	0.21	32 136.8(5)	0.27	0.03 ^a	0.59(4) ^c	0.608(13) ^c	1.7
$4p_{3/2}$ N_3	0.21	32 137.5(5)	0.41	0.03 ^a			1.7

All the values of energy, line width and instrumental resolution are stated in eV. The energies of the M1 and E3 gamma transitions were taken from [Ven06] and [Sle11], respectively. The intensities of the gamma transitions per ^{83}Rb decay are based on [Vai76] and [Wu01]. The electron kinetic energies are stated for gaseous krypton (cf. Eq. 3.15) for $\phi_{\text{spec}} = \phi_{\text{source}}$, using the gamma transitions energies shown in the table and the binding energies summarized in App. A. The intensities of the electron lines per ^{83}Rb decay were determined using interpolated internal conversion coefficients tabulated in [Ros78]. The experimental line widths were obtained from measurements with the condensed $^{83\text{m}}\text{Kr}$ at Mainz MAC-E filter. In the last column the energy resolution is noted for the settings of Mainz spectrometer which was typically used in this work. Remarks: **a** from Table I of [Cam01] (not stated as “recommended”) and [Aks77]. **b** natural line width fixed to 0 in the analysis. **c** the lines N_2 and N_3 -32 were analyzed as a single line $N_{2/3}$ -32.

At this point the individual types of the source based on the $^{83\text{m}}\text{Kr}$ conversion electrons shall be discussed and compared.

Gaseous $^{83\text{m}}\text{Kr}$ source

The gaseous $^{83\text{m}}\text{Kr}$ source is denoted as “calibration source #1” in Fig. 3.5. It is intended to be used directly in the WGTS as an admixture to the tritium gas. This way the distribution of space charge within the WGTS can be studied. Such effect would be observed as broadening of the conversion electron lines [Bel08]. For instance, the natural width of the valence electron line $N\text{-}32$ is practically zero and thus any broadening of the line shape can reveal systematic effects. In addition, the $^{83\text{m}}\text{Kr}$ gas will provide the absolute calibration of the energy scale in KATRIN: this type of source is especially convenient for such purpose, while in the cases of the condensed and solid sources the electron binding energies are affected by surface and solid state effects. The conversion electron lines $L_1\text{-}9.4$ ($\simeq 7.5$ keV), $K\text{-}32$ ($\simeq 17.8$ keV) and $L_3\text{-}32$ ($\simeq 30.4$ keV) are of particular interest as they profit from high statistics. Any contamination of the KATRIN main beam line can be excluded as the $^{83\text{m}}\text{Kr}$ isotope is short-lived and the parent isotope ^{83}Rb can be safely separated from the WGTS setup with the help of cold traps. Rather high activity of ^{83}Rb of the order of 1 GBq will be necessary for KATRIN. An open radioactive source based on ^{83}Rb trapped in zeolite beads [Ven05] seems very well suitable for this task. High activity of ^{83}Rb can be absorbed in a small amount of zeolite beads which ensure a nearly complete release of $^{83\text{m}}\text{Kr}$ but prevent any release of ^{83}Rb . In order to avoid freeze-out of the krypton, the temperature of the WGTS has to be increased from the working value of about 30 K (tritium measurement) up to about 120–150 K.

Condensed $^{83\text{m}}\text{Kr}$ source

The concept of condensed $^{83\text{m}}\text{Kr}$ source (CKrS) dates back to the Mainz Neutrino Mass Experiment [Pic92b, Kra05] where it was used as the calibration source before and after each tritium run. Moreover, the CKrS was used very successfully for various systematic investigations [Pic90, Fle92, Bor03]. The ^{83}Rb atoms were ion-implanted into a copper or Kapton sheet which was kept in a separate vacuum vessel. The gaseous $^{83\text{m}}\text{Kr}$ emanated from the copper sheet and it was led to condense on a helium cooled copper or highly ordered pyrolytic graphite (HOPG) substrate. The surface of the substrate was kept clean via resistive heating and the source region was shielded by cold cylindrical baffles against heat radiation and condensation of residual gas from the spectrometer vacuum. The process was controlled in such a way that only the sub-monolayer amount of $^{83\text{m}}\text{Kr}$ atoms was condensed onto the clean surface. The cleanliness of the substrate and thickness of the $^{83\text{m}}\text{Kr}$ film was monitored with the help of laser ellipsometry.

In [Ost08] the concept of the CKrS was further improved and automatized. The schematic view of the CKrS setup is shown in Fig. 3.9. In Fig. 3.10 the simplified model of the substrate conditions is illustrated. The laser ablation was introduced as another method of substrate cleaning. A NdYAG laser system anneals the HOPG substrate and thus provide

reproducible substrate conditions before each film preparation. As the electron emission rate is governed by the short half-life of $^{83\text{m}}\text{Kr}$ of ≈ 2 h, the $^{83\text{m}}\text{Kr}$ was let to continuously condense on the substrate during the measurement. Overall, the control of the $^{83\text{m}}\text{Kr}$ film properties was improved. In 2006–2007 the long-term energy stability of the conversion lines of CKrS was extensively tested at Mainz MAC-E filter [Ost08]. The high precision HV divider K35 was exploited as the HV reference. It was shown that the CKrS concept provides conversion electrons with the energy stability on the level of ppm month^{-1} .

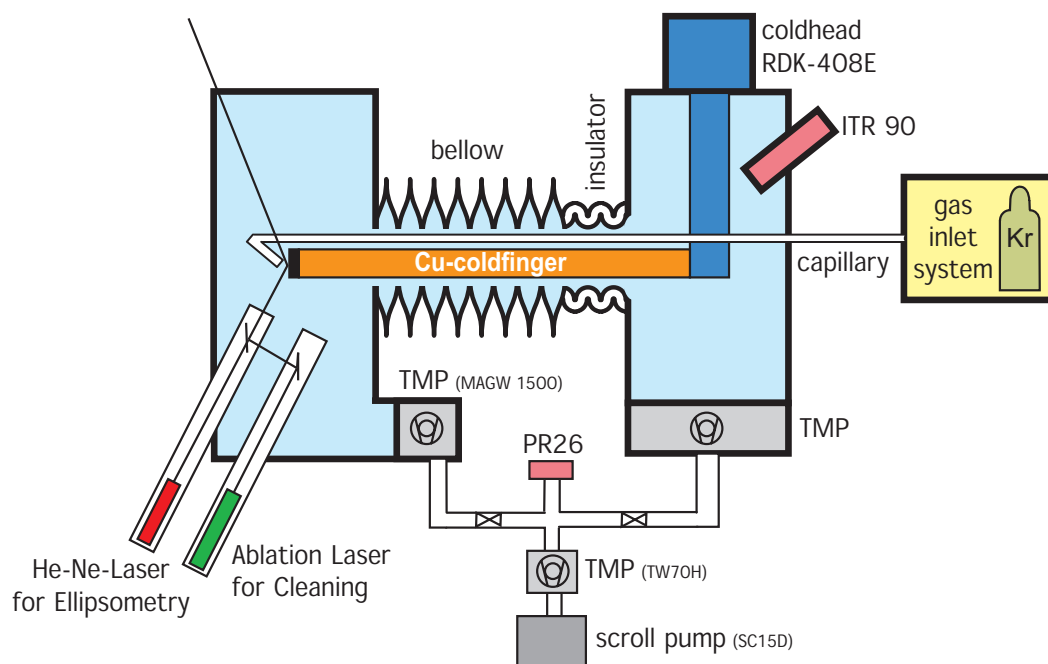


Fig. 3.9: The schematic view of the experimental setup of the condensed $^{83\text{m}}\text{Kr}$ source. From the gas inlet system, depicted on right, the $^{83\text{m}}\text{Kr}$ gas is transported via capillary and is let to condense on the substrate (black spot on the left side). The laser beam, coming either from the ellipsometry He-Ne laser or from the ablation laser, is shown on the left side. The figure is taken from [Thu07].

In Fig. 3.5 the condensed $^{83\text{m}}\text{Kr}$ source (CKrS) was marked as “calibration source #2”. The CKrS setup will be attached to the cryogenic pumping section in the KATRIN main beam line and it will serve as the calibration source for monitoring the HV scale between the individual tritium runs. The features of the CKrS can be listed as follows:

- Thanks to the laser annealing of the substrate, reproducible conditions can be repeatedly prepared before the $^{83\text{m}}\text{Kr}$ atoms are condensed. The concept of the source requires high reproducibility of the cleaning procedure of the substrate.
- The emission of the conversion electrons is isotropic into the forward 2π space.
- High electron count rate of the order of 10^3 counts s^{-1} or more can be reached, limited practically by the amount of parent ^{83}Rb and losses during the $^{83\text{m}}\text{Kr}$ gas transport to the substrate. In any case the amount of condensed $^{83\text{m}}\text{Kr}$ corresponds to a sub-monolayer coverage of the substrate.
- It was shown in [Ost08] that the CKrS can operate for about one week without any cleaning of the HOPG substrate. After this time period, however, the stability of the conversion line energy was hindered by the rest gas adsorption and it was necessary

3. Stability monitoring and calibration...

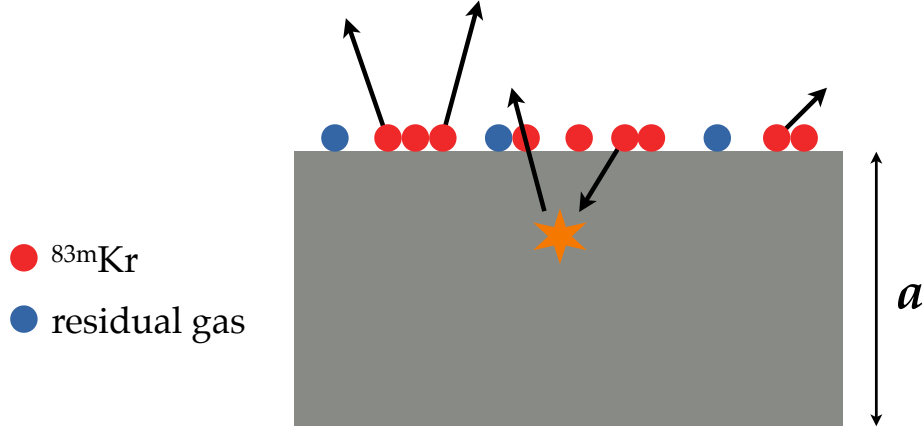


Fig. 3.10: The schematic view of the CKrS substrate illustrating the surface conditions. A small amount of residual gas atoms is depicted on the surface as it is virtually impossible to achieve a perfectly clean surface. However, the substrate contamination is minimized with the help of the laser annealing technique. The arrows denoted the electrons emitted into the space of 4π . The star denotes a backscattering event inside the substrate which leads to the loss of a certain portion of the starting energy of the electron. This way the electron falls out of the elastic peak (“zero-energy-loss peak”) in the electron spectrum and is not useful for the calibration. In addition, the scattered electron may also fall out of the accepted solid angle $\Delta\Omega$, as usually $\Delta\Omega < 2\pi$.

to clean the substrate and prepare a new source.

- The automatized maintenance of the setup is relatively easy, on the other hand, ultrahigh vacuum of 10^{-10} mbar or better is required in the vicinity of the substrate. Moreover, a highly sophisticated setup of the gas purification, gas inlet and overall source positioning is required.
- There is no danger of contamination regarding this source. Any possible release of ^{83m}Kr from the substrate is harmless thanks to the short half-life. Furthermore, the long-lived ^{83}Rb is kept separated from the source vacuum section. Thus, it is possible to place the CKrS in the mean beam line of the KATRIN experiment without the worry of contaminating the main spectrometer.

It should be noted that the kinetic energy of the conversion electron is influenced by the condensation of the ^{83m}Kr atom on the cold substrate. Original Eq. 3.15 is changed to

$$E_{\text{kin}}^{\text{cond}}(i) = E_{\gamma} + E_{\text{rec}, \gamma} - E_{\text{rec}, e}(i) - \left(E_{\text{bin}}^{\text{vac}}(\text{gas}, i) - \Delta E_{\text{bin}}^{\text{vac}}(\text{cond}, i) \right) - \left(\phi_{\text{spec}} - \phi_{\text{source}} \right), \quad (3.20)$$

where by the use of the notation “gas” in $E_{\text{bin}}^{\text{vac}}(\text{gas}, i)$ it is emphasized that this binding energy is valid for the free atom. The term $\Delta E_{\text{bin}}^{\text{vac}}(\text{cond}, i)$ accounts for the change of the electron binding energy due to the image charge [Ost08]. As $\Delta E_{\text{bin}}^{\text{vac}}(\text{cond}, i) > 0$, the electron binding energy of the condensed atom is lower than of the free atom. In [Ost08] the constant correction $\Delta E_{\text{bin}}^{\text{vac}}(\text{cond}, i) \equiv \Delta E_{\text{bin}}^{\text{vac}}(\text{cond}) = 1.74(23)$ eV was used for all krypton atomic shells. As mentioned above, in [Ost08] the values of 32 151.74(35) eV and 9 404.71(35) eV were determined for the energy of the E3 and M1 transitions, respectively.

Solid $^{83}\text{Rb}/^{83\text{m}}\text{Kr}$ source

In order to avoid the repeated condensation of $^{83\text{m}}\text{Kr}$ which is necessary for the operation of the CKrS source, the solid type of $^{83\text{m}}\text{Kr}$ source was introduced in the framework of the KATRIN experiment. The concept is based on the fact that the “ ^{83}Rb -generator” of $^{83\text{m}}\text{Kr}$ lies directly in the source itself. Thus, the count rate of such source is driven by the half-life of ^{83}Rb . The solid type of source is denoted as $^{83}\text{Rb}/^{83\text{m}}\text{Kr}$ henceforth. In the $^{83}\text{Rb}/^{83\text{m}}\text{Kr}$ source an extremely small amount, corresponding to a sub-monolayer quantity, of radioactive material is placed onto or into suitable backing. Changes of the electron binding energy are to be expected due to surface and solid state effects.

The solid $^{83}\text{Rb}/^{83\text{m}}\text{Kr}$ source is highlighted as “calibration source #3” in Fig. 3.5 and its intended application is to serve as a calibration source of stable conversion electron lines in combination with the monitor spectrometer. This type of source is the subject of this work and is thoroughly discussed in coming Chap. 4. In Tab. 3.2 the three types of $^{83\text{m}}\text{Kr}$ source are briefly compared.

Tab. 3.2: The comparison of the three types of the calibration source based on the $^{83\text{m}}\text{Kr}$ conversion electrons.

type of source	gaseous	condensed	solid
source production	$\approx 1 \text{ GBq}$ of ^{83}Rb , probably absorbed in zeolite beads	$\approx 5 \text{ MBq}$ of ^{83}Rb , then repeated cleaning and $^{83\text{m}}\text{Kr}$ condensation onto cooled substrate	$\approx 5 \text{ MBq}$ of ^{83}Rb placed onto or into solid
source handling	high radioactivity	complicated setup	simple, but open radioactive source
expected electron count rate in the K_{32} line [counts s^{-1}]	$\approx 10^4$	$\approx 10^3$	$\approx 10^3\text{--}10^4$
stability of the electron kinetic energy of one source	stable	stable on the level of ppm month^{-1} , verified in [Ost08]	to be proved (this work)
reproducibility of the electron kinetic energy for different sources	reproducible	achieved in [Ost08] thanks to laser ablation	to be proved (this work)
vacuum requirements	compatibility with WGTS	UHV of 10^{-10} mbar (or better) necessary	to be investigated (this work)

4. Solid $^{83}\text{Rb}/^{83\text{m}}\text{Kr}$ electron sources for KATRIN

In Sect. 3.3.2 the metastable $^{83\text{m}}\text{Kr}$ was introduced as a promising source of conversion electrons with sharp and well defined kinetic energies. Of main interest is the internal conversion on the K shell which results in the K -32 electron line (cf. Eq. 3.19) with the energy of $\simeq 17.8$ keV, by only 0.8 keV lower than the endpoint energy E_0 of the tritium β -spectrum. In the KATRIN experiment the $^{83\text{m}}\text{Kr}$ source will be utilized in the form of a) gas, b) atoms condensed on a clean surface and c) atoms adsorbed on or implanted in solid. The option (c) will be discussed in this chapter. The concept of the solid source is actually simple: the parent isotope ^{83}Rb is directly placed onto or into the source substrate itself where it generates the metastable $^{83\text{m}}\text{Kr}$ which emits the useful conversion electron lines. It should be noted already now that the solid $^{83}\text{Rb}/^{83\text{m}}\text{Kr}$ source is not intended as a calibration source in the sense of absolute calibration of the high voltage (HV) scale of the KATRIN spectrometers: due to surface and/or solid state effects, affecting the electron binding energy, the conversion electron energy may vary from source to source. On the other hand, the source is intended for continuous monitoring of the HV scale with the ppm precision. Therefore, the aforementioned effects have to be recognized and controlled.

Firstly, the production and main features of the vacuum-evaporated $^{83}\text{Rb}/^{83\text{m}}\text{Kr}$ sources are introduced in Sect. 4.1. This production technique is based on ultra-pure radiochemistry of trace amount of ^{83}Rb and its subsequent evaporation onto suitable backing in vacuum. Secondly, in Sect. 4.2 the ion-implanted sources are described, together with basic notions of the ion implantation and radiation damage. Here the production technique consists of implanting the ^{83}Rb ions into suitable substrates. Finally, the effects of surface and solid state physics, affecting the conversion electrons emitted from the solid sources, are covered in Sect. 4.3. In the course of coming sections the actual samples will also be described, which were investigated in this work at Mainz MAC-E filter spectrometer.

The non-SI unit of Ångström, $1 \text{ \AA} = 0.1 \text{ nm}$, will be used in this chapter due to its historical use in a number of works, dealing with surface and solid state effects, which are cited here.

Before introducing the production techniques of the solid $^{83}\text{Rb}/^{83\text{m}}\text{Kr}$ sources, the basic properties of the elements $_{36}\text{Kr}$ and $_{37}\text{Rb}$ can be briefly summarized [Gree84]:

- From their nature (Kr being a noble gas, Rb an alkali metal) it follows that these two elements are very different concerning their properties and behavior. Krypton has very weak inter-atomic forces of attraction and consequently very low melting and boiling point. On the other hand, rubidium is a highly reactive and easily surface-ionized low density metal igniting spontaneously in air, reacting violently in water

4. Solid $^{83}\text{Rb}/^{83\text{m}}\text{Kr}$ electron...

and in nature it is never found in the elemental form.

- The electron configurations of these two elements differ by one 5s electron, “Rb = [Kr] 5s¹”, while Kr possesses fully filled s and p electron shells, “Kr = [Ar] 3d¹⁰ 4s² 4p⁶”.
- For Rb the energetically preferred state of achieving a filled electron shell is to lose one electron to form a singly charged positive ion, thus Rb easily reacts mainly with the elements of the groups 17 (halogens) and 16 (chalcogens). Elements of both these groups are willing to acquire the noble gas configuration this way. Various compounds of halides (RbX, X = F, Cl, Br, I), oxides (RbO₂, Rb₂O, Rb₂O₂, Rb₂O₃), chalcogenides (Rb₂X, X = S, Se, Te), and their salts are created.

From the properties listed above it follows that rubidium will be always present in the form of compound in the solid source. However, virtually immediately (within $\approx 10^{-10}$ s or less) after the disappearance of a proton in the ^{83}Rb nucleus during the electron capture the rearrangement of the electron shells occurs and the atom behaves chemically as Kr [Leb11].

4.1. Vacuum-evaporated sources

The idea of the solid $^{83}\text{Rb}/^{83\text{m}}\text{Kr}$ source was introduced in the works [Kov92] (*KLL* and *LMX* Auger spectra from the ^{83}Rb decay) and [Kov93] (conversion electron investigation of the 9.4 keV transition in $^{83\text{m}}\text{Kr}$) where the electrostatic spectrometer ESA-50 [Bri84] operated in the JINR Dubna at the vacuum level of 10^{-6} mbar was used. Here the radioactive ^{83}Rb sources (activities of $\simeq 4.5$ MBq) were prepared by means of evaporation in the vacuum of 10^{-5} mbar onto aluminum backing (cleaned in alcohol by ultrasonics). The source evaporation took about one minute at 800°C. The deposits of 8 mm diameter were invisible on the backing. The shift of about 13–15 eV of the electron lines energies was found in both works, resulting probably from the negative shifts of the electron binding energies in $^{83\text{m}}\text{Kr}$ atoms generated in the solid source. The energy stability of the conversion electron lines was not tested in detail, however, the stability of the order of 1 eV was claimed.

The successful use of the vacuum-evaporated sources in [Kov92, Kov93] led to the systematic investigation of the $^{83}\text{Rb}/^{83\text{m}}\text{Kr}$ sources in the Nuclear Physics Institute Řež/Prague with the perspective to use such sources in the KATRIN experiment. The concept of the vacuum-evaporated source was also appealing due to its compactness and ease of handling. However, being an open radioactive source with the half-life of $\simeq 86$ d, such source requires certain precaution in handling. The investigation started in 2005 and is described in [KAT04, Ven09, Ven10]. Only the main features of the source production technique will be mentioned here.

4.1.1. Vacuum evaporation of ^{83}Rb

The production of the ^{83}Rb activity is accomplished on the U-120M cyclotron facility via the reaction $^{\text{nat}}\text{Kr}(p, x n)^{83}\text{Rb}$ using a water cooled krypton gas target. The pressurized krypton gas is exposed to the external proton beam for several hours. The mixture of rubidium isotopes is then washed out of the target chamber by water. The elution efficiency of ^{83}Rb

from the target amounts to $\simeq 95\%$. After the chemical treatment, the ^{83}Rb water solution is obtained in purified and concentrated form. For the evaporation of ^{83}Rb in the vacuum of 10^{-5} mbar the commercial modular coating system BAL-TEC MED 020 is used. The water solution of ^{83}Rb , containing several tens of μl , is placed onto the tantalum evaporation boat and dried. Then the boat is placed in the coating system and is heated to 200°C for about 10 minutes in order to let the impurities to evaporate. During this phase the boat is shielded by a special mask so that the substrate is kept clean. It was found out that no ^{83}Rb evaporates below 300°C , thus, no ^{83}Rb is lost during this preliminary heating. The evaporation of ^{83}Rb then follows for 30–60 seconds at 800°C . The efficiency of the vacuum-evaporation amounts to 5–30%. Thanks to a suitable mask the evaporated ^{83}Rb activity forms a circle of area of $\simeq 1\text{ cm}^2$. As a backing, metal (Al) or graphite (foil or HOPG) is used.

Typical ^{83}Rb activity evaporated onto the backing is 5–10 MBq. This amount corresponds to an average thickness of only ≈ 0.5 monolayer of radioactive rubidium. However, according to its high reactivity, the ^{83}Rb on the backing is never found in a pure metallic form, rather in the form of compounds which reflect the chemical environment of the source. In addition, during the vacuum evaporation procedure and the consequent storage of the source on air various oxides spontaneously cover the backing, thus creating additional layers on its surface. This process is inevitable¹ even in vacuum conditions of 10^{-10} mbar. Thus, in the application of monitoring the HV scale of KATRIN over several months, the contamination of the source surface with residual gas is inevitable without cleaning. However, some cleaning of the source by means of ion etching is excluded as it would remove also the thin film containing the useful ^{83}Rb . Besides adsorption, another processes involving desorption and surface diffusion can possibly occur. The simplified model of the vacuum-evaporated source is illustrated in Fig. 4.1.

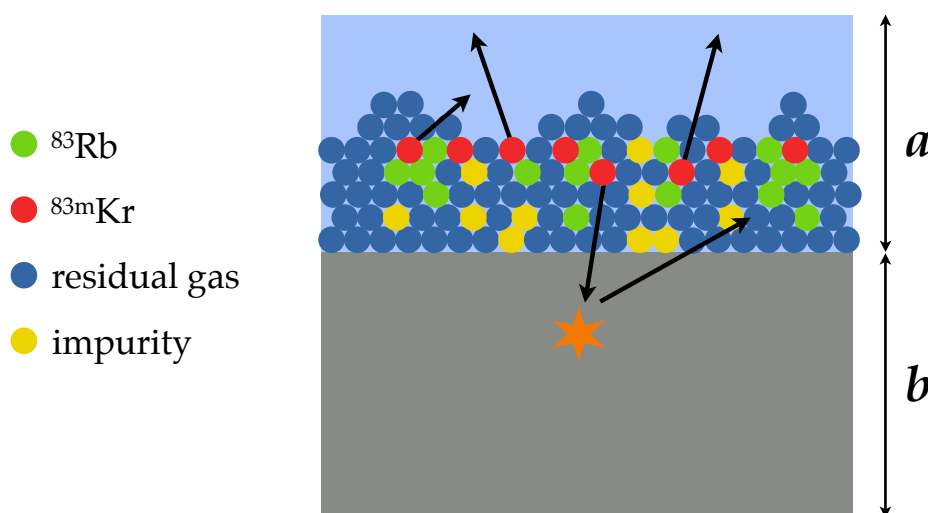


Fig. 4.1: The schematic view of the vacuum-evaporated $^{83}\text{Rb}/^{83\text{m}}\text{Kr}$ source illustrating the surface conditions. On the contrary to the condensed $^{83\text{m}}\text{Kr}$ source (cf. Fig. 3.10), the surface is contaminated due to the adsorption of residual gases. The residual gas adsorption is approximated by a layer of thickness a . The arrows represent the conversion electrons emitted into the space of 4π . The star denotes a backscattering event inside the substrate.

¹The surface area of 1 cm^2 kept on air is covered with a film of residual gas of one monolayer thickness within $\approx 10^{-9}$ s and even in the vacuum of 10^{-10} mbar this process takes only about 6 h [Rot98].

4. Solid $^{83}\text{Rb}/^{83\text{m}}\text{Kr}$ electron...

After the decay, ^{83}Rb atoms convert into chemically inert krypton atoms kept fully or partially in the source solid matrix. With respect to the task of HV scale stability monitoring the aim is to capture both ^{83}Rb and $^{83\text{m}}\text{Kr}$ in a thin film adsorbed on a solid:

- the conversion electrons created in an $^{83\text{m}}\text{Kr}$ atom escaped from the source are not situated in the right place defined for the source position (cf. Fig. 2.3 in Sect. 2.2) and thus are useless for the energy calibration,
- the escape of the $^{83\text{m}}\text{Kr}$ atoms would have to be compensated by a higher ^{83}Rb activity of the calibration source,
- a possible release of ^{83}Rb compounds from the source into the ultrahigh vacuum of the monitor spectrometer would increase the background in the electron spectra.

The bond of ^{83}Rb atoms in the substrate seems to be easily achievable due to its reactivity. On the other hand, it may be difficult to prevent the spontaneous release of the weakly interacting noble gas $^{83\text{m}}\text{Kr}$. The capture (also denoted as retention) of $^{83\text{m}}\text{Kr}$ inside the source was found to significantly vary from source to source even when the various factors affecting the process of vacuum evaporation were reproduced.

The reproducibility and stability of the conversion electron energy is determined by the reproducibility and stability of the source matrix surrounding the $^{83\text{m}}\text{Kr}$ atoms. Such a challenge is complicated by the fact that the vacuum-evaporated $^{83}\text{Rb}/^{83\text{m}}\text{Kr}$ source does not represent a well defined macroscopic sample. On the contrary, sub-monolayer of ^{83}Rb corresponds to trace amount of radioactive material exposed to surrounding conditions. Certain broadening of the conversion electron lines can also be expected in comparison with those obtained from a free $^{83\text{m}}\text{Kr}$ atom.

4.1.2. Samples investigated in this work

Altogether four sources, prepared by vacuum evaporation at the Nuclear Physics Institute Řež/Prague, were tested at Mainz MAC-E filter. They were denoted as "S X", where X is the production number of the given source. In Tab. 4.1 the following properties of the sources $X = 11, 13, 28$ and 29 are presented:

- the date of production,
- the amount of ^{83}Rb [MBq] which was placed into the evaporation boat,
- the element of the substrate onto which the ^{83}Rb was evaporated,
- the distance between the boat and the substrate,
- the efficiency of the evaporation process, determined simply from the comparison of the ^{83}Rb activities of the boat and the substrate,
- the amount of ^{83}Rb [MBq] which was evaporated onto the substrate,
- the retention of $^{83\text{m}}\text{Kr}$ [%], defined as the portion of $^{83\text{m}}\text{Kr}$ which was trapped inside the solid source, and finally
- the amount of ^{83}Rb [MBq] in the source when the measurement of the given source actually started at Mainz MAC-E filter (reference date is also included).

It is clearly seen that reducing the distance between the boat and the substrate increased the efficiency of the evaporation. This enabled to produce strong sources S 28 and S 29 which both contained about 5 MBq of ^{83}Rb . However, their retention of $^{83\text{m}}\text{Kr}$ (denoted here as R_{Kr}) was different: $R_{\text{Kr}}(\text{S 28}) = 19\%$ and $R_{\text{Kr}}(\text{S 29}) = 11\%$ [Ven09].

After the test measurements at the Institute of Physics, University of Mainz, were finished, the source S 28 was transported back to the Nuclear Physics Institute Řež/Prague. The ^{83}Rb activity of the source was remeasured on 20.11.2009 and determined as 0.101(4) MBq [Sle11]. Thus, it was found out that within 16 months which passed since the production date, no ^{83}Rb was released from the source. The uncertainty of the ^{83}Rb activity measurements amounted to 4%. It should be noted that during these 16 months the source S 28 was kept for prolonged periods of time (typically of the duration of $\simeq 1$ month) in the vacuum setup of Mainz spectrometer (10^{-10} mbar). The zero release of the ^{83}Rb atoms from the vacuum-evaporated sources was also reported in [Zbo06] where the ^{83}Rb activity of several sources was repeatedly measured (with the precision of 0.2%) before and after inserting the sources into vacuum of 10^{-6} mbar.

Furthermore, the $^{83\text{m}}\text{Kr}$ retention of the source S 28 was remeasured with the help of two different methods [Sle11]. Both methods utilized the soft gamma ray lines of $^{83\text{m}}\text{Kr}$ of energies 9.4 and 32.2 keV (cf. Eq. 3.16 and Eq. 3.17). The results obtained with both methods agreed well, giving the new value of $R'_{\text{Kr}}(\text{S 28}) = 26.5(14)\%$. Clearly, the new value R'_{Kr} is by 7.5% higher than the value R_{Kr} determined shortly after the source production. It may be speculated that either the $^{83\text{m}}\text{Kr}$ retention of the vacuum-evaporated source changes in time as the source “ages” or the $^{83\text{m}}\text{Kr}$ retention is changed by keeping the source in the ultrahigh vacuum conditions of 10^{-10} mbar for prolonged periods of time. Moreover, during the series of measurements at Mainz spectrometer several abrupt breakdowns of vacuum ($10^{-10} \nearrow 10^{-5}$ mbar or worse) occurred which might affect the vacuum-evaporated source in some way.

Finally, in [Sle11] the spatial distribution of ^{83}Rb atoms over the source S 28 surface was studied with the help of the Timepix detector [Llo07]. The Timepix detector is based on the silicon detector chip with 256×256 pixels, each pixel having the dimensions of $55 \times 55 \mu\text{m}$. Thus, the total sensitive area is a square with the edge of 14.08 mm. The scan of the ^{83}Rb activity of the source S 28 is shown in Fig. 4.2. It was found that the distribution of ^{83}Rb in the x - y plane can be represented by a two-dimensional Gaussian distribution with a given width (FHWM). In the case of the source S 28 the spot of the ^{83}Rb activity was of circular shape of the diameter 7.3 mm. In Fig. 4.2 it is also seen that the spot with the maximum density of ^{83}Rb atoms is off-centered, which comes probably from a slight geometrical misalignment during the process of vacuum evaporation. However, this represents no problem for the utilization of the source.

Tab. 4.1: The overview of the vacuum-evaporated sources investigated in this work.

source no.	date of prod.	^{83}Rb [MBq] in boat	substrate	evaporation dist. [mm]	effic. [%]	^{83}Rb [MBq] as evap.	retention of $^{83\text{m}}\text{Kr}$ [%]	^{83}Rb [MBq] in Mainz	date
11	29.05.2006	140	Al	14	2	2.4	18	0.13	25.05.2007
13	30.01.2007	4.2	Al	11	12	0.5	7	0.23	30.04.2007
28	28.07.2008	18	C	5	27	4.95	19	3.74	28.08.2008
29	28.07.2008	19	C	5	26	4.86	11	1.85	26.11.2008

The description of the columns is given in text beginning on page 62.

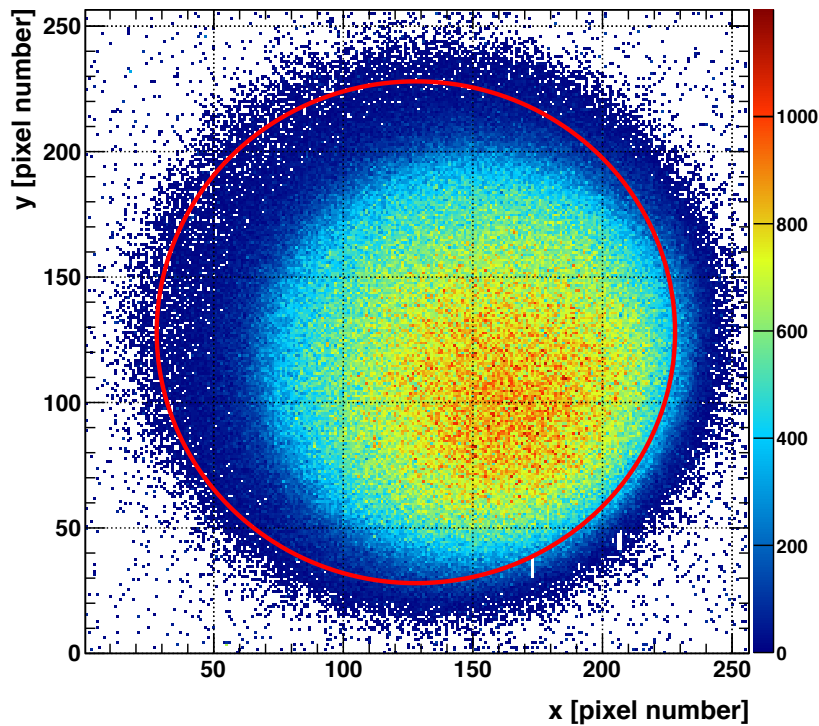


Fig. 4.2: The spatial distribution of the ^{83}Rb activity on the surface of the vacuum-evaporated source S28. The relative intensity of the recorded signal in each pixel is represented by the color scale. The red circle denotes the edge of the source holder of inner diameter 11 mm. The figure is based on [Sle11].

4.2. Ion-implanted sources

The systematic measurements of the energy stability of the $^{83\text{m}}\text{Kr}$ conversion electron lines, carried out at Mainz MAC-E filter, were started with the vacuum-evaporated sources. In the course of these measurements, which are reported later in Chap. 6, it was realized that the sources did not really provide well defined stable conditions for the $^{83\text{m}}\text{Kr}$ atoms. In 2008 an idea arose, to implant the ^{83}Rb ions into suitable substrates. The idea was based on the early work [Por71] where the ^{57}Co ions were a) deposited at very low energy $< 25\text{ eV}$ on the substrate surface and b) implanted at the energy of 500 eV into the substrate lattice. The cleaved surfaces of natural graphite crystals were used as the substrate. The case (a) corresponded to an “oxide state” where the ^{57}Co ions could not penetrate the graphite lattice. The case (b) was denoted as a “metallic state” where oxidation could not occur as the ions penetrated at least one but no more than five atomic planes of graphite. The ^{57}Co (half-life of $\simeq 272\text{ d}$) decays by electron capture into ^{57}Fe which emits electrons of internal conversion from the 14.4 keV gamma transition. The comparison of the “K-14.4” conversion electron lines (internal conversion on the K shell) measured in the two chemical states is shown in Fig. 4.3.

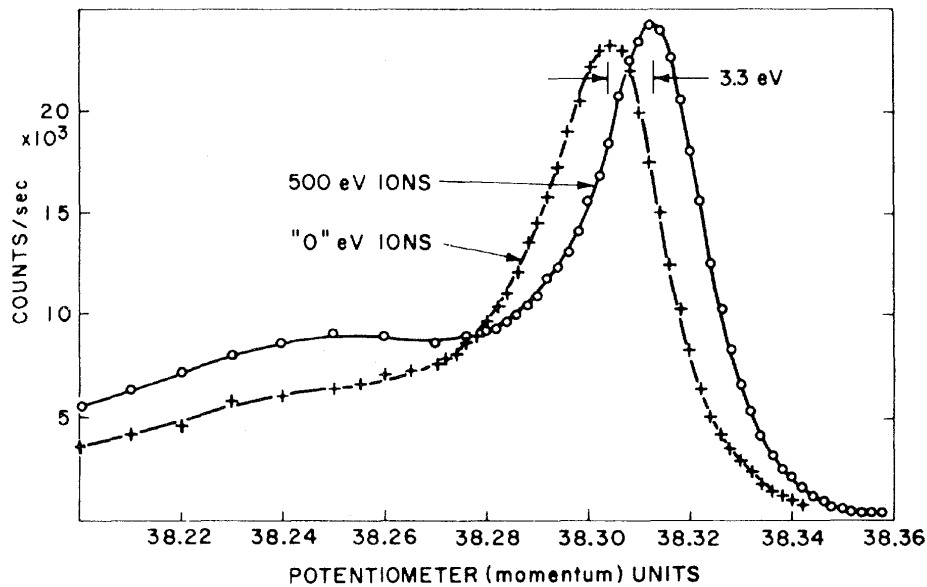


Fig. 4.3: The K -14.4 internal conversion electron lines at 7.3 keV, showing the chemical shift (change in the K binding energy). Ions of ^{57}Co from the electromagnetic isotope separator were allowed to impinge on natural graphite crystals at energies of 0–25 or 500 eV. The “zero” energy ions cannot penetrate the graphite lattice and are oxidized on the surface, whereas the ions with the energy of 500 eV penetrate the lattice and remain in a metal-like environment protected from oxidation. The K shell binding energy differs by about 3.3 eV in these two chemical states, being lower for the 500 eV ions sample. A more pronounced low energy tail of the line corresponding to the implantation at 500 eV was caused by greater energy losses of the conversion electrons emerging from the backing. The figure is taken from [Por71]. In Sect. 4.3 the effects of the binding energy shift and the electron energy losses are discussed in detail.

4.2.1. Basic processes of ion implantation

It is beyond the scope of this work to give a complete overview of the implantation technique. An attempt will be made to cover the following topics:

- The basics of the of ion implantation will be introduced with the help of reviews [Tow76, Dav80b, Nie83, Dez95, For99]. The interplay of a number of factors affecting the process of ion implantation can be comprehended this way.
- The radiation damage will be briefly discussed as it also influences the final structure of the system “target + implants”.

Besides nuclear reactions and diffusion, the ion implantation is the main doping technique with a great versatility: the atoms (which can also be radioactive isotopes) can be implanted into any host lattice. This way the modification of materials is easily achievable which has far-reaching applications, ranging from metal finishing (metal surfaces resistant to corrosion and wear) to production of semiconductors.

The process called ion implantation stands for the phenomenon when the solid is bombarded with ions and the ions remain in the solid. The advantage of this process is that no serious limitations exist for mixing atomic components in the solid. The atoms and the materials can also be brought intentionally to extreme conditions. Fast ions penetrating the solid lose their energy in three stopping processes:

- direct collisions between the ion and a screened nucleus,
- excitation of electrons bound in the solid, and
- charge exchange processes between the ion and the atoms of the solid.

All the three processes are energy dependent and make different contributions to the energy loss along the path of the ion. The quantity which defines the rate of energy loss by the ion in the target is called stopping power S . It represents the measure of the energy loss of the ion per unit distance, thus $S = dE/dx$. The final site of the implanted ions depends in a complex way on the following parameters:

1. the atomic masses and atomic numbers of the incident ion (M_1, Z_1) and the target atom (M_2, Z_2),
2. the crystalline structure of the target,
3. the chemical nature of the incident ion and the target,
4. the impurities inside the host lattice,
5. the incident angle under which the ion hits the surface,
6. the temperature of the target during the implantation process,
7. the implantation energy E_1 of the incident ion,
8. the implanted dose (also called fluence), defined in literature as the total number of implanted ions and usually designated Q [ions cm^{-2}].

While the factors (1) to (4) are usually governed by the given application and choice of materials, the parameters (5) to (8) can be directly controlled during the implantation procedure. Typically, the implantation energy E_1 ranges from hundreds of eV to units of MeV. The implanted dose Q can be expressed as

$$Q [\text{ions cm}^{-2}] = \frac{\text{ion beam current [A]} \cdot \text{time of implantation [s]}}{\text{ion beam scanning area [cm}^2]}. \quad (4.1)$$

The ion implantation is a random process, the average depth below the surface an ion penetrates is called the mean projected range R_p . This depth is typically shorter than the actual distance the ion travels. Generally, the mean projected range increases with the ion energy E_1 and decreases with the masses M_1 and M_2 . The distribution of the implanted atoms inside the target can be represented by a range profile, illustrated in Fig. 4.4. The implanted ions also scatter laterally around the impact point. The range distribution can be roughly approximated by a Gaussian distribution with a standard deviation (straggle) ΔR_p . This longitudinal straggle of the mean projected range can be roughly estimated via

$$\Delta R_p \simeq \frac{2}{3} R_p \frac{\sqrt{M_1 \cdot M_2}}{M_1 + M_2}. \quad (4.2)$$

Following the approximation by the Gaussian distribution, the implanted dose Q can be written as

$$Q = \sqrt{2\pi} \cdot C_p \cdot \Delta R_p, \quad (4.3)$$

where C_p [ions cm^{-3}] denotes the peak concentration of the implants. While the implanted dose Q can be viewed as the total area of the range distribution, the peak concentration

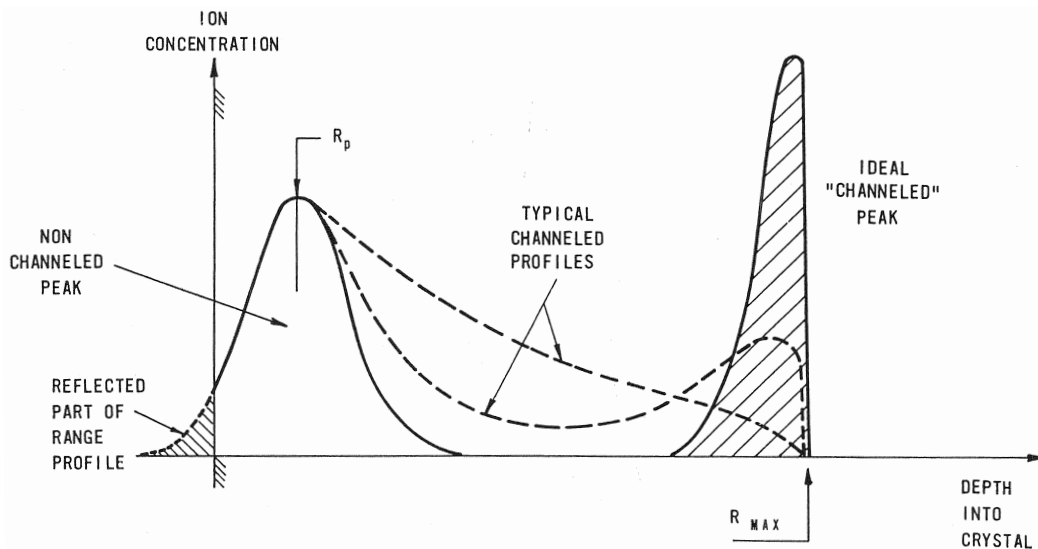


Fig. 4.4: The schematic representation of typical range profiles. The ion concentration is plotted as a function of the implantation depth into the target. The shaded part of the range profile, extending to negative depths, represents a fraction of ions which were reflected upon impinging on the surface. The height and shape of the distribution between R_p and the maximal penetration depth R_{max} depends on many parameters that are difficult to predict or control. The figure is taken from [Dav80b].

C_p corresponds to the concentration of implanted ions at the depth equal to R_p . The range profile also strongly depends on the crystalline structure of the host lattice. During the implantation into a single crystal the ion can travel a significant distance along the crystallographic axis (in an "open channel") while only electronic energy losses occur. This well known effect is denoted as channeling. During the implantation into a polycrystalline target, where the ordering of the individual crystals is random, a certain portion of ions may undergo the channeling and penetrate deeper into the target. This is reflected by a tail of the range profile as shown in Fig. 4.4. The range profiles can be determined experimentally (destructively) by repeated sputtering of the target surface and subsequent measurement of the concentration of the implanted atoms by suitable methods. In the case of implantation of radioactive isotopes, the sputtering may be easily combined with the spectroscopy of ionizing radiation, provided the implanted radioactive isotope emits radiation of measurable energies.

A great amount of work was devoted to the problem of calculating the range profiles of ions in solids theoretically. For a historical review of these efforts the reader is kindly referred to [SRI11]. The first unified approach to the stopping and range theory was made in 1963 by J. Lindhard, M. Scharff and H.E. Schiøtt, using the Thomas-Fermi model of electronic structure of many-body systems. The approach was denoted as "LSS theory" and was widely used for the range estimates for implantation into amorphous materials. The LSS theory enabled predictions of the ranges of ions in solids with the precision of a factor of two over the entire range of atomic species and energies. The LSS theory was the last of the comprehensive theories based on statistical models of atom-atom collisions [SRI11]. Numerical methods, together with further theoretical insights, made it possible to improve the calculation of stopping power and ranges. Nowadays, the overall accuracy of the prediction of

the implantation ranges is about 5% [Zie10, SRI11].

The standard software package SRIM (Stopping and Range of Ions in Matter) [SRI11] was used in this work. In Fig. 4.5 a typical calculation carried out with the SRIM program is presented. A simple configuration was simulated: the Rb ions of the implantation energy 30 keV were hitting the surface of a) gold ($Z = 79$) and b) carbon ($Z = 6$) substrate under zero incident angle. In the SRIM code, the structure of the substrate is assumed to be polycrystalline. In each case the number of simulated Rb ions amounted to 10^5 . The substrate thickness of $25\ \mu\text{m}$ was assumed in the simulation, however, it can be seen in Fig. 4.5 that practically all the ions stopped in the solid within the first $\simeq 400\ \text{\AA}$ in both cases. The range distribution of Rb (30 keV) in C is nearly Gaussian with the parameters $R_p = 227\ \text{\AA}$ and $\Delta R_p = 50\ \text{\AA}$ (direct output of SRIM). Using the approximation in Eq. 4.2 and the standard atomic weights of Rb and C, one comes to the same value for ΔR_p . Assuming that the thickness of one monolayer of carbon $d_{\text{ML}}(\text{C})$ is about $2.15\ \text{\AA}$, the peak concentration of Rb ions lies in the depth of 106 ± 23 atomic layers. The situation is quite different for the case of Rb (30 keV) in Au. Here the mean projected range is much smaller (Au is about 16 times heavier than C), $R_p = 81\ \text{\AA}$, and a tail of the range profile is clearly visible. However, in a rough Gaussian approximation the longitudinal straggle is again $\Delta R_p = 50\ \text{\AA}$. Considering the monolayer thickness of gold as $d_{\text{ML}}(\text{Au}) = 2.57\ \text{\AA}$, the peak distribution is now in the depth of 32 ± 20 atomic layers.

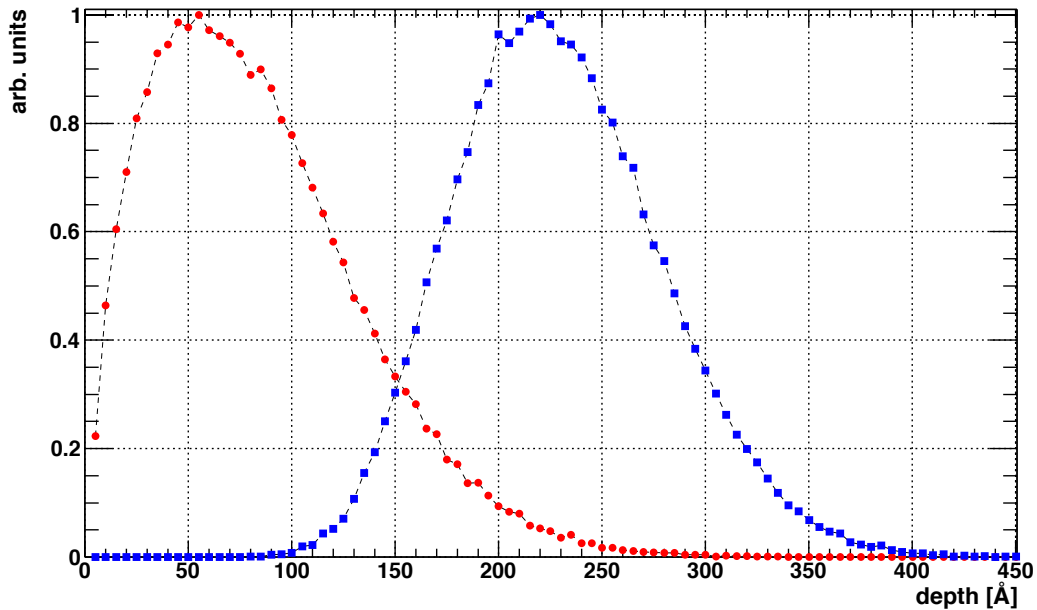


Fig. 4.5: The simulated range profiles of Rb ions implanted at the energy of 30 keV into carbon (blue points) and gold (red points) polycrystalline foils. The distributions were individually scaled to unity. The simulation was carried out with the help of the SRIM code.

In Fig. 4.6 the model of the ion-implanted $^{83}\text{Rb}/^{83\text{m}}\text{Kr}$ source is depicted. The distribution of ^{83}Rb atoms inside the substrate can be assumed in a form similar to distributions shown in Fig. 4.5. In the model the impurities inside the substrate are also included, as their immediate vicinity to the ^{83}Rb atoms (more precisely, the $^{83\text{m}}\text{Kr}$ atoms) can influence the emission of the conversion electrons. One of the main advantages of the ion-implanted source with respect to the vacuum-evaporated one may be seen already now: the rest gas, covering the

4. Solid $^{83}\text{Rb}/^{83\text{m}}\text{Kr}$ electron...

substrate surface, is not affecting the implanted ^{83}Rb atoms. However, few ^{83}Rb atoms are drawn in the figure on the substrate surface. This corresponds to the fact that during the implantation not exactly 100% of implants ends up inside the target.

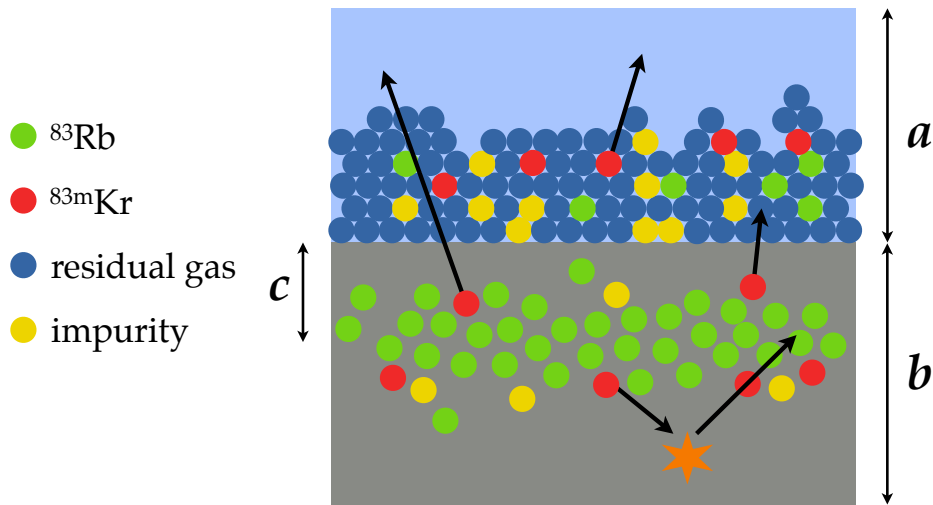


Fig. 4.6: The schematic view of the ion-implanted $^{83}\text{Rb}/^{83\text{m}}\text{Kr}$ source illustrating conditions on the surface and inside the metal foil. Similarly to the vacuum-evaporated source (cf. Fig. 4.1), the surface is contaminated due to the adsorption of residual gases which is represented by a layer of thickness a . Certain portion of ^{83}Rb ions remains in this layer after the implantation. However, more than 90% of the ^{83}Rb ions is brought to the metallic state where the surface conditions do not play a role. The mean projected range is denoted as c . The implanted profile of the ^{83}Rb atoms is not drawn realistically, see Fig. 4.14 below for the simulated distribution of ^{83}Rb atoms along the depth into the foil. The arrows represent the conversion electrons emitted into the space of 4π . The star denotes a backscattering event inside the substrate.

It was shown that from the macroscopic point of view, the location of the implanted ions can be quite accurately predicted. However, the immediate environment of the implanted atom plays a significant role, especially when the atom emits electrons which are intended for the purposes of calibration and monitoring. At this point the radiation damage shall be considered as it influences the internal structure of the irradiated target. The description of the radiation damage involves a complex interplay between the initial collision processes and the subsequent anneal processes.

The elastic collisions of the ion with host nuclei produce radiation damage of crystal structure of the target in the form of a large number of displaced atoms (the lattice atom is "knocked off" its site). The first elastic collisions furnish host atoms with sufficient kinetic energy to induce other displacements in turn. In this way a displacement cascade is built up within $\approx 10^{-13}$ s around each individual ion track, as illustrated in Fig. 4.7. Thus, ion implantation provides almost instantaneous distribution of point defects within an extremely small volume. The cascades can be treated theoretically, similarly to the concept of stopping power and projected range, and the distribution of the damage (disorder) can be predicted. The main parameters involved here are Z_1 , E_1 , Z_2 and channeling. The depth at which a maximum in the damage distribution is observed, is often designated R_d . The distribution can be characterized by its standard deviation ΔR_d .

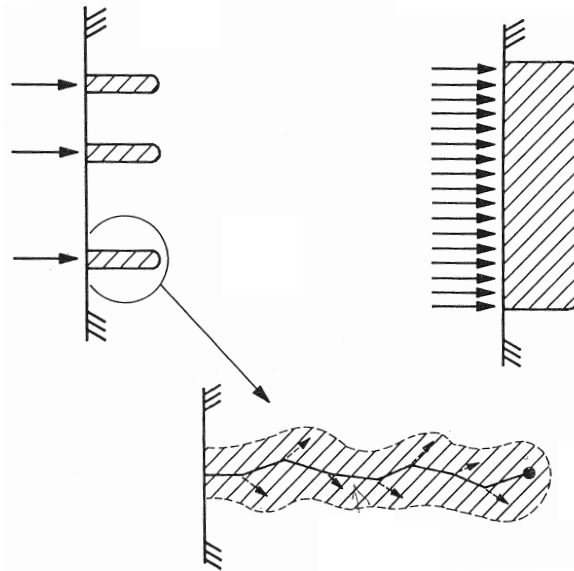


Fig. 4.7: The schematic representation of the lattice disorder in the regimes of low and high implanted dose. The upper left figure shows the individual regions of damage in the low dose limit. At the bottom the individual ion track is depicted in detail. On the upper right side the uniform damage layer in the case of the high dose is shown. The figure is taken from [Dav80b].

After the lattice atom was displaced, the lattice site may remain empty, such site is called vacancy. The displaced atom may come to stop in the solid off site, which creates a so-called interstitial atom. Such an atom occupies an irregular place in the crystal structure. Also, the original vacancy may be re-occupied by some another lattice atom. The relationship between the various effects can be loosely written as

$$\text{displacements} = \text{vacancies} + \text{replacements} = \text{interstitials} + \text{atoms leaving the target}.$$

In the final stage of the slowing-down process, practically every atom in the cascade has acquired an amount of kinetic energy largely exceeding the energy connected with thermal vibrations. This leads to the concept of a "thermal spike". The available kinetic energy at the end of the cascade induces an appreciable amount of damage recovery, *i. e.* reordering takes place and the damaged crystal structure partially "heals itself". Depending on the ratio of the masses of the incident ion and target, there is a probability that the final collision of the implanted ion displaces a host atom, leaving the new (implanted) atom at a substitutional site. Otherwise, the implant will end up interstitially. A large part of the implanted ions finally ends up in their own "depleted zone", in which vacancy concentrations as large as 5% may occur. The abundant energy available at the end of the cascade leads to damage recovery, but can also induce trapping of vacancies or small vacancy clusters, independent of implantation temperature. After the implantation is finished, it is a common practice to remove the lattice damage by thermal annealing of the target. The temperature recommended for the annealing procedure is equal to about $\frac{2}{3} T_{\text{melt}}$ [But11], where T_{melt} is the temperature of the melting point of the host. The thermal annealing usually causes the implanted atoms to become substitutional, *i. e.* to occupy regular lattice sites. However, the implantation profile will be changed by the thermal annealing.

To summarize, the damage events can be categorized as follows:

a) collision processes

Single cascade may result into various point defects: vacancies, interstitials, Frenkel pairs².

b) anneal processes

The high concentration of defects within a single cascade may cause them to recombine or unite to form extended defects: clusters, loops, voids, bubbles. They can migrate and interact with the surface or with other cascades or impurity atoms.

The radiation damage can also be divided according to the implanted dose Q :

a) low dose

Keeping the implanted dose sufficiently low, $Q \lesssim 10^{12}$ ions cm^{-2} , only individual isolated damage regions are created around each ion track and the probability for overlap of the cascades is negligible. In this low-dose limit the collision and anneal processes can be fully separated from one another.

b) high dose

With sufficiently high implanted dose, $Q \gtrsim 10^{14}$ ions cm^{-2} , the complete overlap of the cascades occur and a uniform distribution of damage is obtained, cf. Fig. 4.7. This damage level exhibits complex dependence on the implanted dose and the dose rate.

The illustrative dependence of the substitutional component and the lattice disorder on the implanted dose, studied in the early work [Eri69], is shown in Fig. 4.8. Here the heavy ions of Bi and Tl were implanted into silicon at 25°C without any annealing treatment. At low doses ($Q \simeq 10^{13}$ ions cm^{-2}) a large fraction of implanted ions was found on substitutional sites. At doses greater than 10^{14} ions cm^{-2} , the lattice structure in the implanted region was completely destroyed. The implanted dose of

$$Q_{\text{lim}} \simeq 10^{14} \text{ ions cm}^{-2} \quad (4.4)$$

is generally accepted as a limit above which the lattice is damaged after room temperature implantation [Her86].

The damage of the target upon implantation can be also visualized with the help of the SRIM code. However, the self-annealing effects, occurring at room temperature, are not included in the SRIM calculation. Therefore, the damage calculated with the SRIM code can be interpreted as how the damage would look like for the implantation at 0 K [SRI11]. In Fig. 4.9 the number of vacancies of the targets C and Au created due the implantation of Rb ions of the energy 30 keV (aforementioned example, cf. Fig. 4.5) is shown. While for the carbon target the maximal damage is found in the depth of $R_d \approx 140$ Å, in the case of the gold target the damage distribution peaks at $R_d \approx 40$ Å. It is also interesting to note that at the maximum of the damage distribution, the Rb ion of the initial energy 30 keV creates more than 7 vacancies per Å in the Au lattice, but less than 2 vacancies per Å in the C lattice. This discrepancy reflects the different mechanisms of energy losses in these two cases. The reason for this are the very different ratios of the atomic masses and the atomic numbers of

²Frenkel pair represents a point defect where the displaced atom creates a vacancy and becomes interstitial in the lattice location which is usually unoccupied.

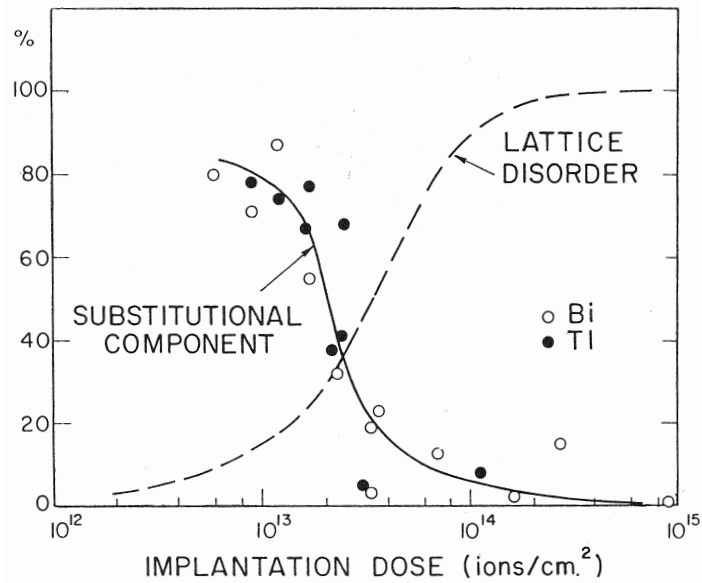


Fig. 4.8: The dose dependence of the substitutional level [%] of un-annealed Tl (●) and Bi (○) implants in silicon at 25°C. The implantation energy amounted to 40 keV. The dashed line indicates the total amount of lattice disorder in the implanted region, expressed as the percentage of silicon atoms displaced by more than 0.2 Å from their equilibrium lattice sites. The figure is taken from [Eri69].

the incident Rb ion and the targets (very light carbon atom vs. heavy gold atom).

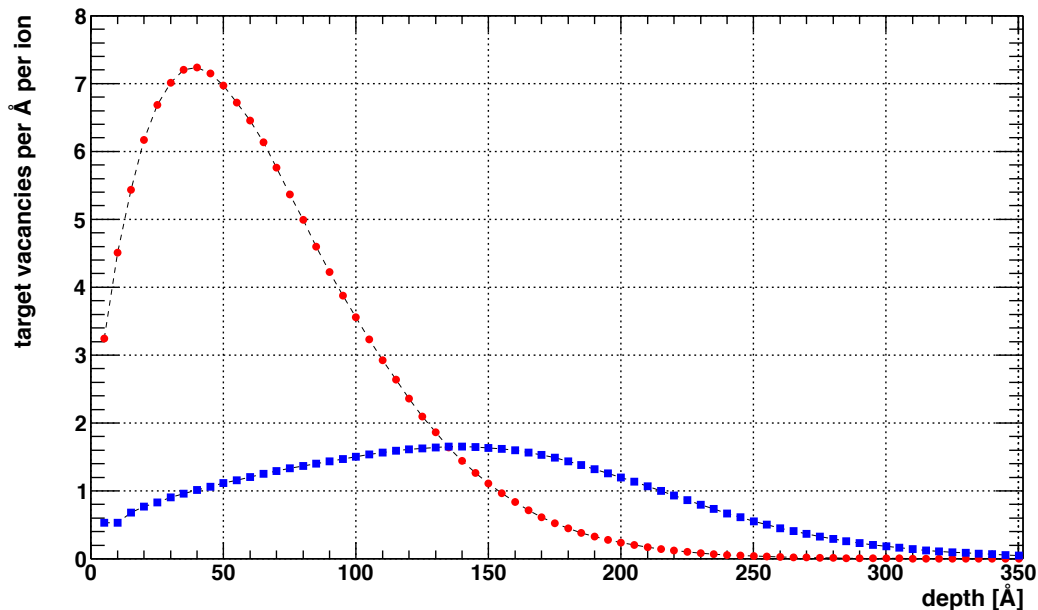


Fig. 4.9: The simulated damage profiles of the implantation of 30 keV Rb ions into carbon (blue points) and gold (red points). The number of vacancies per Å created by one incident Rb ion is plotted as a function of depth. The simulation was carried out with the help of the SRIM code. The corresponding range profiles can be seen in Fig. 4.5.

4.2.2. Ion implantation of ^{83}Rb at the ISOLDE facility

The ion-implanted ^{83}Rb samples investigated in this work were produced at the ISOLDE facility [ISO11] at CERN. The acronym ISOLDE stands for “Isotope Separator On-Line”. The on-line isotope mass separator facility represents the most versatile tool for the production of radioactive isotopes. Here, the production, the chemical separation, the mass separation and the implantation of radioactive isotopes are integrated into one device whereas off-line separators only cover mass separation and implantation. At ISOLDE the radioactive ions are produced by spallation, fragmentation or fission reactions in thick solid or liquid targets hit by an external high energy proton beam [For99].

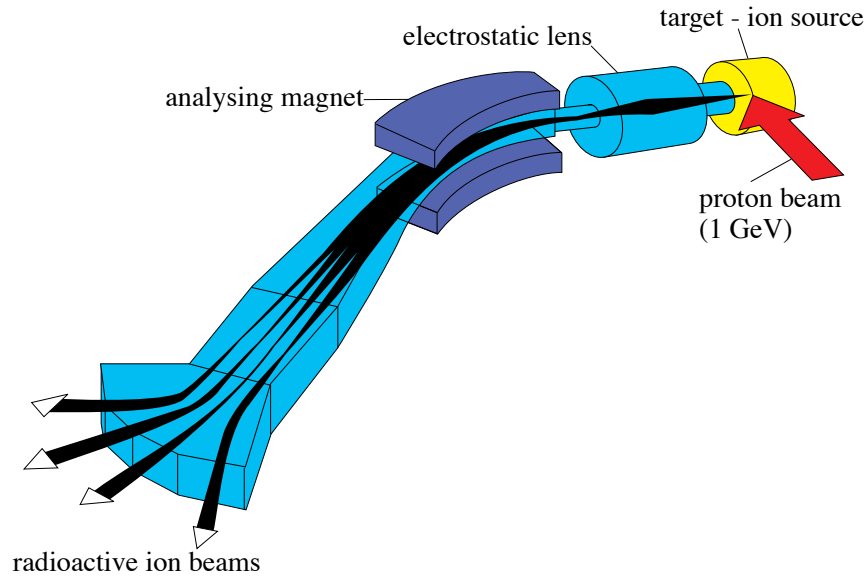


Fig. 4.10: The schematic layout of the on-line mass separator for the radioactive beams at the ISOLDE facility. The figure is taken from [For99].

The scheme of the on-line mass separation for radioactive beams is depicted in Fig. 4.10. The pulsed proton beam of the energy 1–1.4 GeV is delivered by the Proton Synchrotron Booster to the ISOLDE target. In fact, there are two target stations available, one is connected to the general purpose separator (GPS) while the other one is a part of the high resolution separator (HRS). Up to 600 different isotopes of 70 elements can be produced by about 60 different combinations of target material and ion sources [For99]. The target is kept at temperature between 700 and 2 000°C, permitting the rapid diffusion of reaction products into the ion source. The ionization takes place on a hot surface, in a plasma or in the laser ionization source. The ions form an ion beam which is then accelerated to the energy of 30–60 keV and separated by the GPS or HRS separator. The mass resolving power $\Delta m/m$ of the GPS is stated as 2 400 [Kug00]. The mass resolving power of the HRS amounts to 7 000–15 000 with the potential to reach 30 000 in special operational mode. Lastly, the separated ion beams are sent into the ISOLDE beam line system, to which a number of experimental setups is connected. The intensity of the ion beams can be as high as 10^{11} ions s^{-1} . Detailed description of the ISOLDE facility can be found in [Kug00, Her10]. The variety of the experimental applications of the ion beams produced by ISOLDE is reflected in the series of articles [ISO00] describing the research performed at ISOLDE.

In the frame of this work ^{83}Rb ions were implanted at the ISOLDE facility into polycrystalline foils of gold and platinum of high purity. The solid uranium carbide-tantalum ($\text{UC}_x\text{-Ta}$) target was used in combination with the surface ionization, as rubidium, being alkali metal, is easily ionized. The foils of 12 mm diameter, cleaned in alcohol by ultrasonics, were placed into the vacuum chamber of the “solid state physics” (SSP) experimental back-end connected to the beam line of the GPS separator. The arrangement of the foils in the SSP holder can be seen in Fig. 4.11. In order to maximize the number of conversion electrons coming out of the $^{83}\text{Rb}/^{83\text{m}}\text{Kr}$ source without any energy loss, the implantation energy of 30 keV was chosen, which corresponded to the minimal implantation energy available at ISOLDE. In one case, the ion beam was decelerated by the retarding HV of 15 kV. This way the implantation energy of 15 keV was achieved. For this purpose a vacuum chamber was attached to the SSP setup. The schematic layout of the additional setup is shown in Fig. 4.12.

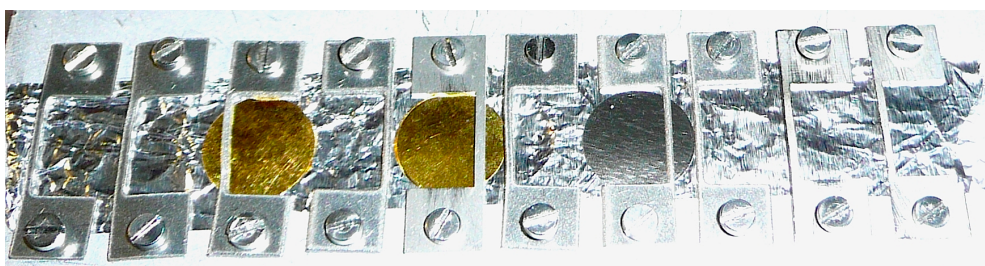


Fig. 4.11: The photograph of gold and platinum foils fastened in the SSP sample holder. It was possible to place up to 10 foils into the holder, however, only three foils were irradiated. The holder geometry was fixed and the ion beam was steered in order to irradiate the individual foils.

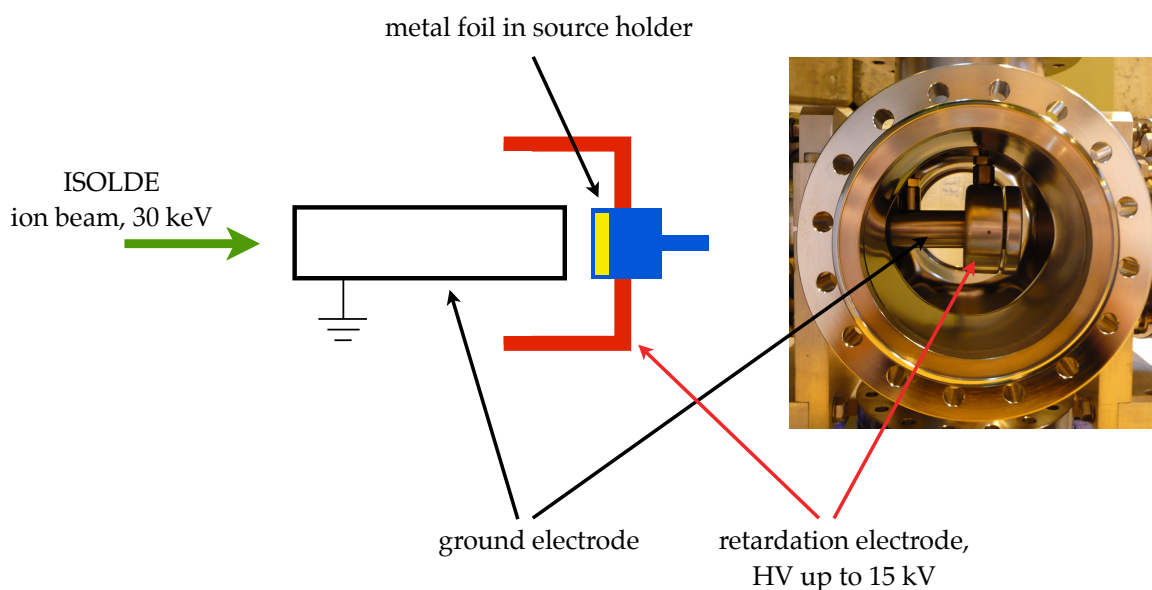


Fig. 4.12: The schematic layout (left side) and the photograph (right side) of the electrode system used for the deceleration of the ISOLDE ion beam.

In all cases the target foils were kept at room temperature and the incident angle was zero. The implantation took place in relatively poor vacuum conditions of 10^{-5} – 10^{-4} mbar. At ISOLDE it is possible to sweep-scan the area of about 2 cm^2 [Joh09] with the ion beam, however, this feature was not utilized during the implantation of ^{83}Rb . Prior to the implantation,

the beam focusing was optimized in the following way: the size and shape of the beam spot at the place of incident was checked with the help of non-radioactive Rb beam of high intensity hitting a paper replacing the foil. This was important especially for the implantation at 15 keV, in which case the foil was placed about 1 m behind the usual place of beam incident. In all cases the ^{83}Rb activity of about 3–4 MBq per sample was aimed for.

During the implantation, the number of collected ^{83}Rb ions was controlled with the help of the current integrator working on the principle of the Faraday cup (FC). The beam intensity was regularly checked by a FC counter placed upstream in the beam line. Typically, the beam intensity amounted to $\approx 2 \times 10^9$ ions s^{-1} , corresponding to the current of ≈ 320 pA. This resulted into the rate of about 0.7 MBq of collected ^{83}Rb per hour in the case of 30 keV implantation. Due to the inevitable defocusing of the ion beam in the case of the 15 keV implantation (cf. Fig. 4.12), here the collection rate was only about 0.2 MBq of ^{83}Rb per hour. After the completion of collections the foils were stored on air in holders preventing any wipe-off. It should be emphasized that *no annealing treatment* of any sample was carried out. The ^{83}Rb activity of the samples was roughly checked at the location at ISOLDE with the help of a commercial detector of ionizing radiation. The range profile of the implanted ^{83}Rb atoms or the size of the irradiated area was not investigated at that moment.

4.2.3. Samples investigated in this work

As the substrate for the implantation of ^{83}Rb the elements of carbon, gold and platinum were considered. At the end, the latter two options were chosen as it was anticipated that noble metals will provide a well defined environment for the ^{83}Rb atoms. Both Au ($Z = 79$) and Pt ($Z = 78$) possess face-centered cubic (fcc) crystal structure [Ash81]. Their electron configurations are “Au = [Xe] $4f^{14} 5d^{10} 6s^1$ ” and “Pt = [Xe] $4f^{14} 5d^9 6s^1$ ”. A noble metal is defined as having the d -bands of the electronic structure filled. Thus, strictly speaking, platinum is not a noble metal in this sense³. In addition, gold is known for its chemical inertness and this seemed appealing with respect to its use in ultrahigh vacuum conditions. The molar volume (also denoted as metallic radius sometimes) of Au and Pt is $V_m(\text{Au}) = 10.2 \text{ cm}^3 \text{ mol}^{-1}$ and $V_m(\text{Pt}) = 9.1 \text{ cm}^3 \text{ mol}^{-1}$, respectively. This quantity is of interest when comparing the sizes of the host lattice and the implant [Nie83]. Rubidium possesses the molar volume of $V_m(\text{Rb}) = 55.8 \text{ cm}^3 \text{ mol}^{-1}$, thus, the ^{83}Rb “impurity” is actually significantly oversized with respect to the host lattices.

As stated in previous section already, polycrystalline foils of high purity were used as the targets for the implantation. The foils were not heated after the collections of the ^{83}Rb ions, thus the damage of the lattice was not healed. However, as the foils were kept at room temperature during the collections, it can be assumed that the lattice underwent self-annealing to some extent. On 11.11.2008 the first collection of ^{83}Rb took place, which resulted into the source denoted as “Pt-30” (^{83}Rb ions of the energy 30 keV hitting the Pt target). The polycrystalline foil of thickness $40 \mu\text{m}$ used for this collection was not a standard commercial foil. Its purity was determined as 99.7% with the help of the X-ray fluorescence method [Sle11]. The 0.3% impurity of rhodium was found in this foil.

For the second series of collections, the commercially available foils of the purity 99.99+%

³By this division, only copper, silver and gold are the noble metals.

[Goo09] were used. The impurities in these foils were specified to be at the level of tens of ppm or less⁴. The thickness of the foils amounted to 25 μm and their diameter was 12 mm. As the first ion-implanted source Pt-30 exhibited promising results concerning the energy stability of the $^{83\text{m}}\text{Kr}$ conversion electrons, the same configuration for the ^{83}Rb implantation was realized once more. This led to the sample designated as “Pt-30 #2”. This way the reproducibility of the source production regarding the relevant source properties (long-term stability of the electron lines energy and portion of the zero-energy-loss electrons) could be verified. However, the two Pt-30 sources were not strictly identical due to the different levels of the impurities. In addition, the ^{83}Rb activities of the two sources were different. In order to investigate another possibilities of the implantation of ^{83}Rb , the sources “Au-30” (30 keV ^{83}Rb ions implanted into gold foil) and “Pt-15” (^{83}Rb ions implanted at lower energy of 15 keV into platinum foil) were produced as well.

In Tab. 4.2 the following properties of the four sources are presented:

- the date of production,
- the element and purity of the substrate,
- the implantation energy,
- the time which was necessary for producing the source,
- the amount of ^{83}Rb [MBq] implanted into the source,
- the retention of $^{83\text{m}}\text{Kr}$ [%] of the source,
- the amount of ^{83}Rb [MBq] in the source when the measurement of the given source actually started at Mainz MAC-E filter,
- the amount of ^{83}Rb [MBq] which was determined at the Nuclear Physics Institute Řež/Prague with the help of gamma ray spectroscopy,
- the dimensions a, b of the elliptic shape of the ^{83}Rb activity spot,
- the mean dose Q [ions cm^{-2}] of ^{83}Rb implanted in the source,
- the peak concentration C_p [ions cm^{-3}] of ^{83}Rb in the source, and
- the peak atomic concentration [%] of ^{83}Rb in the source (which can be presented as the level of ^{83}Rb impurity).

It should be noted that the amount of ^{83}Rb present in the sources just after the implantation and at the beginning of the measurement series at Mainz spectrometer was deduced from precise measurements of the ^{83}Rb activity carried out at the Nuclear Physics Institute Řež/Prague. The spatial distribution of the ^{83}Rb atoms in the x - y plane (over the surface) of the sources was investigated with the same method [Sle11] as described above in Sect. 4.1.2. The results are shown in Fig. 4.13. It can be seen that sources Pt-30 #2 and Au-30 were produced with a well focused beam. On the other hand, the source Pt-15, produced with the help of the retarding electrode, exhibits a circle-segment-like shape. The shape of the ^{83}Rb activity spot of the source Pt-30 is also somewhat blurred.

From the knowledge of the ^{83}Rb activity implanted and of the area of the ^{83}Rb activity spot,

⁴The Au foil, designated as “AU000341/49” by the producer, contained the following impurities [ppm]: As...6, Fe...26, Ir...6, Pd...7 and Rh...8. Similarly, the Pt foil, designated as “PT000240/55” by the producer, contained the impurities [ppm] of B...8, Ca...4, Cu...4, Fe...2, Mo...1, Pd...6 and Rh...31 [Goo09].

Tab. 4.2: The overview of the ion-implanted sources investigated in this work.

source	date of prod.	date of impl.	en. E_1 [keV]	collection time [h]	^{83}Rb [MBq] as impl.	retention of $^{83\text{m}}\text{Kr}$ [%]	^{83}Rb [MBq] in Mainz	in Řež	dimensions $a \times b$ [mm]	^{83}Rb dose Q [10^{14} cm^{-2}]	^{83}Rb conc. C_p [10^{20} cm^{-3}]	^{83}Rb impurity level [%]
Pt-30	11.11.2008	Pt	30	-	3.3	97	2.9	0.16(1)	3.8×2.6	2.3	3.0	0.19
Pt-30 #2	12.06.2009	Pt	30	5.1	4.9	94	3.4	1.35(5)	3.0×1.9	5.8	7.4	0.48
Pt-15	14.06.2009	Pt	15	7.2	1.9	88	1.4	0.54(4)	5.4×2.9	0.9	1.8	0.12
Au-30	12.06.2009	Au	30	4.5	3.3	89	2.3	0.91(2)	2.7×1.5	5.6	6.4	0.43

Detailed description of the columns is given in text beginning on page 77. The last three columns denote the mean implanted dose Q [ions cm^{-2}], the peak concentration C_p [ions cm^{-3}] (see Eq. 4.3) and the peak atomic concentration [%] of ^{83}Rb , calculated on the basis of C_p . The measurement with the source Pt-30 started in the Institute of Physics, University of Mainz, on 26.11.2008. The sources Pt-30 #2, Pt-15 and Au-30 were investigated in the Institute of Physics, University of Mainz, since 27.07.2009. The measurement of the ^{83}Rb activity of all the sources took place in the Nuclear Physics Institute Řež/Prague on 20.11.2009.

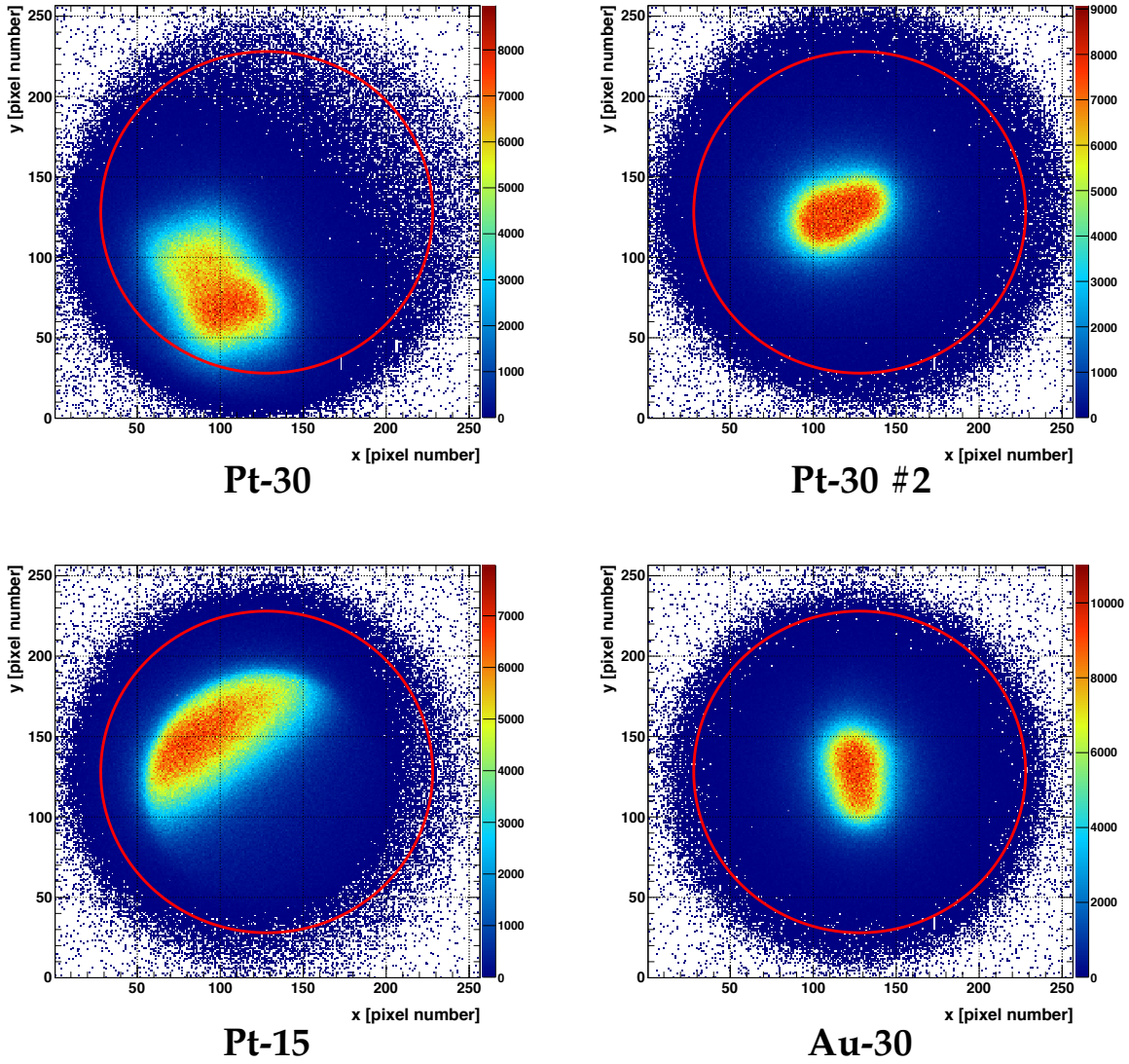


Fig. 4.13: The spatial distribution of the ^{83}Rb activity in the ion-implanted sources. The red circles mark the source holders of the inner diameter of 11 mm. The figure is based on [Sle11].

the implanted dose can be calculated. In all the cases the dose amounted to $\approx 10^{14}$ ions cm^{-2} . As expected, in the case of the well-focused sources Pt-30 #2 and Au-30 the implanted dose was the highest, about 6×10^{14} ions cm^{-2} . This value is already of the same order of magnitude as the dose Q_{lim} (cf. Eq. 4.4) considered as a limit for not destroying the host lattice. The retention of $^{83\text{m}}\text{Kr}$ in the ion-implanted sources was found to be [Sle11] about 90% or more, which is more than 3 times higher retention than in the case of the vacuum-evaporated source S 28. It may seem surprising that the $^{83\text{m}}\text{Kr}$ retention is not 100% here, however, it was pointed out in [Dav80b, San06] that a diffusion of the implants to the surface might occur.

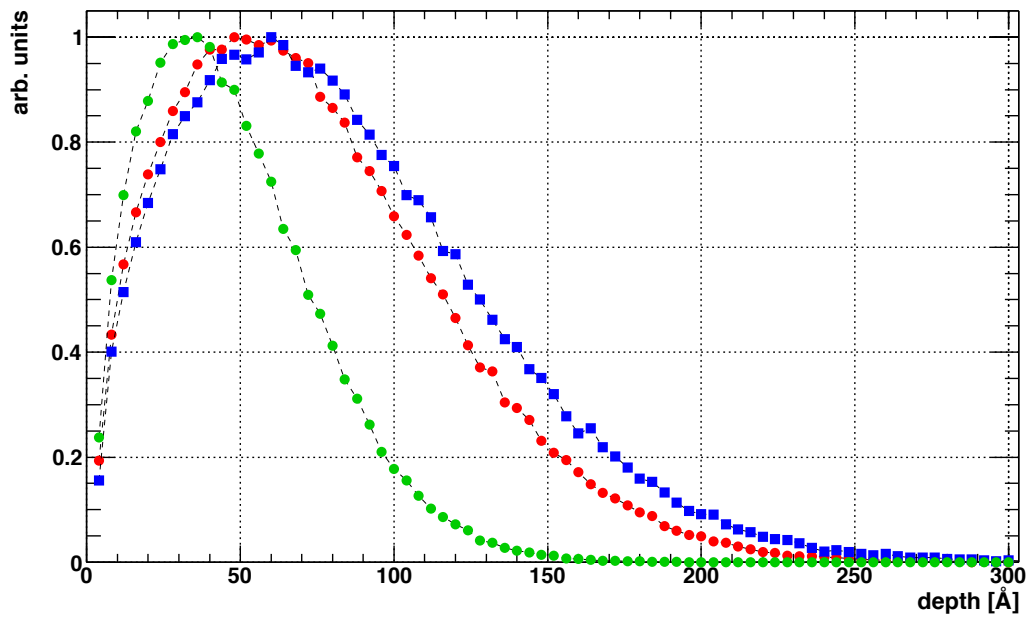
The distribution of ^{83}Rb atoms along the depth of the foils can be assessed with the help of the SRIM code. Fig. 4.14 depicts the results of the simulation, where the following parameters were considered:

- The implantation energy E_1 was set to 30 keV. In one case $E_1 = 15$ keV, which corresponded to the source Pt-15.
- Incident angle was set to zero.
- There is no temperature parameter in the SRIM simulation, as discussed on page 72.
- Polycrystalline structure of the foils is the default and only option in the SRIM code. This correlated well with our situation.
- The thickness of the Au or Pt layer was set to $25 \mu\text{m}$, however, for ^{83}Rb ions of the energy of 15 or 30 keV it virtually represented an infinitely thick layer.
- Due to poor vacuum conditions surrounding the foils during the implantation, there was certainly a considerable amount of water and hydrocarbons adsorbed on the foil surface. This fact was reflected in the simulations by introducing an additional layer above the layer representing the Au or Pt foil. For the sake of simplicity, this “rest gas layer” was set to be a pure carbon layer of the thickness of 30 \AA which was assumed to be a good approximation of the mixture of hydrocarbons *etc.* and surrounding conditions. Moreover, the sputtering effect, produced by ^{83}Rb ions impinging on the surface, is negligible as the ions possess too high energy and penetrate deeper into the metal foil. This statement is supported by the simulations carried out with the SRIM code: the sputtering yield of ^{83}Rb ions with $E_1 = 30$ keV was found to be in the range of 10–20 atoms (Pt or Au) per ^{83}Rb ion which, together with rather low ^{83}Rb ion beam intensities of $\approx 2 \times 10^9$ ions s^{-1} , means that less than one monolayer of the rest gas layer is sputtered during such implantation.

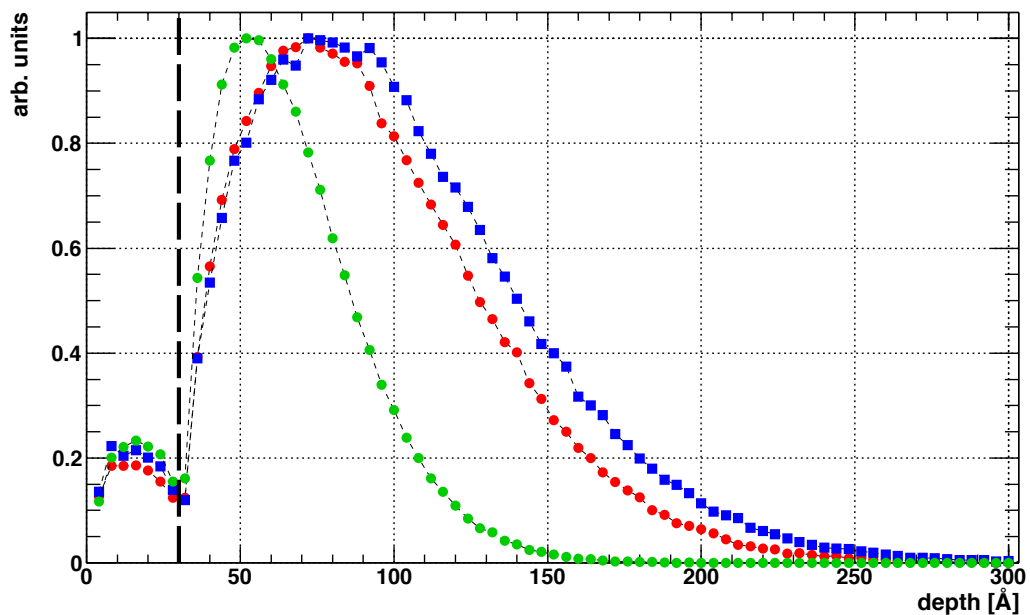
In all the cases the number of simulated ions was set to 1.5×10^5 . The following values of the mean projected range of the ^{83}Rb distribution were found (the values of the longitudinal straggle are stated in parentheses): $R_p(\text{Pt-30}) = 89(42) \text{ \AA}$, $R_p(\text{Au-30}) = 96(47) \text{ \AA}$ and $R_p(\text{Pt-15}) = 61(27) \text{ \AA}$. The stated values are valid for the more realistic case where the rest gas layer was included in the simulation. Obviously, in the case of the source Pt-15 the mean projected range is the smallest one. It is interesting to note that from Fig 4.14(b) it follows that the portion of 5–10% of the incident ^{83}Rb ions gets stopped in the rest gas layer. This environment is non-metal, on the contrary, it corresponds to the “oxide state” mentioned in the introduction to Sect. 4.2. As the foils were not cleaned by ion sputtering or any other means after the implantation, a certain portion of ^{83}Rb is assumed to remain in such a layer. Knowing the values of the implanted dose Q and the longitudinal straggle ΔR_p of the

mean projected range, with the help of Eq. 4.3 one can estimate the peak concentration C_p of ^{83}Rb . In all four cases the peak concentration (cf. Tab. 4.2) lies in the range of $\approx (2-7) \times 10^{20}$ ions cm^{-3} . Considering the number of Pt or Au atoms contained in one cubic cm as 1.53×10^{23} or 1.48×10^{23} , respectively, the aforementioned peak concentrations correspond to the peak atomic concentration of ^{83}Rb of the order of 0.1%. Clearly, in the sources Pt-30 #2 and Au-30 the peak atomic concentration of ^{83}Rb is maximal, about 0.4–0.5%. This way the ^{83}Rb atoms implanted into the foils can be understood as an impurity of a relatively high concentration [Pet10, But11].

At last, the ion-implanted sources shall be discussed regarding the chemical behavior of ^{83}Rb and $^{83\text{m}}\text{Kr}$. It is expected [Leb11] that after its implantation, ^{83}Rb behaves as Rb^+ and bonds to the environment of the Au or Pt lattice. Some kind of diffusion cannot be excluded, but due to its reactivity ^{83}Rb will probably stay on its original place. Some bonding of $^{83\text{m}}\text{Kr}$ in the solid phase is not expected as within $\approx 10^{-10}$ s after the decay of ^{83}Rb the electron shells are reorganized. However, as the metastable $^{83\text{m}}\text{Kr}$ exists for ≈ 2 h before the conversion electron is emitted, the Au or Pt lattice surrounding the $^{83\text{m}}\text{Kr}$ atom might influence the conversion electrons via weak bonds. The processes affecting the conversion electrons emitted from atoms adsorbed onto or implanted into solids will be considered in the coming section.



(a)



(b)

Fig. 4.14: The simulated range profiles of Rb ions implanted into gold and platinum. The situations corresponding to the ion-implanted sources Pt-30 (red points), Pt-15 (green) and Au-30 (blue) were simulated. In (a) only the metallic foil was considered. In (b) the 30 Å thick layer of carbon, mimicking the rest gas adsorption, was included in the simulation. The boundary between the carbon layer and the metallic foil in (b) is denoted by the dashed line. The distributions were individually scaled to unity. The simulation was carried out with the help of the SRIM code.

4.3. Conversion electrons from solid $^{83}\text{Rb}/^{83\text{m}}\text{Kr}$ sources

In previous sections the concepts of the vacuum-evaporated (Sect. 4.1) and ion-implanted (Sect. 4.2) $^{83}\text{Rb}/^{83\text{m}}\text{Kr}$ sources were introduced. Here the processes affecting the conversion electrons emitted from the solid $^{83}\text{Rb}/^{83\text{m}}\text{Kr}$ sources shall be discussed. The most noticeable change regarding the electrons emitted from the solid is their higher kinetic energy when compared to the electrons emitted from a free atom. The reason for this is the shift of the electron binding energy. Moreover, a similar change is also clearly visible when considering the electrons originating in the oxide and metallic state. Such a shift was already visible in Fig. 4.3. Another interesting feature can also be seen in Fig. 4.3: the portion of the zero-energy-loss electrons, *i. e.* the electrons emitted from the solid without any energy loss, is lower in the metallic state.

In this section firstly the shifts of the electron binding energies are considered. Secondly, the so-called shake-up and shake-off effects are described, representing the intrinsic energy losses of the emitted electrons. Finally, the extrinsic energy losses, which the electrons undergo on their path through the solid source, are discussed.

4.3.1. Shifts of electron binding energies

The notion of the electron binding energy in an atom, adsorbed on or implanted in a solid, was extensively studied in the past [Car75, Car78, Ege87]. More precisely, the *shift* of the electron binding energy is of main interest: the electron binding energy of the atom on or in solid is compared to the corresponding binding energy of the free atom. Such a shift can provide significant insights about the chemical and physical nature of the given system. Usually, the core electrons⁵ are studied as they are less perturbed by the environment, on the contrary to the valence electrons.

In this work the electrons resulting from the internal conversion of the gamma radiation are utilized. On the other hand, in literature the binding energy shifts are mostly investigated with the help of the X-ray photoelectron spectroscopy (XPS). One may wonder if the two different ionization mechanisms (photoionization and internal conversion) result in the same electron spectra. Indeed, in [War91] the correspondence of the electron spectra resulting from both mechanisms was verified for the case of gaseous $^{83\text{m}}\text{Kr}$. The *K*-32 line (cf. Tab. 3.1) of $^{83\text{m}}\text{Kr}$ was measured with the help of the iron-free toroidal-field β -electron spectrometer which was originally utilized for the search for the finite neutrino mass [Rob91]. In addition, the Kr $1s_{1/2}$ photo-peak was studied with the help of the synchrotron radiation. It was found that both spectra, including satellites on the low energy side of the primary $1s_{1/2}$ electron peak, are in a good agreement with each other. Thus, the phenomena observed in the XPS spectra may be also anticipated in our case of the internal conversion.

The ^{83}Rb atoms were utilized in two forms: a) adsorbed onto substrates of aluminum and graphite (Sect. 4.1.2) and b) implanted into substrates of gold and platinum (Sect. 4.2.3). These two cases will be discussed here separately.

⁵In krypton (cf. Tab. 3.1) the electrons in states $1s_{1/2}$ (*K* shell) to $3d_{3/2}$ (*M*₅ shell) are considered as core electrons. The states $4s_{1/2}$ (*N*₁ shell) to $4p_{3/2}$ (*N*₃ shell) are denoted as valence electrons.

^{83}Rb adsorbed onto solid

At first sight the situation of the $^{83}\text{Rb}/^{83\text{m}}\text{Kr}$ vacuum-evaporated source might seem fairly similar to the situation of the CKrS (described in Sect. 3.3.2) as in both cases the electron emitter lies on the surface. However, comparison of the two models illustrated in Fig. 3.10 and Fig. 4.1 reveals a significant difference: in the case of CKrS the $^{83\text{m}}\text{Kr}$ atoms are condensed onto clean substrate in well defined conditions. On the contrary, in the case of the vacuum-evaporated source the ^{83}Rb atoms are placed in the contamination layer covering the substrate. This represents rather undefined conditions for the electrons emitted by $^{83\text{m}}\text{Kr}$. In analogy to Eq. 3.20, the kinetic energy of the conversion electron emitted from the vacuum-evaporated source—and measured by the spectrometer with the work function ϕ_{spec} —can be determined as

$$E_{\text{kin}}^{\text{evap}}(i) = E_{\gamma} + E_{\text{rec}, \gamma} - E_{\text{rec}, e}(i) - \left(E_{\text{bin}}^{\text{vac}}(\text{gas}, i) - \Delta E_{\text{bin}}^{\text{vac}}(\text{evap}, i) \right) - \left(\phi_{\text{spec}} - \phi_{\text{source}} \right), \quad (4.5)$$

where the designation “cond” in Eq. 3.20 was replaced by “evap” in order to distinguish these two cases.

In [Ost08] the correction term $\Delta E_{\text{bin}}^{\text{vac}}(\text{cond}, i) \equiv \Delta E_{\text{bin}}^{\text{vac}}(\text{cond}) = 1.74(23)$ eV was used for all electron shells of $^{83\text{m}}\text{Kr}$. The value is based on measurements of the shifts of core level binding energies and Auger electron energies of Kr adsorbed onto oriented graphite (001) [Man85]. The shifts originate in the incomplete screening of the electron hole which can be represented by the notion of the image charge. The theoretical framework, described in [Ege87], enables to predict the shifts of the core level binding energies of the adsorbed atoms and even their dependence on the number of atomic layers lying between the (previously clean) substrate and the atom in question. Usually, rare gases are employed as their bonding is of the van der Waal's type and there is no significant charge transfer [Ege87]. The validity of the correction $\Delta E_{\text{bin}}^{\text{vac}}(\text{cond})$ was verified in [Ost08] in the following way: the electron kinetic energy $E_{\text{kin}}^{\text{cond}}(i)$ was measured for various electron shells i and according to Eq. 3.20 the $^{83\text{m}}\text{Kr}$ transition energy of $E_{\gamma} \equiv E_{\gamma}(\text{conv. el.})$ was obtained as the weighted mean over the shells i . This value was compared with the value $E_{\gamma} \equiv E_{\gamma}(\text{gamma ray})$ determined directly by high precision gamma ray spectroscopy with semiconductor detectors (cf. Eq. 3.16 and Eq. 3.17).

However, in our case there is no available prediction for the correction term $\Delta E_{\text{bin}}^{\text{vac}}(\text{evap}, i)$. Thus, instead of determining the value $E_{\gamma}(\text{conv. el.})$ and comparing it with $E_{\gamma}(\text{gamma ray})$, it seems more sensible to deduce the correction term $\Delta E_{\text{bin}}^{\text{vac}}(\text{evap}, i)$ for each shell i . This can be achieved by measuring the values $E_{\text{kin}}^{\text{evap}}(i)$ and utilizing Eq. 4.5 in the combination with Eq. 3.16 and Eq. 3.17. Such approach will be utilized in Chap. 7. A valid argument can be raised with respect to the “constantness” of the source work function ϕ_{source} in Eq. 4.5. Indeed, it is expected that the oxidation of the substrate surface changes its work function. However, for the sake of simplicity the tabulated values of work functions (valid for clean surfaces) will be used and the only term which will compensate all the changes is $\Delta E_{\text{bin}}^{\text{vac}}(\text{evap}, i)$. The overview of the work functions of materials used in this work is shown in Tab. 4.3.

Tab. 4.3: The overview of work functions of materials used in this work.

material	ϕ [eV]	reference
Al	4.28	[Mic77]
Au	5.1(1)	[Eas70]
C	5.0	[Mic77]
Pt	5.65(10)	[Eas70]
stainless steel *	4.4(2)	[Pic92a]

The values are stated for polycrystalline materials. Remark: * the stainless steel of the type DIN 1.4429 (SAE 316LN) was used for the production of the electrode of Mainz MAC-E filter. Its work function was used as ϕ_{spec} in this work.

^{83}Rb implanted into solid

In comparison with the vacuum-evaporated source, the ion-implanted source (model of which is illustrated in Fig. 4.6) profits from the fact that ^{83}Rb atoms are brought by the ion implantation into metallic environment where the oxidation does not take place. However, without subsequent sputtering of the foil surface, about 5–10 % of the ^{83}Rb ions ends up in the oxidation layer covering the surface. In this oxide layer the ^{83}Rb atoms experience similar conditions as in the vacuum-evaporated source. As this portion of ^{83}Rb can be removed by sputtering, it will not be further discussed here.

In literature the notion of *core level binding energy shifts of rare gases implanted in noble metals* was studied both experimentally [Cit74, Kim75, Bab93] and theoretically [Wat76, Gad76, Wil78, Joh80]. Nonradioactive rare gases (Ne, Ar, Kr and Xe) were implanted into polycrystalline foils of high purity and the XPS method was utilized for measuring the absolute electron binding energies. These were then compared with the binding energies measured for free atoms. The reason for such interest of this issue can be illustrated as follows: the rare gases are closed shells atoms and therefore chemically inert. Thus, the binding energy shifts due to the charge transfer (also called “chemical shifts”) are expected to be negligible. Therefore, the rare gases implanted in noble metals are model systems that provide the possibility of isolating those factors in the binding energies that are *not* related to charge transfer but are characteristic for a neutral atom in a solid environment [Car78].

However, in our case the parent ^{83}Rb atom is implanted and the $^{83\text{m}}\text{Kr}$ atom is then created directly inside the metallic environment. Thus, the similarity of our case with the situation “rare gas implanted in noble metal” may be questioned. The following facts can be considered in order to give an answer:

- Some insight into the radiation damage, produced by implanting Rb or Kr ions, may be done with the help of the SRIM code. In Fig. 4.15 the distribution of the damage events (vacancies and replacements, cf. Sect. 4.2.1) is plotted for the two cases: a) Rb and b) Kr ions of the energy of 30 keV were implanted into Pt substrate covered with 30 Å thick layer of rest gas (geometry was identical to the simulations presented in Sect. 4.2.3). It can be seen that both Rb and Kr ions produce practically identical distributions of damage events in the target. Of course, the processes of self-annealing are not included in the simulation, but certain similarity of Rb and Kr may be claimed

anyhow.

- The sputtering and diffusion studies [San06] of radioactive isotopes ^{85}Kr and ^{86}Rb implanted into polycrystalline gold revealed similarity of these two elements considering their behavior after implantation.
- After the ^{83}Rb atom decays into the metastable $^{83\text{m}}\text{Kr}$, the latter one is not expected to be strongly bonded inside the lattice. A similar behavior can be assumed in the case where the rare gas atom is initially implanted into the lattice.

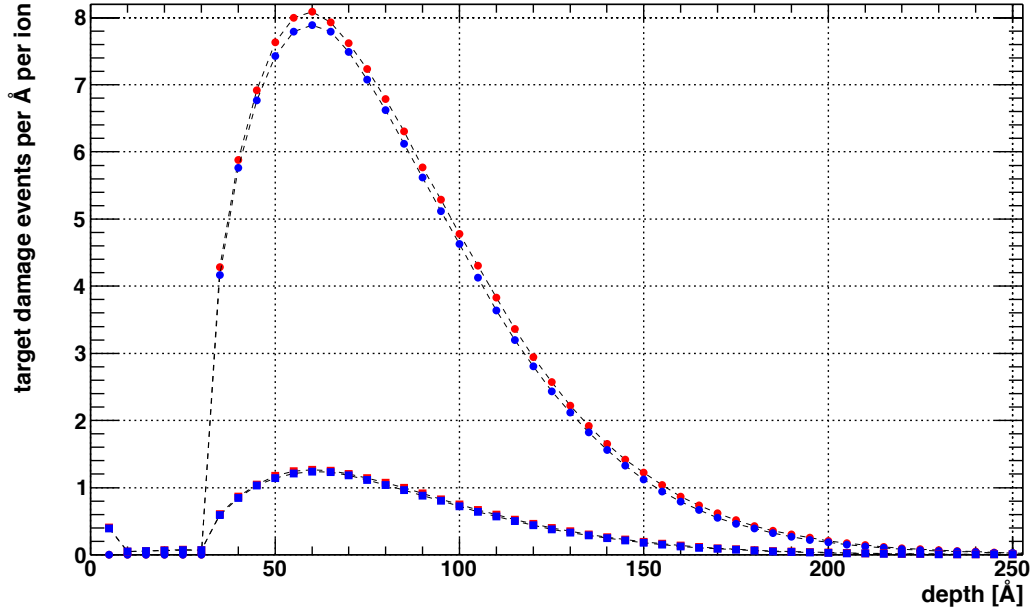


Fig. 4.15: The simulated damage profiles for the implantation of Kr (blue points) and Rb (red points) ions at the energy of 30 keV into platinum. The circles denote the number of vacancies per Å created by one incident ion whereas the squares denote the number of Pt atom displacements per Å created by one incident ion. In the simulation the rest gas layer of the thickness of 30 Å was taken into account. Basically, no significant difference between the cases of the Kr and the Rb ions can be seen. The simulation was carried out with the help of the SRIM code.

Thus, one may rather safely assume that there is no principal difference between a) the rare gas atom of $^{83\text{m}}\text{Kr}$ created in the solid after the electron capture decay of ^{83}Rb and b) the rare gas atom initially implanted into the solid. Therefore, the aforementioned studies of the binding energy shifts may be used for assessing the binding energy shifts of the conversion electrons from $^{83\text{m}}\text{Kr}$.

In [Cit74] the rare gas ions, accelerated by 1 keV, were implanted into high purity metal foils at rather high doses of $\approx 10^{16}$ ions cm^{-2} . Such doses, corresponding to atomic concentrations of tens of %, are by about two orders of magnitude higher than what is assumed as the limit dose at which the lattice does not get destroyed yet, see Eq. 4.4. The rare gas electron levels Ne $1s_{1/2}$, Ar $2p_{3/2}$ and Kr $3p_{3/2}$ were studied. Detailed analysis of the XPS data showed noticeable broadening of the line shapes, but most importantly, the binding energies of the core electrons were found to be significantly *smaller* with respect to corresponding binding energies in free atoms. The experimental binding energy shift was introduced as

$$\Delta E_{\text{bin}}^{\text{vac}}(\text{impl}) = E_{\text{bin}}^{\text{vac}}(\text{gas}) - E_{\text{bin}}^{\text{vac}}(\text{impl}) = E_{\text{bin}}^{\text{vac}}(\text{gas}) - \left(E_{\text{bin}}^{\text{Fermi}}(\text{impl}) + \phi_{\text{source}} \right), \quad (4.6)$$

where

- $E_{\text{bin}}^{\text{vac}}(\text{gas})$ is the electron binding energy of a free atom, related to the vacuum level,
- $E_{\text{bin}}^{\text{vac}}(\text{impl})$ is the electron binding energy of a rare gas atom implanted into solid, referenced to the vacuum level for a direct comparison with $E_{\text{bin}}^{\text{vac}}(\text{gas})$,
- $E_{\text{bin}}^{\text{Fermi}}(\text{impl})$ is the electron binding energy of a rare gas atom implanted into solid, referenced to the Fermi level, and
- ϕ_{source} is the work function of the metal.

Provided the metal is conductively connected to the electron spectrometer of the XPS apparatus, the actual measured quantity is $E_{\text{bin}}^{\text{Fermi}}(\text{impl})$. The shift $\Delta E_{\text{bin}}^{\text{vac}}(\text{impl})$ is positive. A theoretical model was constructed in [Cit74] in which the metal valence s electrons were treated as free, creating a homogeneous electron gas or “jellium”. The density of this gas is equal to that of the host electrons. The rare gas was represented by a pseudopotential filling a spherical cavity in the electron gas. The model enabled to calculate separately a) the shift of the initial-state potential energy of the core levels, corresponding to the implantation in the metal host and b) the polarization energy, corresponding to a binding energy decrease due to the response of the host electrons to a presence of the final-state core hole. A combination of the effects (a) and (b) made it possible to calculate the corresponding shifts which were found in a good agreement with the measured values.

The experimental data of [Cit74] were interpreted in [Wat76] with the help of an alternative approach: while in [Cit74] mainly the response of the electron gas to the introduction of a local perturbation was considered, in [Wat76] the changes suffered by the rare gas atom upon implantation were emphasized. Here the binding energy shift was expressed in terms of two contributions: a) the relaxation shift associated with the extra screening energy provided by the conduction electrons of the host and b) the binding energy shift accompanying the compression of the outer electron wave function of the rare gas when it is forced into the metal matrix [Car78]. The comparison of the theoretical models of [Wat76] and [Cit74] with the experimental data is shown in Fig. 4.16.

Further sophisticated theoretical models [Gad76] (linear-response theory used for calculating the screening and extra-atomic relaxation energies of localized holes on atoms or molecules implanted in or adsorbed on free electron gas solids) and [Joh80] (assumption of a fully screened final state in the metallic case and approximation of the screening valence charge distribution around the core-ionization site) were also developed in the past. Without going into much detail, the observed shift $\Delta E_{\text{bin}}^{\text{vac}}(\text{impl})$ can be loosely divided into following individual shifts [Gad76, Ege87]: chemical, bonding, surface-dipole and relaxation shifts. The investigations of the Ar implanted in noble metals [Cit74] were repeated in [Kim75] (see Fig. 4.16) were in addition the binding energy shifts of various alloyed materials (Au-Ag, Pt-Ag *etc.*) were examined. [Bab93] reported on binding energy shifts of rare gases implanted into polycrystalline titanium and also on the energy shifts of Xe core electrons and Auger electrons upon implantation into various metals (including Pt).

The kinetic energy of the conversion electron emitted from the $^{83\text{m}}\text{Kr}$ atom placed in the metal host and measured by the spectrometer can be derived as follows. Neglecting the binding energy shift at first, one can write

$$E_{\text{kin}}^{\text{impl}}(i) = E_{\gamma} + E_{\text{rec}, \gamma} - E_{\text{rec}, e}(i) - \left(E_{\text{bin}}^{\text{Fermi}}(\text{impl}, i) + \phi_{\text{source}} \right) - \left(\phi_{\text{spec}} - \phi_{\text{source}} \right), \quad (4.7)$$

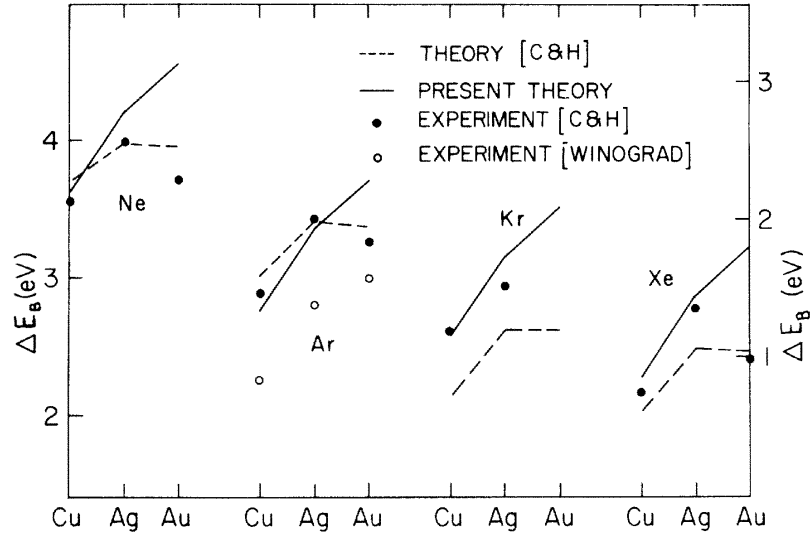


Fig. 4.16: The core level electron binding energy shifts (related to the vacuum level) of the rare gas atoms implanted in Cu, Ag and Au. Measured shifts are given by the filled circles (P.H. Citrin and D.R. Hamman, [Cit74]) and the open circles (K.S. Kim and N. Winograd, [Kim75]). The dashed lines denote the theoretical results of [Cit74] and the solid lines represent the calculations of [Wat76]. The energy scale on the right side is valid for the theoretical values of [Cit74], the rest of data is referred to the scale on the left side. The figure is taken from [Wat76].

where the binding energy $E_{\text{bin}}^{\text{Fermi}}(\text{impl}, i)$ is referenced to the Fermi level (see Fig. 3.7 for the balance of individual terms). It can be seen that the dependence on the source work function ϕ_{source} vanishes. In the next step the binding energy shift can be introduced via utilizing Eq. 4.6 and rewriting the binding energy $E_{\text{bin}}^{\text{Fermi}}(\text{impl}, i)$ as

$$E_{\text{bin}}^{\text{Fermi}}(\text{impl}, i) = E_{\text{bin}}^{\text{vac}}(\text{gas}, i) - \underbrace{\left(\Delta E_{\text{bin}}^{\text{vac}}(\text{impl}, i) + \phi_{\text{source}} \right)}_{= \Delta E_{\text{bin}}^{\text{Fermi}}(\text{impl}, i)}. \quad (4.8)$$

The term $\Delta E_{\text{bin}}^{\text{Fermi}}(\text{impl}, i)$ denotes the binding energy shift referenced to the Fermi level. Thus, finally it can be written

$$E_{\text{kin}}^{\text{impl}}(i) = E_{\gamma} + E_{\text{rec}, \gamma} - E_{\text{rec}, e}(i) - \left(E_{\text{bin}}^{\text{vac}}(\text{gas}, i) - \Delta E_{\text{bin}}^{\text{Fermi}}(\text{impl}, i) \right) - \phi_{\text{spec}}, \quad (4.9)$$

where $E_{\text{bin}}^{\text{vac}}(\text{gas}, i)$ denotes the electron binding energy of gaseous krypton, summarized in App. A for all atomic shells i of krypton. In Eq. 4.9 the term ϕ_{source} is not explicitly written but it is actually included in the term $\Delta E_{\text{bin}}^{\text{Fermi}}(\text{impl})$. Usually, in literature both shifts $\Delta E_{\text{bin}}^{\text{Fermi}}(\text{impl})$ and $\Delta E_{\text{bin}}^{\text{vac}}(\text{impl})$ are stated, differing by ϕ_{source} .

The literature survey did not provide the values $\Delta E_{\text{bin}}^{\text{Fermi}}(\text{impl})$ in a direct way as there are no data available for our cases “Kr in Au” and “Kr in Pt”. In [Cit74] it was reported that Kr could not be successfully implanted in Au. Therefore, an extrapolation of the results “Kr in Cu” and “Kr in Ag” in Fig. 4.16 have to be done, resulting in

$$\Delta E_{\text{bin}}^{\text{vac}}(\text{impl}, \text{Kr in Au}) \simeq 3.1 \text{ eV} \Leftrightarrow \Delta E_{\text{bin}}^{\text{Fermi}}(\text{impl}, \text{Kr in Au}) \simeq 8.2 \text{ eV}. \quad (4.10)$$

In [Bab93] platinum was used as the host metal, however, only Xe was implanted and not Kr. The shift $\Delta E_{\text{bin}}^{\text{Fermi}}(\text{impl}, \text{Xe in Pt}) = 6.8 \text{ eV}$ was reported for the Xe $3d_{5/2}$ electron shell.

The data of [Cit74] allowed to estimate the shift for the system “Kr in Pt” as

$$\Delta E_{\text{bin}}^{\text{vac}}(\text{impl, Kr in Pt}) \simeq 1.9 \text{ eV} \Leftrightarrow \Delta E_{\text{bin}}^{\text{Fermi}}(\text{impl, Kr in Pt}) \simeq 7.5 \text{ eV}. \quad (4.11)$$

It should be noted both estimates in Eq. 4.10 and Eq. 4.11 are based on data obtained with the Kr $3p_{3/2}$ electrons (M_3 shell).

Similarly to the case of the vacuum-evaporated source, the shifts $\Delta E_{\text{bin}}^{\text{vac}}(\text{impl}, i)$ will be determined in Chap. 7 for a series of atomic shells i on the basis of the measurements of the conversion electron lines for both cases “Kr in Au” and “Kr in Pt”.

4.3.2. Shake-up and shake-off effects

Shaking processes can be divided into shake-up and shake-off processes. Generally, they can be denoted as “shake-up/off” processes, representing the intrinsic mechanisms of the energy losses of electrons [Sie69, Car73, Fre74, Koc06]. During the ionization of the core electron the system of atomic shells experience a sudden change of the electric potential. The creation of an inner shell vacancy in the atom may lead to additional *simultaneous* excitation or ionization of outer shell electrons. In the shake-up process a bound electron is excited into an unoccupied bound orbitals. During the shake-off process a bound electron can even be ejected into the continuous spectrum of free electron states. The “original” electron, which was ejected from the inner shell (and thus created the initial inner shell vacancy), is affected by the shake-up/off processes and loses a portion of its energy. This fact can be understood on the basis of many-body interaction and can be well described by the sudden approximation theories. Thus, the shake-up/off processes give rise to satellite structures in the electron spectra. These groups of satellite peaks accompany the inner shell electron lines on the low kinetic energy side. The shake-up effect results in a group of discrete peaks in the spectrum, corresponding to the transitions between the electron bound states. On the other hand, the shake-off effect creates a continuous spectrum with an edge. The shake-up/off processes take place in any ionization process, they are present even in the gaseous phase, where the electron losses caused by the inelastic scattering are negligible. In Fig. 4.17 the XPS spectrum of gaseous neon is depicted, illustrating the shake-up/off effects.

The internal conversion of gamma radiation (see Sect. 1.2) is a ionization process and thus it is accompanied by the shake-up/off processes as well. In [Pic92b] the shake-up/off peaks were recognized in the electron spectra of the various conversion electron lines of condensed $^{83\text{m}}\text{Kr}$. In the case of the K -32 line altogether three satellite peaks S_i were successfully fitted in the spectrum and their shape was described by the Lorentzian function. The peaks S_1 and S_2 were found at 20.3 eV and 33.3 eV below the elastic electron peak, respectively. Their width was determined as 5.8 eV. The intensity of S_1 and S_2 summed up to 18.5% of the main peak which was found to be in a good agreement with the theoretical value of the shake-up/off probability of 20.5% (with a mean energy of 33.4 eV) based on the sudden approximation calculations [Car73]. The third peak S_3 was located about 35 eV below the main peak with the width of about 38 eV and the intensity of 13.2% of the main peak. The large width of S_3 was explained as the result of not only shake processes but also as the indication of the backscattering from the copper substrate. The electron spectrum is shown in Fig. 4.18.

As there are no data available for the shake-up/off probability in the $^{83\text{m}}\text{Kr}$ atom in the solid

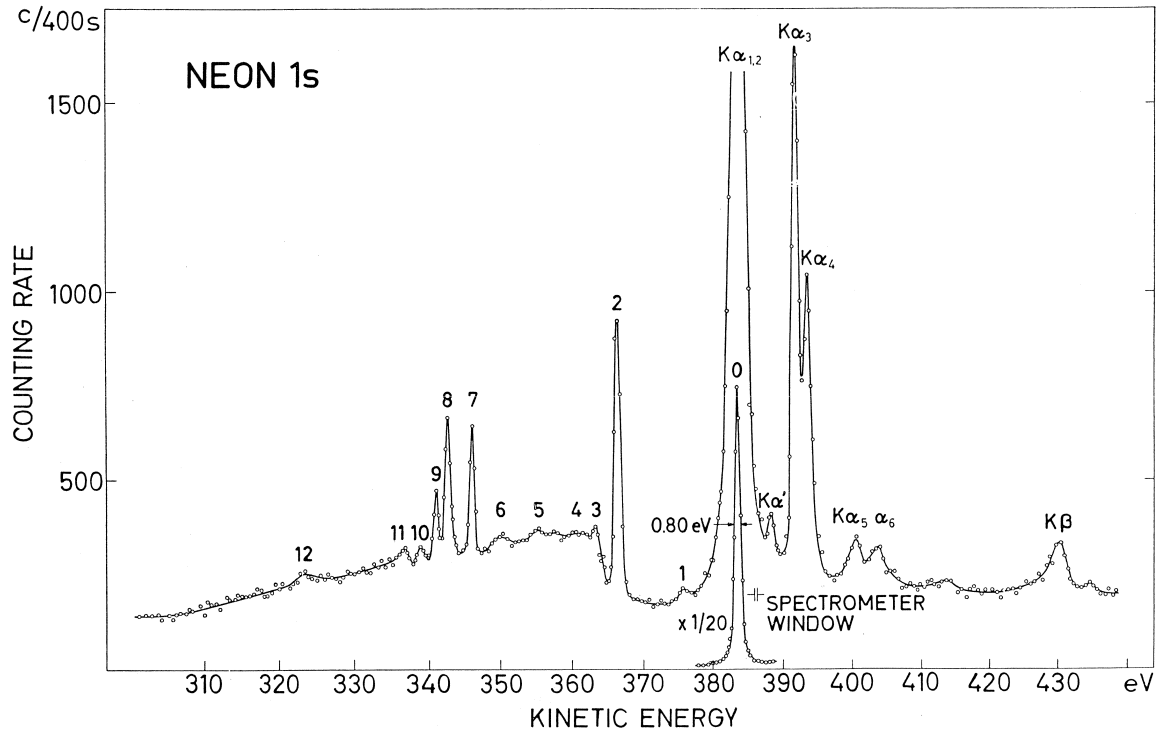


Fig. 4.17: The electron spectrum of neon 1s obtained with the help of the XPS technique. The Mg $K\alpha$ radiation was used as the X-ray source. Gaseous neon was kept at a pressure of about 0.7 mbar. The main peak denoted (0) is the Ne 1s line excited by the Mg $K\alpha_{1,2}$ X-rays. The Mg K X-ray satellites and the Mg $K\beta$ radiation give the peaks of higher kinetic energy. The intensity of the continuum and the peaks (1) to (4), corresponding to the electron energy losses, was found to be pressure dependent. The peaks (7) to (12) resulted from the shake-up and shake-off effects and were found to be pressure independent. The features (5) and (6) were assigned to the Mg $K\alpha_{3,4}$ satellites. The figure is taken from [Sie69].

phase, the value of $P_{\text{shake}}(K-32) = 20.5\%$ will be assumed in this work to be valid for the solid phase as well.

4.3.3. Inelastically scattered electrons

The inelastic scattering of electrons, representing the extrinsic mechanism of electron energy loss, is unwanted in the conversion electron spectroscopy as it reduces the intensity of the useful zero-energy-loss peak. Moreover, it produces complicated structures on the low energy side of the elastic peak in the electron spectrum. However, the energy losses cannot be fully avoided in the case of a solid electron source. The inelastic scattering can be minimized by using the substrate of the thickness which is small compared to the inelastic mean free path (IMFP, denoted as λ) of electrons of interest. Moreover, the elements of low atomic number Z are favored for backing material due to the suppressed probability of the electron backscattering [Dra83]. The energies of the $^{83\text{m}}\text{Kr}$ conversion electrons lie in the range of 7–32 keV and thus the IMFP values are typically of the order of tens to hundreds of Å (depending on the material, of course). In the case of the ion-implanted source,

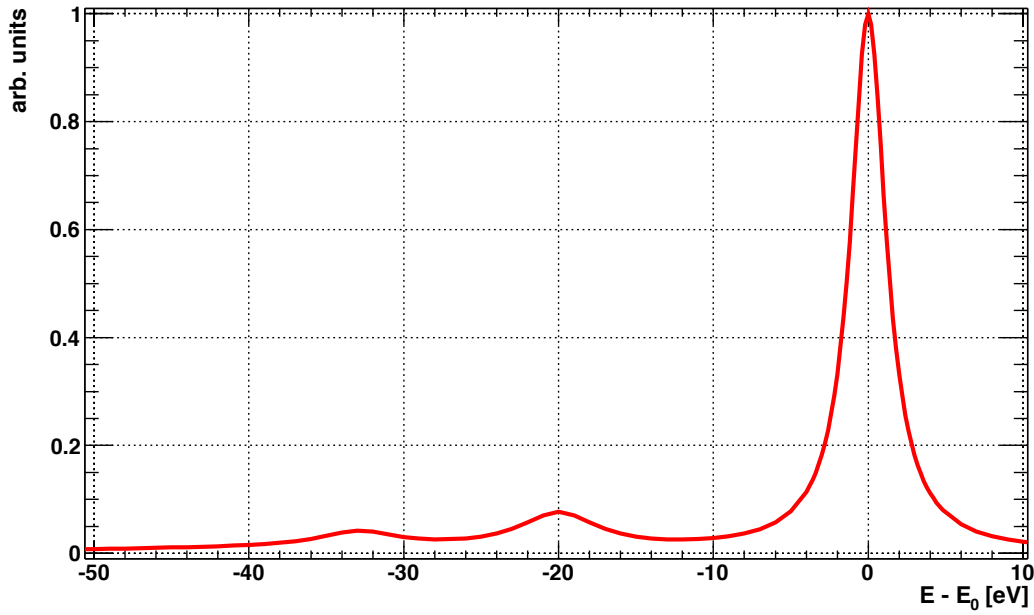


Fig. 4.18: The electron spectrum of the K-32 conversion line measured with the CKrS where $^{83\text{m}}\text{Kr}$ was condensed on cooled copper substrate. Thanks to the knowledge of the transmission function of the MAC-E filter spectrometer the electron spectrum can be obtained from fit of experimental data. The peak at zero energy corresponds to elastic electron peak of the energy of $\simeq 17824$ eV. By naked eye only the two satellites S_1 and S_2 are visible on the low energy side of the elastic peak. The figure is based on [Pic92b, Thu07].

the inelastic electron scattering is expected to be more pronounced than in the case of the vacuum-evaporated source due to the fact that in the former case ^{83}Rb atoms are placed in Au or Pt lattice in the depth of about 50–100 Å.

The electron may appear in the “loss electrons structure” in the spectrum for two reasons which can be divided according to the emission angle θ (taken with respect to the source surface normal). Firstly, if $\theta < 90^\circ$ the electron is emitted into the forward 2π space and it may undergo the inelastic scattering on its path through the source material (*e. g.* through the contamination oxide layer). Secondly, if $\theta > 90^\circ$ the electron is emitted into the backward 2π space and with a high probability such electron will be absorbed in the source. However, there is a certain probability that the electron undergoes a backscattering event during which it generally loses a portion of its energy and the initial emission angle is abruptly changed. Typically, the electron can experience a series of such events and it may be scattered back to the forward space. The backscattering was studied in detail in [Fle92, Pic92b] with the condensed $^{83\text{m}}\text{Kr}$ source.

The situation is further complicated when the solid source is placed in the magnetic field. This corresponds to the situation when the conversion electrons are measured with the help of the MAC-E filter (see Sect. 2.2) where the source is positioned in the magnetic field of given strength B_S . The ratio of B_S to the maximal magnetic field B_{max} (which is reached in the center of the superconducting solenoid) determines the maximal starting angle $\theta_{\text{start}}^{\text{max}}$ cf. Eq. 2.14. All the electrons emitted under angles $\theta \leq \theta_{\text{start}}^{\text{max}}$ are directly “accepted” and are guided by the magnetic field lines to the analyzing plane in the middle of the spectrometer vessel where the energy analysis takes place. This scenario is depicted as option (a) in

Fig. 4.19 where the various situations of the electron scattering are schematically drawn. The ion-implanted $^{83}\text{Rb}/^{83\text{m}}\text{Kr}$ is assumed but the situations discussed here are generally valid for any solid source. The situation (b) in Fig. 4.19 corresponds to the aforementioned backscattering event. The situations (c) and (d) are both specific to the use of the MAC-E filter technique: the electron emitted under angle θ obeying the condition $\theta_{\text{start}}^{\text{max}} < \theta < 90^\circ$ is reflected back onto the substrate due to the magnetic field (magnetic mirror effect [KAT04]). The electron hits the source surface with its original kinetic energy and under the angle identical to θ . Furthermore, the electron can then further undergo backscattering inside the source and may be eventually emitted into the accepted cone (situation (c) in Fig. 4.19). Moreover, the effect of magnetic reflection may occur also in the case of the electron which was initially backscattered in the source. However, in this case the electron would have to experience two backscattering events (the initial one and then the second one after the magnetic reflection) in order to appear in the accepted cone. The probability of such double backscattering event, marked as (d) in Fig. 4.19, is already relatively low with respect to the previous scenarios. Multiple backscattering events may also occur, however, their probability further decreases and they are not considered here.

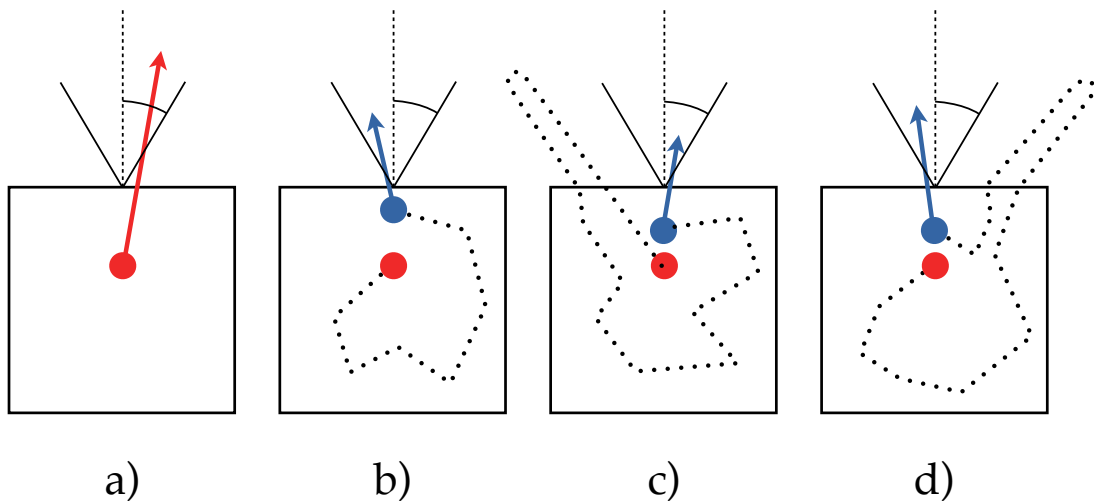


Fig. 4.19: The various situations of the electron emission from the solid source placed in the magnetic field B_S . The maximal acceptance angle $\theta_{\text{start}}^{\text{max}}$ is denoted with respect to the surface normal. The four main scenarios of the electron emission into the accepted cone of $\theta_{\text{start}}^{\text{max}}$ are shown. The red point denotes the place where the electron was created. The blue point marks the “final” position of the electron (prior to the emission from the source) to which the electron was scattered. In (a) the simplest case $\theta < \theta_{\text{start}}^{\text{max}}$ is shown where the electron is emitted without any energy loss. In (b) the electron is emitted under $\theta > 90^\circ$ and is backscattered to the accepted cone. In (c) the electron is firstly emitted under $\theta_{\text{start}}^{\text{max}} < \theta < 90^\circ$, then it undergoes the magnetic reflection and hits the source again, where it is finally backscattered to the accepted cone. The scenario (d) is similar to (c) with the only difference that at the beginning the electron was emitted under $\theta > 90^\circ$ and was backscattered. The figure is based on [Fle92]. In the Monte Carlo simulations, results of which were used in this work, only the scenarios (a) and (b) were considered.

The spectrum of the inelastically scattered electrons may be predicted with the help of Monte Carlo simulations. In this work the results obtained with the simulation code MON3H [Spa94, Dra02] were used for further analysis of the electron spectra obtained with the solid $^{83}\text{Rb}/^{83\text{m}}\text{Kr}$ sources. The MON3H code simulates the electron transport in systems which

can consist of up to three layers, where each layer is specified by the thickness and atomic number. Typically, the three layers correspond to 1) the source backing, 2) the source itself (electron emitter) and 3) the contamination layer of residual gas. It should be noted that thanks to the smallness of the typical IMFP encountered here, the source models were simulated as one-dimensional, *i. e.* only the depth (\equiv axis z) played a role. The scatter of the electrons in the x - y plane was not followed as it would range some hundreds of Å which is negligible compared to the source dimensions (diameter of 12 mm). Two different source models were considered and their individual components can be summarized as follows:

a) vacuum-evaporated source (see Fig. 4.1)

1. Using the notation of Fig. 4.1, the actual thickness $b = 0.2$ mm of the source backing was considered as infinite in the code. This simplification is harmless since the typical IMFP here is by four orders of magnitude smaller than b . The backing was chosen to be carbon, thus, the electron spectra of the sources S28 and S29 (cf. Tab. 4.1) were simulated.
2. The $^{83\text{m}}\text{Kr}$ atom was simulated by a middle “layer” of zero thickness. For the sake of simplicity, the atom was situated directly on the source backing, which might be different from reality where the contamination layer is assumed to cover the backing and the $^{83\text{m}}\text{Kr}$ atom is situated in this contamination layer.
3. The surface contamination (water, hydrocarbons and impurities) was represented by the layer of carbon of the thickness $a = 30$ Å.

b) ion-implanted source (see Fig. 4.6)

1. In this case the metallic foils of Au or Pt were considered. Again, the thickness b was taken as infinite.
2. The distribution of the implantation ranges of the ^{83}Rb ions, simulated with the help of the SRIM code, was considered in the simulation: the distribution of the ^{83}Rb ions (shown in Fig. 4.14(b)) was taken as the probability distribution of the $^{83\text{m}}\text{Kr}$ atoms emitting the electrons. In other words, the output of the SRIM simulation was taken as the input for the MON3H simulation.
3. Again, the surface contamination layer of the thickness $a = 30$ Å was assumed to consist of carbon. In reality, some ^{83}Rb atoms were probably situated in this contamination layer, but this fact was not taken into account in the simulation.

In the MON3H simulation, isotropic emission of electrons with the sharp starting energy E_0 is considered. Each electron is individually followed in a series of elastic and inelastic collisions. Actually, in our case of thin layers, only few collisions can happen. Generally, due to the recoil the electron loses a small portion of kinetic energy even during the elastic scattering, but this is neglected in the simulation [Spa10] as in our case the electron energy loss is of the order of 0.1 eV or less. The elastic scattering is described using the relativistic electron-atom elastic cross sections⁶. The distribution of the electron energy losses in the inelastic collisions is determined according to the differential inelastic cross sections, also called differential inverse mean free paths (DIMFP). The DIMFP functions were derived from optical or electron transmission electron data [Dra02]. In the case of gold a particular “loss function” (function describing the electron energy losses) was utilized, which was

⁶The reader is kindly referred to [Dra02] and citations therein.

derived from the XPS data using deconvolution methods [Yos92]. The loss function was considered as energy independent, *i. e.* the same loss function was used for simulating the losses of the $^{83\text{m}}\text{Kr}$ electrons of the energy $\simeq 17.8$ keV (K -32 line) and $\simeq 30.5$ keV (L_3 -32 line). However, the energy dependency of the elastic scattering cross sections and the IMFP values was taken into account. For example, the IMFP for 17.8 keV electrons in Au reads $\lambda \simeq 133$ Å while for 30.5 keV electrons $\lambda \simeq 217$ Å [Pow10]. The energy dependence of the average energy loss $\langle \Delta E \rangle$ in the inelastic scattering event is rather smooth in the region of our interest, *e. g.* in gold $\langle \Delta E \rangle = 170$ eV for 17.8 keV electrons and $\langle \Delta E \rangle = 183$ eV for 30.5 keV electrons ([Dra02] and citations therein).

During the series of inelastic collisions the summary energy loss ΔE of the electron increases. The simulation of a single electron is stopped if one of the following conditions is fulfilled:

1. The energy loss ΔE exceeds a given limit $(\Delta E)_{\text{lim}}$ which is set prior the simulation. This condition reflects the fact that only the low energy losses (*i. e.* the loss electron structures in the vicinity of the elastic peak in the conversion electron spectrum) were of interest here. Typically, the limit was set to $(\Delta E)_{\text{lim}} = 200$ eV.
2. The electron leaves the source in the forward space.

In the case (1) the electron was not considered in further analysis. In the case (2) the “final” kinetic energy $E_{\text{fin}} = E_0 - (\Delta E)_{\text{fin}}$ of the emitted electron was stored. In addition, the “final” emission angle θ_{fin} , under which the electron left the source, was stored. Usually, about 10^6 electrons were simulated in order to obtain sufficient statistics. The simulation output was organized with respect to the values E_{fin} and θ_{fin} . The results were sorted according to emission angle intervals

$$\frac{n-1}{10} \leq \cos(\theta_{\text{fin}}) \leq \frac{n}{10}, \quad n = 1 \dots 10, \quad (4.12)$$

and the individual electron energy loss spectra $[(\Delta E)_{\text{fin}}, N((\Delta E)_{\text{fin}})]$ were binned with the bin width of 1 eV, usually.

The situations marked as (c) and (d) in Fig. 4.19 were not considered in the simulations presented here, *i. e.* it was assumed that the source is placed in zero magnetic field. The inclusion of the backscattering induced by the magnetic reflection effect would require major changes of the simulation code and, moreover, similar simulations carried out in [Fle92] showed that the effects (c) and (d) play a minor role when the source is in a low magnetic field. During this work the $^{83}\text{Rb}/^{83\text{m}}\text{Kr}$ sources were typically placed in the magnetic field of $B_S = 1.75$ T and correspondingly $\theta_{\text{start}}^{\text{max}} = 32.7^\circ$. Based on [Fle92] the influence of the backscattering induced by the magnetic reflection is assumed to be negligible in our case. Moreover, the magnetic reflection in the MAC-E filter spectrometer was also not included in similar Monte Carlo simulations described in [Dra11a] (where the electron source based on the $^{241}\text{Am}/\text{Co}$ convertor, cf. Sect. 3.3.1, was investigated) and the correspondence with the measured spectra was found to be reasonable.

With help of the MON3H code the electron energy loss spectra of the main $^{83\text{m}}\text{Kr}$ conversion electron lines L_1 -9.4, K -32 and L_3 -32 were simulated for the cases of the vacuum-evaporated source (carbon backing) and the ion-implanted sources Pt-30⁷, Pt-15 and Au-30. The Monte

⁷As the impurities were not included in the simulation models, the sources Pt-30 and Pt-30 #2 were considered identical regarding the electron energy losses.

Carlo simulations were carried out by Dr. A. Špalek⁸. The accuracy of the results obtained with the MON3H code is estimated to be $\simeq 10\%$ on the basis of their comparison with the spectra measured with other electron sources [Spa94, Dra02, Spa10, Dra11a]. In Fig. 4.20 the electron energy loss spectra of the source Au-30 are shown for different ranges of $\cos(\theta_{\text{fin}})$. It can be seen that with increasing θ_{fin} the losses are more pronounced. The influence of E_0 on the electron energy loss spectrum is depicted in Fig. 4.21 for the case of the source Au-30. Here $\theta_{\text{start}}^{\text{max}} = 32.7^\circ$ was considered in such a way that only the corresponding electron spectra (defined according to Eq. 4.12) were taken into account⁹. Clearly, the electron losses are most pronounced in the case of the low energy line L_1 -9.4. Finally, in Fig. 4.22 the electron energy loss spectra simulated for the K -32 line measured in the geometry corresponding to $\theta_{\text{start}}^{\text{max}} = 32.7^\circ$ are compared for all the aforementioned solid sources. As expected, in the case of the vacuum-evaporated source the energy losses are least pronounced. The losses are also less pronounced in the source Pt-15 than in the source Pt-30 as anticipated due to the difference in the mean projected ranges of ^{83}Rb atoms, cf. Fig. 4.14. The energy loss are most pronounced in the Au-30 source.

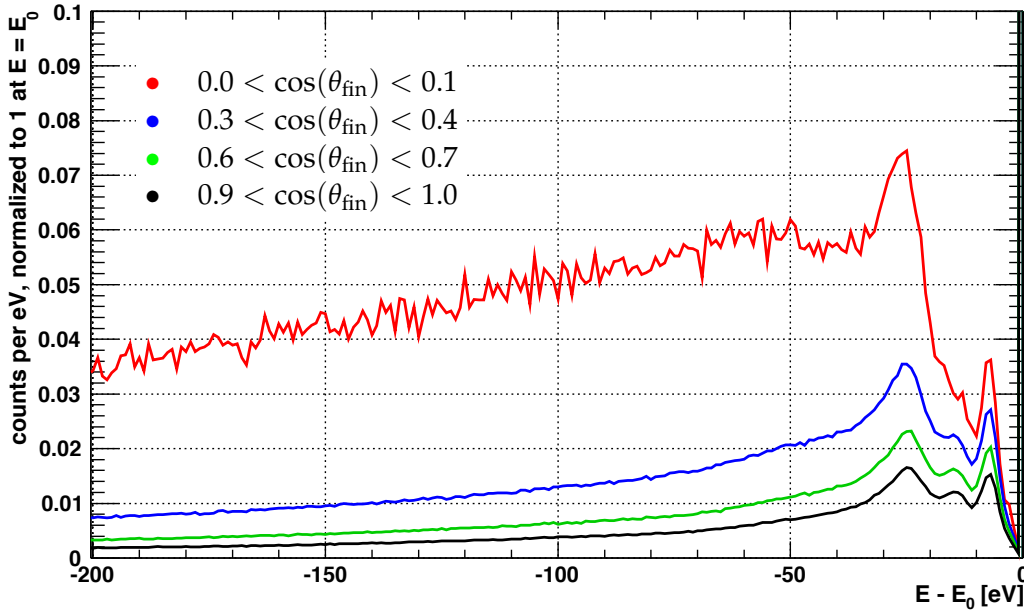


Fig. 4.20: The simulated electron energy loss spectra of the source Au-30 for various ranges of the emission angle θ_{fin} . The starting energy was set to $E_0 = 17824$ eV ($\equiv K$ -32 line of $^{83\text{m}}\text{Kr}$) and the bin width was set to 1 eV. All the events of the zero-energy-loss electrons, corresponding to the elastic peak, lie in one bin at $E = E_0$. The individual spectra are normalized so that the amplitude of this bin is equal to 1. In order to highlight the energy losses, only the zoom of the y axis is shown. It can be clearly seen that the energy losses are more pronounced for large emission angles. The scatter of the red line is due to a poor statistics of events compared to the other angle intervals.

The angular distributions of the zero-energy-loss electrons emitted from all the aforementioned sources are compared in Fig. 4.23 for the case of the K -32 line. It can be seen that in the case of the ion-implanted sources the emission under large emission angles is suppressed in comparison with the vacuum-evaporated source. This clearly stems from the

⁸Nuclear Physics Institute Řež/Prague.

⁹The counts in the individual spectra were weighted corresponding to the portion of the solid angle.

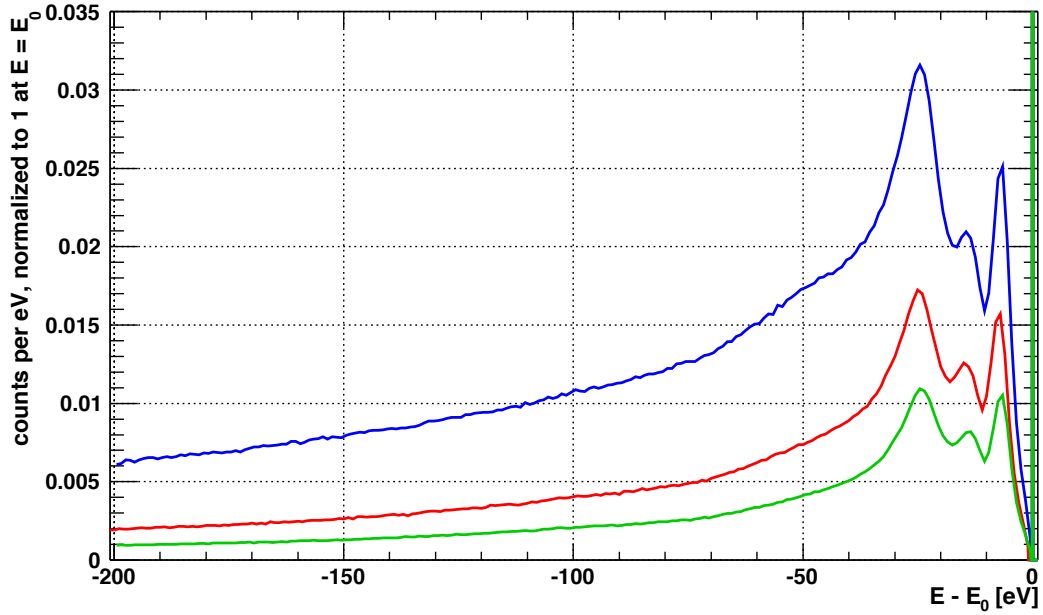


Fig. 4.21: The simulated electron energy loss spectra of the source Au-30 for various starting energies E_0 in the typical geometry $\theta_{\text{start}}^{\text{max}} = 32.7^\circ$ used in this work. The energies E_0 of 7.5 keV (blue line), 17.8 keV (red) and 30.5 keV (green) were chosen, corresponding to $^{83\text{m}}\text{Kr}$ conversion lines L_1 -9.4, K-32 and L_3 -32, respectively. See the caption of Fig. 4.20 for further explanation.

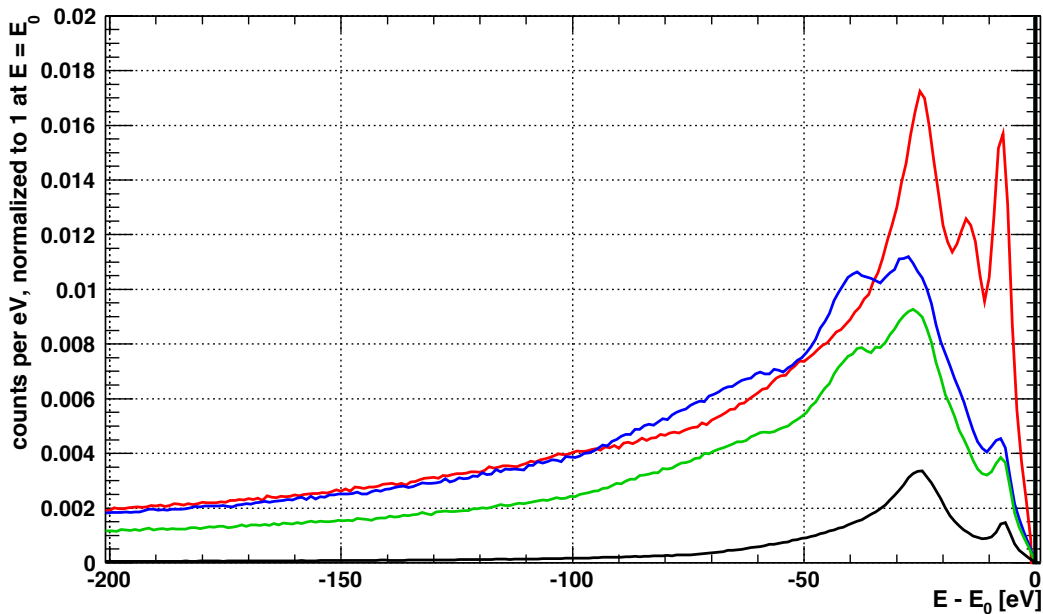


Fig. 4.22: The simulated electron energy loss spectra of the $^{83\text{m}}\text{Kr}$ conversion line K-32 for various solid $^{83}\text{Rb}/^{83\text{m}}\text{Kr}$ sources. In analogy to Fig. 4.21, only the electrons emitted under $\theta \leq \theta_{\text{start}}^{\text{max}} = 32.7^\circ$ were considered. The vacuum-evaporated source (graphite backing) is marked with black line. The spectra of the ion-implanted sources are denoted blue (Pt-30), green (Pt-15) and red (Au-30). See the caption of Fig. 4.20 for further explanation.

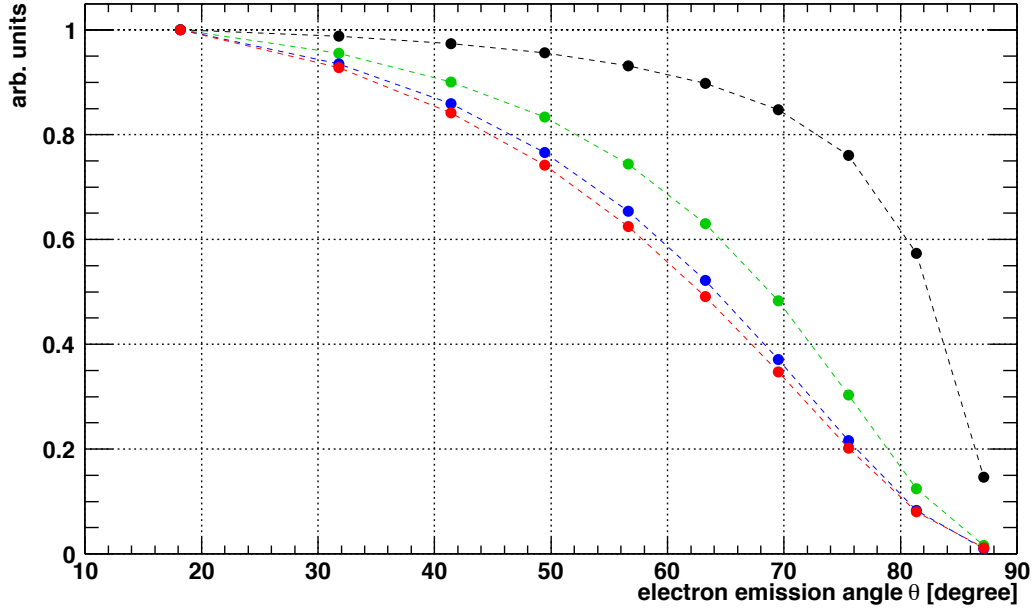


Fig. 4.23: The angular distributions of the zero-energy-loss electrons of the energy $E_0 = 17\,824$ eV emitted from the vacuum-evaporated source (black points) and from the ion-implanted sources Pt-30 (blue), Pt-15 (green) and Au-30 (red). As the output of the simulations is organized according to $\cos(\theta_{\text{fin}})$, cf. Eq. 4.12, the points in this plot are not equidistant on the x axis (shown in $\theta_{\text{fin}} [^\circ]$). For each interval of angles defined by Eq. 4.12 the center was taken, therefore the x axis does not start at $\theta_{\text{fin}} = 0^\circ$. The distributions were scaled to unity. Clearly, the electron emission under large angles is suppressed in the ion-implanted sources.

features of the ion-implanted sources where ^{83}Rb atoms lie in larger depths. However, in our case the important value is the portion of the zero-energy-loss electrons emitted under $\theta \leq \theta_{\text{start}}^{\text{max}} = 32.7^\circ$. The fractions of the zero-energy-loss electrons emitted from each type of source in our geometry can be deduced from Tab. 4.4 where the portions of the inelastically scattered electrons (“loss electrons”) are stated. The following values are summarized in Tab. 4.4 for the three main conversion electron lines of $^{83\text{m}}\text{Kr}$:

- the nominal starting energy E_0 of the electrons,
- the IMFP λ for the electrons of the energy E_0 in carbon, platinum and gold,
- the portion of the inelastically scattered electrons p_{approx} based on a crude approximation (see below), and
- the portion of the inelastically scattered electrons p_{MC} based on Monte Carlo simulations carried out with the help of the MON3H code.

The IMFP values are based on the interpolation of the values tabulated in [Pow10]. The values p_{MC} were calculated from the simulation results described above. The dependence of p_{MC} on the source relative position z —which determines B_S which, in turn, influences $\theta_{\text{start}}^{\text{max}}$ —was briefly studied for the relevant region: $\theta_{\text{start}}^{\text{max}} = 32.7^\circ$ corresponded to $z_0 = 21$ cm (see Sect. 5.1.2 below) and in the region $z_0 \pm 3$ cm the z -dependence was found to be relatively weak, with increasing z (decreasing B_S and $\theta_{\text{start}}^{\text{max}}$) the portion p_{MC} of inelastically scattered electrons generally decreases as $-0.5\% \text{ cm}^{-1}$.

The portion of the inelastically scattered electrons may be also very roughly estimated on

4. Solid $^{83}\text{Rb}/^{83\text{m}}\text{Kr}$ electron...

the basis of knowledge of the IMFP λ and the depth x from which the electrons are emitted. Using the notion of the attenuation of a particle beam, one can write

$$p_{\text{approx}} = 1 - e^{-\frac{x}{\lambda}}. \quad (4.13)$$

However, in this simple model the depth distribution of ^{83}Rb atoms and the angular distribution of the emitted electrons are not considered. In the case of the vacuum-evaporated source $x = 30 \text{ \AA}$ was considered, while for the approximation of the ion-implanted sources x was set equal to the mean projected range of the ^{83}Rb distribution for the corresponding source (see Sect. 4.2.3). The values p_{approx} were found to be in a good agreement (within units of %) with the values p_{MC} , cf. Tab. 4.4. Nevertheless, the values p_{MC} are definitely more reliable than p_{approx} as the former ones are based on realistic models of the sources.

Tab. 4.4: The overview of the inelastically scattered electrons for the three main $^{83\text{m}}\text{Kr}$ conversion lines emitted by the solid $^{83}\text{Rb}/^{83\text{m}}\text{Kr}$ sources.

$^{83\text{m}}\text{Kr}$ conversion electron line	nominal energy E_0 [keV]	IMFP λ at E_0 in C Pt Au [Å]	portion [%] of inelastically scattered electr., calc. based on a) Eq. 4.13 and b) MC sim.						
			evap.		Pt-30		Pt-15 Au-30		
			a)	b)	a)	b)	a)	b)	
L_1 -9,4	7.5	141 66 65	19.2	19.6	78.2	70.9	56.6	57.9	83.1 72.1
K -32	17.8	305 144 133	9.4	9.9	43.0	42.3	28.7	31.3	48.5 49.6
L_3 -32	30.5	497 240 217	5.9	6.3	27.7	30.0	18.0	21.5	32.1 35.2

In the columns marked (a) the portion p_{approx} of inelastically scattered electrons was calculated with the help of Eq. 4.13 using the IMFP values stated in this table. In the columns denoted (b) the portion p_{MC} of the inelastically scattered electrons is based on the results of Monte Carlo simulations.

5. Mainz MAC-E filter used for conversion electron spectroscopy

The samples of the vacuum-evaporated and ion-implanted $^{83}\text{Rb}/^{83\text{m}}\text{Kr}$ sources described in previous Chap. 4 were investigated during several measurement phases at the electron spectrometer of the MAC-E filter type in the Institute of Physics, University of Mainz. This MAC-E filter was previously used as the β -electron spectrometer in the former Mainz Neutrino Mass Experiment [Kra05] until 2001 and later it was upgraded to the high energy resolution¹ of 0.9 eV at 17.8 keV [Thu07]. The measurements were carried out in the time period April 2007–September 2009. In this chapter the experimental setup will be reviewed (Sect. 5.1) and a typical measurement of the conversion electron line and its analysis will be discussed (Sect. 5.2).

The series of the test measurements carried out at this experimental setup will be described in detail the next Chap. 6. At this point it can be noted that the setup was utilized for the measurements of the energy stability of the conversion electrons emitted by the solid $^{83}\text{Rb}/^{83\text{m}}\text{Kr}$ sources. Since the required stability of the conversion electron lines reads $\Delta_{\text{abs}}(\text{HV}) = \pm 60$ meV per one tritium run spanning about two months (cf. Chap. 3), the long-term stability (of the order of month) of the experimental conditions and the understanding of effects, which would limit such stability, were of main interest.

5.1. Experimental setup

The electron spectrometer shown in Fig. 5.1 was rearranged in the course of time into the spectrometer utilized for various test measurements which were necessary during the complex construction of the KATRIN experimental setup. See [Fla04, Thu07, Ost08] for details of the test measurements. After the test measurements of the $^{83}\text{Rb}/^{83\text{m}}\text{Kr}$ sources had been finished, the spectrometer was dismantled, transported to the Karlsruhe Institute of Technology and rebuilt there as the monitor spectrometer for the KATRIN experiment². At this point the individual parts of the setup used in the period 2007–2009 will be shortly described.

¹During the Mainz Neutrino Mass Experiment the spectrometer was typically operated at the energy resolution of about 6 eV.

²The purpose of the monitor spectrometer was discussed above in Sect. 3.2.

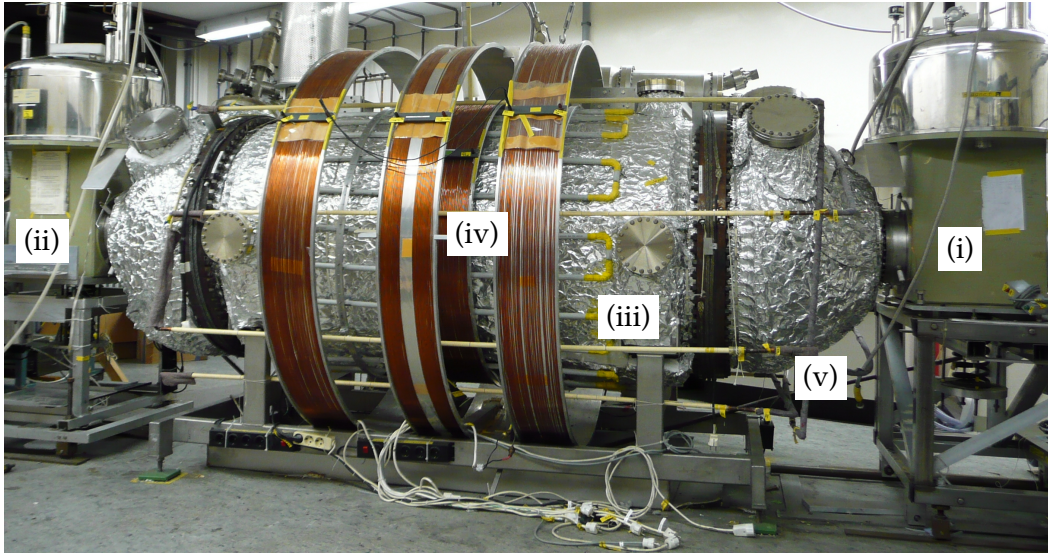


Fig. 5.1: The photograph of Mainz MAC-E filter setup in 2009: (i) solenoid A, (ii) solenoid B, (iii) spectrometer vessel wrapped in thermal insulation, (iv) auxiliary coils for tuning of the spectrometer resolution, (v) auxiliary perpendicular coils for magnetic flux positioning and Earth's magnetic field compensation. The sources were placed in the bore of the solenoid B while the detector section was connected to the solenoid A.

5.1.1. MAC-E filter

The MAC-E filter technique was explained in Sect. 2.2. The filter consisted of an ultrahigh vacuum tank (length of $\simeq 4$ m, diameter of $\simeq 1$ m), massive inner electrodes (Fig. 5.2), two “massless” wire electrodes (Fig. 5.3) and a magnet system. The vacuum tank and the conical massive electrodes on opposite sides were grounded. The wire electrodes were conductively connected with the massive electrode and a negative analyzing voltage of up to -35 kV was applied to them. The massive electrode was produced from 2 mm thick stainless steel sheets (DIN material no. 1.4429). The work function ϕ_{spec} of the central analyzing electrode was measured as $\phi_{\text{spec}} = 4.4(2)$ eV [Pic92a], cf. Tab. 4.3. The magnet system comprised two superconducting solenoids³ “A” and “B” and two sets of auxiliary air coils. The first one, consisting of four coils, was used for tuning the energy resolution of the spectrometer. The second set of two mutually perpendicular windings adjusted the position and shape of the magnetic flux tube inside the spectrometer [Thu07]. The latter set also allowed to compensate for the Earth's magnetic field in the analyzing plane and for misalignments of the source and the detector relative to the lengthwise z axis of the spectrometer.

Working positions of the source and the detector were on the z axis inside the bores of the corresponding superconducting solenoids which provided the guiding magnetic field. The maximal magnetic field achievable in the centre of solenoids amounted to 8.6 T, however, the solenoids were operated at 6.014 T, thus the following notation will be used henceforth: $B_{\text{max}}(\text{A}) = B_{\text{max}}(\text{B}) \equiv B_{\text{max}} \simeq 6$ T. The distance between the centers of the solenoids was 4.02 m. Two spectrometer resolution settings were widely used in this work: 0.9 or 2.0 eV for electrons with the kinetic energy of $E_{\text{start}} = 17.8$ keV ($\equiv K\text{-}32$ line). The spectrometer

³Each superconducting solenoid consisted of 36 447 windings and the dimensions of the coil were the following: inner radius 5.8 cm, thickness 0.8 cm and length 36 cm [Thu07].

resolution was easily tuned by varying the minimal magnetic field B_A in the analyzing plane according to the relation $\Delta E/E_{\text{start}} = B_A/B_{\text{max}}$. The magnetic field configuration used to achieve the resolution of 0.9 eV at 17.8 keV is shown in Fig. 5.4.

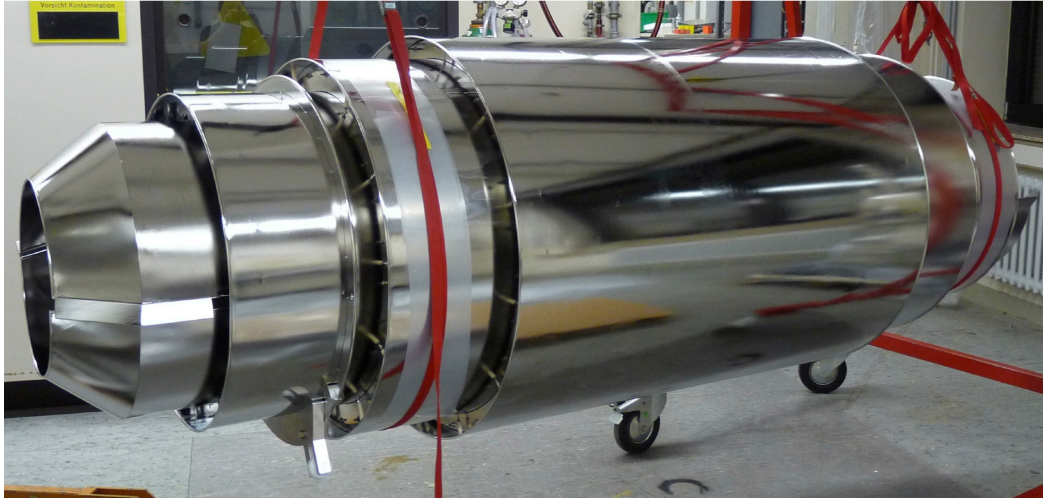


Fig. 5.2: The photograph of the solid electrode after its removal from the MAC-E filter in October 2009.

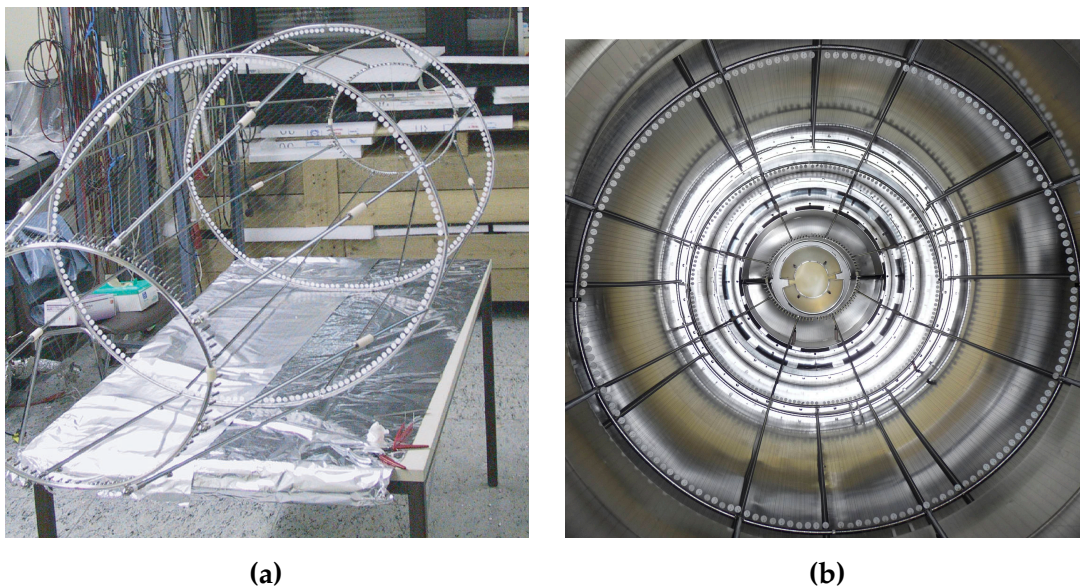


Fig. 5.3: The photographs of the “massless” wire electrode of Mainz MAC-E filter. Figure (a), taken from [Fla04], shows the construction of the electrode in 2003. Figure (b) shows the wire electrode placed inside the massive electrode. The grid is segmented into three parts: one central cylindrical section and two conical wire segments. In addition, there is an outer wire electrode installed in the central part of the spectrometer. This screening electrode was developed [Mul02] for the purpose of background reduction in the MAC-E filter. It served as a prototype of the spectrometer background reduction concept for the KATRIN experiment. However, in this work the screening wire electrode was conductively connected with the solid and massless wire electrodes, and thus it was not utilized for its original purpose.

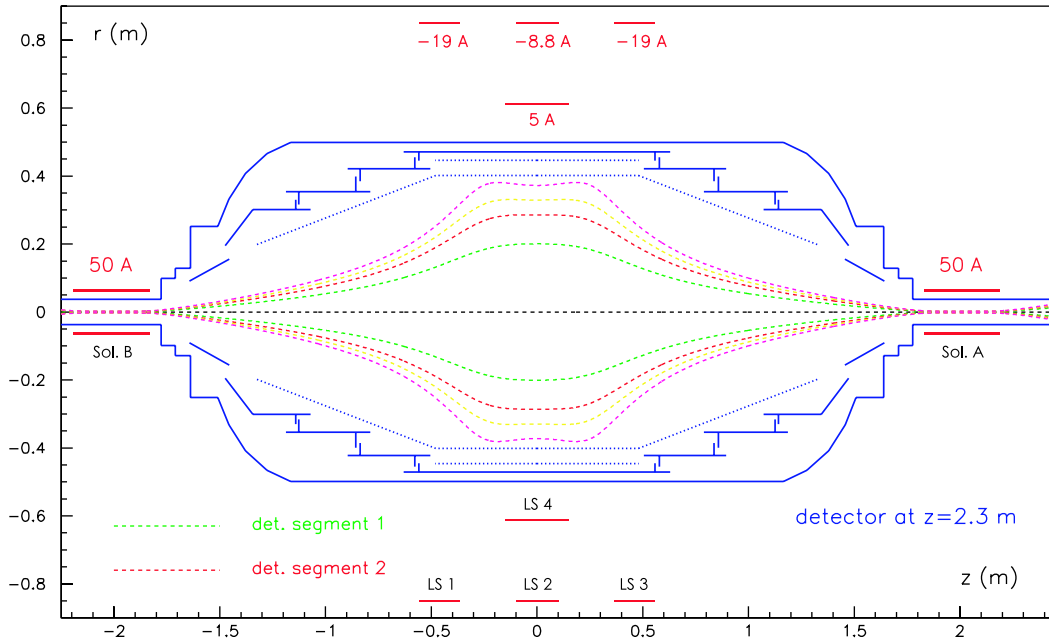


Fig. 5.4: The magnetic field configuration of Mainz MAC-E filter for the energy resolution of 0.9 eV at 17.8 keV. The values of currents (in units of Amper) of the solenoids A, B and the air coils LS 1–4 are indicated. The green dashed line denotes the magnetic flux tube corresponding to the innermost segment of the segmented electron detector (see Sect. 5.1.3) used at the beginning of the measurement series. The figure is taken from [Thu07].

5.1.2. Source section

The electron sources were placed on an in-house made holder (depicted in Fig. 5.5 and Fig. 5.6) which was designed to hold up to four samples in the last measurement phase. This feature made it possible to load simultaneously up to four samples into the source vacuum chamber. The source holder was mounted on a long rod fixed at the rear flange. The flange was connected with the x - y - z table which enabled the adjustment of the given source in the measuring position without deterioration of vacuum. A long, large diameter bellows between the rear flange and the source vacuum chamber allowed the movements, see Fig. 5.7 and Fig. 5.8. The movement in the z direction was motor-driven with the precision of 1 mm. The source could be positioned in the range of 12.5–70 cm relative to the center of the solenoid B. The movement in the x and y directions was done manually with the precision of 0.1 mm. The elevation amounted to ± 1 cm for both directions. The samples were isolated among each other and also relative to the spectrometer. Each sample was connected to the vacuum throughput by a wire which allowed to ground or bias the sample, the maximal applicable high voltage was 3 kV. This way it was possible to separate each electron source electrically.

The usual measurement position of the source was chosen as $z = 21$ cm from the center of the solenoid B. In this case the source magnetic field was $B_S = 1.75$ T and the corresponding acceptance angle amounted to $\theta_{\text{start}}^{\text{max}} = 32.7^\circ$, cf. Eq. 2.14. It was possible to place the samples closer to the center of the magnet bore, *i.e.* in a higher magnetic field and thus to increase the spectrometer efficiency. However, this was avoided as a high magnetic field would guide also the electrons escaping the source under very high angles. This would cause that

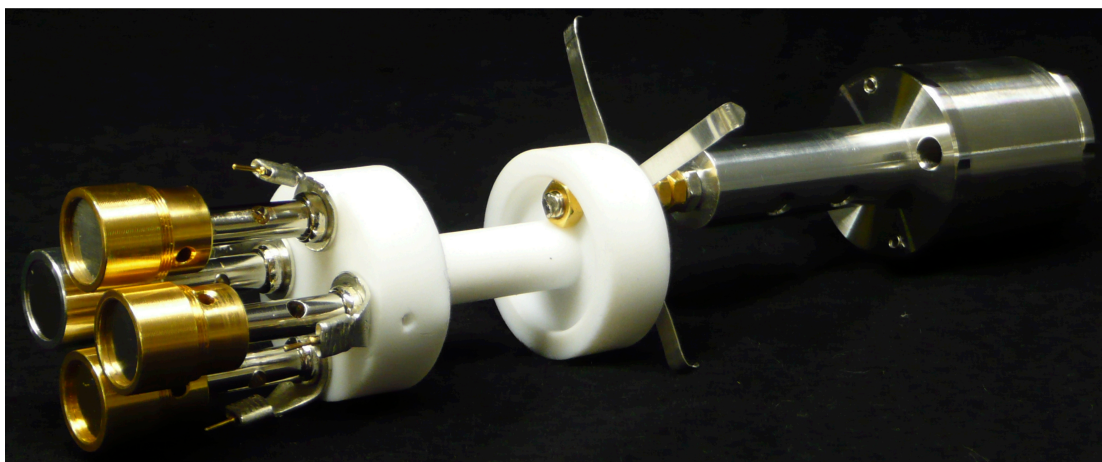


Fig. 5.5: The photograph of the source holder used in the last measurement phase, allowing to investigate up to four samples without a deterioration of vacuum.

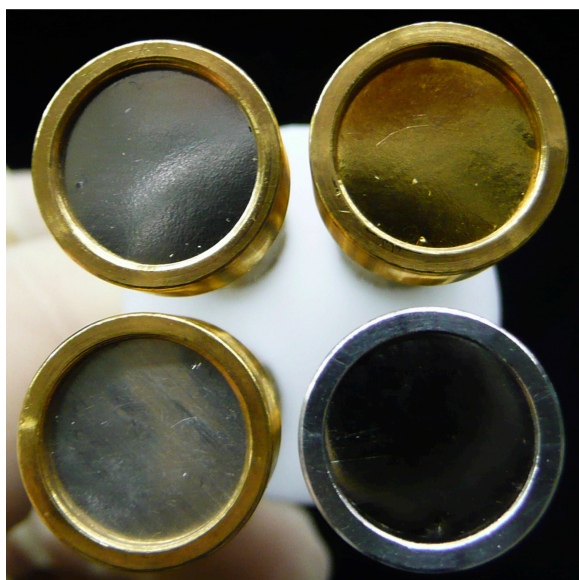


Fig. 5.6: The detail of the four ion-implanted $^{83}\text{Rb}/^{83\text{m}}\text{Kr}$ sources investigated in the last measurement phase. The ^{83}Rb was ion-implanted into four polycrystalline metal foils fixed in the sample holder. The gold foil is recognizable in the top right position, the other three foils of silvery color are the platinum foils. The sample holder in the bottom right position was made from aluminum, whereas the other holders were produced from gold plated copper. The inner and outer diameters of each sample holder were 11 and 14 mm, respectively.

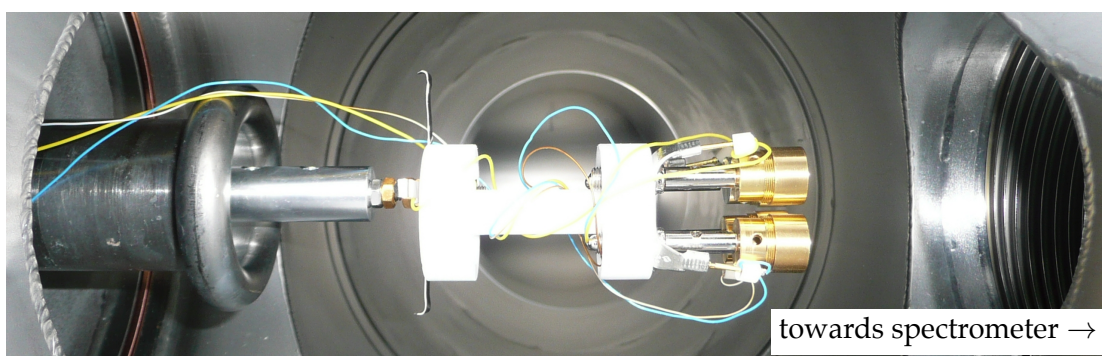


Fig. 5.7: The photograph of the source holder with four samples placed in the vacuum chamber of the source section. Good electrical contact allowed to ground or bias each source separately. Usually, the source to be investigated was connected to the spectrometer ground while all the other sources were biased by +100 V.

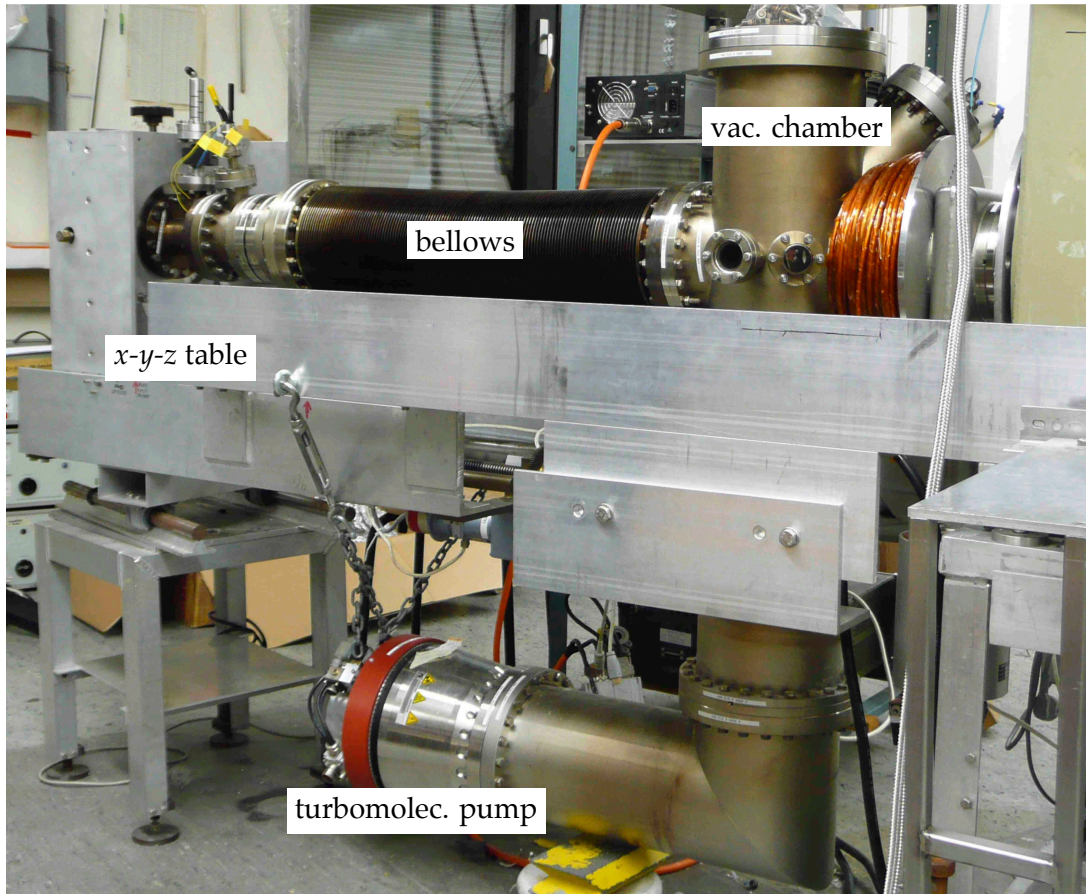


Fig. 5.8: The photograph of the source vacuum section used for the measurements with the solid $^{83}\text{Rb}/^{83\text{m}}\text{Kr}$ sources.

too many electrons with very little energy loss, *i. e.* very close to the zero-energy-loss peak, would be present in the electron spectrum, cf. Fig. 4.20 in Sect. 4.3.3. The maximal diameter of the samples was 14 mm, however, the spot where the ^{83}Rb radioactivity was placed (by the vacuum-evaporation or the ion-implantation) was of the diameter of only about 5 mm which required extra adjustments. The actual samples were described above in Sect. 4.1.2 and Sect. 4.2.3.

5.1.3. Detector section

The first measurement series was started with the Si semiconductor detector which was originally used in the Mainz Neutrino Mass Experiment [Kra05, Thu07]. This segmented detector (five concentric ring segments of the area 1 cm^2 each) allowed spatial resolution of the electron flux. However, due to its malfunction in 2008, the detector was replaced by the unsegmented windowless Si PIN photodiode Hamamatsu S3590-06 with the effective depletion layer of 0.5 mm thickness [Ham06]. Its active area of $9 \times 9\text{ mm}^2$ was mounted beneath a circular mask of diameter 9 mm, see Fig. 5.9.

Both types of detector were placed on a LN_2 cooled finger together with the preampli-

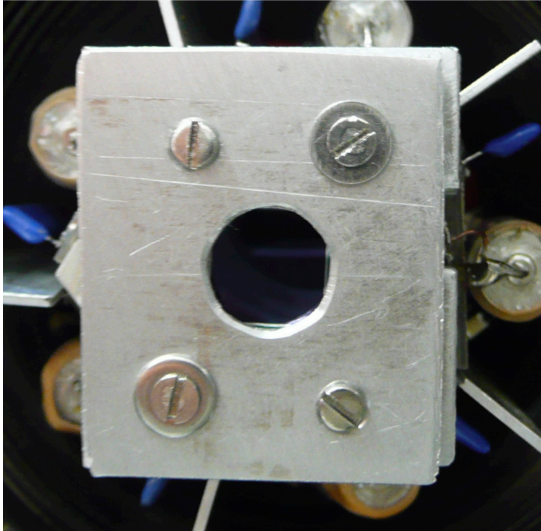


Fig. 5.9: The photograph of the front of the detector setup used for the $^{83}\text{Rb}/^{83\text{m}}\text{Kr}$ measurements. The unsegmented windowless silicon PIN photodiode Hamamatsu S3590-06 with the active area of $9 \times 9 \text{ mm}^2$ was mounted beneath a circular mask of diameter 9 mm.

fier electronics. While the energy resolution of the 5 ring detector was 1.4 keV (FWHM) at 18.6 keV [Kra05], the new photodiode showed the resolution of 3 keV (FWHM) at 17.8 keV. This value was still fully acceptable for the intended purpose. The noise edge of the photodiode was found to be 6.4 keV, thus, the measurements of the low energy conversion lines at 7.5 keV (cf. Tab. 3.1) were still realizable (with some problems as will be seen later). Typically, the photodiode was operated with the bias of -100 V . The response of the photodiode to conversion electrons of the energies of 7–32 keV is illustrated in Fig. 5.10.

The detector setup was mounted on a movable x - y - z table which allowed to adjust the detector inside the bore of the solenoid A with respect to the spectrometer z axis. The usual position of the detector was $\simeq 23 \text{ cm}$ from the solenoid A center, *i. e.* in the magnetic field of 1.06 T.

5.1.4. Vacuum system

The main tank was evacuated by a set of two cascaded turbomolecular pumps with the effective pumping speed of 2000 l s^{-1} . Two pneumatic gate valves separated the spectrometer vessel from the source and detector vacuum sections. Typically, after the bake-out of the entire setup the base pressure of $1 \times 10^{-10} \text{ mbar}$ was reached. The source and detector sections were evacuated by sets of cascaded turbomolecular pumps as well. However, usually the vacuum of $2 \times 10^{-9} \text{ mbar}$ in the source section and only $1 \times 10^{-8} \text{ mbar}$ in the detector section could be achieved. The reasons for a poor vacuum in the detector section were the use of Viton-sealed joints and the fact that it was not possible to bake out the detector components (*e. g.* the first stage of preamplifiers). The elevated pressure in the peripheral sections hindered keeping the tank in the 10^{-10} mbar range for extended periods of time. Thus, the surface of the electrodes was exposed to gradual adsorption of residual gases. This effect can significantly influence the work function ϕ_{spec} of the stainless steel electrode and thus the experimental conditions of the long-term measurement of the energy stability. Actually, ϕ_{spec} was essentially defined by the massless wire electrode (see Fig. 5.3), however, its relatively small surface is assumed to be affected by the rest gas adsorption as well. Both

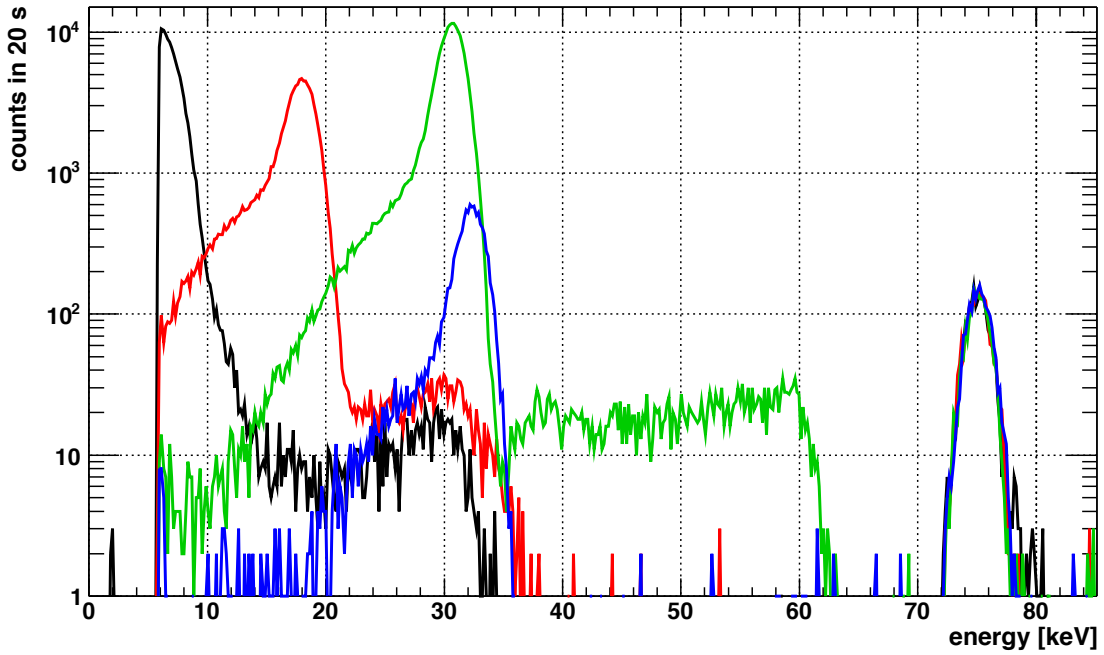


Fig. 5.10: The examples of a typical response of the Si PIN photodiode to $^{83\text{m}}\text{Kr}$ conversion electrons of various energies. The individual spectra of the following electron lines were superimposed into one plot: L_1 -9.4 (black), K -32 (red), L_3 -32 (green) and $N_{2/3}$ -32 (blue). The x axis denotes the energy scale which was calibrated with the help of the X-ray tube directed on the central part of the spectrometer vessel. The width of one bin in the x axis is 4 channels as it was set in the DAQ system for all measurements. The y axis (shown in log scale) denotes the number of events recorded in 20 s measurement time. The low energy cutoff at about 6 keV is due to the low level discriminator of the ADC. The low intensity peaks accompanying the main peaks on their high energy side can be attributed to summation peaks and secondary electrons. The events on the low energy side of the main peaks correspond to backscattered electrons which are magnetically or electrostatically reflected back onto the detector, but have to go three times through the detector dead layer. The peak at 75 keV corresponds to the pulser peak.

negative and positive changes of the metal surface work function after the adsorption of various gases were reported [Aga74, Kaw86, Ish91]. This issue will be further addressed throughout the work. In addition, the quadrupole mass spectrometer was utilized in this work and the changes of the residual gas composition accompanying abrupt changes of vacuum conditions (vacuum breakdowns) were studied.

Moreover, the combination of two circumstances led to sudden vacuum breakdowns which occurred several times during the measurement series. Firstly, the safety system developed in the framework of the Mainz Neutrino Mass Experiment was no longer kept in operation, thus power outages caused severe problems. Secondly, in order to increase the spectrometer efficiency both the source holder and the detector holder were placed in the bores of the solenoids, therefore the automatic closing of the gate valves was not possible. Usually, after each vacuum breakdown the bake-out of the main vacuum vessel and the peripheral sections was carried out.

5.1.5. High voltage system

The high voltage (HV) system used in the framework of this work was basically identical to the one developed in [Thu07] and later on used in [Ost08]. The system is schematically

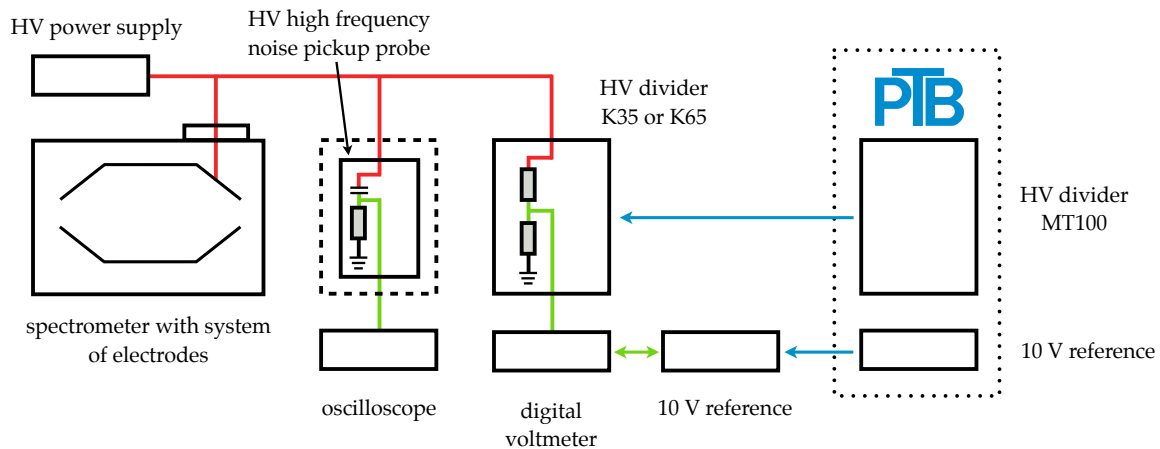


Fig. 5.11: The scheme of the HV setup used for the $^{83}\text{Rb}/^{83\text{m}}\text{Kr}$ measurements, after [Thu07]. The HV connections are indicated red, the low voltage is shown in green. The blue arrows denote the regular calibrations of the HV dividers and the 10 V DC reference with the help of standards of the PTB Braunschweig. The grounding of the HV high frequency noise pickup probe and the HV divider is only schematically drawn here for the sake of example. In reality, a common ground was distributed to the spectrometer and all electrical devices in a star-point manner.

depicted in Fig. 5.11 and can be divided into following parts:

- HV power supply FuG Elektronik HCP-18-35000

The high precision HV power supply delivered the HV to the massive and wire electrodes inside the spectrometer. The stability of the power supply is specified as 2 ppm per 8 hours, the temperature coefficient as 2 ppm K^{-1} and the reproducibility as 10 ppm [FuG06]. The voltage ripple was measured to be 20 mV peak-to-peak and the warmup time into the range of ppm stability was determined to be 2 hours [Thu07].

- HV dividers K35 and K65

The HV was also fed to a high precision HV divider. The divider scaled the HV down to 20 V range which could be easily measured by a commercial digital voltmeter with high precision. The working principle of the HV dividers K35 and K65, used in this work, was described above in Sect. 3.2.1. The main features of these HV dividers are summarized in Tab. 5.1.

The solid $^{83}\text{Rb}/^{83\text{m}}\text{Kr}$ sources are intended for continuous monitoring of the energy scale stability of the KATRIN spectrometers. This way they should act as a stable reference and verify the long-term behavior of the KATRIN HV dividers. Should any fast disturbance in the HV chain occur, the sources should point to it. However, in the test measurements at Mainz MAC-E filter the HV dividers were taken as the reference, on the contrary to the foreseen application in the KATRIN project. The HV dividers K35 and K65 were regularly calibrated at the PTB Braunschweig and the drifts of their dividing ratios were considered to be well known. To our knowledge the dividers K35 and K65, together with the reference divider MT100 of the PTB Braunschweig,

represent the three worldwide best dividers in the given HV range.

- digital voltmeter Fluke 8508A

The divided HV was read by the high precision digital voltmeter. The uncertainty of the DC voltage reading in the 20 V range is specified as 1.1 ppm in 24 hours and in the temperature range $\pm 1^\circ\text{C}$ around the temperature value at which the device was calibrated. Similarly, for the $\pm 1^\circ\text{C}$ range and 1 year period the uncertainty is specified as 4.0 ppm (both values at 99 % C.L.) [Flu08]. The voltmeter was regularly calibrated with a DC reference. Typically, the voltmeter was used in $7\frac{1}{2}$ -digits resolution mode with the integration time of about 2 s (64 power line cycles). The readout speed was increased by the use of the internal buffer memory of the device, practically lowering the integration time down to 1.54 s.

- 10 V DC reference Fluke 732A

In order to verify the performance of the digital voltmeter it was regularly (once per 1–2 days) calibrated with the help of the 10 V DC voltage reference. This in turn was calibrated at the PTB Braunschweig. This way the drift and the offset of the voltmeter were checked. The specified stability of the DC reference is 0.1 ppm year^{-1} [Flu08], however, the drift of the actual (rather old) device used in this work was determined as $0.24\text{ ppm year}^{-1}$ [Bau11]. Nevertheless, such a low drift can be safely neglected in the considerations presented later in this work as the observed drifts of the energies of the conversion electron lines were by two or more orders of magnitude higher.

According to the concept of the continuous monitoring of the energy scale stability in KA-TRIN (see Fig. 3.5 in Sect. 3.2), the $^{83}\text{Rb}/^{83\text{m}}\text{Kr}$ source will be biased by about -800 V when used at the monitor spectrometer. This way it will be ensured that the K -32 conversion electron line of $^{83\text{m}}\text{Kr}$ (17.8 keV) will match the fixed HV of about -18.6 kV applied simultaneously to the main and monitor spectrometers. However, during the test measurements carried out in the Institute of Physics, University of Mainz, the source was grounded and only the HV applied to the spectrometer electrodes was varied. The reason for such configuration was a minimization of the HV measurement uncertainties.

5.1.6. Control and data acquisition system

Both the HV power supply and the digital voltmeter were controlled by the original computer program developed in the Mainz Neutrino Mass Experiment [Bar91, Bar97] and used without major changes since 1997. Later on the program was adapted [Thu07] to control the HV power supply FuG Elektronik HCP-18-35000 and the digital voltmeter Fluke 8508A. Slight changes of the computer program performed in the course of this work made it possible to utilize the internal buffer memory of the digital voltmeter. This proved to be very useful in situations when high count rates were recorded. The program also controlled the CAMAC-based data acquisition (DAQ) system which comprised the following parts:

- bias voltage module set typically to -100 V ,
- spectroscopy amplifier Silena 7614,
- four-input 8064-channel ADC EG&G ORTEC AD413 [ORT08],

Tab. 5.1: The overview of the high precision HV dividers relevant for this work.

HV divider	K35 [Thu07, Thu09]	K65 [Bau09, Bau11]	PTB MT100 [Mar01]
production year	2005	2008	1995
total resistance	184 M Ω	145 M Ω	1 G Ω
maximal voltage [kV]	35	65	100
dividing ratios (nominal)	100 : 1, 1 972 : 1, 3 944 : 1	100 : 1, 500 : 1, 1 818 : 1, 3 636 : 1	100 : 1, 3 334 : 1, 10 000 : 1
warmup time (ppm range)	2 minutes		
warmup time (sub-ppm range)	3 hours		
reproducibility [ppm]	0.33	< 1	< 0.1
temperature stabilization [K]	± 0.1	± 0.1	± 0.15
div. ratio used in this work	1 972.480 16(61) : 1	1 818.109 6(6) : 1	
reference date	Nov 2006	Nov 2009	
calibrated at voltage [kV]	-20	-35	
temperature depend. [ppm K ⁻¹]	< 0.2	< 0.1	0.67
voltage depend. [ppm kV ⁻¹]	0.032(6)	-0.019(2)	
dependance tested in range [kV]	-8 ... - 32	-8 ... - 35	
long-term drift [ppm month ⁻¹]	0.604	-0.13(10)	0.17
drift tested in period	Oct 2005–Nov 2006	Nov 2009–Dec 2010	

Both KATRIN dividers show the reproducibility in the sub-ppm range over the scale of $\simeq 1$ month. The dividing ratios directly used throughout this work are stated together with their reference dates, long-term drifts and temperature- and voltage dependences. The reference HV divider MT100 of the PTB Braunschweig was not directly used in this work, however, the dividers K35 and K65 were calibrated against it.

5. Mainz MAC-E filter...

- FERA-bus histogramming memory EG&G ORTEC HM413 [ORT08],
- research pulser EG&G ORTEC 448 [ORT08],
- precision 1 MHz frequency standard AR 750747, and
- μ -scaler SPEC. 003.

The charge sensitive amplifier delivered the detector pulses to the spectroscopy amplifier set to the shaping time of $0.5 \mu\text{s}$. During the measurements with the original 5 ring detector only the three innermost detector segments were operational and thus three channels of the ADC were read out. Later, only one ADC channel was necessary for the measurements with the photodiode. Besides the electron signals the amplifier was also fed by a periodic signal produced by the pulser. The goal of this procedure was to accomplish a dead time correction similarly to [And69, Deb77]. The shape of the artificial pulses was set⁴ to mimic the true signals from the detected electrons, however, the amplitude of the artificial pulses was chosen so that the pulser peak was clearly separated from the electron signals in the ADC spectra.

Due to the high count rate of the order of $10^4 \text{ counts s}^{-1}$ (in the case of the ion-implanted $^{83}\text{Rb}/^{83\text{m}}\text{Kr}$ sources) the pulser became a crucial item in the DAQ system as the dead time correction of the recorded spectra was necessary. The nominal pulser rate was set to $f = 100 \text{ Hz}$. For the sake of a more precise dead time correction a higher pulser rate would be optimal since the relative uncertainty of the pulser peak area would decrease. Nonetheless, only the rate of 100 Hz was realizable with the specific model which was used. The frequency stability of the pulser was regularly checked in such a way that the pulser signal was delivered directly to the amplifier, while the preamplifier signal was separated from the electronic chain.

In addition to the pulser, the histogramming memory, attached to the ADC module via the FERA-bus interface, was utilized. This measure has significantly decreased the dead time of the DAQ system as the spectral data from the ADC were firstly on-line stored in the histogramming memory and only after each measurement at a given retarding voltage they were transferred to the control computer. Comparative scans were performed with the K_{32} line of a vacuum-evaporated source (total count rate $\approx 1500 \text{ counts s}^{-1}$) and it was found that in the event-by-event mode (information about each signal amplitude separately transferred to the control computer) the dead time τ of the system amounted to $\simeq 40 \mu\text{s}$, while in the histogramming mode (utilizing the histogramming memory) τ got reduced to $\leq 10 \mu\text{s}$. Thus, in order to minimize the losses due to the dead time the histogramming memory was used routinely, also for low count rate measurements, *e.g.* for scans of the $N_{2/3-32}$ line. The precise timing of the measurement was based on the μ -scaler which was used together with the 100 kHz output of the 1 MHz frequency standard.

5.2. Data analysis

In this section the analysis of the data obtained at the aforementioned experimental setup will be described. Basic notions will also be introduced which will be later used throughout

⁴The rise time was set to 20 ns and the decay time constant was set to $5 \mu\text{s}$.

the following chapters discussing the results of the long-term energy stability measurements of the solid $^{83}\text{Rb}/^{83\text{m}}\text{Kr}$ sources.

5.2.1. Typical measurement and data treatment

The z position relative to the solenoid B center was common for all the sources. However, at the beginning of every measurement phase the x - y position of each source was found at which the maximal signal-to-background ratio⁵ was observed. Thus, there was an individual optimal $[x,y]$ position for each source. Such a procedure ensured that each source was individually centered with respect to the spectrometer z axis and that, in turn, the electrons emitted from each source experienced the same potential dip across the analyzing plane (see Sect. 5.2.2 below). The sample under investigation was positioned in the x - y plane and the remaining sources were biased by +100 V. This way it was ensured that the electrons emitted from the remaining sources had a negligible effect on the spectrum measured with the chosen source. In addition, the observed signal-to-background ratio could also be further optimized by tuning the currents in the Earth's magnetic field compensation coils which aligned the electron flux inside the spectrometer.

The actual measurement consisted of scanning a chosen line of the $^{83\text{m}}\text{Kr}$ conversion spectrum described in Sect. 3.3.2. The scanning of the given electron line was realized by stepping the HV in a suitable region (typically ± 25 eV) around the energy of the line. The voltage step was adjusted to the actual resolution of the spectrometer, *e. g.* the usual step for scanning the K -32 line, where the spectrometer resolution amounted to $\simeq 0.9$ eV, was set to 0.5 V. The distribution of the measurement time was not optimized, *i. e.* a uniform measurement time distribution was employed for all measurements. The measurement proceeded as follows:

1. The HV power supply was set to a given step value U_{step} (requested by the control program) and it was let to stabilize for about 5 s.
2. The gate signal was sent to the CAMAC counter and the signals from the ADC were getting stored in the histogramming memory. In parallel, the digital voltmeter started to store the measured low voltage values into its internal buffer memory.
3. After the preset time (specified in the control program) the digital voltmeter stopped recording the low voltage and the gate signal stopped the ADC signal recording. The preset time was usually set to 20–60 s per one measurement, depending on the count rate of the given electron line.
4. The measured low voltage values and the recorded spectrum together with the actual time of measurement were transferred to a disk drive of the control computer.
5. The HV was stepped to another value.

It has to be stated that by the HV stabilization mentioned in (1) the stabilization after a step of typically 0.5 V is meant. The stabilization time of the HV scale due to the initial

⁵Actually, strictly speaking the $[x,y]$ position with the maximal amplitude of the conversion line K -32 was preferred over the position with the maximal amplitude-to-background ratio. It will be shown in Sect. 6.2.4 and Sect. 6.3.5 that the movement of the source in x or y direction by 1 mm changed the amplitude and background values noticeably.

warmup of the various devices (power supply, divider, digital voltmeter) of the order of ~ 12 hours was always ensured. On the other hand, after big HV steps, *e. g.* after switching from -17.8 kV (scan of the K_{32} line) to -30.5 kV (L_{3-32} line), a new measurement was started within ≈ 30 minutes after the previous scan finished. It was stated in Tab. 5.1 that the warmup time of the HV divider K35 to the range of ppm precision amounted about 2 minutes whereas the warmup time for the sub-ppm precision range was about 3 hours. Therefore, in our conditions the HV divider and the whole energy scale was always well stabilized in the ppm precision range.

The following information was obtained for each measurement point at a given HV U_{step} :

- measurement real time t_r (which was close to the preset time),
- N low voltage values $U_{\text{meas}_1} \dots U_{\text{meas}_N}$, measured by the digital voltmeter, from which the mean value U_{meas} and its error were calculated, and
- raw ADC spectrum example of which is depicted in Fig. 5.12.

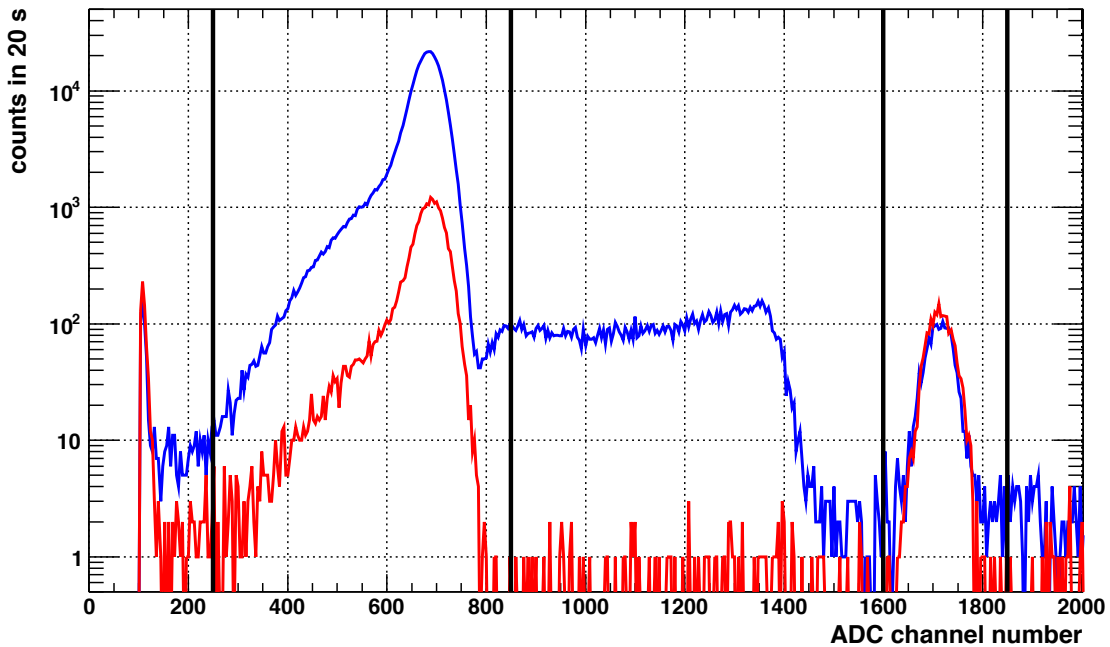


Fig. 5.12: The examples of the raw ADC recorded spectra, obtained during the measurement of the L_{3-32} line of the source Pt-30 #2 (cf. Sect. 4.2.3). The spectrum marked red was recorded in the condition of zero transmission. In this situation the HV applied to the spectrometer electrodes is rejecting all electrons of the L_{3-32} line and only the background—caused by $^{83\text{m}}\text{Kr}$ conversion lines of higher energies and by secondary electrons emitted from the electrodes—is recorded. The spectrum marked blue was recorded in full transmission, *i. e.* when all the L_{3-32} electrons are passing the filter HV. The perpendicular lines frame the summation windows in which the electron and pulser peaks are summed in each spectrum. The width of one bin in the x axis is 4 channels as it was set in the DAQ system for all measurements. The y axis is shown in log scale. The comparison of the electron peak areas in the depicted spectra results in the factor of ≈ 18 . As a consequence of the high count rate in the case of the “full transmission” spectrum the pulser peak area is smaller by about 13% in this case.

The aim is to construct an integral spectrum [retarding energy of spectrometer, count rate] and corresponding uncertainties. A typical integral spectrum is shown in Fig. 5.13. How-

ever, firstly both the U_{meas} values and the count rate had to be corrected for several effects. The energy is defined by the HV, *i. e.* it is dependent on the performance of the HV divider and digital voltmeter as well as on the spectrometer electrodes configuration. The count rate has to be corrected for the dead time in order to ensure a loss-free counting. The corrections of the “horizontal” (energy, or HV) and “vertical” (count rate) scales will be discussed separately in the following two sections.

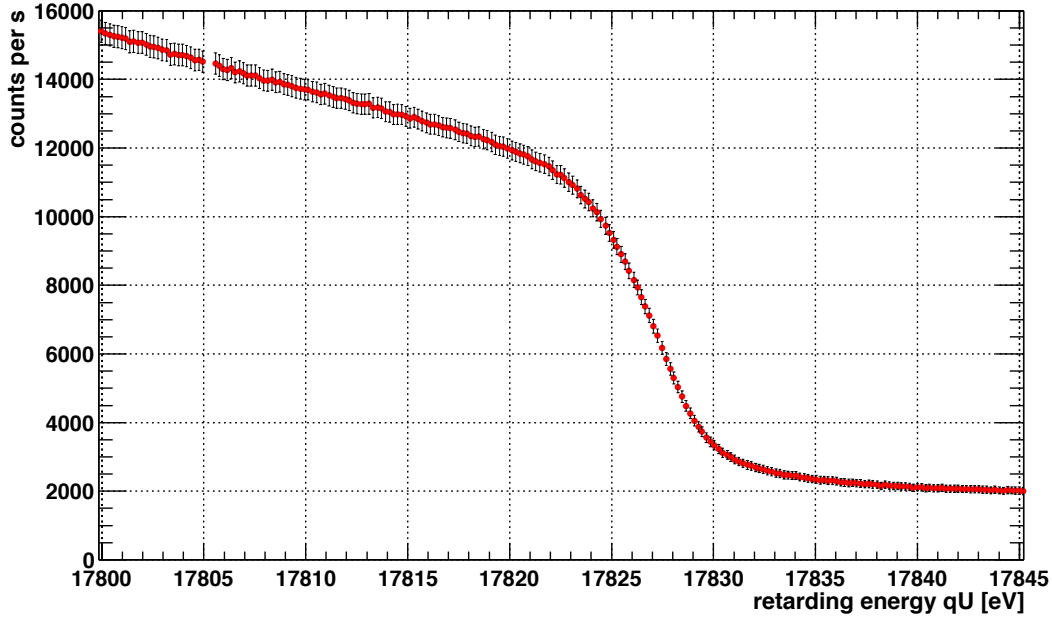


Fig. 5.13: The example of a typical integral spectrum of a conversion electron line recorded with the MAC-E filter spectrometer. The K -32 line of the source Pt-30 #2 is shown as an example. The x axis denotes the retarding energy of the spectrometer. The y axis denotes the count rate, corrected already for the dead time (see Sect. 5.2.3). The spectrum was recorded with the step of 0.2 eV. The error bars of the count rate are multiplied by the factor of 10 for the sake of example. The count rate of about 2000 counts s^{-1} in the right part of the spectrum corresponds to the background “above” the electron line. The electron line itself is seen as the steep rise of the count rate in the region from $\simeq 17835$ to $\simeq 17820$ eV (right to left). Ideally, the count rate “below” the electron line should stay constant, however, inelastically scattered electrons as well as shake-up and shake-off electrons give rise to a structure of satellites on the low energy side of the electron line, therefore, the signal in the integral spectrum further rises with decreasing HV. The spectrum can be visualized as the convolution of the transmission function of the MAC-E filter (see Fig. 2.4 and Eq. 2.15) with the shape of an elastic electron peak (typically Lorentzian with additional broadening, see Sect. 5.2.6) and a structure on its low energy side.

Two scans of the electron line with stepping the HV in a given region “down” (negative HV decreasing) and “up” (negative HV increasing) represented one sweep. One measurement consisted usually of several sweeps. Typically, one sweep took about 0.5–4 hours, depending on the HV step and preset time. As discussed in Sect. 3.3.2, the radioactive decay of the solid $^{83}\text{Rb}/^{83\text{m}}\text{Kr}$ sources is governed by the half-life of ^{83}Rb of $t_{1/2} = 86.2(1)$ d. From this fact it follows that the time duration of one sweep was negligible with respect to $t_{1/2}$ (^{83}Rb) and thus no half-life correction of the counts within the sweeps was necessary.

In previous measurements with the condensed $^{83\text{m}}\text{Kr}$ source [Ost08] it was a common practice to consider each sweep as one spectrum, *i. e.* the sub-sweeps “down” and “up” were av-

eraged in both retarding energy- and count rate axes. However, in [Thu07] it was observed that if the measurement of a given conversion line followed after a significant change of the HV (e.g. $K\text{-}32 \rightarrow L_3\text{-}32$) without a sufficient stabilization, the voltage differences between the corresponding measurement points of the sub-sweeps amounted up to 80 mV (utilizing the divider K35). Such a difference, representing the effect of $\simeq 4$ ppm in the case of the $K\text{-}32$ line, was observed already with a relatively low count rate of ≈ 200 counts s^{-1} . As a remedy to this problem the sub-sweeps were considered separately in the analysis [Thu07]. In this work the count rate in the $K\text{-}32$ line amounted up to $\approx 10^4$ counts s^{-1} which represents the increase of statistics by the factor of 50 with respect to the condensed ^{83m}Kr source. Therefore, the data of the solid $^{83}\text{Rb}/^{83m}\text{Kr}$ sources (mainly of the ion-implanted ones) were even more sensitive to such an effect of HV stabilization.

This problem can be assessed numerically in the following way. Let us assume the weighted mean \bar{X} created from a set of values X_i , $i = 1 \dots n$, each of which has an associated variance σ_i^2 . The weighting factors w_i are usually chosen as reciprocals of the variances, i.e. $w_i = 1/\sigma_i^2$, and it holds

$$\bar{X} = \frac{\sum_{i=1}^n w_i x_i}{\sum_{i=1}^n w_i}. \quad (5.1)$$

The variance of \bar{X} may be derived in two ways [Deb88]: firstly, the ‘‘external’’ variance $\sigma^2(\bar{X}, 1)$ can be obtained with the weighting factors included,

$$\sigma^2(\bar{X}, 1) = \frac{\sum_{i=1}^n w_i (X_i - \bar{X})^2}{(n-1) \sum_{i=1}^n w_i}. \quad (5.2)$$

Secondly, the ‘‘internal’’ variance $\sigma^2(\bar{X}, 2)$ is the value expected from the assigned variances σ_i^2 ,

$$\sigma^2(\bar{X}, 2) = \frac{1}{\sum_{i=1}^n w_i}. \quad (5.3)$$

It can be immediately seen that the internal variance does not depend on the agreement of the data points. In contrast, the external variance includes this factor. The larger of the two variances should be quoted as the variance of \bar{X} [Deb88]. From the definition of the reduced chi squared χ_r^2

$$\chi_r^2 = \frac{1}{n-1} \sum_{i=1}^n w_i (X_i - \bar{X})^2 \quad (5.4)$$

it directly follows

$$\sigma^2(\bar{X}, 1) = \chi_r^2 \cdot \sigma^2(\bar{X}, 2). \quad (5.5)$$

Thus, the magnitude of χ_r^2 , which is expected to be of the order of unity, allows conclusions on the quality of the data. It should be noted that the expressions in Eq. 5.2 and Eq. 5.3 were derived only for Gaussian distributions [Deb88]. Eq. 5.5 can be also interpreted so that for Gaussian distributed data with reasonable uncertainties the variances $\sigma^2(\bar{X}, 1)$ and $\sigma^2(\bar{X}, 2)$ should basically equal.

Such an analysis can be done for the case of averaging the sub-sweeps, thus $n = 2$ and X_1 and X_2 denote the numbers of counts in the sub-sweeps recorded in individual HV measurement points. In Fig. 5.14 the dependence of the ratio $\sigma^2(\bar{X}, 1) / \sigma^2(\bar{X}, 2)$ on the retarding energy is shown for the scan of the K -32 line of the ion-implanted source Au-30 which provided good statistics of $\approx 4 \times 10^3$ counts s^{-1} in the K -32 line. The first three sweeps of two different measurements were considered: in the first case (Fig. 5.14(a)) the high energetic lines $M_{2,3}$ -32 lines were scanned shortly prior the measurement of the K -32 line, thus the HV was freshly changed from -31.9 to -17.8 kV. In the second case (Fig. 5.14(b)) the K -32 line was scanned after the HV was stabilized in the region of -17.8 kV for about 6 days already (as the energy stability of only the K -32 line was investigated at that moment). In all cases the HV divider K65 was used.

It is clearly seen that without a sufficient HV stabilization the ratio $\sigma^2(\bar{X}, 1) / \sigma^2(\bar{X}, 2)$ peaks up to ≈ 100 in the first sweep. The differences between the corresponding measurement points of the sub-sweeps of the first sweep amounted up to 400 mV. It is also apparent that the data are most sensitive to any HV instability—and to possible variations of other experimental conditions—in the region of the peak centroid where the changes of the count rate with the retarding energy are maximal⁶. The effect of the “sub-sweeps mismatch” is much less pronounced in the second and the third sweeps in Fig. 5.14(a) when the HV got gradually stabilized. However, as seen in Fig. 5.14(b) the ratio $\sigma^2(\bar{X}, 1) / \sigma^2(\bar{X}, 2)$ frequently rises above 2–3 even when the HV was kept practically constant (the range of $\simeq 50$ eV was repeatedly scanned) for several days. In contrast to the first case, here the differences between the corresponding measurement points of the sub-sweeps were found to be ≈ 15 mV. Still, the scatter of the sub-sweeps data was found too large in comparison with their uncertainties. Therefore, a safe approach was chosen in further analysis and the sub-sweeps were considered separately as single spectra.

5.2.2. Energy scale corrections

The low voltage $U_{\text{meas}}(t)$ is multiplied by the dividing ratio $M(t)$ of the HV divider,

$$U(t) = M(t) \cdot U_{\text{meas}}(t), \quad (5.7)$$

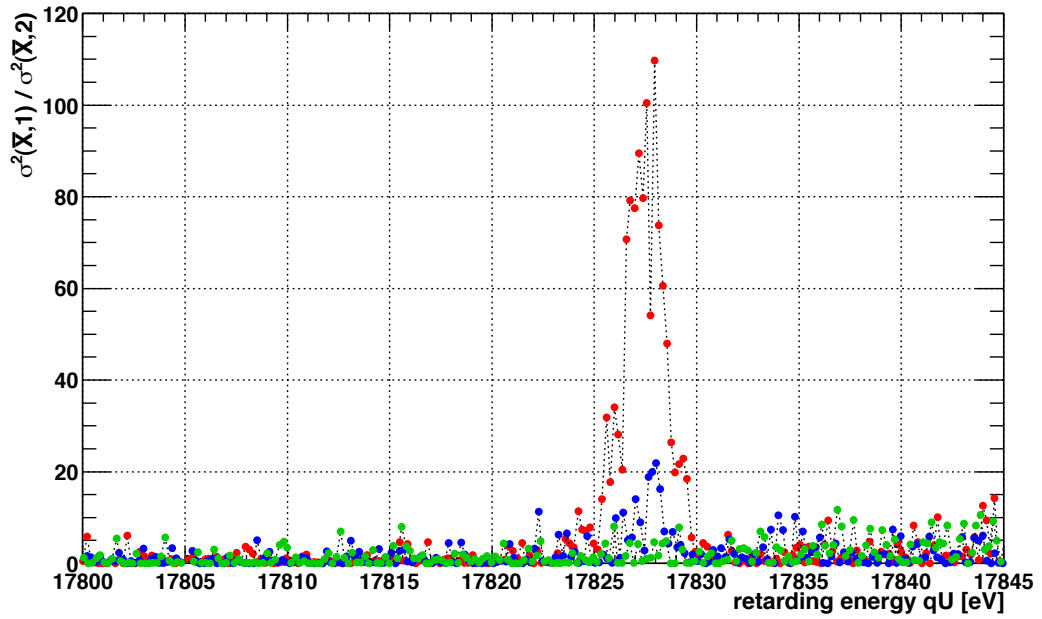
where the time dependence of each quantity was expressed. The value $U(t)$ is equal to the HV delivered by the power supply. This can be significantly different from the nominal preset value U_{step} as some offset is always present⁷. Several corrections have to be taken into account in order to obtain a physically relevant scale. According to [Thu07, Ost08] the

⁶Actually, this notion can be simply quantified as

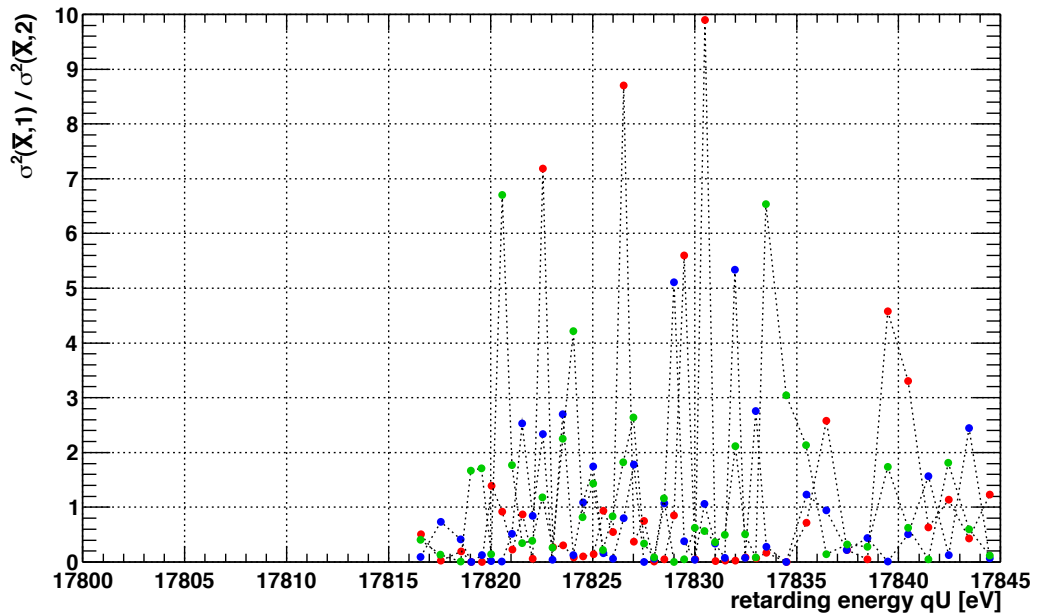
$$\delta N = \frac{\partial n}{\partial U} \Delta U \cdot \delta t, \quad (5.6)$$

where δN denotes the observed change of the number of counts N , $\frac{\partial n}{\partial U}$ represents the sensitivity of the count rate n to the change of the retarding voltage U , ΔU denotes the HV instability and δt is the time span on which the HV stability is considered (requested).

⁷The offset of the HV power supply FuG Elektronik HCP-18-35000 amounted to about -5 V.



(a)



(b)

Fig. 5.14: The values of $\chi_r^2 = \sigma^2(\bar{X}, 1) / \sigma^2(\bar{X}, 2)$ defined in accordance with Eq. 5.2 to Eq. 5.5 are plotted against the retarding energy set to scan the K -32 line of the source Au-30. The y axis represents the measure of difference between the sub-sweeps, *i. e.* between the two “halves” of the given sweep. Basically, for Gaussian distributed data the majority of points should lie in the vicinity of $y = 1$. In **(a)** the K -32 line was scanned practically immediately after the scan of the $M_{2,3}$ -32 lines (retarding energy qU of $\simeq 31.9$ keV) was finished. In **(b)** the K -32 line of the same source was measured when qU was stabilized in the region of 17.8 keV for about 6 days already. In both figures the first sweep is shown in red, the second one in blue and the third one in green. While the top plot shows a measurement performed with a fine step of 0.2 eV over the wide range of 17 800–17 845 eV, the bottom plot was obtained with a step of 0.5 eV over a narrower range of 17 816–17 845 eV, therefore there are fewer data points in the bottom plot.

actual retarding energy qU_{corr} experienced by the electrons reads

$$qU_{\text{corr}}(t) = q \left(U_{\text{meas}}(t) - U_{\text{offset}}(t) \right) \cdot K(t) \cdot \left(M(t) + \frac{\partial M}{\partial U} \underbrace{\left(M \cdot U_{\text{meas}} - U_{\text{ref}} \right)}_{=\delta U} \right) + \delta E_{\text{shift}}, \quad (5.8)$$

where $q = -|e|$ and the following effects are considered:

- The imperfections of the digital voltmeter are described with the zero offset $U_{\text{offset}}(t)$ (not to be confused with the offset of the HV power supply) and the scale factor $K(t)$. Ideally, $U_{\text{offset}}(t) \equiv 0 \text{ V}$ and $K(t) \equiv 1$ but this is never the case. Typically, on the 20 V range the zero offset was found to be of the order of $1 \mu\text{V}$ and the scale factor was different from 1 by $\delta K(t) = 1 - K(t) \simeq 5 \times 10^{-6}$. Regular calibrations of the digital voltmeter with the 10 V DC reference made it possible to track the long-term dependencies $U_{\text{offset}}(t)$ and $K(t)$ which were taken into account.
- The long-term drift of the HV divider must not be omitted when considering the energy stability of the electron lines. In accordance with Eq. 3.12 the time dependence of the dividing ratio $M(t)$ can be expressed as a linear function with the relative drift m [ppm month⁻¹] of the dividing ratio. However, rather than to calculate the dividing ratio $M(t)$ for every moment of the measurement series as $M(t) = M_0(1 + m t)$, the nominal value M_0 was used during the whole measurement series. Later, the observed drift of the given ^{83m}Kr conversion line position was corrected for the drift m .
- The HV dependence of the dividing ratio M is taken into account via the term $\frac{\partial M}{\partial U} \delta U$. As the divider is usually calibrated at the given HV of U_{ref} , for obtaining reliable values in different HV ranges the voltage dependence of M has to be considered. The time dependence of the term $\frac{\partial M}{\partial U} \delta U$ was omitted as typically the difference $\delta U = M \cdot U_{\text{meas}} - U_{\text{ref}}$ spans several units of kV. Moreover, the voltage dependence $\frac{\partial M}{\partial U}$ of both dividers K35 and K65 was determined to be of the order of 0.01 ppm kV^{-1} , cf. Tab. 5.1. In this situation the fluctuations of δU on the ppm scale can be neglected.
- The correction δE_{shift} represents the potential dip across the analyzing plane. The radial variations of the magnetic and electric fields influence the transmission function. The onset of transmission is shifted as the electrons passing the analyzing plane experience different retarding potential, depending on the radius in the analyzing plane. In addition, a radial variation of the magnetic field across the analyzing plane increases (smears) the width of the transmission function. The shift of the transmission onset can be written [Thu07] as

$$\delta E_{\text{shift}} = E_{\text{pot}, r=0} - qU = -2.08 \times 10^{-5} \cdot E_{\text{start}}, \quad (5.9)$$

where $E_{\text{pot}, r=0}$ stands for the retarding potential in the analyzing plane on the symmetry axis, U represents the applied HV and E_{start} is the starting kinetic energy of electrons. In the case of the K-32 line the effect amounts to $\delta E_{\text{shift}}(17.8 \text{ kV}) = -0.371 \text{ eV}$. In Fig. 5.15 the dependence of δE_{shift} on the spectrometer radius and electron kinetic energy is illustrated. With respect to a possible misalignment of the spectrometer setup the uncertainty of δE_{shift} of 5% was assumed in this work as in [Thu07, Ost08].

Finally, the corrected HV is converted into the energy scale via

$$E_{\text{corr}}(t) = qU_{\text{corr}}(t), \quad q = -|e|. \quad (5.10)$$

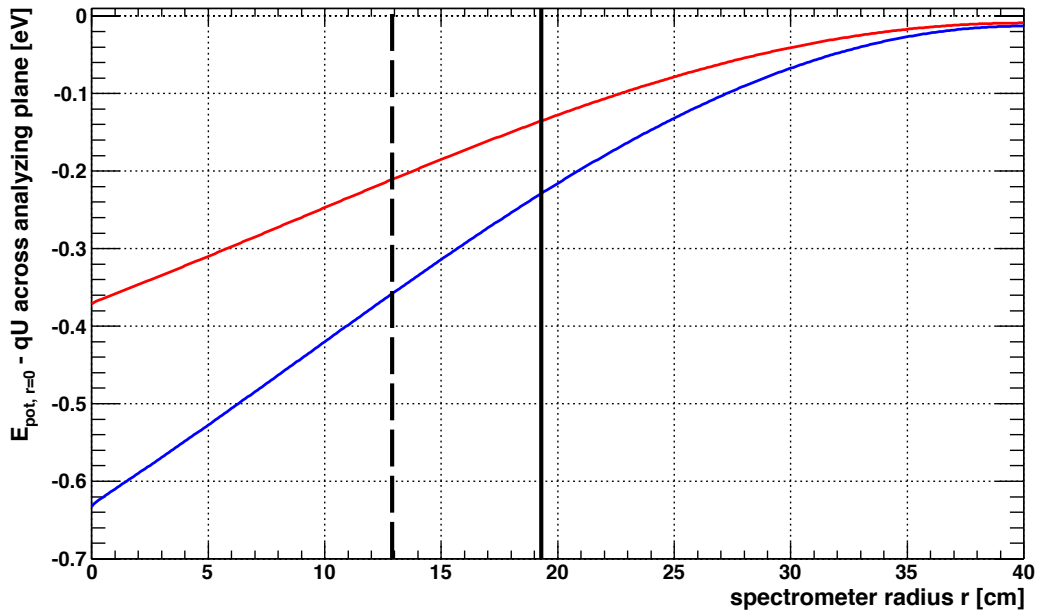


Fig. 5.15: The dependence of the potential dip $E_{\text{pot}, r=0} - qU$ (see Eq. 5.9) on the spectrometer radius in the analyzing plane. The red line shows the dependence calculated for the electrons of the K -32 line, thus here $qU = 17824$ eV. The blue line denotes the case of the L_3 -32 line with $qU = 30473$ eV. The vertical dashed line at $r = 12.9$ cm marks the maximal radius of the magnetic flux tube in the analyzing plane when the spectrometer is operated at the resolution of 2.0 eV at 17.8 keV. Similarly, the vertical full line at $r = 19.3$ cm is valid for the resolution of 0.9 eV at 17.8 keV. The figure is based on [Thu07].

Nevertheless, for the sake of simplicity all the plots of electron spectra in this work are drawn with the quantity qU of the retarding energy of the spectrometer instead of the corrected energy E_{corr} . On the other hand, all the values of the absolute electron energies presented in this work are stated as E_{corr} .

5.2.3. Dead time correction

As the high count rate of several thousands of events per second caused a non-negligible dead time of the electronics, it was necessary to correct the count rate for the dead time with the help of the periodic pulser. The events in the individual raw ADC spectra were summed in suitable ranges of channels. The complete spectrum was summed, giving the total number of counts N_{tot} . Also, the counts in the regions covering the electron peak and the pulser peak were summed up, resulting in peak areas N_e and N_p , respectively. The notions N_e and N_p correspond to the areas marked with vertical lines in Fig. 5.12.

The variance of the pulser peak area N_p was non-zero due to the random signals resulting from the registration of electrons. However, the variance was not equal to $\sigma^2(N_p) = N_p$ which would be the case of Poisson distribution—on the contrary, due to the periodic nature of the pulser the number of events in this peak follows the binomial distribution. In this case

the variance reads

$$\sigma^2(N_p) = N_p \left(1 - \frac{N_p}{f t_r} \right), \quad (5.11)$$

where the probability p of an event (a “success”) was approximated as $p = N_p / (f t_r)$ [Cro05]. Here f represents the frequency of the pulser and t_r the measurement real time. Thus, the periodic nature of the pulser decreases the pulser peak area variance by the factor $1 - N_p / (f t_r)$. In order to prevent any effect of a sudden change of the detector noise (and thus the resolution), the summation windows were chosen big enough to cover the electron and pulser peaks. The nominal value of the pulser rate was 100 Hz, anyway, the actual value of the rate was regularly checked. A clear trend of stabilization was observed within 7 months from the value $f_1 \simeq 102.5$ Hz up to the value $f_2 \simeq 105.0$ Hz. In the further analysis the mean value of the pulser rate $f_0 = 104.0(7)$ Hz was taken into account (the mean value and its error were calculated on the basis of regular calibrations).

For the non-paralyzable model of a radiation detector it holds [Kno00]

$$n_{\text{true}} = \frac{n_{\text{rec}}}{1 - \tau n_{\text{rec}}}, \quad (5.12)$$

where τ is the system dead time and n_{true} and n_{rec} are the true interaction and recorded count rates, respectively. The count rate losses represented by the fraction $1 / (1 - \tau n_{\text{rec}})$ can be compensated by the correction factor CF defined as

$$CF = \frac{f t_r}{N_p} = \frac{n_{\text{true}}}{n_{\text{rec}}}. \quad (5.13)$$

This definition is based on the assumption that the fraction of events lost from the electron peak is equal to the fraction of events lost from the pulser peak. Principally, the dead time correction could be done with the help of Eq. 5.13 in a “point-wise” manner, *i. e.* for each electron peak area N_e the correction factor CF could be calculated from N_p determined in the corresponding ADC spectrum. Then each electron peak area N_e would be corrected for the dead time separately, *i. e.* each point of the resulting integral electron spectrum would be corrected independently on all the other points. However, this approach suffers from large uncertainties which would be introduced to the corrected electron spectrum. Therefore, a more sophisticated approach was chosen: it was based on the least-squares fit of the dependence $CF(N_{\text{tot}})$ shown in Fig. 5.16⁸ over the entire range of N_{tot} . This way all the raw ADC spectra are considered “at once” and the functional description fitted to the $CF(N_{\text{tot}})$ dependence is later used for correcting each point of the integral spectrum. The $CF(N_{\text{tot}})$ dependence was, in accord with Eq. 5.12, assumed in the form

$$CF(N_{\text{tot}}) = \frac{a_1}{1 - a_2 N_{\text{tot}}}, \quad (5.14)$$

where the parameters $a_{1,2}$ correspond to $a_1 \approx 1$ and $a_2 \approx \tau / t_r$. It would be wrong to use N_e in Eq. 5.14 instead of N_{tot} : if some abrupt rise of the detector noise (which is not a part of the electron peak, cf. Fig. 5.12) would significantly increase the dead time, the value of N_e would not change correspondingly and the noise would not be accounted for. Typically, the fit results of the parameters $a_{1,2}$ in Eq. 5.14 were $a_1 \simeq 1.01$ and $a_2 \simeq 10^{-7}$ with relative

⁸Here the dependence $CF(N_{\text{tot}})$ is illustrated for the L_{3-32} line which is the most intense line in the $^{83\text{m}}\text{Kr}$ conversion electron spectrum. Thus, the dead time is maximal during the scan of this line.

errors of 1–10%. From the correspondence $a_2 \approx \tau/t_r$ it can be seen that the dead time τ of the system, assuming the measurement time of 20 s, was $\tau \approx a_2 \cdot t_r \approx 10^{-7} \cdot 20 \text{ s} = 2 \mu\text{s}$, indeed⁹ in the order of several μs .

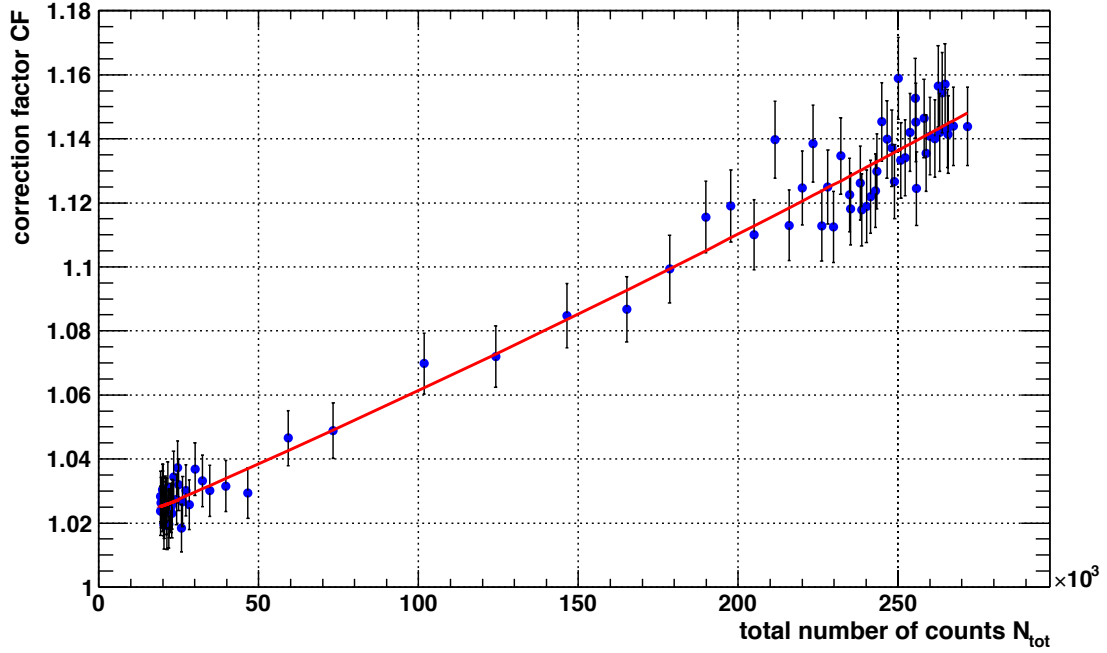


Fig. 5.16: The principle of the dead time correction procedure shown for the case of the L_3 -32 line of the source Au-30. The x axis denotes the total number of counts N_{tot} recorded in the individual ADC spectra. The y axis denotes the correction factor CF defined in Eq. 5.13. The points mark the data $CF(N_{\text{tot}})$ calculated for one sub-sweep of the measurement. The red line represents the least-squares fit of the parameters $a_{1,2}$ according to Eq. 5.14. The fitted dependence $CF(N_{\text{tot}})$ is then used for correcting the individual values of the electron count rate, cf. Eq. 5.16. The result of the dead time correction can be seen in Fig. 5.17.

Finally, the electron count rate

$$n_e = \frac{N_e}{t_r} \quad (5.15)$$

is corrected for the dead time

$$n'_e = CF n_e, \quad (5.16)$$

where n'_e is the loss-free count rate. Its variance $\sigma^2(n'_e)$ is derived as

$$\sigma^2(n'_e) \stackrel{(1)}{=} \frac{\sigma^2(N'_e)}{t_r^2} \stackrel{(2)}{=} \frac{(CF)^2 \cdot N'_e}{t_r^2} \stackrel{(3)}{=} \frac{(CF)^3 \cdot N_e}{t_r^2} \stackrel{(4)}{=} \frac{(CF)^3 \cdot \sigma^2(N_e)}{t_r^2} \stackrel{(5)}{=} (CF)^3 \sigma^2(n_e) \quad (5.17)$$

with the following steps:

1. Here the relation $N'_e = n'_e \cdot t_r$ is used (while the measurement real time t_r is considered to be constant), thus $\sigma^2(N'_e) = t_r^2 \cdot \sigma^2(n'_e)$.
2. The error of the corrected peak area $\sigma(N'_e)$ can be rewritten as $\sigma(N'_e) = CF \cdot \sigma(N_e) = CF \cdot \sqrt{N_e} = \sqrt{CF} \cdot \sqrt{CF} \cdot \sqrt{N_e} = \sqrt{CF} \cdot \sqrt{N'_e}$. However, correctly the error of $\sigma(N'_e)$

⁹It was stated in Sect. 5.1.6 that the use of the histogramming memory within the DAQ system has improved the dead time down to $\leq 10 \mu\text{s}$.

should be enlarged by the additional factor \sqrt{CF} due to the dead time correction itself. This behavior was verified with the help of Monte Carlo simulations carried out in the framework of the Mainz Neutrino Mass Experiment [Wei11] and also in the analysis of the normalized residuals resulting from the fit of dead time corrected spectra. Thus, one can write $\sigma(N'_e) = CF \cdot \sqrt{N'_e}$.

3. Obviously, for the peak areas it holds $N'_e = CF \cdot N_e$.
4. Due to the random nature of the electron peak its variance $\sigma^2(N_e)$ equals N_e .
5. Similarly to (1), $\sigma^2(N_e) = t_r^2 \cdot \sigma^2(n_e)$.

The effect of the dead time correction is clearly visible in Fig. 5.17. The correction is pronounced mainly on the low energy side of the elastic peak. The correction amounted up to $\sim 15\%$ in the case of the L_3 -32 line.

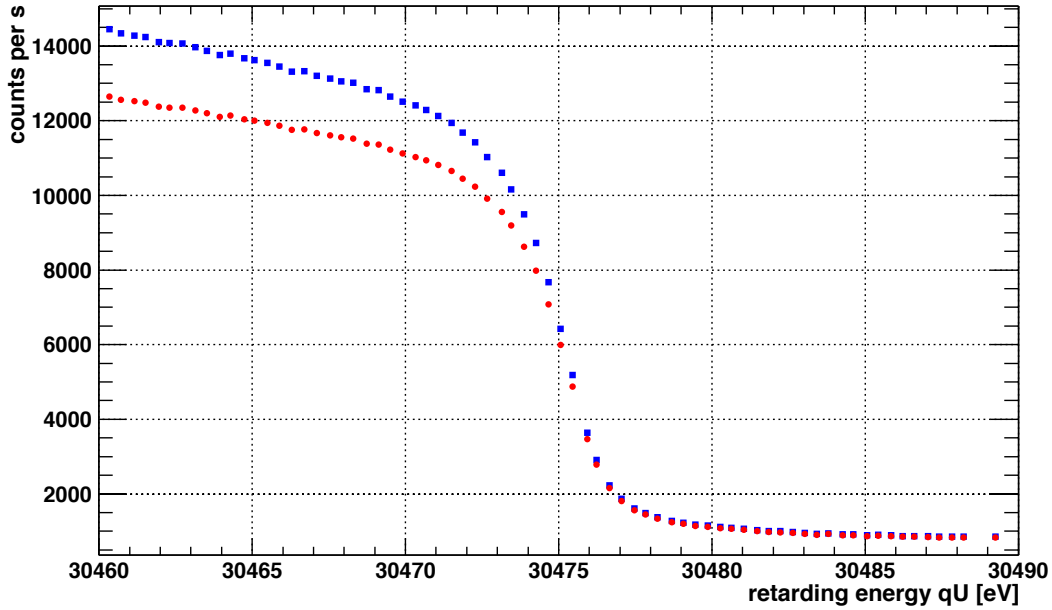


Fig. 5.17: The effect of the dead time correction on the L_3 -32 line of the source Au-30. The spectrum shown in red was calculated without the dead time correction, whereas the spectrum marked blue was corrected for the dead time. The dead time correction was accomplished on the basis of the fit illustrated in Fig. 5.16. The error bars of the count rate are not shown here.

5.2.4. Expected count rate of zero-energy-loss electrons

On the basis of the expected electron count rate registered by the detector, the amplitude A [counts s^{-1}] of a given conversion electron line of the solid $^{83}\text{Rb}/^{83\text{m}}\text{Kr}$ source can be estimated as A_{est} via

$$A_{\text{est}} = \mathcal{A} \cdot d \cdot R_{\text{Kr}} \cdot P_{\text{el. line}} \cdot P_{\text{no-shake}} \cdot \eta_{\text{spec}} \cdot \epsilon_{\text{no-loss}} \cdot \eta_{\text{det}}, \quad (5.18)$$

where the following effects are taken into account:

- \mathcal{A} is the ^{83}Rb activity of the given radioactive source.

5. Mainz MAC-E filter...

- d represents the correction for the radioactive decay of ^{83}Rb with the half-life of $t_{1/2} = 86.2(1)$ d [Fir96].
- The retention factor R_{Kr} , mentioned already in Chap. 4, defines the portion of $^{83\text{m}}\text{Kr}$ atoms which are trapped within the source. $R_{\text{Kr}} = 1$ would mean that 100 % of $^{83\text{m}}\text{Kr}$ atoms remains in the source.
- $P_{\text{el. line}}$ is the probability of the conversion electron emission per ^{83}Rb decay. The values for all significant conversion lines in the $^{83\text{m}}\text{Kr}$ decay are listed in Tab. 3.1.
- The shake-up/off processes were described in Sect. 4.3.2. Both processes reduce the intensity of the zero-energy-loss electron line by the factor $P_{\text{shake}} = 1 - P_{\text{no-shake}}$ which follows from the probability of the shake-up/off processes in the given source.
- The factor η_{spec} corrects the count rate for the spectrometer efficiency. It represents the fraction of electrons emitted into the acceptance code with respect to all the electrons emitted into the full space of 4π . This effect is dependent on the position of the source with respect to the center of the solenoid B.
- In the solid source the electron can undergo an inelastic scattering in which it loses a portion of its energy. The fraction $\epsilon_{\text{no-loss}}$ of the zero-energy-loss electrons for the given source can be estimated with the help of Monte Carlo simulations, see Sect. 4.3.3.
- The detection efficiency η_{det} was estimated as 0.8 for the 5 ring detector originally used in the Mainz Neutrino Mass Experiment¹⁰. As the effective thickness of both the original and the replacement detector amounted to 0.5 mm, $\eta_{\text{det}} = 0.8$ was used throughout this work as well. The slight energy dependency of η_{det} , determined in [Kra05] as $\alpha_{\text{det}} = 4(2) \% \text{ keV}^{-1}$, was omitted in this work.

As an example the K -32 line count rate of the vacuum-evaporated source S 28 (cf. Sect. 4.1.2) measured at the distance of $z = 30$ cm from the solenoid B center will be estimated. At this distance the magnetic field was calculated as $B_S = 0.33$ T, thus, according to Eq. 2.14 the maximal acceptance angle amounted to $\theta_{\text{start}}^{\text{max}} = 13.6^\circ$. This represents the portion of

$$\eta_{\text{spec}} = \frac{\Delta\Omega}{4\pi} = \frac{1 - \cos\theta_{\text{start}}^{\text{max}}}{2} = 0.014 \quad (5.19)$$

of the full space 4π into which the electrons are emitted. The diameter of the source was determined as $d_{\text{source}} = 7.3$ mm and from the conservation of the magnetic flux (cf. Eq. 2.16 and Eq. 2.17) it follows

$$d_{\text{source image}} = d_{\text{source}} \cdot \sqrt{\frac{B_S}{B_D}} \simeq 4.5 \text{ mm}, \quad (5.20)$$

thus, the complete source area was imaged onto the detector ($d_{\text{det}} = 9$ mm) placed in the field of $B_D = 0.86$ T.

The ^{83}Rb radioactivity of the source was $\mathcal{A} = 4.95$ MBq (ref. date 29.07.2008) and the investigation of the source started on 28.08.2008 thus the correction d for the radioactive decay

¹⁰An electron line in the detector spectrum exhibits a significant low energy tail due to backscattering from the detector. The backscattered electrons (20–30 %) come back to the detector after being magnetically or electrostatically reflected by the spectrometer. Thus, they underwent multiple passages through the insensitive dead layer of the detector, causing the low energy tail. Applying an energy window on the ADC spectrum keeps only about 80 % of all events [Wei11].

amounts to $\simeq 0.72$. The $^{83\text{m}}\text{Kr}$ retention was measured as 19% prior to the measurements at Mainz spectrometer and it was re-measured as 26.5(14)% after the measurements were finished, see Sect. 4.1.2. For the purpose of our estimate the average value of $R_{\text{Kr}} \simeq 0.23$ can be taken. The probability $P_{\text{el. line}}$ that the K-32 conversion electron will be emitted in the ^{83}Rb decay is taken from Tab. 3.1 as $P_{\text{K-32}} = 0.1707$. The intensity of the zero-energy-loss line is reduced by the shake-up/off and inelastic scattering processes. The probability of the former one was considered as 20.5% (cf. Sect. 4.3.2), thus, $P_{\text{no-shake}} = 0.795$. In order to estimate the fraction of the inelastically scattered electrons Monte Carlo simulations were carried out, see Sect. 4.3.3. The number of Monte Carlo events, *i. e.* the number of electrons emitted isotropically in the source into the full space was $N_{\text{all}} = 2.0 \times 10^8$. The nominal starting energy of the electrons was set to $E_0 = 17\,824$ eV. The number of zero-energy-loss electrons emitted into the forward cone of 13.6° was found to be $N_{\theta \leq 13.6^\circ, \text{ no loss}} = 2.51 \times 10^6$. This gives the reduction factor of

$$\epsilon_{\text{no-loss}} = \frac{N_{\theta \leq 13.6^\circ, \text{ no loss}}}{\eta_{\text{spec}} \cdot N_{\text{all}}} = 0.906, \quad (5.21)$$

where the product $\eta_{\text{spec}} \cdot N_{\text{all}}$ represents the number of all electrons emitted into the forward cone of 13.6° . Finally, according to Eq. 5.18 the expected count rate in the K-32 line is

$$n_e(\text{K-32}) = 4.95 \times 10^6 \cdot 0.72 \cdot 0.23 \cdot 0.1707 \cdot 0.795 \cdot 0.014 \cdot 0.906 \cdot 0.8 \simeq 1\,129 \text{ counts s}^{-1} \quad (5.22)$$

which is in a good agreement with the observed count rate of $\approx 1\,200 \text{ counts s}^{-1}$. A slight discrepancy can be explained by the uncertainties of the individual factors. In addition, the $^{83\text{m}}\text{Kr}$ retention of the vacuum-evaporated sources was found to change slightly in time as described above. Moreover, the shake-up/off probabilities may differ for the cases of gaseous krypton and krypton adsorbed on or implanted in the solid.

5.2.5. Transmission function

For the description of the experimental data the knowledge of the spectrometer transmission function is of great importance. In an ideal MAC-E filter both the electrostatic retardation potential U and the minimal magnetic field strength B_{A} (see Fig. 2.3 and Eq. 2.15) are invariable along the full extent of the analyzing plane [Val09a]. In reality, however, inhomogeneities both in the electric and the magnetic field will be introduced due to various influences (effects of the finite size of the electrostatic electrodes and the auxiliary coils as well as local distortions of the field configuration). The magnitude of the inhomogeneities in the analyzing plane can be estimated by the two quantities [Val09a]

$$\begin{aligned} \Delta U &= |U(r=0) - U(r=r_{\text{A}}^{\text{max}})| \\ \text{and } \Delta B_{\text{A}} &= |B_{\text{A}}(r=0) - B_{\text{A}}(r=r_{\text{A}}^{\text{max}})|. \end{aligned} \quad (5.23)$$

In Fig. 5.18 the influence of the radial variations of the fields on the transmission function is illustrated. Depending on the radius at which the electrons with the starting energy E_{start} pass the analyzing plane, they experience a different retardation potential. This leads to the shift of the onset of transmission relative to the nominal value, while the width of the

5. Mainz MAC-E filter...

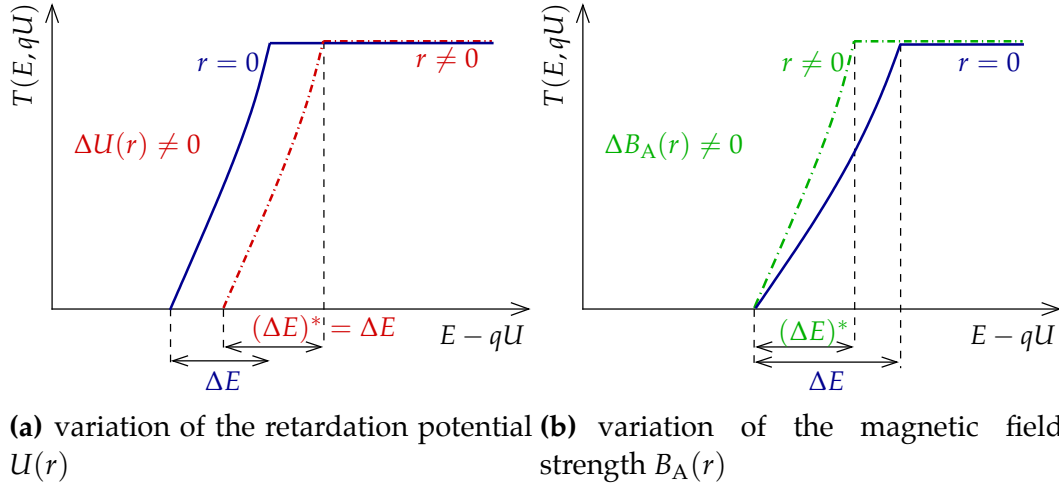


Fig. 5.18: The influence of field inhomogeneities on the shape of the transmission function. In this sketch the cases $\Delta U(r) \neq 0$ (a) and $\Delta B_A(r) \neq 0$ (b) are treated separately in order to disentangle both effects. In practice, however, they will usually be present simultaneously. The figure is taken from [Val09a].

rise is left unchanged: $(\Delta E)^* = \Delta E$ (Fig. 5.18(a)). In contrast, a radial variation of the magnetic field across the analyzing plane will affect the width of the transmission function (Fig. 5.18(b)). As a result, the real transmission function, which integrates over all radii $r \leq r_A^{\max}$, is broadened significantly and the sharp edges of the analytical shape are smeared out [Val09a]. In the case of the K -32 line of $^{83\text{m}}\text{Kr}$ the combination of the aforementioned inhomogeneities causes the smearing of the transmission function by about 4.5% and the shift of the transmission onset of $\delta E_{\text{shift}} = -0.371$ eV for $qU = 17\,824$ eV. [Thu07, Ost08]. The ideal transmission function described by Eq. 2.15 is depicted in Fig. 5.19 together with the “real” one which includes the aforementioned inhomogeneities.

In addition, at high surplus energies $E_{\text{start}} - qU \gtrsim 30$ eV (using the resolution of 0.9 eV at 17.8 keV) the weak magnetic field in the analyzing plane region no longer guides the electrons and the transmission loss occurs [Pic92b]. This effect is clearly visible in the integral spectrum as a strongly dropping signal (towards low energies) on the low energy side of the elastic peak. This effect was systematically studied in [Thu07] where the simulations were compared with the measurements of the $^{83\text{m}}\text{Kr}$ conversion lines of the condensed $^{83\text{m}}\text{Kr}$ source. The simulation results obtained for two different energy resolutions, widely used in this work, are illustrated in Fig. 5.20. A fairly good agreement of the simulations with the experimental results was achieved, however, a non-axial magnetic field had to be introduced in the simulations in [Thu07] in order to match the measured spectra. This can point towards geometrical imperfections of the spectrometer setup. In this work, the simulations of the transmission losses [Thu07] were used for the data description over a wide range of surplus energies, $E_{\text{start}} - qU \lesssim 150$ eV.

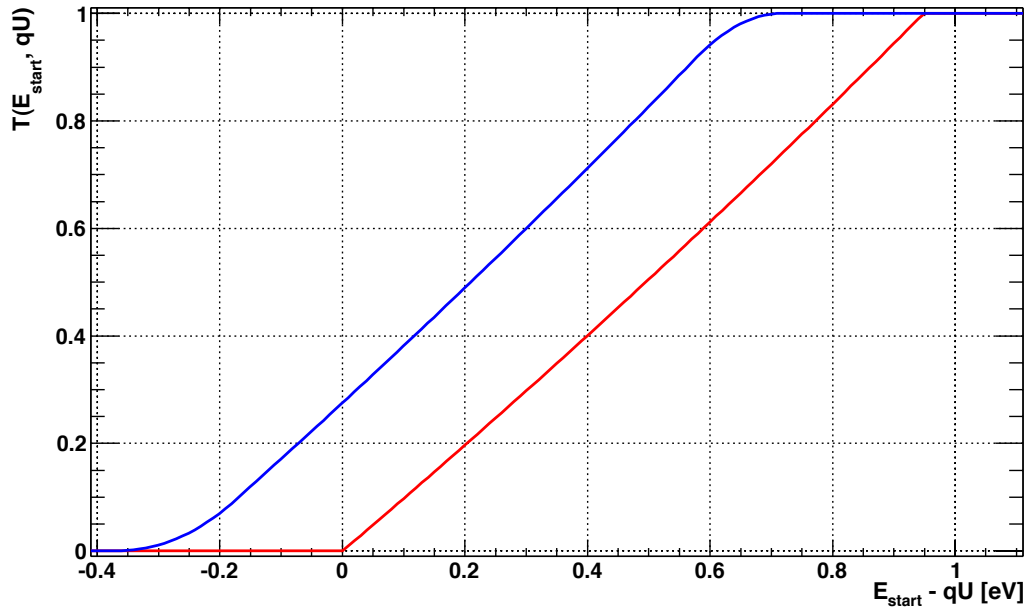


Fig. 5.19: The transmission function of Mainz MAC-E filter calculated for the resolution of 0.9 eV at 17.8 keV. The red line denotes the transmission function without the inhomogeneities of the retardation potential and the magnetic field in the region of analyzing plane. The blue line represents the transmission function where the inhomogeneities are taken into account. The latter one was used in the analysis presented in this work. The figure is based on [Thu07].

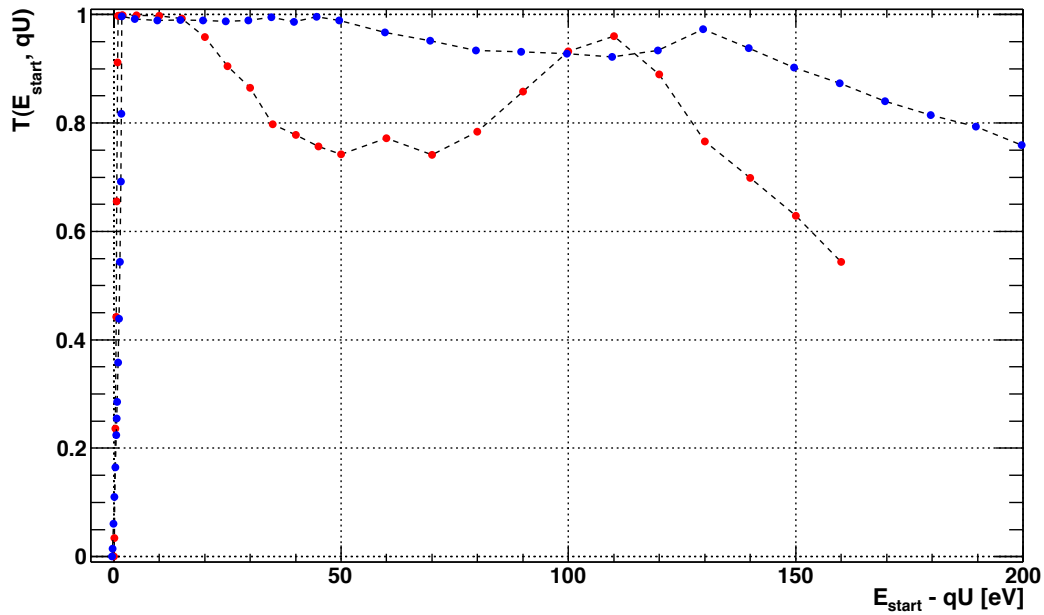


Fig. 5.20: The simulated transmission function for the electrons of high surplus energies. The red points represent the transmission function for the resolution of 0.9 eV at 17.8 keV, while the blue points denote the simulation where the resolution amounted to 2.0 eV at 17.8 keV. A “tradeoff” between the resolution and the transmission can be seen at high surplus energies: in the case of the better resolution (0.9 eV) the transmission breaks down already at $E_{\text{start}} - qU \gtrsim 20$ eV. The figure is based on [Thu07].

5.2.6. Description of the conversion electron line shape

In most cases, the single conversion electron line (as seen in the form of a differential spectrum) is a simple peak-shaped curve characterized by a certain half-width and more or less pronounced low energy tail [Dra83]. The spread around the central energy E_0 , resulting from the natural width Γ of the excited atomic state, can be described by the Lorentzian distribution (see Sect. 1.2)

$$L(E, E_0, \Gamma) = \frac{1}{\pi} \frac{\Gamma/2}{(E - E_0)^2 + (\Gamma/2)^2}, \quad (5.24)$$

where the Γ values range from 0.07 to 70 eV depending on Z and the atomic subshell. The following processes may complicate the shape of the line [Dra83]:

1. The shake-up/off processes give rise to intense satellite structures accompanying the core shell electron lines on the low energy side.
2. The elastic electron peak can be broadened by the Doppler effect. The Gaussian-shaped Doppler broadening is caused by the thermal motion of $^{83\text{m}}\text{Kr}$ atoms due to lattice vibrations in the solid¹¹. For the K -32 electron at room temperature (≈ 300 K) the Doppler broadening was estimated on the basis of kinematic relations [Ger06] as $\Delta E_{\text{Doppler}}(K-32) \simeq 0.26$ eV. The maximal broadening of the $^{83\text{m}}\text{Kr}$ conversion lines occurs in the case of the $N_{2/3}$ -32 line, $\Delta E_{\text{Doppler}}(N_{2/3}-32) \simeq 0.37$ eV.
3. Different chemical environments of the atoms may cause distinct shifts of the electron binding energy. This effect can also influence the electrons of the internal conversion, see Sect. 4.3.1. In the case of a poor energy resolution (several eV) the splitting of the line, resulting from two different environments, may be observed as a broadening of the line.
4. The effect of electron energy losses within the solid source leads to a low energy tail of the elastic peak. With a sufficiently good energy resolution the elastic electron peak can be distinguished from such tail.
5. Furthermore, the line broadening due to the instability of the HV can take place. Obviously, in any electrostatic spectrometer the HV ripple directly influences the sharpness of the transmission function as the electrons are analyzed via the application of the HV on their way to the detector. This effect can play a role in high precision measurements at the ppm scale. Conveniently, the amplitude of the HV instability can be assessed when an electron line of width $\Gamma \simeq 0$ is measured.

To summarize the various effects, the zero-energy-loss electron peak can be distinguished from the satellites and tail structures on the low energy side of the line, provided the energy resolution is sufficiently good. The satellites arise mainly as a result of shake processes (1) and complicated tail structures stem from the inelastic scattering (4). Due to various solid state effects (3) the main line can also be shifted or split. In addition, the whole spectrum is broadened by a combination of effects (2), (3) and (5). The mathematical description of the aforementioned effects shall be briefly discussed. The “basic” Lorentzian shape in Eq. 5.24

¹¹In a gas the Doppler effect is caused by the random motion of atoms or molecules and has to be considered in precision spectroscopy. In the KATRIN experiment it represents one of the systematic effects of the windowless gaseous tritium source. The velocity distribution of the molecules, including the gas flow and the isotopic composition of the gas, has to be taken into account [KAT04].

is smeared by the Gaussian distribution

$$G(E, E_0, \sigma) = \frac{1}{\sigma \sqrt{2\pi}} e^{-\frac{(E-E_0)^2}{2\sigma^2}} \quad (5.25)$$

with the width σ representing the combination of effects (2), (3) and (5). The broadened shape of the elastic electron peak can be conveniently described with a single Voigt function

$$V(E, E_0, \Gamma, \sigma) = \int G(\tau, 0, \sigma) L(E - \tau, E_0, \Gamma) d\tau \Leftrightarrow V = G \otimes L. \quad (5.26)$$

The Voigt function description built in the ROOT environment [ROO10], based on rational approximation algorithm of the complex error function, was used in this work. The width F (FWHM) of the Voigt peak can be approximated [Oli77] as

$$F_{\text{Voigt}} \simeq 0.535 F_{\text{Lorentz}} + \sqrt{0.217 F_{\text{Lorentz}}^2 + F_{\text{Gauss}}^2}, \quad (5.27)$$

where the widths (FWHM) of the Lorentzian and Gaussian profiles are defined as

$$F_{\text{Lorentz}} = \Gamma, \quad F_{\text{Gauss}} = 2\sigma \sqrt{2 \ln 2}. \quad (5.28)$$

Considering the K -32 line of $^{83\text{m}}\text{Kr}$, the typical values are $\Gamma = 2.7$ eV [Ost08] and $\sigma \simeq 1.0$ eV (observed in this work), thus, the FWHM values of the Lorentzian and Gaussian profiles amount to $F_{\text{Lorentz}} = 2.7$ eV and $F_{\text{Gauss}} \simeq 2.4$ eV, respectively. The width (FWHM) of the Voigt profile can be estimated with the help of Eq. 5.27 as $F_{\text{Voigt}} \simeq 4.1$ eV.

The effect of the electron inelastic scattering within the source is described by the loss function $f_{\text{el. loss}}$ which was obtained from the Monte Carlo simulations (see Sect. 4.3.3). The response $R(E_{\text{start}}, qU) \equiv R$ of the complete system to monoenergetic electrons can be written as

$$R = T \otimes f_{\text{trans. loss}}, \quad (5.29)$$

where T is the analytical transmission function (including the inhomogeneities of the electric and the magnetic field, see Fig. 5.19) and $f_{\text{trans. loss}}$ represents the transmission losses discussed in Sect. 5.2.5. Finally, the recorded electron spectrum can be expressed as

$$g(qU) = R(E_{\text{start}}, qU) \otimes f(E_{\text{start}}) + B = \underbrace{T \otimes f_{\text{trans. loss}} \otimes f_{\text{el. loss}}}_{=R'} \otimes f_{\text{shake}} \otimes V + B, \quad (5.30)$$

where $f(E_{\text{start}})$ represents the energy distribution of the electrons emerging from the source and B denotes the recorded background. The term f_{shake} describes the shake-up/off phenomena. As Eq. 5.30 represents a fourfold convolution, it is convenient to save the computing time by calculating the first two convolutions beforehand and taking the resulting function R' as the new response function. Clearly, the function R' is valid only for the given energy resolution of the spectrometer ($\rightarrow T$ and $f_{\text{trans. loss}}$) and for the given type of source, its z position (*i. e.* B_S) and conversion electron line ($\rightarrow f_{\text{el. loss}}$). The new response function R' was calculated with a fine step of 0.1 eV and a linear interpolation of R' was used during the fit procedure.

The function $g(qU)$ was least-squares fitted on the energy- and dead time-corrected spectrum $[E_{\text{corr}}, n'_e]$ with the help of the MINUIT fit routine [Jam75] built in the ROOT environment [ROO10]. Typically, the combination of built-in algorithms SIMPLEX, MIGRAD and

MINOS [Jam75, ROO10] was used for the χ^2 -minimization. The output of the fit routine were the best parameters with their errors and the parameter correlations. The goodness of the fit was verified by checking the structure of the normalized residuals r_i ,

$$r_i = \frac{y_i - g(x_i)}{\sigma_i}, \quad (5.31)$$

with y_i representing the count rate measured in the point x_i of the spectrometer retarding energy, σ_i being the uncertainty of the count rate measurement and $g(x_i)$ denoting the fit function calculated in the point x_i . In addition, the reduced chi squared χ_r^2 and the variance $\sigma^2(\chi_r^2)$ of the χ_r^2 distribution were calculated,

$$\chi^2 = \sum_{i=1}^N r_i^2, \quad \chi_r^2 = \frac{\chi^2}{N_{\text{dof}}}, \quad \sigma^2(\chi_r^2) = \frac{2}{N_{\text{dof}}}, \quad |\chi_r^2 - 1| \stackrel{!}{\leq} k \cdot \sigma(\chi_r^2). \quad (5.32)$$

Here $N_{\text{dof}} = N - N_{\text{par}}$ stands for the number of degrees of freedom and N_{par} denotes the number of free parameters. The last inequality in Eq. 5.32 represents the condition that the χ_r^2 value should be found within k -sigma vicinity of unity. The factor k was usually chosen as $k = 3$. Thus, the fit was considered good only if no structure was found in the residuals and if the condition in Eq. 5.32 was satisfied. All the fit results published in this work obey such conditions of goodness if not stated otherwise.

The following parameters were fitted in Eq. 5.30:

- For one elastic peak altogether four parameters were used: peak centroid E_0 , line amplitude A , Lorentzian width Γ and Gaussian width σ . Usually, Γ was set fixed to the literature value for a given conversion line (see Tab. 3.1), while σ was fitted.
- In the case of fitting a doublet of elastic peaks both widths Γ_1 and Γ_2 were set to literature value, $\Gamma_1 = \Gamma_2 = \Gamma_{\text{lit}}$ and the widths σ_1 and σ_2 were set equal to a common width $\sigma_1 = \sigma_2 = \sigma$ which was fitted. This way it was assumed that the instrumental and physical effects influence both components of the doublet in an identical manner. In order to directly assess the splitting of the doublet of lines, *i. e.* the energy difference $E_{0_1} - E_{0_2}$ of the centroids, the splitting

$$\Delta E_{1-2} := E_{0_1} - E_{0_2} \quad (5.33)$$

was fitted instead of the centroid E_{0_2} . Similarly, instead of the amplitude A_2 the ratio

$$A_{2/1} := \frac{A_2}{A_1} \quad (5.34)$$

of the peak amplitudes was fitted.

- The background B was described with a linear function, however, usually the linear term B_1 was fixed to zero and only the constant term B_0 was fitted.
- In literature the structure of the shake-up/off peaks was described as an exponential tail which reflects the fact that the probability of the process decreases exponentially with excitation energy [Sie69]. In [Pet93] the shake-up/off peaks in the conversion electron spectra recorded with the energy resolution of $\Delta E = 1.8$ eV were described by the function

$$f_{\text{shake}}(E_0, \alpha, \beta, C) = C \operatorname{erfc}[\beta(E - E_0)] e^{\alpha(E - E_0)}, \quad (5.35)$$

where the cutoff on the high energy side was implemented with the complementary error function. The parameters E_0 , α , β and C , representing the centroid, decay constant, scale parameter and amplitude, respectively, were fitted. Since the individual shake-up/off peaks may “merge” into a complicated structure which, in addition, may be unresolved due to insufficient energy resolution (and, moreover, masked by the inelastically scattered electrons), another approach of describing the shake-up/off structure would be to use one or more wide Voigt or even only Lorentzian peaks (large Γ widths). This way the original fit program, easily extended for n Voigt peaks, could be conveniently utilized.

The task of describing the electron line shape can be conveniently split into two complementary parts:

1. For the purpose of the long-term energy stability measurements only the zero-energy-loss peak was fitted on a range which excluded the shake-up/off peaks, the electron losses as well as the transmission losses. In this case the recorded spectrum simplifies to

$$g(qU) = T \otimes V + B. \quad (5.36)$$

2. In order to assess the source-specific details like the shake-up/off phenomena and the energy losses, a wide range of surplus energies $E_{\text{start}} - qU \lesssim 150 \text{ eV}$ has to be considered. Here the full description stated in Eq. 5.30 is necessary.

The function defined in Eq. 5.30 can also be used for simulating the conversion line as it would be measured with the electron spectrometer of the MAC-E filter type: the role of the fit parameters can be reversed, *i. e.* the fit routine can be utilized “the other way around”. After the parameters of the conversion line (amplitude, background, line width and position) are defined together with the spectrometer resolution, a ROOT histogram [ROO10] is filled and then randomized in order to mimic a measured integral spectrum. This approach enabled a better understanding of the structures observed in the residuals in case of a bad fit, *e. g.* if a doublet structure was fitted with a single line.

5.2.7. Cross-correlation method

In Sect. 5.2.6 it became obvious that the precise knowledge of the line shape is crucial for a good fit of the conversion electron line. However, a statement about the long-term stability of the electron line energy can be made even without a detailed knowledge of the line shape. The method of cross-correlation is often used in signal processing for determining the similarity of two signals [Moo00]. Accordingly, two integral conversion electron spectra were compared with each other: one spectrum, usually measured with high statistics and a fine energy step, was considered as a “reference” which was then matched to other spectra. The method was utilized in the following manner:

1. The reference spectrum, in the case of the K -32 line measured with the step of 0.2 eV, was considered on a given range, usually covering only the electron elastic peak.
2. On the defined range the minimal count rate was found and subtracted bin-wise from the spectrum.

3. Similarly, the maximal count rate was found and the spectrum was scaled to 1 on the given range. This way the “template” spectrum with y values between 0 and 1 was created, see Fig. 5.21.
4. The template spectrum was least-squares fitted onto the new spectrum (measured with a usual step of 0.5 eV in the case of the K -32 line), while the amplitude A , the line position shift ΔE and the constant background B_0 were free parameters. Linear interpolation of the template was necessary in order to obtain its y values in the x points (\equiv retarding energy) of the new spectrum.
5. Again, the goodness of the fit was verified with χ_r^2 and the normalized residuals.

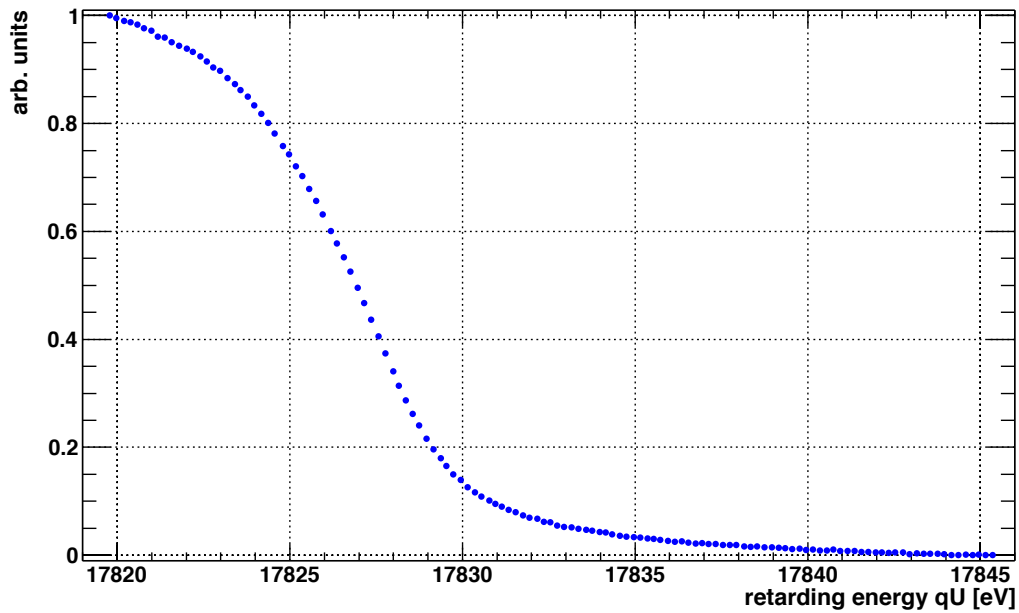


Fig. 5.21: The example of a typical template spectrum of the K -32 line which is used in the cross-correlation method and least-squares fitted on other K -32 spectra of the given source. The integral reference spectrum (example of which is shown in Fig. 5.13) was recorded with the step of 0.2 eV. The constant background B_0 was subtracted and the spectrum was scaled so that the amplitude A is equal to 1 on the range covering the electron elastic peak. The errors bars are not shown.

This way a statement about the electron line shift could be very easily done as the three-parameters fit took a computing time of a fraction of second. Compared to the computing time of up to one hour necessary in some cases for the many-parameters fit described in Sect. 5.2.6, this represented a significant improvement for the analysis of the energy stability measurements. On the other hand, such a method works flawlessly only if the structure of the conversion line does not change with time.

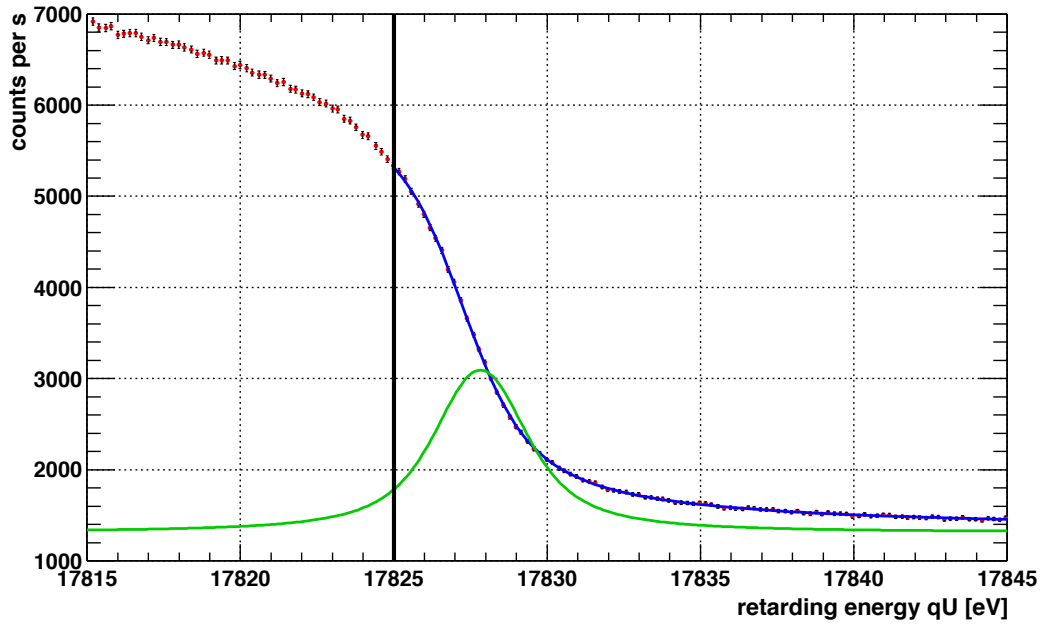
5.2.8. Comparison of cross-correlation and many-parameters fit methods

At this point it shall be verified that both analysis methods, the many-parameters fit (see Sect. 5.2.6) and the cross-correlation method (see Sect. 5.2.7), provide compatible results with respect to the long-term energy stability of the conversion electron line. As an example the data of the K -32 line of the source Au-30, measured with the resolution of 0.9 eV, will be considered. The source provided the count rate of $\approx 4 \times 10^3$ counts s^{-1} in the K -32 line for the typical measurement position in the magnetic field of $B_S = 1.75$ T. Such a high count rate represents a good statistics for the comparison of the methods.

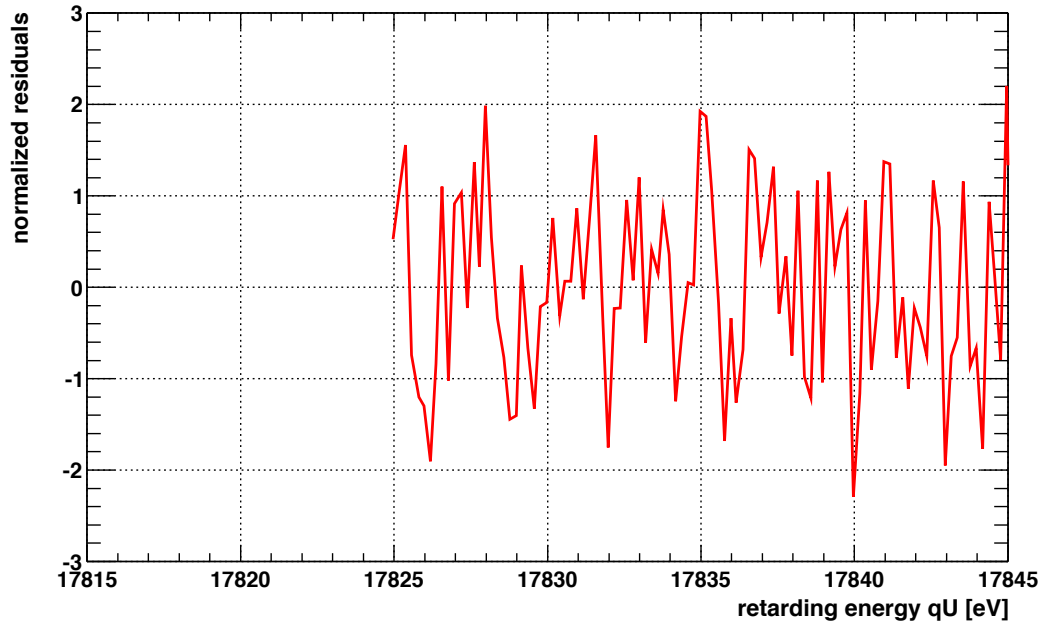
For the fits with the many-parameters description the proper configuration of the magnetic and electric fields together with their inhomogeneities was taken into account. The simplified theoretical description of the line presented in Eq. 5.36 was used, *i. e.* the shake-up/off phenomena and the inelastically scattered electrons were omitted as they play no role in the region of the elastic electron peak. For the sake of simplicity, a single Voigt peak was fitted on the range $[qU_1, qU_2] = [17\,825, 17\,845]$ eV, while σ was a free parameter and Γ was fixed to 2.7 eV [Ost08]. Strictly speaking, the chosen range does not cover the elastic peak completely: while the high energy side of the peak is fully included in the calculation, on the low energy side only about 2.8 eV $\approx 0.68 F_{\text{Voigt}}$ -vicinity of the peak centroid (cf. Eq. 5.27) is considered. The cause of this restriction is the fact that the structure of the line is complicated due to an asymmetry, stemming probably from an additional peak. This phenomenon will be further discussed in Sect. 7.2. Anyhow, for the evaluation of the energy stability such a fit range provides sufficiently precise information about the time drift of the conversion line centroid E_0 . In Fig. 5.22 the fitted function and the normalized residuals of a single fit can be seen. The statistical error of the fitted E_0 amounted to $\simeq 19$ meV. For the determination of the time drift of the electron line energy, carried out with the help of the cross-correlation method, no information about the magnetic and electric fields is necessary. As the template a K -32 spectrum measured with the step of 0.2 V was chosen (shown unscaled in Fig. 5.22(a)). The same fit range $[qU_1, qU_2]$ was used for this method. The normalized residuals of a single fit are shown in Fig. 5.23.

Altogether 178 spectra (sub-sweeps, cf. Sect. 5.2.1), corrected for the dead time, were analyzed with both fit methods. The data were taken in the course of 3 weeks after a bake-out of the complete spectrometer setup when well defined experimental conditions could be assumed. However, the data are considered here only as an example and further HV corrections due to the performance of the devices (HV divider and digital voltmeter) are not discussed at this point. In Fig. 5.24 the results of both methods are compared. The direct output of the cross-correlation method is the shift ΔE_0 of the line position with respect to the reference line position. The shift of the reference spectrum itself ("zero shift") was fitted as 0(9) meV. For the comparison of the methods, the results of the many-parameters fits were related to the same reference spectrum, *i. e.* the differences $E_0 - E_{0, \text{ref}}$ were calculated with a proper error propagation. Both sets of results were least-squares fitted with a linear function yielding the drifts presented in Tab. 5.2.

The absolute term of the linear function describing the results of the many-parameters fit method is shifted towards negative values, however, this has no significance when consid-



(a)



(b)

Fig. 5.22: The example of a typical many-parameters fit of the K -32 line. **(a)** The recorded spectrum corrected for the dead time is shown in red. The error bars of the count rate are multiplied by the factor of 2 for the sake of example. The blue line denotes the least-squares fit of the convolution of the spectrometer transmission function with a single Voigt peak. The fit range $[qU_1, qU_2] = [17825, 17845]$ eV was used, the vertical line at 17825 eV marks its lower limit. The Lorentzian width was kept fixed to $\Gamma = 2.7$ eV, whereas the Gaussian width σ was a free parameter. In this case the fit delivered $\sigma = 0.77(2)$ eV. The centroid was fitted as $E_0 = 17827.827(12)$ eV. **(b)** The normalized residuals (the aforementioned factor of 2 in the error bars taken out) of the fit shown in **(a)** exhibit no significant structure. The number of degrees of freedom was $N_{\text{dof}} = 98$ and the reduced chi squared $\chi_r^2 = 1.10(14)$ (cf. Eq. 5.32). Therefore, the fit can be considered as a good fit.

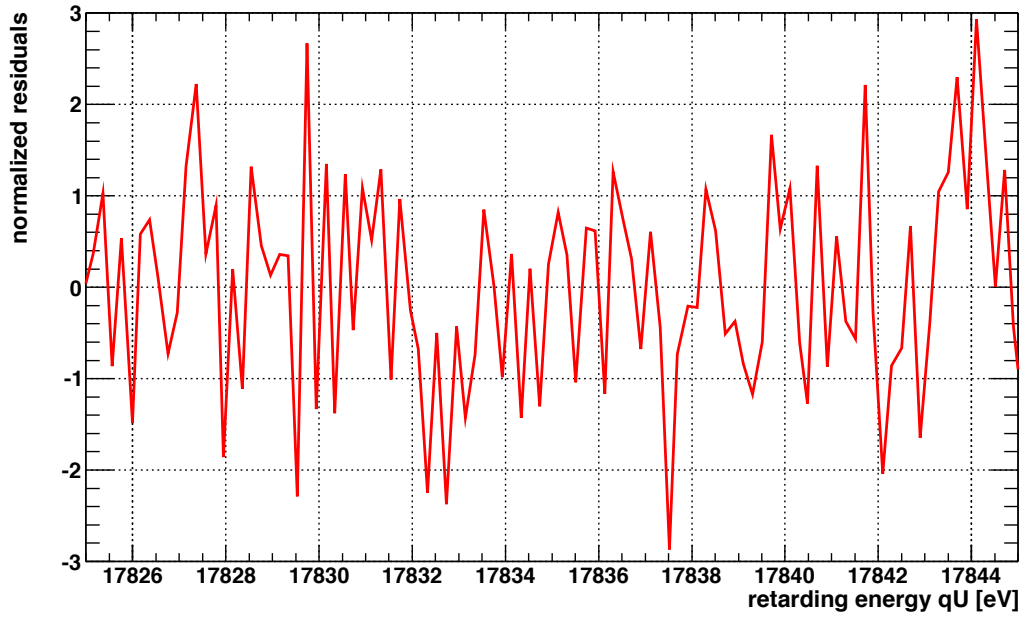


Fig. 5.23: The example of normalized residuals of the least-squares fit performed with the help of the cross-correlation method on the same data as in Fig. 5.22.

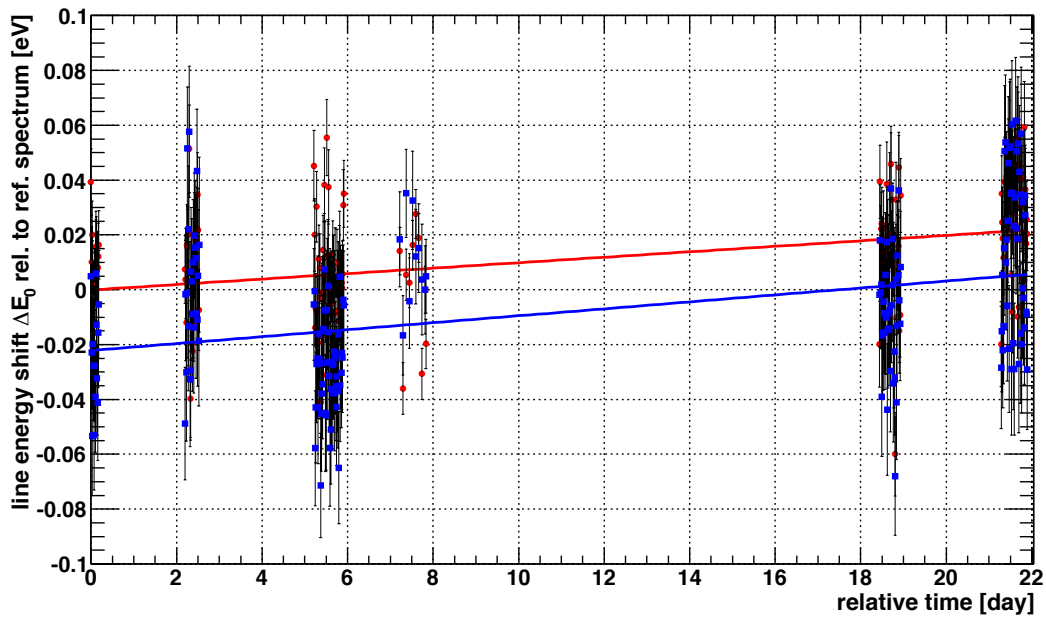


Fig. 5.24: The comparison of the K -32 line position shifts of the source Au-30 analyzed with two fit methods. The red circles mark the results of the cross-correlation method, the blue squares denote the results of the many-parameters fit method. The spectrum scanned at day $\simeq 7.8$ with the step of 0.2 eV was chosen as the reference. The error bars represent the statistical uncertainties of the fits. The red and blue lines denote the linear functions least-squares fitted to the data sets. See Tab. 5.2 for the results of these fits.

Tab. 5.2: The comparison of the results obtained with the many-parameters fit and the cross-correlation method.

fit method	χ_r^2 of fit	linear fit parameters		relative drift*
		absolute [10^{-3} eV]	linear [meV month $^{-1}$]	
cross-correlation	2.05(11)	-0.1(24)	30(6)	1.68(31)
many-param. fit	1.49(11)	-22.2(33)	38(7)	2.13(42)

The data sets obtained with both methods were least-squares fitted with a linear function. Due to slightly increased χ_r^2 values the uncertainties of the fitted parameters were multiplied by $\sqrt{\chi_r^2}$. Remark: * for the calculation of the relative drifts in units of ppm month $^{-1}$ the nominal value of the K-32 line energy of 17 824 eV was used.

ering the long-term energy stability of the electron line. More importantly, both fit methods provide a positive relative drift of the K-32 line position of ≈ 2 ppm month $^{-1}$ with the uncertainty in the sub-ppm range. The relative drifts agree with each other within 1σ , but still, there is a clear difference of $\simeq 4 \times 10^{-7}$ month $^{-1}$ between the values. As the identical data sets were analyzed with both methods, one would expect practically identical results, thus, this discrepancy has to be ascribed to a systematic effect of the fits. Nevertheless, such an effect is still acceptable for the precision of this work. In addition, it should be emphasized that the cross-correlation method was found to be by the factor of $\approx 5 \times 10^3$ faster regarding the computing time. To summarize, keeping in mind the small discrepancy of 0.4 ppm month $^{-1}$, the cross-correlation method significantly reduces the computing time and can be conveniently used for the purpose of determining the energy stability of the ^{83m}Kr conversion lines.

6. Long-term measurements of the conversion electrons energy stability at Mainz MAC-E filter

This chapter describes the course of the long-term energy stability measurements carried out at the MAC-E filter spectrometer setup which was described in previous Chap. 5. By the notion “long-term energy stability” it is meant that the relative stability of the energy of the $^{83\text{m}}\text{Kr}$ conversion electron lines was systematically studied over the time period of the order of months. The motivation for the long-term monitoring of the energy scale in the KATRIN experiment with the precision in the ppm range was discussed in Chap. 3. It should be noted that the requirement of the HV scale stability, expressed in Eq. 3.9, symbolizes the upper limit on the unrecognized fluctuations of the HV scale which are represented by a Gaussian broadening of the width σ . However, in the framework of the measurements presented here the aim was to control (and minimize) the linear drift of the conversion electron lines. This way the HV scale fluctuations, possibly appearing during the KATRIN experimental run, may be recognized on the time scale of tens of minutes¹ to months. On the other hand, the HV scale fluctuations of the order of seconds cannot be recognized with this method. These short-term fluctuations can be assessed with the help of sophisticated HV ripple probes [Thu11].

In contrast to [Ost08], where the long-term energy stability of the condensed $^{83\text{m}}\text{Kr}$ source was studied, in this work the solid $^{83}\text{Rb}/^{83\text{m}}\text{Kr}$ sources (see Chap. 4) were systematically investigated. In these test measurements the focus was made on the stability of the energy of various $^{83\text{m}}\text{Kr}$ conversion electron lines (summarized in Tab. 3.1), however, additional systematic measurements will be discussed here as well. Thanks to them the overall sensitivity and systematic uncertainties of the method can be assessed. A rather chronological approach was chosen for the description of the results so that the progress and logical sequentiality can be easily seen.

In Sect. 6.1 the pilot measurements accomplished with the vacuum-evaporated sources are briefly discussed. A number of imperfections was acknowledged in this phase and later improved. The next Sect. 6.2 reports on the first phase of the systematic tests, this phase being undertaken with a strong vacuum-evaporated source. Further, in the second phase (Sect. 6.3) altogether three solid sources were examined practically simultaneously: two vac-

¹The lower limit of applicability of the calibration source depends on the statistics of the recorded signal. Optimizing the distribution of the measurement time can lower the time which is necessary for recognizing the shift of the HV scale.

uum-evaporated sources and one ion-implanted source. The last phase of the measurements at Mainz setup, during which four ion-implanted sources were tested simultaneously, is presented in Sect. 6.4. Finally, the results are compiled and discussed in Sect. 6.5.

Throughout this chapter the notions similar to "... the conversion electron line *K*-32 was scanned ..." will be used frequently. The experimental setup was described above in Sect. 5.1 and a typical measurement of the conversion electron line carried out with Mainz MAC-E filter was explained in Sect. 5.2.

The uncertainties stated in this chapter represent the statistical uncertainties, resulting from the least-squares fits. The systematic uncertainties are discussed in Sect. 6.5.

6.1. Pilot studies of energy stability of the $^{83}\text{Rb}/^{83\text{m}}\text{Kr}$ sources

6.1.1. Proof of principle

The very first test measurements of the solid $^{83}\text{Rb}/^{83\text{m}}\text{Kr}$ source at Mainz MAC-E filter were carried out in June 2005 [Kas08]. Besides the $^{83}\text{Rb}/^{83\text{m}}\text{Kr}$ source the photoelectron source $^{241}\text{Am}/\text{Co}$ (see Sect. 3.3.1) was also investigated during the measurement campaign. The aim of the $^{83}\text{Rb}/^{83\text{m}}\text{Kr}$ measurements was to provide the evidence of zero-energy-loss electrons coming out of the solid type of source. The sample (designated S4) was vacuum-evaporated on aluminum backing, the ^{83}Rb activity of the source was measured by gamma spectroscopy to be 30 kBq. The conversion electron lines L_1 -9.4, *K*-32 and L_3 -32 were scanned with the resolution of 1.5 eV at 17.8 keV. The amplitude of the *K*-32 line was found to be ~ 20 counts s^{-1} . The energy stability of the conversion lines was not investigated, however, the results proved the solid type of $^{83\text{m}}\text{Kr}$ source to be a promising tool for the energy scale monitoring.

6.1.2. Measurements with vacuum-evaporated sources mounted onto CKrS setup

Besides the encouraging results from June 2005, the idea of the long-term energy stability measurements was supported by the measurements of the L_1 -9.4 line at the electrostatic spectrometer ESA-12 in the Nuclear Physics Institute Řež/Prague. These measurements showed the stability of the L_1 -9.4 line energy of several tens of meV over time periods of $\simeq 2$ months [Ven09, Ven10].

During the time period April–June 2007 two vacuum-evaporated sources designated S11 and S13 were investigated at Mainz spectrometer. Both samples were prepared on Al foil, for other properties of the sources see Sect. 4.1.2. As this measurement phase was complementary to the tests of the CKrS concept (see Sect. 3.3.2), the solid $^{83}\text{Rb}/^{83\text{m}}\text{Kr}$ source was mounted onto the cold end-cup of the CKrS setup. This allowed to investigate the samples in the temperature range of 70–298 K. The HV divider K35 was used as the HV reference for

the tests. An overview of the measurements can be seen in Tab. 6.1.

Tab. 6.1: The overview of the pilot measurements carried out in 2007.

calendar week no.	18	19	20	21	22	23
week of	30.04.	07.05.	14.05.	21.05.	28.05.	04.06.
time since 30.04.2007 [day]	0	7	14	21	28	35
source tested	S 13			S 11		
HV conditions HV divider used	K35					
vacuum conditions CKrS cooled		x	x	x		x
electron line scanned						
L_1 -9.4						
K-32	x	x	x	x	x	x
L_3 -32					x	x
$N_{2/3}$ -32						x

Two vacuum-evaporated sources S 11 and S 13 were investigated during this measurement phase. The given $^{83}\text{Rb}/^{83\text{m}}\text{Kr}$ source was mounted onto the CKrS end-cup. The box **x** denotes that an event or measurement described in the first column occurred in the given week. Each of the columns 2–7 represents one week of measurement.

The measurements were carried out at two main source positions relative to the solenoid B center: 19 cm ($B_S = 2.63$ T, $\theta_{\text{start}}^{\text{max}} = 41^\circ$, cf. Eq. 2.14) and 25 cm ($B_S = 0.77$ T, $\theta_{\text{start}}^{\text{max}} = 21^\circ$). In the case of $B_S = 2.63$ T the measured K-32 line rate of the source S 13 amounted to $\simeq 20$ counts s^{-1} . With the help of Eq. 5.18 the count rate expected in this situation was estimated² as $\simeq 47$ counts s^{-1} which overestimates the measured value by the factor of $\simeq 2.4$. The discrepancy may be caused by the uncertainties of the individual terms in Eq. 5.18.

To achieve the statistical error of 20 meV of the fitted K-32 line position, representing the precision of $\simeq 1$ ppm, a measurement time of ~ 10 hours per one sweep was necessary due to the low statistics. In order to increase the observed count rate, the CKrS end-cup was cooled to about 70 K. This caused the K-32 amplitude to rise up to $\simeq 300$ counts s^{-1} . Assuming that this measured rate corresponds to 100 % retention of $^{83\text{m}}\text{Kr}$ within the source, the rate of $\simeq 20$ counts s^{-1} measured with the source S 13 at room temperature corresponds to $R_{\text{Kr}} = 6.7\%$, in a good agreement with the value of 7 % obtained from measurements in the Nuclear Physics Institute Řež/Prague, cf. Tab. 4.1. Thus, it seems plausible that indeed all the $^{83\text{m}}\text{Kr}$ atoms are trapped on the Al backing cooled to $\simeq 70$ K. The effect of the sample cooling on the K-32 line amplitude is shown in Fig. 6.1.

During the measurements it became obvious that sources of ^{83}Rb activity higher by the factor ~ 30 are necessary for obtaining high statistics in the conversion lines. The increase of

²Here the following factors were used: $A = 0.23$ MBq, $d = 1$, $R_{\text{Kr}} = 0.07$, $P_{\text{K-32}} = 0.1707$, $P_{\text{no-shake}} = 0.795$, $\eta_{\text{spec}} = 0.03$, $\epsilon_{\text{no-loss}} = 0.896$ and $\eta_{\text{det}} = 0.8$. The spectrometer efficiency η_{spec} is reduced due to the fact that only about 24 % of the source area was imaged onto the detector, cf. Eq. 5.20.

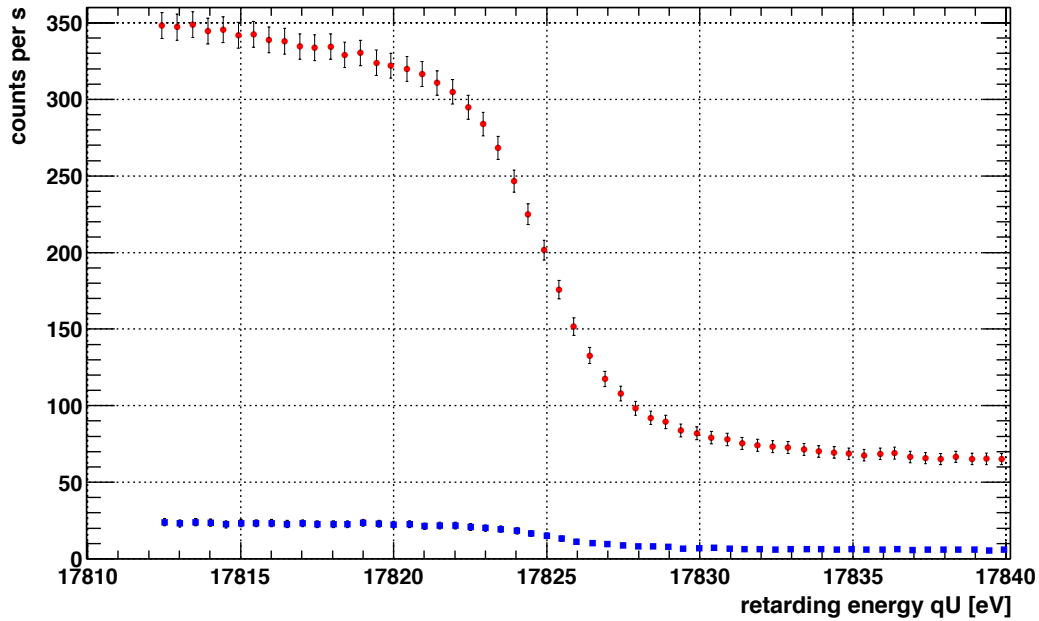


Fig. 6.1: The effect of cooling the vacuum-evaporated source S 13 on the K-32 line amplitude. The spectrum shown in blue was recorded at room temperature, whereas the spectrum marked red was measured at the temperature of $\simeq 70$ K. For the sake of example the error bars in both spectra were multiplied by the factor of 5. The increase of the line amplitude and the background is clearly visible: the blue spectrum corresponds to the $^{83\text{m}}\text{Kr}$ retention factor of $\simeq 7\%$ while in the case of the red spectrum this factor was equal to $\simeq 100\%$. Both spectra were obtained at the energy resolution of 2.0 eV at 17.8 keV.

the $^{83\text{m}}\text{Kr}$ retention factor would be also positive. A noticeable difference to the measurements carried out in June 2005 was the absence of the solenoid “C” increasing the electron flux hitting the detector [Thu07]. Unfortunately, this fact was omitted during the planing of this measurement phase and it was anticipated that even with the sources of low ^{83}Rb activity a sufficiently high count rate would be obtained. It was also concluded that for the next measurement phases the detector should be moved inside the bore of the solenoid A in order to increase the efficiency of the spectrometer when operated without the solenoid C.

Anyway, despite the limited statistics certain statements about the energy stability of the sources could be deduced. In Fig. 6.2 the results of the least-squares fits of the K-32 line performed with the cross-correlation method are depicted. A spectrum obtained with the cooled source S 13 at resolution of 0.9 eV was chosen as the reference as this represented the highest available statistics³. Firstly, the K-32 line of the source S 13 was investigated at room temperature with the spectrometer resolution of 2.0 eV. A relatively large spread of $\simeq 0.17$ eV (RMS) of the line positions was observed. Further, the CKrS setup was cooled down to about 70 K and the K-32 line was scanned with both resolutions of 0.9 eV and 2.0 eV, respectively. Interestingly, the difference of $\simeq 0.4$ eV of the line positions between the two resolution data sets was clearly visible, pointing to possible misalignment of the experimen-

³In somewhat unrigorous manner all the K-32 line data (two different spectrometer resolutions and two different sources) were analyzed with the help of the cross-correlation method using a common reference spectrum. This approach can be justified by the overall poor statistics of the data, especially with the sources investigated at room temperature, cf. Fig. 6.1.

tal setup. After about 12 days the setup was warmed up to room temperature and the K -32 line was scanned again. The source S 11 was tested in a similar way, however, due to the lack of time there was no K -32 line scan at room temperature at the end of the measurement series, unfortunately. The difference between the K -32 line positions measured at room temperature with the source S 13 (days 3–7) and the source S 11 (days 25–28) amounted to 0.46(3) eV. This difference can stem from poor source-to-source reproducibility, however, it must be noted that while the source S 13 was placed in the magnetic field of 2.63 T, the source S 11 was placed in the weaker field of 0.77 T. Thus, a clear conclusion about the source-to-source reproducibility cannot be drawn if there are additional uncertainties caused by the different field values. Altogether five data sets were individually least-squares fitted with a linear function:

1. source S 13 measured at room temperature with the resolution of 2.0 eV,
2. cooled source S 13 measured with the resolution of 0.9 eV,
3. cooled source S 13 measured with the resolution of 2.0 eV,
4. source S 11 measured at room temperature with the resolution of 2.0 eV,
5. cooled source S 11 measured with the 0.9 eV resolution.

The results are summarized in Tab. 6.2.

Tab. 6.2: The drifts of the K -32 line measured with two vacuum-evaporated sources.

source	data set	χ_r^2 of fit	linear fit parameters		relative drift $d_{\text{source}}^{\text{rel}}$ [ppm month ⁻¹]
			absolute [10 ⁻¹ eV]	linear [meV month ⁻¹]	
S 13	room temp.	0.95(27)	-1.5(3)	-101(64)	-5.7(36)
	cooled, res. 0.9 eV	0.82(24)	0.7(2)	-104(40)	-5.8(23)
	cooled, res. 2.0 eV	1.18(22)	-3.1(2)	-214(47)	-12.0(27)
S 11	room temp. *	0.95(27)	6.6(62)	-428(701)	-24.0(393)
	cooled, res. 0.9 eV	1.34(26)	2.9(6)	-464(53)	-26.0(30)

The data depicted in Fig. 6.2 were least-squares fitted with a linear function, the χ_r^2 of the fits is shown in the column (3). The absolute and linear terms of the fitted function are stated in the columns (4) and (5), respectively. The latter one is already corrected for the drifts of the digital voltmeter and the HV divider and thus it is equal to the absolute drift [meV month⁻¹] of the source itself. In the column (6) the relative drift $d_{\text{source}}^{\text{rel}}$ [ppm month⁻¹] of the source is stated. For the calculation of $d_{\text{source}}^{\text{rel}}$ in units of ppm month⁻¹ the nominal value of the K -32 line energy of 17 824 eV was used. Remark: * the large uncertainties of the fit results are caused by the insufficient time span of these measurements.

The source S 13 exhibited a negative long-term drift of the K -32 line of about -6 ppm month⁻¹ at room temperature and also when cooled and measured with the resolution of 0.9 eV. The data set obtained with the resolution of 2.0 eV exhibits a negative drift by the factor of $\simeq 2$ bigger. This can point to some imperfections of the measurement procedure as ideally it should not matter what spectrometer resolution is used. The K -32 line drift of the cooled source S 11 amounted to about -26 ppm month⁻¹. It was not possible to draw a conclusion about the energy stability of the source S 11 kept at room temperature as the parameters of

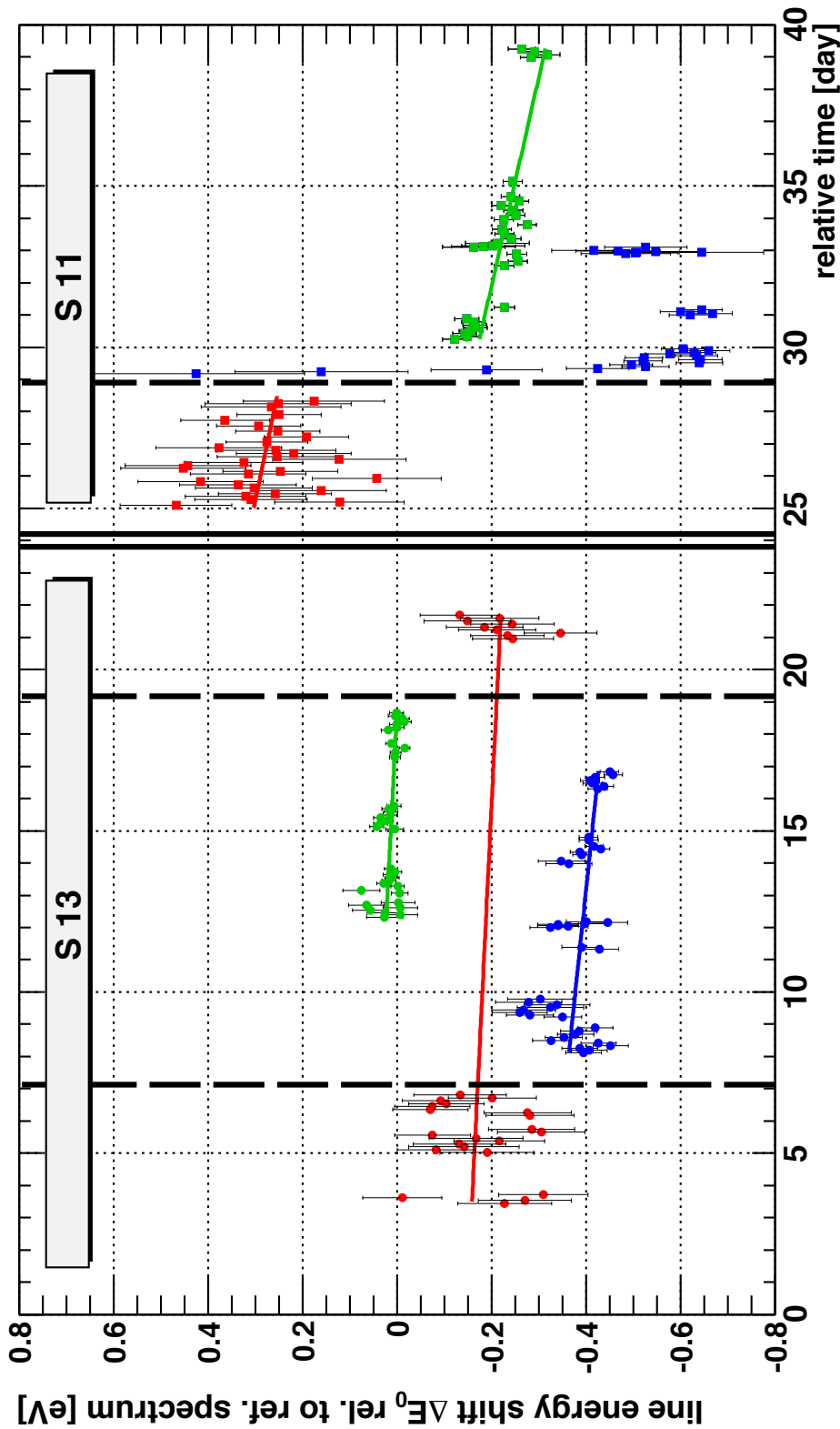


Fig. 6.2: The energy stability measurements of the K-32 line of the vacuum-evaporated sources S11 and S13. The least-squares fits of the individual integral spectra were done with the cross-correlation method. The spectrum obtained with the cooled source S13 measured with the energy resolution of 0.9 eV on day 18 was chosen as the reference. The x axis denotes the relative time in days since 30.04.2007. The y axis shows the K-32 line energy shift ΔE_0 relative to the reference spectrum. The full span of the y axis of 1.6 eV represents the portion of $\simeq 90$ ppm considering the K-32 line energy of 17824 eV. In the time ≤ 3 days introductory tests were performed, therefore no data from this period are considered. The dashed lines represent the moments when the source cooling was switched on or off. The data marked red were measured at room temperature with the resolution of 2.0 eV. The green and blue points show the data taken with the cooled sources at the energy resolution of 0.9 eV and 2.0 eV, respectively. In the time period ≤ 24 days the source S13 was investigated, the double full line on day 24 stands for the exchange of the sources. Later, the source S11 was tested. The colored lines denote the least-squares fits of the individual data sets with a linear function. See Tab. 6.2 for the results of these fits.

the linear function least-squares fitted to this data set suffer from large uncertainties. The reason for this is the insufficient time span of these measurements (in this case about 3 days). The drifts obtained from the fits with a linear function have to be corrected for the drift m_{div} of the dividing ratio $M(t)$ of the HV divider (see Eq. 3.12) and for the drift k_{dvm} of the scale factor $K(t)$ of the digital voltmeter (see Eq. 5.8). Actually, in this particular case these corrections are by one order of magnitude smaller than the observed drifts, however, in the next measurement phases reported below the drifts will be considerably smaller and these corrections will play a role in the analysis. The linear fit of the given data set (obtained with the help of the cross-correlation method) delivers the value d_{total} of the “total” drift which is a combination of the drifts m_{div} , k_{dvm} and the intrinsic drift of the electron line itself, d_{source} . Clearly, the aim is to extract the value of d_{source} from the experimental data. In the course of this chapter the notions of the absolute drift $d_{\text{source}}^{\text{abs}}$ [meV month⁻¹] as well as the relative drift $d_{\text{source}}^{\text{rel}}$ [ppm month⁻¹] will be used. For the conversion between $d_{\text{source}}^{\text{abs}}$ and $d_{\text{source}}^{\text{rel}}$ the nominal value of the energy of the given electron line is used. Analogical notions will be used regarding the total drift d_{total} .

From the considerations based on Eq. 5.8 it can be found⁴ that it holds

$$d_{\text{source}} = d_{\text{total}} + m_{\text{div}} + k_{\text{dvm}} + C. \quad (6.1)$$

The term C stands for the drift of the work function ϕ_{spec} of the spectrometer electrode. As the pilot ⁸³Rb/^{83m}Kr measurements took place in time period when the CKrS was tested and the vacuum conditions were stable for about 2 years without any vacuum breakdown, it can be safely assumed that ϕ_{spec} was stabilized, *i. e.* $C = 0$. The drift of the HV divider K35 was determined as 0.604 ppm month⁻¹ in [Thu07, Thu09] and in this work the uncertainty of 0.1 ppm month⁻¹ was assumed for this value. Such an uncertainty seems reasonable with respect to the uncertainty of the drift of the second divider K65, $-0.13(10)$ ppm month⁻¹ [Bau09, Bau11], cf. Tab. 5.1. Thus, for the K35 divider it was assumed

$$m_{\text{div}}^{\text{PTB}} = 0.60(10) \text{ ppm month}^{-1}, \quad (6.2)$$

where the designation “PTB” denotes the value is based on the calibration procedures carried out in the PTB Braunschweig. Regular calibrations of the digital voltmeter showed that the scale factor K of the 20 V DC range also drifts in time, see Fig. 6.3. The drift of K was determined as

$$k_{\text{dvm}} = -0.59(7) \text{ ppm month}^{-1}. \quad (6.3)$$

In this case the drifts $m_{\text{div}}^{\text{PTB}} \equiv m_{\text{div}}$ and k_{dvm} practically cancel out and thus, $d_{\text{source}} = d_{\text{total}}$. The values d_{source} are stated in Tab. 6.2 as relative drifts $d_{\text{source}}^{\text{rel}}$ in the units of ppm month⁻¹. The negative drifts of the K -32 line position obtained with the cooled sources can be attributed to rest gas adsorption on the cold surface of the sources. The samples were mounted on the CKrS end-cup without any cold shield protection, thus, rest gas adsorption was inevitable. It is a well known fact [Jae63, Hub66, Kaw86, Ish91] that the work function of the metal surface is altered by up to an order of eV due to the adsorption of rest gas molecules. As the spectrometer conditions remained stable during the whole pilot measurement the

⁴In the derivation of Eq. 6.1 from Eq. 5.8 the time dependency of the zero offset $U_{\text{offset}}(t)$ of the digital voltmeter was not considered as it was found that U_{offset} remains stable in the μV range. In addition, the terms of the higher orders, *e. g.* $m_{\text{div}} \cdot k_{\text{dvm}}$, were neglected.

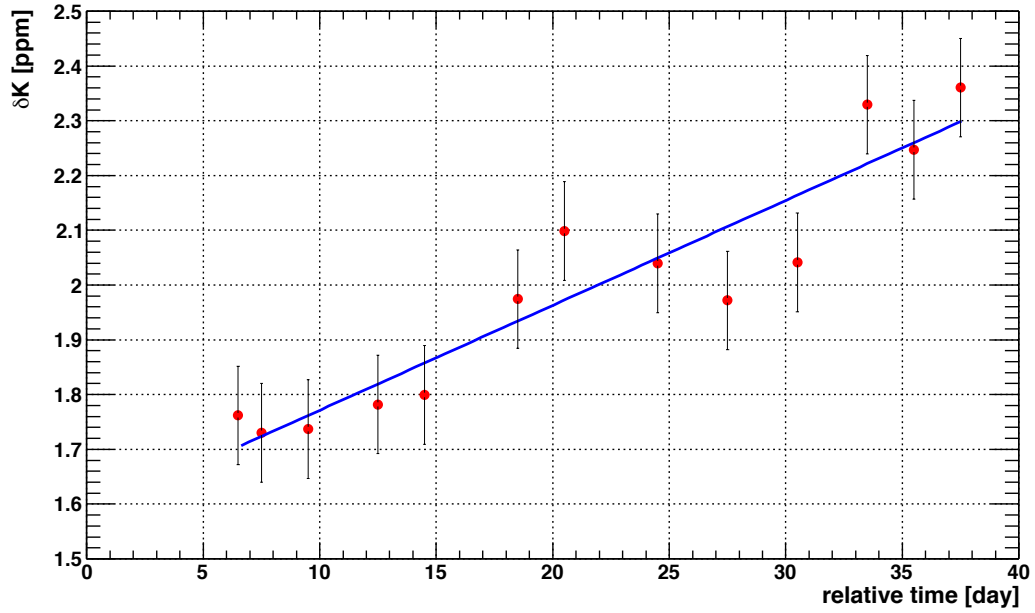


Fig. 6.3: The drift of the scale factor of the digital voltmeter during the pilot measurements. The x axis denotes the relative time in days since 30.04.2007. The y axis shows the deviation of K from unity, $\delta K = 1 - K$, in the units of ppm (relative to one). The positive trend of δK indicates that the deviation of K from 1 is increasing in time. The least-squares fit with $\chi_r^2 = 0.84(43)$ results in the drift $k_{\text{dvm}} = -0.59(7) \text{ ppm month}^{-1}$.

observed K -32 line drifts can be fully ascribed to rest gas adsorption on the source surface and to the vacuum-evaporated sources themselves.

The effect of lowering the electron kinetic energy is clearly seen in Fig. 6.2 where on day 29 the cooling of the source S 11 was started. A sudden drop of $\simeq 0.9 \text{ eV}$ of the K -32 line position was observed during the source cool-down. Similarly, a drop of $\simeq 0.2 \text{ eV}$ was observed in the case of the source S 13. Interestingly enough, the drift of the source S 13 was found to be independent of the source temperature, *i. e.* practically identical drifts were determined for the cooled source as well as for the source kept at room temperature. However, it can be argued that after the source setup was warmed up to room temperature (separated from the spectrometer vacuum vessel by the gate valve), no bake-out of the source setup was performed and thus, the adsorbed rest gas was still covering the source substrate and desorbing only very slowly at room temperature. This way the line positions measured at day = 21 were also possibly affected. It was realized that cooling of the sources has a positive effect on the retention of the $^{83\text{m}}\text{Kr}$ atoms in the vacuum-evaporated sources, but on the other hand, the surface conditions of the source were further kept rather undefined due to rest gas adsorption (see the discussion in Sect. 4.3.1).

Besides the core electron line K -32, the valence electrons of the N shell were also briefly investigated with the cooled source S 11. According to Tab. 3.1 the closely spaced doublet of the lines N_2 -32 and N_3 -32 can be seen at $qU \simeq 32\,137 \text{ eV}$. The splitting of the lines is only about 0.6 eV , therefore, with the spectrometer resolution of 3.6 eV at 32.1 keV the individual lines were not resolved and the unresolved doublet is denoted as $N_{2/3}$ -32. In Fig. 6.4 the recorded spectrum is shown which was successfully least-squares fitted with a single Gaussian peak. The general description with the Voigt function (see Sect. 5.2.6) was simplified

thanks to the negligible natural widths of the $N_{2/3}$ -32 and $N_{3/3}$ -32 lines, thus, $\Gamma = 0$ was fixed in the fit. The width of the peak was determined as $\sigma = 1.45(5)$ eV, including the part of the 0.6 eV separation of the doublet.

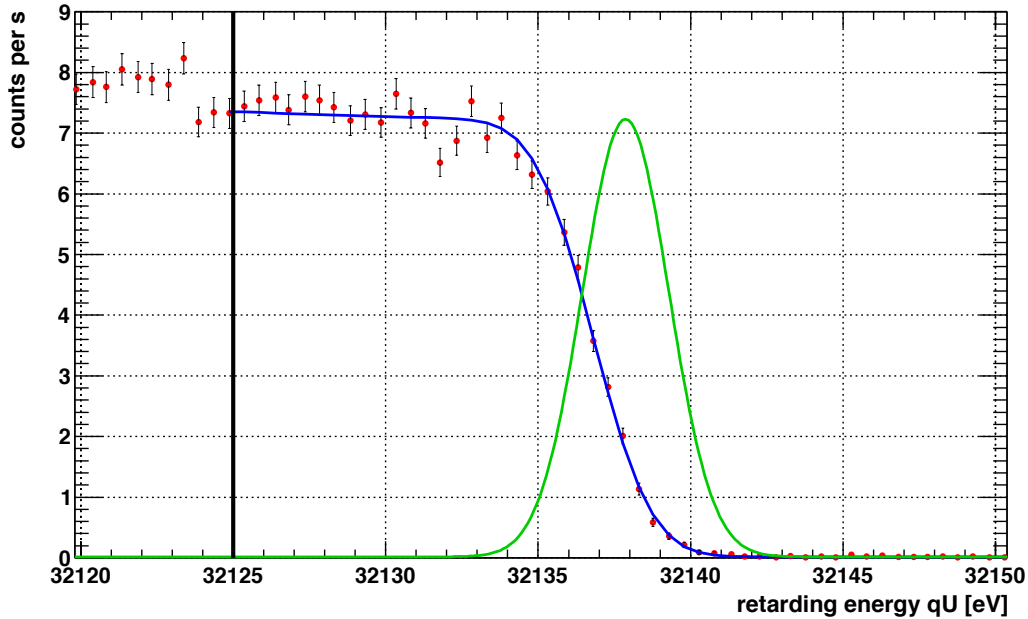


Fig. 6.4: The integral spectrum (shown in red) of the $N_{2/3}$ -32 line of the vacuum-evaporated source S 11 cooled to $\simeq 70$ K. The spectrometer resolution was set to 3.6 eV at 32.1 keV. The blue line denotes the least-squares fit of the convolution of the spectrometer transmission function with the single Gaussian peak. The vertical line at 32 125 V marks the lower limit of the fit range. The green line represents the Gaussian peak of the width $\sigma = 1.45(5)$ eV resulting from the fit. As the $N_{2/3}$ -32 line is the most energetic conversion electron line in the 32 keV gamma transition of the ^{83m}Kr decay the high energy background vanishes.

6.2. First measurement phase: single vacuum-evaporated source

The pilot measurements showed that the spectrometer setup is well suited for investigations of the subtle effects of the long-term energy stability of the conversion electron lines from solid $^{83}\text{Rb}/^{83m}\text{Kr}$ sources in the range of ppm per month. It became obvious that the next systematic tests should proceed with strong sources kept at room temperature in order to avoid any rest gas condensation. After the pilot measurements were finished in the Institute of Physics, University of Mainz, further tests of the production technique based on vacuum evaporation were realized in the Nuclear Physics Institute Řež/Prague. Various sample substrates and settings of the vacuum evaporation setup were tested [Ven09]. Finally, two sources S 28 and S 29 were prepared for the measurements at Mainz MAC-E filter. The properties of the sources were described above in Sect. 4.1.2.

Both samples were prepared on carbon foil (thickness of 0.2 mm) fixed in a holder produced from gold plated copper to ensure good electrical contact. As the prototype of the source holder (improved version of the holder can be seen in Fig. 5.5) allowed to investigate only one sample, firstly the source S 28 was chosen to be investigated, since it was expected that

its higher $^{83\text{m}}\text{Kr}$ retention factor will cause a higher count rate. The overview of the first measurement phase is given in Tab. 6.3. During the preparation phase the HV divider K35 was calibrated with the help of two precision digital voltmeters. This event later turned out to be important for the systematic checks in the long-term energy stability measurements. In addition, the bake-out of the complete setup was carried out about 3 months prior to the start of the measurements.

6.2.1. Systematic measurements of the long-term drifts

The source section was not baked out after the insertion of the source in vacuum in order to avoid any possible release of the ^{83}Rb atoms adsorbed on the graphite substrate. The source was placed in the magnetic field of $B_S = 0.33\text{ T}$, thus, $\theta_{\text{start}}^{\text{max}} = 14^\circ$. An optimal x - y position of the source was found from maximizing the observed amplitude of the K -32 line. Mainly the conversion lines L_1 -9.4, K -32 and L_3 -32 were periodically scanned. The results of the first month of measurement are shown in Fig. 6.5. Due to the scatter of $\approx 1.5\text{ eV}$ of the fitted line positions the electron line L_1 -9.4 was omitted in the plot. Such high scatter can be ascribed to the noise of the detector electronic chain as this low energy line was susceptible to it: in Fig. 5.10 it is clearly seen that the signal of L_1 -9.4 electrons is partially cut off by the low level discriminator of the ADC. The noise edge was found to be unstable in time and it was adjusted throughout the measurement series. As a result the data of the L_1 -9.4 line were not recorded in constant experimental conditions.

Both K -32 and L_3 -32 lines exhibited positive linear trends. The fit of the L_3 -32 data resulted in $d_{\text{total}}^{\text{rel}}(L_3\text{-}32) = 2.27(12)\text{ ppm month}^{-1}$. In the case of the K -32 line the situation is complicated due to the observation of some kind of saturation effect on day 6. Thus, the data "day ≤ 6 " and "day ≥ 6 " were considered separately. The drifts were determined as $d_{\text{total}}^{\text{rel}}(K\text{-}32, \text{day} \leq 6) = 14.4(12)$ and $d_{\text{total}}^{\text{rel}}(K\text{-}32, \text{day} \geq 6) = 3.27(18)\text{ ppm month}^{-1}$. The digital voltmeter was calibrated regularly during the whole measurement phase and its drift was determined as $k_{\text{dvm}} = -0.633(16)\text{ ppm month}^{-1}$, see Fig. 6.6. Again, k_{dvm} practically cancels out with the drift m_{div} in Eq. 6.2 and thus $d_{\text{source}} = d_{\text{total}}$.

The time dependence of the fitted amplitude of the K -32 and L_3 -32 lines is shown in Fig. 6.7. Both lines exhibit an exponential trend following the radioactive decay of ^{83}Rb . This behavior is expected as the ^{83}Rb and $^{83\text{m}}\text{Kr}$ atoms are in equilibrium. The half-life was determined as $t_{1/2}(K\text{-}32) = 79.3(2)\text{ d}$ and $t_{1/2}(L_3\text{-}32) = 81.6(2)\text{ d}$, while the uncertainties were multiplied by $\sqrt{\chi_r^2}$ due to large χ_r^2 values of the fits. The fit results differ by 5–8% from the literature value $t_{1/2} = 86.2(1)\text{ d}$ [Fir96]. The amplitude of the conversion electron lines was fitted as $\approx 1200\text{ counts s}^{-1}$ (K -32) and $\approx 2400\text{ counts s}^{-1}$ (L_3 -32). These values (ref. date 10.09.2008) corresponded well to the expected count rates estimated via Eq. 5.18. From Fig. 6.5 and Fig. 6.7 a conclusion can be drawn that after an initial period of days 0–6, during which the K -32 line drift of $d_{\text{source}}^{\text{abs}}(K\text{-}32, \text{day} \leq 6) \approx 260\text{ meV month}^{-1}$ was observed, the system got stabilized and the source S28 exhibited the drift $d_{\text{source}}^{\text{abs}}(\text{day} \geq 6)$ of 60–70 meV month^{-1} common for both K -32 and L_3 -32 lines. In other words, the two lines, separated by 12.6 keV in the $^{83\text{m}}\text{Kr}$ conversion spectrum, showed practically identical absolute drift. This observation suggests that the complete HV scale (the power supply, the divider and the digital voltmeter) was operating normally and the drift observed on days

Tab. 6.3: The overview of the first phase of measurements performed in 2008.

calendar week no.	20	21	22	23-34	35	36	37	38	39	40	41	42	43	44	45	46	47	48
week of	12.05.	19.05.	26.05.	-	25.08.	01.09.	08.09.	15.09.	22.09.	29.09.	06.10.	13.10.	20.10.	27.10.	03.11.	10.11.	17.11.	24.11.
time since 28.08.2008 [day]	-	-	-	-	-	3	10	17	24	31	38	45	52	59	66	73	80	87
source tested	S 28																	
HV conditions																		
HV divider used									K35									
calibration of HV divider	x											x						
HV scale shift observed								x										
vacuum conditions																		
spectrometer bake-out			x															
electron line scanned																		
L_1 -9.4					x	x	x	x	x	x	x	x	x	x	x	x	x	x
K-32				x	x	x	x	x	x	x	x	x	x	x	x	x	x	x
L_3 -32					x	x	x	x	x	x	x	x	x	x	x	x	x	x
$N_{2/\beta}$ -32						x						x	x					

Single vacuum-evaporated source S 28 was investigated during this measurement phase. In the calendar weeks 20–34 the preparation phase took place. Most importantly, in the week 20 the HV divider was calibrated with the help of two precision digital voltmeters. Moreover, the bake-out of the spectrometer vacuum vessel was performed in the week 22. The actual measurements proceeded in the weeks 35–48. After observing a sudden shift of the HV scale in the week 39, the HV divider was re-calibrated in the week 42.

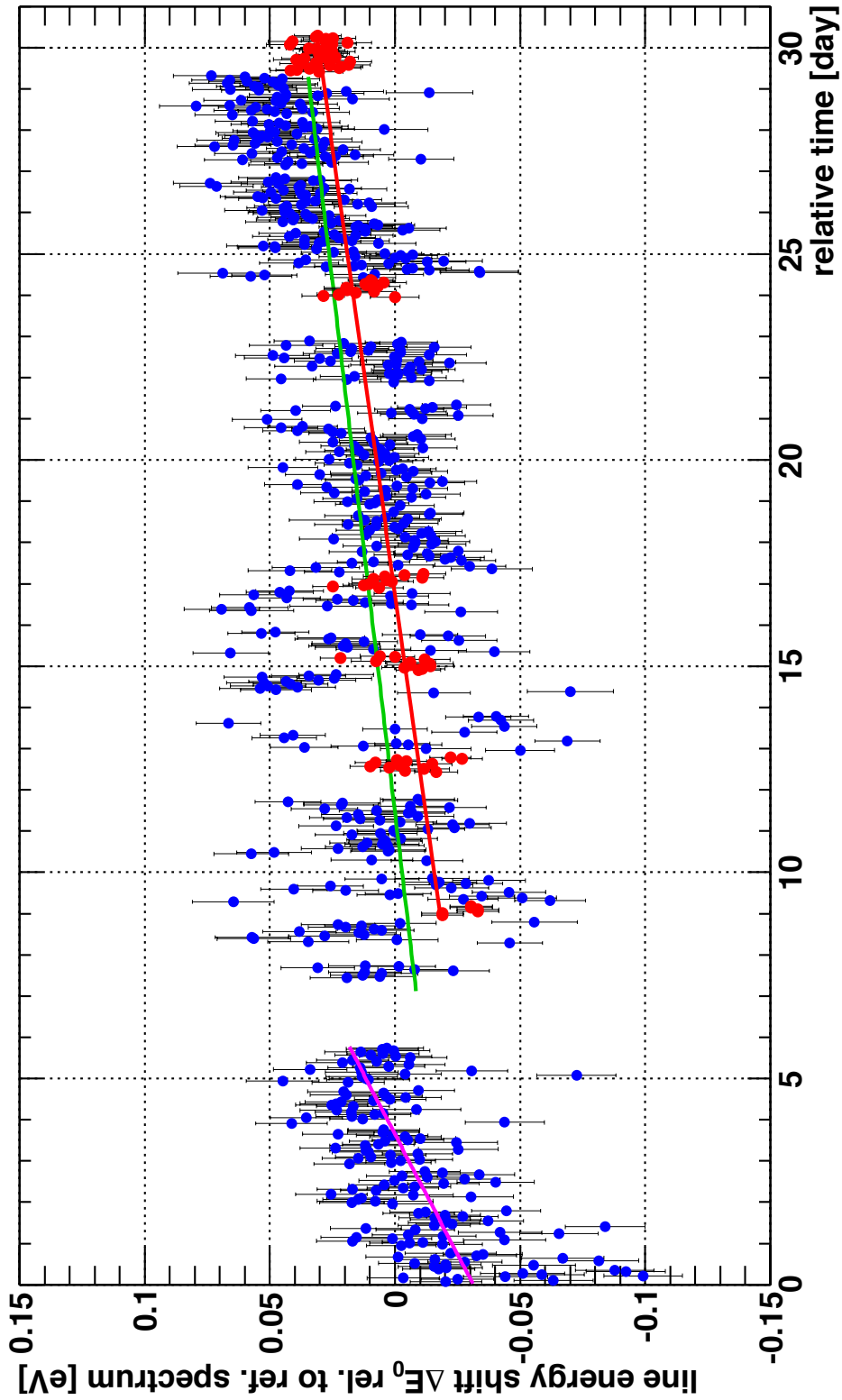


Fig. 6.5: The drifts of the K-32 (blue points) and L_3 -32 (red points) lines of the vacuum-evaporated source S 28. The x axis denotes the relative time in days since 28.08.2008. The y axis shows the line energy shift ΔE_0 relative to the reference spectrum. The least-squares fits were performed with the cross-correlation method, a suitable reference spectrum was chosen for each electron line separately. The magenta and green lines denote the fits of the K-32 data obtained in the time periods of days 0–6 and 6–30, respectively. The red line shows the fit of the L_3 -32 data. The full span of the y axis of 0.3 eV represents the portion of $\simeq 17$ ppm considering the K-32 line energy of 17824 eV.

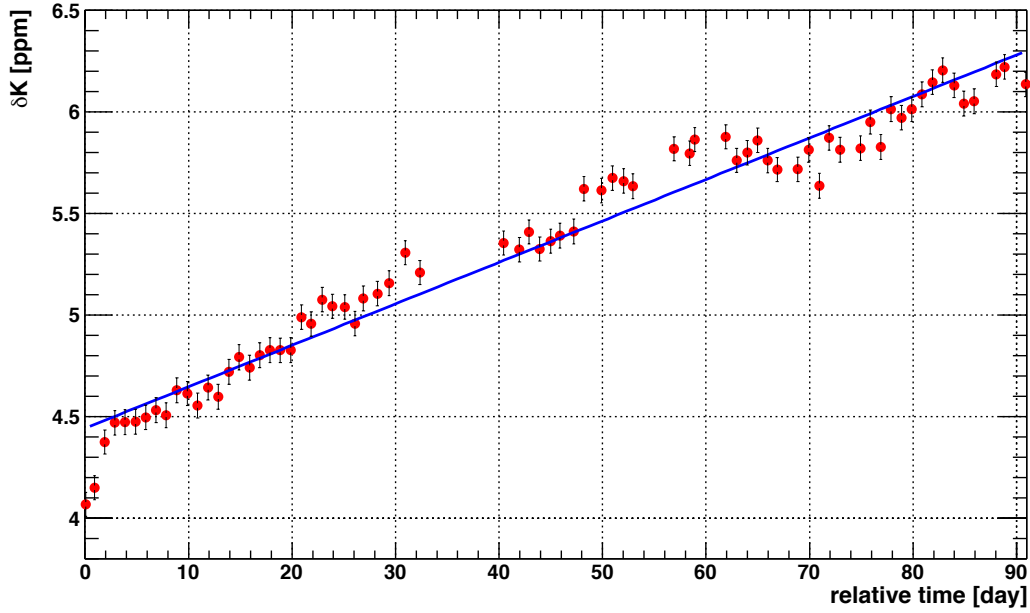


Fig. 6.6: The drift of the digital voltmeter scale factor K during the first measurement phase. The x axis denotes the relative time in days since 28.08.2008. The y axis shows the deviation δK [ppm], see the caption of Fig. 6.3. The time dependence of the K factor was determined as $k_{\text{dvm}} = -0.633(16) \text{ ppm month}^{-1}$. Relatively big scatter of data caused a rather large $\chi_r^2 = 4.02(17)$ which was taken into account via multiplying the uncertainty of k_{dvm} by $\sqrt{\chi_r^2}$.

6–30 can be ascribed to the source itself and/or to the drift of ϕ_{spec} . In addition, as the count rate of the source followed the ^{83}Rb radioactive decay it can be assumed that the source was not significantly affected by the system, *e. g.* a desorption of ^{83}Rb atoms from the graphite substrate did not take place.

The consideration of the drifts of the individual conversion lines can be mathematically expressed as follows. In order to scan the $^{83\text{m}}\text{Kr}$ conversion lines the negative voltage U in the range of -7 to -32 kV is applied to the spectrometer electrodes. The HV divider K35 scales the HV by the factor $M = 1972.480\,16(61) \approx 2000$ to the low voltage U_{meas} in the range of -3.5 to -16 V. The low voltage is measured with the digital voltmeter which is regularly calibrated and traced back to the voltage standards. Supposing the time dependence $M(t)$ is unknown⁵, the remaining drift d_{total} equals, according to Eq. 6.1,

$$d_{\text{total}} = d_{\text{source}} - m_{\text{div}}, \quad (6.4)$$

where the system is assumed to be stable, *i. e.* the term C in Eq. 6.1 is neglected. Thus, the combination of the drifts of the HV divider and the source itself is measured. The drift m_{div} can be obtained from an independent calibration. However, the intended application of the solid $^{83}\text{Rb}/^{83\text{m}}\text{Kr}$ source is to serve as a standard for constant monitoring of the HV stability. Therefore, it should be possible to determine the long-term drift of any HV divider, in principle, which would be used in the monitoring system. For a given electron line, the time dependence of the low voltage $U_{\text{meas}}(t)$ measured with the digital voltmeter can be

⁵Obviously, this is not true for the case of the KATRIN HV dividers K35 and K65, cf. Tab. 5.1. However, here the general case of a HV divider with an unknown drift of the dividing ratio is assumed.

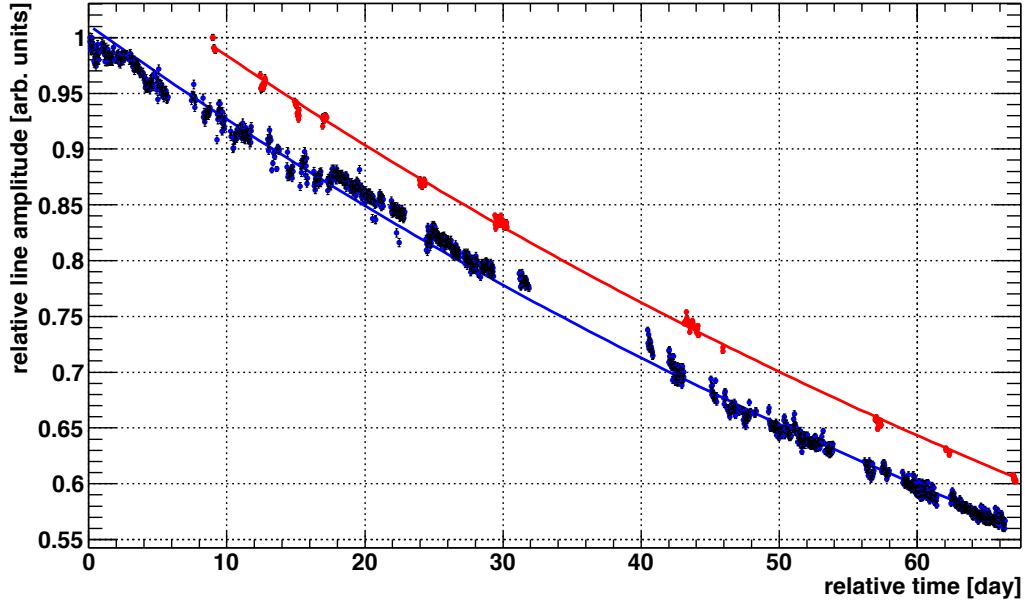


Fig. 6.7: The time dependence of the K -32 (blue points) and the L_3 -32 (red) line amplitude as obtained from the fits carried out with the cross-correlation method. The time 0 corresponds to 28.08.2008. Both data sets were scaled to 1. The blue and red lines indicated the exponential functions fitted onto the data sets. The χ^2_r values were rather large, 7.79(4) and 4.1(1), respectively, which was taken into account by enlarging the uncertainties of the fit results.

expressed (cf. Eq. 5.7) as

$$U_{\text{meas}}(t) = \frac{U(t)}{M(t)} = \frac{U_0 - \frac{1}{q} d_{\text{source}}^{\text{abs}} \cdot t}{M_0(1 + m_{\text{div}} \cdot t)} \approx \frac{1}{M_0} \left(U_0 - \frac{1}{q} d_{\text{source}}^{\text{abs}} \cdot t \right) (1 - m_{\text{div}} \cdot t), \quad (6.5)$$

where $q = -|e|$ and the constants M_0 and U_0 denote the initial values of the dividing ratio M and of the HV corresponding to the conversion electron line position E_0 , respectively. The factor $\frac{1}{q}$ was introduced in the numerator in order to use the aforementioned absolute drift $d_{\text{source}}^{\text{abs}}$ [meV month⁻¹]. This drift is expected to be caused by the surface and solid state effects in the source. In Eq. 6.5 the second and higher order terms were omitted. Omitting further the product $m_{\text{div}} \cdot d_{\text{source}}^{\text{abs}}$, Eq. 6.5 can be rewritten as

$$M_0 \cdot U_{\text{meas}}(t) = U_0 - \left(\frac{1}{q} d_{\text{source}}^{\text{abs}} + m_{\text{div}} \cdot U_0 \right) t, \quad (6.6)$$

thus, in this approximation the measured drift equals $\frac{1}{q} d_{\text{source}}^{\text{abs}} + m_{\text{div}} \cdot U_0$. When at least two conversion lines A and B are periodically measured and their (total) drifts $d_{\text{total}}^{\text{abs}}(A) \equiv a$ and $d_{\text{total}}^{\text{abs}}(B) \equiv b$ are determined from the data, the following set of equations

$$d_{\text{source}}^{\text{abs}}(A) + q \cdot m_{\text{div}}(A) \cdot U_0(A) = a, \quad (6.7)$$

$$d_{\text{source}}^{\text{abs}}(B) + q \cdot m_{\text{div}}(B) \cdot U_0(B) = b$$

can be formed. Assuming that the long-term drift of the HV divider does not depend on the applied voltage one can write

$$m_{\text{div}}(A) = m_{\text{div}}(B) \equiv m_{\text{div}}. \quad (6.8)$$

In addition, to the first approximation the surface and solid state effects are assumed to generally influence all conversion electrons in the same way so the absolute value of the energy drift does not depend on the electron energy,

$$d_{\text{source}}^{\text{abs}}(A) = d_{\text{source}}^{\text{abs}}(B) \equiv d_{\text{source}}^{\text{abs}}. \quad (6.9)$$

These two assumptions simplify the set of equations in Eq. 6.7 to

$$\begin{aligned} d_{\text{source}}^{\text{abs}} + q \cdot m_{\text{div}} \cdot U_0(A) &= a, \\ d_{\text{source}}^{\text{abs}} + q \cdot m_{\text{div}} \cdot U_0(B) &= b \end{aligned} \quad (6.10)$$

which allows for disentangling the drifts m_{div} and $d_{\text{source}}^{\text{abs}}$ of the HV divider and the $^{83}\text{Rb}/^{83\text{m}}\text{Kr}$ source itself.

As an example the data of the $K\text{-}32 \equiv A$ and $L_3\text{-}32 \equiv B$ lines, obtained with the vacuum-evaporated source S 28 on days 6–30, are considered:

1. The nominal HV values corresponding to the line positions are taken as $U_0(A) = -17.82\text{ kV}$ and $U_0(B) = -30.47\text{ kV}$.
2. The total drifts of the data sets depicted in Fig. 6.5 were determined as $d_{\text{total}}^{\text{abs}}(A) = 58(3)\text{ meV month}^{-1}$ and $d_{\text{total}}^{\text{abs}}(B) = 69(4)\text{ meV month}^{-1}$.
3. The total drifts have to be corrected for the drift $k_{\text{dvm}} = -0.633(16)\text{ ppm month}^{-1}$, see Fig. 6.6. The zero offset of the voltmeter was found to be stable in time, $U_{\text{offset}} \simeq -3.01(3) \times 10^{-6}\text{ V}$, and can be neglected in the considerations. The drift of the voltage reference itself was measured at the PTB Braunschweig as $0.24\text{ ppm year}^{-1}$ [Bau11] which is negligible in this case. The relative drift k_{dvm} of the voltmeter scale factor K affects the lines A and B differently: the absolute corrections are $\Delta k_{\text{dvm}}(A) = -11.3(1)\text{ meV month}^{-1}$ and $\Delta k_{\text{dvm}}(B) = -19.3(2)\text{ meV month}^{-1}$. Therefore, the corrected drifts are $d_{\text{total}}^{\text{abs}}(A) \equiv a = 47(3)$ and $d_{\text{total}}^{\text{abs}}(B) \equiv b = 50(4)\text{ meV month}^{-1}$.
4. From Eq. 6.10 it follows $m_{\text{div}} = 0.22(38)\text{ ppm month}^{-1}$ and $d_{\text{source}}^{\text{abs}} = 43(8)\text{ meV month}^{-1}$. The latter one represents the intrinsic absolute drift of the vacuum-evaporated source S 28 as determined on days 6–30 during the first measurement phase. The drift m_{div} stands for the relative drift of the HV divider K35 as determined by this simplified model.

In the case of the divider K35 the drift $m_{\text{div}}^{\text{PTB}}$ was independently determined at the PTB Braunschweig as $0.60(10)\text{ ppm month}^{-1}$ (cf. Eq. 6.2). Of course, this value can be fully traced back to metrological standards and therefore represents more reliable statement about the stability of the divider. Nevertheless, the value m_{div} obtained on the basis of the presented model agrees with the $m_{\text{div}}^{\text{PTB}}$ value within 1σ .

The assumptions on which the introduced method is based shall be briefly discussed:

- The electron binding energy $E_{\text{bin}}(i)$ of the atomic shell i is known to depend on chemical and solid state environment of the atom, see Sect. 4.3.1. This effect is extensively studied in the photoelectron spectroscopy [Sie69, Ege87, Rat09]. In general, the changes $\Delta E_{\text{bin}}(i)$ are not identical for all atomic shells, *e. g.* in [Dec90] the chemical shifts of the binding energy in multiply charged $^{83\text{m}}\text{Kr}$ were determined for several shells: the L_1 , M_1 and $N_1\text{-}9.4$ conversion electron lines were investigated and differences in the

chemical shifts of the order of 1 eV were observed for multiple ionizations “ $n+ \rightarrow (n + 1)+$ ”. Therefore, strictly speaking, the condition expressed in Eq. 6.9 may be unfulfilled with the accuracy needed for the presented purpose.

- In Eq. 6.8 it is assumed that the long-term drift of the HV divider does not depend on the applied voltage. Both dividers K35 and K65 exhibit very low voltage dependence, the coefficient is of the order of 0.01 ppm kV⁻¹ for both devices (cf. Tab. 5.1). In addition, the temperature coefficient lies in the sub-ppm range. Therefore, a very small dependence of the long-term drift on the applied load can be anticipated. So far no voltage dependence of the dividing ratio time drift has been observed [Thu07, Thu09, Bau11].
- The drift k_{dvm} of the voltmeter scale factor K is determined at the voltage of -10 V while the low voltage on the divider output spans the range of about -3.5 to -16 V. It is assumed that the scale factor K is valid for the full measurement range of 20 V, *i. e.* there are no deviations from linearity of the scale. This effect is supposed to be negligible, on the other hand, it could be verified by using two 10 V DC voltage references so the scale factor of the digital voltmeter would be determined at -10 V as well as at -20 V.
- The total drift expressed in Eq. 6.4 does not include the term C standing for the drift of ϕ_{spec} . Should the drift of ϕ_{spec} appear during the measurement, in the first approximation it will influence the drifts of all the conversion lines in the same manner. Thus, assuming the measured drift of the given line in the form of $d_{\text{source}}^{\text{abs}} + q \cdot m_{\text{div}} \cdot U_0$ (see above), the drift of ϕ_{spec} will “mask” the drift $d_{\text{source}}^{\text{abs}}$ as this term is not scaled with the applied HV.

The method introduced in Eq. 6.5 to Eq. 6.10 represents a simple model of disentangling the long-term drifts of the HV divider and the calibration source on the ppm-scale. It suffers mainly from the assumption of Eq. 6.9 that the chemical and solid state environment affects different electron shells of the ^{83m}Kr atom in the same manner. Another method of disentangling the drifts of the HV divider and the source was presented in [Kas08]. This method utilizes the unique feature of the electrostatic spectrometer ESA-12 [Var82]. The spectrometer consists of the double pass cylindrical mirror electron analyzer type and is equipped with a retarding/accelerating lens and a channel electron multiplier used as the detector. The method of [Kas08] is based on the facts that a) the given energy of the studied electrons can be produced by various combinations of the retarding and passing energies and b) the sum of the various retarding and passing energies is different from each other thanks to the factor of 0.56 scaling the passing energy to the passing voltage. Basically, this method is realizable only in the case of the double pass electrostatic spectrometer and is not applicable in the case of the integral spectrometer of the MAC-E filter type which was used in this work. The aforementioned model (Eq. 6.5 to Eq. 6.10) will be further implemented in the following sections when the energy stability of the conversion lines will be discussed.

6.2.2. Sudden unexpected shift of the high voltage scale

On 27.09.2008 an accident occurred during the energy stability measurements of the vacuum-evaporated source S28. The observations can be summarized as follows:

- Since 26.09.2008 the L_3 -32 line was scanned, therefore the HV was stabilized to ≈ -30.5 kV for about 22 hours already.
- During the check routine of the experimental setup the malfunction of the temperature regulation of the HV divider K35 was observed. Typically, the temperature inside the divider vessel was stabilized as $(25.0 \pm 0.2)^\circ\text{C}$, however, at that moment the temperature rose to 27.4°C .
- The power supply driving the auxiliary air coil with the current of 60 A was found to be off as if a power outage would occur. The counter of helium gas evaporating from the superconducting solenoids was found to be out of order as well.
- No significant change of the vacuum was observed. The spectrometer vessel was kept at the UHV level of $\simeq 5 \times 10^{-10}$ mbar.
- The automatic measurement was running flawlessly, *i. e.* the HV power supply and the DAQ system were found functional and were normally regulated by the control program. On the other hand, the digital voltmeter was sending unphysical values to the control computer.

Hence, it can be assumed that some kind of HV spark occurred which affected several devices of the experimental setup. The temperature regulation of the HV divider was not functional since that moment. Most importantly, the HV scale was found to be shifted by $\simeq 0.9$ V. In Fig. 6.8 an example comparing the K -32 line spectra measured before and after the accident is shown. After applying the HV of -17.8 kV to the divider K35 its inner temperature rose to 26.8°C . The temperature coefficient of the divider K35 was < 0.2 ppm K^{-1} (cf. Tab. 5.1), therefore, the dividing ratio M was presumably changed by 0.36 ppm due to the temperature increase. However, the observed shift of 0.9 eV corresponds to the considerable change of 50 ppm of the K -32 energy. Thus, only the temperature regulation malfunction cannot explain this effect.

The most prominent lines of the $^{83\text{m}}\text{Kr}$ conversion spectrum were scanned after the incident. Besides the conversion electrons also the group of the $KL_{2,3}L_{2,3}$ Auger peaks (further denoted as KLL) of the energy $\simeq 10.8$ keV was investigated, see Fig. 6.9. The KLL spectrum of $^{83\text{m}}\text{Kr}$ was studied in the past with the help of the electrostatic spectrometer ESA-50 in the JINR Dubna [Kov92] and altogether eight peaks were identified in the corresponding portion of spectrum. The integral feature of the MAC-E filter and the transmission losses complicated the spectrum in our case. Nonetheless, the shift of the complete KLL spectrum was determined with the help of the cross-correlation method so that no precise knowledge of the line shapes was necessary. In Fig. 6.10 the shifts of the individual electron lines (conversion and Auger) are illustrated for the comparison of the situations before and after the HV scale shift. The low energy line L_1 -9.4 exhibited the shift of 0.98(4) eV while the high energy lines K -32, L_3 -32 and $N_{2/3}$ -32 showed the shifts in the range of 0.93–0.94 eV. The shift of the KLL Auger spectrum was determined as 0.71(3) eV. The data of the L_1 -9.4 line positions suffered from considerable scatter, presumably caused by the noise in the detector electronic chain, as mentioned above already. The low energy lines L_1 -9.4 and KLL were further omitted in the consideration, however, they proved that there was no effect of scaling of the HV shift with the electron energy—the accident resulted in the constant shift of $\simeq 0.93$ V of the HV scale.

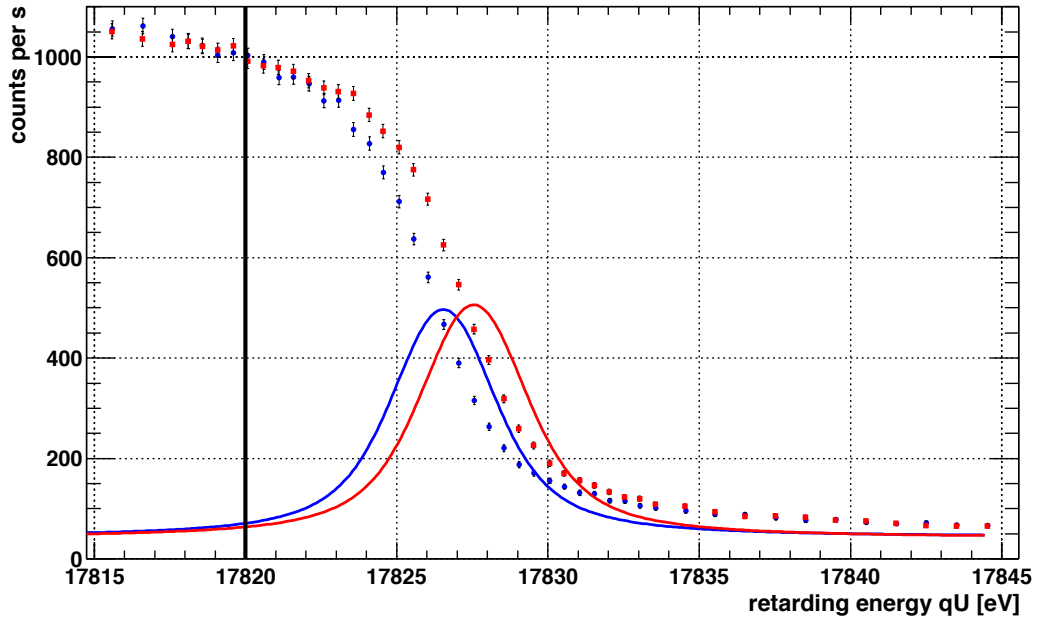


Fig. 6.8: The comparison of the K -32 spectra measured before (blue points) and after (red points) the accident which occurred on 27.09.2008. For the sake of example the error bars were multiplied in both spectra by the factor of 2. The time span between the two scans was about 2 days. The spectra were least-squares fitted with a single Voigt function where $\Gamma = 2.7$ eV was kept fixed and σ was a free parameter (cf. Sect. 5.2.6). The vertical line at $qU = 17820$ eV denotes the lower limit of the fit range. The blue and red lines represent the corresponding Voigt peaks resulting from the fits, including the constant background B_0 . The values of the line amplitude, background and width σ were found to remain unchanged within the fit uncertainties.

The complete experimental setup was checked and no malfunction besides the aforementioned effects was observed. For example, the grounding of the source was verified: when the electrical connection of the source to the spectrometer ground was removed an additional positive shift of $\simeq 0.3$ eV of the K -32 line was observed. Besides the dividing ratio $M_1 \approx 1972 : 1$, which was widely used for the measurements, the second dividing ratio $M_2 \approx 3944 : 1$ of the divider K35 was checked with the help of the K -32 line scans. For the comparison of the data obtained with the dividing ratios M_1 and M_2 , their drifts $m_{\text{div}}(M_1)$ $m_{\text{div}}(M_2)$, determined from the calibrations in the PTB Braunschweig [Thu07, Thu09], were taken into account. The results were found in a perfect agreement, *i.e.* there was no difference of the fitted line positions of the K -32 line regarding the dividing ratio used. This observation suggests that the HV divider itself was working properly but some unexpected offset occurred. The following explanations of the effect were considered:

1. The HV spark has in some way affected the HV divider at its input. This would shift the HV scale by a constant amount independently on the applied voltage. This explanation is supported by the observations during the inspection of the divider in the Institute of Nuclear Physics, University of Münster, later in June 2009 [Bau11]. Black traces of burn-ins were apparent at the upper copper electrode where the HV input was tightened to the divider construction by a bronze spring. In addition, it was found out that the bronze spring was not an ideal connection as it was vulnerable to displacement during the transportation of the divider.

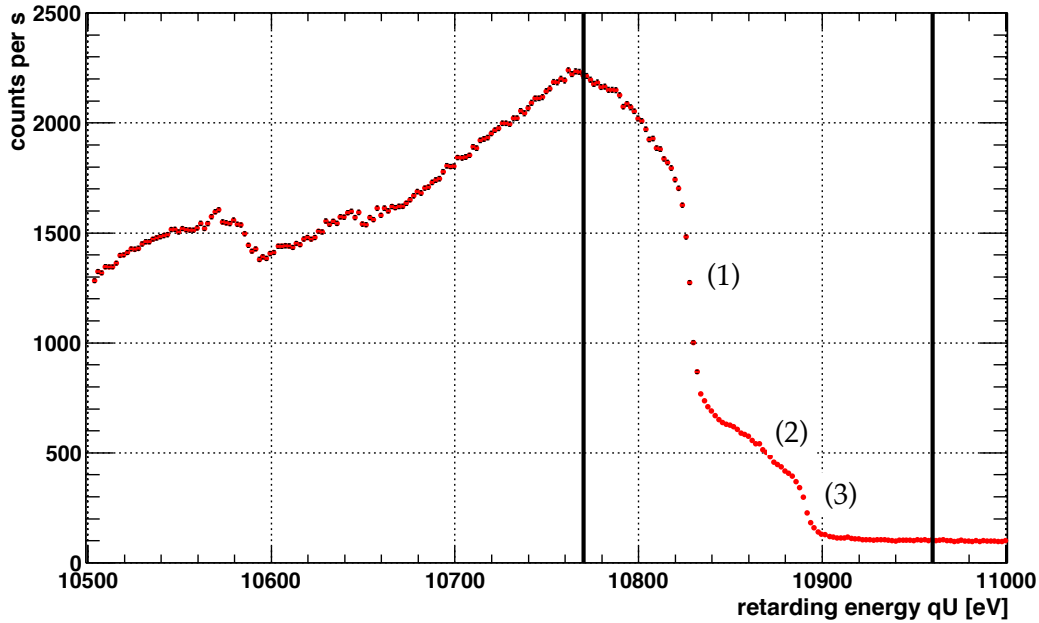


Fig. 6.9: The integral spectrum of the $KL_{2,3}L_{2,3}$ Auger peaks measured with the vacuum-evaporated source S28. The perpendicular lines frame the region of spectrum used for analysis of the HV shift with the help of the cross-correlation method. The most prominent is the 1D_2 peak (marked (1)) of the energy $\simeq 10.83$ keV. The spectrum corresponds well to the differential spectrum obtained with the electrostatic spectrometer [Kov92], however, the integral feature of the MAC-E filter and the transmission losses make the spectrum difficult to evaluate in detail. The transmission losses are clearly visible as the drop of the signal at energies below $\simeq 10.77$ keV. The peak 1D_2 is superimposed on the signal from the higher energy peaks 3P_0 (marked (2)) and 3P_2 (marked (3)).

2. The $^{83}\text{Rb}/^{83\text{m}}\text{Kr}$ source itself could be affected by the HV spark. Due to the auxiliary air coil failure the electron beam flux was significantly off-center and the electrons emitted from the source were hitting the spectrometer electrode surface which was at the potential of -30.5 kV. This could in turn eject secondary electrons and ions which were focused back on the source and could bombard and influence the surface of the source where the ^{83}Rb atoms were adsorbed. This hypothesis is not supported by the fact that according to Fig. 6.7 the amplitudes of the K -32 and L_3 -32 lines were following the ^{83}Rb decay as expected and no significant difference of the amplitudes before and after the accident was visible. However, the source work function ϕ_{source} could be changed by a massive electron and ion bombardment.
3. The spectrometer work function ϕ_{spec} could be also affected by the HV discharge in the spectrometer vessel. As there was no system of online monitoring of vacuum in the setup at that moment, the discharge cannot be rejected from discussion.

In addition, the HV divider K35 was calibrated with the help of two precision digital voltmeters Fluke 8508A. The same procedure was carried out in May 2008 during the preparation phase, thus, the calibration provided an independent check of the divider performance. Fig. 6.11 presents the schematic diagram of the calibration procedure. The voltage of -1 kV was applied to the divider and the divided low voltage of about -0.5 V was read out by

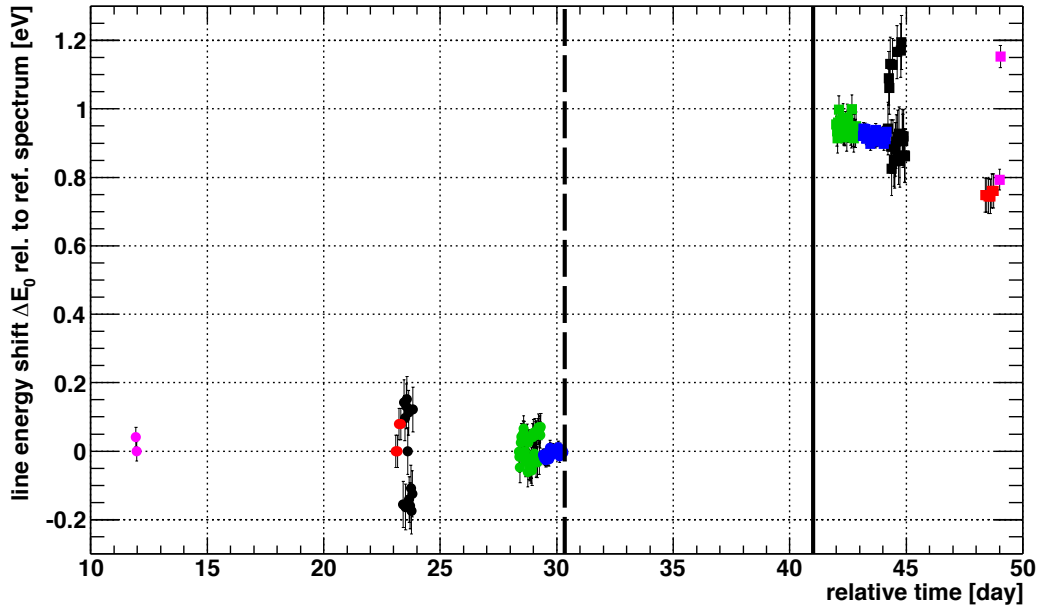


Fig. 6.10: The observation of the sudden change of the HV scale during the measurements with the vacuum-evaporated source S28. The x axis denotes the relative time in days since 28.08.2008. The y axis shows the line energy shift ΔE_0 relative to the reference spectrum. The y error bars were multiplied by the factor of 2 for the sake of clarity. For each electron line, a suitable reference spectrum was chosen from the time period before the accident. The following lines are depicted: conversion electrons L_1 -9.4 in black, K -32 in green, L_3 -32 in blue and $N_{2/3}$ -32 in magenta. The data related to the group of the KLL Auger peaks are shown in red. The dashed line at day $\simeq 30$ represents the moment when the accident took place. The full line at day = 41 denotes the moment when the HV divider was inspected and made ready for the next measurement.

the digital voltmeter set to the 20 V DC range⁶. An additional digital voltmeter set to the 1 000 V DC range was simultaneously measuring the voltage of -1 kV directly. This way the internal divider of the voltmeter is utilized and its stability is specified as 1.8 ppm in the 24 hours period and as 5.8 ppm in the 1 year period (both values at 99% C.L.) [Flu08]. Both voltmeters were set to the maximal resolution of $8\frac{1}{2}$ -digits. Moreover, the voltmeters were also cross-checked against each other by measuring simultaneously the voltage of -1 kV directly. These two arrangements were swapped several times as shown in Fig. 6.11.

The results of this rough calibration of the dividing ratio M_1 are depicted in Fig. 6.12 where the comparison to the values based on the PTB data is also shown. The values obtained with the aforementioned procedure are by $\simeq 20$ ppm lower than the PTB-based values. This difference can be ascribed to the imperfect calibration of the voltmeters as no standard of the -1 kV voltage was available. Moreover, the uncertainty of the calculated dividing ratios amounted to $\simeq 15$ ppm due to the use of two voltmeters. In addition, the thermo-voltages at the cable connectors can play a role when measuring the low voltage of -0.5 V. Obviously, the presented method is not usable for absolute calibration of the high precision HV divider, but it turned out to be very useful method for a quick diagnostics of the divider performance as will be seen later. The calibration of the divider K35 with the help of two voltmeters has

⁶Actually, the DC range of 2 V would be more suitable for such a measurement, however, the range of 20 V was used so that the calibration of the voltmeter with the 10 V DC reference was possible.

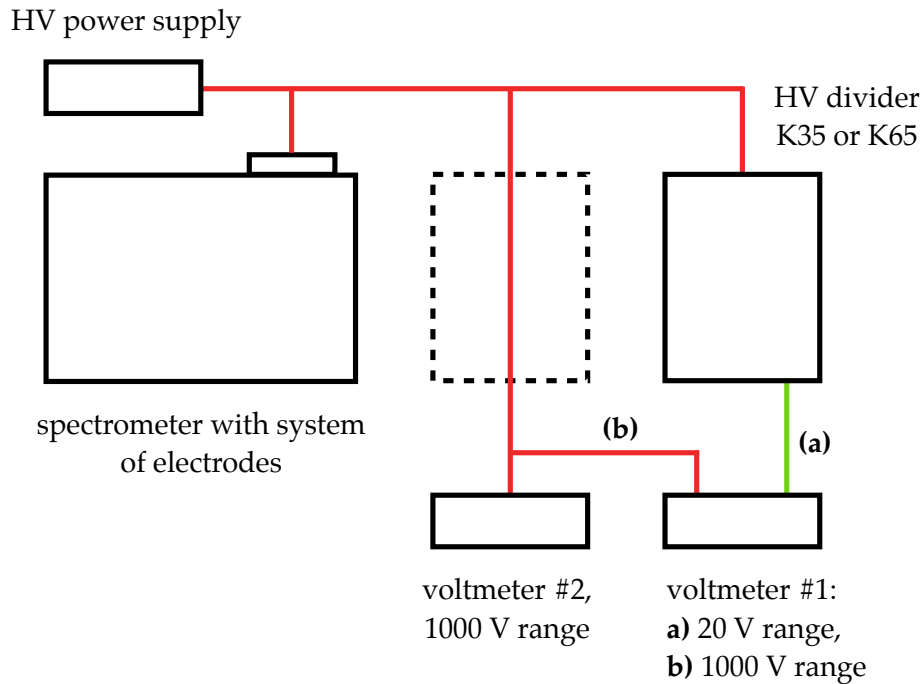


Fig. 6.11: The schematic diagram of the calibration procedure of the HV divider at -1 kV carried out with the help of two high precision digital voltmeters Fluke 8508A. The two arrangements schematically denoted as **(a)** and **(b)** were swapped several times during the procedure. In the connection **(a)** the output of the HV divider was read out by the voltmeter #1 while the voltmeter #2 was connected directly to the -1 kV line. In the connection **(b)** both voltmeters were fed by the voltage of -1 kV and the voltmeter #2 was cross-checked against the voltmeter #1. This procedure allowed to calibrate the dividing ratios of the dividers K35 and K65 with the precision of $\simeq 15$ ppm. More detailed description of the individual devices was given in Fig. 5.11.

not revealed any change of the dividing ratio M_1 on the level of 15 ppm.

6.2.3. Measurements with the shifted high voltage scale

The temperature regulation of the divider K35 was repaired directly in the Institute of Physics, University of Mainz, and the measurements went on with the shifted HV scale as the second high precision divider K65 was under development at that time. The results of the measurements carried out after the HV scale shift are depicted in Fig. 6.13. It was assumed that the drift m_{div} remained unchanged and that the energy stability of the conversion lines of the solid $^{83}\text{Rb}/^{83\text{m}}\text{Kr}$ sources can still be investigated this way. The conversion lines L_1 -9.4, K -32, L_3 -32 and $N_{2/3}$ -32 were periodically scanned. Both the L_1 -9.4 and $N_{2/3}$ -32 line positions suffered from the scatter of $\simeq 0.2$ eV. The cause for the scatter of the L_1 -9.4 line positions was discussed on page 146. In the case of the $N_{2/3}$ -32 line the scatter of the line positions stems from a poor statistics and an insufficient stabilization of the HV prior to the scans of this line. Further on only the K -32 and L_3 -32 lines are considered.

The measurements carried out with the shifted HV scale delivered negative drifts of the K -32 and L_3 -32 line positions, on the contrary to the previous measurements. Both conversion

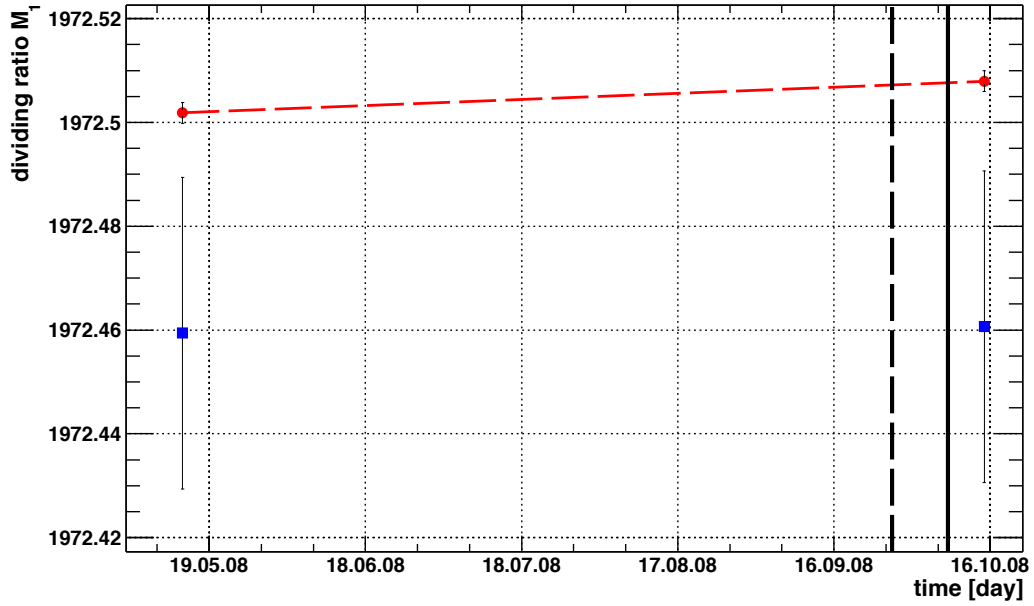


Fig. 6.12: The results of the calibration of the HV divider K35 carried out in the Institute of Physics, University of Mainz, according to the procedure depicted in Fig. 6.11. The blue points show the absolute values of M_1 of the divider as obtained from the calibration procedure. The red points (connected by the red dashed line) represent the M_1 values based on the linear extrapolation ($m_{\text{div}}^{\text{PTB}} = 0.60(10) \text{ ppm month}^{-1}$) of the PTB data from the time period 2005–2006 [Thu07, Thu09]. As in Fig. 6.10, the dashed line represents the moment when the accident occurred and the full line denotes the moment when the HV divider was made ready for the next measurement.

lines exhibited the drift $d_{\text{source}}^{\text{abs}}$ of about $-70 \text{ meV month}^{-1}$. However, this value is based on the assumption that the divider drift m_{div} did not change after the HV scale shift. At this point the simple model of decomposing the observed drift into the individual drifts of the HV divider and the source turns out to be quite useful as a rough check of the system. According to the procedure described in Sect. 6.2.1 one gets $m_{\text{div}} = -0.01(30) \text{ ppm month}^{-1}$ and $d_{\text{source}}^{\text{abs}} = -85(6) \text{ meV month}^{-1}$. Thus, in the approximation utilized in this model the HV divider remained stable as its drift determined from the days 41–74 was compatible within 1σ with the value based on data from 7–30. The results are summarized in Tab. 6.4.

Naturally, the intrinsic drift of the source was determined to be negative as both the observed drifts of the K -32 and L_3 -32 lines were negative. This fact can point back to the explanation (2) of the HV scale shift on page 155: the intrinsic drift of the source changed its sign while the divider drift did not change within the uncertainties. Moreover, the change of ϕ_{spec} (explanation (3) on page 155) cannot be excluded. The negative drift of the conversion electron lines would indicate a slow rise of ϕ_{spec} which was lowered due to the discharge—the electrode surface got “cleaned” by the discharge. Later, ϕ_{spec} was increasing again due to rest gas adsorption. In sum, it is practically impossible to unambiguously explain the drifts of the K -32 and L_3 -32 lines observed before and after the Hv scale shift on the basis of the collected data. Most probably the combination of the source drift and the drift of ϕ_{spec} was measured.

As indicated in Fig. 6.13 on day 74 both the source and the detector were moved into higher magnetic fields (source $0.33 \text{ T} \rightarrow 1.75 \text{ T}$, detector $0.77 \text{ T} \rightarrow 1.06 \text{ T}$), *i. e.* by 9 cm and 1.6 cm

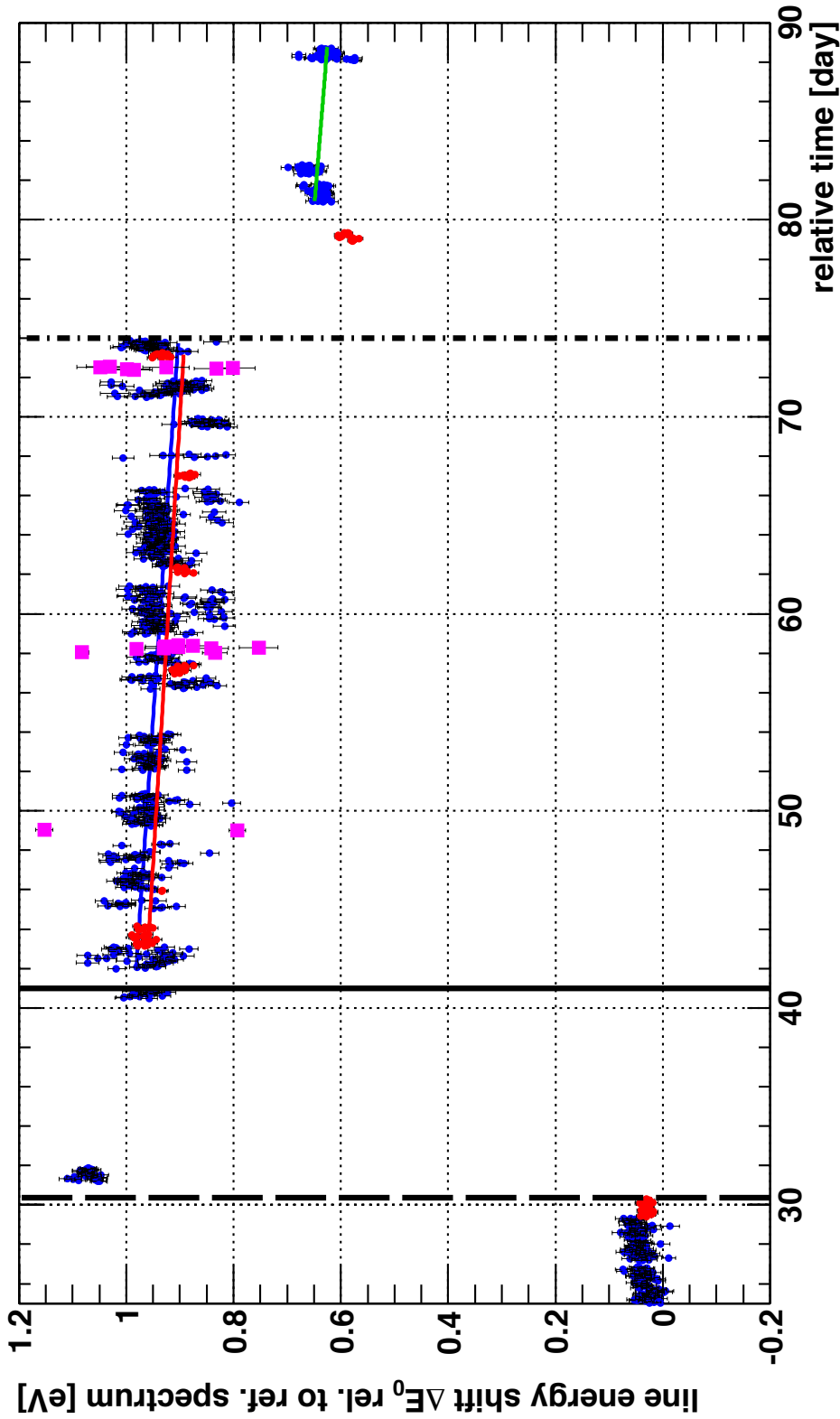


Fig. 6.13: The drifts of the K-32 (blue points) and L₃-32 (red points) lines of the vacuum-evaporated source S 28 obtained after the shift of the HV scale occurred on day 30 (dashed vertical line). The x axis denotes the relative time in days since 28.08.2008. The y axis shows the line energy shift ΔE_0 relative to the reference spectrum. The least-squares fits were performed with the cross-correlation method where the reference spectra were identical to those used in Fig. 6.5. For the sake of illustration, the data of the N_{2/3}-32 line position shifts are also depicted (magenta points). Even after the HV divider was inspected on day 41 (full vertical line) the HV remained at the new level which was by $\simeq 0.93$ eV higher than before day 30. The chain-dotted line on day 74 denotes the movement of the source and the detector into higher magnetic fields. This way the detected count rate was increased, however, the drop of $\simeq 0.3$ eV of the K-32 and L₃-32 line positions was observed. The blue and red lines denote the fits of the corresponding data sets in the time period of days 41–74. The green line shows the fit of the K-32 line positions in the time period of days 80–90.

Tab. 6.4: The drifts of the K -32 and L_3 -32 lines measured with the vacuum-evaporated source S 28.

time period [day]	data set	χ_r^2 of fit	linear fit parameters		relative drift $d_{\text{source}}^{\text{rel}}$ [ppm month ⁻¹]
			absolute [eV]	linear [meV month ⁻¹]	
0–7	K -32	2.2(1)	$-31(3) \times 10^{-3}$	258(33)	14.4(18)
7–30	K -32	2.82(7)	$-22(3) \times 10^{-3}$	58(5)	3.27(30)
	L_3 -32	5.8(1)	$-39(7) \times 10^{-3}$	69(9)	2.27(29)
	source drift $d_{\text{source}}^{\text{abs}} = 43(8) \text{ meV month}^{-1}$ divider drift $m_{\text{div}} = 0.22(38) \text{ ppm month}^{-1}$				
41–74	K -32	15.57(6)	1.09(4)	-74(8)	-4.15(59)
	L_3 -32	7.0(2)	1.05(3)	-66(8)	-2.17(26)
	source drift $d_{\text{source}}^{\text{abs}} = -85(6) \text{ meV month}^{-1}$ divider drift $m_{\text{div}} = -0.01(30) \text{ ppm month}^{-1}$				
80–90	K -32	2.2(1)	0.89(4)	-89(16)	-4.98(89)

The data depicted in Fig. 6.5 and Fig. 6.13 were least-squares fitted with a linear function. The uncertainties of the fit results were multiplied by $\sqrt{\chi_r^2}$ due to the large χ_r^2 values. The procedure described in Sect. 6.2.1 was used for disentangling the drifts of the source and the HV divider.

closer to the center of the spectrometer, respectively. The motivation was to increase the count rate and thus reduce the statistical uncertainty of the line positions. Indeed, the amplitude of the K -32 line was increased by the factor of $\simeq 3.0$ while the background was increased by the factor of $\simeq 3.4$. Strictly speaking, this actually worsened the amplitude-to-background ratio by the factor of 0.9. In addition, a significant negative shift of the line positions was observed. Extrapolating linearly the drifts of the line positions obtained on days 41–74 to the appropriate dates after the change of measurement geometry, the shifts of the K -32 and L_3 -32 line positions were determined as $-0.24(2) \text{ eV}$ and $-0.29(1) \text{ eV}$, respectively. The line position drop can be fully ascribed to the change of the measurement geometry as the whole HV system behaved flawlessly. In the new z position the placement of the source in the x - y plane was again optimized so that the amplitude of the K -32 line was maximal. Thus, ideally the line position should not change, however, in reality some overall misalignment of the experimental setup probably resulted in the fact that the measured kinetic energy of the electrons was very sensitive to the $[x, y, z]$ position of the source and the detector. The K -32 line drift measured on days 80–90 amounted to $-89(16) \text{ meV month}^{-1}$, thus, basically the negative drifts of the K -32 and L_3 -32 lines observed on days 41–74 were reproduced.

6.2.4. Influence of the source position on the K-32 line

It was seen in previous sections that the fitted position E_0 of a given conversion electron line, and generally the kinetic energy of an electron emitted from the source, is very sensitive to the position of the source. The position $[x, y, z]$ of the source can be decomposed as follows (cf. Sect. 5.1.2):

- a) The z position of the source was measured with the precision of 1 mm and it was related to the center of the solenoid B where the magnetic field reached the maximum of B_{\max} .
- b) The displacement $[\Delta x, \Delta y]$ defined the position of the source in the x - y plane with respect to the z axis of the spectrometer. It was assumed that the optimal position of the source, found with the help of maximizing the observed amplitude of the K-32 line, lies on the spectrometer z axis. Obviously, this in turn relied on the overall alignment of the experimental setup. The displacement $[\Delta x, \Delta y]$ was measured with the precision of 0.1 mm.

Since the z position of the source could be always easily measured and related to the spectrometer setup, it was not studied in a great detail. On the other hand, it became obvious that for a given series of the energy stability measurements the z position should be kept constant. In Fig. 6.14 the spectra of the K-32 line obtained at three different z positions ($z = 20, 25$ and 30 cm) are compared. The z position determines the magnetic field B_S into which the source is placed (in this case the field strengths were 2.16, 0.77 and 0.33 T, respectively), thus, also the maximal acceptance angle $\theta_{\text{start}}^{\max}$ varies with z (cf. Eq. 2.14). It was found that with increasing B_S the line background and amplitude rise, however, there seemed to be an optimal spot where the amplitude-to-background ratio A/B peaks: $A/B(2.16 \text{ T}) \simeq A/B(0.33 \text{ T}) \simeq 14$, whereas $A/B(0.77 \text{ T}) \simeq 16$. Similarly, the portion of the inelastically scattered electrons (as compared to the amplitude of the elastic peak) was found to be minimal in the "middle" case of $B_S = 0.77 \text{ T}$. Basically, one could find the optimal z position where the A/B ratio is maximal and the portion of the inelastically scattered electrons minimal. However, as this effect does not represent a significant factor, the z position was simply kept constant at a value where a sufficient count rate of the K-32 was obtained. Moreover, thanks to a good energy resolution the elastic peak was clearly separated from the structure of the inelastically scattered electrons.

Concerning the x - y position of the source, firstly a simple test of the source position reproducibility was carried out in the following manner: firstly, the K-32 line spectrum (1) was scanned at the position $[x_0, y_0, z_0]$. Then the source was moved in both x and y directions while z_0 was kept fixed. The position $[x_0, y_0, z_0]$ was set again and the spectrum (2) was obtained. The procedure was repeated once more and finally the spectrum (3) was scanned. The shifts (2) – (1) and (3) – (1) of the K-32 line positions were determined with the help of the cross-correlation method as $\Delta E_{0(2)-(1)} = 5(9) \text{ meV}$ and $\Delta E_{0(3)-(1)} = 10(8) \text{ meV}$, *i. e.* compatible with a zero shift within 1σ and 2σ , respectively. The values of the line amplitude and background were found unchanged with the uncertainties.

In addition, the influence of the displacement $[\Delta x, \Delta y]$ on the K-32 line shape was studied in two ways:

1. The x - y position of the source was varied while the currents in the auxiliary air coils were kept fixed. In this manner the $[\Delta x, \Delta y]$ displacement was directly examined with

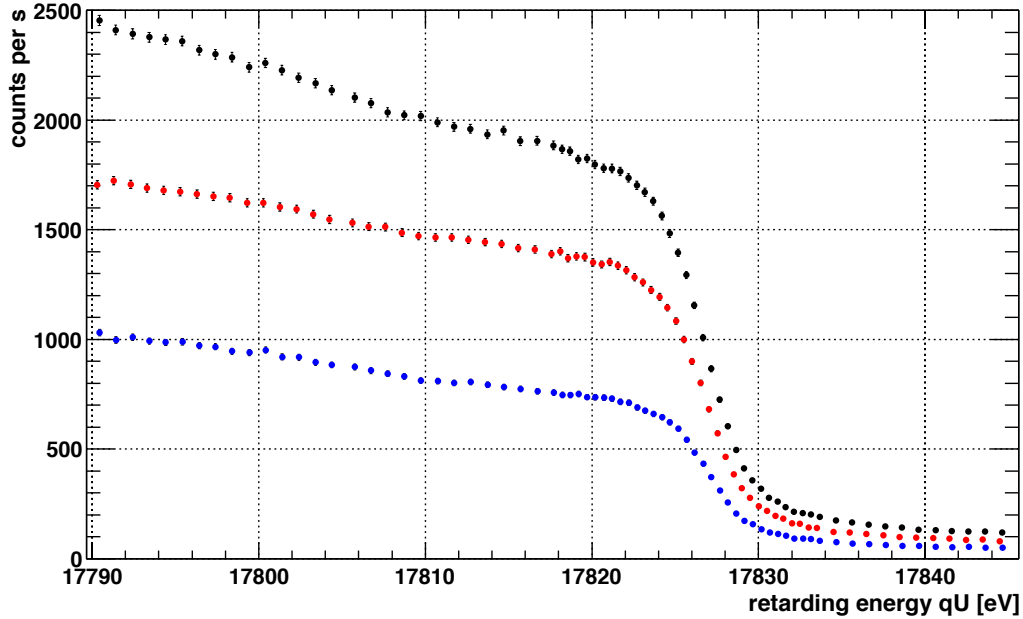


Fig. 6.14: The comparison of the integral spectra of the K -32 line measured at different z positions of the vacuum-evaporated source S28. The blue points denote the K -32 line scan at $z = 30$ cm from the solenoid B center, *i.e.* at the magnetic field of $B_S = 0.33$ T. Here the maximal acceptance angle amounted to $\theta_{\text{start}}^{\text{max}} = 14^\circ$. Similarly, the red points represent the situation $z = 25$ cm, $B_S = 0.77$ T and $\theta_{\text{start}}^{\text{max}} = 21^\circ$. Finally, the spectrum marked black was obtained at $z = 20$ cm, $B_S = 2.16$ T and $\theta_{\text{start}}^{\text{max}} = 37^\circ$. The spectrometer was set to the energy resolution of 0.9 eV at 17.8 keV and the x - y position was kept unchanged during all these scans.

the help of the K -32 line parameters: line position, amplitude and background.

2. The currents of the auxiliary air coils were varied while the x - y position of the source was kept constant. This way the magnetic flux tube was shifted with respect to the z axis of the spectrometer. In [Fla04] this test was used for aligning (“centering”) the spectrometer setup. For a well aligned setup the background rate (no electron source in the setup) should be minimal while its increase indicates that the magnetic flux tube is projecting some portion of the electrode surface onto the detector—the electrons emitted from the electrode surface are guided to the detector. Similarly, for a source well aligned with respect to the spectrometer z axis the background of the K -32 should be minimal.

The results of the test denoted (1) are summarized in Tab. 6.5. The source was displaced by ± 2 mm from the optimal position in both x and y directions. It can be seen that the shift of the K -32 line depends also on the orientation of the displacement. While the displacement by -2 mm in the x (horizontal) axis does not change the line position within uncertainties, the displacement by 2 mm in the other direction increases the K -32 line position by 73(15) meV. The line amplitude was indeed found maximal in the position $[\Delta x, \Delta y] = [0, 0]$, however, the amplitude-to-background ratio A/B was actually maximal for the position $[-2, 0]$: at $[-2, 0]$ the ratio amounted to $A/B = 13.3$ while at $[0, 0]$ it was only $A/B = 11.7$. Anyhow, during the x - y alignment of the source (carried out before this test) the position $[0, 0]$ was chosen so that the maximal amplitude was recorded and the differences of A/B were omitted.

The rather big differences of the line amplitude and background also allowed to immediately disregard or question a given measurement with respect to the proper x - y positioning if the fitted line amplitude did not follow the expected ^{83}Rb decay. In addition, it has to be noted that the source S28 did not represent a point-like source, which would be ideal for this kind of test. Instead, its ^{83}Rb distribution was determined to be of a circular shape with the diameter of 7.3 mm, see Fig. 4.2. During this test the source was placed in the magnetic field of 0.77 T and from the conservation of the magnetic flux (cf. Eq. 2.16) it follows that the diameter of the source image in the analyzing plane (magnetic field of $\approx 3 \times 10^{-4}$ T) amounted to $\simeq 39.7$ cm. Similarly, the displacement of 2 mm corresponded to the shift of about 10 cm of the source image in the analyzing plane.

Tab. 6.5: The influence of the source displacement in the x - y plane on the K -32 line of the vacuum-evaporated source S28.

		horizontal displ. Δx [mm]		
		-2	0	2
vertical displ. Δy [mm]	2		-0.036(11)	
			-24.0(2)	
			21.3(3)	
			11.3	
0		0.006(11)	0.000(7)	0.073(13)
		-8.8(2)	0.0(2)	-18.1(2)
		-20.0(3)	0.0(4)	-5.7(5)
		13.3	11.7	10.1
-2			-0.057(11)	
			-6.8(2)	
			2.9(4)	
			10.6	

The source was displaced by ± 2 mm from the optimal position which was found from maximizing the amplitude prior to the measurement series. Each box represents the weighted average of the results obtained for a given $[\Delta x, \Delta y]$ displacement. The values (top to bottom) in each box denote 1) the K -32 line position shift [eV] with respect to the value obtained at $[0, 0]$, 2) the relative change (in %) of the line amplitude with respect to the $[0, 0]$ value, 3) the relative change (in %) of the line background with respect to the $[0, 0]$ value and 4) the amplitude-to background ratio A/B . The individual integral spectra were analyzed with the help of the cross-correlation method where the reference spectrum corresponds to zero displacement.

In Fig. 6.15 the results of the test denoted as (2) on page 162 are shown. The currents in the auxiliary air coils were varied about the typically used values and at least two scans of the K -32 line were performed for each setting. The plots show a complicated structure, the dependence of each K -32 line parameter (position, amplitude, background and A/B ratio) on the coils currents exhibit a unique map. The K -32 line positions are represented as shifts with respect to the reference spectrum, taken relative to the minimal value, thus all the shifts seem to be positive. However, this does not hamper the considerations. A trend in the K -32 line position is clearly visible, the line position rises with increasing the current

of the horizontal plane coil as well as with decreasing the current of the vertical plane coil. The map of the K -32 line amplitudes exhibits a broad peak of maximal values. This peak only partly overlaps with a flat area where the minimal background was recorded. The plot of the A/B ratios reveals that actually it would have been possible to obtain a slightly better statistics with different settings than with the one typically used.

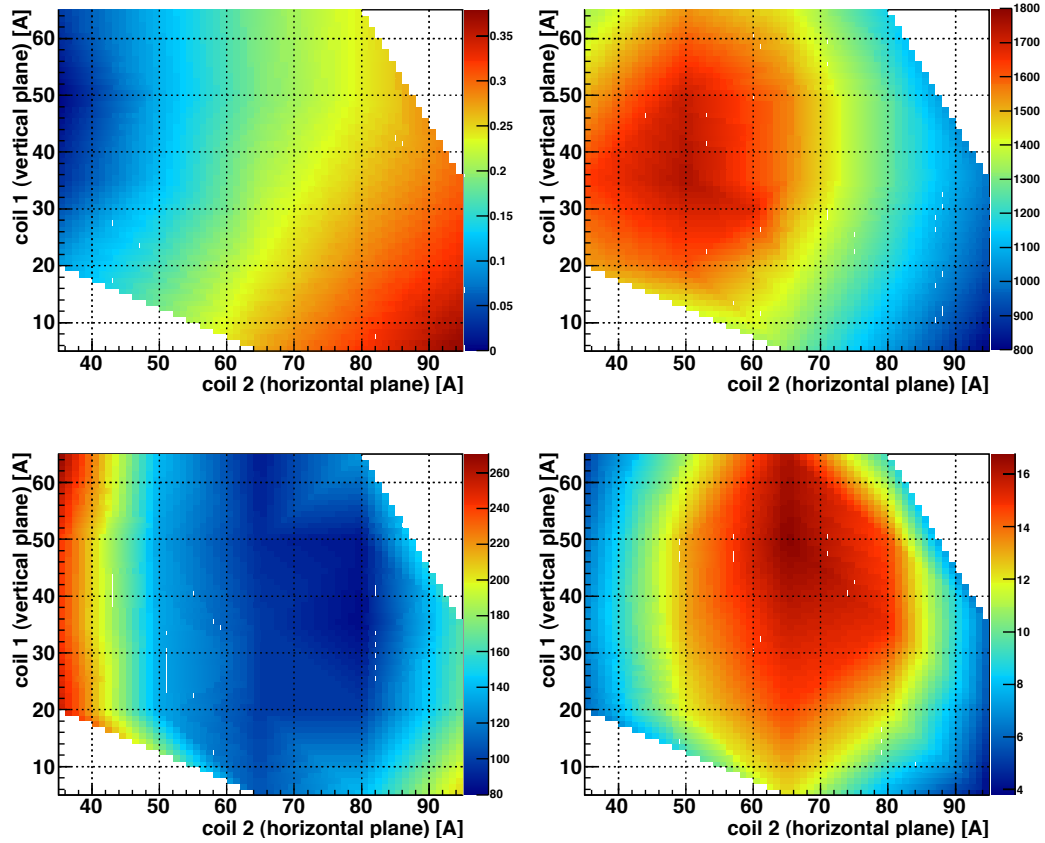


Fig. 6.15: The influence of the settings of the auxiliary air coils on the K -32 line of the vacuum-evaporated source S28. The plots depict 1) the line position shift [eV] (upper left), 2) the line amplitude [counts s^{-1}] (upper right), 3) the line background [counts s^{-1}] (bottom left) and 4) the amplitude-to-background ratio (bottom right) for various combinations of the currents [A] in the air coils. The x -axis represents the coil defining the horizontal plane, the y -axis stands for the vertical plane. The setting used typically for the energy stability measurements was $[x, y] = [60 \text{ A}, 30 \text{ A}]$. The x - y position of the source was kept fixed during this test and the spectrometer resolution was set to 0.9 eV at 17.8 keV. The individual integral spectra were analyzed with the help of the cross-correlation method. The fitted K -32 line position shifts are plotted relative to the minimal value. The measurements were carried out with a step of 15 A in both planes and the interpolation with 100 contour levels was utilized [ROO10].

In sum, it was shown that changing the currents in the auxiliary air coils affects the recorded spectrum practically in the same way as moving the source in the x - y plane. On the other hand, the malfunction of one of the auxiliary air coils would be observed as a significantly shifted spectrum or as a spectrum with a reduced A/B ratio. The stability of the 200 A power supplies driving the auxiliary air coils was specified [Del07] as better than 10^{-4} per 30 hours (constant current mode, ambient temperature $(25 \pm 1)^\circ\text{C}$) which is negligible considering the maps shown in Fig. 6.15. On the other hand, it can be seen in Tab. 6.5 and Fig. 6.15

that both positive and negative changes of the K -32 line position were observed when the source was deliberately misaligned from the measurement position or when the currents in the auxiliary air coils were changed. This points to a certain overall misalignment of the source section with respect to the spectrometer z axis: ideally, the measured line position (energy of conversion electrons) should be maximal when the source is well aligned and any misalignment from the optimal x - y source position should lead to a decrease of the measured line position due to the existence of the potential dip across the analyzing plane (cf. Sect. 5.2.2). Anyhow, as a proper overall alignment of the experimental setup would have required major efforts, the measurements went on with the existing setup in the Institute of Physics, University of Mainz, and the overall alignment of the setup was foreseen for the monitor spectrometer at the Karlsruhe Institute of Technology.

6.3. Second measurement phase: one ion-implanted and two vacuum-evaporated sources investigated simultaneously

When the sudden shift of the HV scale occurred (see Sect. 6.2.2) it was unclear which part of the overall experimental setup could be responsible for this effect. The stability of the conversion lines of the vacuum-evaporated source S 28 was questioned even on the level of 1 eV. Thanks to regular calibrations of the HV divider and a dedicated measurement of a number of conversion lines it became clear that dividing ratio M of the HV divider remained stable⁷. On the other hand, the HV scale was found to be shifted by $\simeq 0.93$ V, with the most probable reason being the HV sparks at the input of the HV divider.



This problem clearly demonstrated that an overall redundancy of the experimental method is necessary. For this reason a new type of source holder was produced which allowed to place simultaneously up to three electron sources into the setup. This way the sources could be alternately measured without a deterioration of vacuum (cf. Sect. 5.1.2). It took only a few minutes to change the sources in the measurement position so one could practically instantly switch from one source to another if some unexpected effect would occur again. As there was no other high precision HV divider available at that moment the HV divider K35 was used further for all the measurements and it was assumed that the drift $m_{\text{div}}^{\text{PTB}} = 0.60(10)$ ppm month⁻¹ remained unaffected.

The overview of the second measurement phase is given in Tab. 6.6. Besides the vacuum-evaporated sources S 28 and S 29 (described in Sect. 4.1.2) the ion-implanted source Pt-30 (see Sect. 4.2.3) was inserted into vacuum as well. Thus, the $^{83\text{m}}\text{Kr}$ conversion electron spectrum of two principally different types of the solid $^{83}\text{Rb}/^{83\text{m}}\text{Kr}$ source was investigated practically simultaneously.

⁷Strictly speaking, the dividing ratio is never stable as its drift m_{div} is non-zero. In this sense it is meant that the dividing ratio did not unexpectedly change when the HV scale shift was observed.

Tab. 6.6: The overview of the second phase of measurements carried out in 2008/2009.

calendar week no.	48	49	50	51	52-1	2	3	4	5	6	7	8-10	11	12	13	14	15-21	22	23
week of time since 26.11.2008 [day]	24.11.	01.12.	08.12.	15.12.	-	05.01.	12.01.	19.01.	26.01.	02.02.	09.02.	-	09.03.	16.03.	23.03.	30.03.	-	25.05.	01.06.
source tested	-	4	11	18	-	39	46	53	60	67	74	-	102	109	116	123	-	179	186
	S 28, S 29 and Pt-30																		
	S 28 and Pt-30																		
HV conditions	K35																		
HV divider used																			
calibration of HV divider																			
HV scale shift observed																			
vacuum conditions																			
breakdown			x	x					x				•	•	Δ				x
spectrometer bake-out		x	x			x	x								x				
electron line scanned																			
L ₁ -9.4	x	x		x							x							x	x
K-32	x	x	x	x					x	x	x	x	x	x	x	x		x	x
L ₃ -32	x	x		x							x	x	x					x	x
N _{2/3} -32	x	x		x							x	x	x	x	x			x	x

During this measurement phase the vacuum-evaporated sources S 28 and S 29 and the ion-implanted source Pt-30 were investigated simultaneously. In the calendar weeks 22 and 23 only the sources S 28 and Pt-30 were measured. In the calendar week 22 another shift of the HV scale was observed and in the week 23 the HV divider was re-calibrated. Several vacuum breakdowns occurred during this measurement phase. The box  stands for the tests with deliberate venting of the source vacuum section carried out in the weeks 11 and 12. The box  represents the test with deliberate venting of the spectrometer vessel realized in the week 13. In the weeks 52-1 and 15-21 no measurement was done due to the winter shutdown and the tests of a prototype of the calibration e-gun [Val09a], respectively.

6.3.1. Comparison of drifts of individual sources

After inserting the samples into the source section no bake-out was carried out and the vacuum level of 10^{-10} mbar was achieved with the help of the turbomolecular pump. At the beginning of the measurement series, the most prominent conversion electron lines were scanned with each source, namely L_1 -9.4, K -32, L_3 -32 and $N_{2/3}$ -32. Similarly to the first measurement phase, the conversion lines were systematically scanned, mainly the K -32 line of each of the three sources. In Fig. 6.16 the drifts of the K -32 line of each source are depicted. The instability of the experimental conditions in the first ~ 60 days is apparent in the graph. The vacuum breakdowns which are designated as vertical dashed lines in Fig. 6.16 will be discussed in detail in the next section. The time dependence of the scale factor K of the digital voltmeter is shown in Fig. 6.17. The drift of K was determined as $k_{\text{dvm}} = -0.143(7)$ ppm month $^{-1}$, thus, the behavior of the voltmeter was not different from previous measurement phases, in principle. However, in this case the drifts $m_{\text{div}}^{\text{PTB}}$ and k_{dvm} do not cancel out in Eq. 6.1, thus $d_{\text{source}} \neq d_{\text{total}}$.

In Fig. 6.18 the time dependence of the K -32 line amplitude of each source is illustrated. During the whole measurement series the spectra were taken with the sources placed in the magnetic field $B_S = 1.75$ T, thus, the amplitudes of all conversion lines of each source should in principle follow the radioactive decay of ^{83}Rb . However, it was observed that the K -32 line amplitude of the vacuum-evaporated sources was strongly affected by the vacuum breakdowns as will be discussed later. On the other hand, it was possible to describe sufficiently well the K -32 data obtained with the source Pt-30 on days 0–127 with the half-life of $t_{1/2}(K\text{-}32, \text{Pt-}30) = 85.8(3)$ d which corresponds well to the literature value.

The only time intervals in which a meaningful determination of the conversion lines drifts was possible were the days 0–15, 53–61 and 64–107, cf. Fig. 6.16. The line positions measured in these time intervals were least-squares fitted with a linear function as in previous sections. In accordance with Sect. 6.2.1 the drifts d_{total} obtained from the raw data were corrected for the drifts $m_{\text{div}}^{\text{PTB}}$ and k_{dvm} . Within the time period of days 64–107 the drifts of the L_3 -32 and $N_{2/3}$ -32 lines of the source Pt-30 were determined in addition to the drift of the K -32 line. The relevant data are shown in Fig. 6.19. The simplified model introduced in Sect. 6.2.1 again allowed to disentangle the drifts of the source and the HV divider in this time period. The drifts of the individual sources and electron lines are summarized in Tab. 6.7.

In the course of the first two weeks of the measurement the K -32 line of all three sources exhibited a negative drift of several hundreds of meV per month: the drifts of the vacuum-evaporated sources were determined as $d_{\text{source}}^{\text{abs}}(K\text{-}32, \text{S}28) = -460(25)$ meV month $^{-1}$ and $d_{\text{source}}^{\text{abs}}(K\text{-}32, \text{S}29) = -546(26)$ meV month $^{-1}$. The ion-implanted source Pt-30 exhibited the negative drift of $d_{\text{source}}^{\text{abs}}(K\text{-}32, \text{Pt-}30) = -240(7)$ meV month $^{-1}$. This behavior of the experimental setup “sources-spectrometer” was actually opposite to what was observed when the source S28 was inserted into vacuum for the first time. The negative drift of all the three sources could indicate that the spectrometer electrodes were slowly getting covered by residual gas atoms from the source section which was not baked out. This could cause a rise of ϕ_{spec} and thus the negative drift of the electron line positions.

As mentioned already, several vacuum breakdowns occurred in the course of the second measurement phase due to an imperfect safety system. They resulted in abrupt changes of the electron line positions of all sources. Precise evaluation of these effects is presented

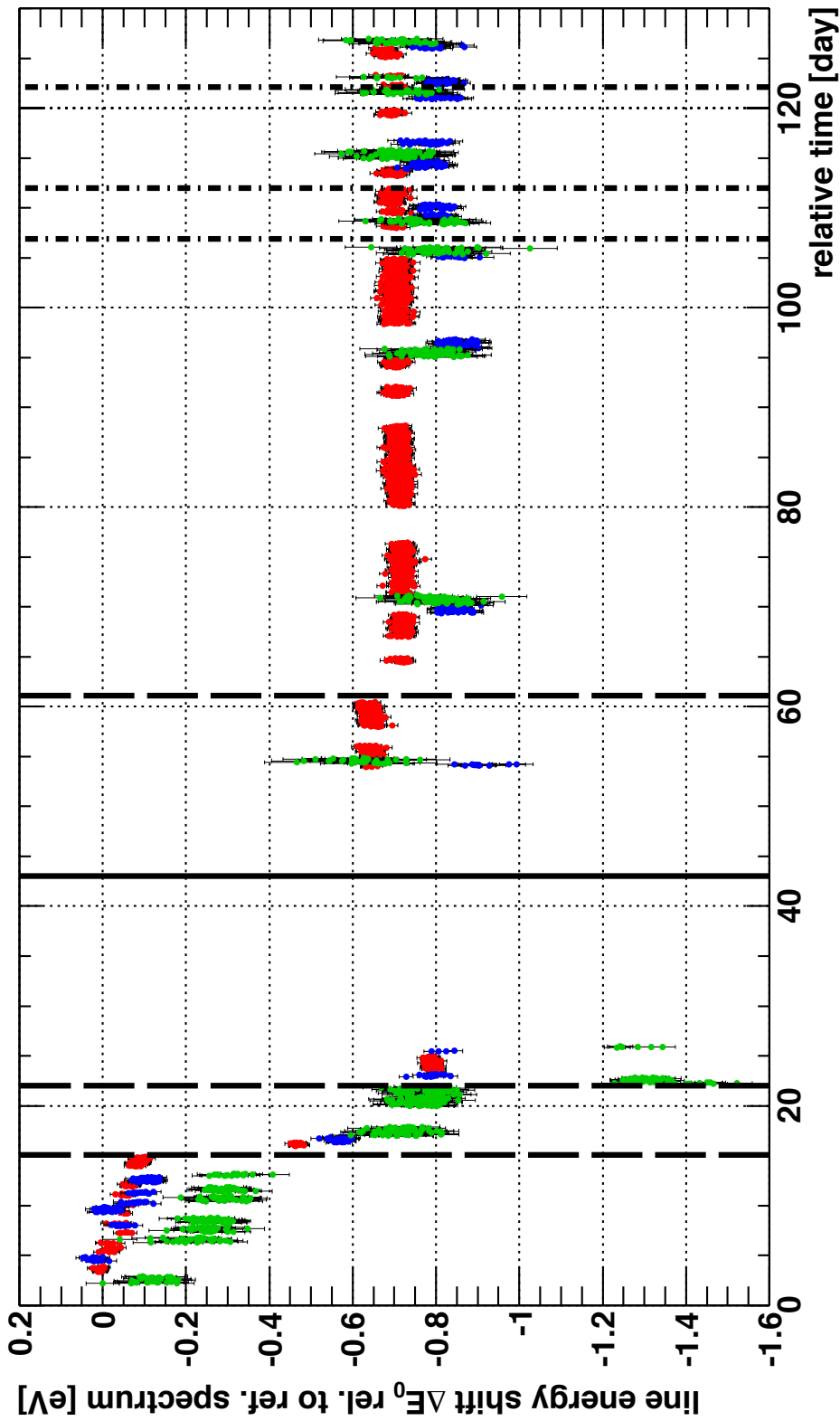


Fig. 6.16: The drifts of the K-32 line of the sources Pt-30 (red points), S28 (blue points) and S29 (green points). The x axis denotes the relative time in days since 26.11.2008. The y axis shows the line energy shift ΔE_0 relative to the reference spectrum. The full span of the y axis of 1.8 eV represents the portion of ≈ 100 ppm considering the K-32 line energy of 17 824 eV. The least-squares fits were performed with the cross-correlation method where the spectra recorded at the beginning of the measurement phase were chosen as the reference spectra. The vertical dashed lines on days 15, 22 and 61 denote the vacuum breakdowns. The solid line on day 43 represents the bake-out of the complete vacuum setup. The chain-dotted lines on days 107, 112 and 122 denote the tests of deliberate venting of the source section and the spectrometer vessel.

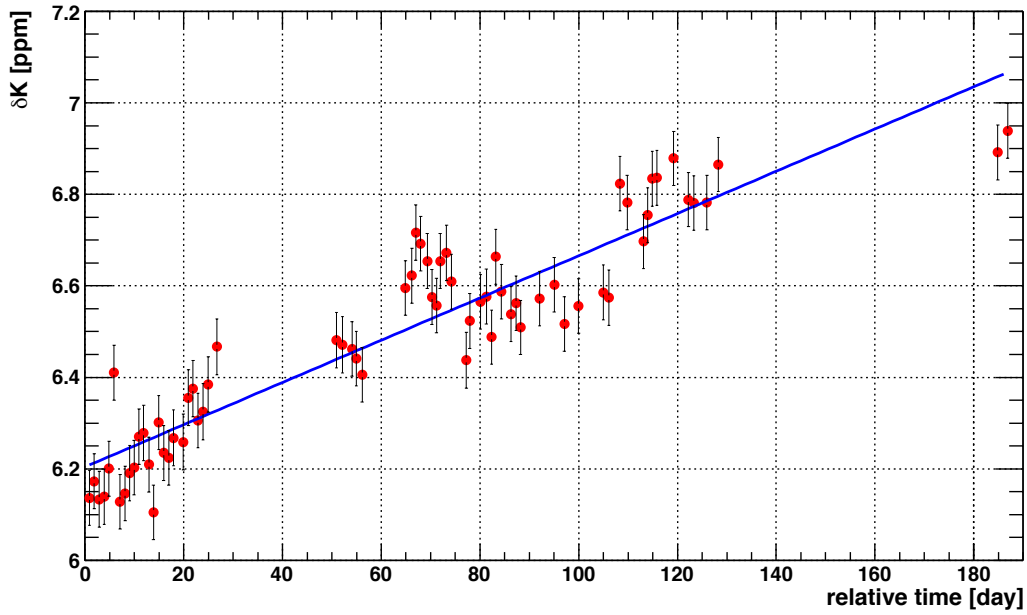


Fig. 6.17: The drift of the digital voltmeter scale factor K during the second measurement phase. The x axis denotes the relative time in days since 26.11.2008. The y axis shows the deviation δK [ppm], see the caption of Fig. 6.3. The least-squares fit with $\chi_r^2 = 2.14(17)$ yielded the drift $k_{\text{dvm}} = -0.143(7)$ ppm month $^{-1}$ (the uncertainty of which was multiplied by $\sqrt{\chi_r^2}$).

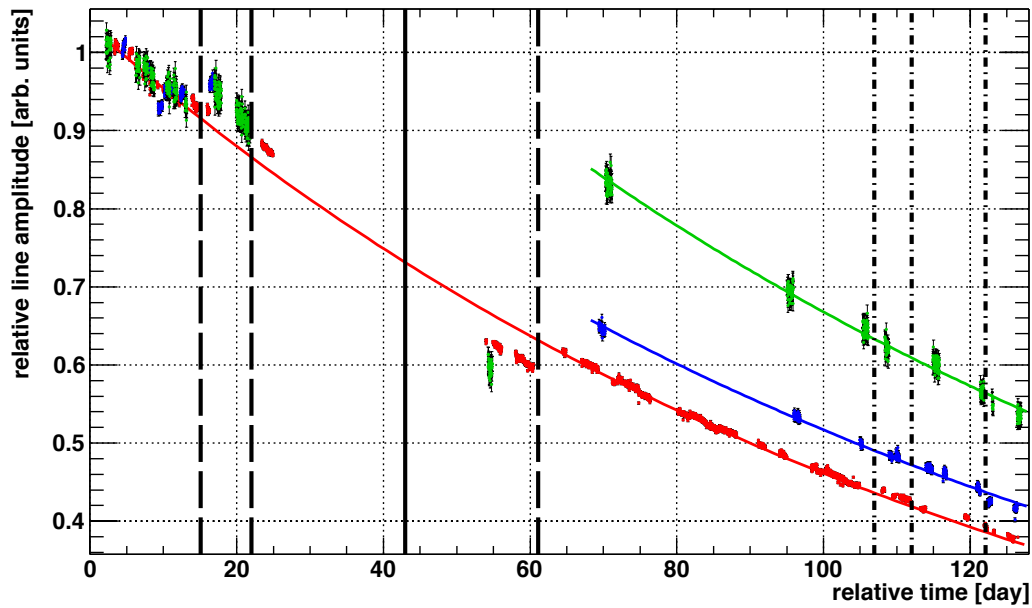


Fig. 6.18: The time dependence of the K -32 line amplitude of the sources Pt-30 (red points), S 28 (blue points) and S 29 (green points) as obtained from the fits carried out with the cross-correlation method. The time 0 corresponds to 26.11.2008. All the data sets were scaled to 1. The vertical lines have the same meaning as in Fig. 6.16. The colored lines denote the fits with an exponential function. The fit of the Pt-30 data over the full range yielded $t_{1/2}(K\text{-}32, \text{Pt-}30) = 85.8(3)$ d where the uncertainty was multiplied by $\sqrt{\chi_r^2}$ due to very large $\chi_r^2 = 95.65(3)$. Meaningful fits of the S 28 and S 29 data were possible only in the time period of days 68–128. The fits resulted in the half-lives of $t_{1/2}(K\text{-}32, \text{S } 28) = 91.5(4)$ d and $t_{1/2}(K\text{-}32, \text{S } 29) = 90.5(5)$ d with the χ_r^2 values of 4.08(7) and 1.10(7), respectively.

Tab. 6.7: The drifts of the K-32, L₃-32 and N_{2/3}-32 lines measured with three solid electron sources S28, S29 and Pt-30.

source	time period [day]	data set	χ_r^2 of fit	absolute [eV]	linear fit parameters [meV month ⁻¹]	relative drift $d_{\text{source}}^{\text{rel}}$ [ppm month ⁻¹]
					linear	
S28	0-15	K-32	2.4(1)	$99(8) \times 10^{-3}$	-460(25)	-25.8(14)
	64-107	K-32	0.8(1)	-0.84(1)	6(4)	0.34(24)
S29	0-15	K-32	0.98(9)	$-92(8) \times 10^{-3}$	-546(26)	-30.6(15)
	64-107	K-32	0.9(1)	-0.81(3)	11(9)	0.61(48)
Pt-30	0-15	K-32	0.7(1)	$31(2) \times 10^{-3}$	-240(7)	-13.5(4)
	53-61	K-32	0.94(9)	-0.69(3)	31(13)	1.77(74)
		K-32	0.85(4)	-0.749(3)	21(1)	1.20(5)
		L ₃ -32	0.1(5)	-0.76(3)	24(10)	0.80(32)
		N _{2/3} -32	12.4(3)	$-90(85) \times 10^{-3}$	35(28)	1.10(88)
	64-107	K-32 & L ₃ -32	source drift $d_{\text{source}}^{\text{abs}} = 17(15)$ meV month ⁻¹ divider drift $m_{\text{div}} = -0.33(85)$ ppm month ⁻¹			
		K-32 & N _{2/3} -32	source drift $d_{\text{source}}^{\text{abs}} = 4(10)$ meV month ⁻¹ divider drift $m_{\text{div}} = 0.38(56)$ ppm month ⁻¹			

The data depicted in Fig. 6.16 and Fig. 6.19 were least-squares fitted with a linear function. The uncertainties of the fit results were multiplied by $\sqrt{\chi_r^2}$ in the cases where $\chi_r^2 \gg 1$. The procedure described in Sect. 6.2.1 was used for disentangling the drifts of the source Pt-30 and the HV divider on the basis of the pairs of data a) K-32 & L₃-32 and b) K-32 & N_{2/3}-32 in the time period of days 64-107. Not listed is the calculation based on the pair of data L₃-32 & N_{2/3}-32 which resulted in the drifts $d_{\text{source}}^{\text{abs}} = -169(245)$ meV month⁻¹ and $m_{\text{div}} = 6(8)$ ppm month⁻¹. Obviously, these values suffer from the fact that the L₃-32 and N_{2/3}-32 are too closely spaced in the spectrum (the energy difference is only 1.7 keV) as otherwise the drifts of both conversion lines were small, of the order of 1 ppm month⁻¹.

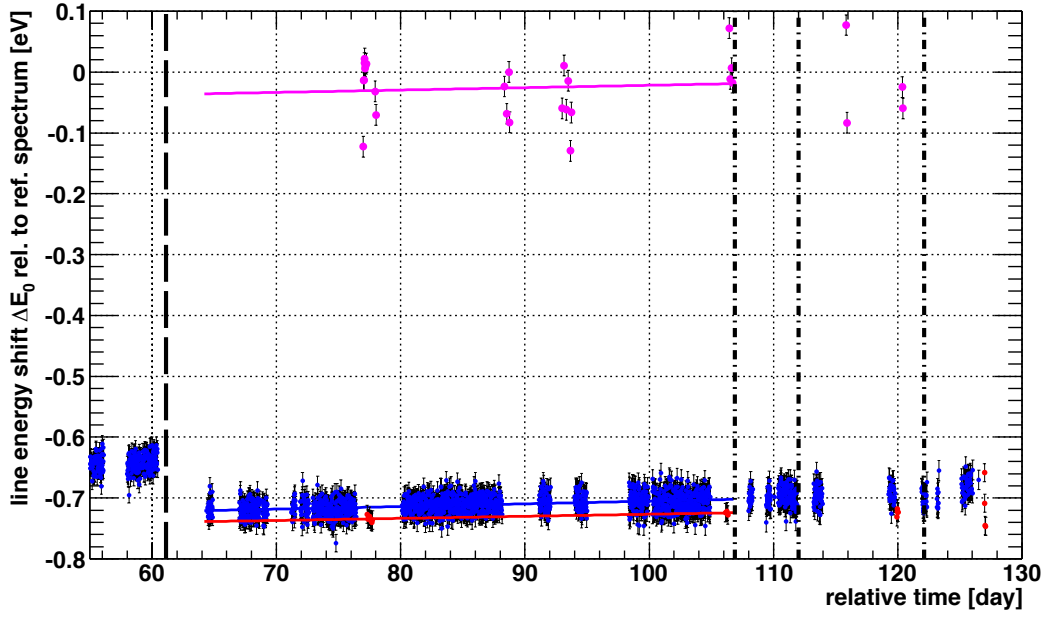


Fig. 6.19: The drifts of the K-32 (blue points), L_3 -32 (red points) and $N_{2/3}$ -32 (magenta points) line positions of the source Pt-30 measured in the time period of days 64–107. The x axis denotes the relative time in days since 26.11.2008. The y axis shows the line energy shift ΔE_0 relative to the reference spectrum. The vertical lines have the same meaning as in Fig. 6.16. The offset of the $N_{2/3}$ -32 data set with respect to the K-32 and L_3 -32 data sets stems from the use of the reference spectra obtained at different moments of the measurement phase. However, only the drift, *i.e.* the slope of the linear functions, is of interest here.

in Sect. 6.3.2. At the beginning of year 2009 the complete vacuum system was baked out for about two weeks. After the bake-out the K-32 line was measured with all the three sources and enough data was collected for determining the drift of the K-32 line position of the source Pt-30 as $d_{\text{source}}^{\text{abs}}(\text{K-32, Pt-30}) = 31(13) \text{ meV month}^{-1}$. On day 61 a complete power outage caused another vacuum breakdown. The system was evacuated again down to the 10^{-10} mbar region but no bake-out was performed after this vacuum problem. In the time period of days 64–107 the measurement of various conversion electron lines of all sources went on without disturbances. The drift of the K-32 line of all sources was found to be relatively low: $d_{\text{source}}^{\text{abs}}(\text{K-32, S28}) = 6(4) \text{ meV month}^{-1}$, $d_{\text{source}}^{\text{abs}}(\text{K-32, S29}) = 11(9) \text{ meV month}^{-1}$ and $d_{\text{source}}^{\text{abs}}(\text{K-32, Pt-30}) = 21(1) \text{ meV month}^{-1}$. The common positive drift can be interpreted as a slow recovery of ϕ_{spec} after the vacuum breakdown, *i.e.* the electrodes were slowly getting clean during the continuous operation of the main turbomolecular pump.

In addition, within the time period of days 64–107 the drift of the L_3 -32 and $N_{2/3}$ -32 lines of the Pt-30 source were determined as $d_{\text{source}}^{\text{abs}}(\text{L}_3\text{-32, Pt-30}) = 24(10) \text{ meV month}^{-1}$ and $d_{\text{source}}^{\text{abs}}(\text{N}_{2/3}\text{-32, Pt-30}) = 35(28) \text{ meV month}^{-1}$. This allowed to disentangle the drifts of the source and the HV divider. Taking into account the pair of the K-32 and L_3 -32 lines, the source drift amounted to $d_{\text{source}}^{\text{abs}} = 17(15) \text{ meV month}^{-1}$ while the divider drift was determined as $m_{\text{div}} = -0.33(85) \text{ ppm month}^{-1}$. Similarly, considering the lines K-32 and $N_{2/3}$ -32, the source drift reduces to $4(10) \text{ meV month}^{-1}$ while the divider drift becomes $0.38(65) \text{ ppm month}^{-1}$. In principle, it is possible to calculate the drifts $d_{\text{source}}^{\text{abs}}$ and m_{div}

on the basis of the L_3 -32 and $N_{2/3}$ -32 data. However, this result suffers from the fact that these lines are too closely spaced in the $^{83\text{m}}\text{Kr}$ conversion electron spectrum. The drifts $d_{\text{source}}^{\text{abs}} = -169(245) \text{ meV month}^{-1}$ and $m_{\text{div}} = 6(8) \text{ ppm month}^{-1}$ have indeed too large uncertainties. Both the calculations based on the data pairs K -32 & L_3 -32 and K -32 & $N_{2/3}$ -32 produced results which are compatible with each other within 1σ . The m_{div} values are also compatible with $m_{\text{div}}^{\text{PTB}}$. This supports the assumption that the divider K35 was performing well according to specifications even after the HV scale was found to be shifted by $\simeq 0.93 \text{ V}$.

To summarize, all the three sources exhibited considerably high negative drifts of the K -32 line in the first two weeks after they were inserted into vacuum. Later, after the bake-out of the complete setup the drift of the K -32 line of the source Pt-30 got reduced to several tens of meV per month. Finally, all the three sources exhibited a small drift of the K -32 line within about 40 days of measurement. During this time period the drifts of the vacuum-evaporated sources were compatible within 1σ uncertainty while the ion-implanted source Pt-30 exhibited the drift by the factor of 2–3 larger. It was noticeable that vacuum conditions strongly influence the measurements of the energy stability of the conversion lines in the sense that ϕ_{spec} was a) changed abruptly or b) slowly varying in time.

6.3.2. Changes of vacuum conditions due to breakdowns and bake-out

The setup of the source section and the overall vacuum system were described in Sect. 5.1.2 and Sect. 5.1.4, respectively. It has to be noted that all the measurement phases carried out at Mainz MAC-E filter suffered from an imperfect slow control system concerning the vacuum system. The slow control system developed in the framework of the Mainz Neutrino Mass Experiment was stripped down to a very basic one. In addition, due to the lack of manpower it was not possible to run the measurements under constant operator control. In order to obtain high statistics of data, the automatized measurement ran practically without interruption. Moreover, in order to increase the observed count rate of the conversion electrons, both the source holder and the detector holder were placed in the bores of the solenoids B and A (cf. Fig. 5.1), thus the automatic closing of the pneumatic gate valves was not possible. This way the experimental setup was strongly affected by several power outages which interrupted the operation of the main turbomolecular pump evacuating the spectrometer vessel. As a result, residual gas filled the complete setup and the pressure rose typically from 10^{-10} to 10^{-5} mbar or even worse. In the literature the unit of langmuir (L) is used to describe the exposure of a surface to the adsorption of gases. One langmuir corresponds to the exposure of the surface to a gas at 10^{-6} Torr for 1 second [IUP93]. In our case the typical residual gas exposure of the vacuum setup surface amounted to $\approx 10^{-5}$ mbar for $\simeq 1$ hour, thus, one can quantify the effect as $\approx 36 \text{ kL}$ (kilolangmuir).

During the second measurement phase there were altogether three vacuum breakdowns, cf. Fig. 6.16. They occurred on days 15, 22 and 61. The first vacuum breakdown occurred during a moderate heating of the source section⁸. The source section was separated from the

⁸The reason for heating of the sources was the assumption that the physical/chemical processes, probably taking place on the surface of the sources after inserting them into vacuum, could be speeded up this way.

spectrometer vessel by the gate valve and the HV was set to zero. The pressure in the spectrometer vessel went up to 2×10^{-5} mbar. Furthermore, the pressure in the detector section went even up to the order of 1 mbar. Once the vacuum was recovered from the breakdown, a very moderate bake-out of the spectrometer vessel at 90°C for about 12 hours was performed. The measurement went on at a rather poor vacuum level of 7×10^{-9} mbar in the main vessel. As the second vacuum breakdown occurred on day 22, the source section was connected to the spectrometer vessel and the HV of -17.8 kV was applied to the spectrometer electrodes. After recovering the vacuum to the level of 4×10^{-9} mbar the measurement continued (without any bake-out) within 5 hours after the problem appeared. A thorough bake-out of the complete vacuum system was performed on days 43–50 and since day 51 a regular measurement went on. On day 61 the third vacuum breakdown occurred due to a total power outage in the laboratory. At this moment the sources were placed in the bore of the solenoid B and the HV of -17.8 kV was applied to the spectrometer electrodes as in the case of the second breakdown. After about 24 hours pump-down the vacuum improved to 4×10^{-10} mbar and the measurements carried on without any bake-out.

The effects of the first two vacuum breakdowns on the K -32 line of all the three sources are depicted in Fig. 6.20. The sudden drop of the K -32 line positions of about -0.4 eV is clearly visible. This observation can be explained as an abrupt increase of ϕ_{spec} upon the residual gas adsorption. The colored dashed lines in Fig. 6.20 represent the extrapolation of the linear drifts which were determined in the first two weeks of the measurement. However, it can be argued that the negative drifts would probably become less steep as the electron line positions would stabilize in time. For this reason only the values obtained prior and after each vacuum breakdown will be considered and mutually compared.

The changes of the K -32 line amplitude are shown in Fig. 6.21. Interestingly, after the first vacuum breakdown (sources separated from the spectrometer) the K -32 line amplitudes of all sources were recorded to be by the factor $\simeq 1.05$ higher than what would be expected due to the ^{83}Rb radioactive decay. However, after the second breakdown, when the sources were directly affected by the abrupt change of vacuum conditions as well, the K -32 line amplitudes of the vacuum-evaporated sources rose even further. In Fig. 6.21 the stabilization of the K -32 line amplitude of the source S 29 at a new level is visible. This level was by the factor $\simeq 1.7$ higher than the expected value. Similarly, the source S 28 exhibited an increase by the factor of $\simeq 1.2$. On the other hand, the K -32 line amplitude of the source Pt-30 remained on the new level (factor 1.05) and was not further affected by the second breakdown. The position shifts and amplitude changes of the conversion lines resulting from the first two vacuum breakdowns are summarized in Tab. B.1. Besides the $\simeq 37\%$ drop of the amplitude in the L_1 -9.4 line—affected anyhow probably by the ADC low level discriminator—and a slight ($\simeq 6\%$) increase of the L_3 -32 line the source Pt-30 remained unaffected by the two vacuum breakdowns. The vacuum-evaporated sources both experienced a significant increase of all line amplitudes except the L_1 -9.4 line which showed a drop of the line amplitude and background similarly to the Pt-30 source. This effect can be attributed to a change of the noise level in the detector electronic chain. The pronounced increase of the line amplitude observed in the rest of the cases should be ascribed to the vacuum-evaporated sources themselves. A layer of residual gas could be adsorbed on the graphite foils and affect the ^{83}Rb atoms in such a way that the $^{83\text{m}}\text{Kr}$ retention was increased.

It was assumed that heating at $\simeq 100^\circ\text{C}$ would stabilize the electron line positions of the sources.

6. Long-term measurements...

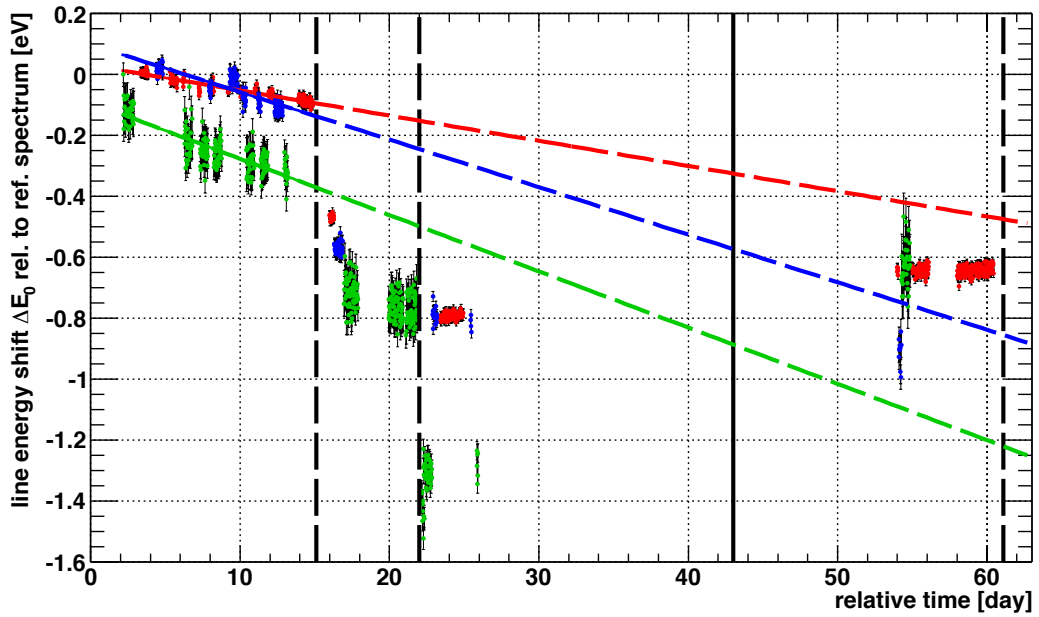


Fig. 6.20: The drifts of the K -32 line of the sources Pt-30 (red points), S 28 (blue points) and S 29 (green points). The x axis denotes the relative time in days since 26.11.2008. The y axis shows the line energy shift ΔE_0 relative to the reference spectrum. The vertical dashed lines on days 15, 22 and 61 denote the vacuum breakdowns. The solid line on day 43 represents the bake-out of the complete vacuum setup. The data sets obtained in the time period of days 0–15 were individually least-squared fitted with a linear function and the trends were extrapolated as indicated by the colored dashed lines.

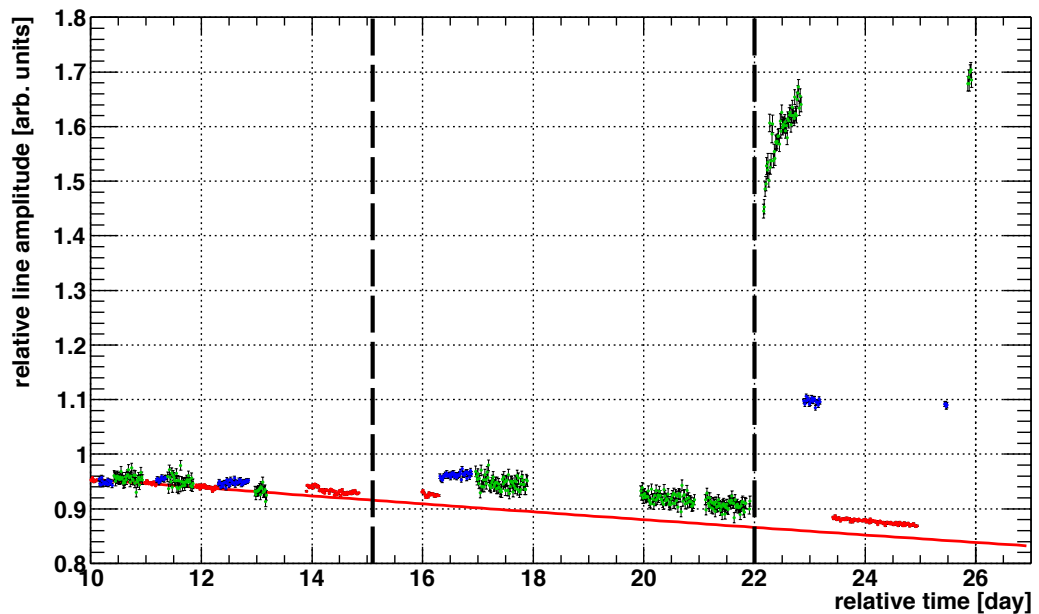


Fig. 6.21: The time dependence of the K -32 line amplitude of the sources Pt-30 (red points), S 28 (blue points) and S 29 (green points) as obtained from the fits carried out with the cross-correlation method. The time 0 corresponds to 26.11.2008. All the data sets were scaled to 1. The plot shows the same data as in Fig. 6.18, however, here the focus is made on the effects of the vacuum breakdowns (vertical dashed lines) on the K -32 line amplitude. The red line represents the fit of the Pt-30 data over the range of days 0–127 as in Fig. 6.18.

A thorough bake-out of the complete vacuum setup was performed after the second vacuum breakdown. However, after about 10 days of measurement a third vacuum breakdown occurred due to a total power outage in the laboratory. The effects on the line positions and amplitudes are summarized in Tab. B.2. After the bake-out the K -32 line position shifts of the sources Pt-30 and S29 were found to be positive while the shift of the source S28 was negative. In addition, in all the three cases the K -32 line amplitude significantly dropped while the line background increased. This rather odd behavior should be probably ascribed to a possible misalignment of the sources with respect to the spectrometer z axis. The x - y positions of the sources were probably set incorrectly prior to the scans of the conversion lines. It was seen in Sect. 6.2.4 that the misalignment of 2 mm of the source in the x - y plane can cause the change of the line amplitude and background as large as 20 %, depending on the direction in the x - y plane. Similarly, the third vacuum breakdown resulted in inconsistent shifts of the K -32 line. This time significant increase of the K -32 line amplitude and background were observed. These observations together with the plot in Fig. 6.18 suggest that the measurements carried out in the time period of days 53–61 should be considered with caution.

The vacuum conditions got stabilized after the third vacuum breakdown, however, the measurements of the energy stability of the conversion electron lines went on without further bake-out of the system. As can be seen in Fig. 6.18 the K -32 line data of the source Pt-30 could be relatively well described on the whole range by the radioactive decay curve. The only significant deviations from this curve were observed in the time period between days 15 and 61. On the other hand, the K -32 line amplitude of the sources S28 and S29 was found to be on an entirely new level after all the vacuum-related problems. It should be kept in mind that the observed changes of the line positions and amplitudes result from the combination of the following effects:

1. effect of the source itself (change of ϕ_{source} and other effects),
2. change of the spectrometer work function ϕ_{spec} ,
3. misalignment of the source.

Ideally, the effect (3) should be negligible, however, it cannot be excluded from the considerations. In the next section the effect (1) will be discussed in detail. The effect (2) should be visible in the first vacuum breakdown (day 15) where the sources were separated from the spectrometer vessel during their moderate heating. If one neglects the effect of the heating on the sources (100°C for 6 hours) then the drop of $\simeq 0.4$ eV of the K -32 line observed with all the three sources corresponds to the positive change of ϕ_{spec} .

Changes of surface work function upon gas adsorption were studied over decades using various techniques ranging from photoelectric technique to Kelvin vibrating capacitor method. Generally, the work function of metal is *lowered* when the surface becomes contaminated [Sch09, Hub66, Eas70, Wel72]. This is the result of the contamination layer “pushing back” the conduction band electrons, thereby reducing the surface dipole. In [Dar73] the stainless steel surface was studied with the help of a Kelvin probe and work function changes upon hydrogen adsorption, charged particles trapping, illumination and electric fields were observed. The work function of stainless steel was found stable in ultrahigh vacuum and after short exposures to hydrogen at pressures below 10^{-6} mbar. It was disturbed, however, by prolonged exposures to hydrogen, illumination, incident charged particles and electric fields. These effects could not easily be explained if the surface was metallic. They were

qualitatively consistent with a hypothesis that the metal surface was oxidized and that the change in work function was due to changes in the density of charge trapped in states either within or on the oxide surface [Dar73].

In this sense the surface of the stainless steel electrode is probably not behaving strictly as metal. In addition, even in vacuum of 10^{-10} mbar the formation time of 1 monolayer of rest gas on a unit area is typically 6 hours [Rot98]. Thus, during the long-term measurements of the energy stability of the solid electron sources the electrode surface is probably not clean. Instead, some stable oxide layer is formed in the course of weeks/months of stable operation of the spectrometer vacuum system. Later, during the vacuum breakdown a considerable amount of oxygen and water vapor can be further adsorbed onto the electrode surface. On the other hand, in several cases there was the HV of typically -18 kV applied to the electrode when the vacuum breakdown occurred. The discharge could also sputter away the adsorbed atoms from the electrode surface. Therefore the vacuum breakdowns represent abrupt changes of vacuum conditions with unpredictable results and they should be certainly avoided during the operation of the monitor spectrometer in the Karlsruhe Institute of Technology.

6.3.3. Tests with deliberate venting of the vacuum setup

It was seen in previous section that abrupt changes of the vacuum conditions resulting from vacuum breakdowns were possibly influencing both the solid sources and the spectrometer work function. In order to disentangle these two notions, several tests with venting of the vacuum setup were carried out. The source section was deliberately vented in order to simulate the vacuum breakdowns which accidentally occurred beforehand. However, this time it was ensured that the spectrometer vessel was not affected by the venting procedure at all. Therefore, ϕ_{spec} could be assumed as constant and any shift of the electron lines should be ascribed to the sources. In addition, during the tests attention was paid to proper alignment of the sources.

The shifts of the conversion electron lines are summarized in Tab. 6.8 and illustrated in Fig. 6.22. Firstly, on day 107 the source section was separated from the spectrometer vessel via the gate valve. The vacuum levels in the source section and in the spectrometer vessel were recorded as 4×10^{-9} mbar and 3×10^{-10} mbar, respectively. The turbomolecular vacuum pump evacuating the source section was stopped and the pressure rose up to 10^{-3} mbar. Still, no air was introduced into the system. After several minutes the vacuum pump was started again and the source section was evacuated for about 24 hours. After that the source section was connected to the spectrometer vessel, sources were aligned in the measurement position and the K -32 line of all the three sources was scanned and compared with the measurements done just prior to the test. The shift of the K -32 line position of the source Pt-30 was determined to be as small as 5(4) meV while the sources S 28 and S 29 exhibited positive shifts of the order of 90 meV and 140 meV, respectively.

On day 112 the test was repeated, however, this time the air was introduced to the vacuum system of the source section while the turbomolecular pump was still evacuating the system. This way a real vacuum breakdown accident was reproduced. Later, the vacuum pump was switched off and the pressure went up to 10^{-1} mbar. Again, after about 28 hours

Tab. 6.8: The overview of the K -32 and $N_{2/3}$ -32 line position shifts observed with the sources Pt-30, S 28 and S 29 as a result of deliberate venting of the source section.

source	electron line	$\Delta E_0(1)$ [eV] "before"	$\Delta E_0(2)$ [eV] "after"	difference [eV] $\Delta E_0(2) - \Delta E_0(1)$
source section vented up to 10^{-3} mbar, day 107				
Pt-30		-0.019(2)	-0.014(3)	0.005(4)
S 28	K -32	-0.057(6)	0.033(5)	0.089(8)
S 29		-0.183(12)	-0.044(21)	0.139(24)
source section vented up to 10^{-1} mbar, day 112				
Pt-30		-0.006(3)	-0.002(3)	0.005(4)
S 28	K -32	-0.004(10)	0.028(4)	0.032(11)
S 29		-0.013(24)	0.094(19)	-0.107(31)
combined effect of the two tests				
Pt-30		0.001(28)	0.003(70)	0.002(75)
S 28	$N_{2/3}$ -32	-0.039(67)	-0.145(21)	-0.106(70)

The spectra were analyzed with the help of the cross-correlation method. For each electron line a spectrum recorded shortly prior to the test was taken as the reference. Thus, the values in the column "before" are close to zero, however, they might be non-zero as typically a group of 10–20 spectra was analyzed in each situation and the results were averaged.

pump-down the K -32 lines were scanned. The shift of the K -32 line of the source Pt-30 was determined to be identical to that one caused by the first venting test, 5(4) meV. The shift of the K -32 line position of the source S 28 was recorded as 32(11) meV, while the source S 29 exhibited the negative shift of $-107(31)$ meV. The changes of the line amplitude and background were below 3% in all cases during the first venting test and below 1% in all cases of the second test. In the case of the sources Pt-30 and S 28 it was also possible to determine the changes of the $N_{2/3}$ -32 line position induced by both venting tests. The shifts of the $N_{2/3}$ -32 line position were determined as 2(75) meV (Pt-30) and $-106(70)$ meV (S 28). Clearly, the shifts of the electron lines observed with the Pt-30 are consistent and compatible with zero within 2σ . On the other hand, the vacuum-evaporated sources were proven to be sensitive to vacuum conditions and susceptible to changes of the line position of the order of tens of meV. The stability of the ion-implanted source against the vacuum conditions represents a major advantage of this type of source over the vacuum-evaporated ones as well as over the condensed ^{83m}Kr source.

In order to assess the effect of venting of the spectrometer vessel on the value of ϕ_{spec} , a third venting test was carried out on day 122. This time the source section and the detector sections were separated from the spectrometer vessel and only the main vessel was vented from 3×10^{-10} mbar up to 10^{-4} mbar. The turbomolecular pump evacuating the spectrometer vessel was kept on running and the HV was set to zero prior to the test. As the spectrometer vessel was vented for about 5 minutes one can quantify this effect as 30 kL. The shifts of the K -32 line are depicted in Fig. 6.22 and summarized in Tab. 6.9. The results are

rather inconsistent: the source Pt-30 exhibited the shift of $-6(9)$ meV, *i. e.* compatible with zero. The source S 28 exhibited the negative shift of $-33(6)$ meV while the shift of the K-32 line of the source S 29 was determined to be slightly positive, $39(33)$ meV. Thus, the observation of a common shift of the K-32 lines of -0.4 eV due to the first vacuum breakdown was not reproduced by this venting test. The only principal difference between these two events was the fact that during the venting test the turbomolecular pump was still running while its operation was automatically stopped as a result of the vacuum breakdown. One can therefore speculate about the fore-vacuum gas back-streaming into the setup in the case when the turbomolecular pump was switched off.

On day 123 a moderate bake-out of the spectrometer vessel was carried out, the spectrometer was heated to 180°C for about 40 hours. The K-32 line of all sources exhibited a positive shift, the sources Pt-30 and S 28 showed a consistent shift of the order of 20 meV. The source S 29 exhibited the shift of $99(38)$ meV. It should be noted that no significant changes of the amplitude and background values were observed in both cases of the spectrometer venting (changes below 2 %) and the spectrometer bake-out (changes below 1 %).

Tab. 6.9: The overview of the K-32 line position shifts observed with the sources Pt-30, S 28 and S 29 as a result of deliberate venting of the spectrometer vessel and a moderate bake-out.

source	electron line	$\Delta E_0(1)$ [eV] "before"	$\Delta E_0(2)$ [eV] "after"	difference [eV] $\Delta E_0(2) - \Delta E_0(1)$
spectrometer vessel vented up to 10^{-4} mbar, day 122				
Pt-30		$-0.017(7)$	$-0.023(6)$	$-0.006(9)$
S 28	K-32	$-0.003(5)$	$-0.035(4)$	$-0.033(6)$
S 29		$-0.116(8)$	$-0.077(32)$	$0.039(33)$
moderate bake-out of spectrometer vessel, day 123				
Pt-30		$-0.003(6)$	$0.013(2)$	$0.016(7)$
S 28	K-32	$0.042(4)$	$0.062(6)$	$0.020(8)$
S 29		$0.019(35)$	$0.118(15)$	$0.099(38)$

See the caption of Tab. 6.8 for the explanation.

6.3.4. Sudden unexpected change of the high voltage divider scale factor

The second phase of the long-term energy stability measurements of the solid $^{83}\text{Rb}/^{83\text{m}}\text{Kr}$ sources was stopped on day 128, the samples Pt-30, S 28 and S 29 were removed from vacuum and stored on air. Within the time period of days 128–170 the spectrometer setup at Mainz was used for tests of other calibration devices foreseen for the KATRIN experiment. Meanwhile, the HV divider K35 was refurbished in the Institute of Nuclear Physics, University of Münster, and transported back to the Institute of Physics, University of Mainz.

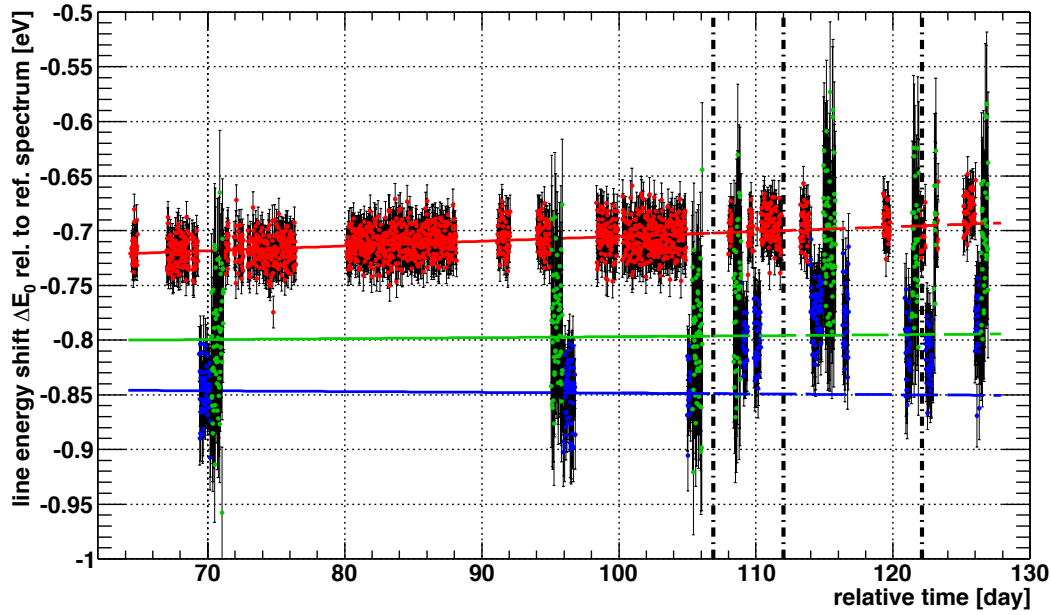


Fig. 6.22: The shifts of the K -32 line of the sources Pt-30 (red points), S28 (blue points) and S29 (green points) resulting from the tests of deliberate venting of the vacuum setup. The x axis denotes the relative time in days since 26.11.2008. The y axis shows the line energy shift ΔE_0 relative to the reference spectrum (the reference spectra are identical to those used in Fig. 6.16). The full span of the y axis of 0.5 eV represents the portion of ≈ 28 ppm considering the K -32 line energy of 17 824 eV. The vertical chain-dotted lines on days 107 and 112 denote the deliberate venting of the source section, see Tab. 6.8. The vertical chain-dotted line on day 122 represents the test of deliberate venting of the spectrometer vessel, see Tab. 6.9. The colored lines stand for the fits of the corresponding data sets on the range of days 64–107, while their extrapolation to the range “day > 107” is marked with the dashed style.

On day 177 the sources Pt-30 and S28 were placed back into vacuum and the source section was heated up to 120°C for 24 hours. The weak source S29 was omitted this time because this measurement was considered as a minor additional test prior to the third measurement phase with new ion-implanted sources.

The z position of the sources with respect to the center of the solenoid B was reproduced with the precision of 1 mm. The arrangement of the two sources in the source holder was different from the one used previously in the case of three sources measured simultaneously. Moreover, there was no unique way of orienting the foils in the x - y plane so the only possible way of positioning the sources was to look for the maximal count rate. On days 185–189 the various conversion electron lines of both sources were scanned and compared to the data obtained before the day 128. The shifts of the line positions are summarized in Tab. 6.10. The shifts shown in the column marked “after” were all measured on days 185–189 without any disturbances (no vacuum breakdown *etc.*). However, the data shown in the column marked “before” were obtained in the course of the second measurement phase where the aforementioned vacuum breakdowns, venting tests *etc.* took place. For each electron line only the measurement carried out closest to the end of the measurement phase was considered. In Tab. 6.10 the circumstances of each “before”-measurement are stated.

Tab. 6.10: The overview of the line position shifts of various conversion lines observed with the sources Pt-30 and S 28 as a result of sudden change of the scale factor of the HV divider K35.

source	electron line	$\Delta E_0(1)$ [eV] "before"	$\Delta E_0(2)$ [eV] "after"	difference [eV]	$\Delta E_0(2) - \Delta E_0(1)$ [ppm]
Pt-30	L_1 -9.4	-0.062(51)	-0.602(90)	-0.54(10)	-72(14)
	<i>day 76 (after 3rd vac. breakdown); changes in amplitude and background values (in %): -47 / -22</i>				
	M_1 -9.4	-0.072(71)	-0.602(96)	-0.53(12)	-58(13)
	<i>day 79 (after 3rd vac. breakdown); -26 / -16</i>				
	K-32	0.008(2)	-1.372(13)	-1.38(1)	-77.4(7)
<i>day 125 (after spec. bake-out); -32 / -25</i>					
	L_3 -32	0.026(18)	-2.080(19)	-2.11(3)	-69.1(9)
<i>day 127 (after spec. bake-out); -32 / -21</i>					
	$N_{2/3}$ -32	-0.009(9)	-2.116(5)	-2.11(1)	-65.6(3)
<i>day 120 (after 2nd venting of sources); -35 / -79</i>					
S 28	L_1 -9.4	0.046(39)	-1.087(114)	-1.13(12)	-152(16)
	<i>day 25 (after 2nd vac. breakdown); -36 / +23</i>				
	K-32	0.030(7)	-1.594(11)	-1.62(1)	-91.1(7)
	<i>day 126 (after spec. bake-out); -66 / -66</i>				
	L_3 -32	-0.001(5)	-2.600(45)	-2.60(5)	-85(2)
<i>day 127 (after spec. bake-out); -65 / -70</i>					
	$N_{2/3}$ -32	-0.009(18)	-2.590(24)	-2.58(3)	-80.3(9)
<i>day 116 (after 2nd venting of sources); -66 / -87</i>					

The spectra were analyzed with the help of the cross-correlation method, see the caption of Tab. 6.8 for the explanation. In the calculation of the amplitude changes the radioactive decay of ^{83}Rb was taken into account.

In the case of the source Pt-30 the lines K -32 and L_3 -32 could be compared to the data collected at the very end of the measurement phase (days 125–127) after the moderate bake-out of the spectrometer vessel. The amplitude and background values of both lines were found to be lowered by about 32 % and 23 %, respectively. Similarly, the K -32 and L_3 -32 lines of the source S 28 were measured in the same experimental conditions and they exhibited a decrease of the amplitude and background of the order of 65–70 %. In all four cases a significant drop of the electron line positions of the order of 1–3 eV was observed.

Interestingly, the shifts of the line positions exhibit a distinct energy dependence. The $N_{2/3}$ -32 line of both sources was measured around the day 118 after the second venting test (source section vented). The decrease of the line amplitudes matches to those of the K -32 and L_3 -32 lines, however, the background decreased by 79 % (Pt-30) and 87 % (S 28). As no significant changes of the amplitude and background values of the K -32 line were observed during the test with spectrometer venting and bake-out, the reason for the drop of the $N_{2/3}$ -32 lines background remains unclear. The L_1 -9.4 and M_1 -9.4 lines of the source Pt-30 were measured around the day 78 after the third vacuum breakdown (which occurred on day 61). Both lines exhibited a drop of the line position of about 0.53 eV. The changes of the amplitude and background are negative as well, however, they do not match the changes in the K -32 and L_3 -32 lines. In the case of the source S 28 the M_1 -9.4 line was not measured during the second measurement phase so only the comparison of the L_1 -9.4 line is available. Here the amplitude has decreased by 36 % while the background has risen by 23 %.

In principle, the combination of the following effects could be responsible for the negative shifts of the conversion electron lines noted in Tab. 6.10:

1. changes of source properties due to their storage on air for two months,
2. misalignment of the sources in the x - y plane,
3. change of the spectrometer work function,
4. refurbishment of the HV divider K35 which consisted of these actions [Bau11]:
 - a) the temperature regulation system was improved,
 - b) the corrupted bronze spring connector at the divider HV input was replaced by a better concept, based on a gold plated connector,
 - c) new scale factor 100 : 1 was implemented.

The individual items should be discussed here. It was shown in Sect. 6.3.3 that the source Pt-30 was practically stable against the venting of the source section up to 10^{-1} mbar: the shift of the K -32 line was reproducibly determined to be 5(4) meV. Therefore, it can be expected that the effect (1) of storing the source Pt-30 on air cannot cause the above mentioned shifts of -1 to -3 eV of the electron lines which are, moreover, scaling with energy. Due to the removal of the complete source holder and its re-construction a certain x - y misalignment of the sources is inevitable. However, it was demonstrated in Sect. 6.2.4 with the source S 28 (and once again in coming Sect. 6.3.5 with the source Pt-30) that the source misplacement in the x or y direction causes the K -32 line shift of the order of tens of meV. As the optimal x - y positions of the sources Pt-30 and S 28 were found via maximizing the count rate observed on the detector the effect (2) cannot really be exclusively responsible for the observed shifts. There was no vacuum breakdown during the test of the alternative KATRIN calibration tools in the time period of days 128–170. Furthermore, the vacuum breakdowns which oc-

curred in the course of the second measurement phase have not influenced the electron line positions in such a way that the line shifts would scale with the electron energy. The effect (3) of a slight change of ϕ_{spec} cannot be definitely excluded, however, it is assumed to play a minor role in this phenomenon.

On the other hand, as discussed already in Sect. 6.2.2 the HV divider K35 was inspected in the Institute of Nuclear Physics, University of Münster, after the sudden shift of $\simeq 0.93$ V of the HV scale was observed in the Institute of Physics, University of Mainz, with the source S28. It was pointed out that the HV connection at the input site of the divider was found imperfect and it was replaced by a more reliable concept. This effect (4b) could be related to eliminating the constant step of $\simeq 0.93$ V and “coming back” to the original HV scale. Finally, as a part of the refurbishment procedure an additional scale factor 100 : 1 was implemented (effect (4c)) into the divider K35 and the chain of precision resistors inside the device was actually slightly altered (resistors were exchanged in their location) [Bau11]. Once the second measurement phase was completed at Mainz setup, the divider K35 was again transported to the Institute of Nuclear Physics, University of Münster. There it was later confirmed that the dividing ratios $M_1 \approx 1972 : 1$ and $M_2 \approx 3944 : 1$ were indeed significantly influenced by this intervention into the device [Bau11]. Therefore, the shifts summarized in Tab. 6.10 were very probably caused mainly by the effect (4c) (and possibly by (4b) as well).

Immediately after observing the scaling property of the electron lines shifts documented in Tab. 6.10, the HV divider K35 was calibrated against two precision digital voltmeters Fluke 8508A. This simple calibration technique was already successfully used in Sect. 6.2.2 when the sudden shift of the HV scale by $\simeq 0.93$ V was observed. The scheme of the calibration is shown in Fig. 6.11. Of course, such a “rough” calibration method cannot compete with the sophisticated calibration methods developed at the PTB Braunschweig, on the other hand, its main advantage consists of immediate accessibility in the laboratory. This way the performance of the HV divider could be quickly checked with the precision of $\simeq 15$ ppm. The result of the calibration is depicted in Fig. 6.23.

It is seen that both calibrations of the HV divider K35 carried out in Mainz in 2008 resulted in the M_1 values by $\simeq 20$ ppm lower than the values based on the extrapolation of the PTB calibration results. However, this statement is not valid for the last two points in Fig. 6.23 which are separated by a short time period of about two days. This “double point” measured in June 2009 appears to lie by $\simeq 84$ ppm higher than the PTB-based value. Extrapolating the first two calibration results obtained in Mainz in 2008 and comparing them with the latest one reveals the positive shift of M_1 of about 107 ppm. It should be emphasized that in all cases of the divider calibration in Mainz the voltage of -1 kV was applied to the divider. Thus, even such a simple calibration procedure indicates that the dividing ratio of the HV divider K35 got unexpectedly shifted to higher values. This observation agrees well with the negative shifts of the conversion electron line which were found to be scaled with the electron energy.

The dependence of the observed line position shifts on the energy of the individual conversion lines is depicted in Fig. 6.24. The negative shifts of the lines determined with the source S28 could be sufficiently well described with a linear function of the following parameters: the linear term amounted to $p_1(S28) = -0.069(2)$ eV keV $^{-1}$ and the absolute term was $p_0(S28) = -0.41(4)$ eV. The value of $p_1(S28)$ would correspond to the change of the

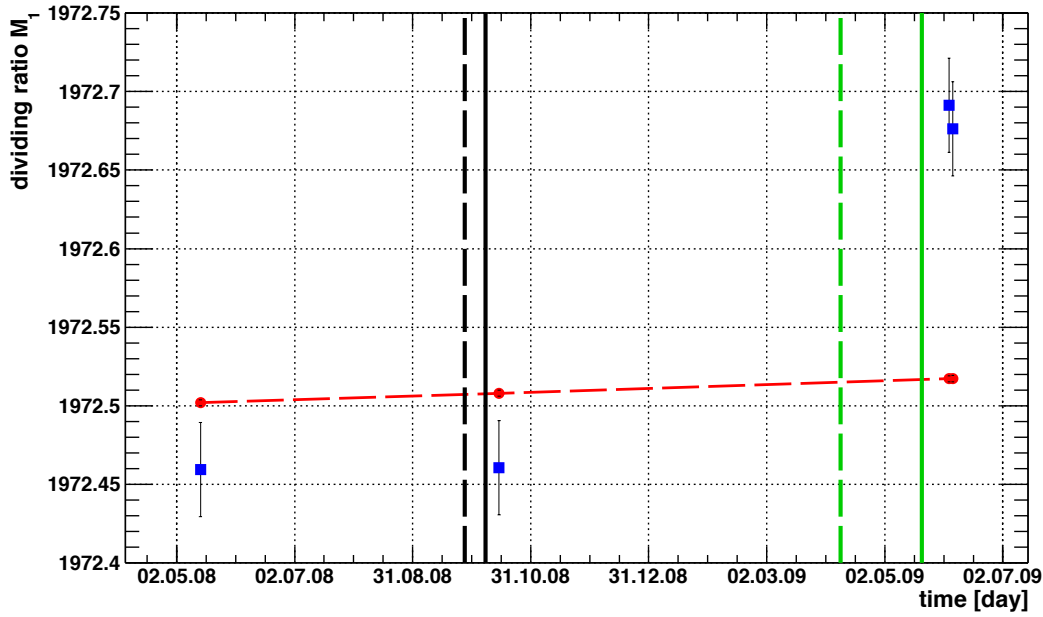


Fig. 6.23: The results of the calibration of the HV divider K35 carried out in the Institute of Physics, University of Mainz, according to the procedure depicted in Fig. 6.11. The blue points show the absolute values of M_1 (scale factor, also denoted as dividing ratio) of the divider as obtained from the calibration procedure. The red points (connected by the red dashed line) represent the M_1 values based on the linear extrapolation ($m_{\text{div}}^{\text{PTB}} = 0.60(10) \text{ ppm month}^{-1}$) of the PTB data from the time period 2005–2006 [Thu07, Thu09]. The black vertical lines denote the first problem of the HV scale shift (cf. Fig. 6.10 and Fig. 6.12). The dashed green line denotes the transport of the divider K35 to the Institute of Nuclear Physics, University of Münster, for refurbishment and additional scale factor implementation. Lastly, the full green line marks the day when the divider K35 arrived to the Institute of Physics, University of Mainz, and was ready for the $^{83}\text{Rb}/^{83\text{m}}\text{Kr}$ measurements. The full span of the y axis corresponds to $\simeq 150$ ppm relative to M_1 value. The positive shift of M_1 of about 107 ppm (based on the extrapolation of the linear trend fitting the first two blue points) is clearly visible.

scale factor of the HV divider of $\frac{\Delta M}{M} = 69(2) \text{ ppm}$ if one would attribute this effect to the HV divider. The shift of the L_1 -9.4 line seems to appear off the linear trend (too negative) of the other lines. However, omitting this point does not change the fit results significantly (changes of $p_{0,1}$ are within their errors) due to a relatively large uncertainty of the L_1 -9.4 data point. On the other hand, the shifts of the L_1 -9.4 and M_1 -9.4 lines of the source Pt-30 appear to be too small in comparison with the fitted linear function. But similarly, these data points suffer from big uncertainties. On the range 7–32 keV the shifts of the conversion lines of the source Pt-30 could be described with the terms $p_1(\text{Pt-30}) = -0.053(2) \text{ eV keV}^{-1}$ and $p_0(\text{Pt-30}) = -0.43(5) \text{ eV}$. Again, the term $p_1(\text{Pt-30})$ would correspond to the change of the divider scale factor of $\frac{\Delta M}{M} = 53(1) \text{ ppm}$.

As already mentioned, the malfunction of the HV divider K35 was independently verified [Bau11] in the Institute of Nuclear Physics, University of Münster, after the negative shifts scaled with the input voltage were observed at Mainz setup. It has to be noted that the divider exhibited a malfunction in the sense that its scale factor was unexpectedly changed by about 84 ppm at -17.8 kV (average of the K -32 line shifts of both sources), besides this problem the divider device was working flawlessly. Of course, such a relatively large change can

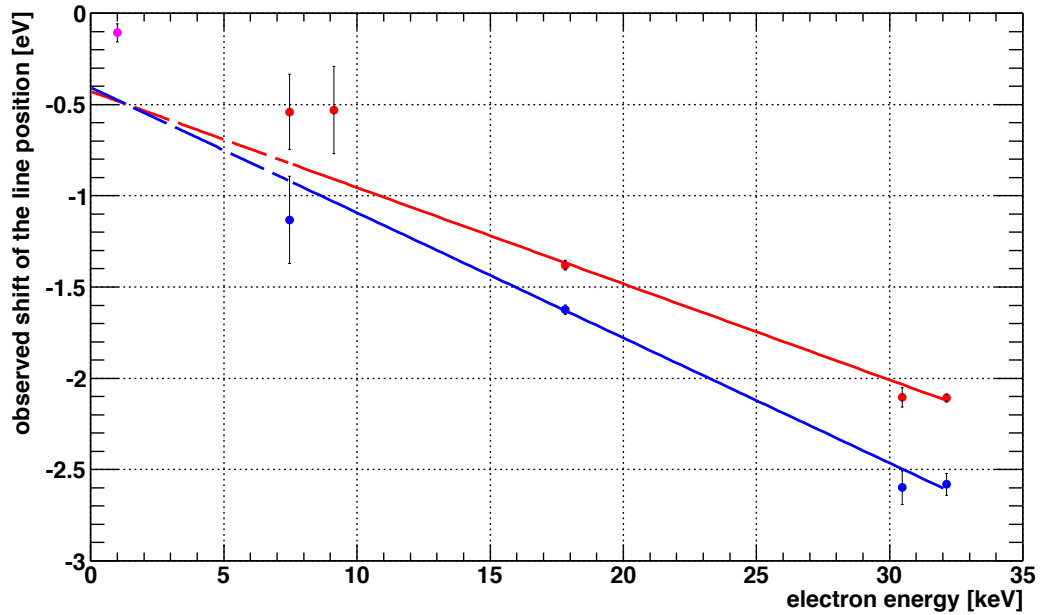


Fig. 6.24: The shifts of $^{83\text{m}}\text{Kr}$ electron lines observed with the sources S28 (blue points) and Pt-30 (red points) as a result of the unexpected change of the divider K35 scale factor, cf. Tab. 6.10. The x axis denotes the nominal energy of the electron lines, the y shows the observed shifts. The error bars of the shifts were multiplied by the factor of 2 for the sake of illustration. The data were least-squares fitted with a linear function, yielding the parameters of p_1 (S28) = $-0.069(2)$ eV keV $^{-1}$, p_0 (S28) = $-0.41(4)$ eV and p_1 (Pt-30) = $-0.053(2)$ eV keV $^{-1}$, p_0 (Pt-30) = $-0.43(5)$ eV. The χ_r^2 values of the fits amounted to 1.1(10) and 2.3(8), respectively. Although the shifts of the low energy conversion lines (below 10 keV) seem to lie off the trends, their large uncertainties do not influence the fitted parameters $p_{0,1}$ significantly. In the upper left corner one point in magenta color is visible—it corresponds to the shift of $\simeq 107$ ppm of the scale factor M_1 determined on the basis of the calibration at -1 kV, see Fig. 6.23. The dashed parts of the colored lines represent the extrapolation of the fitted trends. The discrepancy of $\simeq 0.4$ eV between the extrapolated trends and the calibration point stems probably from the overall uncertainties of both methods (measurements of the conversion lines and a rough calibration technique).

be detected with the help of a commercial measurement equipment (*e. g.* precision voltmeter calibrated in the appropriate DC range). Anyhow, the solid $^{83}\text{Rb}/^{83\text{m}}\text{Kr}$ sources proved to be a very useful and even necessary part of the monitoring concept of the KATRIN experiment. Should a similar problem occur during the real tritium measurement in KATRIN, the signature of the electron lines shifts scaling with the input voltage can be easily checked with the help of the $^{83}\text{Rb}/^{83\text{m}}\text{Kr}$ sources.

6.3.5. Influence of the source position on the K -32 line at two different spectrometer resolutions

The influence of the source $[x, y]$ position on the shape of the K -32 line was already studied in Sect. 6.2.4 with the source S28. These tests were repeated during the second measurement phase (days 65–67) with the help of the source Pt-30. Within this time period stable exper-

imental conditions were reached, thus, any change of the source characteristics occurring during this test can be excluded. The source Pt-30 was moved around its optimal measurement position by ± 1 mm and in each $[x, y]$ position the K -32 was scanned at spectrometer resolutions of 0.9 eV and 2.0 eV at 17.8 keV, respectively. The sources S28 and S29 were present in the setup, however, they were biased by +100 V (this was the usual procedure).

The results are summarized in Tab. 6.11. The data sets obtained with different spectrometer resolutions were evaluated separately with the help of the cross correlation method where the spectrum recorded at the position $[0,0]$ was taken as the reference. The Absolute values of the amplitude and background at the position $[0,0]$ amounted to $A = 4041(2)$ counts s^{-1} and $B = 2308(2)$ counts s^{-1} for the 0.9 eV resolution and $A = 4050(9)$ counts s^{-1} and $B = 7113(10)$ counts s^{-1} for the 2.0 eV resolution. It is seen that $A/B(\text{res. } 0.9 \text{ eV}) \simeq 1.8$, whereas $A/B(\text{res. } 2.0 \text{ eV}) \simeq 0.6$, thus, the A/B ratio is by the factor of 3 higher in the case of the sharper transmission function⁹. The results in Tab. 6.11 indicate that at both widely used spectrometer resolutions the setup is very sensitive to the source misalignment of the order of 1 mm. In the cases where the K -32 line position was not significantly shifted as a result of the source misalignment, the change of the amplitude and/or background of the order of several % was a clear signature. The uncertainties of the “zero shifts”—the shifts of the K -32 lines in the reference $[0,0]$ positions were taken as zero—were 3 meV (0.9 eV resolution) and 16 meV (2.0 eV resolution). Bearing in mind this higher uncertainty of the latter data set, the setup operated with the sharper transmission function was more sensitive to the source misalignment in the sense of the K -32 line position shifts.

Finally, it should be mentioned that comparing mutually the $[0,0]$ positions of both data sets leads to a significant discrepancy: the K -32 line position measured with the resolution of 0.9 eV was found to be by 0.58(1) eV higher than when measured with the resolution of 2.0 eV at 17.8 keV. Ideally, in a well adjusted source–spectrometer geometry it should not matter at which energy resolution a given conversion line is measured. The only difference should stem from the potential dip across the analyzing plane, however, in this case such a difference should amount to ≤ 0.1 eV, cf. Fig. 5.15. Thus, similarly to Sect. 6.2.4, the observed discrepancy points to a certain geometrical misalignment and/or another systematic effect. Still, for the long-term energy stability measurements this does not represent a severe problem as typically only the resolution of 0.9 eV at 17.8 keV was routinely used.

6.3.6. Background and transmission properties of Mainz MAC-E

filter

A short test measurement was carried out in the course of the second measurement phase in order to verify the background properties of the MAC-E filter used in this work. During the test of deliberate venting of the source section (cf. Sect. 6.3.3) the spectrometer vessel was separated from the source section by the pneumatic gate valve. The spectrometer was

⁹From Tab. 6.5 in Sect. 6.2.4 it becomes clear that the K -32 line of the vacuum-evaporated source S28 exhibited $A/B \simeq 12$ which is superior to the case of the ion-implanted source Pt-30. The reason for this is the high background present in the spectra of the ion-implanted $^{83}\text{Rb}/^{83\text{m}}\text{Kr}$ sources in general. This issue is discussed in detail in Chap. 7.

Tab. 6.11: The influence of the source Pt-30 displacement in the x - y plane on the K -32 line.

resolution 0.9 eV at 17.8 keV				
horizontal displ. Δx [mm]				
	-1	0	1	
vertical displ. Δy [mm]	1	-0.018(9)	-0.001(13)	0.029(7)
		-4.5(1)	-1.1(2)	-6.8(1)
		3.6(1)	8.0(4)	-4.5(3)
		1.6	1.6	1.7
	0	-0.002(18)	0.000(3)	0.011(12)
		1.2(3)	0.0(1)	-5.0(2)
		1.9(2)	0.0(1)	-8.0(4)
		1.7	1.8	1.8
	-1	0.034(11)	0.033(3)	0.057(50)
		-3.4(1)	-4.0(1)	-13.9(7)
		-13.7(1)	-11.1(1)	-21.0(8)
		2.0	1.9	1.9

resolution 2.0 eV at 17.8 keV				
horizontal displ. Δx [mm]				
	-1	0	1	
vertical displ. Δy [mm]	1	-0.006(12)	0.012(16)	-0.030(20)
		0.6(3)	0.5(3)	-4.3(3)
		2.7(1)	-3.0(1)	-25.4(1)
		0.6	0.6	0.7
	0	0.014(16)	0.000(16)	-0.003(19)
		0.8(7)	0.0(3)	-9.1(4)
		8.6(2)	0.0(2)	-21.0(2)
		0.5	0.6	0.7
	-1	0.018(19)	0.026(17)	-0.001(12)
		-8.9(6)	-12.4(3)	-24.4(3)
		-1.2(2)	-7.6(2)	-27.5(1)
		0.5	0.5	0.6

The source was displaced by ± 1 mm from the optimal position. The test was carried out at resolutions of 0.9 eV and 2.0 eV at 17.8 keV, respectively. Each box represents the weighted average of the results obtained for the given $[\Delta x, \Delta y]$ displacement. The values (top to bottom) in each box denote 1) the K -32 line position shift [eV] with respect to the value obtained at $[0, 0]$, 2) the relative change (in %) of the line amplitude with respect to the $[0, 0]$ value, 3) the relative change (in %) of the line background with respect to the $[0, 0]$ value and 4) the A/B ratio. The individual integral spectra were analyzed with the help of the cross-correlation method where the reference spectrum corresponds to zero displacement. The relatively large uncertainty of the shifts determined at the resolution of 2.0 eV stems from a poor statistics of the data collected in the $[0, 0]$ position. See Tab. 6.5 for the results obtained with the source S 28.

kept in the vacuum level of 3×10^{-10} mbar and it was not affected by the venting procedure in any way. The time necessary for the pump-down of the source section was conveniently used for the following test: the HV ranging from -15 to -33 kV was applied to the spectrometer electrodes while the detector was kept in the usual measurement position. This way only the events resulting from electrons ejected from the electrodes were detected. In Fig. 6.25 the obtained electron spectra are depicted. In Fig. 6.25(a) altogether four spectra are plotted, they were recorded at voltages U of -15 , -20 , -25 and -30 kV, respectively. The measurement time was 4000 seconds in each case. The noise is visible in all spectra, on the low energy side the cutoff at about 7 keV is caused by the settings of the low level discriminator of the ADC. The noise reaches up to $\simeq 12.5$ keV. In addition, an electron peak is clearly visible in each spectrum at the energy corresponding to the HV applied to the electrodes. Moreover, this peak is accompanied by additional peaks corresponding to multiple background events. In general, the electron peaks can be found at the energies

$$E_k \approx k \cdot (qU - \delta E(qU)) , \quad (6.11)$$

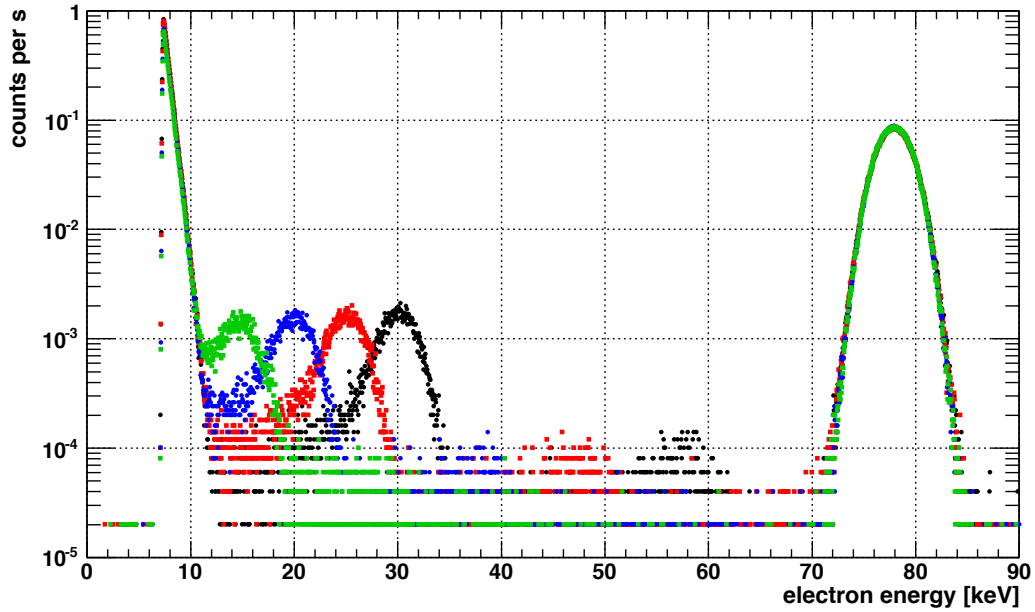
where $q = -|e|$ and $k = 1 \dots N$. The term $\delta E(qU)$ represents the energy losses in the detector dead layer. In the framework of the Mainz Neutrino Mass Experiment these losses were estimated to be $\delta E \approx 0.5$ keV [Wei11] which can be further neglected in our case. The peak at $\simeq 78$ keV present in all the four spectra corresponds to the pulser peak. Summing the pulser peak area verifies that the dead time was negligible in this test. The count rate recorded in the low energy noise structure below 12.5 keV amounted to $\simeq 145$ counts s^{-1} . Subtracting the pulser peak area and the area of the low energy noise from the total number of events in each spectrum results in the average count rate of 2.6 counts s^{-1} . In this value the single as well as all multiple background events are included.

Later, the pulser was disconnected from the preamplifier and the HV was set to $U = -33$ kV. Thus, the retarding potential was higher than the energy of the most energetic line $N_{2/3-32}$ of the ^{83m}Kr conversion electron spectrum. This way it was ensured that any possible contamination of the spectrometer vessel with ^{83}Rb would not affect the measurement. A single spectrum was recorded for $\simeq 13.8$ hours, Fig. 6.25(b) depicts the result in terms of counts per second. Here the low energy noise exhibited the count rate of only 2.1 counts s^{-1} and the summation of the rest of the spectrum yielded the count rate of 3.1 counts s^{-1} . Obviously, the most intensive peak lies at the energy of $E_1 \simeq 33$ keV. In addition, multiple background events are observed: up to fivefold peak is visible at the energy of $E_5 \simeq 165$ keV.

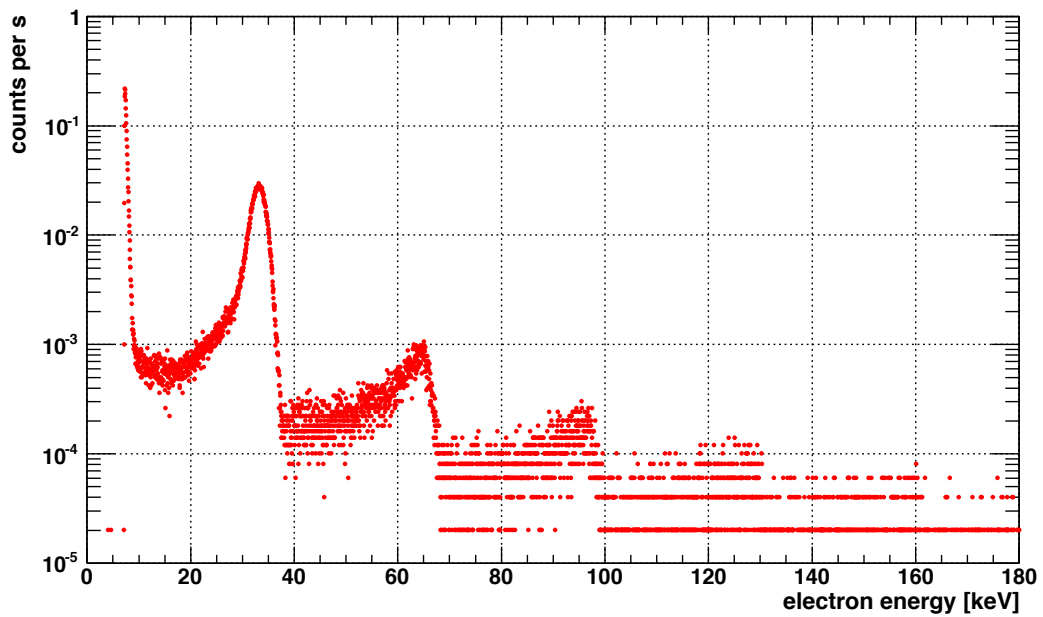
It should be noted that the spectrometer resolution was kept at 0.9 eV at 17.8 keV throughout the tests and the auxiliary set of air coils, used for compensating for the Earth's magnetic field in the analyzing plane, was kept at the same settings as during the long-term measurements of the energy stability of the solid $^{83}\text{Rb}/^{83m}\text{Kr}$ sources. In other words, the spectrometer was not tuned in any special way in order to achieve the low background. Multiple background events observed at Mainz MAC-E filter were studied in [Kas08]. The effect was ascribed to several electrons with the energy equal to qU hitting the detector at the same moment. Secondary electrons emitted from the electrode surface—*e. g.* as a result of the cosmic muons hitting the electrodes—were suggested to be responsible for the effect. In this work no detailed explanation or study of this effect is aimed. Nevertheless, the following conclusions can be drawn from this simple test:

1. Throughout this short-term background measurement as well as during the long-term energy stability measurements the spectrometer was operated with rather conserva-

6. Long-term measurements...



(a)



(b)

Fig. 6.25: The electron spectra (in counts s^{-1}) resulting from the background measurements carried out at Mainz MAC-E filter with the solid sources separated from the spectrometer vessel by the gate valve. In the figure (a) four individual spectra are superposed: spectrum obtained at $U = -15$ kV (green), $U = -20$ kV (blue), $U = -25$ kV (red) and $U = -30$ kV (black) applied to the spectrometer electrodes. The measurement time amounted to 4 000 seconds in each case. The peak at $\simeq 78$ keV corresponds to the pulser peak. Figure (b) shows a similar measurement, however, this time $U = -33$ kV and the pulser was removed from the electronic chain. The spectrum represents about 13.8 hours of data taking. Up to the fivefold peak is visible at the energy of $\simeq 165$ keV.

tive settings. The achieved resolution of 0.9 eV at 17.8 keV was surely the most attractive property of the spectrometer, on the other hand, no sophisticated background reduction as in [Fla04] was attempted here. The massless wire electrode was operated at the same HV as the massive electrode. Therefore, it comes by no surprise that while the background of the MAC-E filter of the order of 0.001 counts s^{-1} was reached in [Fla04], in our case the background rate higher by the factor of $\approx 10^3$ higher was observed.

2. The sensitive area of the spectrometer vessel (imaged onto the detector) was not contaminated with significant amounts of long-lived ^{83}Rb .
3. The spectrometer vessel alone produces very low background of $\simeq 3$ counts s^{-1} in the energy region above $\simeq 13$ keV. The high background observed in the integral electron spectra of the solid $^{83}\text{Rb}/^{83\text{m}}\text{Kr}$ sources comes exclusively from the sources themselves: firstly, the conversion lines of higher energies produce the background under the lines of lower energies, secondly, the electrons which are not transmitted through the spectrometer can be scattered from the source back to the spectrometer volume, and lastly, the not transmitted electrons may hit the spectrometer electrode and produce the secondary electrons.
4. From the observations follows that it does not make sense to aim for ultra low background in the monitor spectrometer currently being commissioned at the Karlsruhe Institute of Technology. The high background of the order of 10^3 counts s^{-1} is inevitable when the solid $^{83}\text{Rb}/^{83\text{m}}\text{Kr}$ sources are used.

In addition to the background measurements, a measurement clearly illustrating the transmission properties of the MAC-E filter was carried out on day 100 (time period without any disturbances, cf. Fig. 6.16). The measurement was accomplished at usual experimental settings, *i. e.* the sources Pt-30, S 28 and S 29 were positioned in the bore of the solenoid B as described above. The source Pt-30 was kept in its optimal $[x, y]$ measurement position and the other two sources were biased by +100 V. The spectrometer resolution was set to 0.9 eV at 17.8 keV. The HV was varied with the step of 10 V between -28 and -32.5 kV. This way the range of 4.5 keV of the $^{83\text{m}}\text{Kr}$ spectrum was covered as can be seen in Fig. 6.26.

Following the integral spectrum from right to left the following features can be recognized:

- above $\simeq 32.15$ keV only the background of about 120 counts s^{-1} is present in the spectrum,
- at $\simeq 32.15$ keV a small “kink” is visible in the spectrum, corresponding to the onset of the $N_{2/3-32}$ conversion line of $^{83\text{m}}\text{Kr}$,
- below $\simeq 32.15$ keV the electron signal stabilizes at the level of 400 counts s^{-1} until the energy of $\simeq 31.9$ keV at which point the effect of the M_{2-32} and M_{3-32} lines is seen as a further increase of the signal up to $\simeq 3.5 \times 10^3$ counts s^{-1} ,
- at the energy of $\simeq 31.84$ keV the signal stops to rise and it gradually falls down to about 780 counts s^{-1} at $\simeq 30.5$ keV,
- at the energy of 30.47 keV a very steep rise of the signal up to $\approx 8 \times 10^3$ counts s^{-1} is visible (L_{3-32} line), followed by a further increase of the count rate up to $\approx 1.57 \times 10^4$ counts s^{-1} at the energy of 30.42 keV (L_{2-32} line),

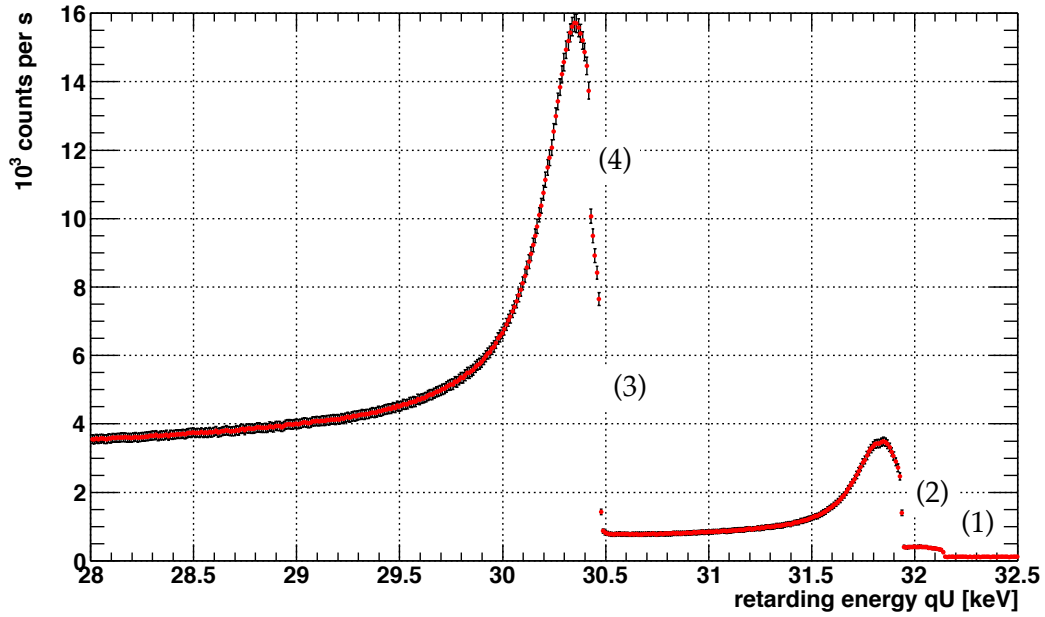


Fig. 6.26: The integral spectrum showing a wide range of energies of 28–32.5 keV covering the high energy $^{83\text{m}}\text{Kr}$ conversion lines of the source Pt-30. The error bars of the count rate were multiplied by the factor of 10 for the sake of illustration. The approximate positions of the electron lines are marked with numbers. From right to left the following lines are recognizable (cf. Tab. 3.1): $N_{2/3}\text{-32}$ (1), $M_{2,3}\text{-32}$ (2), $L_3\text{-32}$ (3) and $L_2\text{-32}$ (4). The resolution of 0.9 eV at 17.8 keV was used for this scan, corresponding to the resolution of 1.6 eV in the high energy range of ≈ 30 keV. The doublet of the $M_2\text{-32}$ and $M_3\text{-32}$ lines is not visible with the naked eye in this figure and therefore the notation $M_{2,3}\text{-32}$ was used. In the region of the $L_3\text{-32}$ (3) and $L_2\text{-32}$ (4) lines it might seem that there are some data points missing, however, this is simply due to the relatively big step of 10 V used in this scan. See text for detailed description of the individual parts of the spectrum.

- again, from the energy of ≈ 30.35 keV the signal gradually falls down to $\approx 3.5 \times 10^3$ counts s^{-1} at 28 keV.

The regions of the spectrum with the falling signal clearly indicate the transmission losses discussed above in Sect. 5.2.5: at high surplus energies the electron is no longer kept on its track passing the analyzing plane and it is not guided to the detector. This effect was already observed and studied at Mainz MAC-E filter [Pic92b, Thu07, Kas08]. It should be noted that the transmission losses are inevitable when the spectrometer is operated with high resolution, in which case the magnetic field in the analyzing plane is considerably weak, of the order of 3 G (Gauss). Less than 48 hours before this “overview scan” a regular measurement of the $K\text{-32}$ line of the source Pt-30 was carried out. Thanks to the short time period between these scans the correction of the count rate due to the ^{83}Rb decay can be safely neglected. The background of the $K\text{-32}$ was found to be $\approx 1.6 \times 10^3$ counts s^{-1} at the energy of ≈ 17.85 keV. Thus, the range of the $^{83\text{m}}\text{Kr}$ spectrum between ≈ 18 and ≈ 28 keV can be viewed as a slowly decaying background (in the direction of low energy) on which then the onset of the $K\text{-32}$ line appears. With a crude linear approximation the fall of the electron signal in the region 18–28 keV can be estimated as ≈ -190 counts s^{-1} per keV.

6.4. Third measurement phase: four ion-implanted sources investigated simultaneously

The tests with deliberate venting of the source section reported in Sect. 6.3.3 showed that the ion-implanted source Pt-30 is stable against abrupt changes of vacuum conditions in its vicinity. The changes of the K -32 line energy (determined with the statistical uncertainty of 4 meV) of the source Pt-30 were found to be of the order of 5 meV, practically compatible with zero. In addition, the relative drifts of various $^{83\text{m}}\text{Kr}$ conversion lines of this source were determined to be of the order of $\approx 1 \text{ ppm month}^{-1}$ (cf. Tab. 6.7) which is very promising with respect to long-term monitoring of the energy scale of the KATRIN spectrometers. Moreover, the amplitude of the Pt-30 K -32 line amounted to $\approx 4 \times 10^3 \text{ counts s}^{-1}$ (with the spectrometer resolution set to 0.9 eV at 17.8 keV). This allowed to determine the position (\equiv energy) of the K -32 line with the statistical uncertainty of 16 meV within 20 minutes, typically¹⁰.

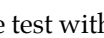
All these positive considerations led to the idea to produce another ion-implanted sources at the ISOLDE facility. The details of the production carried out in June 2009 were described above in Sect. 4.2.2. Altogether three new sources Pt-30 #2, Pt-15 and Au-30 were produced, their properties were discussed in Sect. 4.2.3. During the third measurement phase these new sources were investigated together with the source P-30. This measurement phase turned out to be the last one in the Institute of Physics, University of Mainz, as the MAC-E filter spectrometer was dismantled shortly after this measurement phase was finished. Then the spectrometer was transported to the Karlsruhe Institute of Technology and rebuilt into the monitor spectrometer (cf. Fig. 3.5 in Sect. 3.2).

The overview of the third measurement phase is given in Tab. 6.12. All the four sources were placed into vacuum simultaneously, see Fig. 5.5 and Fig. 5.6. It should be noted that since the beginning of June 2009 two oil rotary pumps were used as backing pumps to the turbomolecular pumps evacuating the source and detector sections. The HV divider K65 was used as the HV reference, cf. Tab. 5.1. Thanks to the use of pre-aged resistors in the divider chain (Sect. 3.2.1), the long-term stability of the dividing ratio was anticipated to be even better than the stability of the previously used divider K35. The long-term stability of the divider K65 was extensively studied in the Institute of Nuclear Physics, University of Münster, over the time period of 13 months [Bau09, Bau11]. The drift of the dividing ratio $M = 1818.1096(6) : 1$ used in this work was determined as $m_{\text{div}}^{\text{PTB}} = -0.13(10) \text{ ppm month}^{-1}$, *i.e.* compatible with a zero drift. Although the drift was determined in the Institute of Nuclear Physics, University of Münster, the notation “PTB” will be used for this value, emphasizing that it was obtained on the basis of calibration equipment which was traced to the standards of the PTB Braunschweig. The value of $m_{\text{div}}^{\text{PTB}}$ was determined with the help of the low voltage calibration method described in [Bau09].

¹⁰It was stated in Sect. 5.2.1 that the distribution of the measurement time was not optimized, *i.e.* the measurement time was always set equal for all the points of a given spectrum. Optimizing the measurement time distribution would allow to investigate the line position shifts on even shorter time scale.

Tab. 6.12: The overview of the third phase of measurements carried out in 2009.

calendar week no.	31	32	33	34	35	36	37
week of	27.07.	03.08.	10.08.	17.08.	24.08.	31.08.	07.09.
time since 27.07.2009 [day]	0	7	14	21	28	35	42
source tested	Pt-30, Pt-30 #2, Pt-15 and Au-30						
HV conditions							
HV divider used	K65						
calibration of HV divider	x	x		x		x	x
vacuum conditions							
breakdown				x		•	
electron line scanned							
L_1 -9.4		x	x		x		x
K-32	x	x	x	x	x	x	x
L_3 -32		x	x	x	x		x
$N_{2/3}$ -32		x	x	x	x		

Four ion-implanted sources were tested simultaneously. The box  denotes the test with deliberate venting of the source section carried out in the calendar week 36. Regular calibrations of the dividing ratio of the HV divider K65 were carried out on the basis of the procedure described in Sect. 6.3.4, however, as no problems with the HV scale occurred during the measurements, the calibrations of the precision of 15 ppm will not be reported.

6.4.1. Comparison of drifts of individual sources

The procedure of measuring the drifts of the conversion line positions was already described in Sect. 6.2.1 and Sect. 6.3.1. The same procedure was followed in this measurement phase. The sources were placed in the magnetic field of $B_S = 1.75$ T, thus, the amplitudes of the electron lines recorded here were directly comparable with those determined in the previous measurement phase. The digital voltmeter was calibrated regularly as well. It should be noted that throughout this measurement phase an another device of the digital voltmeter was used, however, the model of the device was again the high precision voltmeter Fluke 8508A [Flu08].

The time dependence of the scale factor K of the voltmeter is shown in Fig. 6.27. It is obvious that here, in contrast to the previous measurement phases (cf. Fig. 6.3, Fig. 6.6 and Fig. 6.17), no monotonous trend of the dependence $K(t)$ is present. The reason for this can be the fact that on day 30 a malfunction of the laboratory air conditioning system occurred. This caused the room temperature to rise from 25–26°C, which was the typical room temperature in the laboratory in that time period, up to 30°C, see Fig. 6.28. On day 37 the air conditioning system was repaired and the room temperature in the laboratory went back to normal values. However, the decrease of the room temperature back to normal values on day 37 was not reflected by the behavior of the digital voltmeter: as seen in Fig. 6.27 the scale factor K stayed on the new level. In addition, it is interesting to note that the dependence

of the scale factor deviation δK is firstly negative, in contrast to the previous measurement phases. As this given device was used for the first time in the experimental setup of Mainz spectrometer, no conclusion could be made regarding this observation. The further drop of the temperature down to 22.5°C on day 47 in Fig. 6.28 is directly related to the shutdown of majority of the electronic devices (vacuum pumps, power supplies for the air coils *etc.*) in the laboratory.

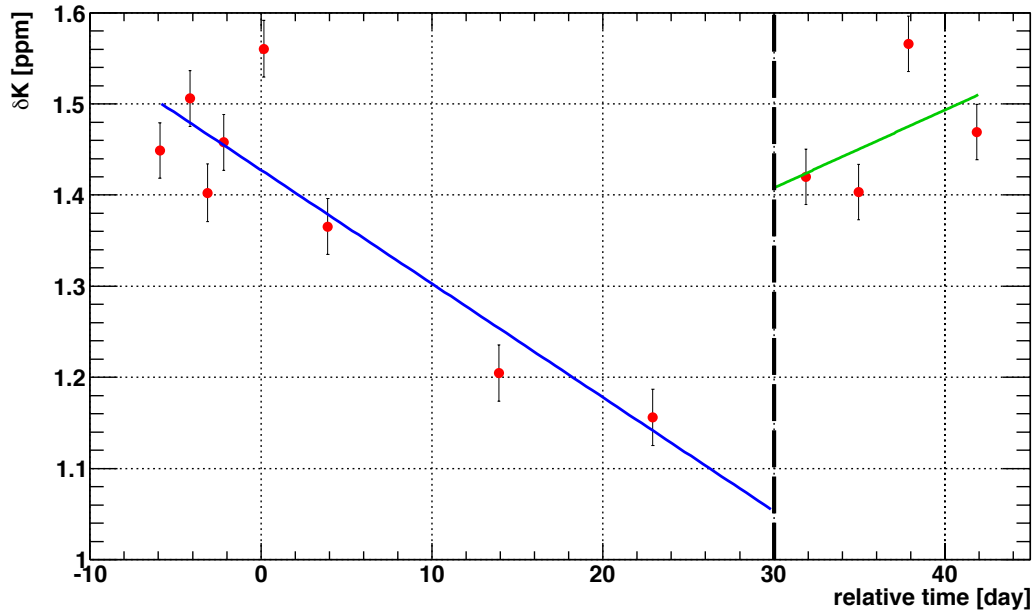


Fig. 6.27: The drift of the digital voltmeter scale factor K during the third measurement phase. The x axis denotes the relative time in days since 27.07.2009. The y axis shows the deviation $\delta K = 1 - K$ [ppm], see the caption of Fig. 6.3. The vertical dashed line on day 30 represents the moment when the malfunction of the air conditioning system in the laboratory occurred. The data sets obtained in the time periods “day ≤ 30 ” and “day ≥ 30 ” were least-squares fitted separately (blue and green lines), yielding the drifts $k_{\text{dvm}}(1) \equiv k_{\text{dvm}}(\text{days} \leq 30) = 0.39(9) \text{ ppm month}^{-1}$ and $k_{\text{dvm}}(2) \equiv k_{\text{dvm}}(\text{days} \geq 30) = -0.27(33) \text{ ppm month}^{-1}$, respectively. The relatively large χ^2_{r} values of 4.9(6) and 6.5(10), respectively, were taken into account via multiplying the uncertainties of k_{dvm} by $\sqrt{\chi^2_{\text{r}}}$. The negative relative time stems from the fact that the voltmeter calibrations were carried out already during the preparation phase of the measurements.

The long-term measurement of the energy stability of the conversion lines went on even during the time period of days 30–37 and the voltmeter reading was obviously used for the data evaluation, in accordance with Eq. 5.8. Therefore, the $K(t)$ data were split into two sets, first one covering the time period of days ≤ 30 and the second one covering the time period of days 30–47. These data sets were separately least-squares fitted with a linear function, yielding the drifts of $k_{\text{dvm}}(1) \equiv k_{\text{dvm}}(\text{days} \leq 30) = 0.39(9) \text{ ppm month}^{-1}$ and $k_{\text{dvm}}(2) \equiv k_{\text{dvm}}(\text{days} \geq 30) = -0.27(33) \text{ ppm month}^{-1}$, respectively. The 10 V DC reference Fluke 732A, which was used for the calibrations of the digital voltmeter, possesses an internal oven which makes it stable within the specifications in the range of $(23 \pm 5)^\circ\text{C}$ [Flu08]. Strictly speaking, this range does not cover the full range of the elevated temperatures, however, the DC reference was regarded stable in this work. In addition, the temperature inside the HV divider was monitored with the help of a built-in sensor. It exhibited no deviation or any unexpected behavior due to the elevated room temperature. Thus, thanks to its own thermal

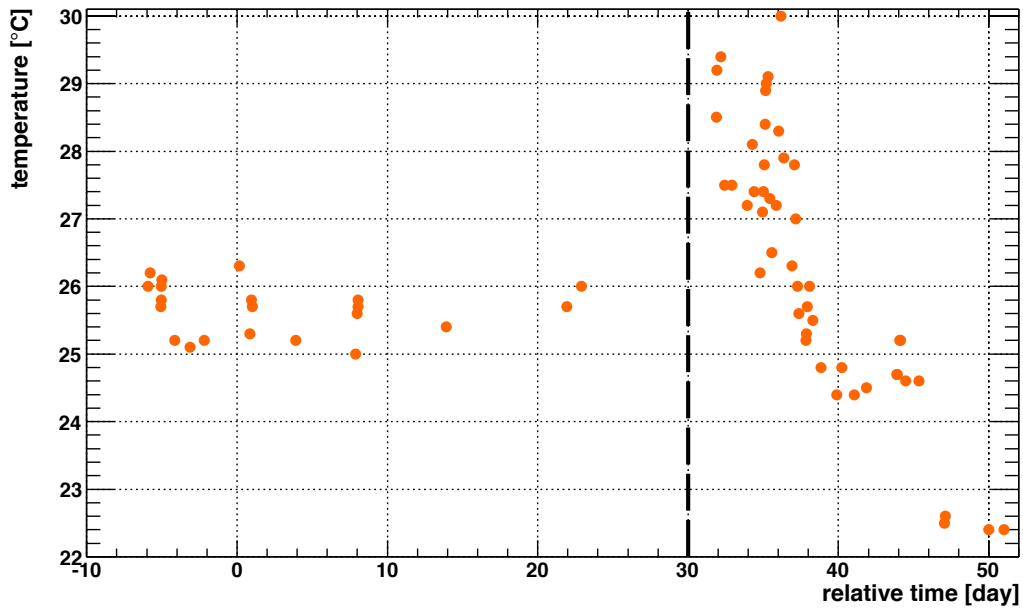


Fig. 6.28: The room temperature [°C] in the laboratory in the Institute of Physics, University of Mainz, where the MAC-E filter spectrometer was situated. The x axis denotes the relative time in days since 27.07.2009. The vertical dashed line on day 30 represents the moment when the malfunction of the air conditioning system in the laboratory occurred.

stabilization the HV divider was not affected by this issue, similarly to the DC reference. It is assumed that the approach of including the two separate drifts $k_{\text{dvm}}(1)$ and $k_{\text{dvm}}(2)$ of the voltmeter scale factor K into the data evaluation procedure fully accounts for the effect of the elevated room temperature in the laboratory.

The drifts of the K -32 line of each source are depicted in Fig. 6.29. The line position shifts were analyzed with the help of the cross-correlation method where the spectra measured with the step of 0.2 eV in the time period of days 9–14 (depending on the given source) were taken as references. The vertical dashed line in Fig. 6.29 denotes the vacuum breakdown which occurred during the measurement (*i. e.* all the vacuum sections were affected) on day 26 as a result of the power outage in the whole institute building¹¹. The vertical chain-dotted line represents the test of deliberate venting of the source section carried out on day 35. These effects will be discussed below.

About one month prior to the start of the measurements a thorough bake-out of the complete vacuum setup was accomplished. Moreover, after inserting the sources into vacuum the source section was moderately heated (32 hours at about 80°C). Such a “pre-conditioning” of the vacuum setup may be responsible for the fact that in Fig. 6.29 no effect of initial stabilization of the K -32 line position was observed (this was not the case of the previous measurement phases, see Fig. 6.5 and Fig. 6.16). In other words, from the very beginning of the measurement the K -32 line positions of each ion-implanted source exhibited very small drift in the ppm month⁻¹ range. It should be noted that the source Pt-30 exhibited a steep negative drift of the K -32 line position at the beginning of the second measurement phase (cf. Sect. 6.3.1). There was a time span of about 8 months between the start of the second

¹¹Unfortunately, no safety system using some kind of uninterruptible power source was in operation in that moment.

and the third measurement phase, thus principally, one cannot exclude some subtle change of the internal properties of the source Pt-30 (stabilization thanks to some natural “aging” of the source). However, the steep negative drift at the beginning of the second measurement phase can be safely ascribed to the stabilization of ϕ_{spec} after inserting the sources into vacuum. This period of initial stabilization was not observed in the case of the third measurement phase.

Another interesting observation is the fact that each source exhibited its own unique drift of the K -32 line energy. This comes by no big surprise as each source was actually unique in its properties: the various parameters of the total implanted dose of ^{83}Rb , the implantation profile (the depth as well as the irradiated area) and the purity of the polycrystalline foil resulted in the fact that no two sources were identical, actually (cf. Sect. 4.2.3). It will be shown in Chap. 7 that each source also exhibited a slightly different kinetic energy of the conversion lines, *i. e.* the electron binding energies differed from source to source.

The drifts of the K -32 line position, corrected for the drifts of the HV divider K65 and the digital voltmeter, are summarized in Tab. 6.13. In the time period of days 0–26 the absolute drifts were determined as follows: $d_{\text{source}}^{\text{abs}}(K\text{-}32, \text{Pt-}30) = -5(6) \text{ meV month}^{-1}$, $d_{\text{source}}^{\text{abs}}(K\text{-}32, \text{Pt-}30 \#2) = 11(3) \text{ meV month}^{-1}$, $d_{\text{source}}^{\text{abs}}(K\text{-}32, \text{Pt-}15) = 4(2) \text{ meV month}^{-1}$ and $d_{\text{source}}^{\text{abs}}(K\text{-}32, \text{Au-}30) = 43(3) \text{ meV month}^{-1}$. The drifts of the sources Pt-30 and Pt-15 are compatible with zero within 1σ and 2σ , respectively. The positive drift of the source Pt-30 #2 is not compatible with zero which makes this source different from its predecessor Pt-30. Considering the relative drifts, the three sources based on the implantation into platinum foils exhibited the drifts in the sub-ppm range, while the relatively high drift of the source Au-30 amounted to $2.39(19) \text{ ppm month}^{-1}$. This observation could be attributed to the difference between the noble metals of gold and platinum. In the case of the source Pt-30 #2 other conversion electron lines besides the K -32 line were measured more than once. In the time period of days 26–46 the L_1 -9.4 and L_3 -32 lines were scanned twice with the time span of about 10 days between the measurements, see Fig. 6.30. These measurements suffered from a low statistics of only several line scans, however, the positive drift of the line positions is present as in the case of the K -32 line.

In Fig. 6.29 the sudden drop of the K -32 line positions of all sources is clearly visible, resulting from the vacuum breakdown on day 26. A detailed evaluation of the shifts of the K -32 and other conversion lines is presented in Tab. B.3. The weighted average of the K -32 line shifts of all the sources amounted to $-0.149(22) \text{ eV}$. In Fig. 6.31 the time dependence of the K -32 line amplitude of each source is shown. It can be seen that in all the cases the K -32 line amplitude follows the radioactive decay of ^{83}Rb and the dependence is disturbed neither by the vacuum breakdown accident nor by the test of the deliberate venting. These results support the findings described in Sect. 6.3.2 and Sect. 6.3.3, *i. e.* that the ion-implanted type of source is stable against abrupt changes of the vacuum conditions. Thus, the sudden drop of the K -32 line positions of $\simeq -0.15 \text{ eV}$ can be ascribed to the change of ϕ_{spec} . The data presented in Fig. 6.31 were least-squares fitted, resulting in the following half-lives: $t_{1/2}(\text{Pt-}30, K\text{-}32) = 77.5(4) \text{ d}$, $t_{1/2}(\text{Pt-}30 \#2, K\text{-}32) = 78.8(3) \text{ d}$, $t_{1/2}(\text{Pt-}15, K\text{-}32) = 77.2(3) \text{ d}$ and $t_{1/2}(\text{Au-}30, K\text{-}32) = 84.3(3) \text{ d}$. Again, a distinct difference between the Pt-based sources and the source Au-30 is seen: the first three values agree relatively well, resulting in the weighted average of $77.9(14) \text{ d}$, while the half-life of the Au-30 K -32 line is by about 8% bigger. Considering the data obtained in the time periods of days 0–26 and 26–46 separately

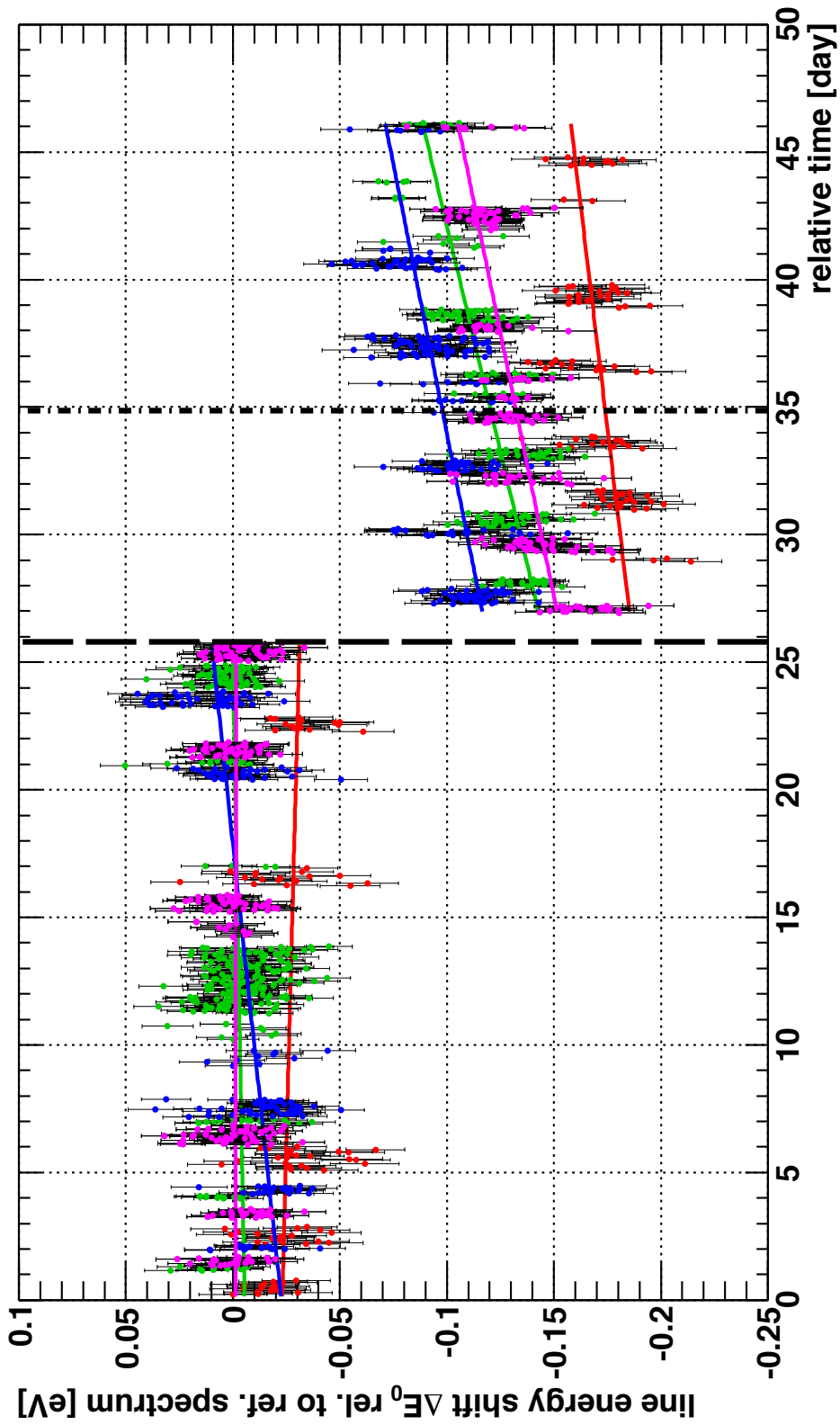


Fig. 6.29: The drifts of the K-32 line positions of the sources Pt-30 (red points), Pt-30 #2 (green), Pt-15 (magenta) and Au-30 (blue). The x axis denotes the relative time in days since 27.07.2009. The y axis shows the line energy shift ΔE_0 relative to the reference spectrum. The full span of the y axis of 0.35 eV represents the portion of ≈ 20 ppm considering the K-32 line energy of 17 824 eV. The least-squares fits were performed with the cross-correlation method where the spectra recorded with the step of 0.2 V in the time period of days 9–14 (depending on the given source) were chosen as the reference spectra. The vertical dashed line on day 26 denotes the vacuum breakdown. The chain-dotted line on day 35 denotes the test of deliberate venting of the source section.

Tab. 6.13: The drifts of the K-32 and other conversion lines measured with the sources Pt-30, Pt-30 #2, Pt-15 and Au-30.

source	time period [day]	data set	χ_r^2 of fit	absolute [eV]	linear fit parameters [meV month ⁻¹]	relative drift $d_{\text{source}}^{\text{rel}}$ [ppm month ⁻¹]
Pt-30	0-26	K-32	1.3(2)	$-23(2) \times 10^{-3}$	-5(6)	-0.27(32)
	26-46	K-32	1.3(1)	-0.22(1)	29(11)	1.60(60)
	full	K-32	0.95(4)*	$-20(2) \times 10^{-3}$	-17(3)	-0.96(17)
Pt-30 #2	0-26	K-32	1.65(8)	$-5(2) \times 10^{-3}$	11(3)	0.63(18)
		L ₁ -9.4	1.2(7)	-0.19(5)	268(32)	35.8(43)
	26-46	K-32	1.5(1)	-0.219(6)	78(6)	4.36(31)
		L ₃ -32	0.0(7)	-0.22(4)	28(33)	0.9(11)
	full	K-32	0.95(4)*	$-8(2) \times 10^{-3}$	18(3)	1.02(16)
Pt-15	0-26	K-32	1.28(9)	$-1(1) \times 10^{-3}$	4(2)	0.23(14)
	26-46	K-32	1.38(9)	-0.217(5)	66(5)	3.68(28)
	full	K-32	0.95(4)*	$-2(2) \times 10^{-3}$	3(3)	0.19(14)
Au-30	0-26	K-32	1.9(1)	$-23(2) \times 10^{-3}$	43(3)	2.39(19)
		L ₃ -32	0.9(3)	$-4(41) \times 10^{-3}$	34(143)	1.1(47)
	26-46	K-32	1.47(9)	-0.180(6)	64(6)	3.59(33)
	full	K-32	0.95(4)*	$-21(2) \times 10^{-3}$	47(3)	2.64(16)

The results of two approaches of analysis are summarized in the table. Firstly, the data depicted in Fig. 6.29 were least-squares fitted with a linear function on the ranges stated in the column (2). Secondly, the analysis described in text beginning page 198 was performed on all data of the K-32 line position shifts of all the four sources. The results of the latter approach are stated in rows marked as "full" in the column (2). With the use of the function defined in Eq. 6.12 it was assumed that in the time period of days 26-46 the exponential recovery of ϕ_{spec} took place, see Fig. 6.32 for the fit. The χ_r^2 value marked with * is common for all the sources. See text for further discussion.

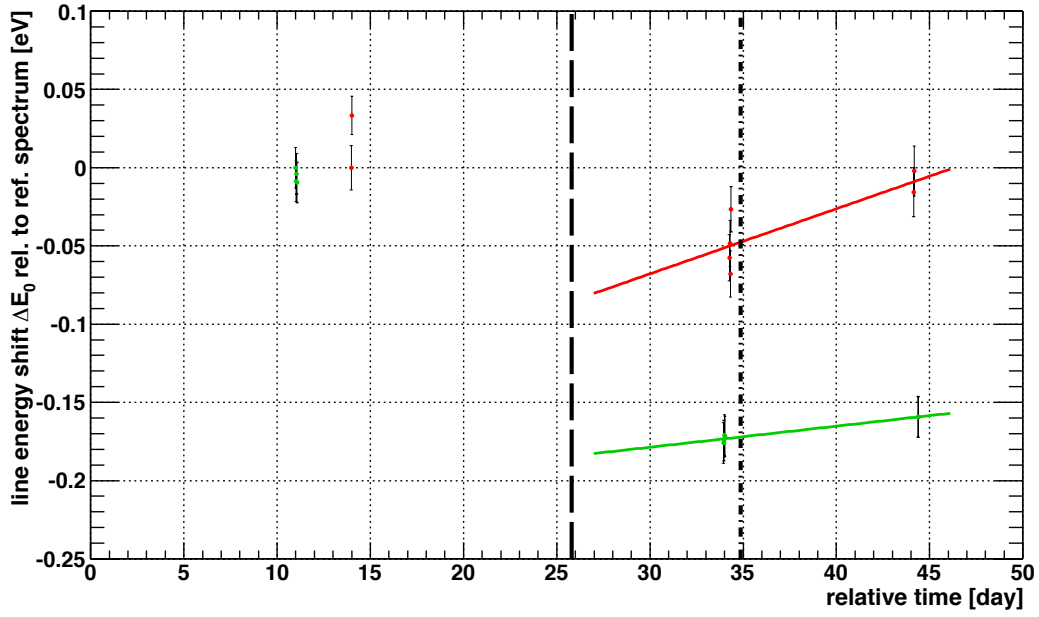


Fig. 6.30: The line position shifts of the lines L_1 -9.4 (red points) and L_3 -32 (green) of the source Pt-30 #2. The x axis denotes the relative time in days since 27.07.2009. The y axis shows the line energy shift ΔE_0 relative to the reference spectrum (chosen individually for each line). The vertical lines have the same meaning as in Fig. 6.29. The drifts are represented by the colored lines. See Tab. 6.13 for the resulting drifts of the line positions.

results in minor changes of the stated values of the order of 3%. The discrepancy between the literature value and the half-life values determined from the fits of measured amplitudes may be interpreted as diffusion of ^{83}Rb atoms deeper into the foils which reduces the number of zero-energy-loss electrons observed in the elastic peak. In addition, the coincidence of electron and pulser signals may give rise to summation events which also reduce the amplitude of the elastic peak in the ADC spectrum.

As already mentioned, on day 35 the test of deliberate venting of the source section was carried out. The philosophy of the test was the same as in the case of the venting tests reported previously in Sect. 6.3.3: the spectrometer vessel was kept intact while the source section was vented with air and the stability of the electron lines of all the four ion-implanted sources was examined. In this case the source section was vented up to atmospheric pressure for about 5 minutes. The results summarized in Tab. B.3 prove that the ion-implanted sources are indeed stable against the vacuum conditions on the meV scale. The observed shifts of the K -32 line position were compatible with zero: 8(9) meV (source Pt-30), 7(4) meV (Pt-30 #2), $-3(5)$ meV (Pt-15) and $-6(12)$ meV (Au-30). These values verify the finding of Sect. 6.3.3 where the first ion-implanted source Pt-30 showed the shift of the K -32 line of 5(4) meV upon venting up to 10^{-1} mbar. In addition, it should be noted that the venting test took place within the time period when ϕ_{spec} was recovering from the vacuum breakdown on day 26. Thus, strictly speaking, the observed shifts of the K -32 line positions may be partially “masked” by the positive drift of ϕ_{spec} in the time period of days 26–46.

In order to disentangle the drift of ϕ_{spec} and the drift of the individual K -32 line positions of the sources, a following approach was chosen: the K -32 data of each source were assumed

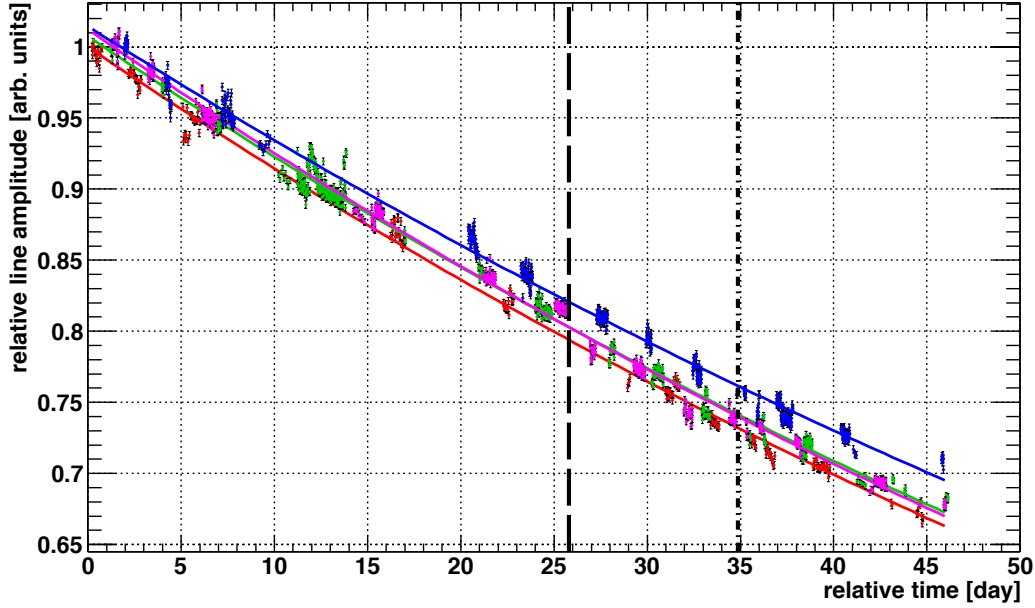


Fig. 6.31: The time dependence of the K -32 line amplitude of the sources Pt-30 (red points), Pt-30 #2 (green points), Pt-15 (magenta points) and Au-30 (blue points) as obtained from the fits carried out with the cross-correlation method. The time 0 corresponds to 27.07.2009. All the data sets were scaled to 1. The vertical lines have the same meaning as in Fig. 6.29. The colored lines denote the fits with an exponential function. The fits resulted into large χ_r^2 values in the range of 7–11 which was taken into account via multiplying the uncertainties of the fit results by $\sqrt{\chi_r^2}$. See text for the results of the fits.

in the form

$$y(t) = \begin{cases} a + b \cdot t & \text{for } t < \text{day } 26 \\ a + b \cdot t + \Delta\phi_{\text{spec}} \cdot e^{-\frac{t-t_0}{\tau}} & \text{for } t \geq \text{day } 26, \end{cases} \quad (6.12)$$

where t denotes time in days, a, b are the parameters of the linear drift of the K -32 line position of the given source, $\Delta\phi_{\text{spec}}$ represents the shift of the spectrometer work function, common for all the sources, and τ stands for the “lifetime” of the exponential recovery of ϕ_{spec} . The definition of such a function assumes that the drift of ϕ_{spec} was equal to zero before the vacuum breakdown occurred on $t_0 = \text{day } 26$. In addition, it is assumed that the drift of the given source was not altered by the vacuum breakdown and that the positive drift observed in the time period of days 26–46 is a combination of the “original” drift of a given source and the ϕ_{spec} recovery. The latter one was anticipated to have the form of an exponential function as a long-term effect of stabilization of experimental conditions. All the K -32 line data depicted in Fig. 6.29 were considered as one data set and the function in Eq. 6.12 was least-squares fitted with altogether 10 free parameters: four pairs of the parameters a, b corresponded to four ion-implanted sources, while $\Delta\phi_{\text{spec}}$ and τ were common for all the sources. The fit with $\chi_r^2=0.95(4)$ is illustrated in Fig. 6.32 and the results are summarized in Tab. 6.13. The common shift $\Delta\phi_{\text{spec}}$ was fitted as $-146(2)$ meV, in a very good agreement with the value of $-0.149(22)$ eV determined from the shifts of individual K -32 lines (see above). The lifetime τ was determined as $68(5)$ days which illustrates the need for a thorough bake-out of the complete system immediately after such a vacuum breakdown accident. The linear terms b [ppm month $^{-1}$], corrected for the drifts of the HV

divider K65 and the digital voltmeter, read $b(\text{Pt-30}) = -0.96(17)$, $b(\text{Pt-30 \#2}) = 1.02(16)$, $b(\text{Pt-15}) = 0.19(14)$ and $b(\text{Au-30}) = 2.64(16)$ ppm month⁻¹. Comparison with the linear drifts determined from the fits of the individual data sets on the range of days 0–26 (see Tab. 6.13) shows that both approaches deliver comparable results: the Pt-based sources exhibit the drifts of the order of 1 ppm month⁻¹ or less while the positive drift of the source Au-30 is the largest one.

6.4.2. Change of residual gas composition in spectrometer vessel resulting from vacuum breakdown

Several accidents of the vacuum breakdown in the spectrometer vessel hindered the measurements of the energy stability of the ^{83m}Kr conversion electrons. Namely the second measurement phase (Sect. 6.3) suffered from a number of vacuum-related problems. In addition, the very promising study of the energy stability of the four ion-implanted sources (Sect. 6.4.1), accomplished in this last phase of measurements, was strongly distorted by the vacuum breakdown on day 26. Obviously, the task of determining the electron energy stability on the level of ppm month⁻¹ requires ultra-stable conditions over a sufficient time span. It was realized in Sect. 6.3.2 that ϕ_{spec} is very sensitive to even sub-monolayer coverage due to rest gas adsorption.

Of course, the safety system and the overall slow control of the spectrometer setup was already greatly improved as the MAC-E filter spectrometer was transported from the Institute of Physics, University of Mainz, to the Karlsruhe Institute of Technology and rebuilt there into the monitor spectrometer. Thus, very likely any vacuum breakdown will be avoided in future measurements and it is not really necessary to study such an effect in a great detail. However, the fact that a commercial quadrupole mass spectrometer was directly attached to the spectrometer vessel was exploited in this work. This way the changes of the residual gas composition resulting from the changes of vacuum conditions in the vessel could be investigated. Such a study could possibly clarify the effects which accompanied the vacuum breakdowns observed during the second and third measurement phases. In this section the changes of the residual gas composition in the spectrometer vessel will be briefly discussed.

The residual gas analysis (RGA)¹² of the vessel volume was performed with the help of the quadrupole mass spectrometer MKS MircoVision Plus [MKS04] attached to the spectrometer vessel in the port of the turbomolecular pump. The mass spectrometer allowed to analyze the gas composition on the mass-to-charge range of $m/z = 0\text{--}100$, anyhow, only the range $m/z = 0\text{--}50$ was usually investigated. Thanks to the channel-plate secondary electron multiplier used as the detector the device was utilizable for detection of the partial pressures as low as 5×10^{-14} mbar. However, in our case we were interested in relatively high partial pressures of 10^{-12} to 10^{-9} mbar. As the device was factory-calibrated the data shown here are stated directly in units of pressure.

The mass spectra recorded at two typical situations, encountered in the course of the energy stability measurements, are depicted in Fig. 6.33. The spectrum depicted in Fig. 6.33(a)

¹²For a detailed introduction to the field of RGA the reader is kindly referred to [Rot98, OHa03] or similar textbooks on vacuum technology.

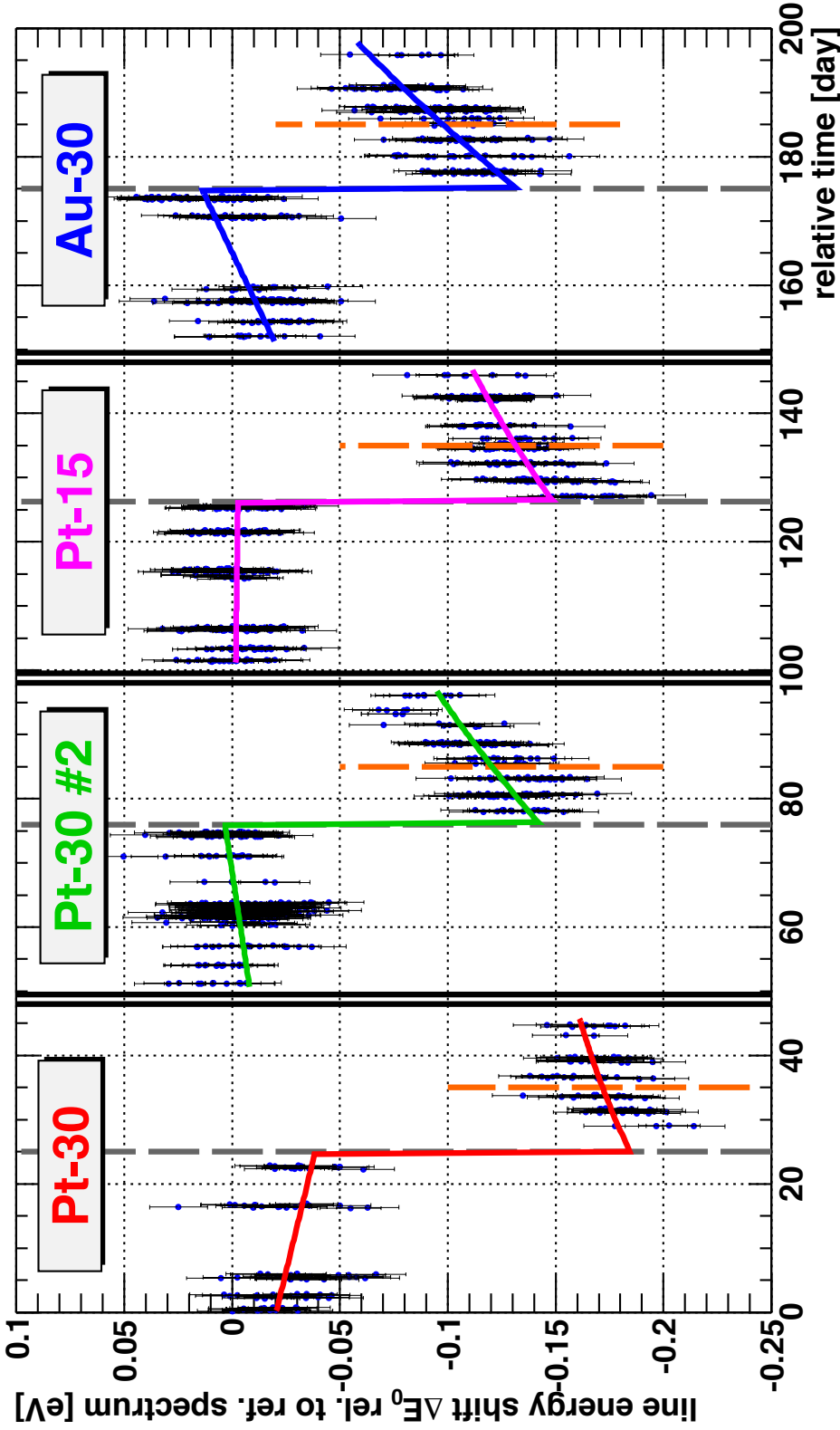


Fig. 6.32: The least-squares fit of the combination of four functions defined in Eq. 6.12 to all data of the K-32 line position shifts of the four ion-implanted sources. The individual integral spectra of the K-32 were analyzed with the help of the cross-correlation method, the results were shown in Fig. 6.29. One complete set of data from Fig. 6.29 was created in such a way that the data set of the source Pt-30 was plotted on the x axis in the time period of days 0–46, while the data sets of the other sources were shifted in time by 50, 100 and 150 days, respectively. Thus, the x axis shows the relative (and shifted) time in the range from 0 to $\simeq 200$ days. The data sets of the individual sources are shown separated by the vertical double lines, however, the fit with 10 free parameters was performed on all data points. The colored lines denote the parts of the fit function relevant for each source. In each data set the sudden shift $\Delta\phi_{\text{spec}}$, caused by the vacuum breakdown, is visible as a negative “jump” and the corresponding time in each data set is denoted by the vertical dashed grey line. The dashed orange lines mark the moment when the test of deliberate venting of the source section was performed. The χ^2_r of the fit amounted to 0.95(4), thus, a sufficiently good description of the data was accomplished with this simplified model. See Tab. 6.13 for the comparison of the fit results with the results obtained with the analysis of each data set separately.

shows the residual gas composition resulting from a moderate bake-out (180°C for 40 hours) of the spectrometer vessel. This bake-out was carried out in the time period between the second and third measurement phases. The total pressure amounted to 1.7×10^{-10} mbar shortly prior to the RGA scan¹³. Fig. 6.33(b) shows the result of the RGA scan performed on day 32 of the third measurement phase, thus, about 6 days after the vacuum breakdown which caused the shift of about -0.15 eV of the K -32 line of all the ion-implanted sources, see Fig. 6.29.

The mass spectrum shown in Fig. 6.33(b) was then scaled in such a way that the area of the peak at $m/z = 2$, corresponding to H_2 , was equal for both mass spectra "vacuum setup after bake-out" $\equiv A$ and "vacuum setup after vacuum breakdown" $\equiv B$. This allowed to perform the subtraction $B - A$ in a point-wise manner, *i. e.* no interpolation of the data points was used. This procedure relies on the stability of the m/z scale of the quadrupole mass spectrometer, which, strictly speaking, may drift in time. However, the aim of this section is to analyze the changes of the residual gas composition only qualitatively rather than to perform a precise quantitative analysis. Therefore, the simple subtraction $B - A$ is assumed to be sufficient for our purpose. The mass spectrum obtained via the subtraction $B - A$ is presented in Fig. 6.34. This spectrum can be fully ascribed to the effect of the vacuum breakdown. It should be emphasized that the interpretation of the RGA spectra is an uneasy task as all the gases have more than one peak in their so-called fragmentation pattern (also denoted cracking pattern). Thus, the main peak is usually accompanied by one or more additional peaks at lower m/z values. Moreover, the fragmentation factors generally vary with pressure and with the settings of the ion source (*e. g.* the kinetic energy of the electrons ionizing the gas molecules).

The five most prominent peaks in Fig. 6.34 are found on $m/z = 19, 18, 20, 28$ and 44 (stated according to the peak intensity). The changes of the gas composition in the spectrometer vessel can be summarized as follows [Rot98, OHa03, MKS04, Lin11]:

- Besides the $m/z = 2$ peak all the other peaks are below 10^{-12} mbar in the range of $m/z = 0-10$ in both spectra A and B . Thus, the differences in this range are clearly not visible in Fig. 6.34. In this mass range only helium at $m/z = 4$ is usually of concern.
- The presence of water causes the peaks at $m/z = 16, 17$ and 18 due to the species of O^+, HO^+ and H_2O^+ . It should be noted that these peaks are also present in the spectrum A , pointing to a probably insufficient bake-out procedure.
- Nitrogen gives rise to the peak at $m/z = 28$ and also 14 , due to the atomic N^+ and doubly ionized N_2^{++} .
- Molecular oxygen shows the peak at $m/z = 32$. An isotope peak can be expected at $m/z = 34$, however, due to the low natural abundance of ^{18}O this peak is not visible in our spectra.
- The $m/z = 40$ peak can be attributed to argon. This peak is not visible in spectrum A . In principle, the doubly ionized Ar^{++} may give rise to a peak at $m/z = 20$, however, the amplitudes ratio of the peaks $m/z = 40$ and $m/z = 20$ in the spectrum B indicates

¹³During the RGA scan the total pressure rose up to $\approx 3 \times 10^{-9}$ mbar due to the outgassing of the heated tungsten filament in the ion source of the quadrupole mass spectrometer. However, all the RGA spectra presented here were recorded about 30 minutes after the heating of the ion source filament was started. Thus, the initial outgassing of the ion source may be neglected in considerations.

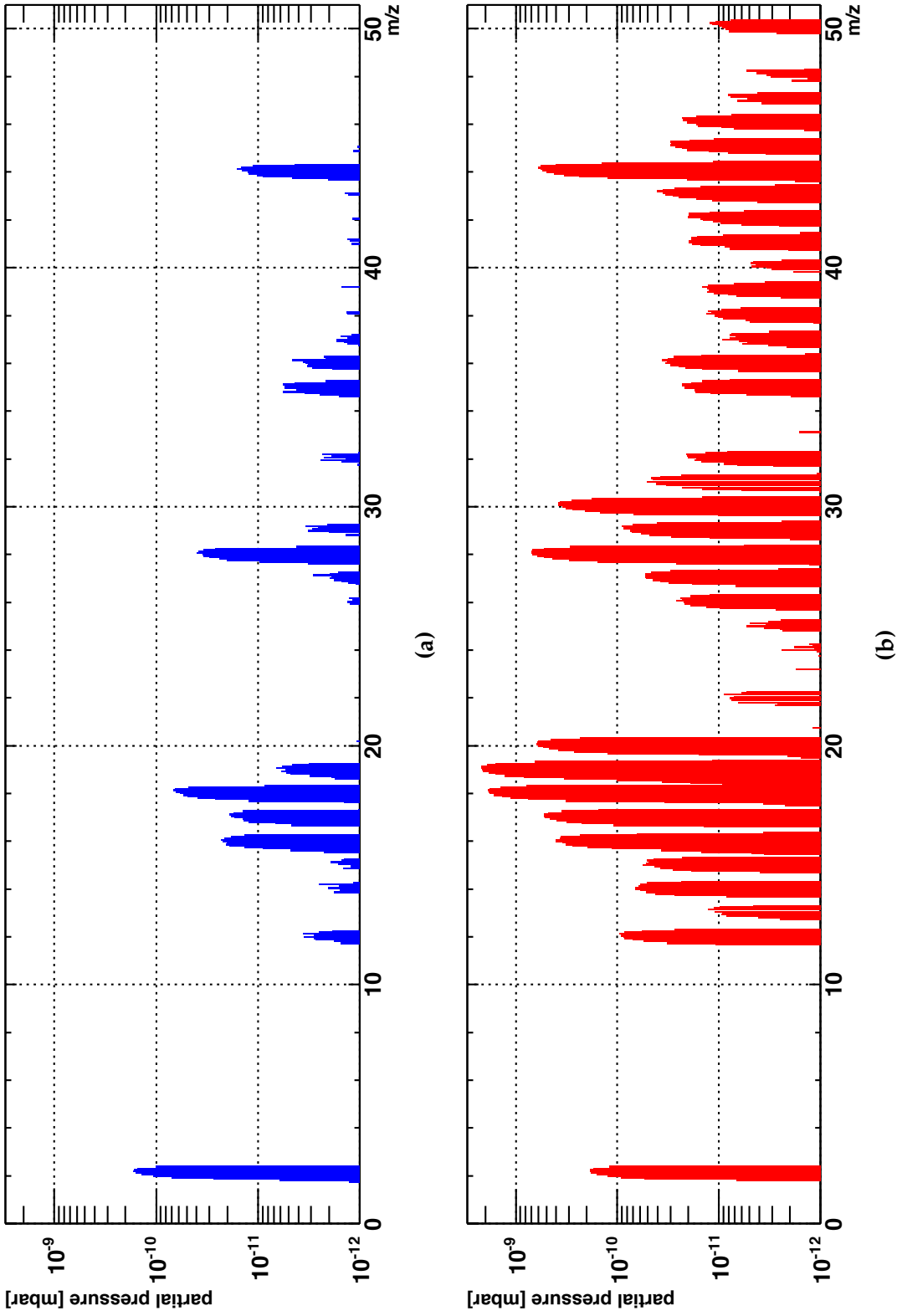


Fig. 6.33: The mass spectra obtained with the help of the RGA scans of vacuum in the MAC-E filter spectrometer vessel. The x axis denotes the mass-to-charge scale in the range of $m/z = 0-50$. The y axis (in log scale) represents the partial pressure of the gases present in the vacuum setup. The mass spectrum shown in (a), denoted as *A* in text, was obtained after a moderate bake-out of the complete vacuum setup. The mass spectrum shown in (b), denoted as *B* in text, was measured about one week after the vacuum breakdown discussed in Sect. 6.4.1. For the sake of clarity only the peaks of amplitudes higher than 10^{-12} mbar are shown.

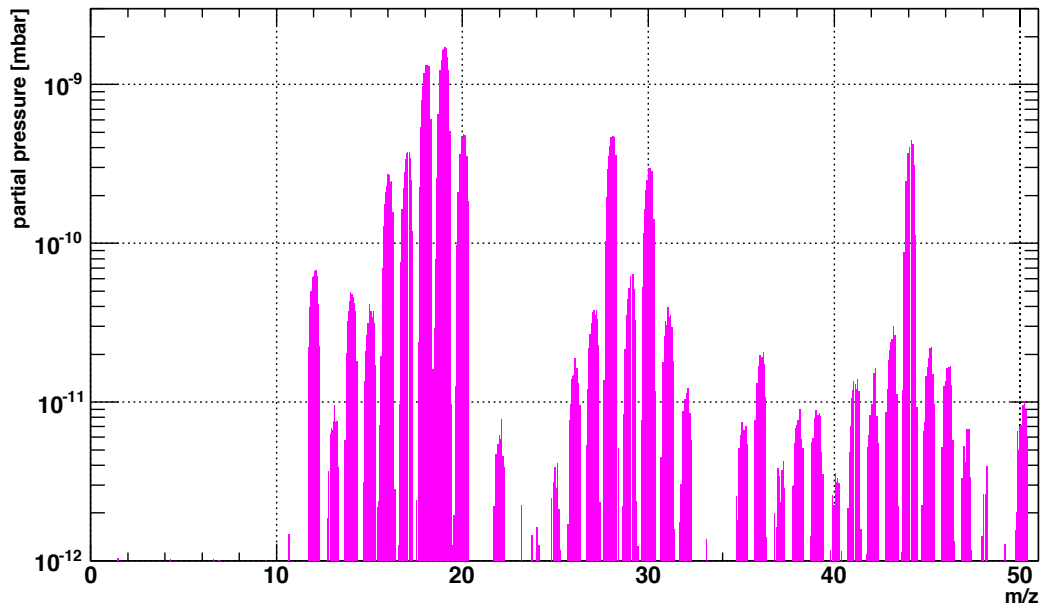


Fig. 6.34: The mass spectrum obtained from the subtraction $B - A$ of the spectra depicted in Fig. 6.33. The x axis denotes the mass-to-charge scale in the range of $m/z = 0$ –50. The y axis (in log scale) represents the changes of the residual gas composition of the spectrometer vessel resulting from the vacuum breakdown. See text for discussion of origin of the individual peaks.

the peak at $m/z = 20$ is not caused by argon. Similarly, the presence of neon in the vacuum setup is not probable. Thus, the peak at $m/z = 20$ suggests some kind of contamination, see below.

- Carbon dioxide has a more complex signature in the mass spectrum: it causes the peak $m/z = 44$ and also 12 and 22 due to C^+ and CO_2^{++} , respectively. Moreover, the fragments of CO_2 result into peaks at $m/z = 12$, 13 and 16.
- Carbon monoxide is also commonly present in the UHV, it can be found on $m/z = 28$ and its fragments on $m/z = 12$ and 16.
- The peak at $m/z = 19$ reveals the contamination of the vacuum setup with an oil containing fluorine. In addition, hydrofluoric acid (HF) matches with the peak at $m/z = 20$. In principle, the peak at $m/z = 20$ may be also caused by Ar^{++} and/or Ne^+ . However, considerations of the fragmentation patterns suggest that the contributions of these gases to the peak at $m/z = 20$ cannot explain the observed amplitude. The presence of HF corresponds well to the fact that the oil rotary pumps were used in the vacuum setup. During the accident of the vacuum breakdown the oil very probably back-streams into the UHV section of the vacuum setup. Interestingly, the peak at $m/z = 19$ is already present in the spectrum A , *i.e.* even after the bake-out. This may again point to an insufficient bake-out procedure after previous vacuum failures. Moreover, it cannot be excluded that the oil back-streaming took place even during normal operation of the turbomolecular pumps. In any case, the oil-based backing pumps should be avoided in the setup in future.

To summarize, the vacuum breakdown resulted into the contamination of the vacuum setup with oil, water and hydrocarbons. The presence of these substances in the setup was re-

vealed even in the spectrum *A* representing the “clean vacuum setup”. One may speculate about some relationship between the observed energy stability of the conversion lines of the ion-implanted $^{83}\text{Rb}/^{83\text{m}}\text{Kr}$ sources in the range of ppm month⁻¹ (see Sect. 6.4.1) and the oil contamination: for example, the oil could also contaminate the sources and form some kind of layer on their surface, stabilizing the physical/chemical properties. On the other hand, the majority of the conversion electrons emitted from the ion-implanted sources comes from the metallic state (cf. Sect. 4.2.3) where the surface effects are not expected to play a role. Therefore, it is anticipated that a comparable or even better energy stability of the conversion lines will be reached with the ion-implanted sources in the coming measurement campaign at the monitor spectrometer in the Karlsruhe Institute of Technology. The vacuum setup of the monitor spectrometer is built as completely oil-free [Gou10].

Unfortunately, similar mass spectra *A* and *B* are not available in the case of the vacuum breakdowns which occurred in the course of the second measurement phase. Nevertheless, it can be assumed that contamination of the vacuum setup with water and hydrocarbons took place there as well.

6.5. Summary of results

The results obtained in the course of the long-term energy stability measurements described in Sect. 6.1 to Sect. 6.4 will be briefly discussed in this section. Firstly, the individual sources will be mutually compared regarding the energy stability of the conversion electrons. Secondly, the various systematic effects encountered in the course of the measurements will be discussed.

6.5.1. Energy stability of conversion electrons emitted by the solid

sources

It was shown in Sect. 3.1 that the relative stability of $\Delta_{\text{rel}}(\text{HV}) = \pm 3.2$ ppm of the retarding potential of 18.6 keV is required in the KATRIN experiment over the time period of one tritium run. As the length of each tritium run is foreseen to be two months, the stability requirement can be expressed as $\Delta_{\text{rel}}(\text{HV}) = \pm 1.6$ ppm month⁻¹. As discussed on page 137, the aim of this work is to minimize the linear drift of the conversion lines of the solid $^{83}\text{Rb}/^{83\text{m}}\text{Kr}$ sources. Thanks to the very low drift of the conversion line energy it shall be possible to recognize the fluctuations of the HV scale in KATRIN on the time scale of tens of minutes to months.

In Fig. 6.35 the relative drifts $d_{\text{source}}^{\text{rel}}$ [ppm month⁻¹] of the *K*-32 conversion line are presented as they were obtained in the course of the long-term measurements carried out with vacuum-evaporated and ion-implanted $^{83}\text{Rb}/^{83\text{m}}\text{Kr}$ sources (see Tab. 6.2, Tab. 6.4, Tab. 6.7 and Tab. 6.13). As the kinetic energy of the *K*-32 conversion electrons amounts to $\simeq 17.8$ keV the relative drifts stated in the units of ppm month⁻¹ can be directly compared to the KATRIN requirement $\Delta_{\text{rel}}(\text{HV})$ defined at 18.6 keV. The drifts $d_{\text{source}}^{\text{rel}}$ are corrected for the drift

6. Long-term measurements...

m_{div} of the dividing ratio of the HV divider as well as for the drift k_{dvm} of the scale factor K of the digital voltmeter, see Eq. 6.1. However, in some cases where the vacuum conditions were not stable, the drift $d_{\text{source}}^{\text{rel}}$ contains also the drift of the spectrometer work function ϕ_{spec} (drift of which was denoted C in Eq. 6.1). As the stability of ϕ_{spec} was not monitored during the measurements of the conversion lines, it is not possible to extract the intrinsic drift of the conversion line energy from the measurements carried out in the time periods where the condition $C = 0$ cannot be assumed—the only exception here was the third measurement phase where the analysis of all data of the four ion-implanted sources enabled to disentangle the linear drifts of the K -32 line and the effect of ϕ_{spec} recovery (assumed to be exponential).

In the pilot measurement phase (vacuum-evaporated sources S 11 and S 13, see Sect. 6.1) considerable negative drifts of the K -32 line energy were observed, exceeding significantly the KATRIN stability requirement. In the case of measurements carried out with sources cooled down to $\simeq 70$ K the negative drift can be attributed to changes of the source work function ϕ_{source} due to rest gas adsorption. The results obtained with the sources kept at room temperature suffered from low statistics and probably also from imperfect vacuum conditions in the source section after the source cooling was stopped: no bake-out was carried out in order to recover ϕ_{source} from rest gas adsorption.

A single vacuum-evaporated source S 28 was investigated in the first measurement phase (see Sect. 6.2). After the initial period of about one week, during which the drift $d_{\text{source}}^{\text{rel}}$ amounted to $\simeq 14$ ppm month $^{-1}$, the experimental conditions stabilized and the three weeks measurement yielded $d_{\text{source}}^{\text{rel}} \simeq 3$ ppm month $^{-1}$. The initial drift is very probably caused by the stabilization of ϕ_{spec} and/or ϕ_{source} . On day 30 the measurement was significantly affected by the sudden unexpected shift of the HV scale (Sect. 6.2.2) which was found to be independent on the voltage and was determined as $\simeq 0.93$ V. However, it was assumed that the drift m_{div} of the HV divider was not influenced by the HV scale shift. This was supported by the results obtained on the basis of a simple method introduced in Sect. 6.2.1 which allowed to disentangle the drifts $d_{\text{source}}^{\text{rel}}$ and m_{div} . Further measurements with the shifted HV scale resulted in negative values of $d_{\text{source}}^{\text{rel}}$.

In the second measurement phase (see Sect. 6.3) two vacuum-evaporated sources S 28 and S 29 were investigated simultaneously together with the ion-implanted source Pt-30. The experimental conditions were rather unstable in the first two months of the measurement when several vacuum breakdowns occurred. Then the six weeks measurement was accomplished during which the sources exhibited drifts compatible with the KATRIN requirement. It should be noted that this measurement in the time period of days 64–107 followed after the vacuum breakdown on day 61 without any bake-out. Thus, some slow recovery of ϕ_{spec} , *i. e.* $C \neq 0$, cannot be excluded in this time period.

Altogether four ion-implanted sources Pt-30, Pt-30 #2, Pt-15 and Au-30 were investigated simultaneously in the third measurement phase, see Sect. 6.4. At the beginning of the measurement phase the source section was moderately heated after the insertion of the sources into vacuum. Moreover, about one month prior to the start of measurements a thorough bake-out of the complete vacuum setup was accomplished. In the time period of days 0–26 the drifts $d_{\text{source}}^{\text{rel}}$ of the K -32 line of the platinum-based sources were found to be of the order of 1 ppm month $^{-1}$ or less, thus, fully satisfying the KATRIN requirement. The K -32 line energy drift of the source Au-30 was determined as $\simeq 2.4$ ppm month $^{-1}$. On day 26 an-

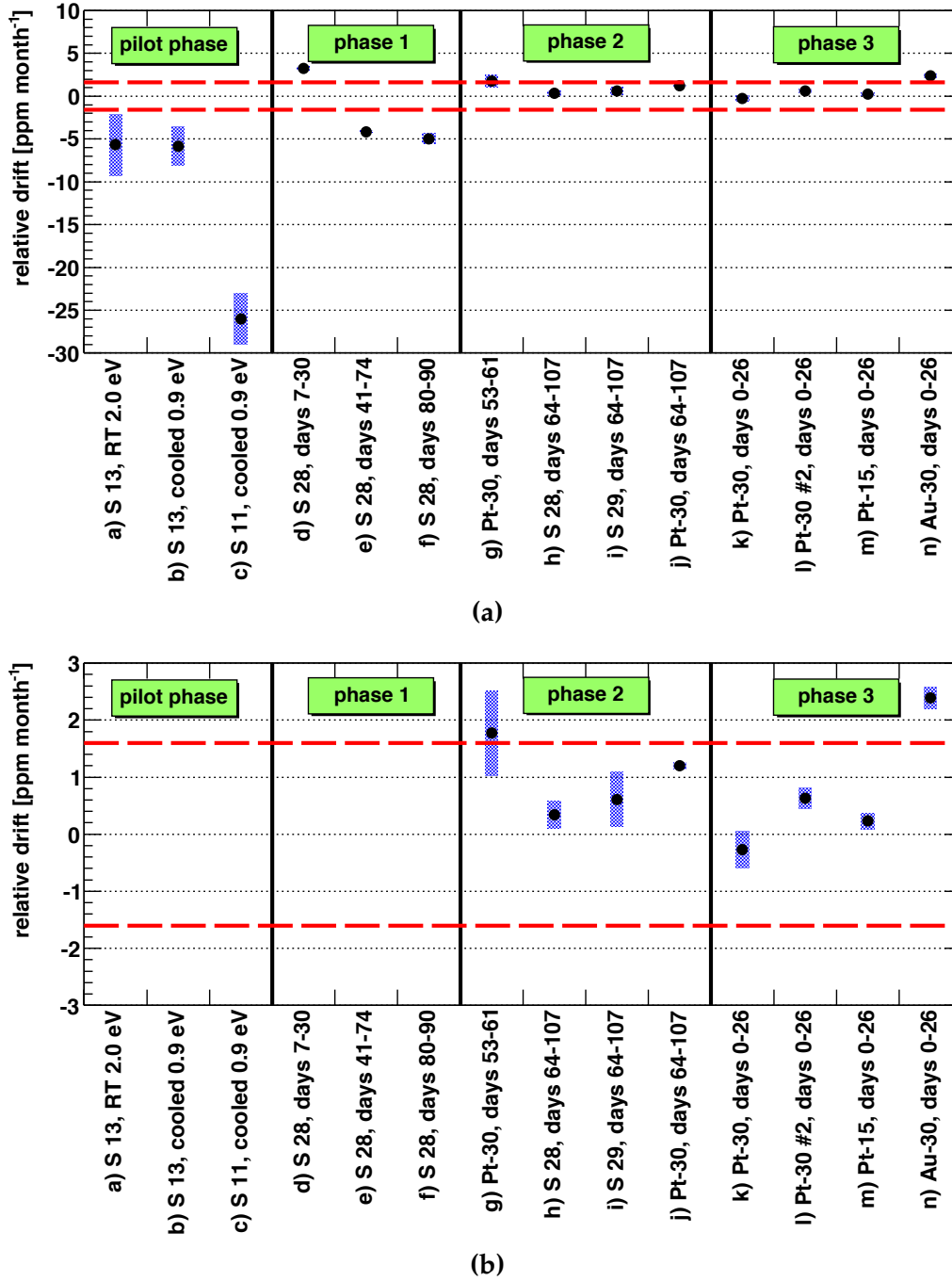


Fig. 6.35: The overview of the relative drifts $d_{\text{source}}^{\text{rel}}$ [ppm month⁻¹] of the conversion electron line K-32 of all the solid sources tested in the framework of this work. The figure is based on the data stated in Tab. 6.2, Tab. 6.4, Tab. 6.7 and Tab. 6.13, however, only the results obtained in well defined experimental conditions (where available) are shown here. The figure (a) covers the span of the y axis from -30 to $+10$ ppm month⁻¹, whereas the figure (b) shows a zoom spanning only ± 3 ppm month⁻¹ of the y axis. The horizontal dashed red lines mark the KATRIN requirement of $\Delta_{\text{rel}}(\text{HV}) = \pm 1.6$ ppm month⁻¹ of the energy scale stability. The vertical lines separate the individual measurement phases accomplished at Mainz MAC-E filter spectrometer. The labels on the x axis denote the source and the time period of the given measurement. The error bars represent only the statistical uncertainties. As discussed in coming Sect. 6.5.2 the overall systematic uncertainty of the drifts was estimated as 0.64 ppm month⁻¹.

other vacuum breakdown occurred which was not followed by any bake-out procedure. In the time period of days 26–46 all the sources exhibited a common positive drift of several ppm month⁻¹. This drift was interpreted as the combination of the drift of a given source and the recovery of ϕ_{spec} . Assuming such a recovery in the exponential form, it was possible to analyze all data in one set and to extract the parameters of the shift and the “lifetime” of ϕ_{spec} recovery, namely $\Delta\phi_{\text{spec}} = -146(2)$ meV and $\tau = 68(5)$ days. The energy of the conversion lines of the ion-implanted sources was reproducibly found to be stable against abrupt changes of the vacuum conditions even on the meV scale, the observed shifts of the K-32 line position were compatible with zero: 8(9) meV (source Pt-30), 7(4) meV (Pt-30 #2), -3(5) meV (Pt-15) and -6(12) meV (Au-30). From this point of view the ion-implanted sources are superior to the vacuum-evaporated ones as well as to the CKrS concept.

Clearly, stable vacuum conditions were crucial for reaching the conversion line energy drifts of the order of ppm month⁻¹ as all other instrumental effects were well controlled, in principle. A summary of the various effects is presented in the coming section.

6.5.2. Overview of systematic effects

So far only the statistical uncertainties were stated, here the systematic effects of the long-term measurements of the conversion electrons energy stability shall be discussed. The various systematic uncertainties can be summarized, following loosely the structure of Chap. 5, as follows:

a) MAC-E filter

1. stability of the energy resolution

The relative energy resolution $\Delta E / E_{\text{start}}$ of the MAC-E filter spectrometer is determined¹⁴, in accordance with Eq. 2.13, by the ratio of the minimal magnetic field strength B_A found in the analyzing plane to the maximal magnetic field strength B_{max} in the center of the superconducting solenoids A and B (see Fig. 5.1). The field of $B_{\text{max}} \simeq 6$ T was realized by providing the current of $I_A = I_B = 50$ A to the windings of the coils. Obviously, the currents I_A and I_B were checked during each procedure of energizing or de-energizing the solenoids. This way it was observed that I_A and I_B practically do not change over time periods spanning several months. Thus, any instability of the resolution ΔE can be expected to stem mainly from the instability of the weak field B_A which usually amounts only to units of G (Gauss), depending on the requested resolution, and is thus susceptible to changes of the Earth's magnetic field *etc.* Of main interest is the z component of B_A , parallel to the axis of the spectrometer. In the course of the long-term test measurements of the condensed ^{83m}Kr source [Ost08] at Mainz MAC-E filter the stability of the z component of B_A was monitored in a close vicinity to the spectrometer vessel¹⁵. A continuous four days measurement showed that the z -

¹⁴ E_{start} denotes the starting kinetic energy of the electron in the source.

¹⁵Of course, it is desirable to know the value of B_A directly on the spectrometer z axis. However, due to vacuum the measurement of B_A has to take place outside the spectrometer vessel. It is not possible to calculate $B_A(0, 0, 0)$ from a single value $B_A(x, y, 0)$, but this does not represent a problem as only the stability is of our concern.

component of B_A was stable in the window of ± 8 mG. Considering $\Delta E = 0.9$ eV and $E_{\text{start}} = 17824$ eV (K -32 line), the minimal magnetic field amounts to $B_A = 3.03$ G and the observed instability would cause the change of ΔE by 0.5 % which can be safely neglected. Unfortunately, such monitoring of the spectrometer resolution was not repeated during the test measurements of the solid $^{83}\text{Rb}/^{83\text{m}}\text{Kr}$ sources, but similar stability of the resolution can be expected here. Thus, this effect does not represent a problem.

2. stability of the currents in the auxiliary perpendicular coils

The influence of the currents in the auxiliary perpendicular coils¹⁶ on the energy and shape of the conversion line was studied in Sect. 6.2.4. The K -32 line of the source S 28 was scanned for various combinations of the currents in the coils. The parameters of the conversion line (position¹⁷, amplitude and background) showed a complicated dependence on the currents, however, it became clear that the auxiliary perpendicular coils affect the line shape in the same way as moving the source in the x - y plane. Most importantly, it was found that the stability of the power supplies delivering the current to the coils is negligible considering the shifts of the K -32 line caused by the changes of the coils currents. In addition, any malfunction of one of the coils would be readily observed as a significantly shifted spectrum or as a spectrum with a reduced amplitude-to-background ratio.

3. stability of the spectrometer work function

In the course of the measurement phases it became obvious that the stability of ϕ_{spec} is a key factor which could not be monitored in some way at that time. The only means of controlling (minimizing) the drift of ϕ_{spec} was a thorough bake-out procedure performed at the beginning of a given measurement phase. Any vacuum breakdown should certainly be avoided in the future measurements—this obviously holds not only for the monitor spectrometer, but for the whole KATRIN setup. In addition, the fluctuations of the work function will be monitored with the help of the Kelvin probe technique [Bec11] on a number of places in the KATRIN setup where the stability of the work function is important regarding the observable $m^2(\nu_e)$.

b) source section: $[x, y, z]$ source position

The $[x, y, z]$ position of the source with respect to the center of the solenoid B influences the magnetic field B_S which, in turn, determines the maximal angle $\theta_{\text{start}}^{\text{max}}$ of the acceptance cone for the emitted electrons. The influence of the source position on the K -32 line was studied in Sect. 6.2.4 with the help of the source S 28 measured at the energy resolution of 0.9 eV and again in Sect. 6.3.5 with the help of the source Pt-30 measured at resolutions 0.9 and 2.0 eV, respectively. The reproducibility of the source positioning in the x - y plane was also verified. The overall setup was found to be very sensitive to the source misalignment of the order of 1 mm: depending on the direction in the x - y plane, the 1 mm misalignment can cause the shift of the K -32 line of 33(3) meV (source Pt-30, resolution 0.9 eV). As the precision of the movement in the x and y directions amounted to 0.1 mm, it is not necessary to consider the effect of the source misalign-

¹⁶They were used for positioning the magnetic flux with respect to the spectrometer axis.

¹⁷More precisely, the shift of the measured conversion line energy was determined with respect to the reference spectrum.

ment in respect with the drift of the conversion line energy observed in the long-term measurements. In order to prevent any sudden shift of the conversion lines energy, the source position should be kept constant during the measurement phase.

c) detector section: $[x, y, z]$ detector position

The $[x, y, z]$ position of the detector with respect to the center of the solenoid A was chosen in the following way: the z position was chosen as close to the solenoid A center as possible¹⁸ and in the x - y plane the detector was positioned so that the observed background was minimal. Thus, the detector was assumed to lie on the spectrometer z axis. Similarly to the source position, the detector position should be kept constant during the measurement phase.

d) high voltage system

1. drift of the dividing ratio of the HV divider

The drift of $M(t)$ was taken into account in the analysis via the term m_{div} . The drifts of the HV dividers K35 and K65, used in the course of the long-term measurements, were determined as $m_{\text{div}}^{\text{PTB}}(\text{K35}) = 0.60(10) \text{ ppm month}^{-1}$ and $m_{\text{div}}^{\text{PTB}}(\text{K65}) = -0.13(10) \text{ ppm month}^{-1}$ (see Tab. 5.1) on the basis of standard calibration procedures. The uncertainty of the drifts of the order of $0.1 \text{ ppm month}^{-1}$ seems to be the limit of the systematic uncertainty of the presented method relying on the long-term stability of the HV dividers, however, the dividers proved to be more than sufficiently stable for our purpose.

2. drift of the scale factor of the digital voltmeter

The drift of $K(t)$ was determined on the basis of regular calibrations. The DC 20 V range of the voltmeter was calibrated at -10 V with the help of the 10 V DC reference (see below). The stability of the voltmeter is specified by the producer as 1.1 ppm in 24 hours [Flu08] (temperature window $\pm 1^\circ\text{C}$ around the temperature value at which the device was calibrated). However, no severe shifts of the scale factor K were observed, the only exception being the shift caused by the malfunction of the air conditioning system in the laboratory which occurred in the third measurement phase (see Fig. 6.27). Instead, K was found to gradually rise or fall in time and the scatter of the data around the least-squares fitted linear function amounted typically to 0.3 ppm.

3. stability of the DC 10 V reference

The stability of the DC 10 V reference is specified by the producer as $0.1 \text{ ppm year}^{-1}$ [Flu08], however, the drift of the device used in this work was determined as $0.24 \text{ ppm year}^{-1}$ [Bau11]. Such a low drift can be neglected in our case as all the other drifts (of the various devices as well as the sources themselves) were at least by the order of 10–100 bigger.

¹⁸Due to mechanical obstacles it was not possible to place the detector in magnetic fields higher than 1.06 T.

e) data acquisition system

1. stability of the scale of the ADC module

One of the factors of the DAQ system which could influence the long-term energy stability measurements of the conversion lines is the stability of the ADC scale. Any unrecognized shift of the ADC scale would directly influence the number of recorded electron events which is then used for the construction of the integral electron spectrum. However, the summation windows in the ADC raw spectra were always chosen wide enough (see Fig. 5.12) so that the shift of the ADC scale should not matter. However, the long-term measurement of the $^{83\text{m}}\text{Kr}$ low energy conversion lines (L_1 -9.4 line *etc.*) suffered from the instability of the noise edge of the detector electronic chain: it can be seen in Fig. 5.10 that the signal of the L_1 -9.4 electrons is partially cut off by the low level discriminator of the ADC. Moreover, the noise edge was optimized throughout the measurement series, thus, a precise determination of the L_1 -9.4 line energy drift was hindered by varying experimental conditions.

2. stability of the pulser frequency

The key item of the DAQ system, regarding the high electron count rates of the order of 10^4 counts s^{-1} , was the research pulser module which enabled to perform the dead time correction (see Sect. 5.2.3). The stability of the pulser frequency is an important factor of the long-term energy stability measurements as any unrecognized instability would influence the dead time-corrected count rate. As stated already in Sect. 5.2.3 the pulser frequency f was regularly checked and some kind of stabilization of f ($f_1 \simeq 102.5$ Hz \rightarrow $f_2 \simeq 105.0$ Hz) was observed during the time period of 7 months. In the analysis the mean value of $f_0 = 104.0(7)$ Hz was taken into account. The effect of the pulser frequency instability can be assessed in the following way: considering for example the K -32 line of the source Au-30, one can produce the integral spectrum with an "improper" pulser frequency $f'_0 = 114.0(7)$ Hz, thus, overestimating the average f_0 by 10 Hz. Similarly, the opposite case of $f''_0 = 94.0(7)$ Hz shall also be investigated. Ten spectra were analyzed with the help of the cross-correlation method where one of the ten spectra produced with f_0 was taken as the reference. In both cases of f'_0 and f''_0 the shift of the K -32 line position was determined as $0(7)$ meV, *i. e.* the fitted line position does not depend on the pulser frequency. On the other hand, the changes of the amplitude and background matched very well with the ratios f'_0/f_0 and f''_0/f_0 , respectively: in the case of f'_0 the amplitude and the background of the line were by 9.6% higher whereas in the case of f''_0 they were by 9.6% lower. Therefore, some unrecognized change of the pulser frequency would be observed as an abrupt change of the amplitude and background of the given conversion line which would otherwise fall exponentially in time due to the radioactive decay of ^{83}Rb . It can be thus assumed that the observed stabilization of the pulser frequency did not affect the drifts of the conversion lines energy.

In sum, an attempt was made to critically assess all known systematic effects which could possibly affect the presented long-term measurements. Considering the aforementioned effects it seem appropriate to safely estimate the limit of the experimental systematic uncertainty of the drifts $d_{\text{source}}^{\text{rel}}$ as 0.5 ppm month^{-1} . Adding this value quadratically with the

6. *Long-term measurements...*

systematic uncertainty of $0.4 \text{ ppm month}^{-1}$ stemming from the use of the cross-correlation method (discussed in Sect. 5.2.8), the overall systematic uncertainty of the drifts $d_{\text{source}}^{\text{rel}}$ summarized in Fig. 6.35 reads $0.64 \text{ ppm month}^{-1}$.

7. Conversion electron spectrum of $^{83\text{m}}\text{Kr}$ in solid sources

In previous Chap. 6 the focus was made on the relative energy stability of $^{83\text{m}}\text{Kr}$ conversion lines of the solid $^{83}\text{Rb}/^{83\text{m}}\text{Kr}$ sources prepared by two different production techniques of vacuum evaporation and ion implantation. The stringent demand on minimizing the linear drift of the conversion lines energy, stemming from the KATRIN requirement of $\Delta_{\text{rel}}(\text{HV}) = \pm 1.6 \text{ ppm month}^{-1}$ at 18.6 keV, was fulfilled in the second (see Sect. 6.3) and the third (see Sect. 6.4) measurement phases when stable vacuum conditions were achieved. Moreover, the ion-implanted sources exhibited considerable stability (on the meV scale) of the conversion line energies against abrupt changes of vacuum conditions.

In this chapter the shapes and absolute kinetic energies of the various $^{83\text{m}}\text{Kr}$ conversion lines of the solid $^{83}\text{Rb}/^{83\text{m}}\text{Kr}$ sources are of main interest. Whereas mainly the cross-correlation method (cf. Sect. 5.2.7) was used in previous chapter, here mainly the many-parameters fit (cf. Sect. 5.2.6) of the conversion spectra will be utilized. Besides the different method of data analysis, the same conversion electron spectra will be considered here, previously used predominantly for determining the drift of the line energy in time. However, only the data obtained in well defined experimental conditions will be considered (thus, *e. g.* spectra measured after a vacuum breakdown will not be used), where available. The choice of data is discussed in Sect. 7.1 together with the anticipated precision of the analysis.

In Sect. 7.2 the shapes and in Sect. 7.3 the absolute kinetic energies of the conversion electron lines will be discussed in detail. It will be shown that while the spectra obtained with the vacuum-evaporated sources can be well described with a single line, the spectra of the ion-implanted sources exhibit some kind of asymmetry on the low energy side of the elastic peak. Several hypotheses attempting at explaining such an asymmetry are discussed in Sect. 7.4. Moreover, in Sect. 7.3 the absolute kinetic energies will be compared with the 9.4 and 32 keV gamma transition energies¹ of $^{83\text{m}}\text{Kr}$, using the electron binding energies of gaseous krypton (tabulated in App. A). The absolute kinetic energies of the various conversion lines also enable us to perform an important test of linearity of the HV scale (or energy scale, actually): the difference of the $^{83\text{m}}\text{Kr}$ gamma transition energies can be compared to the differences of the absolute kinetic energies of the conversion electrons populated in these two gamma transitions. Such a “cross-check” is reported in Sect. 7.3 as well.

All the analyses advertised above deal mainly with the elastic peak in the conversion electron spectrum, corresponding to the zero-energy-loss electrons. In Sect. 7.5 the structure of

¹They are known from independent measurements based on high precision gamma ray spectroscopy with semiconductor detectors, see Sect. 3.3.2.

the electron energy loss spectra, obtained with the solid sources, will be discussed.

7.1. Choice of data and estimate of analysis precision

It became obvious in previous chapter that the vacuum conditions may strongly influence the energy of the conversion lines measured with the electron spectrometer. In the case of the ion-implanted sources, however, it was possible to prove that the energies of the conversion lines themselves are not affected, but on the other hand, the spectrometer work function ϕ_{spec} was significantly affected (abruptly shifted) due to vacuum breakdowns several times. From this point of view it seems reasonable to analyze here only the data obtained in the time periods when ϕ_{spec} can be assumed to be constant.

Consequently, the following data were chosen for the analysis:

0. From the data of the pilot measurement phase (see Sect. 6.1) carried out with the vacuum-evaporated sources S 11 and S 13 mounted onto the CKrS setup only the conversion electron spectra measured with the sources kept at room temperature will be considered. This way it is ensured that the data are not affected by possible changes of the source work function ϕ_{source} due to rest gas adsorption on cooled sources. In Fig. 6.2 the selected data can be seen as red points on days $\simeq 5$ (source S 13) and $\simeq 27$ (S 11).
1. In the first measurement phase (see Sect. 6.2) the vacuum-evaporated source S 28 was investigated for about three months. In Fig. 6.5 it can be seen that after the initial one week period, during which the drift $d_{\text{source}}^{\text{rel}}$ of the K-32 line energy amounted to $\simeq 14 \text{ ppm month}^{-1}$, the experimental conditions stabilized and the three weeks measurement yielded $d_{\text{source}}^{\text{rel}} \simeq 3 \text{ ppm month}^{-1}$. On day 30 a sudden unexpected shift of the HV scale was observed, independent of the input voltage. The positive shift was determined as $\simeq 0.93 \text{ V}$ and the measurements continued with the shifted HV scale (see Fig. 6.13). For the analysis the data obtained in the time periods of days a) 7–30, b) 41–74 and c) 80–90 will be considered. It should be kept in mind, though, that there is the shift of $\simeq 0.93 \text{ eV}$ between the data sets (a) and (b), and, moreover, both the source and the detector were moved in higher magnetic fields between the measurements (b) and (c). This resulted in the shift of of the K-32 line position of about -0.24 eV , pointing to geometrical misalignments of the experimental setup.
2. During the second measurement phase (see Sect. 6.3) one ion-implanted source Pt-30 and two vacuum-evaporated sources S 28 and S 29 were investigated simultaneously. In Fig. 6.16 it can be seen that the experimental conditions were unstable in the first two months of the measurement when several vacuum breakdowns occurred. For the analysis of the absolute kinetic energies the electron spectra obtained in the time periods of days 53–61 (source Pt-30 measured shortly after the bake-out of the spectrometer vessel) and 64–107 (the sources Pt-30 and S 28 measured after the vacuum breakdown which occurred on day 61) were chosen. It should be noted that no bake-out was performed after the vacuum breakdown on day 61. Moreover, this measurement phase was carried out with the shifted HV scale, thus, here the shift of the line positions of about $0.93 - 0.24 = 0.69 \text{ eV}$ should in principle be noticeable with respect

to the data marked (b) in the item (1) of this list. The shift of -0.24 eV, resulting only from the movement of the source and the detector, shall be kept in mind during the estimation of the systematic uncertainties. Data obtained after the sudden change of the scale factor of the HV divider K35 (cf. Sect. 6.3.4) will not be considered in this chapter. Concerning the source S 29, the other conversion lines (different from the K-32 line) were measured only in the time period of days 0–15, thus, this data will be used for the analysis.

3. The third and final measurement phase was reported in Sect. 6.4: altogether four ion-implanted sources Pt-30, Pt-30 #2, Pt-15 and Au-30 were investigated simultaneously. For our purpose the data collected in the time period of days 0–26 (cf. Fig. 6.29) are very suitable as in this time period the vacuum conditions were stable and the sources exhibited very low drifts of the order of 1 ppm month⁻¹ or less². In the case of the source Pt-30 the L_1 -9.4 line was measured only in the time period of days 26–46 when ϕ_{spec} was recovering from the vacuum breakdown.

Concerning the analysis of the electron energy loss spectra, the spectra recorded in “unstable” experimental conditions (in the sense that *e. g.* the recovery of ϕ_{spec} was taking place) can also be considered if necessary: for the purpose of evaluating the complex structure of the shake-up/off peaks (see Sect. 4.3.2) and the inelastically scattered electrons (see Sect. 4.3.3), some shift of the complete spectrum of the order of 1 eV can be safely omitted.

It should be emphasized that for the analysis of a given conversion line always a group of typically 4–20 spectra was used. Therefore, the values presented in the coming sections represent weighted means. Also in the case of the K-32 line, which was frequently scanned for the purpose of precise determination of the line energy drift, not all data are considered. For example, in the case of the ion-implanted sources mainly the K-32 line spectra measured with the fine step of 0.2 eV (used as the reference spectra in the cross-correlation method as mentioned above) will be analyzed here.

Similar analysis of the $^{83\text{m}}\text{Kr}$ conversion spectrum was already carried out for the condensed $^{83\text{m}}\text{Kr}$ source (CKrS, see Sect. 3.3.2) in the early work [Pic92b] and in recent works [Thu07, Ost08]. In these works it became clear that the uncertainty of the absolute kinetic energy of a given $^{83\text{m}}\text{Kr}$ conversion line is dominated by several correction terms (cf. Eq. 3.20): when comparing the absolute kinetic energy of the conversion electron with the gamma transition energy, the knowledge of the electron binding energy and other terms is necessary. The binding energy $E_{\text{bin}}^{\text{vac}}(\text{gas})$ is known with the precision of the order of 0.01 to 0.1 eV. The work functions ϕ_{source} and ϕ_{spec} are known only with the precision of the order of 0.1 and 0.2 eV, respectively (see Tab. 4.3), and the same holds for the term $\Delta E_{\text{bin}}^{\text{vac}}(\text{cond}) = 1.74(23)$ eV (used in [Ost08]) corresponding to the shift of the core level binding energies of condensed krypton. Therefore, it seems unrealistic to aspire for the precision better than tens of meV in such analysis. In this respect the *statistical* uncertainty of the conversion line position of the order of units to tens of meV, stemming from the many-parameters fits of the integral spectra, seems rather satisfactory.

It was stated already in Sect. 5.2.1 that while the amplitude of the K-32 line of the order of 10^2 counts s⁻¹ was observed in the case of the CKrS, in this work the amplitude reached even 10^4 counts s⁻¹ in the case of the ion-implanted sources. In this regard the conversion electron

²With the exception of the source Au-30 which exhibited the drift of the K-32 line energy of ≈ 2.4 ppm month⁻¹.

spectra, obtained in this work, represent much higher statistics and are correspondingly more difficult to analyze facing their high statistical precision.

7.2. Shapes of the conversion electron lines

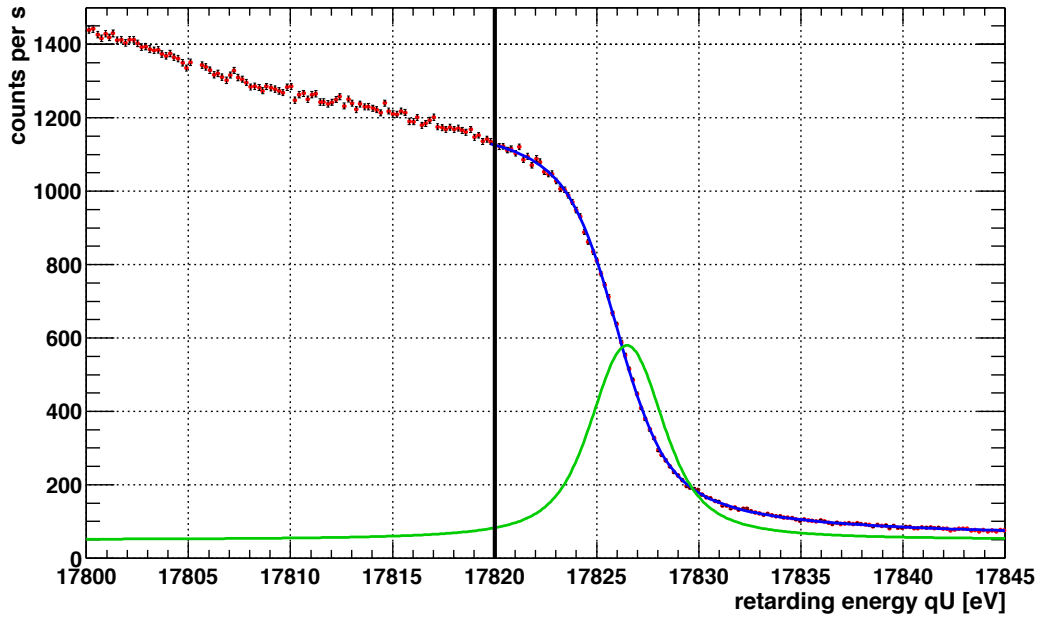
In this section mainly the shapes of the conversion electron lines are considered: the widths and the presence or absence of any asymmetry of the line shapes. In addition, the amplitude and the background of the lines will be of interest at the end of this section.

7.2.1. Description of the conversion lines of the vacuum-evaporated sources with a singlet

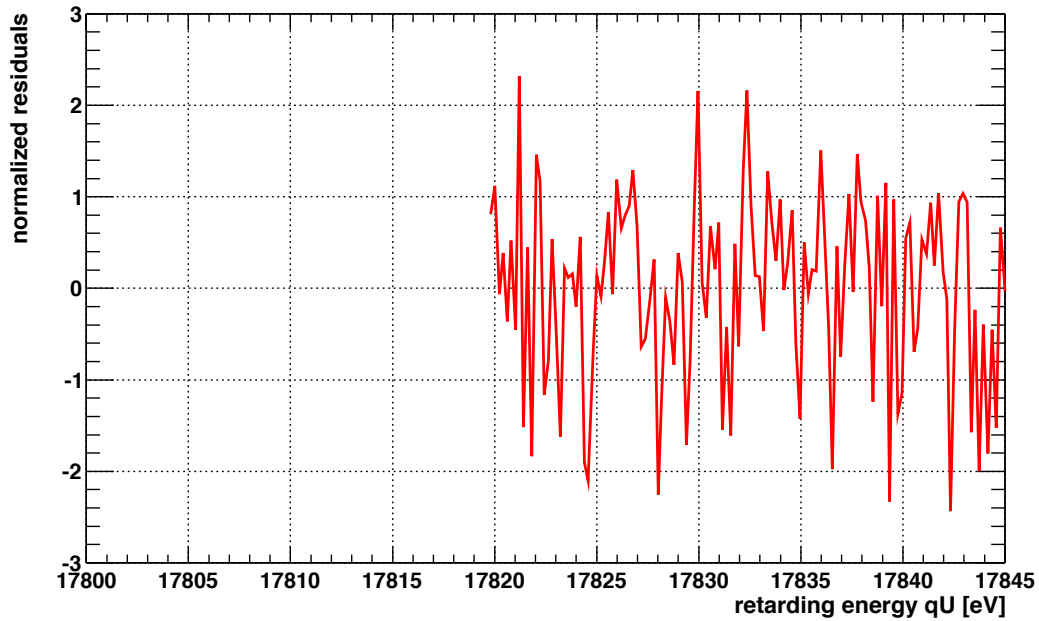
The conversion electron spectra recorded with the vacuum-evaporated sources represent no problem for the analysis carried out with the many-parameters least-squares fit: all the spectra of the sources S 11, S 13, S 28 and S 29 could be well described with a single Voigt function (cf. Eq. 5.26). In [Ost08] the Voigt function was used for the description of the low energy line L_1 -9.4 and of all the high energy lines of the 32 keV gamma transition (besides the $N_{2/3}$ -32 line, see below). In the case of the L_1 -9.4 line the widths resulting from the fit amounted to $\Gamma = 3.72(19)$ eV (Lorentzian width) and $\sigma = 1.38(14)$ eV (Gaussian width). The necessity of the use of the Voigt function was explained in [Ost08] by the increased width of the L_1 -9.4 line due to its proximity to the noise edge of the detector electronic chain. A non-zero width σ introduced in the fits of the high energy lines was explained by the non-vanishing HV noise. In the analysis presented in this work the width Γ was kept fixed and the values recommended in [Cam01] (and tabulated in Tab. 3.1) were used. The width σ was fitted together with the constant background B_0 , the amplitude A and the centroid E_0 of the conversion line. Naturally, a proper transmission function (see Sect. 5.2.5) and its dependences on the electron starting energy, the spectrometer resolution and the source-spectrometer geometry was taken into account.

An example of the many-parameters fit of the K -32 line of the source S 28 is depicted in Fig. 7.1. It can be seen that the elastic peak of a relatively good statistics ($A \approx 1\,200$ counts s^{-1}) could indeed be well described with the single Voigt peak. The results of the analysis of the vacuum-evaporated sources are summarized in Tab. 7.1. In all the cases the value of σ lies in the range of 0.7–1.6 eV while differences line-to-line can be seen, partially also source-to-source. The width σ of the L_1 -9.4 line of all sources was found to lie in the range of 1.3–1.6 eV which corresponds well to the finding of [Ost08]. The K -32 line exhibited σ of $\simeq 0.7$ to 1.1 eV while the L_3 -32 line could be described with σ in the range of 0.9–1.4 eV.

It is also interesting to consider the closely spaced lines N_2 -32 and N_3 -32: the splitting of these lines is only about 0.6 eV which is unresolvable with the spectrometer resolution of 1.7 eV at 32.1 keV, and moreover, the lines possess a negligible natural line width $\Gamma \simeq 0$ eV. Thus, the unresolved doublet $N_{2/3}$ -32 represents a useful tool for the check of the HV noise and other effects broadening the line shape. In [Ost08] the $N_{2/3}$ -32 line was well described



(a)



(b)

Fig. 7.1: The example of a typical many-parameters fit of the K -32 line of the source S28. **(a)** The recorded spectrum corrected for the dead time is shown in red. The blue line denotes the least-squares fit of the convolution of the spectrometer transmission function with the single Voigt peak. The fit range $[qU_1, qU_2] = [17820, 17845]$ eV was used, the vertical line at 17820 eV marks its lower limit. The Lorentzian width was kept fixed to $\Gamma = 2.7$ eV, whereas the Gaussian width σ was a free parameter, $\sigma = 1.07(2)$ eV. The green line denotes the Voigt peak resulting from the fit (including the constant background $B_0 = 50.0(3)$ counts s^{-1}). The centroid was fitted as $E_0 = 17826.483(12)$ eV. **(b)** The normalized residuals of the fit shown in **(a)** exhibit no significant structure. The number of degrees of freedom was $N_{\text{dof}} = 126$ and the reduced chi squared $\chi_r^2 = 1.06(13)$. Therefore, the fit can be considered as a good fit.

Tab. 7.1: The overview of the shapes of the conversion electron lines measured with the vacuum-evaporated $^{83}\text{Rb}/^{83\text{m}}\text{Kr}$ sources.

source	meas. phase	rel. date of scan(s) [day]	source ^{83}Rb [MBq]	mag. field B_S [T]	mag. field B_S [T]	spectrom. eff. η_{spec} [%]	el. line	amplit. A [counts s^{-1}]	backg. B	A/B ratio	line width Lor. Γ Gauss. σ [eV]
S 13	pilot	$\simeq 5$	0.22	2.63	3.0	K-32	17.0(1)	5.18(2)	3.3	2.7	0.71(7)
S 11	pilot	$\simeq 27$	0.13	0.77	0.8	K-32 L_3 -32	8.5(1) 17.0(1)	4.27(2) 2.56(2)	2.0	2.7	1.14(6) 1.35(3)
S 28	1 st	7-30	3.31	0.33	1.4	L_1 -9.4	43.2(2)	34.8(1)	1.2	3.75	1.63(12)
						K-32	1 156(1)	49.9(1)	23.2	2.7	1.063(7)
						L_3 -32	2 266(12)	292(5)	77.5	1.19	0.913(5)
						$N_{2/3}$ -32	60.0(3)	16.6(1)	3.6	0	1.19(2)
						L_1 -9.4	197.7(3)	76.9(2)	2.6	3.75	1.49(4)
						K-32	637(3)	30.1(1)	21.1	2.7	1.115(7)
						L_3 -32	1 328(1)	18.1(1)	73.4	1.19	1.001(5)
						$N_{2/3}$ -32	33.5(2)	8.9(1)	3.8	0	1.32(2)
						L_1 -9.4	774(2)	323(2)	2.4	3.75	1.48(3)
						K-32	1 924(1)	106.0(3)	18.2	2.7	1.125(9)
S 29	2 nd	64-107	0.83	1.75	7.9	L_3 -32	4 175(4)	65.3(6)	64.0	1.19	1.080(3)
						K-32	726.5(4)	117.0(2)	6.2	2.7	0.946(6)
						L_3 -32	1 618(4)	113.5(7)	14.3	1.19	0.984(6)
						$N_{2/3}$ -32	43(1)	66(2)	0.7	0	1.38(3)
S 29	2 nd	0-15	1.8	1.75	7.9	L_1 -9.4	310(5)	181(1)	1.7	3.75	1.33(24)
						K-32	333.0(3)	66.2(2)	5.0	2.7	1.01(1)
						L_3 -32	817(2)	43.2(3)	18.9	1.19	0.95(2)
						$N_{2/3}$ -32	19.9(6)	28.2(4)	0.7	0	0.91(26)

The columns denote the following notions: 1) notation of the given source, 2) the measurement phase and 3) the relative time in days (since the start of the given measurement phase) in which the data were obtained. The columns (4) and (5) indicate the source ^{83}Rb activity A [MBq] and the magnetic field B_S [T] where the source was placed. The column (6) denotes the spectrometer efficiency η_{spec} calculated according to Eq. 2.14 and Eq. 5.19. The notation of the measured line is given in column (7) while the fitted values of the amplitude A and the background B are stated in the columns (8) and (9), respectively. The column (10) summarizes the A/B ratio. Finally, in the columns (11) and (12) the Lorentzian and Gaussian components of the line width are denoted. The uncertainties represent only the statistical uncertainties of the fit results based on the analysis of a group of integral spectra. See text for further discussion of the results.

with a single Gaussian peak with $\sigma = 0.61(1)$ eV which was ascribed to the HV noise. In the case of the vacuum-evaporated sources the fits of the $N_{2/3}$ -32 line resulted in σ ranging from 0.9 to 1.4 eV. Taking into account the fact that the HV setup used in this work was basically identical to that one used in [Ost08], one may conclude that the non-HV related effects (surface and/or solid state effects affecting the ^{83m}Kr atom) are responsible for the broadening of 0.7–1.3 eV (considering the sum of squares) of the conversion lines.

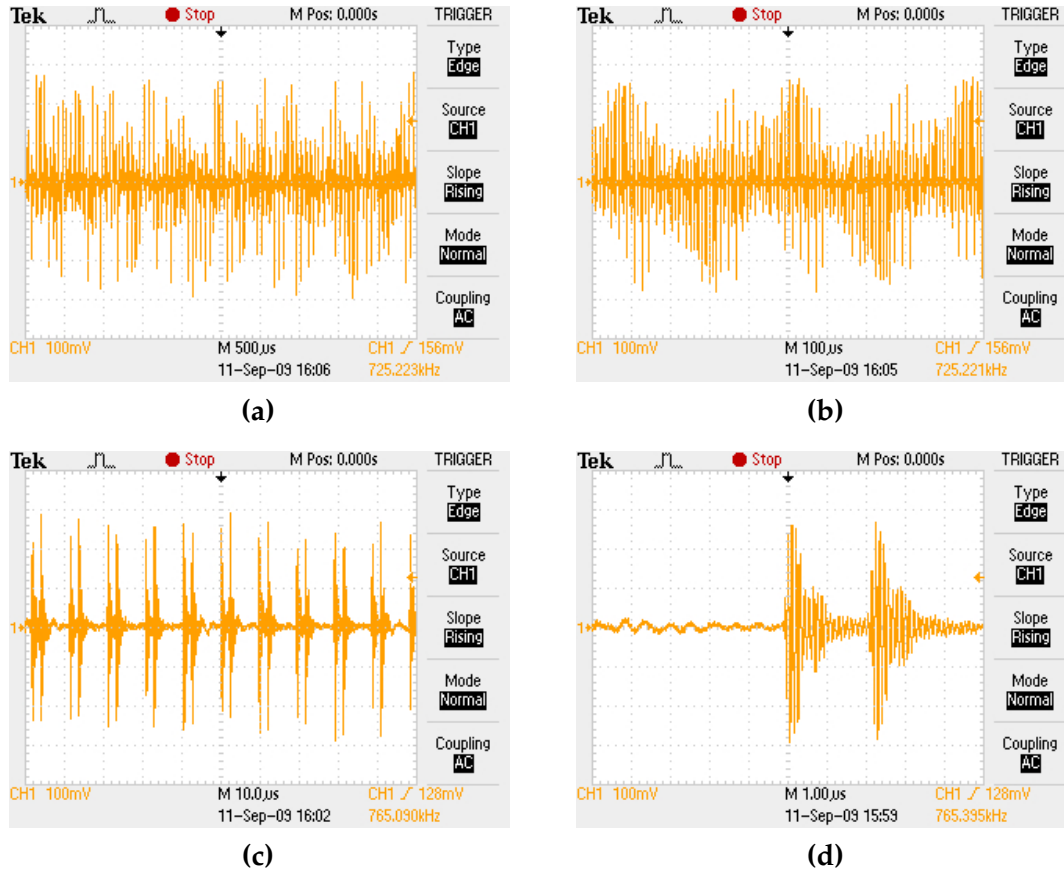


Fig. 7.2: The screenshots of the oscilloscope attached to the HV HF noise pickup probe (see Fig. 5.11) when the HV of -17.8 kV was applied to the spectrometer and the HV divider K35. The full span of the y axis amounts to 800 mV on all figures while the figures differ in the full span of the x axis: in (a) the full span is set to 5 ms, in (b) 1 ms, in (c) $100\ \mu\text{s}$ and in (d) $10\ \mu\text{s}$. The patterns of the macro- and microstructure of the HV HF noise can be seen.

The HV noise was also directly observed with the help of the so-called HV high frequency (HF) noise pickup probe, see Fig. 5.11. In Fig. 7.2 the examples of the oscilloscope screenshot of such a HV HF noise is shown for the situation when the HV of about -17.8 kV was applied to the spectrometer electrodes and the HV divider K35. Unfortunately, the HV HF noise was not monitored throughout all the measurement phases, nevertheless, several observations were accomplished. At -17.8 kV the HV HF noise ripple amounted typically to values of the order of 0.1 V peak-to-peak while at -30.5 kV the ripple of even 2 V peak-to-peak was once recorded. In the example shown in Fig. 7.2 the HV HF noise exhibits certain macro- and microstructure where the highest frequencies range up to ≈ 500 kHz. The maximal ripple amounted to about 0.5 V peak-to-peak. The 50 Hz noise, corresponding to the usual power

line “hum”, was recognized with the ripple of about 0.25 V peak-to-peak. Therefore, the HV noise was certainly present and affected the observed widths of the conversion electron lines. Some scaling of the HV noise ripple was probably observed but no clear statement could be deduced from the limited number of observations. Detailed investigations of the HV HF noise (implementing an artificial AC noise) are foreseen at the monitor spectrometer in the Karlsruhe Institute of Technology where a sophisticated post-regulation circuit will be utilized [Thu11].

In Tab. 7.1 also the values of the amplitude and the background levels of the various conversion lines are stated. These notions will be discussed later in Sect. 7.2.4 together with the values obtained with the ion-implanted sources.

7.2.2. Doublet structure of the conversion lines of the ion-implanted sources

In the case of the ion-implanted sources it turned out to be impossible to describe certain electron spectra reasonably well with a single Voigt peak. This became clear in the course of the second measurement phase when the source Pt-30 was investigated: while the low energy conversion lines (7.5–9.4 keV) of the 9.4 keV gamma transition of $^{83\text{m}}\text{Kr}$ could still be fitted with a single peak, the fits of the conversion lines of the 32 keV gamma transition exhibited clear structures in the residuals. An example of such residuals is illustrated in Fig. 7.3 for the case of the K -32 line of the source Pt-30 #2. These structures indicated the presence of some asymmetry on the low energy side of the elastic peak (or on the high binding energy side, correspondingly). The existing code was enhanced to three Voigt peaks, however, the asymmetric elastic peak could be reasonable well described with a doublet of Voigt peaks. The doublet splitting ΔE_{1-2} (see Eq. 5.33) and the ratio $A_{2/1}$ (see Eq. 5.34) of the low energy peak amplitude A_2 to the amplitude A_1 of the “main” high energy peak were free parameters in the fits. As $\Delta E_{1-2} > 0$ the high energy peak was assumed to correspond to $^{83\text{m}}\text{Kr}$ atoms in the metallic state while the additional component of the doublet was attributed to $^{83\text{m}}\text{Kr}$ in the oxide state where the binding energy is higher than in the metal (see Fig. 4.3 for the example of the shift of the electron binding energy). The Lorentzian widths Γ_1 and Γ_2 were set equal and fixed to the recommended values, $\Gamma_1 = \Gamma_2 = \Gamma_{\text{lit}}$, similarly to the analysis of the vacuum-evaporated sources. The Gaussian widths σ_1 and σ_2 were set equal to a common width $\sigma_1 = \sigma_2 = \sigma$ which was a free parameter. These crude simplifications can be interpreted as the anticipation that both components of the doublet possess the same natural line width and both are affected by the line broadening effects in the same way.

The results of the analysis of the source Pt-30 data obtained in the second measurement phase are summarized in Tab. 7.2. Examples of the various electron lines are depicted in the following figures: in Fig. 7.4 the L_1 , L_2 and L_3 -9.4 lines are shown, Fig. 7.5 depicts the lines M_1 , M_2 and M_3 -9.4 as well as the valence electron line N_1 -9.4. Furthermore, in Fig. 7.6 the lines K , L_2 and L_3 -32 are presented and finally, Fig. 7.7 shows the lines M_2 and M_3 -32, the unresolved doublet³ $M_{4/5}$ -32 and the doublet of the valence lines $N_{2/3}$ -32. The width σ of

³Similarly to the lines N_2 and N_3 -32, the splitting of the lines M_4 and M_5 -32, amounting to about 1.25 eV (cf.

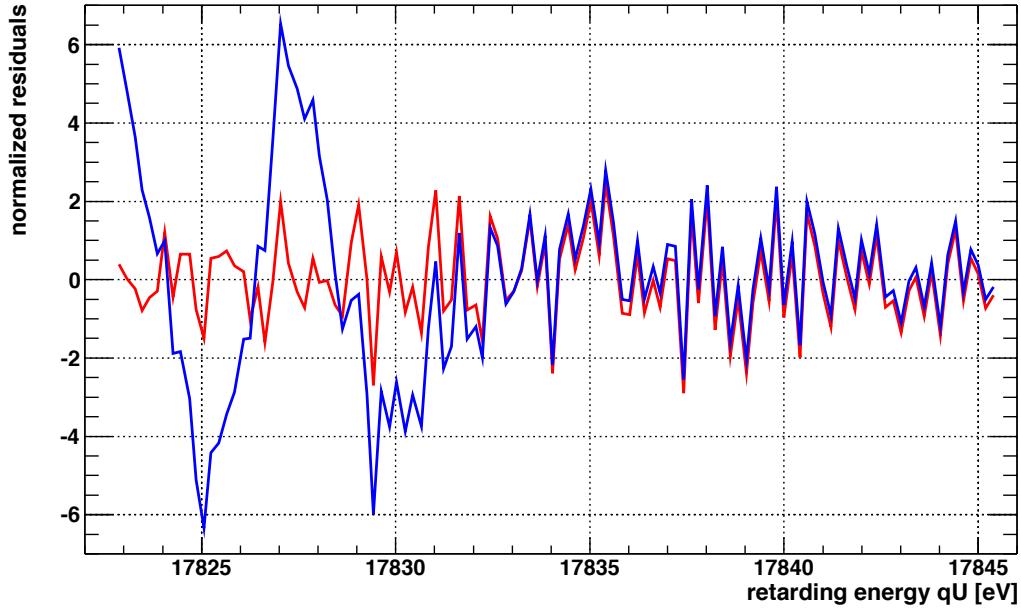


Fig. 7.3: The comparison of normalized residuals of two fits of the same spectrum, illustrating the necessity of including a second Voigt peak in the analysis. The K_{-32} spectrum of the source Pt-30 #2 was scanned with the step of 0.2 eV. The blue line denotes the residuals of the fit ($\chi_r^2 = 5.55(13)$) with a single Voigt peak, the red line represents the residuals of the fit ($\chi_r^2 = 1.26(14)$) with a doublet of Voigt peaks where $\Gamma_1 = \Gamma_2 = 2.7$ eV was fixed and $\sigma_1 = \sigma_2 = \sigma$ was a free parameter. The fit of the doublet resulted into $\sigma = 0.75(4)$ eV, $E_{0_1} = 17828.25(5)$ eV and $\Delta E_{1-2} = 2.78(7)$ eV.

the $L_{1-9.4}$ line of the source Pt-30 was found to be compatible with the values reported above in Sect. 7.2.1. The other lines populated in the 9.4 keV gamma transition were not recorded with the vacuum-evaporated sources, however, a comparison to the CKrS is possible: again, non-vanishing width σ had to be introduced in this analysis, as opposed to the CKrS. The width σ was found to be in the range of 0.4–0.6 eV for all the lines L_2 to $M_{3-9.4}$, while the valence line $N_{1-9.4}$ exhibited the relatively large width of $\sigma = 1.77(20)$ eV.

The lines K and L_{3-32} showed an asymmetric line shape where the ratio $A_{2/1}$ was in all cases in the range of 0.11–0.14. The values of the splitting ΔE_{1-2} exhibited somewhat larger spread, 2.2–3.9 eV. The line L_{2-32} (see Fig. 7.6(b)) was fitted with a single Voigt peak superimposed on a very high background level of the order of $\approx 12 \times 10^3$ counts s^{-1} caused by the L_{3-32} line (see Fig. 7.6(c)). In this case the background was approximated by a linear function. Interestingly, the width σ of the K_{-32} line of the source Pt-30 was determined to be only 0.5–0.7 eV which is smaller than in the case of the vacuum-evaporated sources where $\sigma = 0.7$ –1.1 eV. As no major changes in the HV setup took place during the measurement campaign, the HV noise can probably be excluded from the considerations here. Thus, the discrepancy can be ascribed either to the sources themselves—the ^{83m}Kr atom adsorbed onto the solid surface is probably more influenced by its environment than the ^{83m}Kr atom implanted into metal—or to the description of the line shape with the doublet. The latter explanation would mean that splitting ΔE_{1-2} in some way “masks” the true width σ .

Most striking, however, is the shape of the valence line $N_{2/3-32}$: here it was found that $A_{2/1} > 1$, *i.e.* the amplitude A_2 of the second additional component of the doublet was

Tab. 3.1), is smaller than the spectrometer resolution at this energy, about 1.7 eV at 32.1 keV.

actually greater than A_1 , see Fig. 7.7(c). This behavior was opposite to all the other $^{83\text{m}}\text{Kr}$ conversion electron lines investigated. The ratio $A_{2/1}$ lied in the range of 4.5–4.8 and the splitting ΔE_{1-2} was about 5.6(2) eV, large enough to be recognized with the current spectrometer resolution of 1.7 eV at 32.1 keV. The width σ was determined as $\simeq 1.5$ eV in the case of this doublet. The observation of such unusual line shape naturally raises the questions about the origin of the splitting: are these lines 1) the normally unresolved N_2 and N_3 -32 lines, split due to the environment of the implanted $^{83\text{m}}\text{Kr}$?, 2) the unresolved doublet $N_{2/3}$ -32 split into two separate doublets due to the shift of the electron binding energy? or even 3) does one of the doublet components originate outside of the $^{83\text{m}}\text{Kr}$ atom?

A certain statement about the nature of the splitting can be obtained already from the considerations of the line amplitude. Firstly, the amplitudes of the individual doublet components of this line can be easily compared to the amplitude of the K -32 line. The ratio of the intensities of these lines in gaseous $^{83\text{m}}\text{Kr}$, taken relative to the decay of ^{83}Rb (see Tab. 3.1), reads

$$I_{N_{2/3}\text{-}32/K\text{-}32} := \frac{I(N_{2/3}\text{-}32)}{I(K\text{-}32)} = \frac{0.27\% + 0.41\%}{17.07\%} \simeq 0.04. \quad (7.1)$$

In the case of the solid sources, this factor has to be corrected (see Sect. 7.2.4 below) for the effect of inelastic scattering of electrons as the K -32 electrons are more affected by the inelastic scattering in the sources than the $N_{2/3}$ -32 electrons. From the values summarized in Tab. 7.1 for the vacuum-evaporated sources it follows that the factor $I_{N_{2/3}\text{-}32/K\text{-}32}$ amounted to 5–6% which is in a good agreement with Eq. 7.1 bearing in mind that the shake-up/off peaks decrease the amplitude of the K -32 line while in the case of the $N_{2/3}$ -32 line practically no shake-up/off peaks are present. The amplitude of the K -32 line⁴ can be, in principle, compared to a) the amplitude A_1 of the high energy component of the $N_{2/3}$ -32 line, b) the amplitude A_2 of the second component and c) the total amplitude A of the doublet. On the basis of the values summarized in Tab. 7.2 it turns out that the factor $I_{N_{2/3}\text{-}32/K\text{-}32}$ amounts to a) 0.5–0.9%, b) 3.3–4.3% and c) 4.0–5.0%, respectively. Thus, the high energy component of the doublet clearly cannot alone represent the line $N_{2/3}$ -32 as its amplitude A_1 is too small. Therefore, the high energy component stems probably from 1) a certain splitting of the N_3 -32 line (level $4p_{3/2}$) or 2) an external effect in the sense that it does not originate in the $^{83\text{m}}\text{Kr}$ atom. The nature of the high energy component will be discussed in detail in Sect. 7.4 after the absolute kinetic energies of the lines are determined in Sect. 7.3.

The analysis of the electron spectra obtained with the ion-implanted sources in the third measurement phase was carried out in the same manner as described above. However, in this final measurement phase only the lines L_1 , L_3 and M_1 -9.4 and K , L_3 , M_3 and $N_{2/3}$ -32 were measured. The results are summarized in Tab. 7.3. The L_1 -9.4 line of the three strong⁵ sources Pt-30 #2, Pt-15 and Au-30 had to be described with the doublet, while it was possible to describe well the L_3 and M_1 -9.4 lines with a single Voigt peak. All the lines of the 32 keV gamma transition exhibited an asymmetric line shape with $A_{2/1} < 1$, the doublet $N_{2/3}$ -32 being again the exception with $A_{2/1} > 1$. The $A_{2/1}$ values were found to depend strongly on the source while to be more or less constant for all the lines of the given source. Thus, it can be written $A_{2/1}(\text{Pt-30}) \approx 0.11$, $A_{2/1}(\text{Pt-30 #2}) \approx 0.4$, $A_{2/1}(\text{Pt-15}) \simeq 0.12\text{--}0.25$ and $A_{2/1}(\text{Au-30}) \approx 0.23$. The splitting of the K -32 line was determined as $\Delta E_{1-2} \simeq 2.9$ eV for

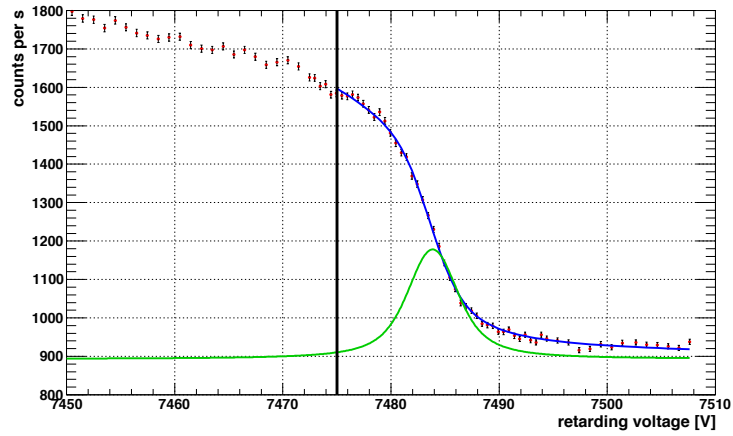
⁴The total amplitude was considered, *i. e.* the amplitudes of the main peak together with the low energy asymmetry.

⁵Meant in the sense of high statistics in the electron lines.

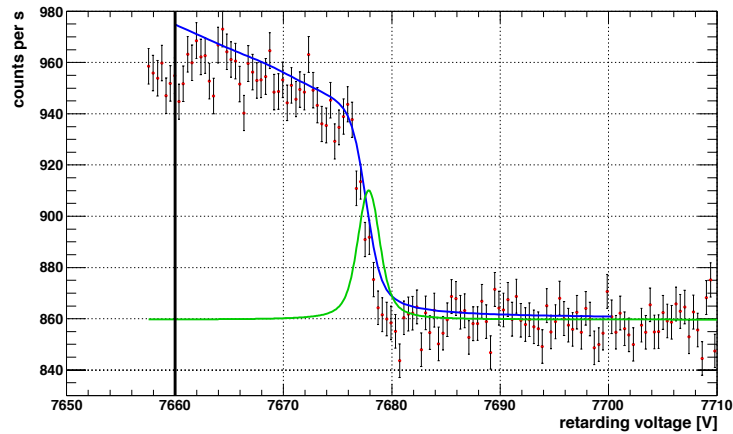
the Pt-based sources while in the case of the source Au-30 the splitting amounted to about 2.5 eV. Due to a high statistical precision of the L_{3-32} line the description of the shape of this line was very sensitive to the parameters Γ and σ . The width Γ was not kept fixed to the recommend value of 1.19 eV in this case, but it was a free parameter. However, the fits resulted into the values $\Gamma \simeq 1.00\text{--}1.15$ eV which is close to the recommended value. The width σ was relatively small, in the range of 0.3–0.6 eV, and the splitting amounted $\Delta E_{1-2} \simeq 2.1\text{--}2.4$ eV. The valence $N_{2/3-32}$ lines exhibited significantly different ΔE_{1-2} values from source to source, ranging from $\simeq 4.3$ eV (source Au-30) to $\simeq 5.5$ eV (source Pt-30 #2).

In sum, the conversion spectra of the ion-implanted sources differed from those of the vacuum-evaporated sources due to the asymmetry of the elastic peak on its low energy side. This was pronounced mainly in the lines recorded with high statistics, *i.e.* $L_{1-9.4}$, K and L_{3-32} . Still, the origin of the asymmetry remains unclear. On the other hand, the spectra of the $N_{2/3-32}$ lines undoubtedly showed a doublet of lines with the splitting of the order of several eV. Considering the line shapes summarized in Tab. 7.2 and Tab. 7.3 an overall discrepancy is visible between the individual ion-implanted sources and even between the individual data sets of a given source. This can be attributed to the fact that each ion-implanted source was unique of its own due to the differences in the implantation procedure. Moreover, the analysis with the doublet of Voigt peaks suffered from a certain instability of the parameters describing the low energy component.

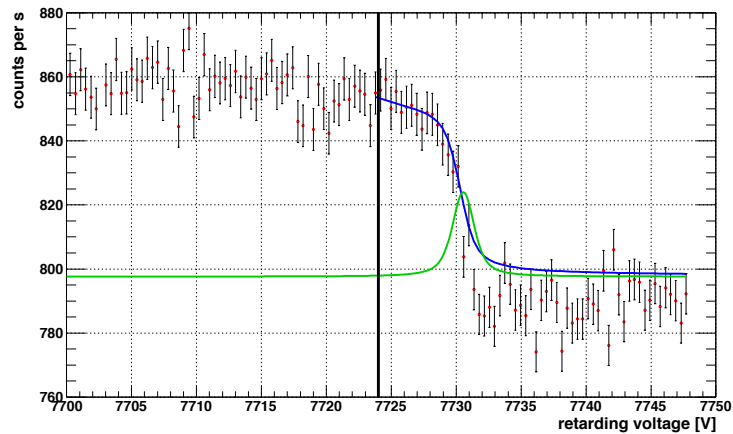
7. Conversion electron spectrum...



(a) line L_1 -9.4



(b) line L_2 -9.4



(c) line L_3 -9.4

Fig. 7.4: The examples of the integral spectra of the conversion lines (a) L_1 -9.4, (b) L_2 -9.4 and (c) L_3 -9.4 of the source Pt-30. The recorded spectra corrected for the dead time are shown in red. The blue lines denote the least-squares fits of the convolution of the spectrometer transmission function with the single Voigt peak. As the simulated spectra of inelastically scattered electrons are included in the description (see Sect. 5.2.6), the fitted function does not remain constant “below” the elastic peak but it rises further. The electron energy losses are most pronounced in the case of these low energy conversion electron lines. The lower limits of the fit ranges are denoted by the vertical lines. The green line denotes the Voigt peak resulting from the fit (including the constant background B_0). The x axis denotes the retarding voltage $|U|$, corresponding to the spectrometer retarding energy qU .

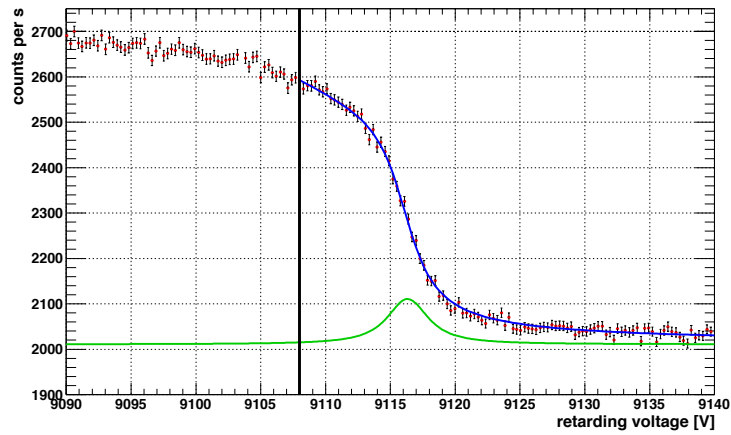
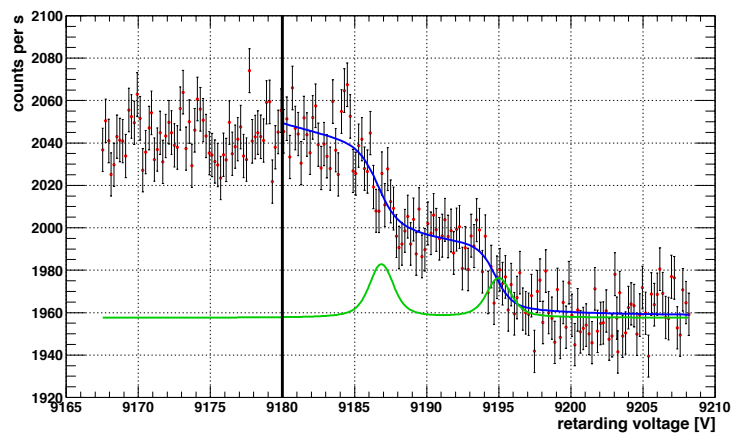
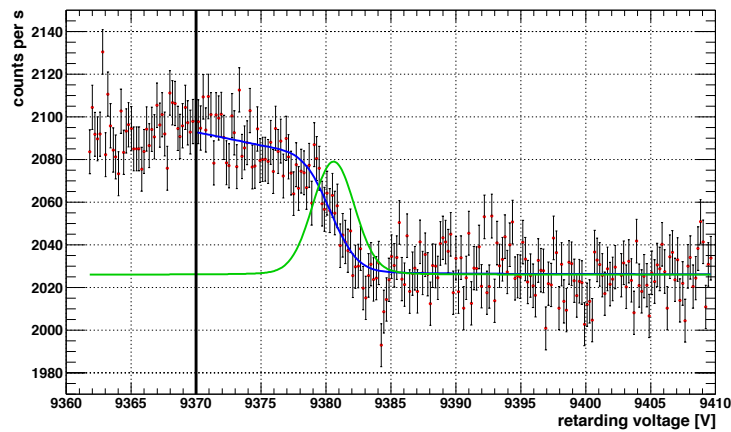
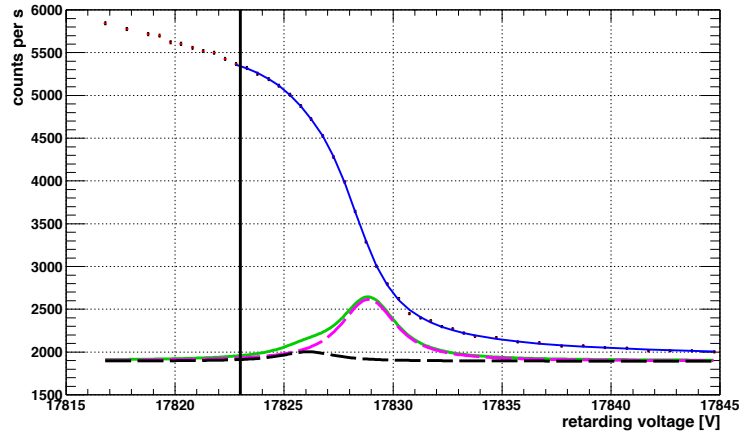
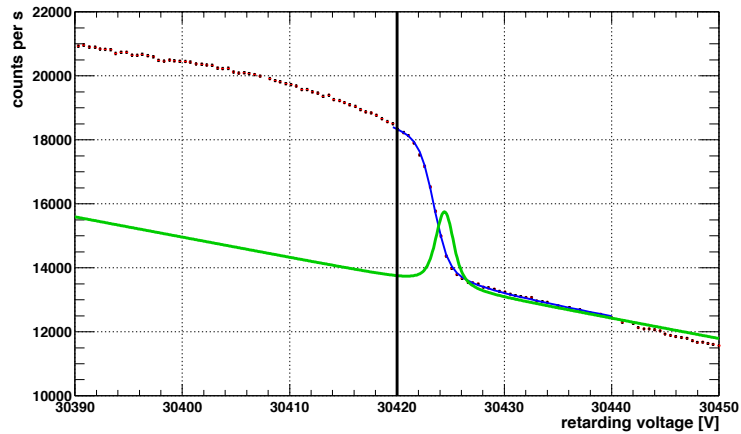
(a) line M_1 -9.4(b) lines M_2 -9.4 and M_3 -9.4(c) line N_1 -9.4

Fig. 7.5: The examples of the integral spectra of the conversion lines (a) M_1 -9.4, (b) M_2 and M_3 -9.4 and (c) N_1 -9.4 of the source Pt-30. See the caption of Fig. 7.4 for the explanation. The fits of the lines M_2 and M_3 -9.4 were carried out on the range covering both lines. The x axis denotes the retarding voltage $|U|$, corresponding to the spectrometer retarding energy qU .

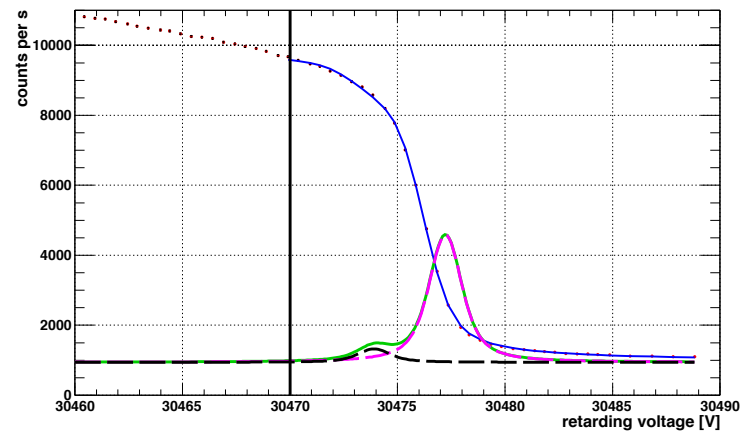
7. Conversion electron spectrum...



(a) line K_{-32}



(b) line L_{2-32}



(c) line L_{3-32}

Fig. 7.6: The examples of the integral spectra of the conversion lines (a) K_{-32} , (b) L_{2-32} and (c) L_{3-32} of the source Pt-30. See the caption of Fig. 7.4 for the explanation. In the case of the lines K_{-32} and L_{3-32} the doublet of Voigt peaks was used to describe the elastic peak. The main component of the doublet is marked with dashed magenta line, while dashed black line denotes the second component of the doublet. The background B_0 was added to both doublet components for illustration. The line L_{2-32} was described with a single Voigt peak superimposed on a linear background caused by the L_{3-32} line. The x axis denotes the retarding voltage $|U|$, corresponding to the spectrometer retarding energy qU . A comparison of residuals of the K_{-32} line fits, carried out with a singlet and a doublet of Voigt peaks, was shown above in Fig. 7.3.

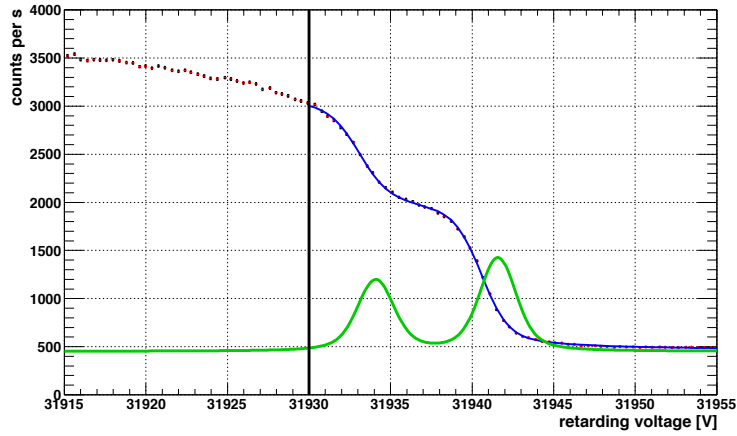
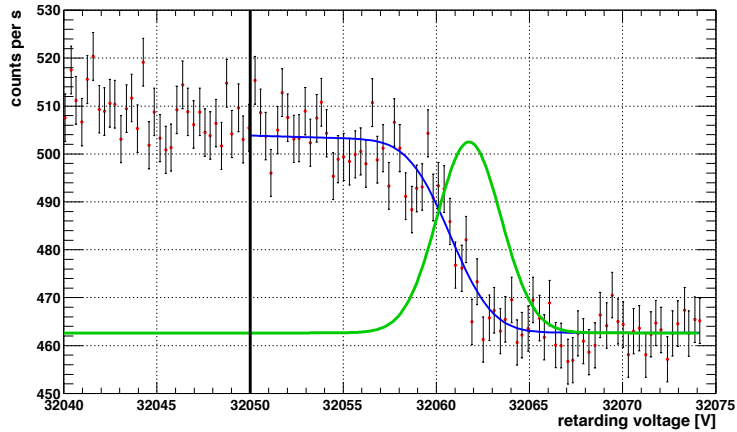
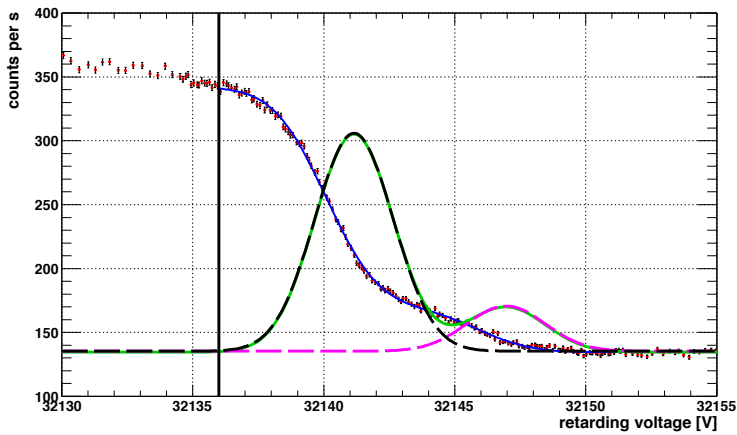
(a) lines M_2 -32 and M_3 -32(b) unresolved doublet of lines $M_{4/5}$ -32(c) doublet $N_{2/3}$ -32

Fig. 7.7: The examples of the integral spectra of the conversion lines (a) M_2 and M_3 -32, (b) $M_{4/5}$ -32 and (c) $N_{2/3}$ -32 of the source Pt-30. See the caption of Fig. 7.4 for the explanation. The fits of the lines M_2 and M_3 -32 were carried out on the range covering both lines. It was not possible to resolve the lines M_4 and M_5 -32, thus, only the unresolved line $M_{4/5}$ -32 was fitted with a single Voigt peak. The normally unresolved doublet of lines N_2 and N_3 -32 exhibited clear splitting of $\Delta E_{1-2} = 5.2(2)$ eV. As in Fig. 7.6(a) and Fig. 7.6(c), the main component of the doublet is marked with dashed magenta line, while dashed black line denotes the second component of the doublet. However, in this case $A_{2/1} \simeq 4.7$ and the high energy component does not correspond to the internal conversion in ^{83m}Kr . The background B_0 was added to both doublet components for illustration. The x axis denotes the retarding voltage $|U|$, corresponding to the spectrometer retarding energy qU .

Tab. 7.2: The overview of the shapes of the conversion electron lines measured with the ion-implanted source Pt-30 during the second measurement phase.

rel. date of scan(s) [day]	gamma transit. line [keV]	el. line	ampl. A_1 [co. s ⁻¹]	$A_{2/1}$ ratio	total ampl. A [counts s ⁻¹]	backg. B	A/B ratio	splitting ΔE_{1-2} [eV]	line width Lor. Γ Gauss. σ [eV]	
0-15	9.4	L_1	-	-	1 432(6)	1 695(1)	0.8	-	3.75	1.412(66)
		K	6 392(17)	0.109(2)	7 087(24)	2 028(1)	3.5	3.89(6)	2.7	0.653(8)
	32	L_3	13 689(163)	0.14(2)	15 667(381)	1 244(2)	12.6	2.24(11)	1.19	0.48(5)
		$N_{2/3}$	74.9(7)	4.54(5)	415(6)	41(2)	10.1	5.88(10)	0	1.59(2)
53-61	32	K	3 862(15)	0.115(4)	4 308(23)	1 977(2)	2.2	3.26(11)	2.7	0.59(2)
64-107		L_1	-	-	659(8)	902(6)	0.7	-	3.75	1.37(2)
		L_2	-	-	89(1)	871(6)	0.1	-	1.25	0.48(14)
		L_3	-	-	61(1)	801(6)	0.08	-	1.19	0.44(11)
	9.4	M_1	-	-	552(3)	2 010.5(9)	0.3	-	3.5	0.44(16)
		M_2	-	-	47(8)	1 961(3)	-	-	1.6	0.57(28)
		M_3	-	-	31(4)	*	0.02	-	1.1	
		N_1	-	-	60(2)	2 035(9)	0.03	-	0.4	1.77(20)
		K	3 312(29)	0.139(9)	3 772(44)	1 893(2)	2.0	3.03(11)	2.7	0.50(3)
		L_2	-	-	4 913(7)	13 403(28)	0.4	-	1.25	0.54(1)
		L_3	8 292(135)	0.110(5)	9 203(155)	941(1)	9.8	3.27(6)	1.19	0.56(6)
	32	M_2	-	-	1 155(12)	451.8(6)	-	-	1.6	0.88(1)
		M_3	-	-	1 499(3)	*	3.3	-	1.1	
		$M_{4/5}$	-	-	40.2(9)	465(2)	0.09	-	0.07	1.49(22)
	$N_{2/3}$	35.4(5)	4.68(7)	201(4)	135.3(6)	1.5	5.23(21)	0	1.40(3)	

All the data were recorded in the geometry with $B_5 = 1.75$ T, thus, the spectrometer efficiency amounted to $\eta_{\text{spec}} = 7.9\%$. The columns in this table are similar to Tab. 7.1, however, here the ratio $A_{2/1}$ and the splitting ΔE_{1-2} of the doublet components were introduced. The total amplitude A is calculated from the fitted values of A_1 and $A_{2/1}$ as $A = A_1 \cdot (1 + A_{2/1})$. The marks “-” in the columns of A_1 , $A_{2/1}$ and ΔE_{1-2} denote that only a single Voigt was used for the fit. The uncertainties represent only the statistical uncertainties of the fit results based on the analysis of a group of integral spectra. Remark: * the fits of the lines M_2 and $M_{3-9.4}$ were carried out on the range covering both lines, therefore the background B was a free parameter common for both lines.

Tab. 7.3: The overview of the shapes of the conversion electron lines measured with the ion-implanted sources during the third measurement phase.

source	gamma transit. [keV]	el. line	$A_{2/1}$ ratio	total ampl.		A/B ratio	splitting ΔE_{1-2} [eV]	line width	
				A [counts s ⁻¹]	backg. B			Lor. Γ	Gauss. σ [eV]
Pt-30	9.4	L_1	–	559(5)	307.3(7)	1.8	–	3.75	1.28(9)
		L_3	–	70(3)	332(2)	0.2	–	1.19	0.66(13)
	32	K	0.111(8)	972(10)	186.3(3)	5.2	3.04(15)	2.7	0.42(3)
		L_3	0.11(1)	2095(34)	110.2(7)	19.0	2.41(23)	1.08(1)	0.35(3)
		$N_{2/3}$	5.12(36)	52(4)	8.7(3)	6.0	4.96(7)	0	1.21(3)
Pt-30 #2	9.4	L_1	0.53(5)	8394(358)	5465(35)	1.5	3.43(6)	3.75	0.91(7)
		L_3	–	835(92)	3605(6)	0.2	–	1.19	1.34(3)
		M_1	–	3076(6)	5859(4)	0.5	–	3.5	1.32(3)
	32	K	0.46(1)	10449(129)	1740(6)	6.0	2.85(3)	2.7	0.75(2)
		L_3	0.43(1)	21049(251)	972(3)	21.7	2.48(3)	1.153(5)	0.58(2)
		M_3	0.38(2)	4018(104)	663.2(8)	6.1	3.12(8)	1.1	0.96(2)
		$N_{2/3}$	7.70(12)	554(10)	8.9(2)	62.0	5.50(3)	0	1.46(3)
Pt-15	9.4	L_1	0.51(5)	4259(159)	2097(2)	2.0	2.62(7)	3.75	0.47(7)
		L_3	–	398(3)	1407(2)	0.3	–	1.19	0.56(3)
		M_1	–	1458(6)	2303(1)	0.6	–	3.5	0.52(7)
	32	K	0.124(9)	4307(49)	657.8(6)	6.5	2.86(9)	2.7	0.53(2)
		L_3	0.158(7)	8607(83)	409(1)	21.1	2.09(8)	1.097(5)	0.46(1)
		M_3	0.25(1)	1820(19)	227.4(3)	8.0	5.47(13)	1.1	0.88(1)
		$N_{2/3}$	4.77(9)	211(5)	9.01(1)	23.4	5.07(4)	0	1.33(2)
Au-30	9.4	L_1	0.28(10)	3934(421)	3440(10)	1.1	3.26(11)	3.75	1.16(25)
		L_3	–	372(13)	2364(5)	0.2	–	1.19	0.84(6)
		M_1	–	1513(4)	3996(6)	0.4	–	3.5	0.99(5)
	32	K	0.22(1)	5066(76)	1310(5)	3.9	2.52(6)	2.7	0.49(2)
		L_3	0.26(1)	11789(153)	684(5)	17.2	2.33(26)	1.08(2)	0.45(5)
		M_3	0.20(2)	2303(59)	419(1)	5.5	3.65(21)	1.1	0.82(4)
		$N_{2/3}$	6.56(13)	306(7)	15.1(3)	20.3	4.34(7)	0	1.10(2)

All the data were recorded in the geometry with $B_S = 1.75$ T, thus, the spectrometer efficiency amounted to $\eta_{\text{spec}} = 7.9\%$. See the captions of Tab. 7.1 and Tab. 7.2 for the explanation. The uncertainties represent only the statistical uncertainties of the fit results based on the analysis of a group of integral spectra.

7.2.3. Verification of the many-parameters fit procedure

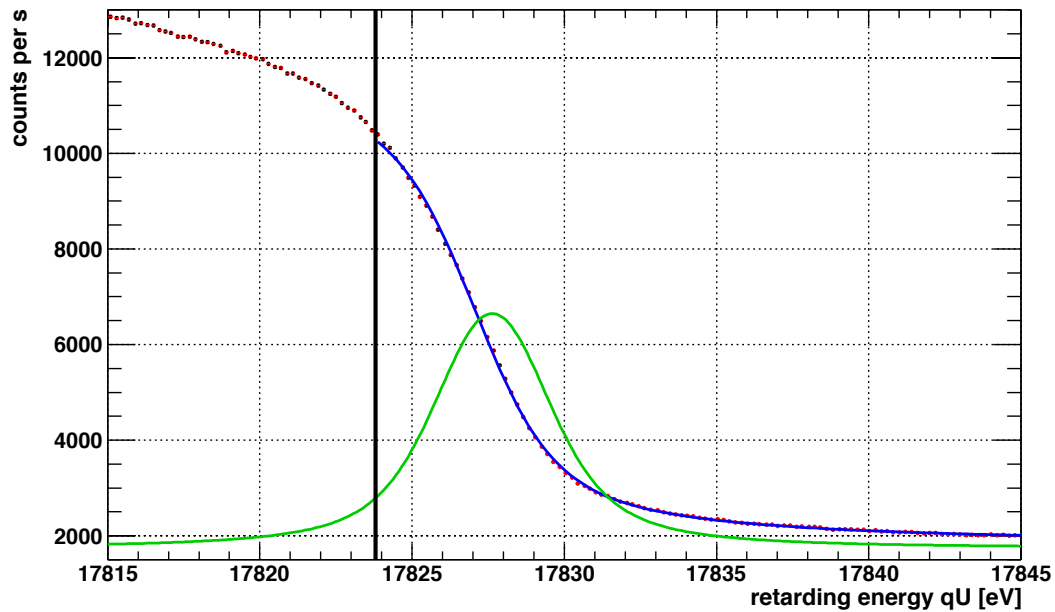
It was seen in previous section that in the analysis of the conversion spectra of the ion-implanted sources the issue of the asymmetric line shape or even the doublet of lines arose. In order to clarify the performance of the many-parameters fit procedure in such cases two approaches were chosen:

- a) The measured spectra of the K -32 line of the source Pt-30 #2 were least-squares fitted with the single Voigt peak on different fit ranges, *i. e.* the lower limit qU_1 of the evaluation interval $[qU_1, qU_2]$ was varied and the dependence of the fitted parameters on qU_1 was investigated.
- b) As described above on page 131 it was possible to simulate a conversion spectrum as it would be measured with the MAC-E filter spectrometer. This possibility was utilized at this point and a series of spectra of the K -32 line was simulated with various values of $A_{2/1}$ and ΔE_{1-2} . These spectra were then least-squares fitted with a single Voigt peak.

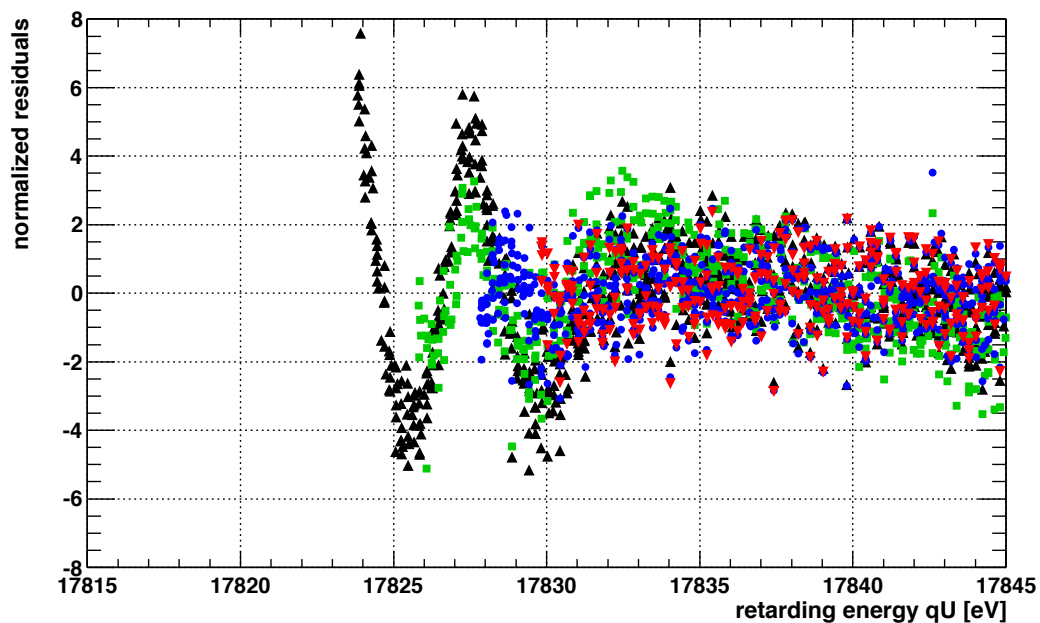
The example of the analysis denoted as (a) is shown in Fig. 7.8(a). Altogether nine spectra, scanned with the step of 0.2 eV and obtained in the course of 16 hours, were fitted while the lower limit qU_1 was varied in the range of 17 822–17 830 eV. Two series of fits were carried out on the group of spectra, in the first case the background was fitted as constant ($B_1 \equiv 0$) and in the second case the background was considered to be linear (free parameters $B_{0,1}$). The overview of the resulting fitted parameters is depicted in Fig. 7.9. Besides the fitted parameters the residuals were also checked for each U_1 . Examples of the normalized residuals can be seen in Fig. 7.8(b). The analysis revealed the following facts:

- The high energy side of the elastic peak can be well described with a single Voigt peak.
- When decreasing the lower limit qU_1 (*i. e.* enlarging the fit interval), the structure in the normalized residuals appears firstly at $qU_1 \simeq 17\,826$ eV. Such an interval already covers the vicinity of the centroid which was determined as $E_0 = 17\,827.86(3)$ eV in this case.
- Decreasing qU_1 further results in more and more pronounced structure in the residuals.
- Both cases of $B_1 \equiv 0$ and $B_1 \neq 0$ deliver compatible results.

In the approach described as (b) the K -32 line spectrum was simulated with the parameters close to the those determined in the fit of the K -32 spectrum of the source Pt-30 #2. The transmission function defining the spectrometer resolution of 0.9 eV at 17.8 keV was used. The background B_0 was chosen as 2 000 counts s^{-1} and the amplitude A_1 of the main peak was set to 10 000 counts s^{-1} which was close to the real spectrum. The widths were set to $\Gamma = 2.7$ eV and $\sigma = 1.0$ eV and the step (corresponding to the HV step during the scan of the spectrum) amounted to 0.2 eV. The ratio $A_{2/1}$ of the amplitudes of the doublet components was varied from 0 (pure singlet) to 2.0 while the splitting ΔE_{1-2} was set to values 0.5, 1.0, 2.0, ..., 5.0 eV. This way a matrix of spectra, describing the various doublet scenarios, was created. In each case a group of 10 simulated spectra was produced. The numbers of counts were randomized in order to mimic the real measured spectra. In Fig. 7.10 the comparison of several simulated scenarios is presented. The conversion line was simulated with the “sharp” energy of $E_0 = 17\,828$ eV and the lower limit of fit range was chosen as $qU_1 =$



(a)



(b)

Fig. 7.8: The example of the analysis used for the verification of the many-parameters fit routine. Figure (a) shows the fit of the measured spectrum of the K_{32} line of the source Pt-30 #2 with a single Voigt peak. The lower limit qU_1 of the fit range in this case amounts to 17824 eV. Though the fit may seem to be a good fit with the naked eye, the normalized residuals plotted in figure (b) reveal a significant structure. In (b) the residuals resulting from fits with different values of qU_1 are shown: red points denote the residuals of the fit with $qU_1 = 17830$ eV (no structure is seen), blue points: $qU_1 = 17828$ eV (certain structure is present), green points: $qU_1 = 17826$ eV (structure is clearly seen) and black points: $qU_1 = 17824$ eV (structure is even more pronounced).

7. Conversion electron spectrum...

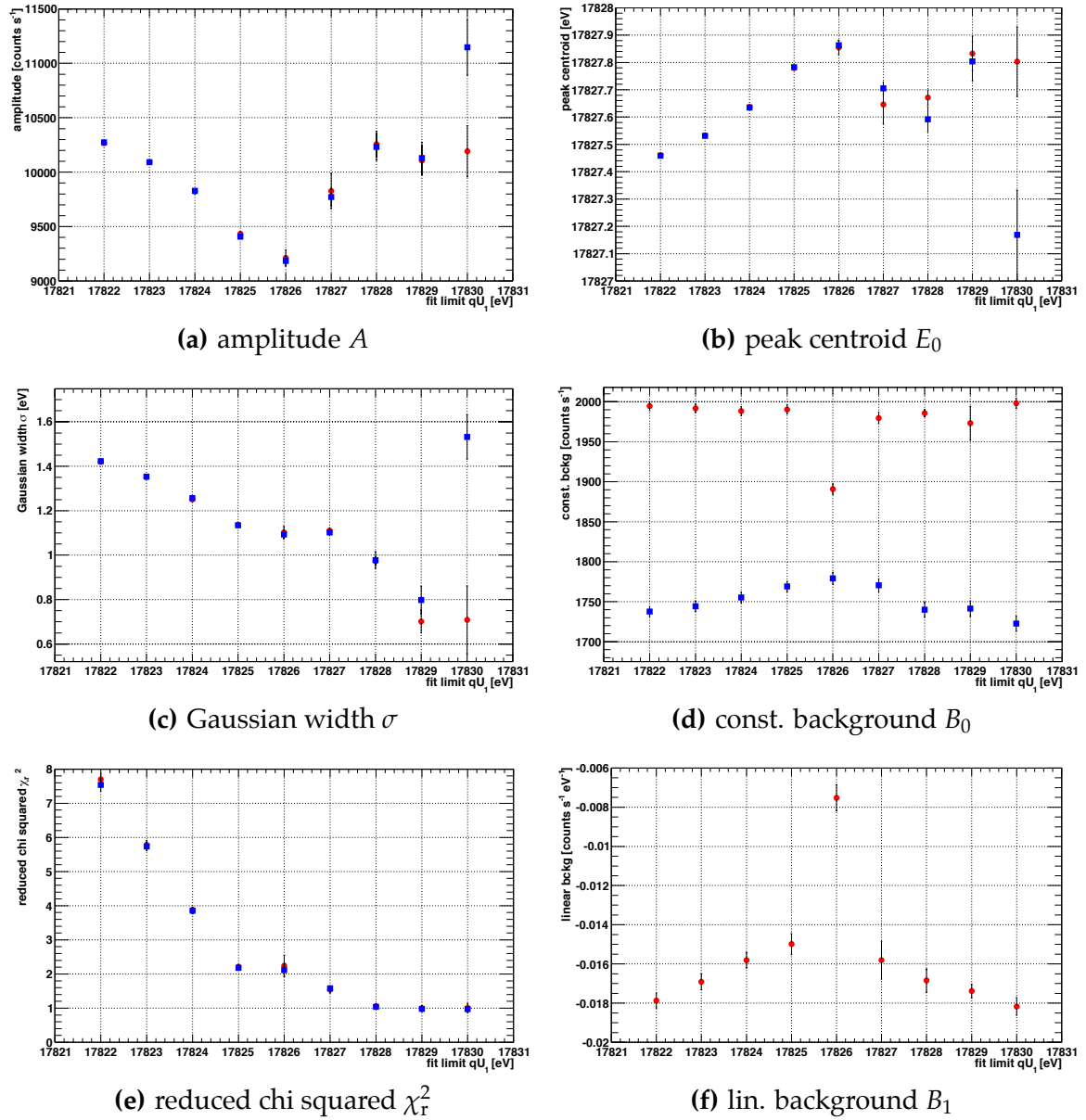


Fig. 7.9: The overview of the fitted parameters and the reduced chi squared resulting from the fits of the measured spectra of the K-32 line of the source Pt-30 #2 with a single Voigt peak. In each figure the x axis denotes the lower limit qU_1 [eV] of the fit range. The blue points mark the results obtained in the case when $B_1 \equiv 0$ whereas the red points denote the results of the fits with linear background B_1 . See text for discussion of the results.

17822 eV, thus $E_0 - qU_1 = 6$ eV, *i. e.* the fit range covered the complete peak (cf. Fig. 7.10).

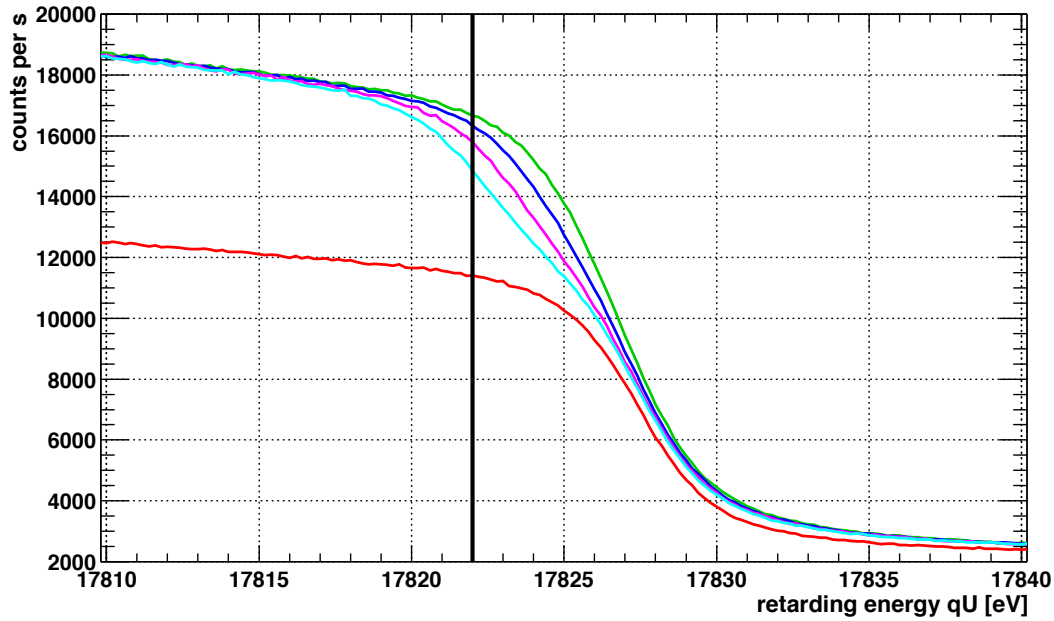


Fig. 7.10: The examples of the simulated integral spectra of the K-32 line produced for the check of the many-parameters fit routine. The red line denotes the simulation with $A_{2/1} = 0$, *i. e.* a pure single Voigt peak with $A_1 = 10\,000$ counts s^{-1} , $B = 2\,000$ counts s^{-1} , $E_0 = 17\,828$ eV, $\Gamma = 2.7$ eV and $\sigma = 1.0$ eV as it would be measured with the resolution of 0.9 eV at 17.8 keV. The rest of the spectra shown were simulated with $A_{2/1} = 0.6$ with different values of the splitting ΔE_{1-2} : 2.0 eV (green line), 3.0 eV (blue), 4.0 eV (magenta) and 5.0 eV (light blue). The vertical line at 17822 eV denotes the lower limit qU_1 of the fit range. The y error bars are not shown.

The results of the analysis of the simulated spectra can be summarized in the following way:

- In all the cases where $\Delta E_{1-2} \leq 1.0$ eV the simulated spectrum was easily described with the single peak where the fitted amplitude A corresponded well to the total amplitude $A = A_1 \cdot (1 + A_{2/1})$. This observation means that if the splitting of the doublet components is roughly equal or less than the width of the spectrometer transmission function then naturally the doublet remains unresolved.
- The structure of the normalized residuals was verified for each $\Delta E_{1-2} - A_{2/1}$ scenario and it was compared with the structure of the normalized residuals observed in the fit of the real K-32 line spectrum of the source Pt-30 #2, see Fig. 7.8(b). For the comparison of the residuals the “real spectrum”-fit was carried out on the corresponding interval $E_0 - qU_1 = 6$ eV. The comparison is schematically tabulated in Tab. 7.4. As already stated, in the case of $\Delta E_{1-2} \leq 1.0$ eV no structure in the residuals was observed (good fit of unresolved doublet). In the case of the scenarios with “ $\Delta E_{1-2} = 2.0$ eV, $A_{2/1} \geq 0.2$ ” and “ $\Delta E_{1-2} = 2.0-5.0$ eV, $A_{2/1} \leq 0.4$ ” a similar residuals structure was observed, however, the amplitude of the structure was lower than in the “real spectrum”-fit. These cases are denoted as “lower amp.” in Tab. 7.4. Practically identical amplitude and structure of the residuals to the “real spectrum”-fit was seen in the spectra simulated with “ $\Delta E_{1-2} = 3.0$ eV, $A_{2/1} \geq 0.6$ ” and “ $\Delta E_{1-2} = 3.0-5.0$ eV, $A_{2/1} = 0.6$ ”. In the rest of the cases the amplitude of the residuals structure was even more pronounced than in the “real spectrum”-fit.

7. Conversion electron spectrum...

- The performance of the fit routine was also verified in an “opposite way”: the spectrum of the *K*-32 was simulated as a pure singlet and it was fitted with a doublet of Voigt peaks with a standard starting values of the parameters, $\Delta E_{1-2} = 3.0$ eV and $A_{2/1} = 0.3$. The fits resulted in suppressing the second component: either via $A_{2/1} \simeq 0.0$ or via $\Delta E_{1-2} \simeq 0.0$ eV. In some cases the fit delivered an unphysical value as $\Delta E_{1-2} \approx 20$ eV, thus the second component was “pushed” out of the fit range.

Tab. 7.4: The overview of the evaluation of the normalized residuals resulting from the fits of the simulated spectra of the *K*-32 line.

ratio $A_{2/1}$	splitting ΔE_{1-2} [eV]					
	0.5	1.0	2.0	3.0	4.0	5.0
0.1	<i>no struct.</i>	<i>no struct.</i>	<i>no struct.</i>	<i>lower amp.</i>	<i>lower amp.</i>	<i>lower amp.</i>
0.2	<i>no struct.</i>	<i>no struct.</i>	<i>lower amp.</i>	<i>lower amp.</i>	<i>lower amp.</i>	<i>lower amp.</i>
0.4	<i>no struct.</i>	<i>no struct.</i>	<i>lower amp.</i>	<i>lower amp.</i>	<i>lower amp.</i>	<i>lower amp.</i>
0.6	<i>no struct.</i>	<i>no struct.</i>	<i>lower amp.</i>	<i>same amp.</i>	<i>same amp.</i>	<i>same amp.</i>
0.8	<i>no struct.</i>	<i>no struct.</i>	<i>lower amp.</i>	<i>same amp.</i>	<i>higher amp.</i>	<i>higher amp.</i>
1.0	<i>no struct.</i>	<i>no struct.</i>	<i>lower amp.</i>	<i>same amp.</i>	<i>higher amp.</i>	<i>higher amp.</i>
1.5	<i>no struct.</i>	<i>no struct.</i>	<i>lower amp.</i>	<i>same amp.</i>	<i>higher amp.</i>	<i>higher amp.</i>
2.0	<i>no struct.</i>	<i>no struct.</i>	<i>lower amp.</i>	<i>same amp.</i>	<i>higher amp.</i>	<i>higher amp.</i>

The residuals of the fits carried out in the various ΔE_{1-2} - $A_{2/1}$ scenarios were compared with the residuals resulting from the fit of the measured spectrum of the *K*-32 line of the source Pt-30 #2. The meaning of the individual boxes is the following: “no struct.” – no structure was observed in the normalized residuals, “low amp.” – a structure was visible in the residuals, however, its amplitude was lower than the one observed in the fits of the real measured spectra, “same amp.” – the amplitude and shape of the structure of residuals was basically identical to the one seen in the fits of the measured spectra, “higher amp.” – the amplitude of the structure of residuals was higher than of the one seen in the fits of the measured spectra. See text for discussion.

Generally, the observations can be interpreted so that the simulations indicate a second component of a doublet to be indeed present in the *K*-32 line spectra of the source Pt-30 #2. The systematic check of the normalized residuals of the fits of the simulated spectra supports the results found in the fits of the real spectra: in Tab. 7.3 it was stated that in the case of the source Pt-30 #2 the fits yielded $A_{2/1} = 0.46(1)$ and $\Delta E_{1-2} = 2.85(3)$ eV which were not excluded in Tab. 7.4. Thus, the doublet structure of the conversion lines of the ion-implanted sources should be treated as a real effect which does not stem from some improper treatment of the data.

7.2.4. Discussion of amplitude and background of the conversion electron lines

In this section the values of the amplitude *A* and the background *B* of the conversion lines shall be briefly discussed. The measured *A* and *B* values of the various conversion lines of the vacuum-evaporated sources were stated above in Tab. 7.1. Similarly, Tab. 7.2 and Tab. 7.3

summarize the A and B values of the conversion lines measured with the ion-implanted sources in the second and the third measurement phases. With respect to the requirements of the task “Calibration and Monitoring” within the KATRIN project it is desirable to maximize the ratio⁶ A/B . The background of the given line (measured with the integrating spectrometer) should be low in order to minimize any possible disturbances resulting from the signal of the conversion lines of higher kinetic energies. In addition, the amplitude should deliver a sufficient number of zero-energy-loss electrons useful for the continuous monitoring of the energy scale stability.

With respect to the considerations of the A/B ratio the L_3 -32 line is superior to the K -32 line⁷: from the internal conversion coefficients (see Sect. 1.2) it follows that the intensities of these lines, taken relative to the decay of ^{83}Rb , are in the ratio (see Tab. 3.1)

$$I_{L_3-32/K-32} := \frac{I(L_3-32)}{I(K-32)} = \frac{27.42\%}{17.07\%} \simeq 1.61. \quad (7.2)$$

The uncertainty of this factor amounts to $\simeq 0.2$. It should be noted though that the values are valid for the ideal case of gaseous $^{83\text{m}}\text{Kr}$ and, moreover, the shake-up/off electrons are neglected. In addition, the high count rate in the L_3 -32 inevitably creates a considerable background of the K -32 line while the background of the L_3 -32 is created only by the lines M_2 and M_3 -32 of low intensity, see Fig. 6.26. Thus, it comes by no surprise that the A/B values are the highest in the case of the L_3 -32 line. In [Ost08] the ratio $I_{L_3-32/K-32}$ was determined as 1.3(2) for the case of the condensed $^{83\text{m}}\text{Kr}$. This represents a fairly good agreement with the literature value keeping in mind that the shake-up/off electrons as well as the inelastically scattered electrons were not taken into account in [Ost08].

From the values presented in Tab. 7.1, Tab. 7.2 and Tab. 7.3 it follows that in the case of the solid $^{83}\text{Rb}/^{83\text{m}}\text{Kr}$ sources the ratio $I_{L_3-32/K-32}$ lies in all the cases in the range of 1.96–2.45. Again, here the shake-up/off electrons as well as the inelastically scattered electrons were neglected at first. Such high values are caused by the fact that in the solid sources the inelastic scattering is more pronounced than in the case of condensed $^{83\text{m}}\text{Kr}$. From the Monte Carlo simulations of electron transport in solids described in Sect. 4.3.3 it follows that the amplitude of K -32 line is more affected by the inelastic scattering than the amplitude of the L_3 -32 line: while the IMFP of the 17.8 keV electrons in platinum is about 144 Å, for the 30.5 keV electrons the IMFP amounts to about 240 Å. This reflects the energy dependence of the losses expressed in Bethe's stopping power formula as $-dE/dx \propto 1/E_{\text{start}}$. On the basis of the estimates of the portion of inelastically scattered electrons in the solid sources (see Tab. 4.4) it can be seen that *e. g.* in the source Pt-30 the amplitude of the L_3 -32 elastic peak is by the factor

$$I_{L_3-32/K-32}(\text{loss, Pt-30}) = \frac{100.0 - 30.0}{100.0 - 42.3} \simeq 1.21 \quad (7.3)$$

more pronounced than the K -32 line. Thus, the ratio of the L_3 -32 and K -32 line amplitudes of the source Pt-30 of 2.16(4) (based on the values $A(L_3-32) = 2095(34)$ counts s^{-1} and $A(K-32) = 972(10)$ counts s^{-1} in Tab. 7.3) has to be corrected for the factor 1.21, resulting in 1.78(4). This value is in a good agreement with the aforementioned value 1.6(2) while in

⁶Usually, in low level counting experiments the quantity A/\sqrt{B} is optimized. However, in accordance with previous Chap. 5 and Chap. 6 the quantity A/B is considered here.

⁷Obviously, the main advantage of the K -32 line over the L_3 -32 line is the fact that the kinetic energy of the K -32 conversion electrons is only by $\simeq 0.8$ keV different from the tritium endpoint.

both cases the shake-up/off electrons are neglected. Should also the shake-up/off electrons be taken into account, one has to consider the values for gaseous krypton [Car73] since there are no literature data for the $^{83\text{m}}\text{Kr}$ atom in solid phase. The ratio of the shake-up/off probabilities of the K -32 and L_3 -32 lines amounts to $P_{\text{shake}}(K-32)/P_{\text{shake}}(L_3-32) = 20.5\%/17.7\% \simeq 1.16$, thus, the recorded amplitude of the K -32 elastic peak is again slightly more affected by these effects than the L_3 -32 elastic peak. Finally, the corrected ratio $I_{L_3-32/K-32}$ reads 1.53(4).

It was shown that the relative intensities of the conversion lines are comparable with those found in [Ost08], however, in the case of the solid sources the electrons undergoing inelastic scattering represent a non-negligible portion. Instead of tabulating the relative intensities of conversion lines of the various sources, here the focus will be made on another feature of the ion-implanted sources: the spectra of the K -32 line of these sources “suffer” from a relatively high background which degrades the useful ratio A/B . Therefore, at this point the background of the K -32 line of the vacuum-evaporated and ion-implanted sources will be compared, in particular the sources S28 and Pt-30. A direct comparison of the values B stated in Tab. 7.1 and Tab. 7.2 is possible for the data series taken in the time period of days 64–107 of the second measurement phase when the sources were investigated simultaneously (together with the source S29). In the case of the source S28 $B = 117.0(2)$ counts s^{-1} when the ^{83}Rb activity of the source amounted to $\mathcal{A} = 0.83$ MBq. Correspondingly, with the 1.52 MBq source Pt-30 the background of $B = 1893(2)$ counts s^{-1} was observed. Thus, correcting B for the ^{83}Rb activity \mathcal{A} , one gets $B'(S28) \simeq 141$ counts $\text{s}^{-1} \text{MBq}^{-1}$ and $B'(Pt-30) \simeq 1246$ counts $\text{s}^{-1} \text{MBq}^{-1}$ which represents the factor of $\simeq 8.8$ by which the background of the source Pt-30 is higher than the background of the source S28 as expected for an ion-implanted source.

One can attempt to estimate B' with the help of the Monte Carlo simulations. As described above in Sect. 4.3.3, in the simulation the electrons are originally created with a certain sharp energy and their scattering inside the source is followed. For the purpose of the background estimate the simulation was carried out⁸ with the parameters $E_0 = 30.5$ keV and $E_{\text{fin}} = 16.8$ keV. In other words, the electrons were simulated as being populated in the L_3 -32 conversion and they were followed down to the region relevant for the background of the K -32 line, see Fig. 7.11. It was discussed in Sect. 5.2.5 that the transmission function of the MAC-E filter significantly “drops” (even approaches zero) with increasing surplus energy, *i. e.* when the K -32 line is measured, at the same time only the electrons of surplus energy of $E_{\text{start}} - qU \approx 200$ eV are still transmitted to the detector and the electrons of higher kinetic energy are practically not transmitted⁹. Based on the simulated transmission function depicted in Fig. 5.20 it can be estimated that actually only the region of 17.8–18.0 keV is relevant for the estimate of the background of the K -32 line measured with the resolution of 0.9 eV at 17.8 keV.

However, the situation is further complicated by the fact that not only the L_3 -32 line is present in the high energy region of the $^{83\text{m}}\text{Kr}$ conversion spectrum, but also another lines are creating the background under the K -32 line. The following simplification was introduced: only the three main groups of the conversion lines were considered, namely the

⁸The Monte Carlo simulations were carried out by Dr. A. Špalek, Nuclear Physics Institute Řež/Prague.

⁹The assumption is based on the simulations of the transmission properties carried out in [Thu07] where the surplus energies higher than ≈ 200 eV were not studied. At this place only a rough estimate of the effect is attempted, for a more detailed calculation one would have to verify the transmission function on the range of $E_{\text{start}} - qU \approx 1$ keV.

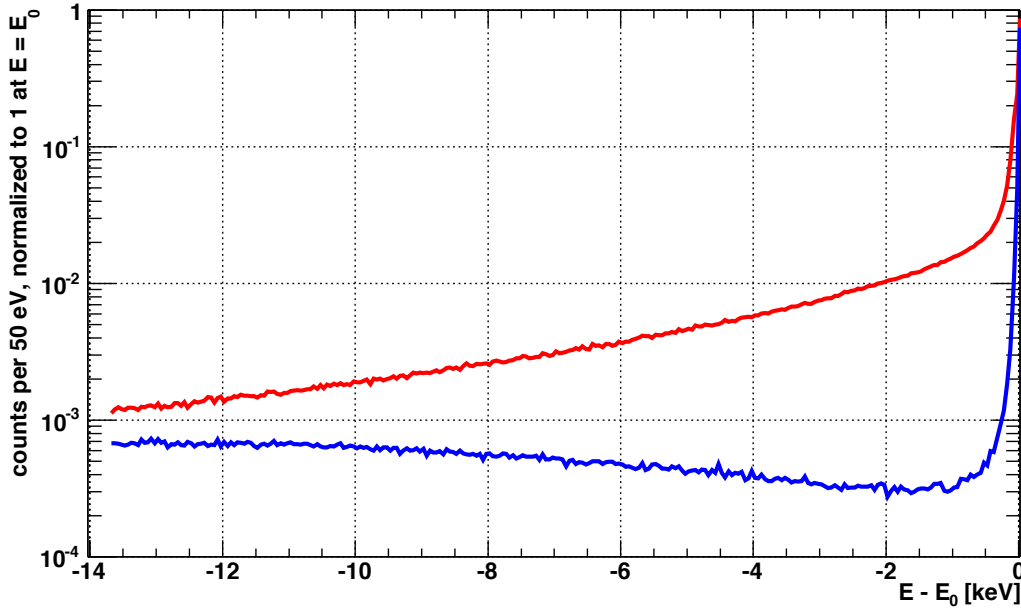


Fig. 7.11: The electron energy loss spectra simulated for the electron starting energy of $E_0 = 30.5$ keV. The bin width was set to 50 eV. All the events of the zero-energy-loss electrons, corresponding to the elastic peak, lie in one bin at $E = E_0$. The spectra are normalized so that the amplitude of this bin is equal to 1. The red line denotes the case of the source Pt-30 and the blue line represents the simulation of the source S28. The spectra are valid for the maximal acceptance angle of $\theta_{\text{start}}^{\text{max}} = 32.7^\circ$. Similar spectra were presented above in Fig. 4.21, however, only for a very narrow range of $E_0 - E \simeq 200$ eV.

L_2/L_3 -32 lines with the nominal energy of $E_0 \simeq 30\,452$ eV and the intensity¹⁰ $I = 17.6 + 27.4 = 45.0\%$, M_2/M_3 -32 lines with $E_0 \simeq 31\,934$ eV and $I = 7.6\%$ and M_4/M_5 -32 lines with $E_0 \simeq 32\,057$ eV and $I = 11.3\%$. This way all the main conversion lines of high energy were taken into account while the lines with the intensity $\leq 1\%$ were neglected (the N_2/N_3 -32 lines, for example). In addition, the spectrum of the inelastically scattered electrons, originally calculated for $E_0 = 30.5$ keV, was shifted relative to the aforementioned nominal energies. This approach can be justified by the fact that the energy dependence of the shape of the loss electron spectra is very smooth and the differences of E_0 of up to ± 1.6 keV encountered here can be safely neglected. The three components of such simulated background under the K-32 line of the source Pt-30 are depicted in Fig. 7.12.

Summing the relevant portions of spectra in Fig. 7.12 (in the case of the source S28 the calculation was done with the proper spectrum shown in Fig. 7.11) and scaling the result with respect to all the Monte Carlo events, and, similarly to Eq. 5.18 in Sect. 5.2.4, taking into account the spectrometer efficiency $\eta_{\text{spec}} = 7.9\%$, the krypton retention R_{Kr} of the sources S28 (0.19, cf. Tab. 4.1) and Pt-30 (0.97, cf. Tab. 4.2) and the detection efficiency $\eta_{\text{det}} = 0.8$, one comes to the estimates $B'_{\text{est}}(\text{S28}) = 23 \text{ counts s}^{-1} \text{ MBq}^{-1}$ and $B'_{\text{est}}(\text{Pt-30}) = 161 \text{ counts s}^{-1} \text{ MBq}^{-1}$, respectively. Clearly, the estimated values are vastly underestimated which suggests that other effects have to be considered as well. Indeed, one has to keep in mind that the secondary electrons (cf. Sect. 6.3.6), produced by the high energy electrons (mainly L_2/L_3 , M_2/M_3 and M_4/M_5 -32), contribute significantly to the background of the

¹⁰Relative to the decay of ^{83}Rb , cf. Tab. 3.1.

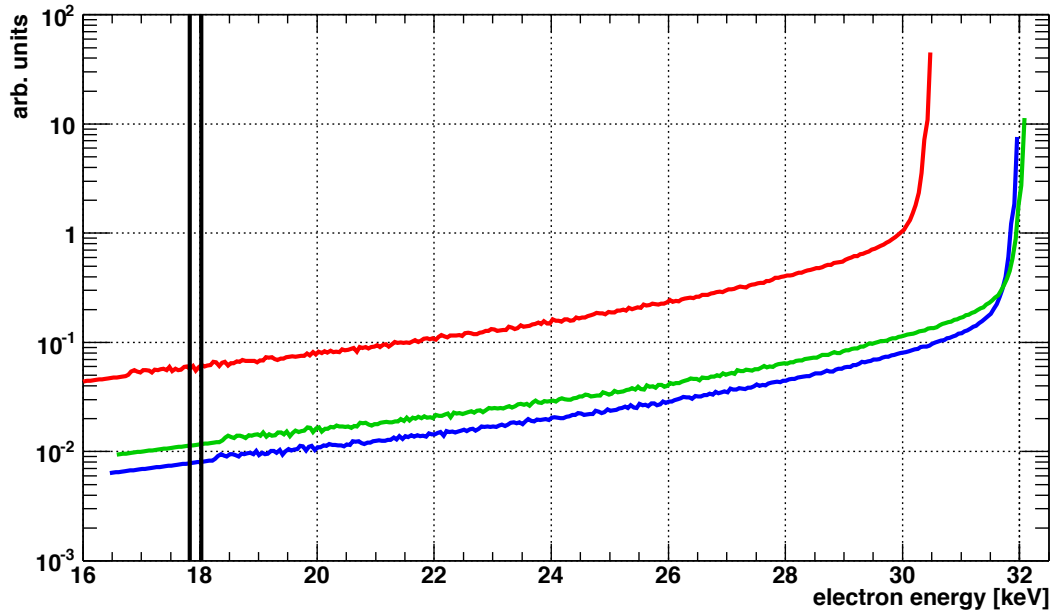


Fig. 7.12: The components of the simulated background of the K -32 line of the source Pt-30. The electron energy loss spectrum depicted in Fig. 7.11 was shifted relative to the corresponding energies of the three groups of high energetic peaks: L_2/L_3 -32 (red line), M_2/M_3 -32 (blue line) and M_4/M_5 (green lines). The intensities of these three spectra were set equal to the intensities (relative to the ^{83}Rb decay) of the groups of the conversion lines. The vertical lines mark the region of 17.8–18.0 keV which was considered in the calculation described in text. The reason for such interval is the fact that the electrons at higher surplus energies are not transmitted when the K -32 line is scanned. The spectrum from Fig. 7.11 used here was extrapolated in the low energy region with an exponential function in order to match the region of interest.

K -32 line measured in this integrating spectrometer. It can be seen the signal coming from the source accounts only for 16% (S28) and 13% (Pt-30) of the total background level. The rest of the background can be attributed to the electrons ejected from the surface of the electrodes. This stems from the fact that not all the electrons, which are rejected in the analyzing plane by the retarding voltage, are reflected back onto the source—certain portion of them is guided to the spectrometer electrode and produces secondary electrons. Still, it should be emphasized that this kind of background is indeed induced by the source itself: when the source section was separated by the gate valve from the spectrometer vessel, the background of only $\approx 3 \text{ counts s}^{-1}$ was observed, see Sect. 6.3.6 for the description of the tests.

7.3. Absolute kinetic energies of the conversion electrons from solid sources

This section deals with the absolute kinetic energies of the various conversion electron lines of the solid $^{83}\text{Rb}/^{83\text{m}}\text{Kr}$ sources. Firstly, the conversion electrons of the 9.4 keV gamma transition (multipolarity M1) of $^{83\text{m}}\text{Kr}$ will be discussed in Sect. 7.3.1. Secondly, in Sect. 7.3.2 the conversion electrons populated in the $^{83\text{m}}\text{Kr}$ 32 keV gamma transition (multipolarity E3)

will be reviewed. Later, in Sect. 7.3.3 the influence of the $^{83\text{m}}\text{Kr}$ atom environment on the electron binding energy of the various electron shells of $^{83\text{m}}\text{Kr}$ will be discussed. Finally, the linearity of the energy scale will be checked in Sect. 7.3.4 on the basis of the results obtained in Sect. 7.3.1 and Sect. 7.3.2.

7.3.1. Conversion electrons of the 9.4 keV gamma transition

The value of the centroid E_0 obtained from the least-squares fit of a given conversion electron line is not directly equal to the absolute kinetic energy of the conversion electrons. Here the calculation of the absolute kinetic energy will be shown for the case of the L_1 -9.4 line of the source Pt-30 measured on day 76 of the second measurement phase. In this measurement phase the HV divider K35 was used as the HV reference.

Altogether 18 spectra of the L_1 -9.4 line were fitted with a single Voigt peak, resulting in the weighted mean value of the centroid of 7 483.830(29) eV. The physically meaningful value of the electron kinetic energy is obtained according to Eq. 5.8: the corrected value of the absolute energy reads 7 483.747 eV. It should be noted that the value represents merely the kinetic energy $E_{\text{kin}}^{\text{impl}}(L_1\text{-}9.4)$, used above in Eq. 4.9, and this value is *not* corrected for the recoil energies $E_{\text{rec}, \gamma}$ and $E_{\text{rec}, e}(L_1\text{-}9.4)$ nor for the work functions ϕ_{source} and ϕ_{spec} . The stated uncertainty of 29 meV represents only the statistical uncertainty resulting from the fits. The full uncertainty of the final value was calculated in the same way as in [Thu07, Ost08] where the following effects were considered:

1. It was stated in Sect. 5.2.2 that the integral spectra used in this work were produced with a fixed nominal value of the dividing ratio M_0 of the HV divider. Then, the linear drift of the energy of a given line was always corrected in Chap. 6 for the time dependence $M(t)$ which was considered to be a linear function with the relative drift m [ppm month $^{-1}$]. Naturally, in the analysis reported in this chapter the proper dividing ratio was used as well. In this particular case the nominal value amounted to $M_0(\text{K35}) = 1\,972.480\,16(61)$ (cf. Tab. 5.1) and the actual value used at this point was equal to $M(\text{K35}) = 1\,972.513$, differing by $\simeq 16$ ppm from the nominal value. In [Thu07] the relative uncertainty of M was stated as 1.6 ppm at the HV of -20 kV.
2. The voltage dependence of the dividing ratio of the HV divider K35 was also taken into account: the HV divider K35 was absolutely calibrated at -20 kV whereas during the scan of the L_1 -9.4 line the HV was set to -7.5 kV. Thus, considering the voltage dependence of the dividing ratio as $0.032(6)$ ppm kV $^{-1}$ (cf. Tab. 5.1), the HV difference of $\simeq 12.5$ kV causes the shift of the dividing ratio of about 0.4 ppm. Such a shift is actually negligible compared to other corrections in this exemplar calculation. The uncertainty of this shift was included in accordance with [Thu07].
3. The time dependence of the scale factor $K(t)$ of the digital voltmeter was taken into account, see Fig. 6.17 for the result of the regular calibrations of the digital voltmeter. The relative uncertainty of the readout of the low voltage (at the output of the HV divider) amounted typically to ≤ 0.5 ppm during all the measurement phases. The absolute uncertainty of the voltage readout then scales with the applied HV via the factor $K \cdot M$.

7. Conversion electron spectrum...

4. Similarly, the uncertainty of the zero offset of the digital voltmeter scales via the factor $K \cdot M$. As this offset was always observed to be about $-3 \mu\text{V}$ (see page 151), this correction represents the shift of about -6 meV of the energy scale. Its uncertainty was included in the analysis as well.
5. In Eq. 5.8 the potential dip δE_{shift} (see Eq. 5.9 and Fig. 5.15) across the analyzing plane, stemming from the radial variations of the magnetic and electric fields influencing the transmission function, is also included. According to Eq. 5.9 the potential dip amounts to $\delta E_{\text{shift}} = -0.157 \text{ eV}$ in the case of the L_1 -9.4 line. The correction of this effect lowers the absolute kinetic energy. The relative uncertainty of this correction was estimated in [Thu07] as 5 %.
6. In [Ost08] the uncertainty of the source position was also included in the analysis of the absolute kinetic energies. This systematic effect was studied (with the help of the K -32 line of the sources S 28 and Pt-30) in this work already in Sect. 6.2.4 and Sect. 6.3.5 in order to assess the sensitivity of the overall experimental setup to a possible misalignment. In these tests the maximal relative shift of the K -32 line energy of 4.1(7) ppm was observed in the case when the source S 28 was misplaced by 2 mm from its optimal $[x, y]$ position (used routinely for the measurements). Therefore, a rather conservative estimate of this effect was used and the relative uncertainty of 4.1(7) ppm was involved in the analysis.
7. Lastly, the stability of the line energy itself, studied in detail in previous Chap. 6, was also considered as one of the systematic effects. In the time period of days 64–107 of the second measurement phase, very low drifts of the lines energies were observed (cf. Fig. 6.16 and Tab. 6.7), of the order of ppm month⁻¹ or less. On the other hand, as the L_1 -9.4 line usually exhibited a considerably higher scatter of the energy than the other conversion lines, a conservative estimate of 0.1 eV of the line stability was considered at this place.

Taking into account all the listed corrections and their uncertainties, the final uncertainty in this case reads 0.111 eV. Thus, the absolute kinetic energy can be stated here as

$$E_{\text{kin}}^{\text{impl}}(L_1\text{-}9.4, \text{ day } 76) = 7483.75(11) \text{ eV}. \quad (7.4)$$

However, it should be emphasized that the data were obtained in the time period when the HV scale was shifted by $\simeq 0.93 \text{ V}$. The uncertainty of this was safely estimated as 0.2 V, thus, the energy scale was shifted by $+0.93(20) \text{ eV}$. Therefore, the corrected value should actually read

$$E_{\text{kin}}^{\text{impl}}(L_1\text{-}9.4, \text{ day } 76, \text{ HV corr.}) = 7482.82(23) \text{ eV}. \quad (7.5)$$

On the basis of Eq. 4.7 to Eq. 4.9 this value can be compared to the absolute kinetic energy of the L_1 -9.4 electrons emitted by gaseous ^{83m}Kr. Eq. 4.9 can be conveniently rewritten into the form

$$E_{\text{kin}}^{\text{impl}}(i) = \underbrace{E_{\gamma} + E_{\text{rec}, \gamma} - E_{\text{rec}, e}(i) - E_{\text{bin}}^{\text{vac}}(\text{gas}, i)}_{= E_{\text{kin}}^{\text{gas}}(i) \text{ in Tab. 3.1}} + \underbrace{\Delta E_{\text{bin}}^{\text{Fermi}}(\text{impl}, i)}_{= \Delta E_{\text{bin}}^{\text{vac}}(\text{impl}, i) + \phi_{\text{source}}} - \phi_{\text{spec}}, \quad (7.6)$$

where the term of the kinetic energy $E_{\text{kin}}^{\text{gas}}(i)$ of the conversion electrons in gaseous ^{83m}Kr (tabulated in Tab. 3.1), already contains the corrections for the recoil energies, in this case amounting to $E_{\text{rec}, \gamma}(9.4 \text{ keV}) = 0.002 \text{ eV}$ and $E_{\text{rec}, e}(L_1\text{-}9.4) = 0.049 \text{ eV}$. In addition, it is

convenient to introduce the term $\Delta\phi$ describing the potential difference of the source and spectrometer work functions

$$\Delta\phi(\text{Pt}) := \phi_{\text{spec}} - \phi_{\text{source}}(\text{Pt}) = 4.4(2) - 5.65(10) = -1.25(22) \text{ eV}, \quad (7.7)$$

where the values are taken from Tab. 4.3. Finally, one can further rewrite Eq. 7.6 as

$$\Delta E_{\text{bin}}^{\text{vac}}(\text{impl}, i) = E_{\text{kin}}^{\text{impl}}(i) - E_{\text{kin}}^{\text{gas}}(i) + \Delta\phi(\text{Pt}). \quad (7.8)$$

The *positive* shift $\Delta E_{\text{bin}}^{\text{vac}}(\text{impl}, i)$, related to the vacuum level, represents the shift of the electron binding energy of the conversion electron emitted by the $^{83\text{m}}\text{Kr}$ atom implanted into polycrystalline platinum. Its meaning is identical to the shift introduced in Eq. 4.6 where it denoted the shift observed in [Cit74] for noble gases implanted into noble metals. In our exemplar case the shift amounts to

$$\Delta E_{\text{bin}}^{\text{vac}}(\text{impl}, L_1-9.4) = 7482.82(23) - 7481.16(89) - 1.25(22) = 0.41(95) \text{ eV}. \quad (7.9)$$

Due to the large uncertainties, dominated by the uncertainty of $E_{\text{kin}}^{\text{gas}}(i)$ which, in turn, stems from the uncertainties of $E_{\text{bin}}^{\text{vac}}(i)$ and $E_{\gamma}(9.4)$ (cf. Eq. 3.17), the determined shift is compatible with zero shift.

The presented analysis was carried out in analogous way for all $^{83\text{m}}\text{Kr}$ electron shells of the various solid $^{83}\text{Rb}/^{83\text{m}}\text{Kr}$ sources. In the case of the ion-implanted source Au-30 Eq. 7.8 was utilized where the work function difference $\Delta\phi(\text{Au}) = -0.70(22) \text{ eV}$ was taken into account. Similar shifts of the kinetic energies of the conversion electrons were also determined for the vacuum-evaporated sources. In this case the shift was calculated as (cf. Eq. 4.5)

$$\Delta E_{\text{bin}}^{\text{vac}}(\text{evap}, i) = E_{\text{kin}}^{\text{evap}}(i) - E_{\text{kin}}^{\text{gas}}(i) + \Delta\phi, \quad (7.10)$$

where the term $\Delta\phi$ was different for the two pairs of the sources. The sources S 11 and S 13 were evaporated onto aluminum backing, and therefore $\Delta\phi(\text{S 11/13}) = 0.12(22) \text{ eV}$, whereas for the sources S 28 and S 29, prepared by the vacuum evaporation onto graphite, the term equals $\Delta\phi(\text{S 28/29}) = -0.60(22) \text{ eV}$. Furthermore, on the basis of the results obtained in [Ost08] it was also possible to determine the electron binding energy shifts $\Delta E_{\text{bin}}^{\text{vac}}(\text{cond}, i)$ of the conversion electrons emitted from $^{83\text{m}}\text{Kr}$ condensed onto clean HOPG substrate. Rewriting Eq. 3.20 one arrives at

$$\Delta E_{\text{bin}}^{\text{vac}}(\text{cond}, i) = E_{\text{kin}}^{\text{cond}}(i) - E_{\text{kin}}^{\text{gas}}(i) + \Delta\phi(\text{CKrS}), \quad (7.11)$$

with the term $\Delta\phi(\text{CKrS}) = -0.17(26) \text{ eV}$, based on the value $\phi(\text{HOPG}) = 4.57(16) \text{ eV}$. This way the reevaluation of $E_{\text{kin}}^{\text{cond}}(i)$ from [Ost08] delivered the values $\Delta E_{\text{bin}}^{\text{vac}}(\text{cond}, i)$. The latter ones could be then compared to the correction term $\Delta E_{\text{bin}}^{\text{vac}}(\text{cond}, i) \equiv \Delta E_{\text{bin}}^{\text{vac}}(\text{cond}) = 1.74(23) \text{ eV}$ used in [Ost08] for all the electron shells of $^{83\text{m}}\text{Kr}$ (see Sect. 3.3.2 and Sect. 4.3.1). The results of the analysis are summarized in Tab. 7.5. In the upper part of the table the absolute kinetic energies are stated, uncorrected for the recoil energies. In the case of the ion-implanted sources Pt-30 #2, Pt-15 and Au-30, where the $L_1-9.4$ line was well described only with a doublet of Voigt peaks, the energy stated in the table corresponds to the doublet component of higher kinetic energy. It is assumed at this point that this component indeed represents the $^{83\text{m}}\text{Kr}$ atom implanted into noble metal. This question is discussed later in this chapter. In the lower part of Tab. 7.5 the corresponding shifts of the electron binding energies are summarized. The errors of the shifts are correlated due to the uncertainties of the energies of the $^{83\text{m}}\text{Kr}$ gamma transitions.

Tab. 7.5: The overview of the absolute kinetic energies of the conversion electrons populated in the 9.4 keV gamma transition of ^{83m}Kr .

source	gas calc. acc. to Eq. 3.15	CKrS reevaluation of [Ost08]	S 28 1 st 41-74	80-90	S 29 2 nd 0-15	Pt-30 2 nd 0-15	64-107	Pt-30 #2 3 rd	Pt-15 3 rd	Au-30 3 rd
L_1	7481.2(9)	7481.05(5)	7481.46(75)	7481.74(29) *	7481.58(29) *	7481.61(35) *	7482.82(23) *	7483.78(8)	7484.67(7)	7483.23(21)
L_2	7673.8(4)	7674.65(6)					7676.86(23) *			
L_3	7726.5(4)	7727.40(7)					7729.43(24) *	7729.22(15)	7730.41(4)	7729.43(5)
$E_{\text{kin}}(f)$										
M_1	9113.0(5)	9113.47(5)					9115.32(23) *	9115.29(5)	9116.33(5)	9115.48(5)
M_2	9183.5(4)	9184.62(15)					9185.99(45) *			
M_3	9191.3(4)	9192.23(14)					9194.01(34) *			
N_1	9378.2(4)	9378.91(5)					9379.51(30) *			
L_1		-0.28(93)	-0.30(119)	-0.02(97) *	-0.15(99) *	1.06(98) *	0.41(95) *	1.37(93)	2.26(92)	1.37(95)
L_2		0.63(48)					1.77(51) *			
L_3		0.68(48)					1.63(52) *	1.42(48)	2.61(46)	2.18(46)
$\Delta E_{\text{bin}}^{\text{vac}}(i)$										
M_1		0.30(56)					1.07(59) *	1.03(54)	2.08(54)	1.77(54)
M_2		0.91(54)					1.20(67) *			
M_3		0.80(51)					1.50(58) *			
N_1		0.51(48)					0.03(55) *			

The kinetic energies of the conversion electrons emitted from gaseous ^{83m}Kr were calculated according to Eq. 3.15 where the work function difference $\phi_{\text{spec}} - \phi_{\text{source}}$ was omitted. The shifts determined for the ^{83m}Kr condensed onto clean HOPG substrate (CKrS) represent the shifts $\Delta E_{\text{bin}}^{\text{vac}}(\text{cond}, i)$ in Eq. 7.11. The shifts $\Delta E_{\text{bin}}^{\text{vac}}(\text{evap}, i)$ (cf. Eq. 7.10) are stated, whereas the shifts $\Delta E_{\text{bin}}^{\text{vac}}(\text{impl}, i)$ (cf. Eq. 7.8) are shown for the ion-implanted sources. The values marked with * were corrected for the shift of the energy scale of +0.93(20) eV. The errors of the shifts are correlated due to the uncertainties of the electron binding energies $E_{\text{bin}}^{\text{vac}}(i)$ and the energies of the ^{83m}Kr gamma transitions. See text for further discussion of the results.

7.3.2. Conversion electrons of the 32 keV gamma transition

The analysis described in previous section for the conversion electrons of the 9.4 keV gamma transition of $^{83\text{m}}\text{Kr}$ was accomplished in analogous way for the 32 keV $^{83\text{m}}\text{Kr}$ gamma transition. The results are summarized in Tab. 7.6 (vacuum-evaporated sources) and Tab. 7.7 (ion-implanted sources). Again, the tables state the absolute kinetic energies as well as the binding energy shifts, defined above via Eq. 7.8, Eq. 7.10 and Eq. 7.11. In the latter table, the absolute kinetic energy of the doublet component of higher energy is again presented in all the cases where the conversion line spectrum had to be fitted with a doublet of peaks, the only exception being the $N_{2/3}$ -32 line where it was shown that the high energy component does not correspond to the internal conversion of $^{83\text{m}}\text{Kr}$. The values of the splitting ΔE_{1-2} , summarized in Tab. 7.2 and Tab. 7.3, can be used to deduce the absolute kinetic energy of the second doublet component. The results based on the data obtained with the shifted HV scale have to be used with caution, stated are the values corrected for the shift of +0.93(20) eV. In all the cases the shifts were found to be positive and the uncertainties amounted to about 0.6–0.8 eV. Detailed discussion of the results takes place in coming section.

Tab. 7.6: The overview of the absolute kinetic energies of the conversion electrons populated in the 32 keV gamma transition of ^{83m}Kr in the vacuum-evaporated $^{83}\text{Rb}/^{83m}\text{Kr}$ sources.

source meas. phase rel. time [day]	gas calc. acc. to Eq. 3.15	CKrS reevaluation of [Ost08]	S11 pilot	S13 pilot	S28 1 st 41-74	S28 2 nd 64-107	S29 2 nd 0-15
K	17 824.3(5)	17 826.18(6)	17 825.67(9)	17 825.35(9)	17 826.27(8)	17 825.37(21) *	17 826.05(23) *
L_2	30 419.6(5)	30 421.64(10)					
L_3	30 472.3(5)	30 474.36(10)	30 473.36(12)		30 474.67(11)	30 473.52(23) *	30 474.23(24) *
$E_{\text{kin}}(i)$							
M_2	31 929.3(5)	31 931.05(34)					
M_3	31 937.0(5)	31 938.73(34)					
$M_{4/5}$	32 057.2(7)						
$N_{2/3}$	32 137.2(7)	32 139.15(10)			32 139.43(12)	32 138.58(26) *	32 138.99(26) *
K		1.68(57)	1.47(56)	1.14(56)	1.34(55)	1.40(60) *	1.12(60) *
L_2		1.87(57)					
L_3		1.90(57)	1.20(56)		1.79(56)	1.71(60) *	1.35(60) *
$\Delta E_{\text{bin}}^{\text{vac}}(i)$							
M_2		1.58(68)					
M_3		1.55(67)					
$M_{4/5}$							
$N_{2/3}$		1.74(76)			1.60(75)	1.59(80) *	1.16(79) *

The table summarizes the data obtained with the vacuum-evaporated sources which are compared to the kinetic energies of the conversion electrons emitted from gaseous ^{83m}Kr (Eq. 3.15 where $\phi_{\text{spec}} = \phi_{\text{source}}$). The shifts determined for the ^{83m}Kr condensed onto clean HOPG substrate (CKrS) represent the shifts $\Delta E_{\text{bin}}^{\text{vac}}(\text{cond}, i)$ in Eq. 7.11. The shifts $\Delta E_{\text{bin}}^{\text{vac}}(\text{cond}, i)$ were obtained from reevaluation of the data obtained in [Ost08]. In the case of the vacuum-evaporated sources the electron binding energy shifts $\Delta E_{\text{bin}}^{\text{vac}}(\text{evap}, i)$ were calculated according to Eq. 7.10. The values marked with * were corrected for the shift of the energy scale of +0.93(20) eV. The errors of the shifts are correlated due to the uncertainties of the electron binding energies $E_{\text{bin}}^{\text{vac}}(i)$ and the energies of the ^{83m}Kr gamma transitions. See text for further discussion of the results.

Tab. 7.7: The overview of the absolute kinetic energies of the conversion electrons populated in the 32 keV gamma transition of $^{83\text{m}}\text{Kr}$ in the ion-implanted $^{83}\text{Rb}/^{83\text{m}}\text{Kr}$ sources.

source meas. phase rel. time [day]	gas calc. acc. to Eq. 3.15	CKrS reevaluation of [Ost08]	Pt-30 2 nd 53–61	Pt-30 3 rd 64–107	Pt-30 #2 3 rd	Pt-15 3 rd	Au-30 3 rd
K	17 824.3(5)	17 826.18(6)	17 827.73(22) *	17 827.70(22) *	17 827.94(6)	17 828.34(6)	17 827.76(6)
L_2	30 419.6(5)	30 421.64(10)		30 423.17(23) *			
L_3	30 472.3(5)	30 474.36(10)		30 475.90(23) *	30 476.05(10)	30 476.35(9)	30 475.75(10)
$E_{\text{kin}}(i)$							
M_2	31 929.3(5)	31 931.05(34)		31 932.80(23) *			
M_3	31 937.0(5)	31 938.73(34)		31 940.29(23) *	31 940.25(11)	31 940.58(10)	31 940.04(10)
$M_{4/5}$	32 057.2(7)			32 060.69(31) *			
$N_{2/3}$	32 137.2(7)	32 139.15(10)		32 139.86(37) *	32 139.49(11)	32 140.17(11)	32 139.63(13)
K		1.68(57)	2.75(60) *	2.15(59) *	2.13(59) *	2.76(55)	2.73(55)
L_2		1.87(57)		2.32(59) *			
L_3		1.90(57)	3.18(60) *	2.36(59) *	2.51(56)	2.81(56)	2.76(56)
$\Delta E_{\text{bin}}^{\text{vac}}(i)$							
M_2		1.58(68)		2.25(62) *			
M_3		1.55(67)		2.03(61) *	2.00(57)	2.32(57)	2.33(57)
$M_{4/5}$				2.25(81) *			
$N_{2/3}$		1.74(76)	1.95(79) *	1.38(81) *	1.01(75)	1.69(75)	1.69(75)

The table summarizes the data obtained with the ion-implanted sources which are compared to the kinetic energies of the conversion electrons emitted from gaseous $^{83\text{m}}\text{Kr}$ (Eq. 3.15 where $\phi_{\text{spec}} = \phi_{\text{source}}$). The shifts determined for the $^{83\text{m}}\text{Kr}$ condensed onto clean HOPG substrate (CKrS) represent the shifts $\Delta E_{\text{bin}}^{\text{vac}}(\text{cond}, i)$ in Eq. 7.11. The shifts $\Delta E_{\text{bin}}^{\text{vac}}(\text{cond}, i)$ were obtained from reevaluation of the data obtained in [Ost08]. In the case of the ion-implanted sources the electron binding energy shifts $\Delta E_{\text{bin}}^{\text{vac}}(\text{impl}, i)$ were calculated according to Eq. 7.8. The values marked with * were corrected for the shift of the energy scale of +0.93(20) eV. The errors of the shifts are correlated due to the uncertainties of the electron binding energies $E_{\text{bin}}^{\text{vac}}(i)$ and the energies of the $^{83\text{m}}\text{Kr}$ gamma transitions. In the case of the $N_{2/3}$ -32 line the values are valid for the low energy component of the doublet which was attributed to the internal conversion of $^{83\text{m}}\text{Kr}$. See text for further discussion of the results.

7.3.3. Influence of $^{83\text{m}}\text{Kr}$ atom environment on the electron binding energy

The results of previous two sections were analyzed in such a way that for each source one final value of the electron binding energy shift (related to the vacuum level) was obtained for as many electron shells as possible. In the case of the sources S 28 and Pt-30 several measurements were available. A weighted mean was calculated from the data while the final uncertainty was multiplied by $\sqrt{\chi_r^2}$ (χ_r^2 being used in the sense of Eq. 5.5) in order to account possible discrepancies of the individual measurements. It was stated above already that the errors of the shifts are correlated due to the uncertainties of the energies of the $^{83\text{m}}\text{Kr}$ gamma transitions. Therefore, in Fig. 7.13 the results plotted without the uncertainties of 0.4 and 0.5 eV of the 9.4 and 32 keV $^{83\text{m}}\text{Kr}$ gamma transitions (cf. Eq. 3.17 and Eq. 3.16), respectively. Still, the uncertainties of the individual electron binding energies are included in the calculation. The shifts observed in the 9.4 keV gamma transition are shown in Fig. 7.13(a) while Fig. 7.13(b) summarizes the shifts relevant for the electrons populated in the 32 keV gamma transition. The observations can be summarized as follows:

- From the reevaluation of the data of [Ost08] the shifts $\Delta E_{\text{bin}}^{\text{vac}}(\text{cond}, i)$ (see Eq. 7.11) of the $^{83\text{m}}\text{Kr}$ condensed onto a clean HOPG substrate were obtained. It can be clearly seen in Fig. 7.13 that the binding energy shifts found in the 9.4 keV gamma transition are considerably lower than the ones found in the 32 keV gamma transition. The former set of data gives the weighted mean of $\langle \Delta E_{\text{bin}}^{\text{vac}}(\text{cond}, i-9.4) \rangle = 0.60(20)$ eV whereas the latter set of data results in $\langle \Delta E_{\text{bin}}^{\text{vac}}(\text{cond}, i-32) \rangle = 1.74(25)$ eV (denoted by the red dashed line in Fig. 7.13(b)). The fact that $\langle \Delta E_{\text{bin}}^{\text{vac}}(\text{cond}, i-32) \rangle$ is actually identical to the value $\Delta E_{\text{bin}}^{\text{vac}}(\text{cond}) = 1.74(23)$ eV used in [Ost08] comes by no surprise. The reason for this agreement is that in [Ost08] the kinetic energy of each conversion electron line was corrected by $\Delta E_{\text{bin}}^{\text{vac}}(\text{cond})$ and the energy of the 32 keV gamma transition was determined as $E_\gamma(\text{conv. el.}) = 32\,151.74(35)$ eV. On the other hand, in this work the value $E_\gamma(\text{gamma ray}) = 32\,151.7(5)$ eV (see Eq. 3.16) was used and the shifts were deduced. This may seem as an unnecessary calculus since $E_\gamma(\text{conv. el.})$ and $E_\gamma(\text{gamma ray})$ perfectly agree in the case of the 32 keV gamma transition. However, the shifts smaller by $\simeq 1.1$ eV observed in the 9.4 keV gamma transitions reflect a small discrepancy of the values $E_\gamma(\text{conv. el.}) = 9\,404.71(35)$ eV determined in [Ost08] and $E_\gamma(9.4) = 9\,405.8(4)$ eV (see Eq. 3.17) used in this work.
- Due to a relatively poor precision of 0.8 eV of the value $E_{\text{bin}}^{\text{vac}}(L_1)$ taken from [Sie69] the data of the $L_1-9.4$ electrons suffer from large uncertainties, however, a clear trend of increasing shift is visible when going from condensed and vacuum-evaporated $^{83\text{m}}\text{Kr}$ to ion-implanted sources.
- In the case of the other electron shells the uncertainties of the shifts are smaller and the overall discrepancy between the individual solid $^{83}\text{Rb}/^{83\text{m}}\text{Kr}$ sources is clearly seen.
- With the source Pt-30 a nearly complete spectrum of $^{83\text{m}}\text{Kr}$ conversion electrons was measured. The shifts $\Delta E_{\text{bin}}^{\text{vac}}(\text{impl}, i)$ (see Eq. 7.9) were in almost all the cases considerably larger than the corresponding shifts $\Delta E_{\text{bin}}^{\text{vac}}(\text{cond}, i)$ of the condensed $^{83\text{m}}\text{Kr}$, the only exception being the valence electrons (lines $N_1-9.4$ and $N_{2/3}-32$).
- No good agreement between the data sets of the sources Pt-30 and Pt-30 #2 was found,

thus, in this respect a poor source-to-source reproducibility of the absolute energies of the conversion electrons was observed. It has to be kept in mind though that the sources differ in a) the total implanted dose of ^{83}Rb , b) the peak atomic concentration of ^{83}Rb and c) the level of other impurities in the platinum foils (mainly rhodium impurity was present in the source Pt-30, cf. Sect. 4.2.3).

- Generally speaking, for each electron shell the conversion electrons of both $^{83\text{m}}\text{Kr}$ gamma transitions exhibited shifts of the binding energy following a trend which can be symbolically written as

$$E_{\text{bin}}^{\text{vac}}(\text{gas}) > E_{\text{bin}}^{\text{vac}}(\text{cond}) \simeq E_{\text{bin}}^{\text{vac}}(\text{evap}) > E_{\text{bin}}^{\text{vac}}(\text{impl}). \quad (7.12)$$

In addition, the shifts $\Delta E_{\text{bin}}^{\text{vac}}(\text{impl}, M_3)$ can be directly compared to the literature values $\Delta E_{\text{bin}}^{\text{vac}}(\text{impl}, \text{Kr in Pt}) \simeq 1.9 \text{ eV}$ (cf. Eq. 4.11) and $\Delta E_{\text{bin}}^{\text{vac}}(\text{impl}, \text{Kr in Au}) \simeq 3.1 \text{ eV}$ (cf. Eq. 4.10) based on the XPS measurements [Cit74] of the $3p_{3/2}$ electrons (M_3 shell) of krypton implanted into polycrystalline foils. Our values read $\Delta E_{\text{bin}}^{\text{vac}}(\text{Au-30}, M_3\text{-32}) = 2.33(57) \text{ eV}$, $\Delta E_{\text{bin}}^{\text{vac}}(\text{Pt}, M_3\text{-32}) = 2.12(33) \text{ eV}$ (weighted mean over all Pt-based sources) and $\Delta E_{\text{bin}}^{\text{vac}}(\text{Pt-30}, M_3\text{-9.4}) = 1.50(55) \text{ eV}$. There is an overall agreement of the values within 1σ (Kr in Pt) and 2σ (Kr in Au).

7.3.4. Energy difference of the 9.4 keV and 32 keV gamma transitions

It was already advertised at the beginning of this chapter that the absolute kinetic energies of the conversion lines can be also used for a check of the linearity of the HV scale (represented in this measurement campaign by the HV dividers K35 and K65, cf. Sect. 3.2.1). Namely, the L_3 shell of $^{83\text{m}}\text{Kr}$ is very suitable for this kind of check as both the $L_3\text{-9.4}$ and $L_3\text{-32}$ conversion lines can be measured with the MAC-E filter spectrometer with a good statistics. This way the HV scale can be checked on the energy range 7.7–30.5 keV.

In the case of the vacuum-evaporated sources, Eq. 4.5 can be rewritten in the form

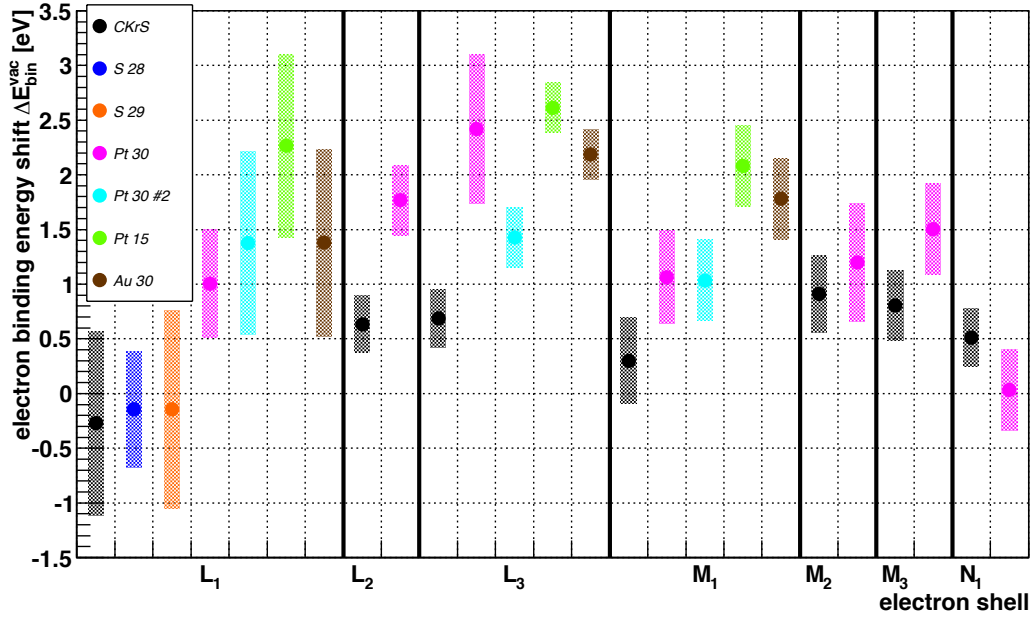
$$E_{\gamma} = \underbrace{E_{\text{kin}}^{\text{evap}}(i) - E_{\text{rec}, \gamma} + E_{\text{rec}, e}(i)}_{= E_{\text{kin, corr}}^{\text{evap}}(i)} + \left(E_{\text{bin}}^{\text{vac}}(\text{gas}, i) - \Delta E_{\text{bin}}^{\text{vac}}(\text{evap}, i) \right) + \Delta\phi, \quad (7.13)$$

where $E_{\text{kin, corr}}^{\text{evap}}(i)$ denotes the absolute kinetic energy corrected for the recoil terms and $\Delta\phi$ has the same meaning as in Sect. 7.3.1. The energy difference of the 9.4 and 32 keV gamma transitions can be then written as

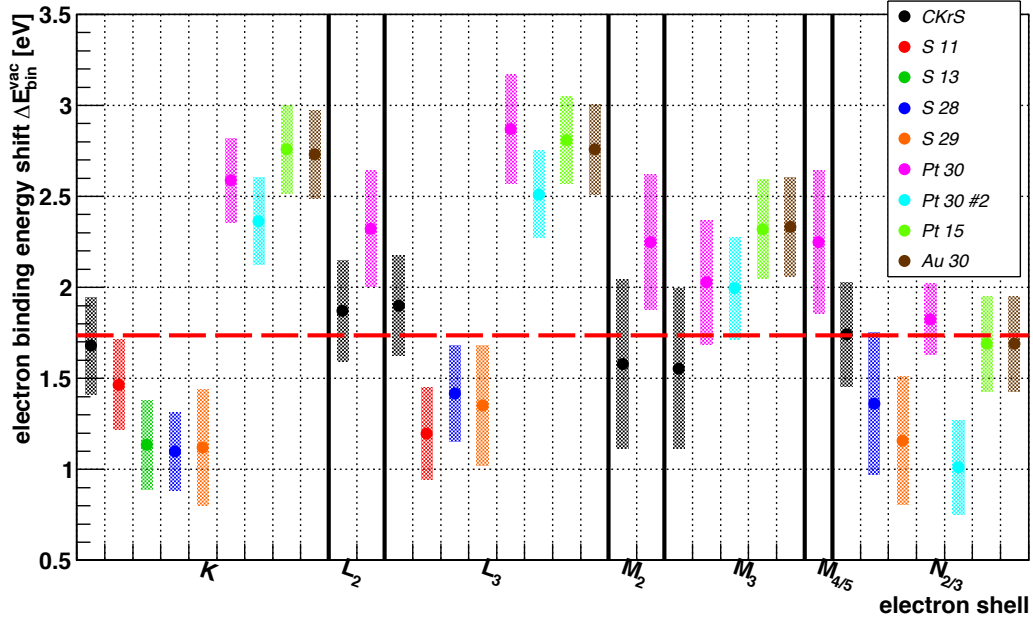
$$E_{\gamma}(32) - E_{\gamma}(9.4) = E_{\text{kin, corr}}^{\text{evap}}(L_3\text{-32}) - E_{\text{kin, corr}}^{\text{evap}}(L_3\text{-9.4}) + \underbrace{\Delta E_{\text{bin}}^{\text{vac}}(\text{evap}, L_3\text{-9.4}) - \Delta E_{\text{bin}}^{\text{vac}}(\text{evap}, L_3\text{-32})}_{\simeq 0}. \quad (7.14)$$

Here the difference of the binding energies cancels out as both lines are populated from the electron shell L_3 ($2p_{3/2}$). The difference of the terms $\Delta\phi$ vanishes as well as it is assumed that the work function ϕ_{source} is identical for the $L_3\text{-9.4}$ and $L_3\text{-32}$ electrons. In addition, the shifts $\Delta E_{\text{bin}}^{\text{vac}}(\text{evap})$ of the electron binding energies are compatible on the level of \simeq

7. Conversion electron spectrum...



(a) 9.4 keV gamma transition



(b) 32 keV gamma transition

Fig. 7.13: The comparison of the electron binding energy shifts for $^{83\text{m}}\text{Kr}$ condensed onto a clean HOPG substrate (CKrS, cf. Sect. 3.3.2), vacuum-evaporated on Al and C substrates and ion-implanted in Pt and Au lattices. For the condensed $^{83\text{m}}\text{Kr}$ the shifts $\Delta E_{\text{bin}}^{\text{vac}}(\text{cond}, i)$ are shown, obtained from the reevaluation of data measured in [Ost08]. The shifts $\Delta E_{\text{bin}}^{\text{vac}}(\text{evap}, i)$ and $\Delta E_{\text{bin}}^{\text{vac}}(\text{impl}, i)$ are shown for the vacuum-evaporated and ion-implanted $^{83}\text{Rb}/^{83\text{m}}\text{Kr}$ sources, respectively. Figure (a) shows the shifts determined on the basis of conversion electrons populated in the 9.4 keV gamma transition of $^{83\text{m}}\text{Kr}$, in figure (b) the analogous shifts are shown for the 32 keV gamma transition. The x axis denotes the individual electron shells i of krypton, the vertical lines separate the individual (sub)shells. The y axis shows the shifts in [eV]. The rectangles mark the uncertainties where the uncertainty of 0.4 and 0.5 eV, respectively, of the $^{83\text{m}}\text{Kr}$ gamma transitions was taken out in order to see possible discrepancies between the sources. The red dashed line in (b) marks the value $\Delta E_{\text{bin}}^{\text{vac}}(\text{cond}) = 1.74(23)$ eV used in [Ost08]. See text for further discussion.

0.3 eV with each other for the cases L_3 -9.4 and L_3 -32 electrons¹¹. Still, this assumption is not perfectly valid in the case of the ion-implanted sources as can be seen in Fig. 7.13. There is a discrepancy of up to $\simeq 1$ eV between the binding energy shifts observed in the 9.4 and 32 keV gamma transitions of $^{83\text{m}}\text{Kr}$. Eq. 7.14 greatly simplifies the calculation and the difference of the gamma transitions energies equals the difference of the kinetic energies of the L_3 -9.4 and L_3 -32 electrons, corrected for the recoil energies. On the other hand, the energies of the $^{83\text{m}}\text{Kr}$ gamma transitions (see Eq. 3.16 and Eq. 3.17) can be subtracted as

$$\Delta E_\gamma(32 - 9.4) := E_\gamma(32) - E_\gamma(9.4) = 32\,151.7(5) - 9\,405.8(4) = 22\,745.90(64) \text{ eV}, \quad (7.15)$$

where the term $\Delta E_\gamma(32 - 9.4)$ is identical (under the aforementioned assumptions) to the energy difference $E_\gamma(32) - E_\gamma(9.4)$ in Eq. 7.14. Similarly, the presented analysis can be done also with the data of the ion-implanted sources. In this case the shifts $\Delta E_{\text{bin}}^{\text{vac}}(\text{impl})$ replace the shifts $\Delta E_{\text{bin}}^{\text{vac}}(\text{evap})$ and all the assumptions are still valid.

As the pairs of the L_3 -9.4 and L_3 -32 spectra were intentionally always measured in a short time period, the changes of the work functions ϕ_{source} and ϕ_{spec} can be neglected. Furthermore, even the shift of the HV scale described above does not represent a problem here as the shift was observed to be constant and here actually only the difference of the HV values plays a role. Both the many-parameters fit routine and the cross-correlation method were (independently) used for the analysis. The results of both methods are summarized in Tab. 7.8.

The use of the many-parameters fit method was straightforward: the absolute kinetic energies of the L_3 -9.4 and L_3 -32 electrons were calculated in the same manner as in Sect. 7.3.1 and Sect. 7.3.2. As discussed above, the spectra of the L_3 -32 line of the ion-implanted sources had to be fitted with a doublet of Voigt peaks. For this analysis only the components of higher kinetic energy were considered. In Tab. 7.8 the results achieved with the many-parameters fit method are denoted as $\Delta E_{\text{kin}}(L_3, \text{m.p.f.}) := E_{\text{kin, corr}}(L_3\text{-}32) - E_{\text{kin, corr}}(L_3\text{-}9.4)$.

The cross-correlation method (see Sect. 5.2.7) does not require any detailed knowledge of the doublet structure of the L_3 -32 lines. The procedure was as follows:

1. A certain spectrum X of the L_3 -32 line was used as the reference spectrum and the group of other L_3 -32 spectra of the same measurement (*i. e.* all the spectra were obtained in the course of several hours) were fitted with the help of the cross-correlation method. The fits resulted in a weighted mean Δ_1 of the shifts of the spectra with respect to the spectrum X . The shift Δ_1 was close to a zero shift.
2. The spectrum X was manually shifted by the fixed value $\Delta_2 \equiv 22\,476.0$ eV in order to match the region of the low energy line L_3 -9.4. This way a spectrum X' was created, with the same shape and statistics as the X spectrum (the count rate values and uncertainties were not altered). This step was necessary as the fit procedure in the cross-correlation method is not capable of comparing two spectra differing by ≈ 22 keV.
3. The group of the L_3 -9.4 spectra was fitted via the cross-correlation method where the X' spectrum was taken as the reference spectrum. This resulted into the weighted

¹¹The shift determined for the L_3 -9.4 line of the vacuum-evaporated source S28 is not stated in Fig. 7.13 as it was not included in the analysis presented in Sect. 7.2 and Sect. 7.3. The reason for that is the fact that this line was measured at the end of the second measurement after the tests of deliberate venting of the vacuum setup were carried out. Thus, due to possible changes of the values ϕ_{spec} and ϕ_{source} this measurement was not considered above. However, for our purpose these data can now be used, see discussion in the text.

Tab. 7.8: The overview of the differences of the kinetic energies of the conversion lines $L_{3-9.4}$ and L_{3-32} .

source	meas. phase	rel. time [day]	$E_{\text{kin}}(L_{3-9.4})$ [eV]	$E_{\text{kin}}(L_{3-32})$ [eV]	$\Delta E_{\text{kin}}(L_{3, \text{m.p.f.}})$ [eV]	$\Delta E_{\text{kin}}(L_{3, \text{c.c.m.}})$ [eV]	"m.p.f. - c.c.m."
S 28	2 nd	127	7 728.27(6)	30 474.61(9)	22 746.18(11)	22 746.29(7)	-0.11(14)
	2 nd	78	7 730.35(13)	30 476.83(11)	22 746.32(17)	22 746.60(18)	-0.28(25)
		127	7 730.37(11)	30 476.92(12)	22 746.39(16)	22 746.47(11)	-0.08(20)
Pt-30	3 rd	23	7 730.81(18)	30 476.54(11)	22 745.58(21)	22 745.53(42)	0.05(47)
		45	7 730.47(15)	30 476.39(13)	22 745.76(20)	22 745.81(7)	-0.05(21)
	mean				22 746.08(43)	22 746.08(71)	0.00(83)
		-2 *	7 729.17(10)	30 475.76(10)	22 746.44(14)	22 746.11(5)	0.33(15)
	3 rd	11	7 729.22(15)	30 476.05(10)	22 746.67(18)	22 746.07(6)	0.60(19)
Pt-30 #2		34	7 729.18(7)	30 475.55(9)	22 746.21(12)	22 746.03(6)	0.19(13)
		44	7 729.23(6)	30 475.60(9)	22 746.21(11)	22 746.04(7)	0.17(13)
	mean				22 746.32(14)	22 746.07(3)	0.25(14)
	3 rd	15	7 730.41(4)	30 476.35(9)	22 745.78(10)	22 745.69(6)	0.10(12)
Pt-15		45	7 730.27(4)	30 476.08(9)	22 745.65(10)	22 745.73(5)	-0.08(12)
	mean				22 745.72(7)	22 745.71(4)	0.01(8)
	3 rd	8	7 729.43(5)	30 475.75(10)	22 746.16(11)	22 745.93(6)	0.23(13)
Au-30		45	7 729.38(7)	30 475.57(9)	22 746.03(11)	22 745.99(7)	0.04(13)
	mean				22 746.09(8)	22 745.96(5)	0.14(9)
mean of all data					22 745.99(28)	22 745.97(37)	0.02(46)
difference [eV] to $\Delta E_{\gamma}(32 - 9.4)$ in Eq. 7.15					0.09(70)	0.07(74)	

The values $E_{\text{kin}}(L_{3-9.4})$ and $E_{\text{kin}}(L_{3-32})$ were obtained with the many-parameters fits. Their difference, corrected for the recoil energies and potential dip in the analyzing plane of the spectrometer, is denoted $\Delta E_{\text{kin}}(L_{3, \text{m.p.f.}})$. The results of the cross-correlation method are marked $\Delta E_{\text{kin}}(L_{3, \text{c.c.m.}})$ and they are also corrected for the recoil and potential dip terms. In addition, they were corrected for the shift of 0.82(1) eV discussed in the text. The last column shows the absolute differences between the results derived with both methods. In the calculation of the weighted means the final uncertainty was multiplied by $\sqrt{\chi^2}$ in order to account for discrepancies between the individual sources. Remark: * the measurement took place before the start of the third phase of the long-term energy stability measurements.

mean Δ_3 . This shift was found to be typically of the order of 0.1 eV.

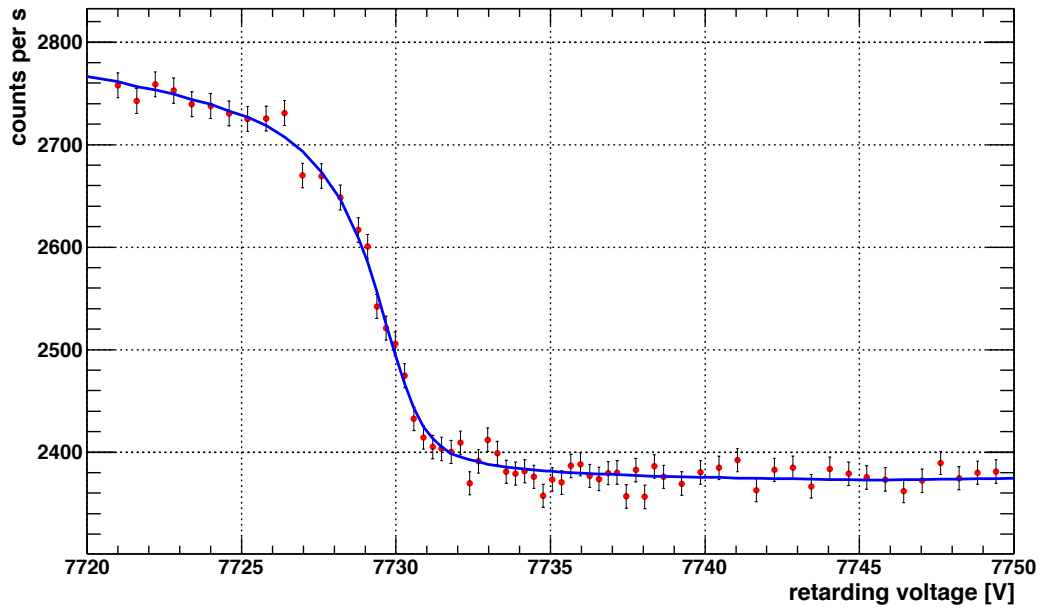
4. Finally, the difference of the kinetic energies of the two groups of spectra was calculated as $\Delta_{\text{fin}} := \Delta_1 + \Delta_2 - \Delta_3$.
5. The value Δ_{fin} was corrected for the difference of the recoil energies as well as for the difference of the terms accounting for the potential dip (see Sect. 7.3.1). The resulting values are denoted $\Delta E_{\text{kin}}(L_3, \text{c.c.m.})$ in Tab. 7.8.

The example of the fit described in step (3) is shown in Fig. 7.14. It may seem inappropriate to attempt at describing the L_3 -9.4 spectrum with the help of the artificially shifted spectrum of the L_3 -32 line. As both the lines are populated in the L_3 shell, their natural line width is equal and reads $\Gamma = 1.19$ eV (see Tab. 3.1). However, the energy resolution of the MAC-E filter spectrometer rises linearly with the kinetic energy of the electrons, cf Eq. 2.13. Thus, in the case of the L_3 -9.4 electrons the width of the transmission function is 0.4 eV which is very narrow compared to the width of 1.6 eV of the transmission function when measuring the L_3 -32 electrons.

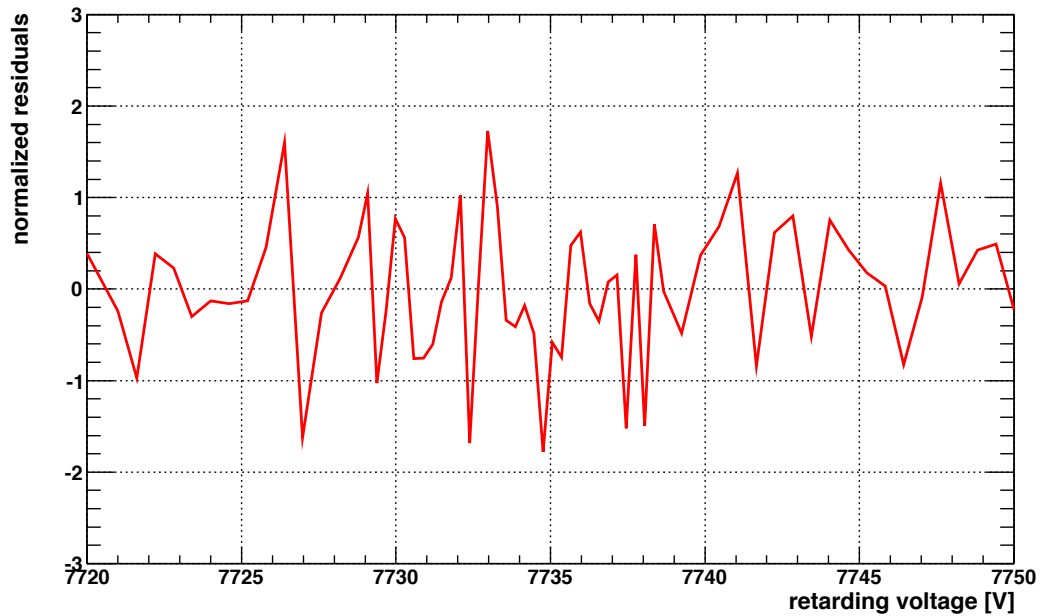
The use of the cross-correlation method for determining the energy difference of these widely spaced lines was also examined on the basis of simulated spectra. The L_3 -9.4 and L_3 -32 spectra were simulated with values typical for the source Pt-30 #2: the line L_3 -9.4 was simulated with the amplitude $A = 850$ counts s^{-1} , the background $B = 4200$ counts s^{-1} and the width $\sigma = 1.3$ eV. The energy was set to $E_0 = 7730$ eV. Similarly, the L_3 -32 was simulated with typical values of $A = 18\,000$ counts s^{-1} , $B = 1\,000$ counts s^{-1} , $\sigma = 0.9$ eV and $E_0 = 30\,476$ eV. Thus, the difference of these “sharp” energies is 22 746 eV which equals Δ_2 . Both lines were simulated as Voigt peaks with the width $\Gamma = 1.19$ eV. Naturally, the corresponding transmission function was used in both cases. Altogether ten spectra of the L_3 -9.4 line were produced (differing slightly in the number of counts due to the randomization) and they were fitted with the help of the reference spectrum—the simulated L_3 -32 spectrum shifted by the value Δ_2 as in steps (2) and (3) above. Thus, in this ideal case of $\Delta_1 \equiv 0$ (single L_3 -32 spectrum) the fits should actually result into $\Delta_{\text{fin}} \simeq \Delta_2$, or in other words, $\Delta_3 \simeq 0$. However, the weighted mean of the fitted shift gave the value $\Delta_3 = +0.82(1)$ eV. This result means that the cross-correlation method underestimates the real difference of the widely spaced spectra: $\Delta_{\text{fin}}(\text{fit}) = \Delta_{\text{fin}}(\text{real}) - 0.82(1)$ eV. Therefore, the differences obtained with the cross-correlation method have to be increased by 0.82(1) eV. The values summarized in Tab. 7.8 are already corrected in the described way. This effect stems probably from different line shapes and different widths of the transmission functions.

In total 13 pairs of the L_3 -9.4 and L_3 -32 spectra (or, more precisely, groups of spectra) were obtained in the course of the second and third measurement phases. A very good agreement was achieved between the results of both methods of the analysis: the weighted means over all data read $\Delta E_{\text{kin}}(L_3, \text{m.p.f.}) = 22\,745.99(28)$ eV and $\Delta E_{\text{kin}}(L_3, \text{c.c.m.}) = 22\,745.97(37)$ eV, respectively. They agree with the value $\Delta E_\gamma(32 - 9.4)$ in Eq. 7.15 on the level of 0.1 eV or better, however, due to the uncertainty of $\Delta E_\gamma(32 - 9.4)$ of 0.64 eV no more precise comparison is possible. Still, the results suggest that all the terms affecting the absolute energy scale on the level of 0.1 eV were recognized and well understood in this work. Actually, this observation contradicts the results summarized in Fig. 7.13 where the discrepancy of $\simeq 1$ eV between the electron binding energy shifts corresponding to the 9.4 and 32 keV gamma transitions was visible. The reason for this is that in the evaluation of the L_3 -9.4 and L_3 -32 kinetic energy difference also other data were used which were not considered for the calculation

7. Conversion electron spectrum...



(a)



(b)

Fig. 7.14: The example of the fit of the L_3 -9.4 spectrum (source Au-30) with the help of the cross-correlation method where the spectrum of the L_3 -32 line was taken as the reference spectrum. The L_3 -32 spectrum was beforehand artificially shifted by 22 746 eV to match the region of interest. Figure (a) shows a typical fit and in figure (b) the normalized residuals are presented. The correctness of this method is discussed in the text.

presented in Fig. 7.13. These measurements suffered from unstable experimental conditions (e. g. the recovery of ϕ_{spec}), however, for the analysis presented in this section they can be used as the pairs of the L_3 -9.4 and L_3 -32 spectra were always measured in a short time period. In addition, the discrepancies between the individual solid $^{83}\text{Rb}/^{83\text{m}}\text{Kr}$ sources are reflected in the results summarized in Tab. 7.8. In [Ost08] not only the difference between the L_3 -9.4 and L_3 -32 kinetic energies was determined, but also the analogous difference of the L_2 -9.4 and L_2 -32 kinetic energies. The values of 22 747.10(12) eV and 22 747.14(12) eV, respectively, were obtained in [Ost08]. The disagreement of $\simeq 1.1$ eV of the results of [Ost08] with the values determined in this work stems from the aforementioned difference of the $^{83\text{m}}\text{Kr}$ 9.4 keV gamma transition energy values.

7.4. Hypotheses for the explanation of the asymmetry and splitting in the $^{83\text{m}}\text{Kr}$ conversion electron spectra of the ion-implanted $^{83}\text{Rb}/^{83\text{m}}\text{Kr}$ sources

It was seen in Sect. 7.2 that the conversion electron spectra of the core shells of the ion-implanted sources exhibited a certain asymmetry on the low kinetic energy side of the elastic peak. It was possible to describe the spectra with a doublet of Voigt peaks with the common natural line width Γ fixed to the recommended value and the common broadening of the width σ which was a free parameter in the fits. The ratio $A_{2/1} = A_2/A_1$ of the amplitudes $A_{1,2}$ of the doublet components was less than unity in all core electron spectra. On the other hand, the valence line $N_{2/3}$ -32 showed a clear splitting E_{1-2} of about 4–5 eV while the doublet components were found to be “reversed”, i. e. $A_{2/1} > 1$. On the basis of the results summarized in Sect. 7.2 and Sect. 7.3, at this point several hypotheses attempting at the explanation of these interesting features will be discussed.

7.4.1. Different environments of the ^{83}Rb atoms

It was discussed in Sect. 4.3.1 that the shifts of the electron binding energies (with respect to the gaseous phase) are characteristic for the atom adsorbed onto surface or implanted into solid. In addition, the shifts are typically higher for the implanted atom than for the adsorbed atom (cf. Eq. 7.12). Thus, a mixture of two different environments of the ^{83}Rb atoms would explain the asymmetry of the $^{83\text{m}}\text{Kr}$ conversion electron lines: the individual components of the doublet would correspond to ^{83}Rb atoms in two environments differing in the electron binding energy.

There are at least two scenarios how the ^{83}Rb ions, accelerated to the implantation energy of 15 or 30 keV, could end up in two chemically different environments directly after bombarding the polycrystalline foils (Pt or Au):

1. As the ion-implantation took place in relatively poor vacuum and no subsequent sputtering of the foils was carried out, there was a certain portion of ^{83}Rb ions which did

not enter the metallic state. Instead, they stopped in the oxide layer covering the foils. On the basis of the simulations performed with the SRIM code (see Sect. 4.2) the portion of the ^{83}Rb atoms in the oxide state was estimated to be 5–10 %.

2. Even after being implanted into the high purity metal foil (99.7 % for the source Pt-30 and 99.99+ % for the other ones) the ^{83}Rb ion can still encounter various processes as *e. g.* diffusion (in both directions into and out of the foil), trapping on impurities or cluster formation. Moreover, the implanted dose Q was determined to lie in the range of $\approx (1-6) \times 10^{14}$ ions cm^{-2} (cf. Tab. 4.2) for all the ion-implanted sources tested in this work. It was discussed in Sect. 4.2.1 that 10^{14} ions cm^{-2} is generally considered as the limit value above which the lattice is damaged after room temperature implantation (cf. Eq. 4.4). This further complicates our situation.

With respect to the aforementioned facts the presence of chemically different environments for the ^{83}Rb atoms cannot be excluded [But11, Vet11]. Furthermore, it is an open question how the metastable $^{83\text{m}}\text{Kr}$ atom behaves during its existence for ≈ 2 h before the conversion electron is emitted.

In the framework of this thesis the attempt was made to investigate the location of the ^{83}Rb atoms in the ion-implanted sources. For this purpose the non-radioactive isotope ^{85}Rb was implanted into gold foils of the same properties as described in Sect. 4.2.3. The implantation was carried out at the radioisotope separator and implanter at the Helmholtz-Institut für Strahlen- und Kernphysik, University of Bonn. The minimal implantation energy was 30 keV as in the case of the implantations at the ISOLDE facility (when omitting the retardation of the ISOLDE ion beam down to 15 keV). The implantation took place at room temperature and the incident angle was zero. In addition, no thermal annealing was carried out after the implantation. Thus, it was anticipated that the non-radioactive samples imitate well the ion-implanted radioactive sources as the main parameters of the implantation process were identical. Altogether three non-radioactive samples were produced with the implanted doses Q of 5×10^{13} , 5×10^{14} and 5×10^{15} atoms cm^{-2} [Nol10]. The advantage of such non-radioactive samples is that they can be investigated by methods of surface physics where the radioactive $^{83}\text{Rb}/^{83\text{m}}\text{Kr}$ sources could possibly contaminate the experimental setup.

The samples were tested at the Physikalisches Institut, University of Münster, with the help of the XPS method. The Al anode was used as the X-ray source, utilizing the $K\alpha$ radiation of the energy 1 486.6 eV. The photoelectrons ejected from the sample were analyzed in the 180° hemispherical energy analyzer PHOIBOS 100 [SPE08] and detected with a single channel electron multiplier detector system. The $K\alpha$ X-ray line was not monochromatized, thus, the instrumental resolution was limited by the natural line width of Al $K\alpha$, $\Delta E = 0.85$ eV (FWHM) [SPE08]. In addition, the transfer lens system was used for defining the analysis area and angular acceptance by imaging the sample onto the entrance slit. Unfortunately, due to misalignment of the sample holder with respect to the energy analyzer the sensitivity of the measurements was degraded by a factor of $\approx 10^2$ [Lin10]. This resulted in the fact that no peaks of Rb were observed in the XPS electron spectra even with the sample of $Q = 5 \times 10^{15}$ atoms cm^{-2} . A brief description of the measurements is given in App. C.

The site location of $^{83\text{m}}\text{Kr}$ implanted into solid was also studied in early works [Kem79, Spi81] with the help of the Mössbauer spectroscopy¹². Here the ^{83}Rb ions were implanted

¹²For an introduction to the Mössbauer spectroscopy the reader is kindly referred to [Gon75] or similar text-

in the group IV semiconductors (diamond, Si, Ge and Sn) and in the cubic metals (Cu, Ag, Au, Mo, W, Al, Ir, Pt and Pb). Obviously, the cases “ $^{83\text{m}}\text{Kr}$ in Au” and “ $^{83\text{m}}\text{Kr}$ in Pt” are the most interesting ones with respect to our study. The parent isotope was identical to our case, *i. e.* the ^{83}Rb ions were implanted. In [Kem79] the sources of doses $(3-6) \times 10^{14}$ ions cm^{-2} were obtained via room temperature implantation at implantation energies of 60–120 keV and rates of 5×10^{11} ions $\text{cm}^{-2} \text{s}^{-1}$. In [Spi81] the implantation energy amounted to 20 keV. In both works the 9.4 keV gamma transition of $^{83\text{m}}\text{Kr}$ was investigated in the so-called transmission geometry of the Mössbauer effect with the source and the absorber cooled down to 4 K. In the former study the case “ $^{83\text{m}}\text{Kr}$ in Au” was investigated. In the “as implanted” sample non-zero isomer shift and line width were observed while the consecutive thermal annealing of the sample (1 h at 300°C and further 1 h at 650°C) reduced the isomer shift to a zero shift, but the line width increased. This was interpreted as vacancy trapping at the impurities, producing a line broadening. In other words, ^{83}Rb was not purely on substitutional sites in the host. In the latter work both cases “ $^{83\text{m}}\text{Kr}$ in Au” and “ $^{83\text{m}}\text{Kr}$ in Pt” were studied. The Mössbauer spectra of both Rb-Pt and Rb-Au samples were fitted with two single lines, and, moreover, a quadrupole interaction was deduced from the analysis of the Rb-Au spectrum. This finding was ascribed to the presence of vacancies near the ^{83}Rb probe.

An asymmetric line shape was reported in [Cit74] (discussed in detail in Sect. 4.3 regarding the shifts of the core level binding energies) for the core level line 1s of neon implanted into copper. The XPS spectrum is illustrated in Fig. 7.15 where the asymmetry on the high binding energy side is clearly visible. The asymmetry was ascribed to creation of small neon gas clusters at rather high doses ($Q \approx 10^{16}$ ions cm^{-2}): a photoionized neon atom in a gas cluster is expected to polarize its immediate environment less efficiently than a single atom surrounded by more mobile metal-conduction electrons [Cit74]. Such reduced screening would produce an apparently higher Ne 1s binding energy as observed in Fig. 7.15.

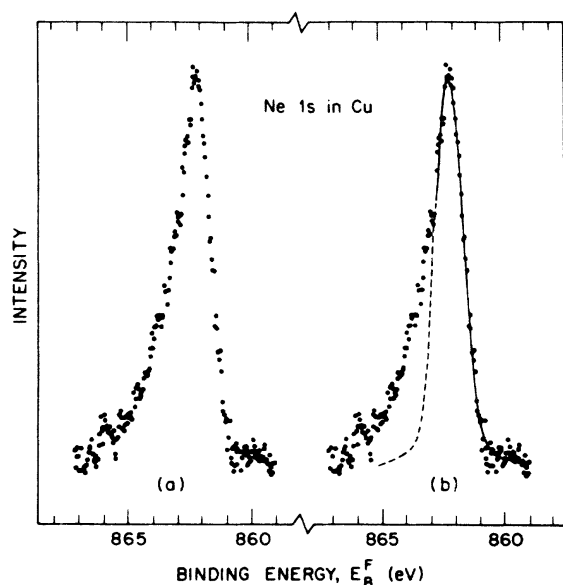


Fig. 7.15: The XPS spectrum of the level 1s of neon implanted into copper. The x axis denotes the binding energy, increasing in the direction right to left. In (a) the raw data is shown, in (b) the least-squares fit of fraction of the curve (denoted by the solid line) emphasizes the high binding energy line asymmetry. The figure is taken from [Cit74].

In sum, various processes are to be expected in the ion-implanted $^{83}\text{Rb}/^{83\text{m}}\text{Kr}$ sources which may lead to the doublet structure of the conversion electron lines. From this point of view it

books.

is desirable to test in the near future the thermal annealing of the sources which could “heal” the lattice and bring the ^{83}Rb atoms immediately into well defined environment. In addition, complementary measurements (with the help of the XPS or other suitable method) would be required for unambiguously clarifying the nature of the effects observed. However, it can be assumed that the valence electrons would be affected in a similar way to the core electrons, *i. e.* the considerable splitting of the $N_{2/3}$ -32 line with the feature $A_{2/1} > 1$ probably does not stem from this effect.

7.4.2. Surface plasmons

Surface plasmon excitations are induced by the electrons moving at the interface between two materials. They are characterized by the so-called surface excitation parameter (SEP), defined as the average number of surface plasmons excited by electrons outside the solid. In our case the surface plasmons could, in principle, be created when the conversion electrons are escaping from the solid source to vacuum. This phenomenon is not included in the Monte Carlo simulations of the inelastically scattered electrons (see Sect. 4.3.3) of the solid $^{83}\text{Rb}/^{83\text{m}}\text{Kr}$ sources. Thus, one may consider this to be the reason for insufficient description of the core level lines with a single peak: neglecting the surface plasmon peak at about 3–6 eV below the elastic peak would result into bad fit of the spectrum with a single peak. This was particularly the case of the ion-implanted sources. The presence of the surface plasmons shall be briefly discussed here.

In [Poll74] a peak corresponding to surface plasmons is recognized in the energy loss electron spectra (XPS method) for a clean surface of aluminum probe in a vacuum of 10^{-11} mbar. However, this peak “disappeared” in the spectrum once the surface oxide was formed. Typically, various studies of the energy loss electron spectra are done with very clean surfaces after *in situ* preparation and sophisticated sputtering techniques, moreover, the cleanliness of the surface is routinely monitored (*e. g.* with the Auger electron spectroscopy). Therefore, the phenomenon of surface plasmons is probably less pronounced or not present at all in our case of the solid sources as they were stored on air and not cleaned once put into vacuum.

In addition, the energy and angular dependency of the SEP was described in [Kwe06] as $P_{\text{SEP}}(\alpha, E) = a / [E^b (\cos \alpha)^c]$ with α denoting the electron crossing angle (solid \rightarrow vacuum) and E being the electron energy. The material-specific parameters a, b, c were determined for Au as $a = 1.8695$, $b = 0.4052$ and $c = 0.80$. Thus, the surface plasmons play a role only at low electron energies and for example in our case of 17.8 keV electrons (K -32 line) they can be neglected in the description of the spectrum.

7.4.3. Electron-hole interaction in metals

In the XPS process, the emission of a core electron from an atom situated in metal is accompanied by a number of excitation processes which are not encountered in the isolated atom (gaseous phase). Once the electron is ejected from the atom, the ion interacts with the surrounding electrons: some of the electrons from the filled conduction band states move to the ion to screen the positive charge and the so-called electron-hole (e-h) pair is produced

[Wer78]. Without going into details, it can be stated that the result of such e-h interactions in metals is the asymmetric line shape of the peaks observed in the XPS spectra. In [Don70] the so-called Doniach-Šunjić shape of the XPS line was theoretically derived in the form

$$DS(E, E_0, \alpha, \gamma) = \frac{\Gamma(1 - \alpha) \cos\left(\pi\frac{\alpha}{2} + (1 - \alpha) \arctan\left(\frac{E - E_0}{\gamma}\right)\right)}{((E - E_0)^2 + \gamma^2)^{(1-\alpha)/2}}, \quad (7.16)$$

where Γ denotes the gamma function, E_0 denotes the peak centroid, γ is the line width (defined so that $\text{FWHM} = 2\gamma$) and α represents the skew parameter. An example of the line shape is shown in Fig. 7.16. Nowadays the Doniach-Šunjić shape is included in many commercial codes for the XPS spectra evaluation, however, due to the ill-defined area (for $\alpha > 0$ the integral $\int_{-\infty}^{\infty} DS(E) dE$ is infinite) its use is complicated when intensities have to be derived.

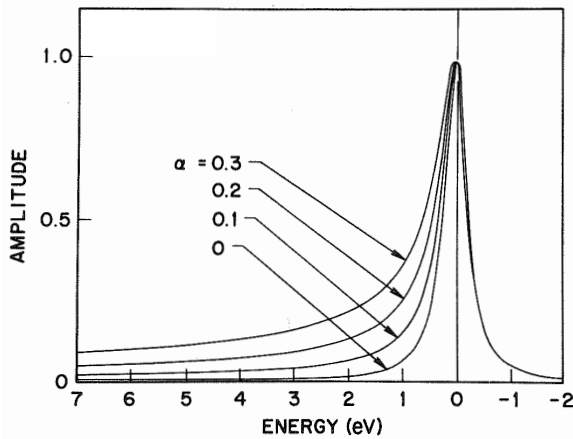


Fig. 7.16: The examples of the Doniach-Šunjić line shape, incorporating the Lorentzian effect of finite lifetime. All the four functions in the plot have the same width ($\text{FWHM} = 2\gamma = 0.5 \text{ eV}$) and they differ in the skew parameter α . The case of $\alpha = 0$ represents a pure Lorentzian shape. The Gaussian broadening is not included in the plot. The figure is taken from [Wer78].

As already discussed in Sect. 4.3.1, in [War91] the correspondence of the electron spectra resulting from the internal conversion and photoionization was verified for the case of gaseous $^{83\text{m}}\text{Kr}$. Thus, in principle, the Doniach-Šunjić shape should be applicable also to our case of $^{83\text{m}}\text{Kr}$ conversion electron spectra of solid sources. However, here the function $DS(E)$ has to be convoluted with the Gaussian broadening and then plugged into Eq. 5.30 instead of the Voigt function V . In the scope of this work such analysis was not carried out but the hypothesis of asymmetric shape of the core level lines seems plausible. On the other hand, an asymmetric line could be sufficiently well fitted with a doublet of Voigt peaks together with the low energy tail of the inelastically scattered electrons.

7.4.4. Strong electric fields in polycrystalline foils

At this point the nature of the splitting of the valence line $N_{2/3-32}$ shall be discussed. It was shown already in Sect. 7.2.2 that from the comparison of the amplitudes of the doublet components it turned out that the high energy component (see 7.7(c)) cannot alone represent the line $N_{2/3-32}$ as its amplitude is too small. Moreover, its absolute energy was found too high to correspond to the internal conversion in $^{83\text{m}}\text{Kr}$. Therefore, the high energy component stems probably from 1) a certain splitting of the N_{3-32} line (level $4p_{3/2}$) or 2) an external

effect in the sense that it does not originate in the $^{83\text{m}}\text{Kr}$ atom. In this section the scenario (1) will be discussed while the option (2) will be discussed further in Sect. 7.4.5.

In this work the ^{83}Rb ions were implanted into polycrystalline foils of gold and platinum, both elements being face-centered cubic (fcc) metals. The consequence of this is the fact that there is no electric field gradient (EFG) for the ^{83}Rb atoms on the substitutional sites [But11, Vet11]. Thus, the splitting of the $4p_{3/2}$ level could be caused only by atoms which are not substitutional. It was mentioned above in Sect. 7.4.1 that in the un-annealed samples a certain portion of ^{83}Rb atoms is indeed not substitutional and various defects can influence the ^{83}Rb atoms as well. Therefore, EFGs are generally expected in the ion-implanted sources.

The metastable state of $^{83\text{m}}\text{Kr}$ (energy of 41.5 keV, see Fig. 3.8 in Sect. 3.3.2) has the nuclear spin of $\frac{1}{2}^-$, hence there is no quadrupole interaction. However, the 9.4 keV state has the spin of $\frac{7}{2}^+$ and is sufficiently long-lived (half-life of 147 ns) to give rise to quadrupole interactions, as does the ground state with the spin of $\frac{9}{2}^+$. The quadrupole moment of the ground state is $Q = 0.25$ eb (electron-barn, $1 \text{ b} = 10^{-28} \text{ m}^2$), thus, quadrupole splittings in un-annealed samples are to be expected [But11]. Further study of such effects would be possible with the method of time differential perturbed angular correlations (TDPAC).

The quadrupole splitting ΔE_Q can be described via [Gon75]

$$\Delta E_Q \simeq \frac{1}{2} e Q V_{zz}, \quad (7.17)$$

where Q denotes the quadrupole moment and $V_{zz} = \partial^2 V / \partial z^2$ is the principal component of the diagonalized EFG tensor. From the aforementioned value of Q one can estimate the EFG necessary for causing the splitting ΔE_{1-2} of about 5 eV as $V/z \approx 6 \times 10^{14} \text{ V m}^{-1}$. The quadrupole splitting takes place only in the $4p_{3/2}$ level (N_3 -32 line) but not in the $4p_{1/2}$ level (N_2 -32 line). Therefore, altogether three lines should be present in the spectrum: $\ell_1 \equiv N_2$, $\ell_2 \equiv N_3(\text{a})$ and $\ell_3 \equiv N_3(\text{b})$. However, due to the width of 1.7 eV of the transmission function at 32.1 keV two of the peaks could merge to give the final doublet structure observed in our spectra. The ratio of the intensities of the N_2 and N_3 -32 lines reads (Tab. 3.1)

$$I_{N_2-32/N_3-32} := \frac{I(N_2-32)}{I(N_3-32)} = \frac{0.27\%}{0.41\%} \simeq 0.66, \quad (7.18)$$

thus, the stronger line N_3 -32 splits into two lines ℓ_2 and ℓ_3 which are equal in intensity. Though, the decomposition of the $N_{2/3}$ -32 spectra summarized in Tab. 7.2 and Tab. 7.3 does not correspond to this scenario as the ratio $A_{2/1}$ was determined to lie in the range of 4.8–7.7.

7.4.5. Internal conversion at neighboring atoms

Another hypothesis which could explain the observation of the high energy component of the $N_{2/3}$ -32 line in the spectra of the ion-implanted sources involves the internal conversion on Pt or Au atoms surrounding the $^{83\text{m}}\text{Kr}$ atom. Such effect would be analogous to the prompt excitation of neighbor atoms of the tritium molecule T_2 condensed onto cooled substrate by a β -decaying tritium atom. This phenomenon was recognized in the framework of the Mainz Neutrino Mass Experiment [Kol88, Kra05].

In our case the conversion of the 32 keV gamma transition of $^{83\text{m}}\text{Kr}$ could possibly took place on the valence electrons of Pt or Au surrounding the $^{83\text{m}}\text{Kr}$ atom. The relevant electron shells are the valence $O_{4/5}$ levels. Their binding energies, related to the Fermi level, read [Fir96]

$$E_{\text{bin}}^{\text{Fermi}}(\text{Pt}, O_{4/5}) = 2.1(5) \text{ eV} \Leftrightarrow E_{\text{bin}}^{\text{vac}}(\text{Pt}, O_{4/5}) = 7.8(5) \text{ eV} \quad (7.19)$$

and

$$E_{\text{bin}}^{\text{Fermi}}(\text{Au}, O_{4/5}) = 2.5(13) \text{ eV} \Leftrightarrow E_{\text{bin}}^{\text{vac}}(\text{Au}, O_{4/5}) = 7.6(13) \text{ eV}, \quad (7.20)$$

where the work functions of Pt and Au (see Tab. 4.3) were used for referencing the binding energies to the vacuum level. Thus, using the energy of the 32 keV gamma transition from Eq. 3.16 one arrives at the absolute kinetic energies

$$E_{\text{kin}}(\text{Pt}, \text{conv. on } O_{4/5}) = 32\,143.3(7) \text{ eV} \quad (7.21)$$

and

$$E_{\text{kin}}(\text{Au}, \text{conv. on } O_{4/5}) = 32\,143.4(14) \text{ eV}. \quad (7.22)$$

The values in Eq. 7.21 and Eq. 7.22 were already corrected for the potential dip of -0.675 eV (see Eq. 5.9) in the analyzing plane of the spectrometer. Besides this spectrometer-related correction no other correction (recoil energies) is necessary as the values stated in Tab. 7.7 were neither corrected for recoil. The weighted mean of the absolute kinetic energies of the high energy component of the $N_{2/3}$ -32 line of the Pt-based sources¹³ reads $32\,145.18(22) \text{ eV}$ (the uncertainty was multiplied by $\sqrt{\chi_r^2}$ due to $\chi_r^2 = 3.4$) which is by $1.9(7) \text{ eV}$ higher than $E_{\text{kin}}(\text{Pt}, \text{conv. on } O_{4/5})$. For the source Au-30 the measured absolute kinetic energy of the high energy component amounts to $32\,143.97(12) \text{ eV}$. This value is in a good agreement with $E_{\text{kin}}(\text{Au}, \text{conv. on } O_{4/5})$ as the difference of $0.5(14) \text{ eV}$ is compatible with zero.

Unfortunately, higher precision of such comparison is hindered by the uncertainties of the binding energy values. Nevertheless, the hypothesis is capable to explain the doublet structure of the $N_{2/3}$ -32 lines. It seems desirable to theoretically estimate the densities of the $O_{4/5}$ electrons in the close vicinity of the $^{83\text{m}}\text{Kr}$ atom in polycrystalline gold and platinum. Theoretical calculations of $^{83\text{m}}\text{Kr}$ $N_{2/3}$ -32 and $O_{4/5}$ Pt or Au electron densities in a close vicinity of the $^{83\text{m}}\text{Kr}$ nuclei would be valuable. From such densities the relevant conversion coefficients could be established the ratio of which should equal to the ratio of the intensities of the electron lines in question. Moreover, it would be interesting to verify this hypothesis with another systems, *e. g.* ^{83}Rb implanted into iridium which is also a fcc metal. Here the $O_{4/5}$ binding energy amounts to $3.8(4) \text{ eV}$ which should shift the high energy component of the $N_{2/3}$ -32 line towards lower values and the splitting ΔE_{1-2} should decrease correspondingly. Besides the effect of internal conversion of $^{83\text{m}}\text{Kr}$ at neighboring atoms one could also speculate about the shake-up / off effects of neighboring atoms. In this case the internal conversion would take place in the $^{83\text{m}}\text{Kr}$ atom and the ejected electron would then induce shaking effects in the electron configuration of a neighboring atom. However, such an effect would lead to a certain loss of energy of the "original" conversion electron, but in our case the high energy component of the $N_{2/3}$ -32 line doublet possesses *higher* energy than what is expected in the case of $^{83\text{m}}\text{Kr}$ implanted in Au or Pt lattice. Therefore, such an effect does not seem to explain our observation.

¹³In the case of the source Pt-30 only the value obtained in the third measurement phase was used for this calculation.

7.5. Electron energy loss spectra of the solid sources

In this section the electron energy loss spectra of the solid $^{83}\text{Rb}/^{83\text{m}}\text{Kr}$ sources will be briefly discussed. The spectra, depicted in Fig. 7.17, were obtained with the spectrometer resolution set to 2.0 eV at 17.8 keV and show the region of about 200 eV “below” the elastic peak of the K -32 line, *i. e.* its low energy tail. The integral spectra were scaled so that the amplitude of the elastic peak equals to unity. The spectrum obtained with the $^{83\text{m}}\text{Kr}$ condensed onto clean HOPG substrate [Ost08] is also shown for comparison. Clearly, both types of the solid source, vacuum-evaporated as well as ion-implanted sources, suffer from considerable losses of the zero-energy-loss electrons (useful for the monitoring of the energy scale stability) due to the inelastically scattered electrons. The electron signal on the low energy side of the elastic peak is influenced by the following effects:

1. inelastically scattered electrons, often denoted “loss electrons”,
2. shake-up/off electrons,
3. background stemming from conversion lines of higher energy, and
4. losses of the transmission function due to high surplus energies.

The effect of item (1) was described in this work with the help of the Monte Carlo simulations described in Sect. 4.3.3. The shake-up/off electrons (2) were not included in these simulations. The background (3) caused mainly by the lines L_2 and L_3 -32 can be approximated by a constant B_0 . The behavior of the transmission function at high surplus energies (4) was studied in detail in [Thu07] and the results of the simulation carried out therein (see Fig. 5.20) were used in this work. It can be seen in Fig. 5.20 that the transmission function losses are much less pronounced when the spectrometer resolution is “worsen”. This is the reason for measuring the spectra discussed here at the resolution of 2.0 eV instead of the settings of resolution of 0.9 eV at 17.8 keV which was routinely used for the long-term measurements of the energy stability of the conversion lines (see Chap. 6).

A simple estimation of the portion of the zero-energy-loss electrons with respect to all the electrons emitted from the given source can be done on the basis of Fig. 7.17: the amplitude A_{elast} of the elastic peak is compared to the total amplitude A_{tot} of the integral spectrum. Then the ratio $\zeta := A_{\text{elast}}/A_{\text{tot}}$ represents the portion of electrons emitted from the given source without energy losses. Correcting this ratio for the losses of the transmission function by the factor of 0.9 (cf. Fig. 5.20) results in $\zeta(\text{CKrS}) \simeq 0.85$, $\zeta(\text{S 28}) \simeq 0.44$, $\zeta(\text{Pt-30}) \simeq \zeta(\text{Pt-30 \#2}) \simeq 0.35$, $\zeta(\text{Pt-15}) \simeq 0.41$ and $\zeta(\text{Au-30}) \simeq 0.29$. Thus, as expected the CKrS source is superior to the solid sources regarding the portion of useful electrons. The vacuum-evaporated source S 28 already suffers from the considerable portion of inelastically scattered electrons due to the oxide layer. From this point of view the best source out of the ion-implanted sources is Pt-15 where the simulated distribution of the ^{83}Rb atoms implanted into the polycrystalline foil peaks at $R_p(\text{Pt-15}) = 61 \text{ \AA}$ (see Fig. 4.14 in Sect. 4.2.3). The scaled spectra of the sources Pt-30 and Pt-30 #2 were found in a good agreement which is to be expected as in both cases the implantation energy amounted to 30 keV (the distribution of simulated ranges peaks at $R_p(\text{Pt-30}) = 89 \text{ \AA}$). A slight discrepancy between the scaled spectra could point to differences in the foils used for implantation (99.7 % and 99.99+ %) or to differences in the implanted dose which may affect the lattice damage. The source Au-30 suffers from highest losses of the zero-energy-loss electrons, this also comes by no surprise

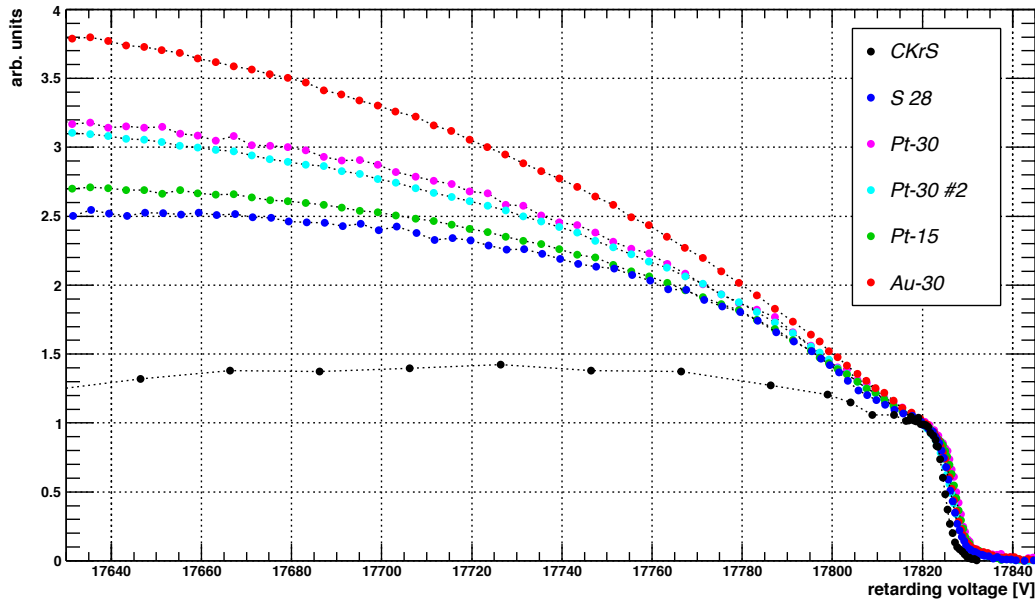


Fig. 7.17: The comparison of the integral electron spectra covering the range of the K -32 line with its low energy tail down to ≈ 200 eV below the elastic peak. The x axis denotes the retarding voltage applied to the spectrometer electrode. The y axis denoting the count rate was scaled so that the amplitude of the elastic peak amounts to unity. The error bars were omitted in the plot. Without any low energy tail of the elastic peak the spectrum would ideally equal to unity over the whole range. However, the effects discussed on page 260 give rise to the structure consisting of shake-up/off and inelastically scattered electrons. In addition, the effect of the transmission losses at high surplus energies plays a role here. The data of the CKrS (^{83m}Kr on clean HOPG substrate) were taken from [Ost08] for comparison.

as $R_p(\text{Au-30}) = 96 \text{ \AA}$.

A more sophisticated analysis of the electron energy loss spectra was carried out in the following way. The aforementioned effects (1) and (4) were considered as known thanks to the results of the simulations and the effect (3) was taken into account as a constant background B_0 . Thus, the only item “missing” in the description of the low energy tail of the elastic peak is the effect (2) of the shake-up/off electrons. The many-parameters fit routine, described in Sect. 5.2.6, was enhanced to incorporate altogether five Voigt peaks: two peaks $S'_{1,2}$ were used for the elastic peak of the K -32 line (where the line shape asymmetry was observed in the spectra of the ion-implanted sources, see Sect. 7.2.2) and three peaks $S_{1,2,3}$ were used to describe the shake-up/off electrons—in Sect. 4.3.2 it was stated that similar spectra obtained with ^{83m}Kr condensed onto clean copper substrate [Pic92b] were successfully described with three peaks attributed to the shake-up/off peaks. In the presented analysis the Lorentzian width of $S'_{1,2}$ was fixed to $\Gamma = 2.7$ eV and the Gaussian broadening σ was a free parameter common for both peaks. For the sake of simplicity the peaks $S_{1,2,3}$ were considered to have a pure Lorentzian shape. This way the total number of free parameters was reduced and as the large widths Γ were expected, the difference between the Voigt and Lorentzian line shape was not significant. It was discussed in Sect. 5.2.6 that in other works of high resolution conversion electron spectroscopy (*e.g.* [Pet93]) the shake-up/off peaks were well described with the function consisting of complementary error function combined with an exponential decay (see Eq. 5.35). However, as the individual shake-up/off

peaks are usually “merged” into complicated structure, the description with three Lorentzian peaks seems sufficient. Also with respect to the accuracy of the individual simulated spectra (inelastically scattered electrons and transmission function losses), which were used as the total response function R' (see Eq. 5.30), this approach seems appropriate.

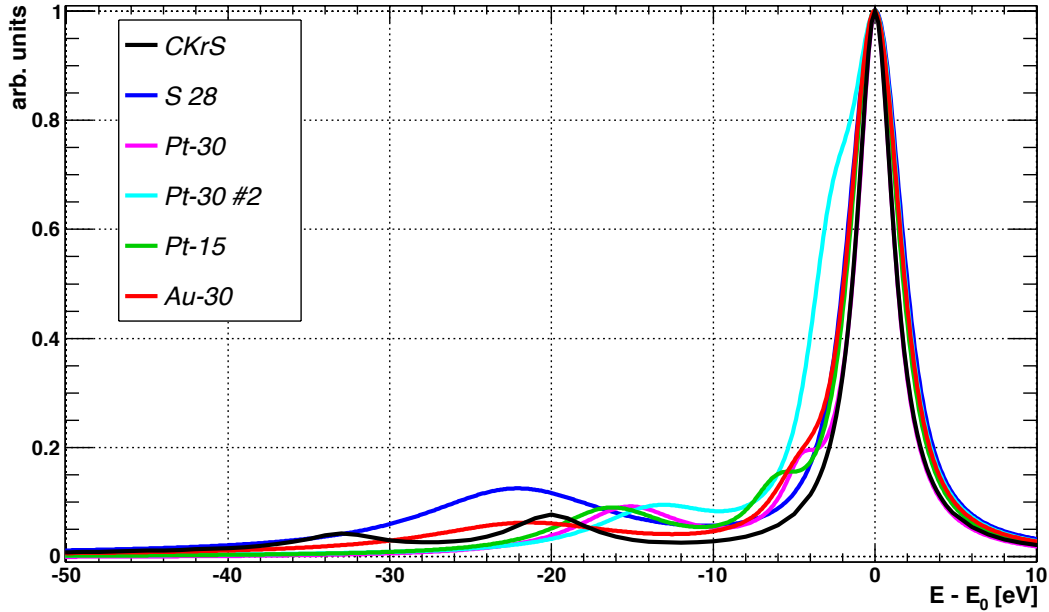


Fig. 7.18: The results of the least-squares fits of the shake-up/off peaks in the electron energy loss spectra depicted in Fig. 7.17. The x axis denotes the electron energy taken relative to the centroid energy E_0 of the elastic peak of the K -32 line. The y axis is scaled to unity in the point $E = E_0$. Only the energy interval of 50 eV below the elastic peak is shown as due to the large widths Γ the peaks are very small compared to the elastic peak amplitude. The spectrum of CKrS is taken from [Pic92b] where $^{83\text{m}}\text{Kr}$ was condensed onto clean copper substrate, thus, strictly speaking, it is not directly comparable with the integral spectrum of the CKrS shown in Fig. 7.17. The asymmetry of the K -32 line on its low energy side is clearly visible in the spectra of the ion-implanted sources, mostly in the Pt-30 #2 spectrum (light blue).

The results (de-convoluted line shapes) are shown in Fig. 7.18. The three peaks S_i , $i = 1, 2, 3$, were described with the help of the energy differences $\Delta E_i := E_0(S'_1) - E_0(S_i)$ and the amplitude ratios $A_i := A(S_i) / A(S'_1)$ with respect to the corresponding parameters of the elastic peak. All the Pt-based sources exhibited very similar results regarding the position of the peaks, $\Delta E_1 \simeq 15$ eV, $\Delta E_2 \simeq 31$ eV and $\Delta E_3 \simeq 67$ eV. The parameters of the peak S_1 closest to the elastic peak were determined as $\Gamma_1 \simeq 8.5$ eV and $A_1 \simeq 0.23$ for all the Pt-based sources while the values Γ_2 and A_2 were found in wide ranges of 7–17 eV and 0.18–0.41, respectively. Similarly, $\Gamma_3 = 37$ –48 eV and $A_3 = 0.38$ –0.47. The amplitudes A_i of the three peaks are the highest in the case of the source Au-30, however, the widths Γ_i are also larger here. In detail, S_1 : $A_1 \simeq 0.29$, $\Gamma_1 \simeq 15$ eV, S_2 : $A_2 \simeq 0.50$, $\Gamma_2 \simeq 26$ eV and S_3 : $A_3 \simeq 0.61$, $\Gamma_3 \simeq 42$ eV. In addition, the peaks were slightly shifted towards lower energies, *i. e.* $\Delta E_1 \simeq 20$ eV, $\Delta E_2 \simeq 45$ eV and $\Delta E_3 \simeq 76$ eV, respectively. The spectrum of the source S28 was fitted with the peaks of the following parameters, S_1 : $\Delta E_1 \simeq 22$ eV, $A_1 \simeq 0.52$, $\Gamma_1 \simeq 15$ eV, S_2 : $\Delta E_2 \simeq 46$ eV, $A_2 \simeq 0.36$, $\Gamma_2 \simeq 20$ eV, and S_3 : $\Delta E_3 \simeq 79$ eV, $A_3 \simeq 0.49$, $\Gamma_3 \simeq 35$ eV.

In [Pic92b] the width of the first two peaks amounted to $\Gamma_1 = \Gamma_2 = 5.8$ eV, thus, the shake-up/off peaks are considerable wider in the spectra of the solid $^{83}\text{Rb}/^{83\text{m}}\text{Kr}$ sources. On the

other hand, the intensities of the shake-up/off peaks are higher for $^{83\text{m}}\text{Kr}$ in solid phase as in [Pic92b] the intensities amounted to $A_1 + A_2 = 0.18$ in a good agreement with calculations based on the sudden approximation [Car73]. Unfortunately, no theoretical predictions or measurements of the shake-up/off probabilities and energies are available in the literature for $^{83\text{m}}\text{Kr}$ implanted in metal, therefore no detailed comparison of the obtained parameters is possible. Moreover, the accuracy of the presented results is limited by the simulations of the aforementioned effects involved. Thus, in other words, the fitted peaks may also account for some effects of energy losses of the emitted conversion electrons which were not taken into account in the simulations.

8. Conclusions and outlook

Since W. Pauli's postulation in 1930 the neutrino has been one of the most interesting elementary particles and this is valid even nowadays: the absolute scale of neutrino masses is still unknown and it is pointing towards new physics beyond the Standard Model. Thanks to large efforts of both experimental and theoretical physicists it is clear that the neutrinos are massive and oscillate in the sense that the flavor state, undergoing weak interaction processes, is a linear superposition of the mass eigenstates via the so-called Pontecorvo-Maki-Nakagawa-Sakata mixing matrix. The absolute neutrino mass scale can be directly investigated on the basis of precise study of the kinematics of weak decays. In contrast to other methods, such as the search for neutrinoless double β -decay or cosmological neutrino mass studies using large scale structures and cosmic microwave background radiation data, the direct kinematic method provides a completely model-independent measurement of the neutrino mass, based only on kinematic relations and energy-momentum conservation. The β -decay of tritium with the endpoint energy of $Q = 18.6$ keV is of particular interest: even a very small non-zero neutrino mass will modify the β -spectrum in its endpoint region which can be precisely studied with the methods of high-resolution electron spectroscopy.

The Karlsruhe TRitium Neutrino (KATRIN) experiment [KAT04], presently being set up at Karlsruhe Institute of Technology, represents a next-generation tritium β -decay experiment designed to perform a high precision direct measurement of the electron antineutrino mass $m(\nu_e)$ with the sensitivity of $0.2 \text{ eV } c^{-2}$ (90 % C.L.). KATRIN is the successor experiment of the neutrino mass experiments carried out in Mainz (Germany) and Troitsk (Russia), which set the upper limit of $m(\nu_e) < 2 \text{ eV } c^{-2}$ [PDG10]. Therefore, the aim of the KATRIN experiment represents the improvement of the neutrino mass sensitivity by one order of magnitude. Such an improvement causes numerous experimental challenges, including, among others, a windowless gaseous tritium source of high luminosity, a very large main spectrometer (length of 23 m and diameter of 10 m) achieving an energy resolution of 0.93 eV at electron energies around the tritium endpoint, and very low background. For the latter purpose two successive electrostatic retardation filters with the magnetic adiabatic collimation (called "MAC-E filters") will be used, where a smaller pre-spectrometer eliminates the bulk part of the low energy β -electrons, carrying no information on the neutrino mass.

The stability of the energy scale of the KATRIN spectrometers is one of the main systematic effects: the principle of the MAC-E filter technique relies on the precise knowledge of the retarding potential which is experienced by the β -electrons on their path through the spectrometer. Therefore, the challenge of knowing the electric retarding potential precisely enough in every moment during the measurement is inevitable in the KATRIN experiment. Besides the use of the state-of-the-art equipment for a direct measurement of the high voltage, including specially developed precision high voltage dividers, a method based

on atomic/nuclear standards will be utilized in KATRIN. Namely, a very stable calibration electron source will be continuously measured by an additional MAC-E filter spectrometer (“monitor spectrometer”) to which the high voltage will be applied, corresponding at the same time to the filtering potential of KATRIN. This way a two-fold monitoring system will be formed.

The objective of this work was the test of feasibility of solid electron source based on the metastable isotope krypton-83m ($^{83\text{m}}\text{Kr}$, $t_{1/2} = 1.83$ h). This type of source is intended for use at the monitor spectrometer for continuous monitoring of the stability of KATRIN energy scale. The process of internal conversion of $^{83\text{m}}\text{Kr}$ is utilized in such source, where $^{83\text{m}}\text{Kr}$ is continuously generated by rubidium-83 (^{83}Rb , $t_{1/2} \simeq 86$ d). The K-32 conversion electron line of the kinetic energy $E = 17.8$ keV and the width $\Gamma = 2.7$ eV is particularly suitable for the purpose of energy scale monitoring as its energy is only by 0.8 keV lower than the tritium endpoint energy.

In the course of this dissertation project altogether eight samples of the solid $^{83}\text{Rb}/^{83\text{m}}\text{Kr}$ sources, produced by two different techniques of vacuum evaporation and ion implantation, were investigated with the help of the former Mainz MAC-E filter spectrometer. The possible instability of the energy scale of the β -spectrometers was identified as one of the six main systematic uncertainties of the KATRIN experiment. The importance of continuous monitoring of the energy scale stability and of absolute calibration of the energy scale was discussed in detail. It was shown that the monitoring task of KATRIN demands the energy stability $\Delta E/E$ of the K-32 line of ± 1.6 ppm per month. The two-fold concept of monitoring of the KATRIN energy scale was presented together with a discussion of feasibility of possible candidates for monoenergetic electron sources, based on atomic/nuclear standards. In the KATRIN experiment the $^{83\text{m}}\text{Kr}$ source will be utilized in three different forms: as a gas, as a condensed source and as a solid source. Two production techniques of the $^{83}\text{Rb}/^{83\text{m}}\text{Kr}$ solid sources were described and the actual samples, investigated in this work, were presented. The vacuum-evaporated sources were produced at the Nuclear Physics Institute Řež/Prague, while the ion-implanted sources were obtained at the ISOLDE facility, CERN. The experimental setup of Mainz MAC-E filter spectrometer, used in this work for long-term measurements of energy stability of the $^{83\text{m}}\text{Kr}$ conversion lines of the solid $^{83}\text{Rb}/^{83\text{m}}\text{Kr}$ sources, was reviewed and the analysis of the collected data was described. Altogether four measurement phases of the long-term energy stability measurements were carried out at Mainz MAC-E filter. Finally, the shapes and the absolute kinetic energies of the various conversion lines of the solid $^{83}\text{Rb}/^{83\text{m}}\text{Kr}$ sources were investigated.

At this point the results presented in the individual chapters of this work will be summarized, together with the outlook on the future production and use of the solid $^{83}\text{Rb}/^{83\text{m}}\text{Kr}$ sources in the KATRIN experiment.

Results obtained with the solid $^{83}\text{Rb}/^{83\text{m}}\text{Kr}$ sources

The most important results achieved in this work can be summarized as follows:

- The long-term stability of the kinetic energy of the conversion electrons was quantified in this work with the notion of the relative linear drift $d_{\text{source}}^{\text{rel}}$ [ppm month⁻¹] of the given conversion line of the given source. Four vacuum-evaporated and four

ion-implanted $^{83}\text{Rb}/^{83\text{m}}\text{Kr}$ sources were investigated in the course of the measurements at Mainz MAC-E filter. The stability of the electrical devices used in this work, namely the high precision HV divider, the HV power supply and the digital voltmeter, allowed to extract the intrinsic drifts $d_{\text{source}}^{\text{rel}}$ from the data. The stability of the spectrometer work function ϕ_{spec} turned out to be one of the key factors affecting the measurements. Unfortunately, the setup used in this work did not allow to monitor the stability of ϕ_{spec} in some way. The only means of controlling (minimizing) the drift of ϕ_{spec} was a thorough bake-out procedure performed at the beginning of a given measurement phase. The best results were achieved in the final measurement phase when the ion-implanted sources Pt-30, Pt-30 #2, Pt-15 and Au-30 were investigated. The designation Pt-30 means that the ^{83}Rb ions were implanted at the energy of 30 keV into polycrystalline platinum foil, cf. Sect. 4.2.3. In the time period of 26 days the drifts of the K-32 conversion line were determined as

$$d_{\text{source}}^{\text{rel}}(\text{Pt-30}) = -0.27 \pm 0.32_{\text{stat}} \pm 0.64_{\text{syst}} \text{ ppm month}^{-1}, \quad (8.1)$$

$$d_{\text{source}}^{\text{rel}}(\text{Pt-30 \#2}) = 0.63 \pm 0.18_{\text{stat}} \pm 0.64_{\text{syst}} \text{ ppm month}^{-1}, \quad (8.2)$$

$$d_{\text{source}}^{\text{rel}}(\text{Pt-15}) = 0.23 \pm 0.14_{\text{stat}} \pm 0.64_{\text{syst}} \text{ ppm month}^{-1}, \quad (8.3)$$

$$d_{\text{source}}^{\text{rel}}(\text{Au-30}) = 2.39 \pm 0.19_{\text{stat}} \pm 0.64_{\text{syst}} \text{ ppm month}^{-1}. \quad (8.4)$$

In this time period the stability of ϕ_{spec} can be safely assumed and the observed drifts can be ascribed to the solid state effects in the sources affecting the electron binding energy. The systematic uncertainty of $0.64 \text{ ppm month}^{-1}$ was determined on the basis of safe estimates of various effects, cf. Sect. 6.5.2. All the three Pt-based sources fulfilled the stringent demand of $\pm 1.6 \text{ ppm per month}$ on the energy stability $\Delta E/E$ set by the KATRIN project. The source Au-30 exhibited non-zero drift and one can speculate about the reason for such a relatively high drift: due to the well focused ion beam the implanted dose of ^{83}Rb might be too high and serious damage of the lattice could occur. However, the same holds for the source Pt-30 #2 where the drifts was low. This may reflect the differences between the elements of gold and platinum.

- The ion-implanted sources were found to be superior to the vacuum-evaporated ones concerning the resistibility of the conversion line energies to vacuum conditions. Several vacuum breakdowns occurred during the measurement campaign which caused severe temporal worsening of the vacuum from 10^{-10} mbar up to 10^{-5} mbar. In general, these vacuum breakdowns resulted in negative shifts of the measured kinetic energies. Thanks to the tests of deliberate venting of the source section separated from the spectrometer vessel it was found that the shift of ϕ_{spec} is responsible for the observed shift of conversion lines energies. Still, a non-zero shift of the order of tens of meV was found to stem from the vacuum-evaporated sources where the ^{83}Rb atoms are adsorbed in the oxide layer. On the other hand, the ion-implanted sources exhibited no shift of the conversion line energy even after exposure to air. This feature was reproducibly tested with the precision of 4 meV.
- The analysis of the full set of data of the four ion-implanted sources allowed to describe sufficiently well the long-term measurements of the K-32 line of these sources over the time period of 46 days, including the accident of vacuum breakdown. An exponential recovery of ϕ_{spec} was assumed in the time period after the vacuum breakdown and the sources were assumed to be resistive against vacuum conditions, *i.e.* the linear

8. Conclusions and outlook

drift of a given source was considered on the full range of 46 days. The full data set was least-squares fitted with altogether 10 free parameters (four pairs of parameters describing the linear drifts of the K -32 lines plus two parameters describing the shift of ϕ_{spec} and its subsequent exponential recovery, common for all the sources) delivered results compatible with the aforementioned drifts.

- It is worth mentioning that the source Pt-30 exhibited the aforementioned drift, compatible with a zero drift, after almost 9 months since its production at the ISOLDE facility. In this sense such solid $^{83}\text{Rb}/^{83\text{m}}\text{Kr}$ source is indeed very well suited for the long-term application in the KATRIN experiment.
- The electron count rate recorded in the K -32 line amounted up to $\approx 10^4$ counts s^{-1} in the case of the source Pt-30 #2. Therefore, the concept of dead time correction utilized in this work was an important part of the data treatment procedure. The amplitudes of the conversion lines generally followed the radioactive decay of ^{83}Rb with the half-life of $t_{1/2} = 86.2$ d, however, occasionally significant deviations from this trend were caused due to the misalignment of the source with respect to the spectrometer axis. Analysis of data revealed that the fitted half-life was actually lower than the literature value of 86.2 d, however, here it should be noted only the electrons emitted from the sources without any energy loss were taken into account this way. The lower than expected half-life can point towards the fact that ^{83}Rb diffusion processes take place in the sources. In addition, it can not be excluded that $^{83\text{m}}\text{Kr}$ retention of the sources changes in time.
- The shapes of the conversion lines were studied in detail. The spectra obtained with the vacuum-evaporated sources could be well described with a single Voigt peak where the half-life width Γ (Lorentzian component) was fixed to values recommended in [Cam01] while the broadening σ (Gaussian component) was a free parameter. The width σ was found of the order of 1 eV which was caused by the combination of Doppler broadening (thermal motion of $^{83\text{m}}\text{Kr}$ atoms), noise of the HV and solid state effects. On the other hand, the spectra of the ion-implanted sources could not be well described with a single peak and the description by a doublet of Voigt peaks had to be introduced. The conversion lines of the core shells exhibited a clear asymmetry on the low energy side which was quantified by the amplitude $A_{2/1}$ relative to the amplitude A_1 of the main component of the doublet and the energy splitting ΔE_{1-2} between these components. Both $A_{2/1}$ and ΔE_{1-2} were found to be strongly line- and source-specific, the typical values were $A_{2/1} = 0.1\text{--}0.5$ and $\Delta E_{1-2} = 2.2\text{--}5.5$ eV. Several hypotheses were suggested to explain such findings: chemically different environments of the ^{83}Rb atoms, surface plasmons and electron-hole interaction in metals. The most probable seems to be the first hypothesis as in our case the samples were not thermally annealed after the ^{83}Rb implantation. Therefore, the effects resulting from the radiation damage, such as vacancies and clusters, are to be expected, which might significantly affect the immediate environment of the ^{83}Rb atom. Then the asymmetry can be understood as a certain portion of ^{83}Rb atoms which possess higher electron binding energy. Still, the majority of ^{83}Rb atoms are expected on the substitutional sites, *i. e.* in a “truly” metallic state.
- In the spectra of the valence line $N_{2/3}$ -32 (unresolved lines N_2 and N_3 -32) of the ion-implanted sources an interesting doublet feature was observed, namely $A_{2/1} = 4.8\text{--}7.7$

and $\Delta E_{1-2} = 4.3\text{--}5.5$ eV, in the aforementioned notation. In other words, the low energy component was actually of larger amplitude than the high energy one, in contrast to the spectra of core electrons. The effect of quadrupole splitting of the state $4p_{3/2}$ due to strong electric fields on the not substitutional sites of ^{83}Rb atoms was discussed in this work, however, the measured ratio of amplitudes did not correspond to the hypothesis. Another hypothesis was suggested: the high energy component could stem from the interval conversion of $^{83\text{m}}\text{Kr}$ at neighboring atoms in the immediate vicinity of the $^{83\text{m}}\text{Kr}$ atom. The comparison with the binding energies of the $O_{4/5}$ shells of platinum and gold indeed supports this idea. Moreover, the fitted amplitude of the high energy peak was by the factor of 5.5–8.7 lower than expected from the comparison of the internal conversion coefficients of the lines $K\text{-}32$ and $N_{2/3}\text{-}32$. Thus, the high energy component could be ascribed to the conversion on neighboring atoms and the low energy component represents the unresolved doublet of the $N_{2/3}\text{-}32$ lines.

- The absolute kinetic energies of the $^{83\text{m}}\text{Kr}$ conversion lines were deduced from the data and compared with the corresponding values for gaseous krypton and for $^{83\text{m}}\text{Kr}$ condensed onto a clean HOPG substrate [Ost08]. For the electron shells K , L , M and N the general trend

$$E_{\text{bin}}^{\text{vac}}(\text{gas}) > E_{\text{bin}}^{\text{vac}}(\text{cond}) \simeq E_{\text{bin}}^{\text{vac}}(\text{evap}) > E_{\text{bin}}^{\text{vac}}(\text{impl}) \quad (8.5)$$

was observed, *i. e.* the maximal electron binding energy is found in the gaseous phase and decreases when the originally free atom is adsorbed onto solid surface. It further decreases when the atom is implanted into solid, in our case into polycrystalline metal foil of high purity. In the presented analysis the energies of the 9.4 keV and 32 keV gamma transitions of $^{83\text{m}}\text{Kr}$, determined in [Ven06] and [Sle11] by high precision gamma ray spectroscopy with semiconductor detectors, were used as external values. On the basis of these values and the binding energies for gaseous krypton the shifts of the binding energies in our solid sources were deduced. This approach was chosen due to the fact that no detailed theoretical predictions for these shifts were available.

- The electron binding energy shifts, denoted in Eq. 8.5 and summarized in Fig. 7.13, were found to strongly vary source-to-source as well as line-to-line. This observation requires further tests of the reproducibility of the production technique. Strictly speaking, each of the sources tested in this work was unique on its own, thus, identical sources should be produced and tested regarding the absolute kinetic energies of $^{83\text{m}}\text{Kr}$ conversion electrons.
- The measured absolute kinetic energies were used for an important check of linearity of the energy scale, represented by the HV scale used in this measurement campaign. The HV scale is affected by a number of items: HV divider, digital voltmeter, configuration of the spectrometer electrodes, work functions. The difference of the $^{83\text{m}}\text{Kr}$ gamma transition energies reads [Ven06, Sle11]

$$E_{\gamma}(32) - E_{\gamma}(9.4) = 32\,151.7(5) - 9\,405.8(4) = 22\,745.90(64) \text{ eV}, \quad (8.6)$$

which can be compared with the value derived from the difference of the kinetic energies of the lines $L_3\text{-}9.4$ and $L_3\text{-}32$. In this work the analysis was carried out with two independent methods: with a usual many-parameters fit and with the cross-correlation

method based on determining the similarity of two spectra (cf. Sect. 5.2.7). The former method delivered the value

$$\Delta E_{\text{kin}}(L_3, \text{m.p.f.}) = 22\,745.99 \pm 0.28_{\text{stat}} \pm 1.00_{\text{syst}} \text{ eV}, \quad (8.7)$$

while the latter one resulted in the value

$$\Delta E_{\text{kin}}(L_3, \text{c.c.m.}) = 22\,745.97 \pm 0.37_{\text{stat}} \pm 1.00_{\text{syst}} \text{ eV}. \quad (8.8)$$

The large systematic uncertainty of the results reflects the aforementioned discrepancies between the absolute kinetic energies of the conversion electrons of the individual sources. A very good agreement was achieved between the two methods of analysis, in addition, the values in Eq. 8.7 and Eq. 8.8 are in a good agreement with the difference of the gamma transition energies in Eq. 8.6. A similar procedure was carried out already in [Ost08] where besides the pair of the L_3 lines also the pair of L_2 lines was considered and the final result reads $\Delta E_{\text{kin}} = 22\,747.12(8) \text{ eV}$. The discrepancy of $\simeq 1.1 \text{ eV}$ stems from the difference of the $^{83\text{m}}\text{Kr}$ 9.4 keV gamma transition energy values used in this work and determined in [Ost08].

Comparison of the ion-implanted $^{83}\text{Rb}/^{83\text{m}}\text{Kr}$ sources and the CKrS

The solid ion-implanted sources proved to be a very promising alternative to the concept of the CKrS. These two sources shall be briefly compared here:

- The measurements have shown that the stability of a single source is comparable for both concepts. The solid source profits from the fact that the ^{83}Rb generator is placed directly in the source, thus, the long half-life allows a long-term application of the order of months. On the other hand, in [Ost08] the so-called “continuous” source, where $^{83\text{m}}\text{Kr}$ gas was let to adsorb continuously during the measurement, had a limited applicability of maximum one to two weeks.
- From the point of view of the source-to-source reproducibility the CKrS is superior to the solid sources. In the CKrS the substrate surface can be always cleaned prior to the $^{83\text{m}}\text{Kr}$ condensation. As in this work only four ion-implanted sources were produced, moreover with different parameters, no strong statement can yet be done regarding the reproducibility. Still, it is promising that three different sources based on platinum exhibited stability compatible with the requirements of KATRIN. The reproducibility of the absolute kinetic energies is to be proved in future when two identical samples shall be produced.
- The CKrS concept requires rather complicated vacuum setup which is not the case with the solid sources. However, the production of the ion-implanted sources at the ISOLDE facility turned out to be an uneasy task depending on a number of parameters and may be unavailable in some time periods for the KATRIN project. Therefore, alternative ways of implantation of ^{83}Rb into metals shall be pursued.
- The electron count rate recorded in the K -32 line was by the factor of $\approx 10^2$ higher in the case of the ion-implanted sources. This feature will allow to check the stability of the energy scale with the precision of $\pm 15 \text{ meV}$ within several minutes.

- With respect to vacuum requirements the ion-implanted sources are very advantageous: it was demonstrated that the conversion electrons emitted by these sources are not influenced even by abrupt vacuum changes or controlled deliberate venting from 10^{-10} mbar up to air.
- Thanks to its compactness, the ion-implanted source can be also used in other applications, *e. g.* for the tests of alignment and transmission properties of the KATRIN main beam line. However, it has to be kept in mind that this type of source represents an open radioactive source with the half-life of $\simeq 86$ d, therefore any contamination of the KATRIN setup has to be prevented.

Outlook on the further production of the ion-implanted $^{83}\text{Rb}/^{83\text{m}}\text{Kr}$ sources

Although very promising results were obtained already with the first samples of the ion-implanted sources, the following details of the production technique could be improved. Stated are also suggestions concerning the future sources which could clarify the open issues:

- The implanted dose $Q \approx 10^{14}$ ions cm^{-2} of the current samples shall be lowered by at least one order of magnitude in future. This way the lattice damage induced by the ^{83}Rb ions should be reduced. In order to achieve the ^{83}Rb activity sufficient for long-term application of the source, the option of sweep-scanning of the ion beam over the substrate can be utilized at the ISOLDE facility.
- Thermal annealing of the sources after the ^{83}Rb collection should be tested. Together with the previous item this procedure shall minimize the lattice damage and also the asymmetry of the conversion lines. It is also a common procedure to thermally anneal the substrate even prior the implantation—such a process could be tested as well.
- It was realized in this work that according to simulations about 5–10 % of ^{83}Rb ions do not reach the metallic state during the implantation, but they end up in the oxide layer covering the metal foil. Although this fact did not actually proved to be important in the presented measurements, the surface of the metal foil could, in principle, be cleaned by simple means of argon ion sputtering. Such a procedure would ensure that virtually no ^{83}Rb atoms are present in the oxide state.
- Very promising results were obtained also with the source Pt-15 which, furthermore, profited from reduced portion of inelastically scattered electrons, cf. Sect. 7.5. The option of implantation at low energies ($\approx 2\text{--}10$ keV) should be tested as it would increase the number of zero-energy-loss electrons, useful for the energy scale monitoring.
- As the substrate the polycrystalline platinum foils of high purity (99.99+ %) seem to be sufficient for our purpose. One could also attempt to implant ^{83}Rb into the HOPG substrate for further reduction of the inelastic scattering of electrons. The use of gold foils does not seem promising with respect to the non-zero shift of the $K\text{-}32$ line energy. However, the thermal annealing could have possibly improved the performance of such a source.

8. Conclusions and outlook

- In parallel to the implantation at the ISOLDE facility, the ^{83}Rb collection could, in principle, be done also at the radioisotope separator and implanter at the Helmholtz-Institut für Strahlen- und Kernphysik, University of Bonn. The tests are currently ongoing, the main issue being a very low efficiency of the ionization of ^{83}Rb . Having two production sites of ion-implanted sources would be a great benefit for the KATRIN project.
- The option of the so-called table-top implanter was also currently discussed in the KATRIN collaboration. Such an instrument would allow to implant the ^{83}Rb ions at very low energies without the necessity of using the complicated facilities as ISOLDE. However, due to the absence of an expensive magnetic separator the ion beam would definitely not be clean.
- Besides the classical implantation, the process of diffusion can be also used for bringing the ions into a solid. Here the main advantage is the fact that the damage lattice is minimal in comparison with the implantation.
- Independently on the production technique used, it is necessary to perform a test of reproducibility of the source production regarding the absolute kinetic energies of the conversion electrons.

Recommendations on future measurements at the monitor

spectrometer

Finally, on the basis of the long-term measurements performed at Mainz MAC-E filter, several remarks can be made about the upcoming measurements at the monitor spectrometer in the framework of the KATRIN experiment:

- The $[x, y, z]$ position of the source and the detector should be kept fixed during a given measurement phase (tritium run).
- The vacuum breakdowns should be definitely avoided in future. In addition, a thorough bake-out of the overall vacuum setup should be done prior to every measurement phase. Regular analysis of the residual gas composition seems advantageous. The systematics of the method of continuous monitoring of the energy scale stability would greatly benefit from monitoring the work function ϕ_{spec} of the monitor spectrometer. For this purpose a system based on the Kelvin probe is foreseen [Bec11].
- The drifts of the K -32 line energy stated in Eq. 8.1 to Eq. 8.4 were determined in the course of 26 days. Thus, it seems reasonable that the measurement of the conversion lines stability at the monitor spectrometer should start at least 7–14 days before the actual tritium run starts. This way the drift of the given source will be already sufficiently well known and it may serve for the check of the HV scale stability.
- At least two ion-implanted $^{83}\text{Rb}/^{83\text{m}}\text{Kr}$ should be placed in the source section simultaneously and their conversion electron lines should be measured on a regular basis. It can be also highly recommended to measure other conversion lines besides the K -32 line. This procedure proved to be very useful for checking the stability of the HV scale and the effects of abrupt changes of ϕ_{spec} .

- The structure and ripple of the high frequency HV noise at the monitor spectrometer should be regularly monitored as well.
- The time needed to scan *e. g.* the *K-32* conversion line can be conveniently reduced using an optimized distribution of the measurement time.

The presented solid electron sources, namely the ion-implanted ones, can be of interest in other applications where a source of electrons of precise and ultra-stable energy is necessary. The energy resolution should amount to $\Delta E < 5$ eV in such applications in order to separate the electrons undergoing the inelastic scattering from the zero-energy-loss electrons.

A. Electron binding energies of gaseous krypton

In Tab. A.1 the electron binding energies $E_{\text{bin}}^{\text{vac}}$ of gaseous krypton are summarized. A literature survey was carried out in order to obtain the precise value $E_{\text{bin}}^{\text{vac}}(i)$ for every atomic shell $i = K, \dots, N_3$ of krypton. For each atomic shell the “final” value, which was used throughout this work, was obtained.

In the case of the shells K , L_2 and L_3 the values derived in [Dra04] were directly taken as they represent accurate reevaluation of previous experimental works. For the L_1 shell the value of [Sie69] was taken, since the value of [Dra04] suffers from incorrect calculation [Dra11b]. In the case of the N_4 and N_5 shells, only the values of [Moo58] were available. In the rest of the cases the weighted mean of the collected values was taken. The uncertainties and the agreement of the individual values was checked and taken into account in the calculation of the error of the weighted mean. Actually, the values were found to agree well within the uncertainties.

In fact, there are another sources of the $E_{\text{bin}}^{\text{vac}}$ values available. However, the binding energies taken from work [Kra65] and indicated in the table were omitted here as according to [Sie69] this measurement was carried out with a less precise calibration. The work [Sve76] states the values $E_{\text{bin}}^{\text{vac}}$ without uncertainties and thus was also not considered.

Tab. A.1: The overview of electron binding energies $E_{\text{bin}}^{\text{vac}}(i)$ of gaseous krypton.

Electron level Reference	K 1s _{1/2}	L ₁ 2s _{1/2}	L ₂ 2p _{1/2}	L ₃ 2p _{3/2}	M ₁ 3s _{1/2}	M ₂ 3p _{1/2}	M ₃ 3p _{3/2}	M ₄ 3d _{1/2}	M ₅ 3d _{3/2}	N ₁ 4s _{1/2}	N ₂ 4p _{1/2}	N ₃ 4p _{3/2}
Moore [Moo58]										27.52(5)	14.66(5)	14.00(5)
Codling [Cod64]								95.04(5)	93.82(5)			
Krause [Kra65]		1921.2(8)	1727.2(6)	1674.8(6)								
Bearden [Bea67]	14325.6(8)	1921.0(6)	1727.2(5)	1674.9(5)		222.7(11)						
Stiegbahn [Stie69]		1924.6(8)	1730.9(5)	1678.4(5)	292.8(3)	222.2(2)	214.4(2)	94.9(2)	93.7(2)	27.4(2)		
Johansson [Joh73]							214.55(15)		93.80(10)			
Svensson [Sve76]						221.8*	214.2*					
King [Kin77]								95.038(25)	93.788(20)			
Sevier [Sev79]					292.1(10)	222.1(6)	214.4(6)					
Deslattes [Des03]	14327.19(13)	1920.4(12)	1730.9(5)	1679.07(39)								
Dragoun [Dra04]	14327.26(4)	1921.4(3)	1731.91(3)	1679.21(3)								
value used in this work	14327.26(4) [Dra04]	1924.6(8) [Sie69]	1731.91(3) [Dra04]	1679.21(3) [Dra04]	292.74(29) <i>aver.</i>	222.20(19) <i>aver.</i>	214.49(12) <i>aver.</i>	95.04(2) <i>aver.</i>	93.79(2) <i>aver.</i>	27.51(5) <i>aver.</i>	14.66(5) [Moo58]	14.00(5) [Moo58]

All values are stated in eV. In columns the individual atomic shells of krypton are exhibited, in rows the references are listed in chronological order. The last two rows denote the values which were used in this work, together with their origin. The designation *aver.* means that the value used in this work is a weighted mean of the values listed in the given column. The values marked with * were not taken into account while calculating the weighted mean. See text for further discussion.

B. Evaluation of the energy shifts of the $^{83\text{m}}\text{Kr}$ conversion lines resulting from abrupt changes of vacuum conditions

B.1. Second measurement phase

In Sect. 6.3.2 the effects of various sudden changes of vacuum conditions on $^{83\text{m}}\text{Kr}$ conversion lines of the solid $^{83}\text{Rb}/^{83\text{m}}\text{Kr}$ sources Pt-30, S 28 and S 29 were studied. In Tab. B.1 the line position shifts resulting from the first two vacuum breakdowns are summarized. Also noted are the changes of the line amplitude and background values. The effects of the bake-out of the complete experimental setup on the conversion line positions are listed in Tab. B.2 together with the effects of the third vacuum breakdown.

Tab. B.1: The overview of the $^{83\text{m}}\text{Kr}$ conversion lines position shifts observed as a result of the vacuum breakdowns in the second measurement phase.

source	electron line	$\Delta E_0(1)$ [eV] "before"	$\Delta E_0(2)$ [eV] "after"	difference [eV] $\Delta E_0(2) - \Delta E_0(1)$	weighted mean [eV]
first vacuum breakdown, day 15					
Pt-30		0.010(2)	-0.370(9)	-0.380(9)	
S 28	K-32	0.021(3)	-0.448(10)	-0.469(10)	-0.419(141)
S 29		0.026(20)	-0.381(6)	-0.407(21)	
<i>no significant changes (all below 5%) in amplitude and background values in all cases</i>					
second vacuum breakdown, day 22					
Pt-30		-0.015(2)	-0.337(2)	-0.322(3)	
S 28	K-32	0.015(4)	-0.242(5)	-0.257(6)	—
S 29		-0.100(13)	-0.676(5)	-0.576(13)	
<i>increase of amplitudes: S 28 by 20%, S 29 by 70%, Pt-30 without change</i>					
combined effect of the first and the second vacuum breakdowns					
Pt-30	L_1 -9.4	0.076(60)	-0.832(40)	-0.908(72)	
	L_3 -32	-0.012(4)	-0.791(2)	-0.779(5)	-0.779(17)
	$N_{2/3}$ -32	0.021(33)	-0.665(55)	-0.686(64)	
<i>changes of amplitudes: L_1-9.4 by -37%, L_3-32 by +6%, rest without change</i>					
S 28	L_1 -9.4	0.111(39)	-0.714(23)	-0.824(45)	
	L_3 -32	-0.006(7)	-0.848(5)	-0.842(8)	-0.832(188)
	$N_{2/3}$ -32	0.036(22)	-0.480(41)	-0.517(46)	
<i>changes of amplitudes: L_1-9.4 by -23%, L_3-32 by +31% and $N_{2/3}$-32 by +10%</i>					
S 29	L_1 -9.4	0.117(72)	-0.637(86)	-0.754(113)	
	L_3 -32	0.018(9)	-1.106(14)	-1.124(17)	-1.095(588)
	$N_{2/3}$ -32	-0.027(40)	-0.333(95)	-0.305(103)	
<i>changes of amplitudes: L_1-9.4 by -4%, L_3-32 by +83% and $N_{2/3}$-32 by +6%</i>					

The effects of the first two vacuum breakdowns on the electron lines were analyzed with the help of the cross-correlation method. For each electron line a spectrum recorded shortly prior to the vacuum breakdown was chosen as the reference. Thus, the values in the column "before" are close to zero, however, they might be non-zero as typically a group of 10–20 spectra was analyzed in each situation and the results were averaged. The uncertainties of the weighted mean were multiplied by $\sqrt{\chi^2_{\text{r}}}$ in cases where $\chi^2_{\text{r}} \gg 1$. The effect of the first and second vacuum breakdown could be determined separately only for the K-32 line of all the three sources. All the other electron lines were scanned before the first and after the second vacuum breakdown, thus, only the combined effect of these two could be determined. In the calculation of the amplitude changes the radioactive decay of ^{83}Rb was taken into account.

Tab. B.2: The overview of the $^{83\text{m}}\text{Kr}$ conversion lines position shifts observed as a result of the bake-out and the third vacuum breakdown in the second measurement phase.

source	electron line	$\Delta E_0(1)$ [eV] "before"	$\Delta E_0(2)$ [eV] "after"	difference [eV] $\Delta E_0(2) - \Delta E_0(1)$
complete bake-out, days 43–53				
Pt-30		0.000(1)	0.145(5)	0.146(5)
S 28	K-32	−0.062(7)	−0.174(12)	−0.113(14)
S 29		0.062(12)	0.666(10)	0.604(16)
<i>changes of amplitude / background values (in %):</i>				
Pt-30 ... −10 / +55, S 28 ... −60 / +24, S 29 ... −60 / +170				
third vacuum breakdown, day 61				
Pt-30		0.006(6)	−0.073(2)	−0.079(6)
S 28	K-32	−0.080(17)	0.032(3)	0.113(18)
S 29		0.137(13)	0.017(8)	−0.120(15)
<i>changes of amplitude / background values (in %):</i>				
Pt-30 ... +6 / +19, S 28 ... +110 / +90, S 29 ... +60 / +7				
combined effect of the bake-out and the third vacuum breakdown				
	L_1 -9.4	−0.093(43)	0.091(37)	0.184(57)
Pt-30	L_3 -32	−0.007(4)	0.037(2)	0.044(4)
	$N_{2/3}$ -32	0.070(28)	0.018(30)	−0.052(40)
<i>changes of amplitude / background values (in %):</i>				
L_1 -9.4 ... +23 / +33, L_3 -32 ... −6 / +33, $N_{2/3}$ -32 ... −2 / +410				

See the caption of Tab. B.1 for the explanation.

B.2. Third measurement phase

In Sect. 6.4.1 the vacuum breakdown was encountered during the measurements of the ion-implanted sources Pt-30, Pt-30 #2, Pt-15 and Au-30. The changes of the *K*-32 line and other conversion lines of these sources, resulting from the vacuum breakdown, are summarized in Tab. B.3. There the results of the test of deliberate venting of the source section are stated as well.

Tab. B.3: Overview of the $^{83\text{m}}\text{Kr}$ conversion lines position shifts observed with the four ion-implanted sources Pt-30, Pt-30 #2, Pt-15 and Au-30 as a result of the vacuum breakdown and deliberate venting of the source section.

source	electron line	$\Delta E_0(1)$ [eV] "before"	$\Delta E_0(2)$ [eV] "after"	difference [eV] $\Delta E_0(2) - \Delta E_0(1)$	weighted mean [eV]
vacuum breakdown up to 10^{-4} mbar, day 26					
Pt-30		-0.007(3)	-0.153(8)	-0.146(9)	
Pt-30 #2	K-32	-0.002(1)	-0.145(2)	-0.143(2)	-0.149(22)
Pt-15		-0.001(2)	-0.167(2)	-0.166(3)	
Au-30		-0.006(3)	-0.151(2)	-0.144(4)	
<i>amplitude and background values without changes</i>					
	L_1 -9.4	-0.017(17)	-0.068(8)	-0.052(19)	
Pt-30 #2	L_3 -9.4	-0.011(57)	-0.259(98)	-0.248(114)	-0.157(42)
	L_3 -32	-0.009(3)	-0.169(2)	-0.161(4)	
	$N_{2/3}$ -32	0.050(49)	-0.111(13)	-0.161(51)	
<i>L_1-9.4 ... -17 % / -14 %, L_3-9.4 ... -17 % / -10 %, rest without change</i>					
source section vented up to atmospheric pressure, day 35					
Pt-30		0.011(3)	0.019(8)	0.008(9)	
Pt-30 #2	K-32	0.011(2)	0.019(3)	0.007(4)	0.003(3)
Pt-15		0.003(2)	0.000(4)	-0.003(5)	
Au-30		0.012(11)	0.005(4)	-0.006(12)	
<i>amplitude and background values without changes</i>					
combined effect of vacuum breakdown and deliberate venting					
Pt-30	L_3 -9.4	0.093(80)	-0.135(42)	-0.228(91)	—
	L_3 -32	0.006(4)	-0.102(6)	-0.108(7)	
<i>L_3-9.4 ... -16 % / -23 %, L_3-32 no change</i>					
	L_1 -9.4	-0.010(10)	-0.131(9)	-0.121(13)	
Pt-15	L_3 -9.4	-0.078(32)	-0.150(22)	-0.072(39)	—
	L_3 -32	-0.003(2)	-0.119(2)	-0.116(3)	
<i>L_1-9.4 ... -27 % / -26 %, L_3-9.4 ... -26 % / -22 %, L_3-32 no change</i>					
	L_1 -9.4	-0.015(23)	-0.089(15)	-0.073(28)	
Au-30	L_3 -9.4	-0.097(46)	-0.103(67)	-0.006(81)	—
	L_3 -32	-0.013(1)	-0.079(2)	-0.066(2)	
<i>L_1-9.4 ... -18 % / -23 %, L_3-9.4 ... -19 % / -21 %, L_3-32 no change</i>					

See the caption of Tab. B.1 for the explanation.

C. Investigation of different environments of the ^{83}Rb atoms in the ion-implanted $^{83}\text{Rb}/^{83\text{m}}\text{Kr}$ sources with the XPS method

After observing the doublet structure of the conversion electron lines in the solid sources, as described in Sect. 7.2, an idea of confirming the results by a complementary measurement arose. It was realized that implanting a non-radioactive Rb ions into Au or Pt foil would imitate the radioactive samples tested at Mainz MAC-E filter. The advantage of such non-radioactive sample is that it can be easily investigated by methods of surface physics.

The non-radioactive ^{85}Rb ions were implanted at the radioisotope separator and implanter at Bonn. The minimum possible implantation energy was 30 keV as in the case of the implantations at ISOLDE facility [Joh09, Nol10]. As a substrate the Au foil (purity 99.99+ %, thickness 0.025 mm, diameter 12 mm [Goo09]) was chosen. The foils were at room temperature and the angle of incidence of the ion beam was zero. No thermal annealing was carried out after the implantation, similarly to the ^{83}Rb collections. Thus the implantation profiles described in Sect. 4.2.3 are valid for this case, too. Altogether three samples were produced with implanted doses of 5×10^{13} , 5×10^{14} and 5×10^{15} atoms cm^{-2} [Nol10].

The method of X-ray photoelectron spectroscopy (XPS), also know as electron spectroscopy for chemical analysis (ESCA), was chosen for investigating the non-radioactive samples. In this surface chemical analysis technique the solid sample is irradiated with a beam of photons of energy $h\nu$. The photo-emitted electrons escape from the top layer of 1–10 nm thickness with the kinetic energy

$$E_{\text{e,kin}} = h\nu - E_{\text{bin}}^{\text{Fermi}} - \phi_{\text{sample}}, \quad (\text{C.1})$$

where $E_{\text{bin}}^{\text{Fermi}}$ is the binding energy with respect to the Fermi level and ϕ_{sample} represents the sample work function. The kinetic energy of the electrons is measured by a spectrometer, typically of the 180° hemispherical energy analyzer type. The spectrometer and the sample are connected to ensure that the Fermi-energies are at the same reference level. The spectrometer actually measures the electron kinetic energy as

$$E'_{\text{e,kin}} = h\nu - E_{\text{bin}}^{\text{Fermi}} - \phi_{\text{spectr.}} \quad (\text{C.2})$$

as the relation

$$E_{\text{e,kin}} + \phi_{\text{sample}} = E'_{\text{e,kin}} + \phi_{\text{spectr.}} \quad (\text{C.3})$$

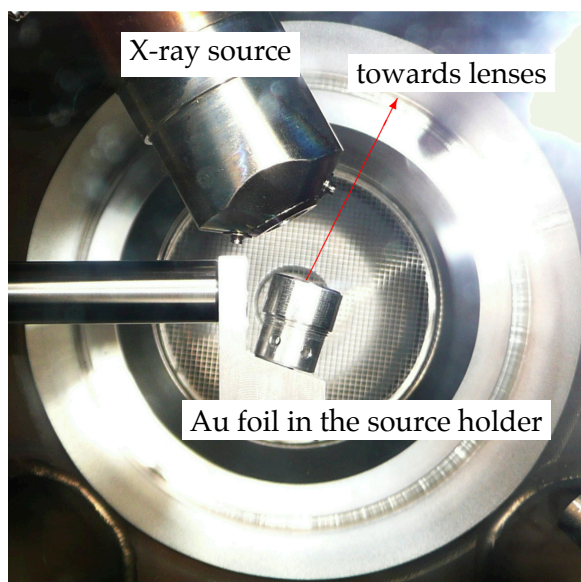


Fig. C.1: The non-radioactive Rb sample placed inside the XPS setup at the Physikalisches Institut, University of Münster.

holds [SPE08]. Thus knowing the photon energy $h\nu$, measuring $E'_{e,\text{kin}}$ and calibrating the spectrometer work function $\phi_{\text{spectr.}}$ yields the electron binding energy $E_{\text{bin}}^{\text{Fermi}}$ without knowing the sample work function ϕ_{sample} . The aim of the XPS measurements presented here was to investigate a possible structure of the binding energies $E_{\text{bin}}^{\text{Fermi}}$ of Rb electrons implanted in Au foils.

The samples were tested at the Physikalisches Institut, University of Münster, in the time period March–May 2010. As the X-ray source the Al anode was used, utilizing the $K\alpha$ X-ray line of energy $h\nu = 1486.6$ eV. The ejected photoelectrons were analyzed with the help of the 180° hemispherical energy analyzer PHOIBOS 100 and a single channel electron multiplier detector system [Lin10, SPE08]. The $K\alpha$ X-ray line was not monochromatized thus the instrumental resolution was limited by the natural line width of Al $K\alpha$, $\Delta E = 0.85$ eV (FWHM) [SPE08]. In addition, the transfer lens system was used for defining the analysis area and angular acceptance by imaging the sample onto the entrance slit. The actual geometry is depicted in Fig. C.1.

The setup was evacuated down to 10^{-9} mbar range and the XPS spectra were recorded with the energy step of 0.1–0.5 eV and with an integrating time of 0.5–3.5 s per point. Firstly, the sample with the highest dose of 5×10^{15} atoms cm^{-2} was investigated. This implanted dose was by one order of magnitude higher than the typical dose obtained in the case of radioactive $^{83}\text{Rb}/^{83\text{m}}\text{Kr}$ sources. A typical spectrum of the scan over the E_{bin} (for the sake of simplicity the notation “Fermi” is omitted from here on) range 0–800 eV is shown in Fig. C.2 as recorded and in Fig. C.3 after the background of Tougaard type [Rep92, Tou88] was subtracted. The E_{bin} peaks of Rb were expected at the following positions [Car78]: $4p_{3/2}$... 15.3 eV, $4p_{1/2}$... 16.3 eV, $4s$... 30.5 eV, $3d_{5/2}$... 112.0 eV, $3d_{3/2}$... 113.0 eV, $3p_{3/2}$... 239.1 eV, $3p_{1/2}$... 248.7 eV and $3s$... 326.7 eV. The structure observed at the position $E_{\text{bin}} \simeq 110$ eV can be assigned to the photoelectrons undergoing inelastic scattering in the foil.

Obviously, only the material of the Au foil and the contamination layer of carbon on top

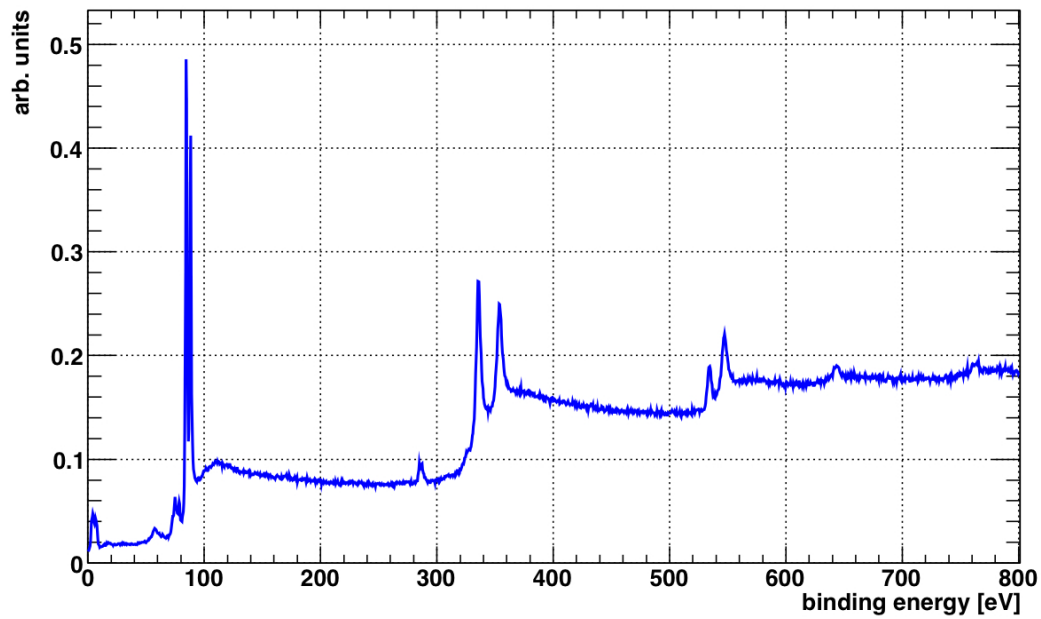


Fig. C.2: The XPS spectrum of the high dose sample.

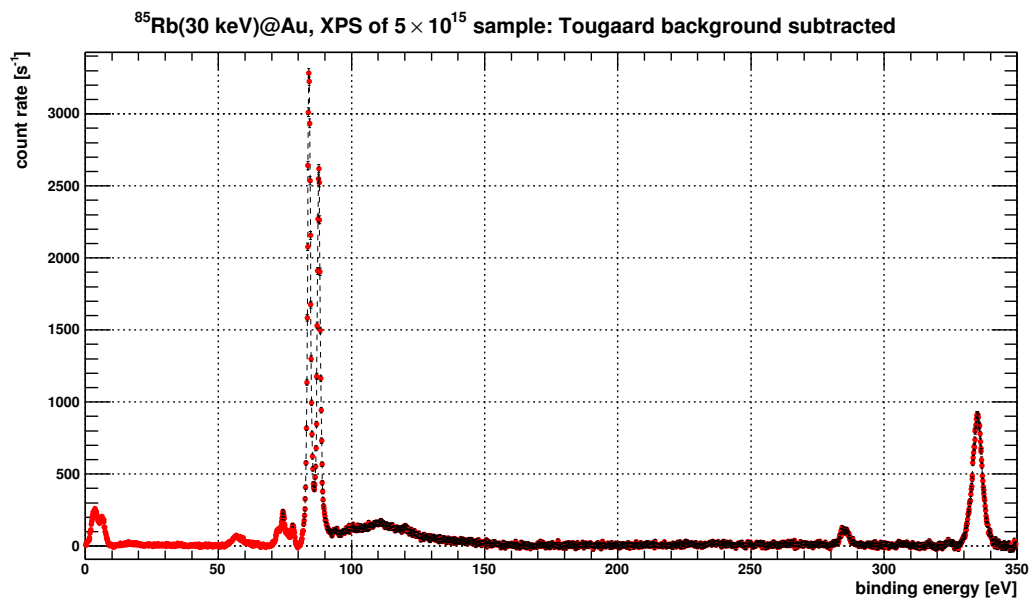


Fig. C.3: The XPS spectrum of the high dose sample, after subtraction of the Tougaard spectrum.

of it could be identified in the spectra. The tests proceeded further with measurements of the sample with a low dose of 5×10^{13} atoms cm^{-2} . If some difference would be observed between the E_{bin} spectra of 5×10^{13} atoms cm^{-2} sample and 5×10^{15} atoms cm^{-2} sample, it could be directly attributed to the effect of implanted Rb atoms as otherwise the bulk of Au foil was identical for both samples. The E_{bin} spectra were scaled so that the areas of the Au doublet ($4f_{5/2}$, $4f_{7/2}$) were identical in both spectra. The difference can be seen in Fig. C.4 as calculated pointwise with the help of linear interpolation (the spectra were not measured in exactly identical points of E_{bin}). In addition, the calculated difference has been re-binned in

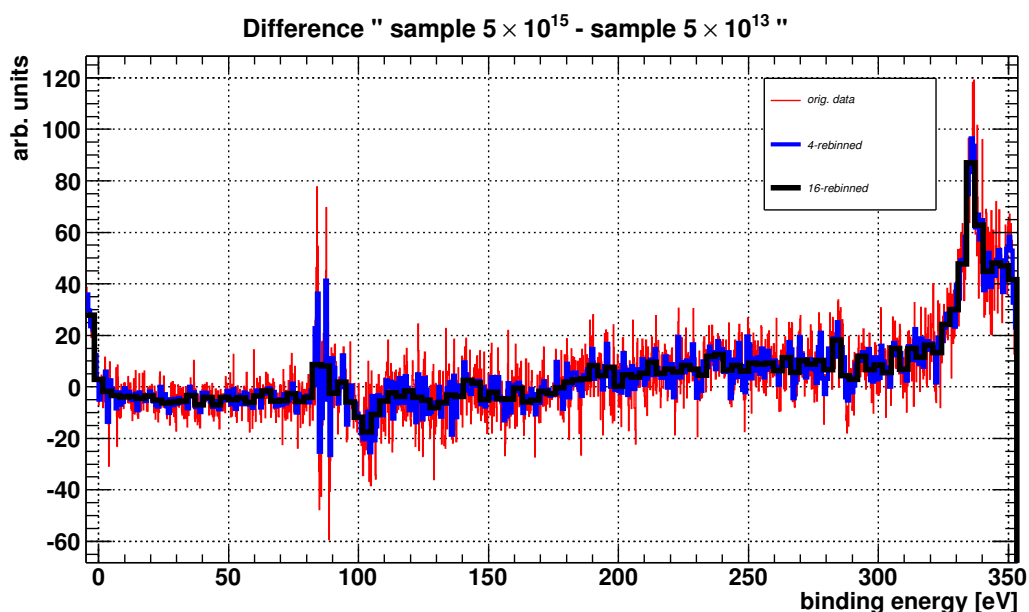


Fig. C.4: The difference of the scaled XPS scans obtained with the high dose and the low dose sample.

order to smear out possible fluctuations of the count rate. The following differences between the aforementioned spectra have been found:

- a minute structure at $E_{\text{bin}} \simeq 90$ eV which can be attributed to the imperfect scaling of the spectra
- a small peak at $E_{\text{bin}} \simeq 285$ eV which can be safely identified as a change in the C concentration ($C 1s = 284.2$ eV [Car78])
- a clearly visible peak at $E_{\text{bin}} \simeq 335$ eV which value corresponds well to Au $4d_{5/2}$ peak [Car78]

However, no signature of Rb was found in the difference of the scaled spectra, *i. e.* the XPS technique was not sensitive enough to observe the Rb atoms buried in the Au foil.

As can be deduced from the implantation profile in Fig. 4.14, the peak concentration of the Rb ions implanted with energy of 30 keV into amorphous Au foil lies in the depth of $\simeq 6$ nm. In order to increase the registration probability of Rb the sample with dose of 5×10^{15} atoms cm^{-2} has been sputtered with Ar ions with energy of 2.5 keV. With the help of the SRIM code [Zie10] it has been estimated that the sputtering yield of the Ar ions of energy 2.5 keV is about 6 Au atoms ion $^{-1}$. However, even after intensive sputtering no Rb signal has been observed in the XPS scans.

Lastly, the performance of the XPS apparatus has been checked with the help of a massive Rb sample. This sample was prepared by drying out a RbCl solution on Au foil. There was about 1×10^{18} atoms cm^{-2} of Rb, the film on the foil was visible by naked eye. The BE spectrum corrected for the Tougaard background is shown in Fig. C.5. The following peaks were clearly visible in the spectrum [Car78]:

- $BE \simeq 15$ eV ... it can possibly be H, Rb, Cl or K,
- $BE \simeq 112$ eV ... Rb ($3d_{5/2}$ and $3d_{3/2}$),

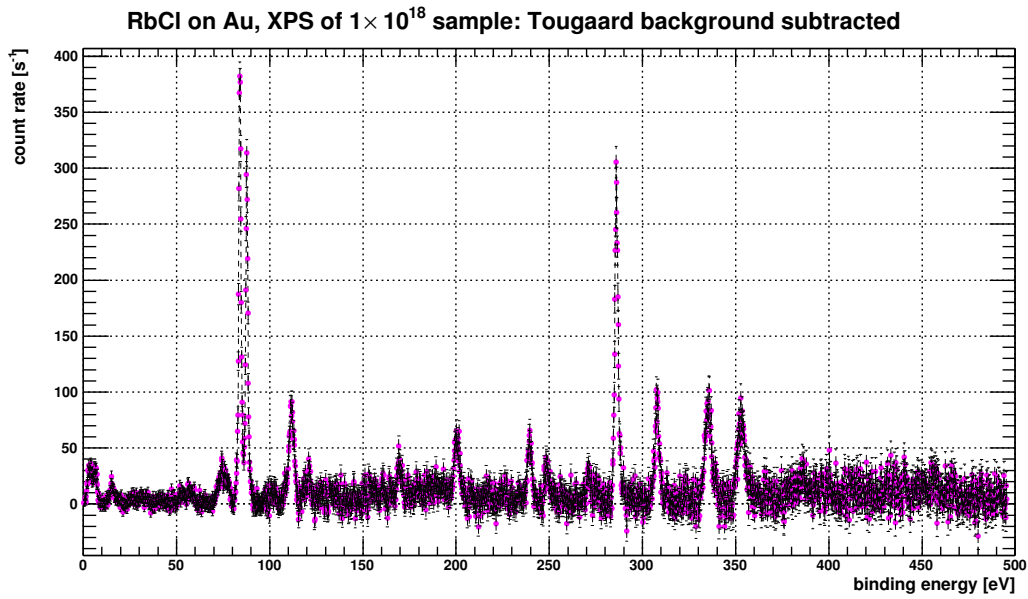


Fig. C.5: The XPS spectrum of the massive RbCl sample, after subtraction of the Tougaard spectrum.

- $BE \simeq 169$ eV ... possibly sulphur,
- $BE \simeq 200$ eV ... group of Cl peaks,
- $BE \simeq 239$ eV ... Rb $3p_{3/2}$,
- $BE \simeq 248$ eV ... Rb $3p_{1/2}$,
- $BE \simeq 271$ eV ... Cl,
- $BE \simeq 285$ eV ... C and Cl,

It can be concluded that the XPS technique is unfortunately not well suited for investigating such trace amounts of atoms implanted in the depth of several nm. No signal of Rb has been found in the spectra of the sample with the dose of 5×10^{15} atoms cm^{-2} . On the other hand, the measurement of the massive RbCl source with 1×10^{18} atoms cm^{-2} reliably showed Rb peaks on the expected E_{bin} positions. In order to observe a reliable Rb signal from an implanted sample with the XPS technique, it would be necessary to implant a high dose of $\approx 10^{18}$ atoms cm^{-2} and to lower the implantation energy significantly (~ 1 keV). However, these conditions (high dose and low implantation energy) would cause the sample to be totally different from the investigated $^{83}\text{Rb}/^{83\text{m}}\text{Kr}$ sources. Another possibility would be the use of the secondary ion mass spectrometry (SIMS) technique which has a depth resolution of 5–30 nm and a detection limit of 10^{12} – 10^{17} atoms cm^{-3} .

Bibliography

Note: the number behind each reference denotes the number of page where the reference was cited.

- [Aga74] V.K. Agarwala and T. Fort, Jr., *Surf. Sci.* **45** (1974) 470. 108
- [Aks77] H. Aksela, S. Aksela *et al.*, *Phys. Rev.* **A 15** (1977) 985. 53
- [ALE98] The ALEPH collaboration (R. Barate *et al.*), *Eur. Phys. J.* **C 2** (1998) 395. 11
- [Alt03] G. Altarelli and K. Winter, Eds., *Neutrino Mass*, Springer, 2003. 1
- [And69] O.U. Anders, *Nucl. Instrum. Methods* **68** (1969) 205. 112
- [Ash81] N.W. Ashcroft and N.D. Mermin, *Solid State Physics*, Saunders College, 1981. 76
- [Ass96] K. Assamagan, Ch. Brönnimann *et al.*, *Phys. Rev.* **D 53** (1996) 6065. 11
- [Bab93] Y. Baba, H. Yamamoto and T. Sasaki, *Surf. Sci.* **287/288** (1993) 806 and also *Nucl. Instrum. Meth.* **B 66** (1992) 424. 85, 87, 88
- [Bae10] O. von Baeyer and O. Hahn, *Phys. Z.* **11** (1910) 488. 13
- [Bar91] H. Barth, *Aufbau des Datenaufnahmesystems für das Mainzer Neutrinomassenexperiment*, diploma thesis, University of Mainz, 1991. 110
- [Bar97] H. Barth, dissertation, University of Mainz, 1997. 110
- [Bau09] S. Bauer, *Aufbau und Inbetriebnahme des zweiten Präzisions-ochspannungsteilers bis 65 kV für das KATRIN-Experiment*, diploma thesis, University of Münster, 2009, available at <http://www-ik.fzk.de/~katrin/publications/thesis.html>. 47, 111, 143, 191
- [Bau11] S. Bauer, private communication, 2009–2011. 110, 111, 143, 151, 152, 154, 181, 182, 183, 191, 210
- [Bea67] J.A. Bearden and A.F. Burr, *Rev. Mod. Phys.* **39** (1967) 125. 276
- [Bec10] M. Beck, K. Valerius *et al.*, *Eur. Phys. J.* **A 44** (2010) 499. 31
- [Bec11] M. Beck, *Work function measurements with a Kelvin probe*, presentation at the 20th KATRIN collaboration meeting, Karlsruhe, 2011, available at KATRIN BSCW, 95 General Meetings and Review Panels, 1 Collaboration Meetings, 20. Collaboration Meeting, Session - C1, 95-TRP-5043-C1-MBeck.pdf. 209, 272
- [Bel08] A.I. Belesev, E.V. Geraskin *et al.*, *Phys. Atom. Nucl.* **71** (2008) 427. 50, 54

Bibliography

- [Bla10] K. Blaum, Yu.N. Novikov and G. Werth, *Contemp. Phys.* **51** (2010) 149. 41
- [Bor03] B. Bornschein, J. Bonn *et al.*, *J. Low Temp. Phys.* **131** (2008) 69. 54
- [Bri84] Ch. Briançon, B. Legrand *et al.*, *Nucl. Instrum. Methods* **221** (1984) 547. 60
- [But11] T. Butz, private communication, 2011. 71, 81, 254, 258
- [Cal01] D.O. Caldwell, Ed., *Current Aspects of Neutrino Physics*, Springer-Verlag, Berlin Heidelberg, 2001. 1
- [Cam01] J.L. Campbell and T. Papp, *Atom. Data Nucl. Data* **77** (2001) 1. 18, 52, 53, 216, 268
- [Car78] M. Cardona and L. Ley, *Introduction*, in *Photoemission in Solids I: General Principles*, Eds. M. Cardona and L. Ley, Springer-Verlag, Berlin, 1978, p. 1. 83, 85, 87, 284, 286
- [Car73] T.A. Carlson and C.W. Nestor, Jr., *Phys. Rev. A* **8** (1973) 2887. 89, 236, 263
- [Car75] T.A. Carlson, *Photoelectron and Auger Spectroscopy*, Plenum Press, 1975. 83
- [Cha14] J. Chadwick, *Distribution in intensity in the magnetic spectrum of the β -rays of radium*, *Verh. Dtsch. Phys. Ges. (Germany)* **16** (1914) 383. 1
- [Cit74] P.H. Citrin and D.R. Hamann, *Phys. Rev. B* **10** (1974) 4948 and also *Chem. Phys. Lett.* **22** (1973) 301. 85, 86, 87, 88, 89, 241, 247, 255
- [Cod64] K. Codling and R.P. Madden, *Phys. Rev. Lett.* **12** (1964) 106. 276
- [Cro05] S. Croft, R. Venkataraman *et al.*, *Appl. Rad. Isot.* **63** (2005) 575. 121
- [Dan62] G. Danby, J.-M. Gaillard *et al.*, *Phys. Rev. Lett.* **9** (1962) 36. 2
- [Dar73] R.J. D'Arcy and N.A. Surplice, *Surf. Sci.* **34** (1973) 193. 175, 176
- [Dav80b] J.A. Davies and L.M. Howe, *Basic Implantation Processes*, in *Site Characterization and Aggregation of Implanted Atoms in Materials*, Eds. A. Perez and R. Coussement, Plenum Press, New York, 1980, p. 7. 66, 68, 71, 80
- [Deb77] K. Debertin and U. Schötzgig, *Nucl. Instrum. Methods* **140** (1977) 337. 112
- [Deb88] K. Debertin and R.G. Helmer, *Gamma- and X-Ray Spectrometry with Semiconductor Detectors*, North-Holland, 1988. 116
- [Dec90] D.J. Decman and W. Stoeffl, *Phys. Rev. Lett.* **64** (1990) 2767. 151
- [Del07] Delta Elektronika BV, *SM3000-Series Power Supplies Data Sheet*, 2007. 164
- [Des03] R.D. Deslattes, E.G. Kessler, Jr. *et al.*, *Rev. Mod. Phys.* **75** (2003) 35. 48, 276
- [Dez95] I. Dézsi, *J. Radioanal. Nucl. Ch.* **190** (1995) 225. 66
- [Don70] S. Doniach and M. Šunjić, *J. Phys. C: Solid State* **3** (1970) 285. 257
- [DON08] The DONuT collaboration (K. Kodama *et al.*), *Phys. Rev. D* **78** (2008) 052002. 2
- [Dra83] O. Dragoun, *Adv. Electron. El. Phys.* **60** (1983) 1. 13, 18, 90, 128
- [Dra02] O. Dragoun, A. Špalek *et al.*, *Nucl. Instrum. Meth.* **B 194** (2002) 112. 92, 93, 94, 95

- [Dra04] O. Dragoun, A. Špalek and F.J. Wuilleumier, Czech. J. Phys. **54** (2004) 833. 52, 275, 276
- [Dra11a] O. Dragoun, A. Špalek *et al.*, Appl. Rad. Isot. **69** (2011) 672. 48, 50, 94, 95
- [Dra11b] O. Dragoun, private communication, 2011. 275
- [Dun08] J.A. Dunmore, M.L. Leber and the KATRIN collaboration J. Phys. Conf. Ser. **136** (2008) 042056. 32
- [Eas70] D.E. Eastman, Phys. Rev. **B 2** (1970) 1. 85, 175
- [Ege87] W.F. Egelhoff, Jr., Surf. Sci. Rep. **6** (1987) 253. 83, 84, 87, 151
- [Eic09] F. Eichelhardt, *Measurement of the Tritium Pumping Properties of a 4.2 K Argon Condensate for the Cryogenic Pumping Section of KATRIN*, dissertation, University of Karlsruhe (TH), 2009, available at <http://www-ik.fzk.de/~katrin/publications/thesis.html>. 25, 30, 31
- [Ell87] S.R. Elliott, A.A. Hahn and M.K. Moe, Phys. Rev. Lett. **59** (1987) 2020. 9
- [Eri69] L. Eriksson, G.R. Bellavance and J.A. Davies, Radiat. Eff. Defect. S. **1** (1969) 71. 72, 73
- [Fer34] E. Fermi, Z. Phys. **88** (1934) 161. 1
- [Fir96] R.B. Firestone, V.S. Shirley *et al.*, *Table of Isotopes*, 8th Edition, John Wiley & Sons, New York, 1996. 17, 47, 50, 51, 124, 146, 259
- [Fix02] D.J. Fixsen and J.C. Mather, Astrophys. J. **581** (2002) 817. 7
- [Fla04] B. Flatt, *Voruntersuchungen zu den Spektrometern des KATRIN-Experiments*, dissertation, University of Mainz, 2004. 30, 101, 103, 162, 189
- [Fle92] L. Fleischmann, *Untersuchung der Rückstreuung von keV-Elektronen im Rahmen des Mainzer-Neutrinoruhemasseexperimentes*, diploma thesis, University of Mainz, 1992. 54, 91, 92, 94
- [Flu08] Fluke Corporation, *8508A Reference Multimeter Extended Specifications and 732A DC Reference Standard Data Sheet*, 2008. 110, 156, 192, 193, 210
- [For99] D. Forkel-Wirth, Rep. Prog. Phys. **62** (1999) 527. 66, 74
- [Fra11] F.M. Fränkle, L. Bornschein *et al.*, Astropart. Phys. **35** (2011) 128. 29
- [Fre74] M.S. Freedman, Ann. Rev. Nucl. Sci. **24** (1974) 209. 89
- [FuG06] FuG Elektronik GmbH, HCP-18-35000 Power Supply Technical Manual, 2006. 109
- [Gad76] J.W. Gadzuk, Phys. Rev. **B 14** (1976) 2267. 85, 87
- [Ger06] C. Gerthsen, H. Vogel and D. Meschede, *Physik*, 23rd Edition, Springer-Verlag, Berlin, 2006. 128
- [Goe35] M. Goepfert-Mayer, Phys. Rev. **48** (1935) 512. 9
- [Gol58] M. Goldhaber, L. Grodzins, and A.W. Sunyar, Phys. Rev. **109** (1958) 1015. 2

- [Gon75] U. Gonser, Ed., *Mössbauer Spectroscopy*, Springer-Verlag, Berlin, 1975. 254, 258
- [Goo09] Goodfellow Cambridge Ltd., <http://www.goodfellow.com>, 2009. 77, 283
- [Gou10] J.D. Goullon, *Installation and commissioning of the monitor spectrometer of KATRIN*, diploma thesis, University of Karlsruhe (TH), 2010, available at <http://www-ik.fzk.de/~katrin/publications/thesis.html>. 205
- [Gree84] N.N. Greenwood and A. Earnshaw, *Chemistry of the Elements*, Pergamon Press, Oxford, 1984. 59
- [Gro09] S. Grohmann, *Cryogenics* **49** (2009) 413. 29
- [Hah24] O. Hahn and L. Meitner, *Z. Phys.* **26** (1924) 161. 13
- [Ham06] Hamamatsu Photonics K. K., *Si PIN photodiode S3590 series data sheet*, 2006. 106
- [Hel00] R.G. Helmer and C. van der Leun, *Nucl. Instrum. Meth. A* **450** (2000) 35. 48
- [Her10] A. Herlert, *Nuclear Physics News* **20** (2010) 5. 74
- [Her86] P. Herzog, in *Low-Temperature Nuclear Orientation*, Eds. N.J. Stone and H. Postma, North-Holland, Amsterdam, 1986, p. 748. 72
- [Hil11] B. Hillen, *Untersuchung von Methoden zur Unterdrückung des Spektrometeruntergrunds beim KATRIN Experiment*, dissertation, University of Münster, 2011. 31
- [Hub66] E.E. Huber, Jr. and C.T. Kirk, Jr., *Surf. Sci.* **5** (1966) 447. 143, 175
- [Hug10] K. Hugenberg, *Prog. Part. Nucl. Phys.* **64** (2010) 288. 32, 42
- [Hul32] H.R. Hulme, *Proc. Roy. Soc. Lond. A* **138** (1932) 643. 13
- [Ish91] S. Ishi and B. Viswanathan, *Thin Solid Films* **201** (1991) 373. 108, 143
- [ISO00] *Hyperfine Interact.* **129** (2000) 1–553, a series of articles describing the research carried out at the ISOLDE facility. 74
- [ISO11] The ISOLDE facility, <http://isolde.web.cern.ch/ISOLDE/>, additional information in http://www.scholarpedia.org/article/The_ISOLDE_facility, 2011. 74
- [IUP93] The International Union of Pure and Applied Chemistry (I. Mills *et al.*), *Quantities, Units and Symbols in Physical Chemistry*, 2nd Edition, Blackwell Science, 1993. 172
- [Jae63] R. Jaeckel and B. Wagner, *Vacuum* **13** (1963) 509. 143
- [Jam75] F. James and M. Roos, *Comput. Phys. Commun.* **10** (1975) 343. 129, 130
- [Joh80] B. Johansson and N. Mårtensson *Phys. Rev.* **B 21** (1980) 4427. 85, 87
- [Joh73] G. Johansson, J. Hedman *et al.*, *J. Elec. Spec. Rel. Phenom.* **2** (1973) 295. 276
- [Joh09] K. Johnston, private communication, 2009. 75, 283
- [Kam05] The KamLAND collaboration (T. Araki *et al.*), *Phys. Rev. Lett.* **94** (2005) 081801. 3
- [Kas04] J. Kašpar, M. Ryšavý *et al.*, *Nucl. Instrum. Meth. A* **527** (2004) 423. 39, 40

- [Kas08] J. Kašpar, *Am/Co photoelectron source for energy scale monitoring of the KATRIN neutrino experiment*, dissertation, Czech Technical University in Prague, 2008, available at <http://www-ik.fzk.de/~katrin/publications/thesis.html>. 34, 48, 50, 138, 152, 187, 190
- [KAT01] The KATRIN collaboration (A. Osipowicz *et al.*), *Letter of Intent – KATRIN: A next generation tritium beta decay experiment with sub-eV sensitivity for the electron neutrino mass*, 2001, arXiv:hep-ex/0109033v1. 21, 36
- [KAT04] The KATRIN collaboration (J. Angrik *et al.*), *KATRIN Design Report 2004*, FZKA Scientific Report 7090, 2005, available at <http://bibliothek.fzk.de/zb/berichte/FZKA7090.pdf> 8, 21, 26, 27, 28, 29, 31, 32, 33, 34, 35, 36, 39, 40, 41, 43, 45, 47, 48, 60, 92, 128, 265
- [Kaw86] H. Kawano, S.I. Itasaka and S. Ohnishi, *Int. J. Mass Spectrom.* **73** (1986) 145. 108, 143
- [Kaz08] O. Kazachenko, B. Bornschein *et al.*, *Nucl. Instrum. Meth.* **A 587** (2008) 136. 30
- [Kem79] G.J. Kemerink, S. Bukshpan and H. de Waard, *Hyperfine Interact.* **7** (1979) 339. 254, 255
- [Kib08] T. Kibédi, T.W. Burrows *et al.*, *Nucl. Instrum. Meth.* **A 589** (2008) 202, see also <http://bricc.anu.edu.au>. 16
- [Kim75] K.S. Kim and N. Winograd, *Chem. Phys. Lett.* **30** (1975) 91. 85, 87, 88
- [Kin77] G.C. King, M. Tronc *et al.*, *J. Phys. B: Atom. Mol. Phys.* **10** (1977) 2479. 276
- [Kla01] H.V. Klapdor-Kleingrothaus, A. Dietz *et al.*, *Eur. Phys. J.* **A 12** (2001) 147. 10
- [Kla04] H.V. Klapdor-Kleingrothaus, I.V. Krivosheina *et al.*, *Phys. Lett.* **B 586** (2004) 198. 10
- [Kla06] H.V. Klapdor-Kleingrothaus and I. V. Krivosheina, *Mod. Phys. Lett.* **A 21** (2006) 1547. 10
- [Kno00] G.F. Knoll, *Radiation Detection and Measurement*, John Wiley & Sons, New York, 2000. 121
- [Koc06] A.G. Kochur and V.A. Popov, *Radiat. Phys. Chem.* **75** (2006) 1525. 89
- [Kol88] W. Kołos, B. Jeziorski *et al.*, *Phys. Rev.* **A 37** (1988) 2297. 258
- [Kov92] A. Kovalík, V.M. Gorozhankin *et al.*, *J. Elec. Spec. Rel. Phenom.* **58** (1992) 49. 60, 153, 155
- [Kov93] A. Kovalík and V.M. Gorozhankin, *J. Phys.* **G 19** (1993) 1921. 60
- [Kra88] K.S. Krane, *Introductory Nuclear Physics*, John Wiley & Sons, 1988. 13, 16
- [Kra05] C. Kraus, B. Bornschein *et al.*, *Eur. Phys. J.* **C 40** (2005) 447. 3, 12, 44, 54, 101, 106, 107, 124, 258
- [Kra65] M.O. Krause, *Phys. Rev.* **140** (1965) A1845. 275, 276

Bibliography

- [Kri11] A. Krieger, C. Geppert *et al.*, Nucl. Instrum. Meth. **A 632** (2011) 23. 47
- [Kug00] E. Kugler, Hyperfine Interact. **129** (2000) 23. 74
- [Kwe06] C.M. Kwei, Y.C. Li and C.J. Tung, Surf. Sci. **600** (2006) 3690. 256
- [Leb11] O. Lebeda, private communication, 2009–2011. 60, 81
- [Lin11] P.J. Linstrom and W.G. Mallard, Eds., *NIST Chemistry WebBook*, Standard Reference Database Number 69, National Institute of Standards and Technology, Gaithersburg MD, 2011, available at <http://webbook.nist.gov/chemistry>. 202
- [Lin10] S. Linden, private communication, 2009–2010. 254, 284
- [Llo07] X. Llopart, R. Ballabriga *et al.*, Nucl. Instrum. Meth. **A 581** (2007) 485. 63
- [Lob85] V.M. Lobashev and P.E. Spivak, Nucl. Instr. Meth. **A 240** (1985) 305. 25
- [Lob03] V. M. Lobashev, Nucl. Phys. **A 719** (2003) C153. 3, 12
- [Lor02] T.J. Loredo and D.Q. Lamb, Phys. Rev. **D 65** (2002) 063002. 11
- [Mak62] Z. Maki, M. Nakagawa and S. Sakata, Prog. Theor. Phys. **28** (1962) 870. 2
- [Man85] T. Mandel, M. Domke *et al.*, Surf. Sci. **162** (1985) 453. 84
- [Mar01] R. Marx, IEEE Trans. Instrum. Meas. **50** (2001) 426. 44, 111
- [MAR10] The MARE collaboration (A. Nucciotti *et al.*), arXiv:1012.2290v1, 2010. 12
- [Mei24] L. Meitner, Z. Phys. **26** (1924) 169. 13
- [Mic77] H.B. Michaelson, J. Appl. Phys. **48** (1977) 4729. 85
- [MKS04] MKS Instruments, Inc., *RGA MicroVision Plus Data Sheet*, 2004. 200, 202
- [Moo00] T.D. Moon and W.C. Stirling, *Mathematical Methods and Algorithms for Signal Processing*, Prentice Hall, 2000. 131
- [Moo58] C.E. Moore, *Atomic Energy Levels*, Volume III, Nat. Bureau Stand., Washington, 1958. 275, 276
- [Mul02] B. Müller, *Umbau des Mainzer Neutrinomassenexperiments und Untergrunduntersuchungen im Hinblick auf KATRIN*, diploma thesis, University of Mainz, 2002, available at <http://www-ik.fzk.de/~katrin/publications/thesis.html>. 103
- [Nag06] Sz. Nagy, T. Fritioff *et al.*, Europhys. Lett. **74** (2006) 404. 41
- [Nas05] A.F. Nastoyashchii, N.A. Titov *et al.*, Am. Nucl. Soc.: Fusion Sci. Technol. **48** (2005) 743. 33, 43
- [Nie83] L. Niesen, Hyperfine Interact. **13** (1983) 65. 66, 76
- [Nol10] C. Noll, private communication, 2009–2010. 254, 283
- [OHa03] J.F. O'Hanlon, *A User's Guide to Vacuum Technology*, John Wiley & Sons, New Jersey, 2003. 200, 202

- [Oli77] J.J. Olivero and R.L. Longbothum, *J. Quant. Spectrosc. Ra.* **17** (1977) 233. 129
- [ORT08] EG&G ORTEC Products Group, *CAMAC Quad 8k ADC AD413A, CAMAC FER-Abus Histogramming Memory HM413 and Research Pulser 448 data sheets and operating manuals*, 2008. 110, 112
- [Ost08] B. Ostrick, *Eine kondensierte ^{83m}Kr -Kalibrationsquelle für das KATRIN-Experiment*, dissertation, University of Münster, 2008, available at <http://www-ik.fzk.de/~katrin/publications/thesis.html>. 33, 52, 53, 54, 55, 56, 57, 84, 101, 109, 115, 117, 119, 126, 129, 133, 137, 208, 215, 216, 219, 235, 236, 239, 240, 241, 242, 244, 245, 246, 248, 253, 260, 261, 269, 270
- [Ott94] E.W. Otten, *Prog. Part. Nucl. Phys.* **32** (1994) 153. 33
- [Ott06] E.W. Otten, J. Bonn and C. Weinheimer, *Int. J. Mass Spectrom.* **251** (2006) 173. 40
- [Ott08] E.W. Otten and C. Weinheimer, *Rep. Prog. Phys.* **71** (2008) 086201. 10, 13, 21, 23, 24, 41
- [Pau30] W. Pauli, letter to a local meeting on radioactivity at Tübingen, Germany (dated December 4, 1930), original German version reprinted in: R. Kronig and V. Weisskopf, Eds., *Wolfgang Pauli, Collected Scientific Papers*, Vol. 2, Interscience, New York (1964) 1316. For the English translation see, e. g. L.M. Brown, *Physics Today* **31** (1978) 23. 1
- [PDG10] Particle Data Group (K. Nakamura *et al.*), *J. Phys. G* **37** (2010) 075021, available at <http://pdg.lbl.gov>. 3, 5, 11, 12, 265
- [Pen65] A.A. Penzias and R.W. Wilson, *Astrophys. J.* **142** (1965) 419. 7
- [Per75] M.L. Perl, G.S. Abrams *et al.*, *Phys. Rev. Lett.* **35** (1975) 1489. 2
- [Pet93] J.W. Petersen, A. Svane and E. Holzschuh, *Phys. Rev. B* **47** (1993) 1811. 130, 261
- [Pet10] J.W. Petersen, private communication, 2010. 81
- [Pic90] A. Picard, *Aufbau und Test eines Solenoid-Retardierungs-Spektrometers zur Bestimmung der Neutrino Ruhemasse aus dem Tritium-Beta-Zerfall*, dissertation, University of Mainz, 1990. 54
- [Pic92a] A. Picard, H. Backe *et al.*, *Nucl. Instrum. Meth. B* **63** (1992) 345. 25, 27, 85, 102
- [Pic92b] A. Picard, H. Backe *et al.*, *Z. Phys. A* **342** (1992) 71. 50, 52, 53, 54, 89, 91, 126, 190, 215, 261, 262, 263
- [Poll74] R.A. Pollak, L. Ley *et al.*, *J. Elec. Spec. Rel. Phenom.* **3** (1974) 381. 256
- [Pon67] B. Pontecorvo, *Zh. Eksp. Teor. Fiz.* **53** (1967) 1717 [*Sov. Phys. JETP* **26** (1968) 984]. 2
- [Por71] F.T. Porter and M.S. Freedman, *Phys. Rev. C* **3** (1971) 2285. 65, 66
- [Pow10] C.J. Powell and A. Jablonski, Eds., *NIST Electron Inelastic-Mean-Free-Path Database, Version 1.2, Standard Reference Database Number 71*, National Institute of Standards and Technology, Gaithersburg MD, 2010, available at <http://www.nist.gov>.

- gov/srd/nist71.cfm. 94, 97
- [Pra11] M. Prall, *Background Reduction of the KATRIN Spectrometers: Transmission Function of the Pre-Spectrometer and Systematic Tests of the Main-Spectrometer Wire Electrode*, dissertation, University of Münster, 2011. 30
- [Rat09] B.D. Ratner and D.G. Castner, *Electron Spectroscopy for Chemical Analysis*, in *Surface Analysis - The Principal Techniques*, 2nd Edition, Eds. J.C. Vickerman and I.S. Gilmore, John Wiley & Sons, 2009, p. 47. 49, 151
- [Rei96] F. Reines, *Rev. Mod. Phys.* **68** (1996) 317. 2
- [Rep92] M. Repoux, *Surf. Interface Anal.* **18** (1992) 567. 284
- [Rob88] R.G.H. Robertson and D.A. Knapp, *Ann. Rev. Nucl. Part. Sci.* **38** (1988) 185. 37
- [Rob91] R.G.H. Robertson, T.J. Bowles *et al.*, *Phys. Rev. Lett.* **67** (1991) 957. 50, 83
- [ROO10] ROOT, Object-Oriented Data Analysis Framework, <http://root.cern.ch>, 2010. Version 5.26.00 was used throughout this work. 129, 130, 131, 164
- [Ros78] F. Rösel, H.M. Fries *et al.*, *Atom. Data Nucl. Data* **21** (1978) 91 and *Atom. Data Nucl. Data* **21** (1978) 291. 13, 16, 50, 52, 53
- [Rot98] A. Roth, *Vacuum Technology*, Elsevier, Amsterdam, 1998. 61, 176, 200, 202
- [Sae00] A. Saenz, S. Jonsell and P. Froelich, *Phys. Rev. Lett.* **84** (2000) 242. 32
- [San06] D.C. Santry, *Appl. Radiat. Isotopes* **64** (2006) 1528. 80, 86
- [Sch09] R. Schlaf, private communication, 2009. 175
- [Sev79] K.D. Sevier, *Atom. Data Nucl. Data* **24** (1979) 323. 276
- [Sie68] K. Siegbahn, Ed., *Alpha-, beta- and gamma-ray spectroscopy*, North-Holland, Amsterdam, 1968. 13, 16
- [Sie69] K. Siegbahn, C. Nordling *et al.*, *ESCA Applied to Free Molecules*, North-Holland, Amsterdam, 1969. 89, 90, 130, 151, 246, 275, 276
- [Sim10] F. Šimkovic, *Prog. Part. Nucl. Phys.* **64** (2010) 219. 10
- [Sis04] M. Sisti, C. Arnaboldi *et al.*, *Nucl. Instrum. Meth. A* **520** (2004) 125. 12
- [Sle11] M. Slezák, *The source of monoenergetic electrons for the monitoring of spectrometer in the KATRIN neutrino experiment*, diploma thesis, Charles University in Prague, 2011, available at <http://www-ik.fzk.de/~katrin/publications/thesis.html>. 51, 53, 63, 65, 76, 77, 79, 80, 269
- [SNO07] The SNO collaboration (B. Aharmim *et al.*), *Phys. Rev. C* **75** (2007) 045502. 3
- [Spa94] A. Špalek and O. Dragoun, *Czech. J. Phys.* **44** (1994) 277. 92, 95
- [Spa10] A. Špalek, private communication, 2010. 93, 95
- [SPE08] SPECS Surface Nano Analysis GmbH, *Hemispherical Energy Analyzer PHOIBOS 150 data sheet and User's Manual of the SpecsLab program*, 2008. 254, 284

- [Spi81] W.J.J. Spijkervet, F. Pleiter and H. de Waard, *Hyperfine Interact.* **9** (1981) 333 and also *Hyperfine Interact.* **8** (1980) 173. 254, 255
- [SRI11] J. Ziegler, Software package SRIM (Stopping and Range of Ions in Matter), <http://www.srim.org>, 2011. Version SRIM-2008.04 was used throughout this work. 68, 69, 72
- [Stu10] M. Sturm, M. Schlösser *et al.*, *Laser Phys.* **20** (2010) 493. 32
- [Sup05] The Super-Kamiokande collaboration (Y. Ashie *et al.*), *Phys. Rev. D* **71** (2005) 112005. 3
- [Sve76] S. Svensson, N. Mårtensson *et al.*, *Phys. Scripta* **14** (1976) 141. 275, 276
- [T2K11] The T2K collaboration (K. Abe *et al.*), *arXiv:1106.2822*, 2011. 5
- [Thu07] T. Thümmler, *Präzisionsüberwachung und Kalibration der Hochspannung für das KATRIN-Experiment*, dissertation, University of Münster, 2007, available at <http://www-ik.fzk.de/~katrin/publications/thesis.html>. 41, 45, 46, 47, 55, 91, 101, 102, 104, 106, 109, 110, 111, 116, 117, 119, 120, 126, 127, 140, 143, 152, 154, 158, 183, 190, 215, 236, 239, 240, 260
- [Thu09] T. Thümmler, R. Marx and C. Weinheimer, *New J. Phys.* **11** (2009) 10307. 46, 111, 143, 152, 154, 158, 183
- [Thu11] T. Thümmler, *HV - Status & Outlook*, presentation at the 20th KATRIN collaboration meeting, Karlsruhe, 2011, available at KATRIN BSCW, 95 General Meetings and Review Panels, 1 Collaboration Meetings, 20. Collaboration Meeting, Session - 3, 95-TRP-5008-S3-TThuemmler.pdf. 41, 43, 45, 137, 220
- [Tou88] S. Tougaard, *Surf. Interface Anal.* **11** (1988) 453. 284
- [Tow76] P.D. Townsend, J.C. Kelly and N.E.W. Hartley, *Ion implantation, sputtering and their applications*, Academic Press, 1976. 66
- [Ubi09] M. Ubieto-Díaz, D. Rodríguez *et al.*, *Int. J. Mass Spectrom.* **288** (2009) 1. 33
- [Vai76] S. Väisälä, G. Graeffe *et al.*, *Phys. Rev. C* **13** (1976) 372. 53
- [Val06] K. Valerius for the KATRIN collaboration, *Prog. Part. Nucl. Phys.* **57** (2006) 58. 30
- [Val09a] K. Valerius, *Spectrometer-related background processes and their suppression in the KATRIN experiment*, dissertation, University of Münster, 2009, available at <http://www-ik.fzk.de/~katrin/publications/thesis.html>. 6, 8, 28, 30, 31, 125, 126, 166
- [Val09b] K. Valerius, M. Beck *et al.*, *New J. Phys.* **11** (2009) 063018. 32
- [Val10] K. Valerius, *Prog. Part. Nucl. Phys.* **64** (2010) 291. 30
- [Val11] K. Valerius, H. Hein *et al.*, *J. Instrum.* **6** (2011) P01002. 32
- [Var82] D. Varga, I. Kádár, *et al.*, *Nucl. Instrum. Methods* **192** (1982) 277. 152
- [Ven05] D. Vénos, A. Špalek *et al.*, *Appl. Radiat. Isotopes* **63** (2005) 323. 54

Bibliography

- [Ven06] D. Vénos, O. Dragoun *et al.*, Nucl. Instrum. Meth. **A 560** (2006) 352. 51, 53, 269
- [Ven09] D. Vénos, J. Kašpar *et al.*, Report NPI ASCR Řež/Prague, EXP-01/2009, arXiv:0902.0291v1. 50, 60, 63, 138, 145
- [Ven10] D. Vénos, M. Zbořil *et al.*, Meas. Tech. **53** (2010) 573. 60, 138
- [Vet11] U. Vetter, private communication, 2011. 254, 258
- [War91] D.L. Wark, R. Barlett *et al.*, Phys. Rev. Lett. **67** (1991) 2291. 83, 257
- [Wat76] R.E. Watson, J.F. Herbst and J.W. Wilkins, Phys. Rev. **B 14** (1976) 18. 85, 87, 88
- [Wei09] C. Weinheimer, arXiv:0912.1619, 2009. 26
- [Wei11] C. Weinheimer, private communication, 2011. 123, 124, 187
- [Wei27] V. Weisskopf and E. Wigner, Z. Phys. **63** (1927) 54. 18
- [Wel72] R.L. Wells and T. Fort, Jr., Surf. Sci. **32** (1972) 554. 175
- [Wer78] G.K. Wertheim and P.H. Citrin, *Fermi Surface Excitations in X-Ray Photoemission Line SHapes from Metals*, in *Photoemission in Solids I: General Principles*, Eds. M. Cardona and L. Ley, Springer-Verlag, Berlin, 1978, p. 197. 257
- [Wil78] A.R. Williams and N.D. Lang, Phys. Rev. Lett. **40** (1978) 954. 85
- [WMA11] The WMAP collaboration (E. Komatsu *et al.*), Astrophys. J. Suppl. S. **192** (2011) 18. 9
- [Wol09] J. Wolf, J. Vac. Soc. Jpn. **52** (2009) 278. 30, 43
- [Wu57] C.S. Wu, E. Ambler, *et al.*, Phys. Rev. **105** (1957) 1413. 2
- [Wu01] S.C. Wu, Nucl. Data Sheets **62** (2001) 893. 53
- [Yos92] H. Yoshikawa, R. Shimizu and Z.J. Ding, Surf. Sci. **261** (1992) 403. 94
- [Zbo06] M. Zbořil, *Vacuum Stability of $^{83}\text{Rb}/^{83\text{m}}\text{Kr}$ Electron Source for the Neutrino Experiment KATRIN*, diploma thesis, Czech Technical University in Prague, 2006, available at <http://www-ik.fzk.de/~katrin/publications/thesis.html>. 63
- [Zha90] G.L. Zhang and L. Niesen, Hyperfine Interact. **53** (1990) 253.
- [Zie10] J.F. Ziegler, M.D. Ziegler and J.P. Biersack, Nucl. Instrum. Meth. **B 268** (2010) 1818. 69, 286
- [Zub04] K. Zuber, *Neutrino Physics*, Institute of Physics Publishing, 2004. 1, 5, 6, 22

